

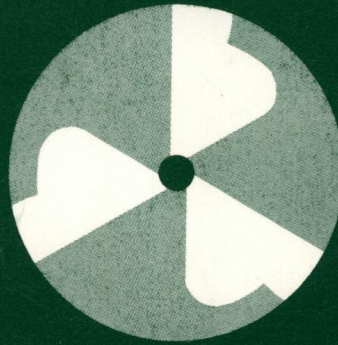
2 copy

COO-1779-71

**MASTER**

# Annual Report

1970 - 71



**Cyclotron Laboratory**

**Dept. of Physics**

**Michigan State University**

**DISTRIBUTION OF THIS DOCUMENT IS UNLIMITED**

## **DISCLAIMER**

**This report was prepared as an account of work sponsored by an agency of the United States Government. Neither the United States Government nor any agency Thereof, nor any of their employees, makes any warranty, express or implied, or assumes any legal liability or responsibility for the accuracy, completeness, or usefulness of any information, apparatus, product, or process disclosed, or represents that its use would not infringe privately owned rights. Reference herein to any specific commercial product, process, or service by trade name, trademark, manufacturer, or otherwise does not necessarily constitute or imply its endorsement, recommendation, or favoring by the United States Government or any agency thereof. The views and opinions of authors expressed herein do not necessarily state or reflect those of the United States Government or any agency thereof.**

## **DISCLAIMER**

**Portions of this document may be illegible in electronic image products. Images are produced from the best available original document.**

COO-1779-71

ANNUAL REPORT  
of the  
MICHIGAN STATE UNIVERSITY  
CYCLOTRON LABORATORY\*  
for the period  
July 1, 1970 to July 1, 1971

NOTICE

This report was prepared as an account of work sponsored by the United States Government. Neither the United States nor the United States Atomic Energy Commission, nor any of their employees, nor any of their contractors, subcontractors, or their employees, makes any warranty, express or implied, or assumes any legal liability or responsibility for the accuracy, completeness or usefulness of any information, apparatus, product or process disclosed, or represents that its use would not infringe privately owned rights.

By  
Project Staff

September 1971  
East Lansing, Michigan

\*Supported jointly by National Science Foundation, Atomic Energy Commission, Office of Naval Research and Michigan State University (see Preface for details).

DISTRIBUTION OF THIS DOCUMENT IS UNLIMITED

This year we have made a major change in the format of our Annual Report by including a new section consisting of a series of brief writeups on Research in Progress. Such a section is more difficult to prepare than the compilation of reprints and preprints which has previously constituted our Annual Report; the result is however much more useful in that a very current picture of our program is conveyed—more up to date in fact than any other common channel of information exchange.

This year's Annual Report is also different in that it includes all of the programs in the laboratory, which contrasts with previous years when results were sorted out in accord with the source of funds and individual annual reports were submitted for each grant or contract. These individual reports inevitably involved substantial duplication since collaborations in the laboratory have always been a very flexible pattern depending on particular scientific interests and quite independent of funding boundaries. Moreover all the programs use the laboratory facilities which were entirely obtained through grants from the National Science Foundation and all programs are then in a real sense supported to a substantial degree by NSF, even though operating support may be from some other source. We are then submitting this combined Annual Report to all the agencies supporting programs here. To indicate the relative contribution of these sources we show in Table I the percentage operating support from each source for the year 1970-71 and, in Table II, the faculty and postdoctoral staff attached to each grant or contract.

Let me then turn to a few general remarks on the overall state of the laboratory in the year 70-71. In its early years our program

mainly centered on instrumentation; as a result our instrumentation now has many exceptional characteristics and these facilities are in a state of vigorous use on a broad spectrum of problems in nuclear physics. Summarizing the accomplishments of our nuclear program in any brief way I find in fact to be very difficult. In a real sense this whole report is such a summary. As I leaf through the manuscript pages the main summary thought which comes to me is a feeling of seeing a large amount of high quality data on a broad variety of topics. Included in this I note a number of topics showing close collaboration between theorist and experimentalist, a pattern which we expect to occur even more in the future now that George Bertsch has joined our faculty filling the last of our Science Development positions. I also note that we are managing to handle an increasing number of experiments involving collaboration with visitors from other laboratories, an arrangement which we have found nearly always to be both productive and stimulating. Our desire in fact is to accommodate any experiment for which the facilities of this laboratory are particularly appropriate independent of questions of institutional affiliation. If you have an idea for an experiment we would be pleased to hear from you.

Finally I wanted to thank those who in years past have taken the trouble to comment on our Annual Report. This feedback has been most valuable in our discussions of pros and cons of various formats and we hope readers will keep on letting us know what they find useful or not useful. We appreciate such help greatly.

Henry Blosser

Table I. Sources of support for MSU Cyclotron Laboratory programs for year 1970-71.

Institution or Agency	Grants or Contracts	Per Cent of Total
1-National Science Foundation	Grants GP-6760 & GP-27483	60.5
2-Atomic Energy Commission	Contract AT(11-1)-1051	6.7
3-Atomic Energy Commission	Contract AT(11-1)-1779	6.9
4-Office of Naval Research	Contract N-00014-68-A-0109-0008	2.5
5-National Aeronautics & Space Agency	Contract NGR-23-004-056	1.9
6-Michigan State University		21.5

Table II. List of faculty and postdoctoral personnel as of June 1971 and source of salary funds. Numbers refer to grants and contracts listed in Table I.

Professors	Assoc. Professor
S. Austin 1,6	W. Benenson 1,6
H. Blosser 1,6	F. Bernthal 3,6
A. Galonsky 1,6	G. Bertsch 2,6
M. Gordon 1,6	J. Borysowicz 2,6
C. Gruhn 1,6	G. Crawley 1,4,6
E. Kashy 1,6	J. Nolen 1,6
W. Kelly 1,6	H. Wildenthal 1,6
W. McHarris 3,6	
H. McManus 2,6	
	Postdoctorals
	M. Dworzecka 2
	R. Hinrichs 1
	O. Katyal 5
	B. McKellar 2
	P. Miller 1
	F. Petrovich 2
	H. Robertson 1
	R. Warner 3
Asst. Professors	
T. Arnette 1,6	
R. Jolly 1,6	

## CONTENTS

## I. Research in Progress (August 1971)

Page

	Page		Page
The Effective Two Nucleon Force from Inelastic Nucleon Scattering, Sam M. Austin.....	1	Study of Proton Rich Nuclei Using the ( $^3\text{He}, ^6\text{He}$ ) Reaction at 70 MeV, W. Benenson, J. Dreisbach, E. Kashy, B.M. Freedom, I. Proctor, and F. Trentelman.....	36
Renormalized Operators and Collective Particle-Hole Excitations in $^{40}\text{Ca}$ , M. Dworzecka and H. McManus.....	3	A Survey of the ( $^3\text{He}, ^7\text{Be}$ ) Reaction, G.M. Crawley, P.S. Miller, and W.F. Steele.....	38
Electron and Proton Inelastic Scattering from $^{40}\text{Ca}$ and $^{208}\text{Pb}$ , G.R. Hammerstein and F. Petrovich.....	5	Search for $^{64}\text{Ge}$ , R.G.H. Robertson, S.M. Austin, and Wm.C. McHarris.....	39
An Eikonal Approximation for Electron-Nucleus Scattering, G.R. Hammerstein.....	7	The Decay of $^{40}\text{Sc}$ to $^{40}\text{Ca}$ , J. Black.....	40
Concerning Calculation of Strong Absorption Parameter in the Strong Cut Regge Absorption Model, David Perry.....	8	Use of the He Thermalizer-Jet Transport, K.L. Kosanke, G.C. Giesler, and Wm.C. McHarris.....	42
The Structure of the Lighter N=82 Nuclei, B.H. Wildenthal and D.C. Larson.....	10	Progress with the On-Line Isotope Separator, K.L. Kosanke, Wm.C. McHarris, and H.P. Hilbert.....	43
Proton Induced Spallation of $^{14}\text{N}$ , $^{16}\text{O}$ , and the Astrophysical Production of Li, Be, and B, Helmut Laumer, Lolo Panggabean, and Sam M. Austin.....	12	Rabbit-Pneumatic Target System, K.L. Kosanke, H.P. Hilbert, and C.B. Morgan.....	45
Proton Induced Spallation of $^{20}\text{Ne}$ and the Astrophysical Production of the Lithium Isotopes, L.M. Panggabean, H. Laumer, and Sam M. Austin.....	13	Electron Capture Decay of $^{205}\text{Bi}$ , K.L. Kosanke, Wm.C. McHarris, and W.H. Kelly.....	47
The $^{14}\text{N}(p,p')^{14}\text{N}$ Reaction at 29.8, 36.6, and 40.0 MeV, S.H. Fox, S.M. Austin, and D. Larson.....	14	The Decay of $^{202}\text{mPb}$ , J. Guile.....	49
Inelastic Proton Scattering on Zr at 40 MeV and Monopole Transitions, R.A. Hinrichs, B.M. Freedom, and D. Larson.....	16	The Decay of $^{170}\text{Lu}$ to Levels in $^{170}\text{Yb}$ , D.C. Camp and F.M. Bernthal.....	51
Inelastic Proton Scattering from N=82 Nuclei, D. Larson, S.M. Austin, B.H. Wildenthal, and S.H. Fox.....	17	Study of Levels in Even-Even Deformed Nuclei by ( $^3\text{He}, d$ ) and ( $^4\text{He}, t$ ) Reaction Spectroscopy, F.M. Bernthal and R.A. Warner.....	53
Inelastic Scattering from Pb and Bi Isotopes, W.T. Wagner, G.M. Crawley, and P.S. Miller....	19	In-Beam ( $\alpha, xny$ ) and ( $^3\text{He}, xny$ ) Studies of Rotational Band Structure in Transitional Odd-Mass Deformed Nuclei, F.M. Bernthal and R.A. Warner.....	54
The ( $p, n\bar{p}$ ) Reaction Near A=208, G.M. Crawley and P.S. Miller.....	20	The ( $p, t$ ) Reaction on Rare Earth Nuclei, R. Gales.....	55
Proton Spin-Flip, R.H. Howell and A.I. Galonsky.....	22	The $\beta^+/\epsilon$ Decay of $^{143}\text{Eu}$ , Richard B. Firestone.....	57
Study of the Asymmetry Potential by ( $p, n$ ) Quasi-Elastic Scattering, R.K. Jolly, T. Amos, A. Galonsky, and R. St.Onge.....	24	The $\beta^+/\epsilon$ Decay of $^{143}\text{Sm}$ , Richard B. Firestone.....	59
The Ghost Anomaly in the $^9\text{Be}(p, d)^8\text{Be}$ Reaction P.S. Miller, G.M. Crawley, W.F. Steele, and F.C. Barker.....	25	The Decay of $^{141}\text{Pm}_{80}$ to States in $^{141}\text{Nd}_{81}$ , F.Y. Yap, R.R. Todd, R. Warner, W.H. Kelly, and Wm.C. McHarris.....	61
Studies of Odd-Odd Nuclei in the sd-shell J.A. Rice, B.H. Wildenthal, and B.M. Freedom.....	26	The Electron Capture Decay of $^{56}\text{Ni}$ , L. Samuelson.....	63
The $^{40}\text{Ca}(p, t)^{46}\text{Ca}$ Reaction at 39 MeV, G.M. Crawley, P.S. Miller, and G. Igo.....	28	Low-Lying States of $^{56}\text{Co}$ from $^{56}\text{Fe}(p, ny)$ Thresholds and $\gamma$ -ray Angular Distributions, L. Samuelson.....	65
Direct ( $p, \alpha$ ) Reactions, Jerry Nolen and Paul Zemaný.....	30	Decay of the Neutron Deficient A=63 Isotopes, G. Giesler.....	67
70 MeV $^3\text{He}$ Elastic Scattering, R.R. Doering, R.A. Hinrichs, and A. Galonsky.....	31	Decay of the Neutron Deficient A=62 Nuclei and the Possibility of $\beta$ -Delayed $\alpha$ Emission, G. Giesler and K. Kosanke.....	69
Reaction Mechanism and Spectroscopic Studies with the ( $^3\text{He}, t$ ) Reaction		The Search for Three-Particle Isomeric States in $^{43}\text{Ti}$ and $^{43}\text{Sc}$ , J. Black.....	71
Transitions to $0^+$ Antianalog States in $^{64,66}\text{Ga}$ and $^{40}\text{K}$ , R.A. Hinrichs, R. Sherr, G.M. Crawley, and I. Proctor....	33	The $\gamma$ Decay of $^{53\text{m}}\text{Co}$ , J. Black.....	73
The Reaction $^{89}\text{Y}(^3\text{He}, t)$ to $T_2$ States, R.A. Hinrichs and G.F. Trentelman.....	33	Nitrogen Fixation, C.P. Wolk, S.M. Austin, J. Bortins, and A. Galonsky.....	75
Spectroscopy of $^{34}\text{Cl}$ via the $^{34}\text{S}(^3\text{He}, t)$ Reaction, R.A. Hinrichs, B.H. Wildenthal, D. Show, and J.A. Rice.....	34	Neutron Yields from Proton Bombardment of Thick Targets, T. Amos, A. Galonsky, and R.K. Jolly.....	76
		Elemental Analysis by Elastic Scattering, R.K. Jolly and H.B. White.....	77
		New Computer Program for Field Trimming Calculations, M.M. Gordon and D.A. Johnson.....	80
		Studies of Orbit Centering, L. Learn and M.M. Gordon.....	81

Stabilization of Cyclotron Main Field with Beam Phase Sensing, H.G. Blosser, J. Collins, and R.A. deForest.....	82	Shell-Model Calculations for Nuclei with A=23-29, B.H. Wildenthal and J.B. McGroory.....	92
Computer Compatible Servo-System for Cyclotron RF, P. Sigg.....	83	The Ghost Anomaly in the ${}^9\text{Be}(p,d){}^8\text{Be}$ (g.s.) Reaction, P.S. Miller, G.M. Crawley, W.F. Steele, and F.C. Barker.....	92
Additions and Improvements to Laboratory Computer, Richard Au.....	85	Isobaric Yields of Masses 6 to 11 from Proton Spallation of ${}^{14}\text{N}$ in the Energy Range 17 to 42 MeV, H. Laumer, C.N. Davids, and S.M. Austin.....	93
An Ultra-Thin-Window Gas Cell, H. Laumer.....	86	Internal Conversion Studies of the 2.3 keV Transition from the Electron Capture Decay of ${}^{205}\text{Bi}$ , W.C. Johnston, K.L. Kosanke, S.K. Haynes, W.C. McHarris, and W.H. Kelly.....	93
Preparation of Thin Film Deposits from Biological, Environmental and Other Matter, R.K. Jolly and H.B. White.....	88	Decay of ${}^{141m}\text{Sm}$ , R.R. Todd, R.E. Eppley, W.H. Kelly, Wm.C. McHarris, and R.A. Warner.....	93
II. Abstracts of Talks at Meetings (July 1970-June 1971)		<u>Cleveland APS Meeting - April 1971</u>	
<u>Houston APS Meeting - October 1970</u>		Study of Local Modes of Lithium and Boron in Silicon, E. Dounce, O.P. Katyal, and C.R. Gruhn.....	93
The Effects of Compton Scattering on Ge(Li)-Ge(Li) Coincidence Experiments, G.C. Giesler, R.A. Warner, W.C. McHarris, and W.H. Kelly....	90	<u>Washington APS Meeting - April 1971</u>	
The Sum-Coincidence Method Applied to the Evaluation of Ge(Li)-Ge(Li) Coincidence Results, G.C. Giesler, K.L. Kosanke, R.A. Warner, W.C. McHarris, and W.H. Kelly.....	90	${}^3\text{He}$ Elastic Scattering at 70 MeV ${}^{50}\text{Ti}$ and ${}^{51}\text{V}$ , R.A. Hinrichs, R.R. Doering, and A. Galonsky..	93
Energy of the Second Excited State of ${}^{12}\text{C}$ and the $3\alpha$ Reaction Rate, S.M. Austin, G.F. Trentelman, and E. Kashy.....	90	Inelastic Proton Scattering on N=82 Nuclei, D. Larson, S.M. Austin, B.H. Wildenthal, and S.H. Fox.....	93
Neutron Yields from Proton Bombardment of Thick Targets, T. Amos, A. Galonsky, and R. Jolly.....	90	Asymmetry in the Inelastic Scattering of 40.5 MeV Protons from ${}^{16}\text{O}$ and ${}^{12}\text{C}$ , W. Benenson and P.J. Locard.....	94
Ultra-High Resolution Spectrometer System for Charged Particle Studies of Nuclei, H.G. Blosser, G.M. Crawley, R. deForest, E. Kashy, and B.H. Wildenthal.....	90	Inelastic Proton Scattering from ${}^{16}\text{O}$ at Bombarding Energies from 24.6 to 40.1 MeV, D.L. Bayer, I.D. Proctor, and F.L. Petrovich.....	94
Proton Spin-Flip in (p,p') Reaction on ${}^{120}\text{Sn}$ and ${}^{124}\text{Sn}$ , R.H. Howell, R.R. Doering, and A. Galonsky.....	90	Shapes of ( ${}^3\text{He},t$ ) Angular Distributions to T <sub>c</sub> States in ${}^{89}\text{Zr}$ , R.A. Hinrichs.....	94
${}^{27}\text{Al}(p,n){}^{27}\text{Si}$ at $E_p=30$ MeV, R.K. Jolly, T. Amos, A. Galonsky, and R. St.Onge.....	91	Decay of ${}^{141}\text{Pm}$ , F.Y. Yap, R.R. Todd, R.A. Warner, W.H. Kelly, and Wm.C. McHarris.....	94
The Michigan State University Isochronous Cyclotron, Neutron Time-of-Flight Facility, R. St.Onge, T. Amos, A. Galonsky, and R. Jolly.....	91	<u>Nuclear Science Application Symposium, New York, Nov. 1970</u>	
Electron-Capture Decay Scheme of ${}^{203}\text{Bi}$ , Wm. C. McHarris, J.B. Cross, and W.H. Kelly.....	91	Determination of Trace Elements in Samples by Nuclear Scattering and Reaction Techniques, R.K. Jolly, C.R. Gruhn, and C. Maggiore.....	94
Electron-Capture Decay Scheme of ${}^{204}\text{Bi}$ , J.B. Cross, W.C. McHarris, and W.H. Kelly.....	91	<u>Nuclear Structure Symposium, Jyvaskyla, Finland April 1971</u>	
The (p,t) Reaction on ${}^{141}\text{Pr}$ , R.W. Goles, Wm. C. McHarris, W.H. Kelly, and R.A. Warner.....	91	Inelastic Scattering of Protons from ${}^{16}\text{O}$ and the Effective Two-Body Interaction, S.M. Austin, P.J. Locard, S.N. Bunker, J.M. Cameron, J.R. Richardson, J.W. Verba, and W.T.H. Van Oers.....	94
E6 and M5 Gamma-Ray Transitions in the ${}^{53m}\text{Fe}$ Decay, J.N. Black, Wm.C. McHarris, and W.H. Kelly.....	91	III. Abstracts of Papers in Press (August 1970)	
The ${}^3\text{S}({}^3\text{He},t)$ Reaction at 35 MeV, R.A. Hinrichs, B.H. Wildenthal, and J.A. Rice.....	92	Proton Scattering and the Optical Model Differences Between ${}^{40}\text{Ca}$ and ${}^{48}\text{Ca}$ , C.J. Maggiore, C.R. Gruhn, T.Y.T. Kuo, and B.M. Freedom.....	95
<u>New York APS Meeting - February 1971</u>		Neutron Hole State Structure in N=81 Nuclei. I ${}^{144}\text{Sm}$ and ${}^{142}\text{Nd}(p,d)$ , R.K. Jolly and E. Kashy.....	95
Levels of ${}^{56}\text{Co}$ Below 2 MeV Excitation from ${}^{56}\text{Fe}(p,n\gamma){}^{56}\text{Co}$ and ${}^{56}\text{Ni}$ EC Decay, L.E. Samuelson, R.A. Warner, W.H. Kelly, R.R. Todd, and Wm.C. McHarris.....	92	Neutron Hole State Structure in N=81 Nuclei. II ${}^{140}\text{Ce}$ and ${}^{138}\text{Ba}(p,d)$ , R.K. Jolly and E. Kashy.....	95
(p,t) Reactions on N=82 Nuclei at $E_p=35$ MeV, R.K. Jolly and E. Kashy.....	92	The Mass of ${}^{25}\text{Si}$ and the Isobaric Multiplet Mass Equation, G.F. Trentelman and I.D. Proctor.....	95
The (p,t) Spectra of ${}^{169}\text{Tm}$ , ${}^{165}\text{Ho}$ , and ${}^{159}\text{Tb}$ , R.W. Goles, R.A. Warner, Wm.C. McHarris, and W.H. Kelly.....	92		

	Page		Page
Calculations with a $1s, 0d$ Shell Model for $A=34-38$ Nuclei, B.H. Wildenthal, E.C. Halbert, J.B. McGrory, and T.T.S. Kuo.....	96	Measurement of $T_Z=-3/2$ Masses and the Iso-baric Multiplet Mass Equation, G.F. Trentelman, B.M. Preedom, and E. Kashy.....	193
Shapes of Angular Distributions in the $^3\text{He}(^3\text{He}, t)^{90}\text{Zr}$ Reaction to Antianalog and Other $T_Z$ States, R.A. Hinrichs and G.F. Trentelman.....	96	Use of Thin Semiconductor Position Sensitive Detectors in Magnetic Spectrographs. R.K. Jolly, G.F. Trentelman, and E. Kashy.....	196
The Structure of Nuclei with Masses $A=30-35$ , as Calculated in the Shell-Model, B.H. Wildenthal, J.B. McGrory, E.C. Halbert, and H.D. Graber.....	96	Experimental Studies of Neutron-Deficient Gadolinium Isotopes. III. The Strange Case of $^{145}\text{Gd}$ , R.E. Eppley, Wm.C. McHarris, and W.H. Kelly.....	200
Study of Charge-Exchange Coupling in Proton Induced Reactions on $^{93,94,100}\text{Mo}$ and $^{92,94}\text{Zr}$ , R.A. Hinrichs, G.W. Phillips, J.G. Cramer, and H. Wieman.....	96	$(p, d)$ Reaction in the Titanium Isotopes, P.J. Plauger and E. Kashy.....	214
The $(p, t)$ Reaction on Even-Even $N=Z$ Nuclei in the $2s_{1/2}$ Shell, R.A. Paddock.....	97	Experimental Studies of the Neutron-Deficient Gadolinium Isotopes. II. $^{145}\text{Gd}$ , R.E. Eppley, Wm.C. McHarris, and W.H. Kelly.....	236
Preparation of Thin Film Deposits from Biological, Environmental and Other Matter, R.K. Jolly and H.B. White.....	97	Ultra-High Resolution Spectrometer System for Charged Particle Studies of Nuclei, H.G. Blosser, G.M. Crawley, R. deForest, E. Kashy, and B.H. Wildenthal.....	242
<b>IV. Reprints of Published Papers (July 1970-June 1971)</b>			
Inelastic Scattering of Protons from $^{16}\text{O}$ and the Spin-Dependent Part of the Effective Interaction, Sam M. Austin, P.J. Locard, S.N. Bunker, J.M. Cameron, J. Reginald Richardson and J.W. Verba.....	98	Precision Mass Measurement of $^{13}\text{C}$ , $^{13}\text{O}$ , and $^{24}\text{Mg}$ and the Iso-baric Multiplet Mass Equation, G.F. Trentelman, B.M. Preedom, and E. Kashy.....	247
Determinations of Trace Elements in Samples by Nuclear Scattering and Reaction Techniques, R.K. Jolly, C.R. Gruhn, and C. Maggiore.....	112	$\text{Ge}(\text{Li})-\text{Ge}(\text{Li})$ Sum Coincidence: A Bonus from $\text{Ge}(\text{Li})-\text{Ge}(\text{Li})$ Megachannel Coincidence Experiments, G.C. Giesler, K.L. Kosanke, R.A. Warner, Wm.C. McHarris, and W.H. Kelly.....	256
Spurious Peaks Produced by Compton Scattering in $\text{Ge}(\text{Li})-\text{Ge}(\text{Li})$ Coincidence Gamma-ray Spectrometer Systems, G.C. Giesler, Wm.C. McHarris, R.A. Warner, and W.H. Kelly.....	117	$N$ -Shell Conversion Electrons from the 2.33 keV Transition in $^{205}\text{Pb}$ , W.C. Johnston, W.H. Kelly, S.K. Haynes, K.L. Kosanke, and Wm.C. McHarris.....	266
Study of the Level Structure of $N=82$ Nuclei via Proton-Transfer Reaction, B.H. Wildenthal, E. Newman, and R.L. Auble.....	125	Inelastic Deuteron Scattering from $^{56}\text{Fe}$ and $^{58}\text{Fe}$ , R.K. Jolly.....	270
Energy of the Second Excited State of $^{12}\text{C}$ and the Rate of the Triple-Alpha Reaction, S.M. Austin, G.F. Trentelman, and E. Kashy...	147	A Truncated Shell-Model Calculation of $^{23}\text{Na}$ , $^{24}\text{Mg}$ , and $^{28}\text{Si}$ , J.B. McGrory and B.H. Wildenthal.....	279
$E6$ and $M5$ Transitions Observed in $^{59}\text{mFe}$ Decay, J.N. Black and Wm.C. McHarris.....	151	States in Odd-Odd $^{200}\text{Tl}$ Populated by the Electron-Capture Decay of $^{200}\text{Pb}$ , R.E. Doebler, Wm.C. McHarris, and W.H. Kelly....	283
Proton Scattering and the Optical Model Difference Between $^{40}\text{Ca}$ and $^{48}\text{Ca}$ , C.J. Maggiore, C.R. Gruhn, T.Y.T. Kuo and B.M. Preedom.....	155	<b>V. Ph.D. Thesis Titles (July 1970-June 1971) 300</b>	
Static Quadrupole Moments in $A=18-38$ Nuclei as Predicted in the Shell-Model, B.H. Wildenthal, J.B. McGrory, and P.W.M. Glaudemans.....	158		
Anomalous $L=1$ Shapes of Angular Distributions for $(^3\text{He}, t)$ Transitions to $0^+$ Anti-analog States in $^{64,66}\text{Ga}$ and $^{40}\text{K}$ , R.A. Hinrichs, R. Sherr, G.M. Crawley, and I. Proctor.....	162		
Experimental Studies of Neutron-Deficient Gadolinium Isotopes. I. The Electron-Capture Decay of $^{145}\text{Gd}$ , R.E. Eppley, Wm.C. McHarris, and W.H. Kelly.....	165		
Properties of the $^{203}\text{Bi}$ Ground-State Analog in $^{203}\text{Po}$ , G.M. Crawley, W. Benenson, P.S. Miller, D.L. Bayer, R. St.ONGe, and A. Kromminga.....	182		
Shell-Model Structure of $^{35}\text{Cl}-^{35}\text{Ar}$ , B.H. Wildenthal, E.C. Halbert, J.B. McGrory, and T.T.S. Kuo.....	189		



Section I  
Research in Progress.  
August 1971

There have been two main approaches to determining an effective interaction suitable for microscopic model analyses of inelastic scattering and charge exchange data. It has been shown<sup>1,2</sup> that "realistic" forces, similar to those often used in bound state calculations, describe the scattering data reasonably well in the 20-60 MeV range. These forces, however, have rather complex radial shapes and are difficult to use in commonly available DWA codes. Further it is difficult to assess the accuracy of the assumptions made in their derivation.

An alternative procedure<sup>3</sup> is to assume a force of a convenient form and to attempt to fix the parameters of the force by comparison with experiment in particularly favorable circumstances. In this report we present preliminary results of a survey of the available information on the effective two-body interaction  $V$  assuming  $V$  has the form

$$V_{ip}(r) = [V_0 + V_{10} \vec{\sigma}_i \cdot \vec{\sigma}_p + V_{01} \vec{\tau}_i \cdot \vec{\tau}_p + V_{11} \vec{\sigma}_i \cdot \vec{\sigma}_p \vec{\tau}_i \cdot \vec{\tau}_p] \frac{e^{-\alpha r}}{\alpha r}$$

Here the subscripts on the  $V_{ST}$  are the transferred spin and isospin while  $p$  refers to the projectile and  $i$  to the valence nucleon. The quantity  $\alpha$  is the inverse range of the force and was taken to be  $1.0F^{-1}$ .

Corrections for exchange have been made in a number of cases where only direct processes out were included in the original calculation. Most of

the transitions relevant to  $V_{10}$ ,  $V_{01}$ , and  $V_{11}$  had an angular momentum ( $L$ ) transfer of 0 or 1 and these corrections were small.<sup>3</sup> In the case of  $V_{00}$  the transitions were  $L=2,3$  and inclusion of exchange enhanced the cross-section by a factor between two and four.<sup>1,4</sup> In the  $V_{00}$  case the selection of relevant analyses was rather limited since it was necessary that the wavefunctions adequately describe the collective properties of the states. The results of this survey are given in Figs. 1 to 4 and references to the original analyses are in Table I. (Note  $V_{00} \equiv V_0$ ,  $V_{10} \equiv V_\sigma$ ,  $V_{01} \equiv V_\tau$ ,  $V_{11} \equiv V_{\sigma\tau}$ ). The numbers shown near the points are the mass number  $A$  of the target and the  $L$  transfer where appropriate ( $A, L$ ). Also shown on the figures are other estimates of the  $V_{ST}$ . The points or lines labelled impulse approximation give the strengths of 1.0F range Yukawas that yield the same cross-section as the impulse approximation pseudopotential of Petrovich, *et al.*<sup>1</sup> The lines labelled KK, KKD, and HJ are the Yukawas which have the same volume integrals<sup>2</sup> as the long range parts of the Kallio-Kolltveit force (with and without density dependence (D)<sup>5</sup>) and the Hamada-Johnston force, respectively. Finally, the points labelled optical model in Fig. 1 were determined by matching the volume integral of the optical-model-real-potentials of Greenlees, *et al.*<sup>6</sup> and making a correction<sup>7</sup> for exchange contributions.

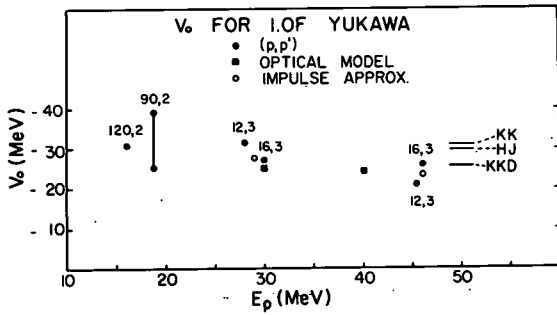


Figure 1

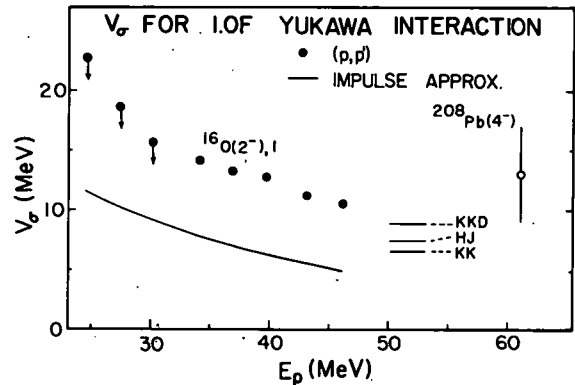


Figure 2

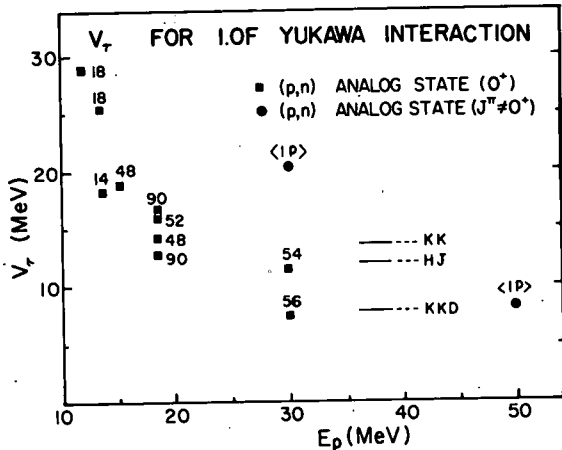


Figure 3

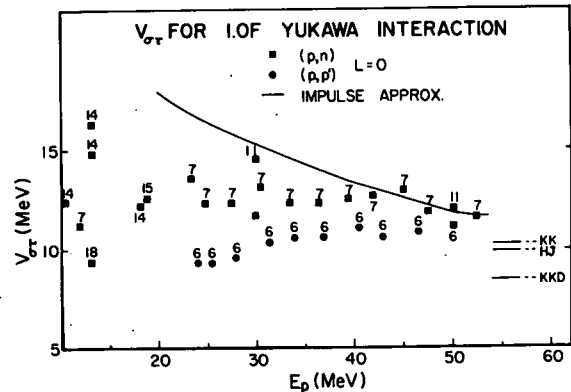


Figure 4

In an empirical procedure such as that described here the main test of the approximation is the consistency of the results. For  $E_p > 20$  MeV, the results for  $V_0$  and  $V_{\sigma\tau}$  are quite encouraging but data on  $V_\sigma$  and  $V_\tau$  are quite scanty. This survey is being extended to include the spin orbit and tensor forces.

#### References

1. F. Petrovich, H. McManus, V.A. Madsen, and J. Atkinson, Phys. Rev. Letters 22, 895(1969).
2. W.G. Love and G.R. Satchler, Nuclear Physics A159, 1(1970).
3. G.R. Satchler, Nuclear Phys. A95, 1(1967).
4. J. Atkinson and V.A. Madsen, Phys. Rev. C1, 1377(1970).
5. A.M. Green, Phys. Letters 24B, 384(1967).
6. G.W. Greenlees, W. Makofske and G.J. Pyle, Phys. Rev. C1, 1145(1970).
7. D. Slanina and H. McManus, Nucl. Phys. A116, 271(1968).
8. S.M. Austin, P.J. Locard, S.N. Bunker, J.M. Cameron, J.R. Richardson, J.W. Verba, and W.T.H. van Oers, Phys. Rev. C3, 1514(1971).
9. A. Scott, N.P. Mathur and G.R. Satchler, to be published.
10. J.D. Anderson, S.D. Bloom, C. Wong, W.F. Hornyak, and V.A. Madsen, Phys. Rev. 177, 1416(1969).
11. C.J. Batty, B.E. Bonner, E. Friedman, C. Tschalär, L.E. Williams, A.S. Clough, and J.B. Hunt, Nuclear Phys. A116, 643(1968).

Table I

Figure	Mass	Ref.	Figure	Mass	Ref.
$1(V_{00} \equiv V_0)$	12	1	$3(V_{01} \equiv V_\tau)$	14,18	10
	16	8		48	3,10
	90,120	4		52	3
	Optical Model	6,7		54,56	11
				90	3,10
$2(V_{10} = V_\sigma)$	$^{16}\text{O}$	8	$\langle 1p \rangle$		12
	$^{20}\text{Pb}$	9	$4(V_{11} \equiv V_{\sigma\tau})$	6,7	12,13,14
		11		12	
		14 <sup>+</sup>		10,15	
		15		10	
			18	2,10	

<sup>+</sup> Results for  $^{14}\text{C}(p,n)^{14}\text{N}(\text{g.s.})$  were excluded since these are known to be dominated by the tensor part of the effective interaction.

#### References (con't.)

12. A.S. Clough, C.J. Batty, B.E. Bonner and L.E. Williams, Nucl. Phys. A143, 385(1970). The quantities given are averages of the results of this paper.
13. S.M. Austin, P.J. Locard, W. Benenson, and G.M. Crawley, Phys. Rev. 176, 1227(1968).
14. A.S. Clough, C.J. Batty, B.E. Bonner, C. Tschalär, L.E. Williams, and E. Friedman, Nucl. Phys. A137, 222(1969).
15. C. Wong, J.D. Anderson, V.A. Madsen, F.A. Schmittroth, and M.J. Stomp, Phys. Rev. C3, 1904(1971).

Renormalized Operators and Collective  
Particle-Hole Excitations in  $^{40}\text{Ca}$

M. Dworzecka and H. McManus

ABSTRACT

Collective particle-hole excitations in  $^{40}\text{Ca}$  are calculated with Sussex matrix elements in Tamm-Dancoff approximation. Calculations are done both with bare and renormalized operators. Renormalization is accomplished by including core polarization effects by perturbation in both the two-body interaction and transition moments. The results are similar to those obtained in random-phase approximation using realistic forces with core polarization screening.

Considerable success has been achieved by Gillet, *et al.* Nucl. Phys. **88**, 321(1966); **54**, 472(1964); **54**, 321(1964); **57**, 698(1964); in describing negative parity collective excitations in closed shell nuclei by means of a simple particle-hole model with ground state correlations taken into account via the R.P.A. The ground state correlations so treated consist of multiplet excitations within the single particle and hole configurations originally picked for the description of the state (model space), and give, compared with the T.D.A. calculations in the original model space, a large energy shift and an increase in collectivity as measured, for instance, by the BE3 of a  $3^-$  state. However, the calculations used a force whose parameters were fixed by comparing calculation with experiment. Kuo, *et al.*, Phys. Letters **29B**, 544(1969), did a similar calculation using realistic forces, i.e. derived from the G-matrix. In this case the force between nucleons near the Fermi surface is altered by another type of correlation, core-polarization. This involves excitations, for instance, of positive parity particle-hole excitations, not included in the ground state correlations in the R.P.A. approximation. The results of the calculation were very sensitive to the way the core-polarization effects were taken into account, though some of the variations were due to an incorrect choice of backward going graphs in the R.P.A. Similar calculations were done by Dieperink, Nucl. Phys. **A116**, 556(1968). This method treats one type of correlation—core-polarization, by perturbation theory, and another, ground state correlations, by a different approximation, the R.P.A. The present calculation compares the results of treating both effects by perturbation theory with the results of using R.P.A. taking the  $3^-$  states of  $^{40}\text{Ca}$  as an example. In perturbation theory both the effective interaction and the effective transition operator have to be calculated. The effective interaction is calculated from the diagrams of Fig. 2.  $V$  is the bare force, in this case Sussex matrix elements,  $V_{2p-2h} = V_{ph} + V_{pp} + V_{hh}$  the lowest order core-polarization contributions involving energy denominators  $2h$ .  $V_{\text{GSC}}$  gives the effect on the interaction of ground

state correlations, via  $3p-3h$  intermediate states and hence should not be used in R.P.A. calculations. The effective operator is given by the diagram of Fig. 3.  $t_{\text{DIR}}$  being the bare operator if all correlations are neglected and  $t_{\text{cp}}$  the addition to the bare operator from correlations. In the present case, the whole effect of  $t_{\text{cp}}$  comes from ground state correlations, so it corresponds to the effect of the Y parts of the vectors in R.P.A. For the perturbation calculation, vectors were calculated in the usual T.D.A. with an effective force and the transition operators BE3 calculated from these vectors with a corresponding effective operator. Thus if the bare force  $V$  was used, neglecting all correlations, then the bare operator  $t_{\text{DIR}}$  was used for calculating BE3. If ground state correlations were included then  $V = V + V_{\text{GSC}}$ , and  $t = t_{\text{DIR}} + t_{\text{cp}}$ . The corresponding R.P.A. calculation used  $V$  in both A and B matrices. If core polarization was included  $V = V + V_{2p2h} + V_{\text{GSC}}$ , then  $t = t_{\text{DIR}} + t_{\text{cp}}$  and the corresponding R.P.A. calculation used  $V = V + V_{2p2h}$  in the A matrix and  $V = V$  in the B matrix. The results for the lowest  $3^-$  state of  $^{40}\text{Ca}$  are shown in Table 1.

Table 1

Interaction	Transition Operator	TDA		Corresponding RPA	
		E(MeV)	BE3(WU)*	E	BE3
None					
Pure $f_{7/2}d_{3/2}^{-1}$	$t_{\text{DIR}}$	7.1	0.72	*1WU=	$665\text{fm}^6$
$V$	"	6.14	9.0	-	-
$V + V_{2p2h}$	"	6.34	6.75	-	-
$V + V_{\text{GSC}}$	$t_{\text{DIR}} + t_{\text{cp}}$	5.43	16.5	4.74	23.4
$V + V_{2p2h} + V_{\text{GSC}}$	"	5.68	14.2	5.16	19.6

The main configuration  $f_{7/2}d_{3/2}^{-1}$  lies originally at 7.1 MeV, and has a small BE3 of 0.72 W.U. Switching on the interaction (Col. 2) immediately creates a moderately collective state lowering the energy to 6.14 MeV and increasing the BE3 to 9.0 W.U. The overall effect of correlations is to decrease the energy further to 5.68 MeV and increase the transition rate to 14.2 W.U., most of the effect coming from ground state correlations, essentially similar to the R.P.A. results.

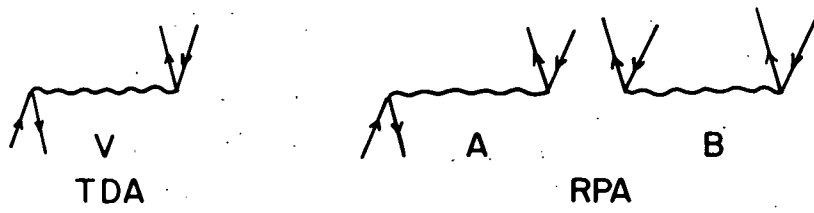


Fig.1

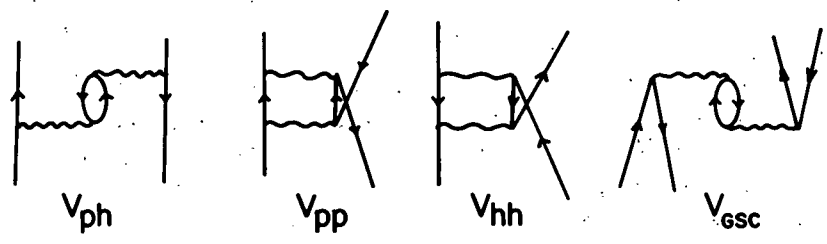


Fig.2

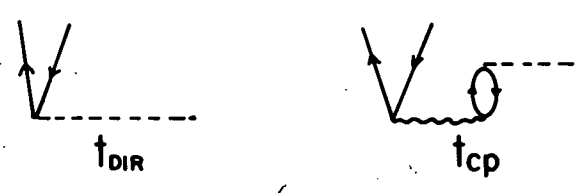


Fig.3

The differential cross-section for inelastic electron-nucleus scattering can be written

$$\frac{d\sigma}{d\Omega} = \sigma_m \left\{ |F_{\text{LONG}}(q)|^2 + \frac{1}{2}(1 + 2 \tan^2 \frac{\theta}{2}) |F_{\text{TRANS}}(q)|^2 \right\}$$

where  $\sigma_m$  is the Mott cross-section and  $F_{\text{LONG}}$  and  $F_{\text{TRANS}}$  are the longitudinal and transverse form factors.

For normal parity excitations the longitudinal form factor provides the dominant contribution except at very large angles, so the transverse form factor usually is neglected.

In Born approximation  $F_{\text{LONG}}$  as a function of linear momentum transfer,  $q$ , for the excitation of a nucleus with charge  $Z$  and a spin zero ground state to a final state of angular momentum  $J$  is

$$F_{\text{LONG}}(q) = \frac{1}{Z} [(4\pi)(2J+1)]^{1/2} \int_0^\infty j_J(qr) \rho_J(r) r^2 dr$$

where  $j_J$  is a spherical Bessel function. The relevant nuclear information is contained in the radial charge transition density  $\rho_J$ .

Since the electromagnetic interaction is well understood, reliable charge transition densities can be extracted from empirical form factors.

Similarly, the physical information required for a distorted wave approximation calculation of inelastic proton-nucleus scattering is contained in form factors

$$F_{\text{LSJ}}^{\text{LSJ}}(r) = \sum_{x=p,n} \int_0^\infty v_{\text{px}}^{\text{SL}}(r, r_0) F_x^{\text{LSJ}}(r_0) r_0^2 dr_0$$

where  $L$ ,  $S$ , and  $J$  are the orbital, spin, and total angular momenta transferred in the interaction and  $x$  refers to the protons or the neutrons.  $v^{\text{SL}}$  is the  $L$ th multipole coefficient of the proton-target nucleon interaction; the functions  $F_{\text{LSJ}}$  are transition densities, which contain the nuclear structure information.

For normal parity transitions the two functions  $F_p^{\text{JOJ}}$  and  $F_n^{\text{JOJ}}$  are important.  $F_p^{\text{JOJ}}$  is essentially the same as the function  $\rho_J$ , which can be inferred from an electron scattering experiment; thus only  $F_n^{\text{JOJ}}$  remains to be determined.

For  $T=0$  excitations in  $N=Z$  nuclei neutrons and protons play symmetric roles, so in these cases we can set  $F_p^{\text{JOJ}} = F_n^{\text{JOJ}}$ . Since

$$V_{T=0} = V_{pp} + V_{pn}$$

we are left with the single form factor

$$F^{\text{JOJ}} = 2 \int_0^\infty v_{T=0}^{\text{JOJ}}(r, r_0) F_p^{\text{JOJ}}(r_0) r_0^2 dr_0$$

Confrontation with experiment of an angular distribution calculated using this form factor essentially tests the quality of our choice of the nonspin-flip, isoscalar part of the projectile-nucleus interaction.

In the case of the  $3^-$ ,  $T=0$  excitation at 3.73 MeV in  $^{40}\text{Ca}$ , we took the charge transition density to be of the form

$$\rho(r) = N \frac{d}{dr} [1 + \exp(\frac{r-R}{C})]^{-1}$$

and adjusted  $N$ ,  $R$ , and  $C$  to obtain the form factor shown and compared with experiment in Fig. 1. The calculation was done in Born approximation employing finite proton size and local wave number corrections. Using this transition density in the manner discussed above, we calculated the angular distribution for proton scattering in the same transition, assuming a projectile-nucleus interaction which was the long range part of the Kallio-Kolltveit (KK) potential. The possibility of exchange of the projectile with one of the target nucleons was taken into account in an approximate way. The result is compared with experiment in Fig. 2.

Heisenberg and Sick recently extracted a charge transition density from inelastic electron scattering on the  $3^-$  excitation at 2.63 MeV in  $^{208}\text{Pb}$ .

While for lead the connection between charge and matter transition densities is not as clear as in the  $^{40}\text{Ca}$  case, we nonetheless expect, in the spirit of the collective model, that neutrons and protons play rather similar roles in a strong vibrational excitation. Therefore we set  $F_n^{\text{JOJ}} = \frac{N}{Z} F_p^{\text{JOJ}}$  and obtain a proton scattering form factor

$$F^{\text{JOJ}}(r) = \frac{A}{Z} \int_0^\infty [v_{T=0}^{\text{JOJ}}(r, r_0) - \frac{N-Z}{A} v_{T=1}^{\text{JOJ}}(r, r_0)] F_p^{\text{JOJ}}(r_0) r_0^2 dr_0$$

We neglected the second term in brackets both because of the  $\frac{N-Z}{A}$  term and because for the KK force the isovector term is smaller than the isoscalar by a factor of three. The angular distribution of scattered protons predicted using this form factor with the same force and treatment of exchange as in the  $^{40}\text{Ca}$  case is shown as the solid line and compared with experiment in Fig. 4.

We also calculated transition densities and a proton scattering angular distribution for the same  $3^-$  state using a wave function obtained by Kuo in a preliminary random phase approximation calculation which included 47 low particle-hole excitations but no higher excitations. The matter transition density is shown as the dashed curve in Fig. 3 and the angular distribution is the dashed curve in Fig. 4.

The similarity of the two angular distributions for lead—despite the differences in transition density for points in the nuclear interior—suggest that proton inelastic scattering is sensitive primarily to structural features which lie near the nuclear surface.

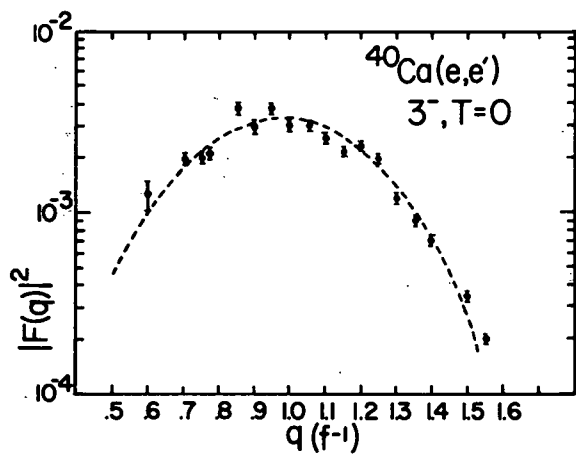


Figure 1

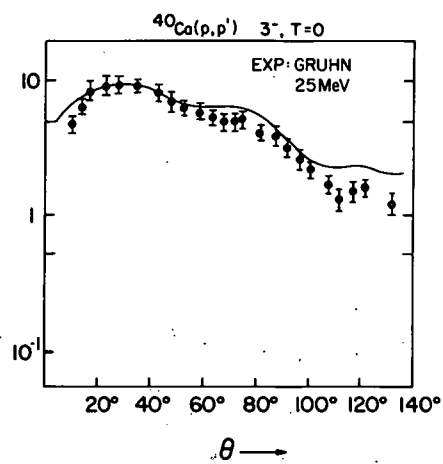


Figure 2

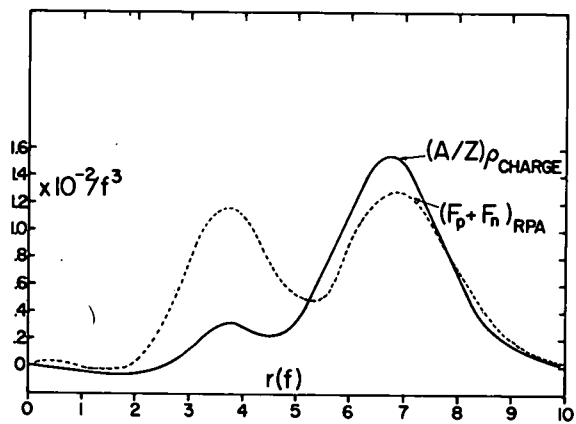


Figure 3

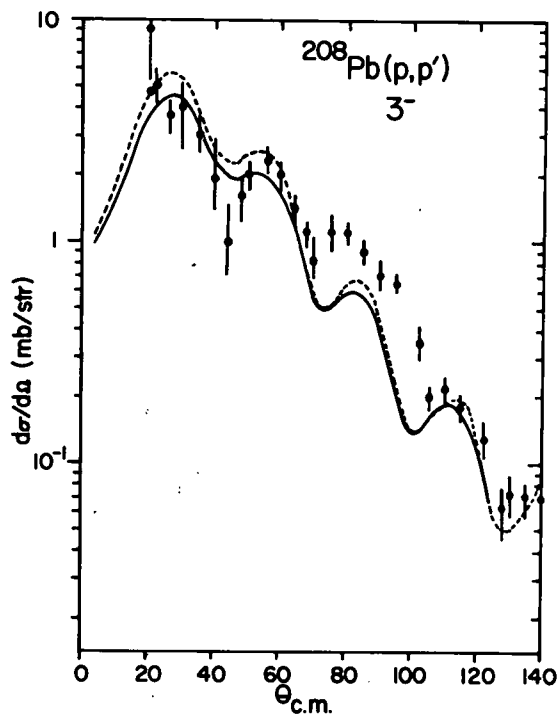


Figure 4

# An Eikonal Approximation for Electron-Nucleus Scattering

G.R. Hammerstein

An important problem in any theoretical description of electron-nucleus scattering is treatment of the electron wave's distortion in the nuclear Coulomb field.

The familiar Born (plane wave) approximation gives a fairly accurate account of the gross features of cross-sections. But while experimental cross-sections display marked diffraction minima, the Born approximation predicts absolute zeros and these are shifted to too large values of linear momentum transfer. Thus we need to employ a calculational method which takes into account Coulomb distortion if we are to be able to study details of nuclear structure.

A method which has been used extensively describes the electron wave through numerical, partial wave solutions of the Dirac equation. Since this method is highly accurate, it probably will not be superceded in last-step analysis of nuclear data. Nonetheless, it suffers from two drawbacks: it is time consuming and, more importantly, when it is employed everything happens inside the computer. Direct connections are difficult to see between details of proposed nuclear models and details of the resultant cross-sections.

It is of interest then to devise a calculational method which takes Coulomb distortion into account but retains the perspicuity of the Born approximation.

A number of years ago Yennie, Boos, and Ravenhall proposed an eikonal approximation for elastic electron-nucleus scattering. While their quoted results agreed well with partial wave calculations, the wave function they obtained was such a complicated object that their procedure was hardly to be preferred to the exact numerical method.

The method described here employs the YBR eikonal treatment of the wave function, but with a constant spinor and a minimum of analytic approximations. The result is almost identical in form to the Born approximation. It should be of interest primarily in the treatment of longitudinal inelastic scattering and can be employed in a straightforward way in the case of transverse excitations as well, but we will describe here the formally simpler case of elastic scattering.

The S-matrix element for elastic electron scattering can be written in position space as

$$S_{FI} = \delta_{FI} - ie \int d^4x \bar{\psi}_F(X) \gamma^\mu \psi_I(X) A^\mu(X)$$

where  $\psi_I$  solves the Dirac equation

$$(i\gamma^\mu \partial_\mu - m) \psi_I = e\gamma^\mu A^\mu \psi_I.$$

The function  $A^\mu$  is the nuclear four-potential and  $\psi_F$  is a Dirac plane wave.

We neglect the electron mass compared to the incident energy and suppose that only distortions due to the Coulomb field are important  $A_\mu \rightarrow V$ . The basic assumption is that  $\psi$  can be represented as

$$\psi = U \exp(-iEt) \exp(iS)$$

where  $U$  is a constant spinor and  $S$  depends only on the spatial coordinates. Then the Dirac equation becomes

$$(-\vec{\gamma} \cdot \vec{\nabla} S + \gamma^0(E-V)) \psi(x) = 0.$$

Solutions exist only if the Hamilton-Jacoby equation

$$(E-V)^2 = (\vec{\nabla} S)^2$$

is satisfied.

The appropriate boundry condition is that  $\psi$  reduce to a logarithmically distorted plane wave at large distances. Then

$$S(\vec{x}) = S(o) + \vec{k} \cdot \vec{x} - \int_0^{\vec{x}} V(\vec{x}') dr$$

where  $k$  is the incident wave number,  $dr$  is an increment along the classical trajectory, and  $S(o)$  is the phase at the origin. Since  $dr$  depends on  $V$ , the remaining integral is quite complicated. We assume that it can be written as a series in powers of the fine structure constant:

$$S(\vec{x}) = S(o) + \vec{k} \cdot \vec{x} + S_1(\vec{x}) + S_2(\vec{x}) + \dots$$

Substituting this series in the above Hamilton-Jacoby equation and requiring that  $S_1(o) = 0$ , we find that

$$S_1(\vec{x}) = - \int_0^{\vec{x}} V(\vec{x}') dz + \int_0^{\infty} [V(z) - V(\vec{x}')] dz$$

$$S_2(\vec{x}) = -(1/2k) \int_{-\infty}^{\vec{x}} (\partial S_1 / \partial y)^2 dz$$

and so on, where  $dz$  is along the path through the origin and  $dy$  is in a direction perpendicular to that path.

Then

$$\psi(X) = U \exp(-iEt) \exp(S(o) + \vec{k} \cdot \vec{x} + S_1(\vec{x}) + \dots)$$

is the desired wave function.

Inserting this function in the S-matrix expression for Coulomb scattering and forming a cross-section in the standard fashion, we obtain

$$\frac{d\sigma}{d\Omega} = 4e^2 k^2 \cos^2(\theta/2) \left| \int d^3x V(\vec{x}) \exp(iS) \exp(-i\vec{k}_F \cdot \vec{x}) \right|^2$$

which differs from the Born approximation solely in the presence of  $\exp(iS)$  instead of a plane wave.

The actual performance of calculations has proved to be fraught with numerical difficulties. Nonetheless preliminary calculations have been encouraging in that they indicate the desired contributions by the correction terms. The trouble seems to lie with the rather roundabout treatment of the underlying Born approximation.



Concerning Calculation of Strong Absorption Parameter  
in the Strong Cut Regge Absorption Model.

David Perry

Preliminary Remarks: Two body high energy processes ab cd show a definite preference for small momentum transfers, and the early attempts to incorporate this forward peaked behavior into calculations of differential cross-sections for inelastic reactions revolved around Born terms, i.e., single particle exchanges which produce a certain amount of peaking due to the presence of the propagator of the exchanged particle.

$$\Rightarrow T_{ab \rightarrow cd} \sim v_{ace} \frac{1}{T - M_e^2} v_{deb}$$

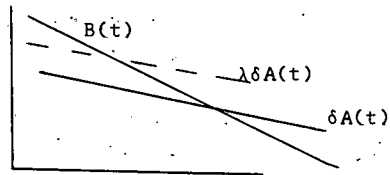
The  $\pi$  since it is the particle of small s+mass, would give the greatest peaking and could be exchanged in many reactions, e.g.  $\pi p \rightarrow \rho p$ . Even for this reaction the forward peaking was not enough, but density matrix arguments suggested that the basic mechanism was correct.

To induce sharper peaking than afforded by the Born term alone, absorptive corrections (among others) were introduced. This correction accounts for the loss of flux from ab, cd into inelastic channels—flux not available for the exchange reaction we are considering. The procedure is to partial wave analyze the Born term in an eikonal sense  $B_{fi}(t) \rightarrow B_{fi}(b)$ , write  $A_{fi}(b) = B_{fi}(b)I(b)$  where  $I(b)$  is a factor obtained from elastic scattering account for loss of flux and resum the series to obtain  $A_{fi}(t)$ .  $I(b)$  is obtained from the forward elastic peak,  $I(b) = 1 - CC^{-\gamma b^2}$  which suppresses lower partial waves and so pronounces the forward peak. If we write  $A(b) = B(b) - ce^{-\gamma b^2} B(b)$  on resumming the series we have  $A(t) = B(t) - A(t)$  and we can call the first term Born and the second, cut.

Strong Regge Cut Absorption Model

While the above procedure worked pretty well for exchanges, it was clearly wrong (in both energy and angular dependence) for exchanges like  $\rho$ , present in reactions like  $\pi^- p \rightarrow \pi^0 n$ . Great improvement came with (for both s and t) the introduction of a Reggeized version of the exchange particles which treatments  $J_{exch} = a(t)$ . Absorption corrections are again introduced the same way

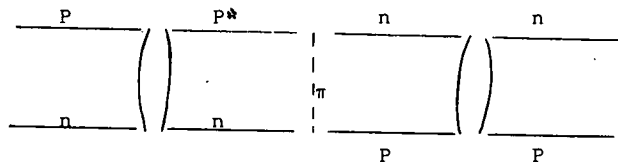
$A_{fi}(b) = B_{fi}(b)I(b)$  but now  $B(b)$  represents a reggeon exchange. If  $I(b) = 1 - CC^{-\gamma b^2}$ , then  $A(t) = R(t) - A(t)$  and it was found by U.M. group that one can fit the dip present at  $t = -0.6 \text{ BeV}^{-2}$  if one uses instead  $A(t) = R(t) - \lambda \delta A(t)$  with  $\lambda \sim 2$ . This is the strong cut regge absorption model. Amplitudes are now a sum of two terms pole + cut or Born + absorption correction, the second is (mostly) negative with respect to 1st, and varies more slowly with angle. The effect of  $\lambda$  is to remove the dips in.



This mechanism has been found to fit many other quantum exchange reactions well.

Calculations: My attempts have been to see if so large a cut enhancement factor,  $\lambda$ , could emerge naturally from a calculation. The initial approach taken was to see if it could be due to the coherent action of inelastic states (the reason originally given by the U.M. group).

For the reaction  $\pi n \rightarrow \pi p$  for the part that goes by  $\pi$  exchange this amounts to calculation of graphs of the type



By treating the  $N^*$  as a quasi-spinor particle of effective coupling  $g(\pi NN^*)$ , and relating  $g^*$  to the decay, one can calculate a scaling factor—and we found  $\lambda \pi < 1.4$ . The calculation is extremely crude but one at least obtains an estimate. It agrees roughly with previous calculations by Ravenhall for  $\pi^- p \rightarrow \pi^0 n$  who found  $\lambda(e) < 1.2$ . Because of the small values emerging from calculations of this sort we decided to look elsewhere. One attempt was to try improvements in  $I(b)$  where  $I(b)$  is now assumed to fit large t elastic data as well. A number of forms were used some theoretical, some phenomenological, some just guessed at. The result is that at small t the  $n=0$  amplitudes (zero net flip amplitudes) can have  $\lambda \sim 1.4, 1.5$  but that  $n \neq 0$  amplitudes do not change much or can even be renormalized downward. At larger t they will all rise and take on a curvature induced by  $I(b)$ . A look at the data shows that this cannot be correct.

Another attempt was to look at reactions through a quark model, and one can calculate things using the Glauber formalism developed for the scattering of composite systems (mostly nuclei).

Single scattering of quarks by other quarks when summed over all constituents supplies a Born term; double scattering supplies a cut. The quark-quark amplitudes must then be related back to  $A_{ab \rightarrow cd}$ .

It was found that no enhancement is possible in this model, if you stay with quark-quark amplitudes.

Other mechanisms considered and rejected were polynomial  $t$  dependence of the residue functions, and possible spin-flip contribution in the elastic amplitude.

Conclude: So large an enhancement factor is pretty difficult to obtain. Entirely different mechanisms are now being pursued.

Recent advances in experimental techniques have made possible the quantitative study of the lighter mass nuclei having 82 neutrons.<sup>1-4</sup> Spectra have been obtained for  $^{133}\text{Sb}$ ,  $^{134}\text{Te}$ , and  $^{135}\text{I}$ ; these nuclei correspond respectively to one, two and three protons outside the Z=50, N=82 doubly-magic  $^{132}\text{Sn}$  core. The properties of these systems are interesting because their presumed structural simplicity permits a relatively unambiguous delineation of the various facets involved in nuclear structure phenomena. The nuclei around  $^{208}\text{Pb}$  have been extensively studied in this same spirit in order to extract such quantities as effective charges and effective g-factors. Next to the  $^{208}\text{Pb}$  neighborhood, the N=82 region may well exhibit the best "closed shell" behavior available to us. In addition the N=82 nuclei provide what the lead region does not, namely a long string of nuclei (14 have been studied at present) built by adding protons to the doubly-magic core. Thus for N=82 we will have the opportunity to pursue the consequences of our deductions based on the simple, "few" nucleon systems through a series of "many" nucleon systems.

Actually, of course, because of the accidents of nuclear stability, the situation has been inverted in the N=82 region. The naturally stable, many-proton, systems have been extensively studied both experimentally and theoretically for some time, and the few-proton nuclei have just become available for study within the last year or so. In this note we present theoretical predictions for the structure of the Z=(50+1,2,3, and 4), N=82 nuclei and compare these results to the presently available experimental data.

Our predictions for  $^{133}\text{Sb}$ ,  $^{134}\text{Te}$ , and  $^{135}\text{I}$  are based on previous shell-model calculations for heavier N=82 nuclei.<sup>5</sup> These calculations employ an MSDI residual interaction<sup>6,7</sup> and a model space comprised of all  $0g_{7/2}$ - $1d_{5/2}$  configurations plus all configurations formed by exciting one particle from the  $0g_{7/2}$ - $1d_{5/2}$  subspace to either a  $2s_{1/2}$  or  $1d_{3/2}$  orbit. In our initial work<sup>5</sup> we chose values for the SDI strength and for the single-particle-energy (SPE) splittings which optimized agreement between model and experimental excitation energies for all known positive-parity N=82 states in A=136-145 inclusive. Subsequently, because the model space is most appropriate for the lighter N=82 nuclei, we readjusted the SDI strength and the SPE splittings to optimize agreement only for A=136-140. The significant change which resulted from the new approach was an increase, from 0.48 MeV to 0.88 MeV, of the  $0g_{7/2}$ - $1d_{5/2}$  SPE splitting.

We have used these A=136-140 parameters, and the same model space assumptions, to calculate the structure of the one, two, three, and four proton systems. The predicted and experimentally observed

energies are given in Table 1. The agreement is satisfactory. Several other data are available on these nuclei which bear on the wave functions of these states. In Table II we present some predictions from our wave functions for purposes of comparison to experiment.

The  $^{133}\text{Sb}$  nucleus does not offer much material for discussion from our point of view, of course. The single gamma-ray ( $E_\gamma=0.963$  MeV) attributed to this system presumably corresponds to the "single-proton"  $1d_{5/2}$  to  $0g_{7/2}$  transition. Any additional energy levels below the  $0h_{11/2}$ ,  $1d_{3/2}$ , and  $2s_{1/2}$  single-proton states at  $\sim 3$  MeV excitation would signal the breaking of the assumed model core and problems for our approach.

In addition to the level energies of  $^{134}\text{Te}$ , the lifetime of the 1691 keV to 1576 keV transition has been measured<sup>2,3</sup> and the transition interpreted as a  $J^\pi=6^+$  to  $4^+$  electric quadrupole decay. The B(E2) extracted from the 162 ns lifetime of this decay is  $85 e^2 F^4$ . The calculated B(E2) for the transition between the lowest  $6^+$  and  $4^+$  state in our  $^{134}\text{Te}$  model spectrum (under the assumptions of harmonic oscillator single-particle wave functions ( $M_\omega=41 A^{-1/3}$ ) and a proton charge of  $1e$ ) is  $39 e^2 F^4$ . This implies an effective charge for protons in this region of  $E_p(\text{eff})=1.47e$ . Our model wave functions for each of the lowest  $0^+$ ,  $2^+$ ,  $4^+$ , and  $6^+$  states are dominated ( $\sim 80\%$ ) by the  $(g_{7/2})^2$  configuration. However, the difference between the effective proton charge derived from a pure  $g_{7/2}$  assumption for these states and our present value is  $1.74e$  vs  $1.47e$ .

The structure of the low-lying levels of  $^{135}\text{I}$  have been studied both by gamma-ray decay and by proton pickup<sup>8</sup> from  $^{136}\text{Xe}$ . The  $^{136}\text{Xe}(d, ^3\text{He})^{135}\text{I}$  reaction populates the 0.604 and 0.871 MeV states with  $\ell=2$  transfer. Systematics argue against interpreting the higher energy state as being fed by  $1d_{3/2}$  pickup, yet study of the heavier N=82 nuclei gives no evidence for any but the lowest  $5/2^+$  state being populated in such a pickup reaction. The experimental and calculated S-factors are presented in Table II and it can be seen that our theory predicts this phenomenon with quantitative accuracy. Its occurrence depends upon the drawing close of the  $[(g_{7/2})^2_{J=0}(d_{5/2})]_{J=5/2}$  state and the  $[(g_{7/2})^3]_{J=5/2}$  state so that their amplitudes mix. In the BCS language we would speak of the  $1d_{5/2}$  one-quasiparticle state mixing with the  $0g_{7/2}$  three-quasiparticle  $J=5/2$  state. That is, in the three proton system we witness the transition from the "super-conducting" type of nuclear structure characteristic of the heavier N=82 systems to a more typical "shell-model" structure. Of course, our present shell-model treatment encompasses both types of structure simultaneously, the changes in overt behavior

just arising from the different numbers of active particles.

Although  $^{136}\text{Xe}$ , the 4-proton system, is a stable isotope, rather little is experimentally known about the structure of its low-lying states either. One feature that has been recently discovered<sup>4</sup> is an isomeric gamma-ray transition that appears to be a  $6^+$  to  $4^+$  E(2) transition analogous to that discussed for  $^{134}\text{Te}$ . The strength of this transition in  $^{136}\text{Xe}$  is  $0.6 e^2 F^4$ , as opposed to the value of  $85 e^2 F^4$  in  $^{134}\text{Te}$ . Our predicted B(E2), using the effective proton charge of  $1.47e$ , is  $3.5 e^2 F^4$ . This marked reduction in strength in going from the 2 proton to the 4 proton system arises in the model because of a selection rule forbidding E2 transitions between components having the same seniority and a half-full j-shell.

#### References

1. G.B. Holm, S. Borg, and B. Rydberg, Conference on the Properties of Nuclei Far from the Region of Beta-Stability, Leysin, Switzerland.
2. W. John, F.W. Guy, and J.J. Wesolowski, Phys. Rev. C2, 1451(1970).
3. S. Borg, P. Carlé, L.E. DeGeer, G. Holm, and A. Kerek, Annual Report, Research Institute for Physics, Stockholm, Sweden.
4. L.C. Carraz, J. Blachot, E. Monnard, and A. Moussa, Nucl. Phys. A158, 403(1970).
5. B.H. Wildenthal, Phys. Rev. Letters 22, 1118(1969).

6. R. Arvieu and S.A. Moszkowski, Phys. Rev. 145, 830(1966).
7. P.W.M. Glaudemans, P.J. Brussaard, and B.H. Wildenthal, Nucl. Phys. A102, 593(1967).
8. B.H. Wildenthal, E. Newman, and R.L. Auble, Phys. Rev. C3, 1199(1971).

Table II. Electromagnetic and single-nucleon transition strengths in  $^{134}\text{Te}$ ,  $^{135}\text{I}$ , and  $^{136}\text{Xe}$ .

Nucleus.	$J_{\nu}^{\pi} \rightarrow J_{\nu}'^{\pi}$	Calc.	Expt.
B(E2)'s in units of $e^2 F^4$			
$^{134}\text{Te}$	$2_1^+ \rightarrow 0_1^+$	81 <sup>b</sup>	
	$4_1^+ \rightarrow 2_1^+$	81	
	$6_1^+ \rightarrow 4_1^+$	39	85
$^{136}\text{Xe}$	$2_1^+ \rightarrow 0_1^+$	122	
	$4_1^+ \rightarrow 2_1^+$	9	
	$4_2^+ \rightarrow 2_1^+$	65	
	$6_1^+ \rightarrow 4_1^+$	1.6	0.6
	$6_2^+ \rightarrow 4_1^+$	11	
Single Nucleon S-factors			
$^{136}\text{Xe} \rightarrow ^{135}\text{I}$	$0_1^+ \rightarrow 7/2_1^+$	318	274
	$0_1^+ \rightarrow 5/2_1^+$	58	34
	$0_1^+ \rightarrow 5/2_2^+$	17	12

<sup>b</sup> $b_{ep}$  assumed to be 1.0e.

Table I. Characteristics of Low-Lying Levels of  $^{133}\text{Sb}$ ,  $^{134}\text{Te}$ ,  $^{135}\text{I}$ , and  $^{136}\text{Xe}$

Nucleus	$J_{\nu}^{\pi}$	$E_{\text{calc.}}$	$E_{\text{expt.}}$	Model Wave Function (Largest Components) <sup>a</sup>
$^{133}\text{Sb}$	$7/2^+$	0.00	0.00	1.00 $g_7$
	$5/2^+$	0.88	0.963	1.00 $d_5$
$^{134}\text{Te}$	$0_1^+$	0.00	0.00	.90( $g_7$ ) <sup>2</sup> + .43( $d_5$ ) <sup>2</sup>
	$2_1^+$	1.39	1.279	.90( $g_7$ ) <sup>2</sup> + .26( $g_7 d_3$ ) + .22( $d_5$ ) <sup>2</sup>
	$4_1^+$	1.76	1.576	.93( $g_7$ ) <sup>2</sup> - .27( $g_7 d_5$ )
	$6_1^+$	1.93	1.691	.93( $g_7$ ) <sup>2</sup> - .37( $g_7 d_5$ )
$^{135}\text{I}$	$7/2_1^+$	0.00	0.00	.90( $g_7$ ) <sup>3</sup> <sub>J=7</sub> - .42( $g_7$ ) <sup>1</sup> ( $d_5$ ) <sup>2</sup> <sub>J=0</sub>
	$5/2_1^+$	0.65	0.604	.84( $g_7$ ) <sup>2</sup> <sub>J=0</sub> ( $d_5$ ) <sup>1</sup> <sub>J=5</sub> - .40( $g_7$ ) <sup>3</sup> <sub>J=5</sub> + .27( $d_5$ ) <sup>3</sup> <sub>J=5</sub>
	$5/2_2^+$	0.82	0.871	.42( $g_7$ ) <sup>2</sup> <sub>J=0</sub> ( $d_5$ ) <sup>1</sup> <sub>J=5</sub> + .80( $g_7$ ) <sup>3</sup> <sub>J=5</sub> + .19( $d_5$ ) <sup>3</sup> <sub>J=5</sub>
$^{136}\text{Xe}$	$0_1^+$	0.00	0.00	.80( $g_7$ ) <sup>4,0</sup> + .58( $g_7$ ) <sup>2</sup> <sub>J=0</sub> ( $d_5$ ) <sup>2</sup> <sub>J=0</sub> + .16( $d_5$ ) <sup>4</sup>
	$2_1^+$	1.38	1.313	.80( $g_7$ ) <sup>4,2</sup> + .37( $g_7$ ) <sup>2</sup> <sub>J=2</sub> ( $d_5$ ) <sup>2</sup> <sub>J=0</sub> + .24( $g_7$ ) <sup>2</sup> <sub>J=0</sub> ( $d_5$ ) <sup>2</sup> <sub>J=2</sub>
	$4_1^+$	1.76	1.694	.82( $g_7$ ) <sup>4,2</sup> + .38( $g_7$ ) <sup>2</sup> <sub>J=4</sub> ( $d_5$ ) <sup>2</sup> <sub>J=0</sub> + .26( $g_7$ ) <sup>3</sup> <sub>J=7</sub> ( $d_5$ ) <sup>1</sup> <sub>J=5</sub>
	$6_1^+$	1.92	1.892	.79( $g_7$ ) <sup>4,2</sup> - .44( $g_7$ ) <sup>3</sup> <sub>J=7</sub> ( $d_5$ ) <sup>1</sup> <sub>J=5</sub> - .37( $g_7$ ) <sup>2</sup> <sub>J=6</sub> ( $d_5$ ) <sup>2</sup> <sub>J=0</sub>
	$4_2^+$	2.20		.81( $g_7$ ) <sup>4,4</sup> + .24( $g_7$ ) <sup>3</sup> <sub>J=7</sub> ( $d_5$ ) <sup>1</sup> <sub>J=5</sub> - .21( $g_7$ ) <sup>3</sup> <sub>J=9</sub> ( $d_3$ ) <sup>1</sup> <sub>J=3</sub>
	$6_2^+$	2.33		.80( $g_7$ ) <sup>3</sup> <sub>J=7</sub> ( $d_5$ ) <sup>1</sup> <sub>J=5</sub> + .44( $g_7$ ) <sup>4,2</sup> - .30( $g_7$ ) <sup>3</sup> <sub>J=7</sub> ( $d_5$ ) <sup>3</sup> <sub>J=5</sub>

<sup>a</sup>Half-integral spins are given as two times their value, i.e.  $7/2=7$ . The additional quantum numbers labeling a few components are the seniorities, e.g. ( $g_7$ )<sup>4,2</sup> refers to the seniority 2, coupling of four 7/2 particles coupled to total angular momentum J.

Proton Induced Spallation of  $^{14}\text{N}$ ,  $^{16}\text{O}$  and  
the Astrophysical Production of Li, Be, and B  
Helmut Laumer, Lolo Panggabean, and Sam M. Austin

The program for measuring the production cross-sections of the light elements Li, Be, B from proton spallation of  $^{14}\text{N}$  and  $^{16}\text{O}$  has been completed. We have made measurements at proton beam energies from 17 MeV to 42 MeV. The gas cell described elsewhere in this report was an essential part of the measuring apparatus. We found total cross sections by measuring differential cross-sections at a number of angles and integrating the resulting distribution over angle. Particle mass identification was accomplished by a time-of-flight technique in which one simultaneously measures the time-of-flight  $t$  and energy  $E$  of a particle and forms the product  $Et^2$  which is proportional to the particle mass ( $Et^2 = 1/2MV^2 \times (\frac{\text{distance}}{V})^2 \times M$ ). Mass identification is sufficient<sup>1</sup> since for all possible product nuclei only one isobar is stable and all others decay to it on astrophysical time scales.

Particles produced in a gas target were detected in a thin (between  $78\mu$  and  $150\mu$ ) Ortec silicon surface barrier detector placed about 27 cm from the target. A timing signal derived from this energy ( $E$ ) pulse starts a time-to-amplitude converter (TAC); a second timing signal from the Cyclotron RF system stops the TAC. Linear signals  $E$  and TAC are decoded by Northern Scientific-629 ADC's. Using the all purpose code TOOTSIE<sup>2</sup> the Sigma-7 computer calculates the quantities  $t = T_0 - \text{TAC}$  and  $Et^2$  and displays  $Et^2$  vs.  $E$  in a two dimensional array (128x128 channels) on a storage oscilloscope.  $T_0$  is adjusted so the mass bands displayed can be easily identified. For the proper choice of  $T_0$ , ( $T_0 - \text{TAC}$ ) at the particle flight time between the reaction site and the detector.

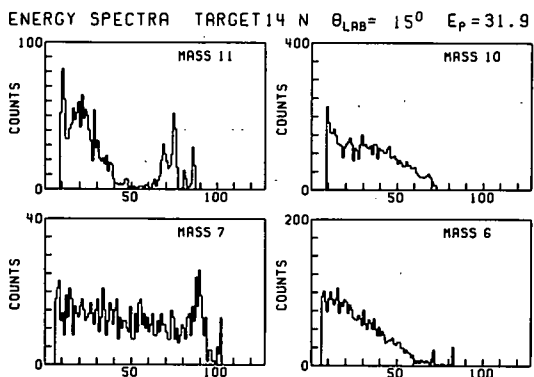


Figure 1

Energy spectra are obtained by defining mass bands on the scope display and storing the energy spectra for each mass. Examples of the energy spectra obtained are shown in Fig. 1. The low energy cutoff evident in these spectra is due to the finite flight time available between consecutive beam bursts; heavy low energy particles from one

burst can arrive at the same time as light particles at the same energy from the next burst. The burst spacing is beam energy dependent; it is 53 nsec at 42 MeV and 72 nsec at 22 MeV. For mass 6 the sensitivity of the timing pulse pickoff unit also can limit the low energy particle detection. The low energy portion of the energy spectra are mainly made up of particles from multi-body break up rather than from two-body final states. From phase space arguments<sup>3</sup> one finds that the energy spectrum goes to zero at zero particle energy. In calculating the differential cross-sections a low energy extrapolation of the energy spectra was performed by assuming the channels below the cutoff have the same number of counts as an average of the last few non-zero channels. One half of this contribution to the differential cross-section is assigned as error. This is the major contributor to the error quoted for the total production cross-section.

At beam energies below 26 MeV mass 11 production from  $^{14}\text{N} + \text{P}$  is dominated by the reaction  $^{14}\text{N}(\text{P}, ^{11}\text{C}^*)^3\text{He}$ . Since  $^{11}\text{C}$  excited above 7.5 MeV particle decays, there is a natural energy cutoff in the spectra at forward angles and no extrapolation need be made.

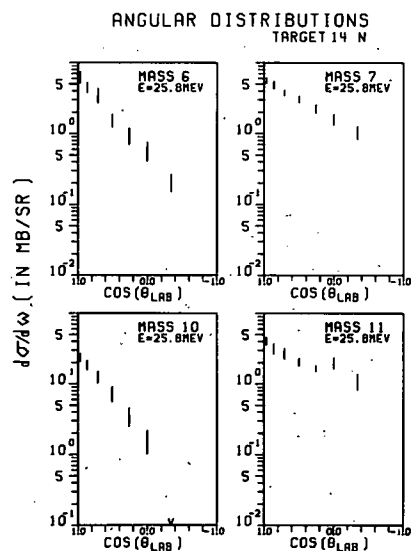


Figure 2

Due to the low energy cutoff there is also always a maximum detection angle beyond which no particles can be detected. As seen from sample angular distributions in Fig. 2, this usually represents a small error contribution in the cross-section integration. Again  $^{14}\text{N}(\text{P}, ^{11}\text{C}^*)^3\text{He}$  is an exception, the contribution of two-body final states at back angles now represents a large uncertainty.

Continued on  
Page 87.

Proton Induced Spallation of  $^{20}\text{Ne}$  and  
the Astrophysical Production of the Lithium Isotopes  
L.M. Pānggabean, H. Laumer, and Sam M. Austin

It is believed that Li, Be, B (masses 6 through 11) are not part of the products of thermonuclear reactions which is assumed to be the process that generates the different elements in the stars. It has been suggested that another mechanism, spallation by high energy protons, produced these elements. The important targets in this case are  $^{12}\text{C}$ ,  $^{14}\text{N}$ ,  $^{16}\text{O}$ ,  $^{20}\text{Ne}$ ,  $^{24}\text{Mg}$ ,  $^{28}\text{Si}$ .<sup>1-3</sup>

There have been many data obtained on the production cross-sections of Li, Be, B from most of these targets in the high energy region.<sup>4</sup> However, data on the lower energy region (20-70 MeV) are needed.<sup>4</sup> In this laboratory effort is being made to measure the production cross-sections of Li, Be, B with protons energy ranges from 22 to 42 MeV. Charge particle time-of-flight techniques, which were used in the previous work,<sup>5</sup> have been applied to measure the similar cross-sections from proton spallation of  $^{20}\text{Ne}$ .

The reaction  $\text{Ne}+p$  has been studied at three different energies i.e. 30, 35, 40 MeV. An isotopically enriched (99.95%  $^{20}\text{Ne}$  out of a gross composition of 99.5% neon)  $^{20}\text{Ne}$  gas target<sup>6</sup> in an ultra thin gas cell is used. A pressure of about 0.052 atm which is, at 15°, equivalent to an 80  $\mu\text{g}/\text{cm}^2$  target, is used. This enables one to measure down to about 1 MeV particles of mass-6 and 7. The low energy cutoffs for mass 8, 9, and 10 are about 1.5 MeV. A background run has always been taken and total yields have been calculated by subtracting the normalized background counts at each angle.

A two dimensional display (mass versus energy) of the data indicates that masses 6,7,8,9, and 10 can be well separated except for the very low energy region (below 5 MeV). The band of mass 11 is mostly covered by the band of mass 12 and therefore is not extractable. Angular distributions are taken for each bombarding energy. They slowly rise at forward angles. The overall feature of the cross-sections at different energies shows a small dependence on bombarding energy. (see Figs. 1 and 2). At the time this report is written data on 30 MeV are being analyzed and not shown on the diagrams. The cross-sections get smaller as the bombarding energy goes down. The preliminary analysis shows that the integrated cross-section at 40 MeV is about 1.97 mb. for mass-6, 1.75 mb for mass-7, 0.90 mb for mass-8, .92 mb for mass-9 and 1.92 mb for mass-10. Plans are being made to extrapolate the yields into the zero energy region. The numbers quoted above do not include these regions and hence can be considered as their lower limits.

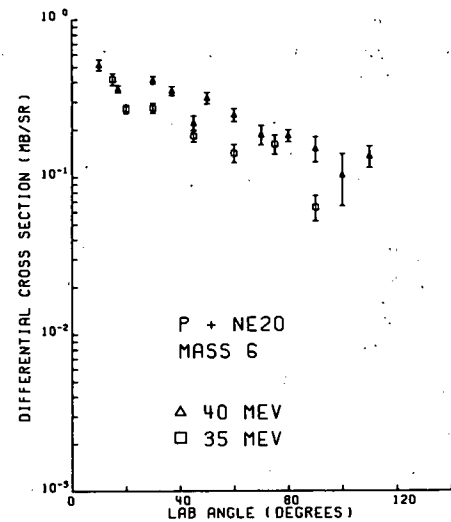


Fig. 1 Comparison between the cross-sections of mass-6 at 40 and 35 MeV.

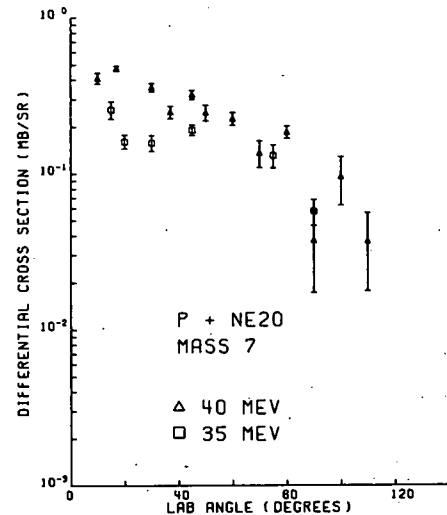


Fig. 2 Comparison between the cross-sections of mass-7 at 40 and 35 MeV.

#### References

1. D.D. Clayton, Principle of Stellar Evolution and Nucleosynthesis, Ch. V, McGraw-Hill, 1968.
2. R. Bernas et al. Annals of Physics **44**, 426(1967).
3. H. Reeves et al. Nature **226**, 727(1970).
4. B.S.P. Shen (ed.) High Energy Nuclear Reactions in Astrophysics, Benjamin, 1967.
5. C. Davids et al. PRL **22**, 1388(1969).
6. See topic on Ultra-thin Window Gas Cell in this report.

The reaction  $^{14}\text{N}(p,p')^{14}\text{N}^*(\text{Ex}=2.31)$  has been of interest to a number of investigators.<sup>1-4</sup> The L=0 inelastic scattering matrix element for the  $1^+(T=0)$  to  $0^+(T=1)$  transition in  $^{14}\text{N}$  is nearly proportional to the matrix element for the Gamow-Teller beta decay of  $^{12}\text{C}$  which is strongly inhibited. Hence if one assumes only a central effective interaction in microscopic model calculations of the reaction, the normally dominant L=0 contribution to the inelastic scattering cross-section should be almost vanishing<sup>4</sup> and the L=2 component would be expected to dominate the cross-section. Since the L=2 contribution fits the angular distribution poorly,<sup>1</sup> the  $^{14}\text{N}(p,p')^{14}\text{N}^*(\text{Ex}=2.31)$ ,  $1^+(T=0)$  to  $0^+(T=1)$  reaction is a good case for which to consider the effects of a possible tensor component of the effective interaction.

To explore tensor effects in the effective two-body interaction and possible energy dependences 29.8, 36.6, and 40.0 MeV protons from the MSU Sector-Focussed Cyclotron were scattered from  $^{14}\text{N}$  targets and cross-sections for the excitation of the 2.31 and 3.95 states in  $^{14}\text{N}$  and elastic scattering were obtained. Most of the 28.9 MeV data and the forward angle points of the 36.6 and 40.0 MeV elastic angular distributions were obtained using gas targets and silicon solid state detectors. The 36.6 and 40.0 MeV data and check points for the 2.31, 29.8 MeV angular distribution were obtained using targets of melamine evaporated on carbon foil backings in conjunction with the MSU Enge split-pole spectrograph and a 300  $\mu$  thick, 3.0 cm long position sensitive solid state detector. The gas cell data was taken with a  $\Delta E, E$  detector telescope consisting of a 500  $\mu$  thick surface barrier silicon detector and a 5000  $\mu$  Si(Li) back detector. The  $\Delta E, E$  signal pairs from particles of different masses are separated into different mass bands and energy spectra by the code TOOTSIE<sup>5</sup> running in the Sigma-7 computer. The position sensitive detector data was acquired through the XE/E option of TOOTSIE. Here two signals are obtained from the detector. One is proportional to the product of the position of the incident particle along the face of the detector and the energy lost by the particle and the other proportional only to the energy lost. The code does the numerical division necessary to define the particles' incident position. Point to point normalization of the spectrograph data was done by means of a 5000 mm Si(Li) detector used as a monitor, while overall normalization was obtained from the gas cell data.

The angular distributions for the elastically scattered protons and the reactions to the 2.31

and 3.95 states in  $^{14}\text{N}$  for 29.8, 36.6 and 40.0 MeV incident protons are given in Figs. 1, 2, and 3. The errors shown on the data points are preliminary estimates of the total errors. The elastic cross-sections should be good to within 5%. A problem particular to the 2.31 angular distribution for 29.8 MeV incident protons taken with the E, E silicon detector telescope is the excitation of the 1.78 MeV state of  $^{28}\text{Si}$  by inelastic proton scattering in the solid state detectors. Figure 4 is one of the spectra taken in the spectrograph.

A good bit of effort has gone into finding optical model parameters for the elastic scattering angular distributions. Using GIBELUMP, an optical model search code,<sup>6</sup> and starting with parameters similar to those used by van Oers and Cameron<sup>7</sup> to fit p- $^{16}\text{O}$  elastic scattering from 23-53 MeV, the optical model parameters in Table 1 were obtained. The explicit optical potential used was:

$$U(r) = U_c - V_R f_R(x) + \left(\frac{\hbar}{2m_p c}\right)^2 (V_s + iW_s) \vec{L} \cdot \vec{\sigma} \frac{1}{r} \frac{d}{dr} f_s(x)$$

$$-i[W_s - 4W_D \frac{d}{dx_I}] f_I(x). \text{ Where } U_c \text{ is the potential of a uniformly charged sphere of radius } r_c A^{1/3}.$$

$$f(x) = (1 - e^{-x})^{-1} \quad x = \frac{r-R}{a} \quad R = r_0 A^{1/3}$$

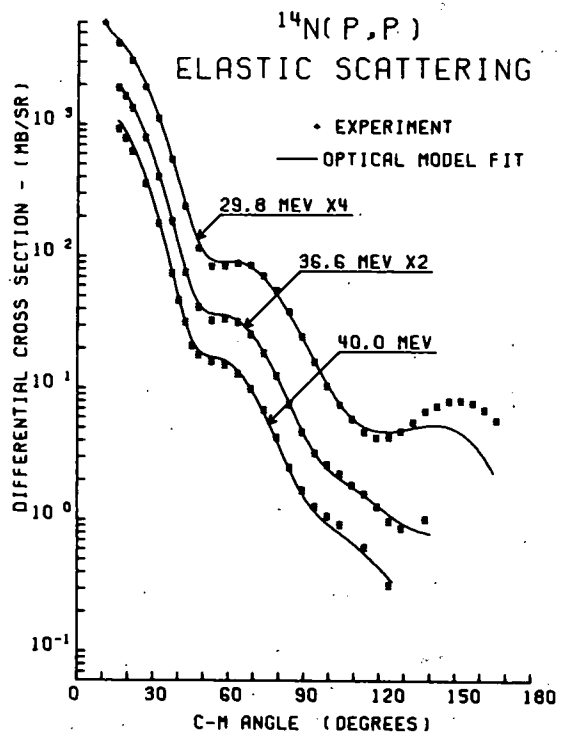


Figure 1

The hope was to fit 24.9, 29.8, 36.6 and 40.0 MeV p- $^{14}\text{N}$  elastic scattering data with average real and imaginary well geometries while the spin-orbit well geometry was set equal to the real.

geometry. The geometry used was  $R_R=R_S=1.133\text{fm}$ ,  $A_R=A_S=0.6515\text{fm}$ ,  $R_I=1.345\text{fm}$ , and  $A_I=0.5090\text{fm}$ . The fits in Fig. 1 were obtained with slightly different parameters than those in Table 1. The final fits whose parameters are in Table 1 were actually better than shown in Fig. 1 especially at forward angles for 40.0 MeV.

Table 1

$E_{\text{LAB}}$ (MeV)	$V_R$ (MeV)	$W_S$ (MeV)	$W_O$ (MeV)	$V_S$ (MeV)	$\chi^2/N$
24.9	51.36	1.56	4.75	766.0	4.2
29.8	48.50	2.65	3.52	959.1	4.7
36.6	46.45	6.26	1.63	1012.6	1.2
40.0	43.84	5.74	2.07	1555.2	0.56

The transition to the 2.31 state will be analyzed using a microscopic DWBA code (DWBA 70 by Raynal and Schaeffer) in which exchange effects as well as the tensor and L·S interactions may be included.

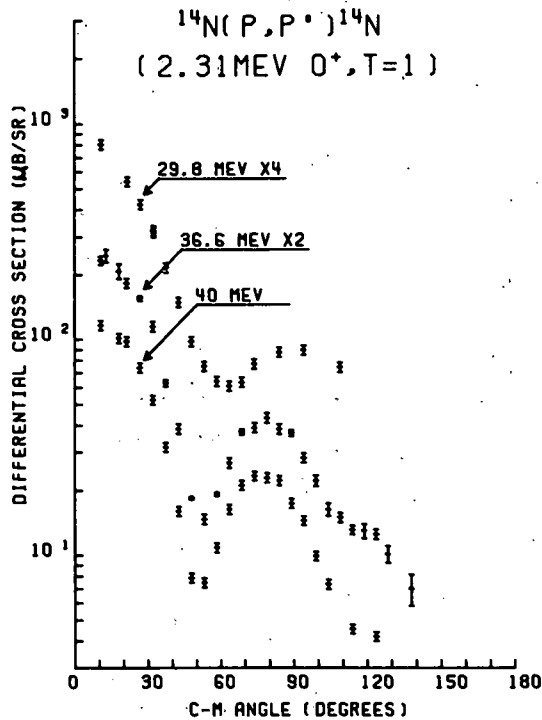


Figure 2

References

- G.M. Crowley, S.M. Austin, and W. Benenson, and V.A. Madsen, F.A. Schmittroth and M.J. Stomp, Phys. Letters 32B, 92(1970).
- J.L. Esceidie, A. Tarrats, and J. Raynal Proceedings of the Third International Symposium on Polarization Phenomena in Nuclear Reactions edited by H.H. Barschall and W. Haeberti (The University of Wisconsin Press) p. 705-707.

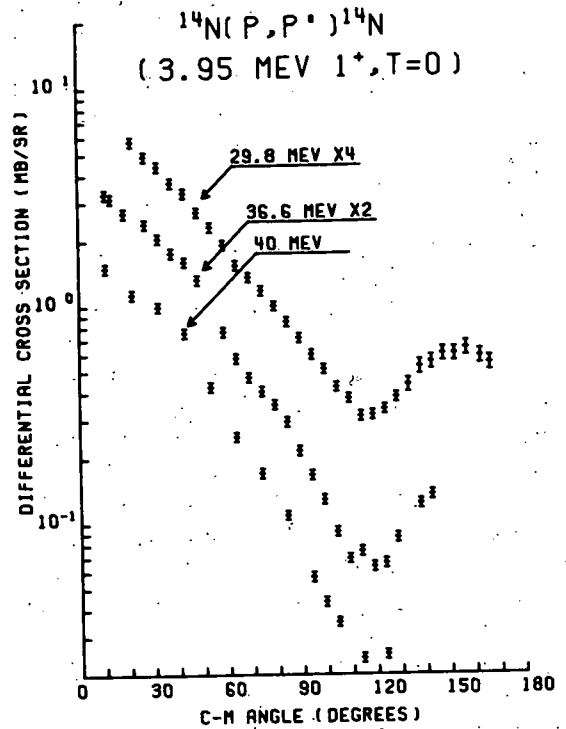


Figure 3

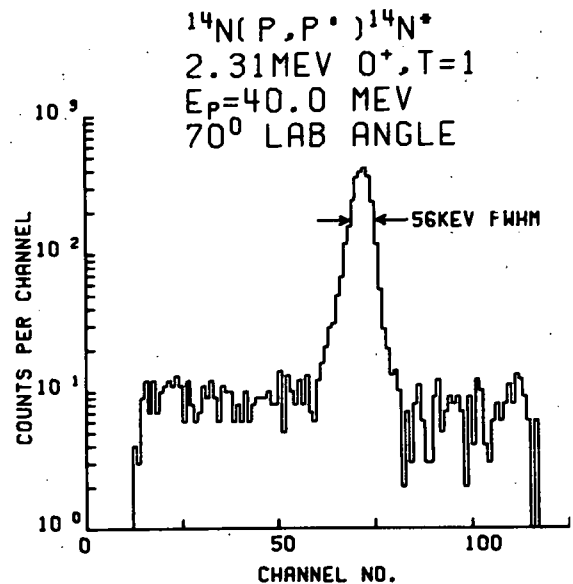


Figure 4

- C. Wong, J.D. Anderson, V.A. Madsen, F.A. Schmittroth and H.J. Stomp, Phys. Rev. C3, 1904(1971).
- C. Wong, J.D. Anderson, J. McClure, B. Pohl, V.A. Madsen, F.A. Schmittroth, Phys. Rev. 160, 769(1967).
- D.L. Bayer, MSUCL-31 (MSU, East Lansing, Michigan) (1971).
- Written by F.G. Perey and modified by R.M. Haybron.
- W.T.H. van Oers and J.M. Cameron, Phys. Rev. 184, 1061(1969).



Inelastic Proton Scattering on Zr at 40 MeV and Monopole Transitions  
 R.A. Hinrichs, B.M. Freedom,\* and D. Larson

We have initiated a study of inelastic proton scattering on the Zr isotopes at 40 MeV with a special interest in the excitation of the well known excited  $0^+$  states in these nuclei. Such  $0^+$  to  $0^+$  transitions in the Zr isotopes have only been observed at much lower energies<sup>1</sup> (12.7 MeV); a study of these monopole transitions is particularly interesting in that their angular distributions are quite sensitive to the radial shape of the interaction form factor. Core polarization effects should also not cloud a microscopic description of the interaction as first order monopole collective oscillations of the core should be zero.

Data has been taken so far on  $^{90,92}\text{Zr}$  at angles from  $10^\circ$  to  $120^\circ$  using plates in our Enge split-pole spectrograph. Long and short exposures were taken at each angle to study the  $0^+$  as well as other more strongly excited states. Figure 1 shows a partial angular distribution for excitation of the first excited  $0^+$  state in  $^{90}\text{Zr}$  at 1.75 MeV. Pronounced structure is seen, as well as the smallness of the cross-section.

Data for the sequence of levels  $2^+$ ,  $4^+$ ,  $6^+$ ,  $8^+$  (due to re-coupling of two  $g_{9/2}$  protons) has also been obtained. This sequence is interesting as it can provide information on the importance of exchange and spin-orbit effects as a function of angular momentum transfer. Analysis along these lines is being carried out with the use of the recently acquired computer code DWBA-70, written by R. Schaeffer and J. Raynal.

Reference

1. J.K. Dickens, E. Eichler, and G.R. Satchler, Phys. Rev. 168, 1355(1968).

\* Univ. of South Carolina, Columbia, S.C.

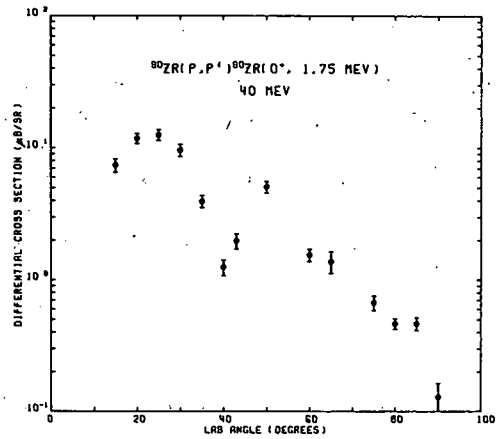


Fig. 1 Angular distribution for the reaction  $^{90}\text{Zr}(p,p')$  at a bombarding energy of 40 MeV for excitation of the  $0^+$  state at 1.75 MeV.

We are using 30 MeV protons to study inelastic scattering from nuclei with 82 neutrons. There are seven such stable nuclei, with four to twelve valence protons outside the Z=50 shell. Since the density of states is quite high, we are using the specular system developed by Blosser et al. which allows us to routinely obtain resolutions of 10 keV or less at 30 MeV. The specular system is basically a feedback system which operates on the elastic peak. It regulates the magnetic field of the spectograph in a compensating manner to keep the elastic peak at a constant point on the focal plane. During setup it is used to minimize the line widths of the peaks of the scattered particles. Dispersion matching is used to compensate for the beam energy spread, thus eliminating the need for slits to minimize the beam energy resolution. Beam currents on target were 100 nA for Ba<sup>138</sup> and 900 nA for Pr<sup>141</sup> and Sm<sup>144</sup>.

Targets were made by vacuum evaporation of isotopically enriched Ba<sup>138</sup>, Sm<sup>144</sup> and natural Pr<sup>141</sup> onto 20 μg/cm<sup>2</sup> carbon foils. The targets were stored and transferred under vacuum to prevent oxidation. Typical target thicknesses ranged from 50-300 μg/cm<sup>2</sup>.

Data on Ba<sup>138</sup>, Pr<sup>141</sup> and Sm<sup>144</sup> is now being analyzed. Typical spectra are shown in Fig. 1-2. Figure 1 shows a spectrum from Ba<sup>138</sup> taken at a lab angle of 35°. The resolution here is 11 keV fwhm. The elastic peak is not shown. The first excited 2<sup>+</sup> state at 1.436, and the 3<sup>-</sup> at 2.880 MeV were uncountable on this plate. The 4<sup>+</sup> state at 1.899

is followed by a state at 2.09 MeV which has not been seen in gamma ray work on this nucleus, but has been seen in La<sup>139</sup> (d,He<sup>3</sup>).<sup>2</sup> A 6<sup>+</sup> assignment for this state is consistent with the shell-model calculations of Wildenthal,<sup>3</sup> both with respect to the energy position and the spectroscopic factors for proton pickup.

Figure 2 shows a spectrum from Sm<sup>144</sup> taken at a lab angle of 40°. The resolution is 7 keV fwhm. The elastic peak is not shown. The first excited 2<sup>+</sup> state at 1.67 and the 3<sup>-</sup> at 1.82 MeV were uncountable on this plate. The strong state in the region of 2.43 MeV is probably the 2<sup>+</sup> seen by Barker and Hiebert<sup>4</sup> and is not the 0<sup>+</sup> level which is known at 2.48 MeV.<sup>5</sup>

Figure 3 shows that the cross-sections for the first 2<sup>+</sup> excited states in Ba<sup>138</sup> and Sm<sup>144</sup> are nearly identical in shape and differ in magnitude by less than 10%. In Fig. 4 we see that for the first 3<sup>-</sup> states in these nuclei the shapes are again the same, but the Sm<sup>144</sup> cross-section is 25% larger than the Ba<sup>138</sup> cross-section.

Future work includes extending the experiments to the remaining N=82 nuclei, and doing microscopic DWBA calculations using the wave functions of Wildenthal with realistic forces.

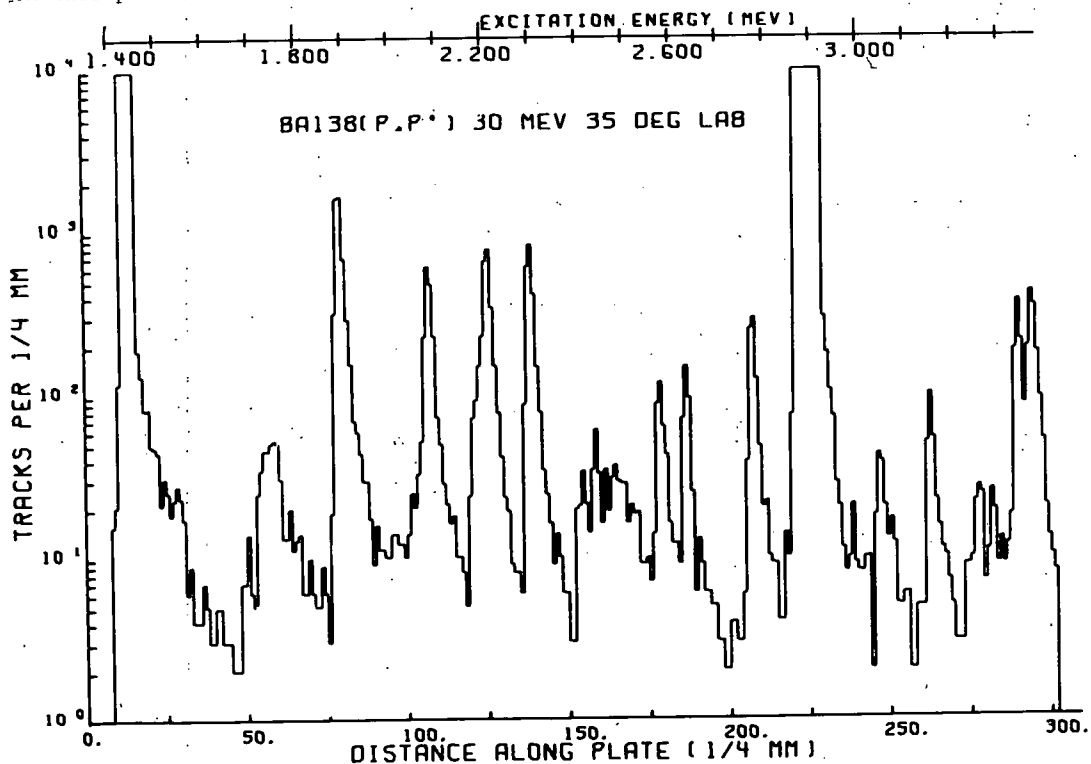


Figure 1

REFERENCES

1. H.G. Blosser et al., Nucl. Instr. and Meth. 91(1971)61.
2. W.P. Jones, L.W. Borgman, K.T. Hecht, John Bardwick, and W.C. Parkinson, Phys. Rev. 4, (1971)580.
3. B.H. Wildenthal, to be published.
4. J.H. Barker, J.C. Hiebert, to be published.
5. J.S. Geiger, R.L. Graham, Ark. Fys. 36(1967)191.

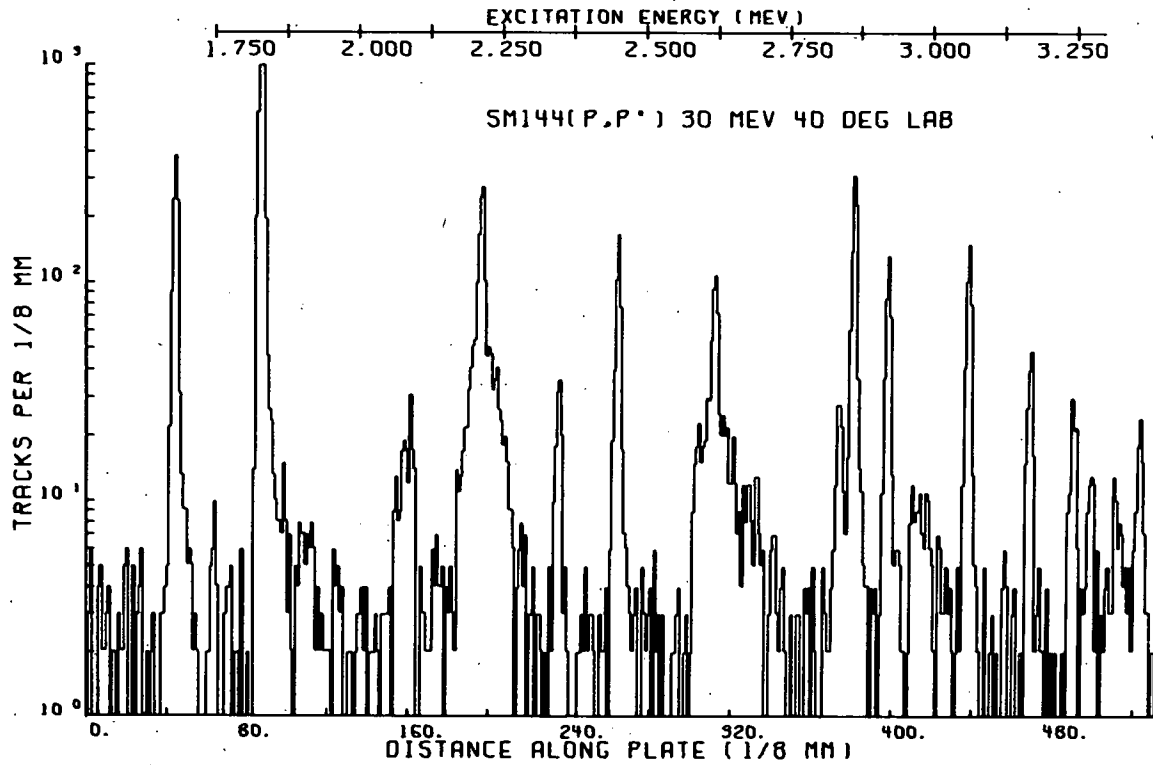


Figure 2

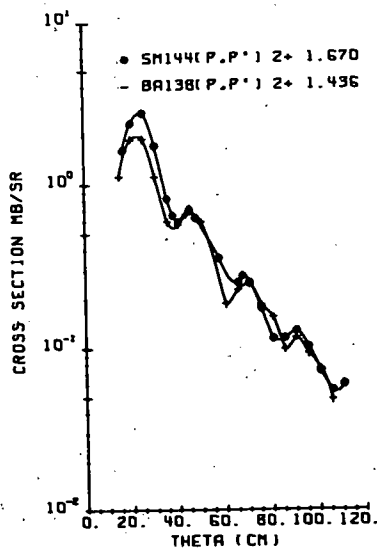


Figure 3

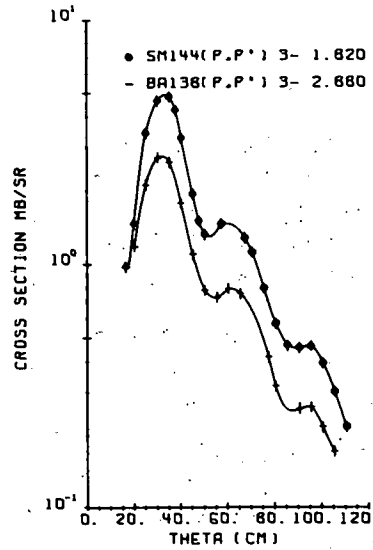


Figure 4

Information on both nuclear structure and nuclear reaction mechanisms can be obtained from inelastic scattering experiments. However, experimental difficulties have limited the range over which various models and theories can be tested effectively. The shell-model structure of many Pb and Bi isotopes has been well established and good predictions of scattering and related phenomena have been given via a microscopic description of these nuclei. Also, the weak coupling model has seen success when applied to low-lying multiplets in this region and it would be of interest to extend this treatment to higher energies. Inelastic scattering also gives information on the collective properties of the predominantly single particle states in the odd A isotopes. With facilities for ultra-high resolution nuclear experiments, the Michigan State University Cyclotron Laboratory allows previous experimental difficulties to be overcome.

Therefore, much new information can now be obtained by a study of proton inelastic scattering from  $^{206}\text{Pb}$ ,  $^{207}\text{Pb}$ ,  $^{208}\text{Pb}$ , and  $^{209}\text{Bi}$ . While an inelastic study of the three lead isotopes has been done,<sup>1</sup> resolution and choice of bombarding energy were not optimum. Because of the MSU accelerator stability and predicted sensitivity of the data at this energy, the experiment will be performed at 40 MeV incident energy. With the use of the ultra-high resolution spectrometer system<sup>2</sup> recently developed at MSU, resolution of about 5 keV has been obtained.

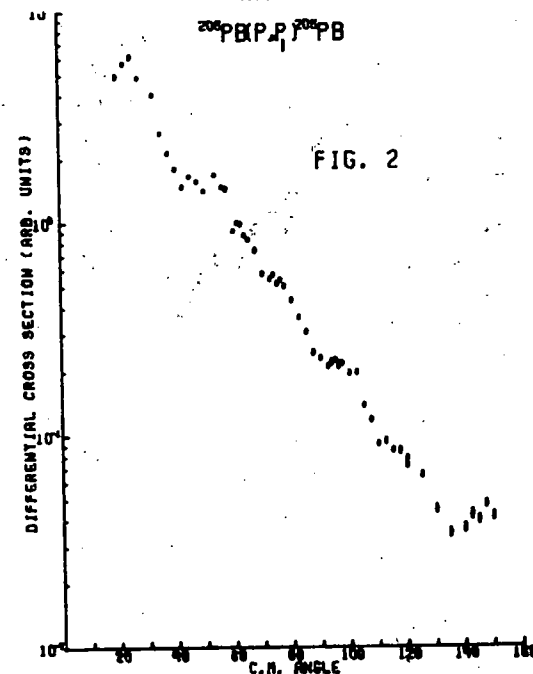
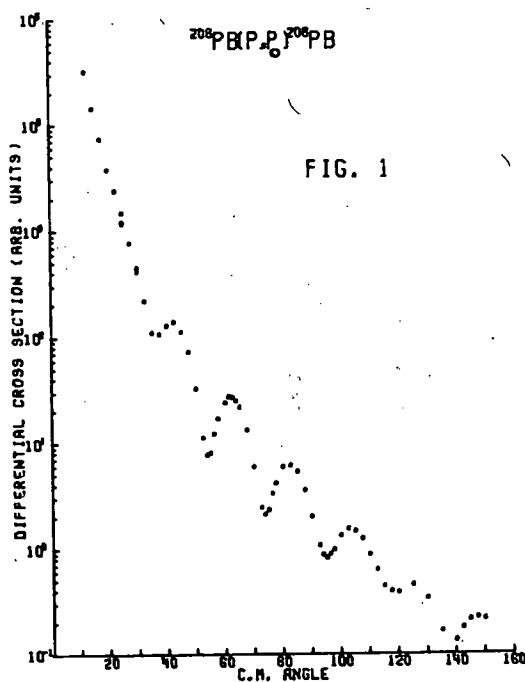
Preliminary data have been taken at a few angles on  $^{207}\text{Pb}$  and  $^{208}\text{Pb}$  in the Enge spectrograph using photographic plates. Such data provides necessary information regarding exposure length versus total charge collected and their relation to plate fogging. The targets used in this preliminary run were made by vacuum evaporation of isotopically enriched lead on a thin carbon-formvar backing. It was found necessary to subject the backing to a glow discharge (exposure to low pressure, low energy ionized gas bombardment) to insure adhesion of the Pb. The targets were stored in reasonable vacuum to prevent unnecessary oxygen contamination. Another study is being made to determine the optimum relationship between target thickness, counting rate, and energy resolution.

Most of the reaction theories to be compared with the final inelastic scattering data require optical model parameters which are, of course, obtained from elastic scattering angular distributions. Also for a normalization aid in the inelastic experiments and to give data on the more strongly excited states, we are currently

using the 40" scattering chamber and a  $\Delta E-E$  detector telescope arrangement using two 5 mm Si(Li) detectors to study proton scattering at 40 MeV. The angular distributions for scattering from the ground state and first excited  $3^-$  state of  $^{208}\text{Pb}$  are shown respectively. In Figs. 1 and 2, similar studies on  $^{206}\text{Pb}$ ,  $^{207}\text{Pb}$ , and  $^{209}\text{Bi}$  are planned.

## References

1. G. Vallois, Thesis, CEN-Saclay, Report CEA-R-3500 (unpublished).
2. H.G. Blosser, G.M. Crawley, R. deForest, E. Kashy, and B.H. Wildenthal, Nucl. Instr. and Methods 91, 61(1971).



Studies of the (p,n̄p) reaction allow the determination of the position and in some cases the width of the isobaric analogue state populated in the (p,n) reaction without the difficulty of neutron detection. In principle proton decay widths can also be measured but this is usually difficult because of uncertainties in the (p,n) cross section. This situation is improved in the lead region where decay to more than one final state is observed and therefore relative proton decay widths can be obtained. Another advantage of the (p,n̄p) reaction is that can be used to study nuclei not readily reached by resonant elastic and inelastic scattering.

Earlier measurements of the partial widths for decay of the IAS in  $^{208}\text{Bi}$  had shown agreement between the resonance measurements<sup>1</sup> and the (p,n̄p) experiment.<sup>2</sup> However measurements of the  $^{209}\text{Bi}(p,n̄p)$  reaction<sup>3</sup> gave relative proton widths for the IAS in  $^{209}\text{Po}$  which were significantly different from the measurements in  $^{208}\text{Bi}$ . This discrepancy encouraged us to repeat the  $^{208}\text{Pb}(p,n̄p)$  experiment as a check on the earlier measurement. In addition, the (p,n̄p) reaction on  $^{206}\text{Pb}$ ,  $^{207}\text{Pb}$  was also studied.

The experiment used protons of various energies from 21.3 to 35 MeV from the Michigan State Isochronous Cyclotron. A standard counter telescope of cooled silicon detectors was used to detect the protons. Deuteron spectra were taken simultaneously since these reach the same final nuclei and help provide an energy calibration. The deuteron resolution also gives an accurate check of the target thickness measurements. Spectra were taken at many angles to avoid contaminant peaks and to check kinematic effects.<sup>3</sup>

The results of the Coulomb energy measurements are shown in Fig. 1 together with the results of other Coulomb energy measurements in the Pb isotopes. These data are plotted relative to the predictions of Fox and Long<sup>4</sup> which appear to be a reasonable approximation although the experimental values are consistently lower than the predictions. It should be noted that the measurements for  $^{206}\text{Pb}$  and  $^{209}\text{Bi}$  cannot be obtained from resonance measurements since no suitable target is available.

A spectrum of protons from  $^{208}\text{Pb}$  at a laboratory angle of  $158^\circ$  is shown in Fig. 2. The low lying excited states of  $^{208}\text{Pb}$  including the ground state have been excluded from the figure. The peaks observed correspond to decays to the first three single particle states in  $^{207}\text{Pb}$  with  $J^\pi$  of  $1/2^-$ ,  $5/2^-$ , and  $3/2^-$  respectively. It is clear that although the peaks are broad, presumably due to the intrinsic width of the IAS, the  $f_{5/2}$  state can be distinguished.

Similarly a proton spectrum from  $^{207}\text{Pb}$  showing the large  $\bar{p}$  feature at backward angles is shown in Fig. 3. The situation is more complex here since decays take place to a number of excited states of varying  $J^\pi$  too close in energy to be distinguished. A feature of this spectrum is the large width of the  $\bar{p}$  peaks which are significantly broader than the  $^{208}\text{Pb}$  case.

In contrast, the  $\bar{p}$  peaks from the  $^{206}\text{Pb}(p,n̄p)$  reaction shown in Fig. 4 are narrower than even the  $^{208}\text{Pb}$  case, the decays here going again to the hole states in  $^{205}\text{Pb}$  with spins  $5/2^-$  (plus possibly  $1/2^-$ ) and the  $3/2^-$  state at 262 keV. The  $^{206}\text{Pb}$  target has more impurities and care must be taken to position the  $\bar{p}$  peak in a reasonably clear region of the spectrum by suitable choice of bombarding energy and observation angle.

The yield for proton decay to a particular final state (or multiplet in the case of  $^{209}\text{Bi}$ ) of the residual nucleus is given by

$$\frac{d\sigma}{d\Omega}(\bar{p}) \propto \sum_i \frac{\Gamma_i p_i}{(E-E_i)^2 + 1/4\Gamma^2}$$

where in general the sum is over all members of a multiplet. Penetrability corrections are made to the partial decay widths ( $\Gamma_i$ ) appearing in the equation. Corrections for target thickness and kinematics are also folded into the fitting equation. A smooth background was substrated from the original experimental spectrum as were contributions from impurity peaks. The remaining spectrum was fitted using a least squares method searching on the relative partial widths and gridding on the total width.

An example of such a fit is shown in Fig. 5. Although the total width is not well determined by the fitting procedure, a smaller  $\chi^2$  is ob-

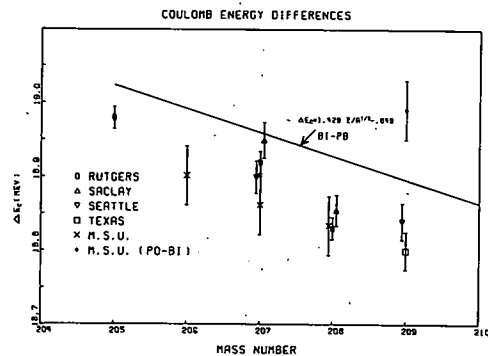


Figure 1

tained for total widths near 380 keV rather than the value of 22 keV obtained from resonance measurements.<sup>1</sup> However the partial widths extracted are relatively stable for a range of total widths. These calculations are still proceeding and the indications are that the earlier measurements did indeed give too low a value for the  $f_{5/2}$  decay width although reasonable agreement is obtained with more recent measurements.

References

1. G.H. Leng and G.M. Temmer, Phys. Letters 24B, 370(1967) and B.L. Anderson, J.P. Bondorf, and B.S. Madsen, Phys. Letters 22, 651(1966).
2. G.J. Igo, C.A. Whitten, Jr., Lean-Luc Perreouod, J.W. Verba, T.J. Woods, J.C. Young, and L. Welch, Phys. Rev. Letters 22, 724(1969).
3. G.M. Crawley, W. Benenson, P.S. Miller, D.L. Bayer, R. St.Onge, and A. Kromminga, Phys. Rev. 2, 1071(1970).
4. J.D. Fox, and D.D. Long, FSU preprint 1969 and D.D. Long, P. Richard, C.F. Moore and J.D. Fox, Phys. Rev. 149, 906(1966).
5. P.S. Miller, Ph.D. Thesis, Princeton University 1968 (unpublished), P.S. Miller and G.T. Garvey, Nucl. Phys. A163, 65(1971).

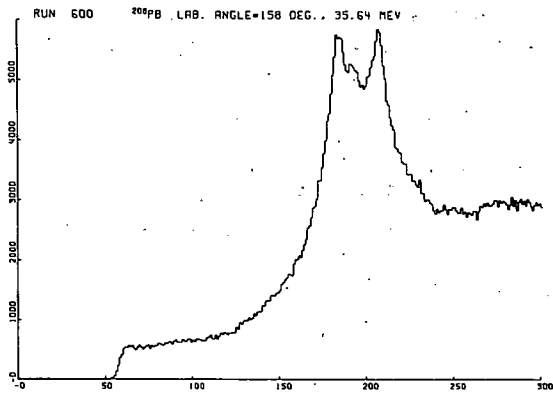


Figure 2

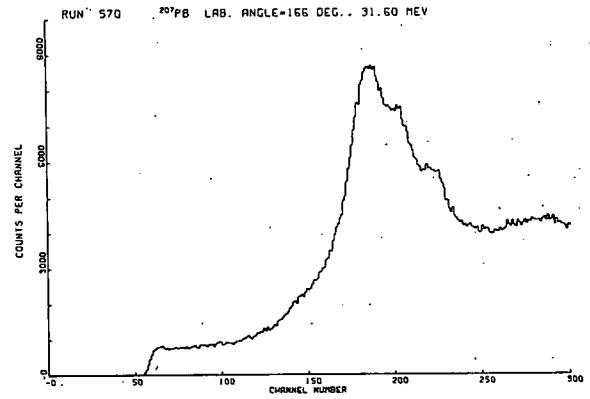


Figure 3

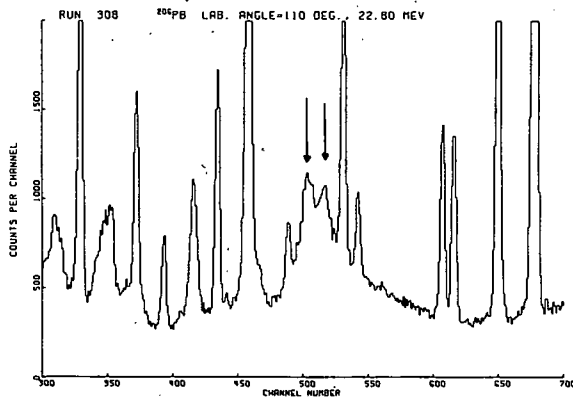


Figure 4

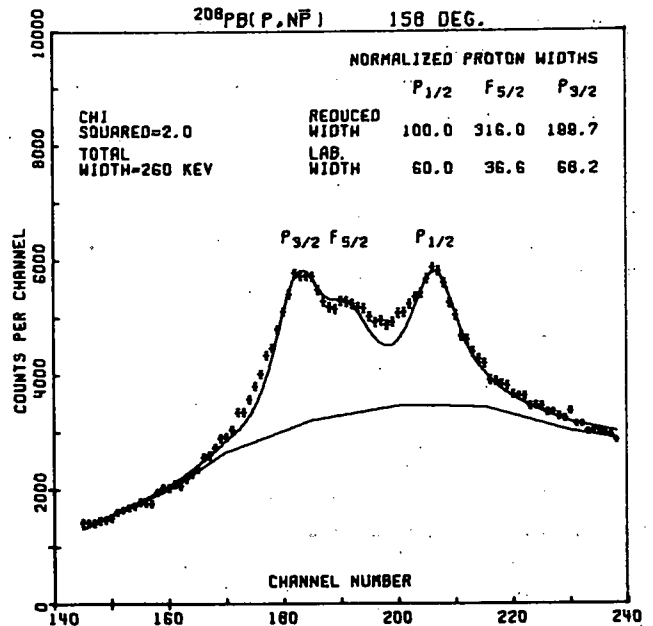


Figure 5

PROTON SPIN-FLIP

R.H. Howell and A.I. Galonsky

Experiments are being conducted to measure the proton spin-flip in inelastic scattering using the (p,p'γ) coincidence technique. Measurements have recently been completed for the following reactions.

	Ep	Ex	J <sup>π</sup>
$^{120}\text{Sn}(p,p'\gamma)^{120}\text{Sn}^*$	30 MeV	1.17 MeV	2 <sup>+</sup>
$^{124}\text{Sn}(p,p'\gamma)^{124}\text{Sn}^*$	30 MeV	1.13 MeV	2 <sup>+</sup>

The scattering chamber has been described.<sup>1</sup> A new lead shield with motor drive has been added to the gamma-ray detector assembly.

Targets were isotopically enriched foils of 5 mg/cm<sup>2</sup> for  $^{124}\text{Sn}$  and 10 mg/cm<sup>2</sup> for  $^{120}\text{Sn}$ . Detectors were a 2 inch diameter by 3 inch long NaI(Tl) gamma-ray detector and a cooled 500mm<sup>2</sup>x5mm Si(Li) particle detector.

An electronics system was developed to collect coincidence events as a 2-dimensional function of proton energy and gamma-ray pulse height.

The data are seen in Figs. 1 and 2. Finite solid angle corrections were calculated as a function of proton scattering angle and relative sub-state populations with a published formula.<sup>2</sup>

Optical Model parameters for all DWA calculations were taken from Becchetti and Greenlees.<sup>3</sup>

Collective-model DWA calculations were performed here with the code written by H. Sherif at the University of Washington. This code included the deformed spin-orbit part of the optical potential in the full Thomas form.<sup>4</sup> Varying the strength of the spin-orbit deformation effected the spin-flip fits slightly and produced much better fits to published asymmetry data.<sup>5</sup> (See Fig. 3.)

Microscopic DWA calculations were performed with the real, central Kallio-Kolltveit interaction and the quasi-particle wave function of Clement and Baranger.<sup>6</sup> Fits to the spin-flip were acceptable but fits to the asymmetry were not as good as in the collective case (see Fig. 4). Addition of the imaginary part of the collective model improves the asymmetry fit while having little effect on the spin-flip fits. Addition of the imaginary term also showed improvement to the fits to the cross section (see Fig. 5).

REFERENCES

1. J.J. Kolata and A. Galonsky, Phys. Rev. 182, 1073(1969).
2. H.H. Hippelein, R. Jahr, J.A.H. Pflieger, F. Rott, and H.M. Vieth, Nucl. Phys. A142, 369(1970).
3. E.D. Becchetti and G.W. Greenlees, Phys. Rev. 182, 1190(1969).

4. H. Sherif and J.S. Blair, Phys. Letters 26B, 489(1968); H. Sherif, Thesis, Univ. of Washington, 1968 (unpublished).
5. O. Karban, P.D. Greaves, V. Hnizdo, J. Lowe, and G.W. Greenlees, Nucl. Phys. A147, 461 (1970).
6. D.M. Clement and E.U. Baranger, Nucl. Phys. A120, (1968) and private communication.

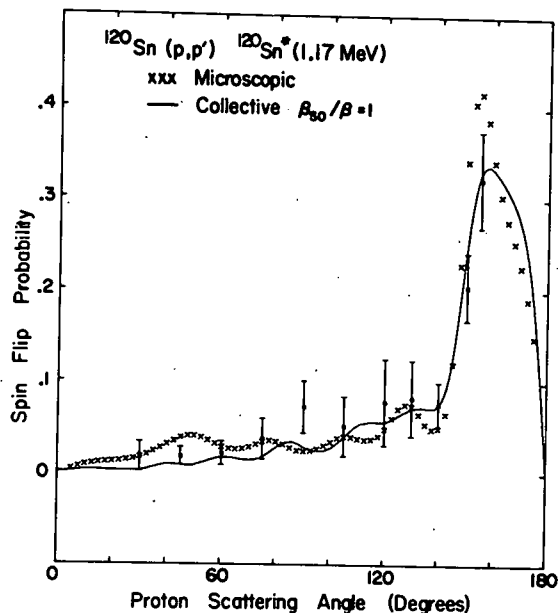


Fig. 1 Spin-flip probability for  $^{124}\text{Sn}$ . The data have been corrected for the use of finite detector apertures. The curves are the collective model with a full Thomas term (solid line) and the microscopic model with the KK force (x's).

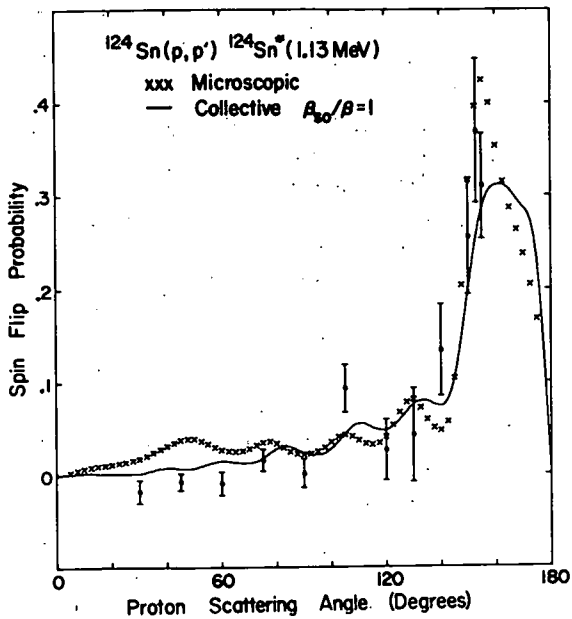


Fig. 2 Spin-flip probability for  $^{124}\text{Sn}$ . The correction for finite detector apertures reduces the values of the data at forward angles. The curves are the collective model with a full Thomas term (solid line) and the microscopic model with the KK force ('x's').

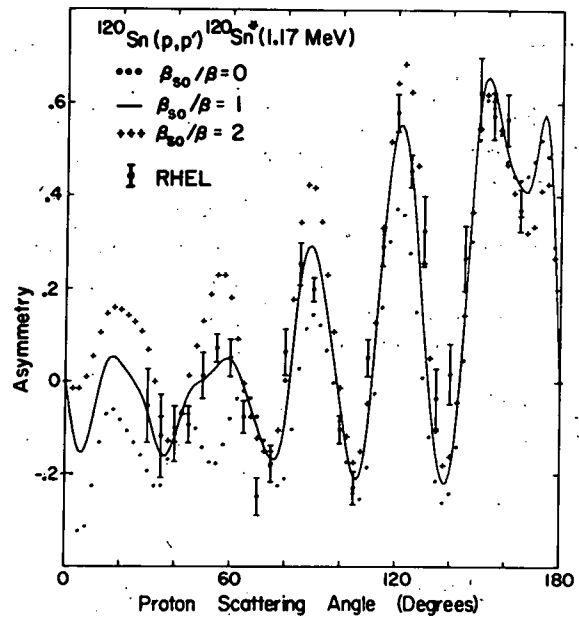


Fig. 3 Collective model calculations of the asymmetry with the full Thomas term. Increasing the strength of the spin orbit deformation from 0 to 2 has the greatest effect at forward angles where the central collective model is in least agreement with the data.

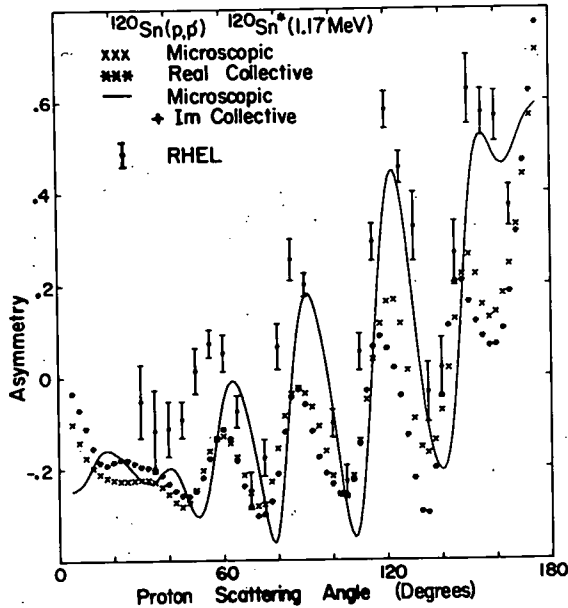


Fig. 4 The fits to the asymmetry with the real microscopic force ('x's') and real part of the collective model ('star's') are degraded at all angles. Adding an imaginary part to the microscopic form factor (solid line) improves the fit over most of the angular range.

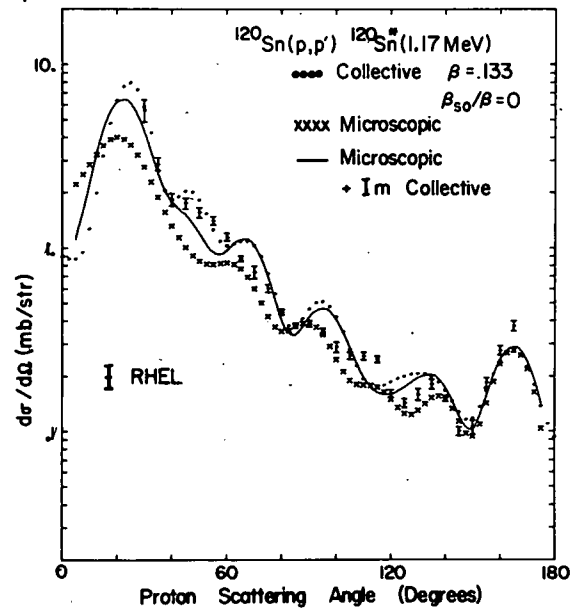


Fig. 5 Adding an imaginary part to the real microscopic form factor (solid line) improves the fit to the cross-section over that of the real microscopic form factor alone ('x's'). The complex collective model (dots) without spin orbit deformation also fits the data well.



The proton-nucleus potential is more strongly attractive than the neutron-nucleus potential. This "asymmetry effect" can be described by a term in the scattering potential proportional to  $\frac{N-Z}{A}$  or, alternatively, by one proportional to  $\frac{\vec{t} \cdot \vec{T}}{A}$ , where  $\vec{t}$  and  $\vec{T}$  are the nucleon and nucleus isospin vectors, respectively. Attempts to determine both the shape and strength of the asymmetry potential by systematic analysis of nucleon scattering data have not produced entirely conclusive results; the basic reason being that the asymmetry potential is a small part of the total potential responsible for scattering.

In (p,n) reactions between analogue states, however, the asymmetry potential is the entire potential responsible for the transition. To begin our study we have measured (p,n) angular distributions on aluminum with protons of 22, 30 and 40 MeV. In this case the analogue transition leads to the ground state of the residual nucleus,  $^{27}\text{Si}$ . The data are shown in the figure along with DWBA fits computed with the code JULIE using a derivative surface form factor and optical model parameters of Perey<sup>1</sup> (22 and 30 MeV) and of Fricke and Satchler<sup>2</sup> (40 MeV). A pure volume interaction does not give a good fit at any of the three energies.

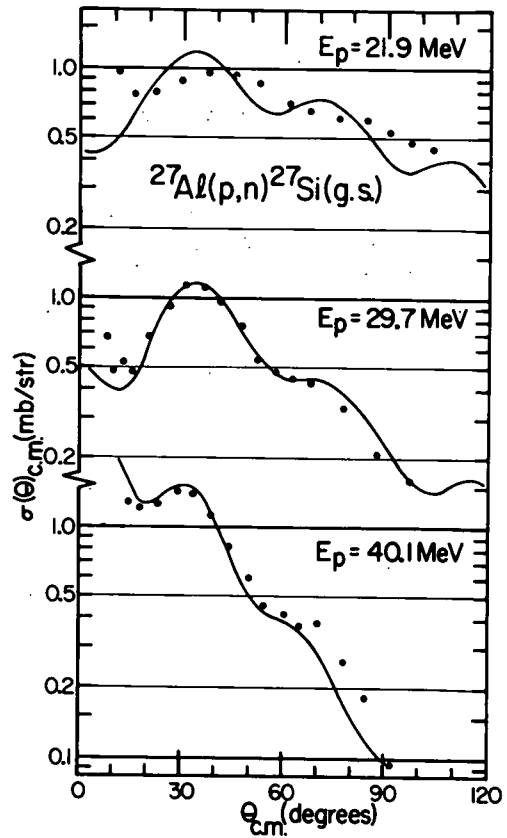
The eyeball normalizations in the figure of theory to experiment are for strengths of the surface interaction  $V_1'$  given in the table below. The asymmetry potential most commonly used in elastic scattering analyses has a volume shape with a depth  $V_1 \approx 27$  MeV. From the  $V_1^n$  ambiguity in elastic scattering, we can relate an effective volume strength,  $V_1(\text{eff})$ , to our surface strengths through the relation  $V_1(\text{eff}) = \frac{na}{R} V_1'$ . The values of  $V_1(\text{eff})$  in the table are for  $n=2$ .

$E_p$	$V_1'$	$V_1(\text{eff})$
22	80	28
30	67	23
40	71	28

All values in MeV.

References

1. F.G. Perey, Phys. Rev. **131**, 745(1963).
2. M.P. Fricke and G.R. Satchler, Phys. Rev. **139**, B567(1965).



A ghost anomaly is a distortion of the line profile of a nuclear level caused by the occurrence of a breakup threshold near the energy of the level. The ground state of  ${}^8\text{Be}$ , which has a measured decay width in the range 6 to 8 eV, possesses an interesting ghost because the state lies just 92 keV above the  $\alpha$ - $\alpha$  breakup threshold. The spectrum of deuterons from the  ${}^9\text{Be}(p,d){}^8\text{Be}$  reaction in Fig. 1 shows this ghost which is the broad group extending from near the ground state to beyond 2 MeV excitation energy. This anomaly is a feature of the ground state line shape, so it cannot vary with respect to the main peak except in so far as the line shape may be further distorted by interference from other  $0^+$  states. The ghost can be calculated by a reaction theory, such as R-matrix theory, which includes the effects of the barrier and the interference of several levels on the line shape of the ground state.<sup>1</sup> The ghost line shape can help to constrain the R-matrix parameters for the  $0^+$  states used to fit  $\alpha$ - $\alpha$  scattering phase shifts. The ghost is especially sensitive to the channel radius  $a_0$ , whose value is ambiguous in the fits to scattering data ( $5.5 \text{ fm} \leq a_0 \leq 7.0 \text{ fm}$ ).<sup>2</sup> An earlier measurement of the ghost by the  ${}^8\text{Be}(p,d)$  reaction<sup>3</sup> was done at 5.2 MeV bombarding energy where the compound nucleus contribution to the cross section may not be negligible. This weakened the conclusion that could be drawn because of practical difficulties in the analysis. The  ${}^8\text{Be}$  ghost has been investigated recently by several different reactions<sup>4</sup> at low energies, but only a preliminary theoretical analysis has been performed on the data. We are measuring the ghost line shape near 40 MeV bombarding energy where the direct (p,d) amplitude is expected to predominate over compound nucleus.

The deuterons from the natural Be target (thickness 1.8 mg/cm<sup>2</sup>) enter the Enge split-pole magnetic spectrograph and are detected in the focal plane. Preliminary measurements of the line shape were made with 3cm- and 5cm-long position sensitive solid state detectors, but they required large corrections for efficiency variation and non-linearity of the detector response. In addition the short lengths made splicing together several runs a necessity and introduced normalization difficulties.

Nuclear emulsions were used to obtain the spectrum shown in Fig. 1. Due to the large dynamic range required to see both the ghost and the main peak, three exposures (for approximately 1, 10 and 100 microcoulombs of integrated beam current) were taken and the countable parts of each were scanned. Similar data were recorded at a laboratory angle of 15°.

Recently an experimental position sensitive gas proportional counter has been used successfully at 30 MeV bombarding energy (see Fig. 2). A practical model of this detector is under construction, and we intend to use it shortly to measure angular distributions of the ghost at several energies to try to verify the hypothesis that compound nuclear effects are negligible.

Analysis of the spectra using a 3 level approximation for the  $0^+$  and the  $2^+$  states will be performed as described elsewhere.<sup>5</sup>

#### References

1. F.C. Barker and P.B. Treacy, Nucl. Phys. **38**, 33(1962).
2. F.C. Barker, H.J. Hay, and P.B. Treacy, Aust. J. Phys. **21**, 239(1968).
3. H.J. Hay, E.F. Scarr, D.J. Sullivan, and P.B. Treacy, Aust. J. Phys. **20**, 59(1967).
4. E.H. Berkowitz, S.L. Marolt, A.A. Rollefson, C.P. Browne, B.A.P.S. **15**, 520(1970), and to be published.
5. P.S. Miller, G.M. Crawley, W.F. Steele, and F.C. Barker, B.A.P.S. **16**, 35(1971).

\* Australian National University, Canberra, Australia.

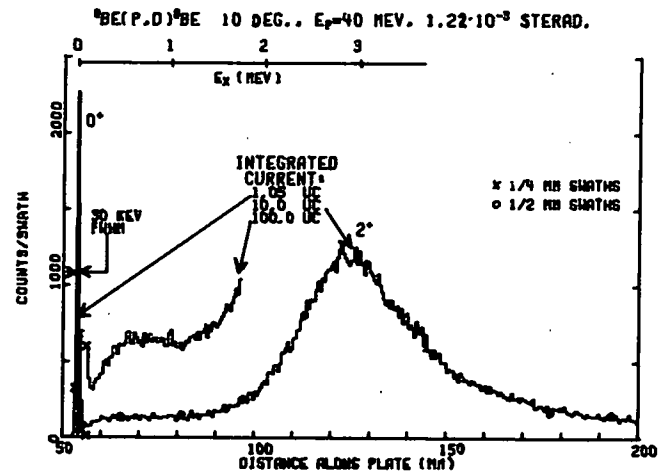


FIG. 1

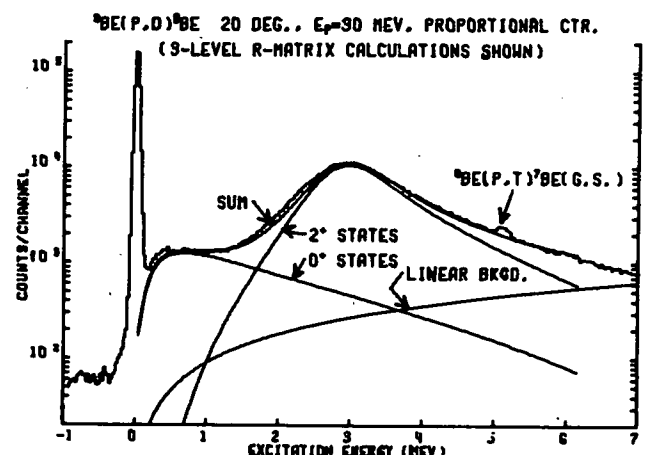


FIG. 2

Examination of the results of recent detailed shell-model theories<sup>1,2</sup> for the nuclei of the sd-shell (A=17-39) shows that nuclei with odd numbers of both neutrons and protons occupy pivotal positions in so far as evaluation of these theories is concerned. We are studying several such nuclei with the (p,d) reaction. Our experimental goals are to resolve and identify as many levels in the residual nuclei as possible and assign accurate excitation energies to them, and to measure the (p,d) angular distributions to very small angles so as to allow an unambiguous extraction of both  $l=0$  and  $l=2$  spectroscopic factors. The experiments are carried out with photographic plates and the split-pole spectrograph. Bombarding proton energies are 35 MeV. Targets of Na<sup>35</sup>Cl, Li<sup>35</sup>Cl, <sup>23</sup>Na, Na<sup>37</sup>Cl, and <sup>34</sup>S have been studied to date. Plate scanning and analysis of the energy level spectra have been completed for the Na and <sup>35</sup>Cl target data and DWBA analysis of these angular distributions is in progress. Representative spectra are shown in Fig. 1. The FWHM energy resolution for these data is approximately 14 keV. The energy levels we identify in <sup>34</sup>Cl and <sup>22</sup>Na are listed in Tables I and II, along with the results of gamma-ray and other charged particle studies. Our excitation energy assignments are obtained by making a small correction

to our absolute momentum vs. focal plane position calibration in order to produce an rms best fit to the set of  $\pm 1$  keV energy assignments available from Ge(Li) gamma-ray detector studies. We find that in order to simultaneously fit both the <sup>22</sup>Na and <sup>34</sup>Cl energies we must use a value  $Q[<sup>23</sup>Na(p,d)<sup>22</sup>Na]-Q[<sup>35</sup>Cl(p,d)<sup>34</sup>Cl] = +229$  keV rather than the value  $+218 \pm 9$  keV in the literature.<sup>3,4</sup>

References

1. E.C. Halbert, J.B. McGrory, B.H. Wildenthal, and S.P. Pandya, *Advances in Nuclear Physics*, Vol. 4.
2. B.H. Wildenthal, E.C. Halbert, J.B. McGrory, and T.T.S. Kuo, to be published in *Physical Review*.
3. C. Maples, G.W. Goth, and J. Cerny, *Nuclear Reaction Q-Values*, Lawrence Radiation Laboratory, Berkeley, California, 1966.
4. J.H.E. Mattauch, W. Thiele, and A.H. Wapstra, *Nuclear Physics* **67**, 32(1965).

Table II  
 Energy Levels in <sup>22</sup>Na

$E_x^a$ (MeV)	$E_x^d$ (MeV)	$E_x^e$ (MeV)
0.000	0.000	
0.583	0.583	
0.657	0.657	
0.891	0.891	
1.529	1.528	
	1.937	
1.950	1.952	
1.983	1.984	
2.210	2.211	
2.569	2.572	
2.968	2.969	
3.057	3.059	
3.518	3.521	
3.708	3.708	
3.943	3.944	
4.071	4.069	
4.295	4.294	
4.321	4.319	
4.361	4.360	
	4.466	
	4.522	
	4.583	
4.585	4.622	
4.625	4.708	
4.707	4.770	
4.773	4.770	
5.062	5.061	
5.100	5.099	
	5.117	
5.129		
5.173	5.165	
5.321	5.317	
5.441	5.446	5.440
5.606	5.605	5.605
5.726	5.734	
5.754	5.745	
	5.837	5.803
5.868	5.871	5.858
	5.938	
	5.953	
5.925		
5.964		
5.998	5.988	5.995
6.089	6.089	6.088
6.183	6.190	6.185
6.245	6.241	6.247
6.329	6.329	6.326
6.436	6.435	

Table I  
 Energy Levels in <sup>34</sup>Cl

$E_x^a$ (MeV)	$E_x^b$ (MeV)	$E_x^c$ (MeV)
0.000	0.000	0.000
0.147	0.146	0.147
0.462	0.461	0.461
0.667	0.666	0.666
1.232	1.230	1.229
1.886	1.888	1.886
		1.924
		2.157
2.156	2.158	
2.178	2.181	
2.374	2.377	
2.578		2.579
2.609	2.611	2.608
2.720	2.722	2.720
3.127		3.126
3.333		3.332
3.382		3.381
3.543	3.545	3.544
	3.601	
3.632	3.632	3.630
	3.771	3.771
3.860		
3.942		
3.965		
3.983	3.982	3.982
4.079	4.075	4.075
	4.137	4.143
4.149		
4.219		
4.331		
	4.353	4.352
	4.416	4.416
4.447		
4.467		
	4.514	4.514
4.612		4.605
4.641	4.639	4.636
4.719		

Table I Con't.

$E_X^a$ (MeV)	$E_X^b$ (MeV)	$E_X^c$ (MeV)
4.860		
4.943		
4.963		
4.975		
5.005		
5.118		
5.186		
5.339		
5.368		
5.452		
5.560		
5.583		
5.614		
5.643		
5.760		
5.873		
5.948		
5.984		
6.057		
	6.167	
6.187		
	6.206	
6.228		
6.279		
6.372		

Table II cont.

$E_X^a$ (MeV)	$E_X^d$ (MeV)	$E_X^e$ (MeV)
	6.450	
6.534	6.528	6.521
6.569	6.556	6.557
	6.591	6.582
	6.640	
6.670	6.671	6.664
6.722	6.713	6.715

<sup>a</sup>Present work ( $\pm 1$  keV/MeV)

<sup>d</sup>Olness, Harris, Paul, Warburton, Phys. 1c, 958(1970).  
for levels below 5.2 MeV ( $\pm 0.5$  keV/MeV) and Hinds,  
Marchant and Middleton, Nucl. Phys. 51, 427(1964)  
for levels above 5.2 MeV ( $\pm 10-15$  keV).

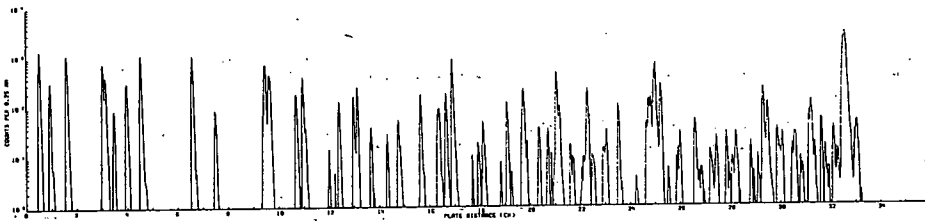
<sup>e</sup>J.D. Garrett, Ph.D. Dissertation, University of  
Pennsylvania, (1970) ( $\pm 4$  keV).

<sup>a</sup>Present work ( $\pm 1$  keV/MeV)

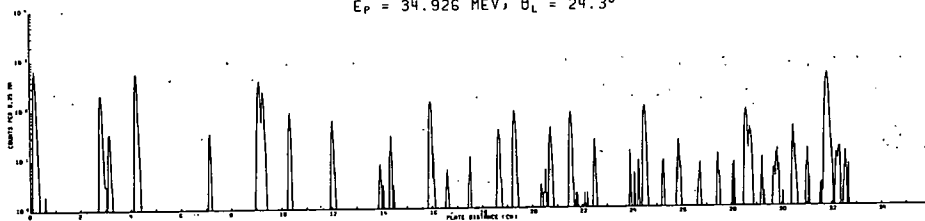
<sup>b</sup>A.K. Hyder, Jr. and Gale I. Harris, to be  
published. ( $\pm 1$  keV)

<sup>c</sup>J.R. Erskine, D.J. Crozier, J.P. Schiffer, and  
W.P. Alford, Phys. Rev. 3C, 1976(1971).

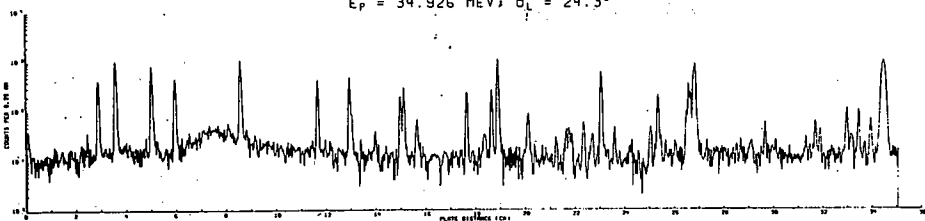
$^{35}\text{Cl}(P,D)^{34}\text{Cl}$ ;  $^{23}\text{Na}(P,D)^{22}\text{Na}$   
 $E_p = 34.926$  MEV;  $\theta_L = 24.3^\circ$



$^{23}\text{Na}(P,D)^{22}\text{Na}$   
 $E_p = 34.926$  MEV;  $\theta_L = 24.3^\circ$



$^{35}\text{Cl}(P,D)^{34}\text{Cl}$   
 $E_p = 34.926$  MEV;  $\theta_L = 24.3^\circ$



This reaction has been investigated by a number of authors<sup>1-3</sup> but the previous work has suffered from either a lack of good energy resolution or too low a bombarding energy. Both of these difficulties can be overcome using the Enge spectrometer with the MSU Cyclotron. One of the major aims in such an experiment is to obtain accurate cross sections for various  $0^+$  states excited in this reaction since this serves as a good test of shell-model configurations in the Ca isotopes. Since there have also been some careful (t,p) studies<sup>4,5</sup> populating the same states from  ${}^{44}\text{Ca}$ , a complete comparison of all the  $0^+$  states populated by these two reactions serves as an even more stringent constraint on both the reaction theory and the nuclear wave functions used. Unfortunately the previous (p,t) studies have only been able to observe the first excited  $0^+$  state at 2.43 MeV and have not been able to make comparisons with the remaining four  $0^+$  states observed in the (t,p) reaction.

Preliminary data have been obtained at three laboratory angles  $20^\circ$ ,  $24^\circ$ ,  $28^\circ$  for this experiment using a beam of 39 MeV protons from the MSU Cyclotron. The proton energy has been chosen so that the maximum energy tritons were obtained which could be bent by the Enge spectrometer. A thin  ${}^4\text{Ca}$  isotopically enriched target ( $60 \mu\text{g}/\text{cm}^2$  96% enriched), evaporated onto a carbon backing and transferred under a vacuum, was used in the preliminary run. The  $28^\circ$  triton plate is the only one scanned yet, and this spectrum is shown below. The energy resolution is approximately 11 keV FWHM and the initial indication is that at least some single states are resolvable up to 7.5 MeV. Since the specular system<sup>6</sup> was used with the ground state peak, this peak does not appear in the spectrum on the plates.

All of the states seen in the previous (t,p) and (p,t) experiments are also observed here although states at 4.29, 4.99, 5.64, and 5.85 MeV are very weakly excited. One state which was seen in a (p,p') experiment<sup>7</sup> at 3.780 MeV is completely missing in our data and in fact has not been observed in any other experiment. However we do observe about 10 or 12 new states up to 6 MeV excitation including what appear to be doublets at 4.43, 4.47, 4.78, 4.80, and 5.93, 5.94 MeV where for the first two cases the higher energy member is weakly excited. In addition new states are observed at 4.01, 4.52, 5.03, 5.09, 5.26, 5.47, 5.49, 5.79 MeV although it should be remembered that some of these may be impurity peaks which will become distinguishable when spectra at other angles are compared.

It is also interesting to note that the strong excitation of the first  $4^+$  and  $6^+$  states at 2.58 and 2.98 MeV which one might class mainly as

members of the  $(\nu_{f7/2}^{-1})^2$  configuration. At 20 MeV these are much weaker than the first  $2^+$  state but at 39 MeV all three states are of comparable strength at this angle (which should probably enhance the lower J states). Similarly the  $3^-$  and  $5^-$  states at 3.61 and 4.75 MeV are in the ratio 1:3 at 39 MeV whereas at 20 MeV the ratio was closer to 3:1.

The six  $0^+$  states observed in (t,p)<sup>4</sup> are all observed at approximately the same energy in this experiment the main difficulty being with the state observed in (t,p) at 5.628 MeV, where only a weak peak is seen in the (p,t) reaction at about 5.64 MeV. The intensities of these  $0^+$  states, relative to the 1st excited  $0^+$  at 2.43 MeV are shown in Table 1, although these numbers should be treated with great caution since they are only derived from one spectrum.

Further experiments and analysis on this reaction are being carried out.

Table 1  
 Relative Strengths of  $0^+$  States in  ${}^6\text{Ca}$ , Normalized  
 to  $0^+$  State at 2.43 MeV

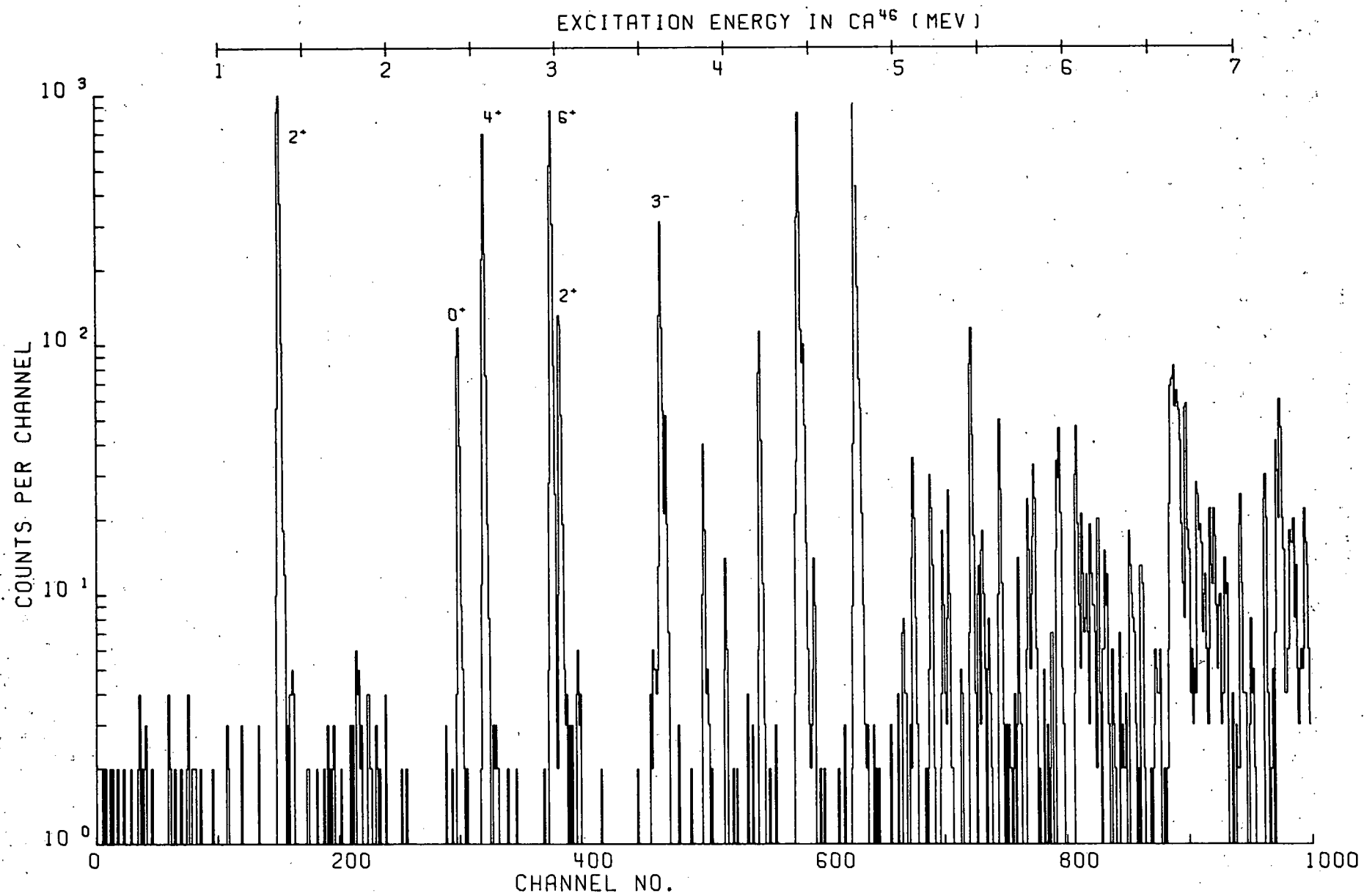
(Energy (MeV))	Relative Strength at $28^\circ$ Lab
2.43	10.0
5.29	2.5
5.59	5.0
5.64	0.3
6.05	4.5

#### References

1. R. J. Peterson, Phys. Rev. 170, 1003(1968).
2. Y. Dupont, P. Martin and M. Chambre, Phys. Letters 31B, 68(1970).
3. H. Hefele, U. Lynen and R. Santo, Nucl. Phys. A157, 93(1970).
4. D.C. Williams, J.D. Knight and W.T. Leland, Phys. Rev. 164, 1419(1969).
5. J.H. Bjerregaard, O. Hansen, O. Nathan, R. Chapman, S. Hinds and R. Middleton, Nucl. Phys. A103, 33(1967).
6. H.G. Blosser, G.M. Crawley, R. deForest, E. Kashy, and B.H. Wildenthal, Nucl. Instr. and Methods 91, 61(1971).
7. T.A. Belote, J.H. Bjerregaard, O. Hansen and G.R. Satchler, Phys. Rev. 138, B1067(1965).

\* Univ. of California, Los Angeles, California.

CA48(P,T) 28DEG EP=39.0MEV



Direct (p,  $\alpha$ ) Reactions  
Jerry Nolen and Paul Zemaný

We have recently begun to use the direct (p,  $\alpha$ ) reaction to obtain nuclear structure information about several nuclei. Very few angular distributions have yet been measured, but preliminary data indicate this promises to be a very useful nuclear probe.

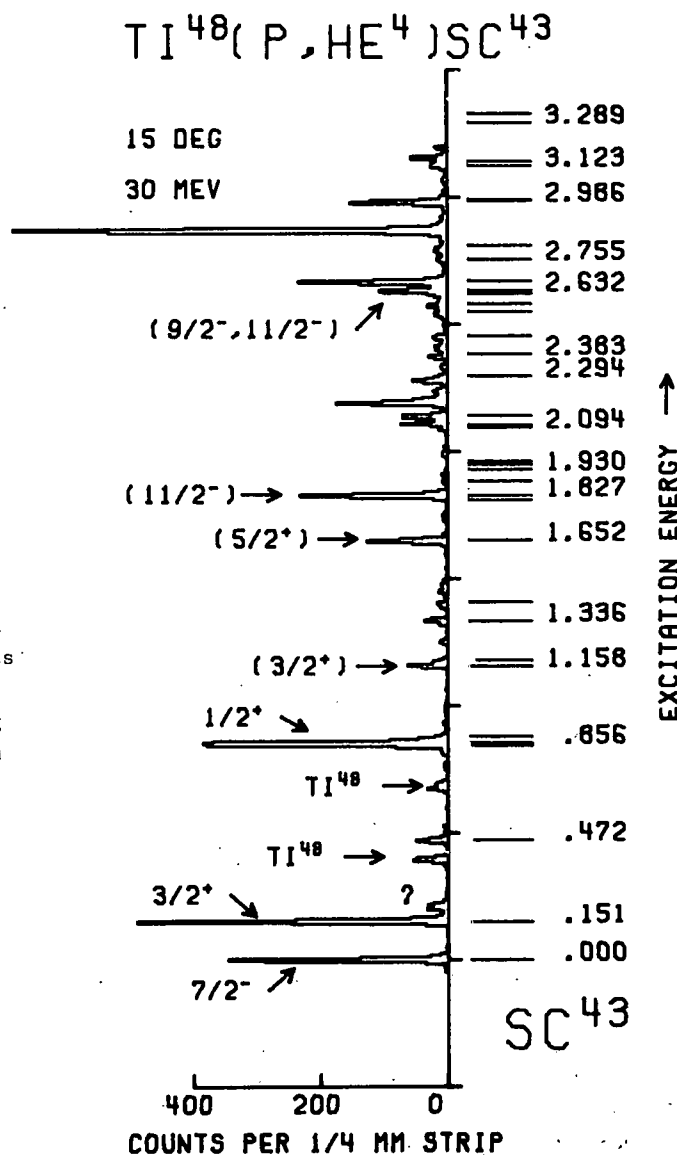
The data are being recorded on nuclear emulsions with the dispersion-matching technique in the Engesplit-pole magnetic spectrograph. The resolution is partially limited by target thickness due to the relatively low cross-sections for many of the energy levels of interest. However, typical data recorded at a proton energy of 30 to 35 MeV has about 15 keV (1/2 mm) FWHM resolution.

The reactions currently being studied are  ${}^{46}\text{Ti}(p, \alpha){}^{43}\text{Sc}$  and  ${}^{44}\text{Ca}(p, \alpha){}^{41}\text{K}$ . In both of these cases one primary interest is in determining to what extent the high spin states are populated. A  $15/2^+$  state from the configuration  $(\pi d_{3/2}^{-1})(\nu f_{7/2}^2)$  is expected around 4 MeV excitation in  ${}^{41}\text{K}$ , this would be populated via L=8 angular momentum transfer in this reaction. Similarly, the  $19/2^-$  state from the  $(f_{7/2}^3)$  configuration in  ${}^{43}\text{Sc}$  has recently been located by the Stockholm group as a short-lived isomer at 3.123 MeV excitation energy. Shell-model selection rules generally inhibit the population of these seniority three high spin states in one and two nucleon direct transfer reactions, but allow them to be populated in three nucleon transfer. Preliminary DWBA calculations also indicate that the (p,  $\alpha$ ) reaction is not restricted kinematically from a wide range of angular momentum transfer, i.e. it does not enhance particular L-values to a large extent. Thus it is hoped these "extended" shell-model configurations can be located and identified with the (p,  $\alpha$ ) reaction. If so, the resulting information on these states will provide valuable new tests of shell-model calculations.

A sample spectrum of the  ${}^{46}\text{Ti}(p, \alpha){}^{43}\text{Sc}$  reaction is given in the figure. It is clear that many states of the  $f_{7/2}^3$  as well as states involving s-d proton holes are strongly populated. Since this scattering angle was small the lower spin states are emphasized in this spectrum. It had been previously inferred from their low yields in proton stripping reactions as well as life-time work that the low-lying  $3/2^+$  and  $1/2^+$  states in  ${}^{43}\text{Sc}$  were dominantly proton hole states. Their strong yields in the (p,  $\alpha$ ) pickup reaction confirm this interpretation. The energy levels indicated on the figure are largely from particle-gamma and gamma-gamma correlation work. The (p,  $\alpha$ ) data will help to clear up many of the existing ambiguities in spin and configuration assignments.

The preliminary angular distributions for the  ${}^{44}\text{Ca}(p, \alpha)$  reaction to the low-lying levels of  ${}^{41}\text{K}$  indicate some probable new spin assignments. For example, the doublet at 1.560-1.582 MeV was well resolved with the lower member having an L=2 shape and the upper an L=0 shape. Thus the probable spin assignments are 1.560 MeV ( $3/2, 5/2^+$ ) and 1.582 MeV ( $1/2^+$ ).

An example of the difference between (p,  $\alpha$ ) and (d,  ${}^3\text{He}$ ) reaction is indicated by the different relative yields to states of the same spin. The (d,  ${}^3\text{He}$ ) reaction essentially measures the relative amounts of  $2s_{1/2}$  proton hole configuration in these two  $1/2^+$  states of  ${}^{41}\text{K}$ . However, in the (p,  $\alpha$ ) reaction coherence between the simple proton hole components and seniority three components can greatly change the relative yields. Thus the two reactions yield complementary information about the wave functions.



We have begun an investigation of  $^3\text{He}$  elastic scattering from  $f_{7/2}$ -shell nuclei at 70 MeV. Thus far we have bombarded  $^{51}\text{V}$ ,  $^{50}\text{Ti}$ , and  $^{48}\text{Ti}$  targets. The positive  $Q$ -values ( $\sim 10$  MeV) of the ( $^3\text{He}, ^4\text{He}$ ) reactions on these nuclei necessitate the use of particle identification. Thus, with E- $\Delta E$  detector telescopes we have also collected data on the associated neutron pickup and inelastic scattering reactions. Preliminary elastic angular distributions for  $^{51}\text{V}$  and  $^{50}\text{Ti}$  are presented in Fig. 1. We are currently in the process of extracting final angular distributions for as many of the aforementioned reactions as our resolution will allow.

The dominant feature of the  $^{50}\text{Ti}$  and  $^{51}\text{V}$  elastic scattering cross-sections is a dramatic drop-off with increasing angle. From  $5^\circ$  to  $140^\circ$  they span about ten orders of magnitude, which is a source of major experimental difficulties. To measure the small cross-sections, we used "thick" ( $> 1$  mg/cm $^2$ ) targets, large solid angles, and minimal beam energy selection. These factors coupled to give  $\sim 150$  keV FWHM resolution. Thus we do not expect to analyze more than a few of the low-lying excited states.

The principal objective of this study is to extend the optical model to 70 MeV for  $^3\text{He}$  scattering. A secondary interest has been to obtain further information relevant to the question of the necessity for target-spin dependent terms in the optical model potential, such as:  $\vec{L} \cdot \vec{I} U_1(r)$  and/or  $\vec{\sigma} \cdot \vec{I} U_2(r)$ . We have employed the optical model code GIBELUMP to search for parameters yielding reasonable fits to our preliminary  $^{51}\text{V}$  and  $^{50}\text{Ti}$  angular distributions. The parameters obtained differ little from the starting sets, which were found at 30-37 MeV by Gibson<sup>1</sup> and by Luetzelschwab and Hafele<sup>2</sup> for various  $f_{7/2}$ -shell nuclei. In particular, the discrete ambiguity in the strength of the real potential is still present. Of the various parameter families giving reasonable fits, the one with  $V^2_{110}$  has the least  $\chi^2$ , especially if large angle data are included (Fig. 2a). In general, the back angle cross-sections were difficult to fit. However, significant improvements resulted from including a spin-orbit potential of about 2-3 MeV (Fig. 2b) and using a surface rather than volume form of the imaginary potential. Some of the best fits were obtained with the parameter sets listed in the table.

At Oak Ridge Hafele and Fulmer have done similar studies with 50 MeV helions scattering from  $^{59}\text{Co}$  and  $^{60}\text{Ni}$ .<sup>3</sup> They interpret an observed damping of the  $^{59}\text{Co}$  elastic angular distribution oscillations with respect to those of  $^{60}\text{Ni}$  beyond  $70^\circ$  as evidence for including a target-spin dependent term in the optical model potential. We

chose  $^{51}\text{V}$  and  $^{50}\text{Ti}$  as our initial targets because they are another pair of neighboring nuclei with the same spins as  $^{59}\text{Co}$  and  $^{60}\text{Ni}$  ( $7/2^-$  and  $0^+$ ; respectively). However, we have not observed a similar damping of back angle cross-section oscillations for  $^{51}\text{V}$  with respect to  $^{50}\text{Ti}$ . In fact the data for both nuclei are strikingly similar (Fig. 1). Two possible explanations of this result have been suggested. Hafele and Fulmer also have a  $^{60}\text{Ni}$  angular distribution at 71 MeV which is much smoother beyond  $70^\circ$  than the one at 50 MeV.<sup>4</sup> Thus, it may be that the target-spin effect is more pronounced at 50 MeV. The other obvious difference between our experiments is the choice of targets. Perhaps  $^{60}\text{Ni}$  is "anomalously spherical" for its neighborhood of the nuclide spectrum and yields larger elastic scattering oscillations than  $^{59}\text{Co}$  due to a smaller diffuseness rather than greater target-spin forces. To explore these possibilities, we have decided to include  $^{58}\text{Ni}$ ,  $^{59}\text{Co}$ , and  $^{60}\text{Ni}$  in our next series of targets.

## References

1. E.F. Gibson, *et al.*, Phys. Rev. **155**, 1194(1967).
2. J.W. Luetzelschwab and J.C. Hafele, Phys. Rev. **180**, 1023(1969).
3. J.C. Hafele, C.B. Fulmer, and F.G. Kingston, Phys. Letters **31B**, 17(1970).
4. C.B. Fulmer and J.C. Hafele, ORNL-4649, 48(1970).

## OPTICAL MODEL PARAMETERS - 70 MEV

	V	R <sub>0</sub>	A	W <sub>0</sub>	R <sub>1</sub>	A <sub>1</sub>	V <sub>50</sub>	CHISO
$^{51}\text{V}$	155.0	1.24	.621	26.1	1.16	.805	2.9	130
	102.1	1.24	.715	18.9	1.24	-.830	1.6	55
$^{50}\text{Ti}$	158.3	1.24	.641	25.1	1.13	.860	1.3	33
	157.1	1.24	.628	28.15	1.43	.891	0.7	70
$^{50}\text{Ti}$	106.7	1.24	.739	20.0	1.29	.765	2.4	27
	107.0	1.24	.742	20.2	1.31	.744	0.0	31
30 MEV $^{51}\text{V}$ (LUETZELSCHWAB, HAFELE)								
	156.5	1.24	.639	23.7	1.04	.934	3.2	29

Note: All parameter sets shown are with a surface form of the imaginary potential except the one labelled S, which is spherical. The set at 30 MeV was obtained from our fit to the data of Luetzelschwab (Ref. 2).



Fig. 1 Comparison of  $^3\text{He}$  elastic scattering from  $^{50}\text{Ti}$  and  $^{51}\text{V}$  at 70 MeV.

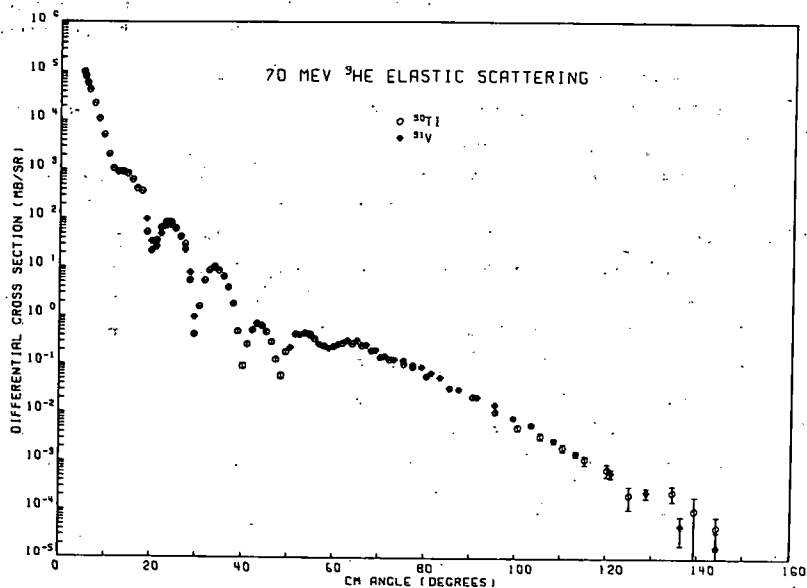
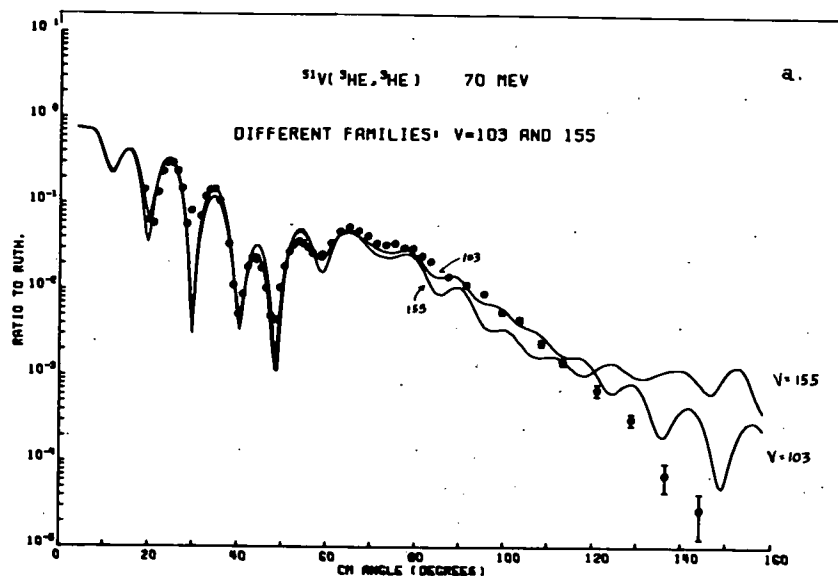
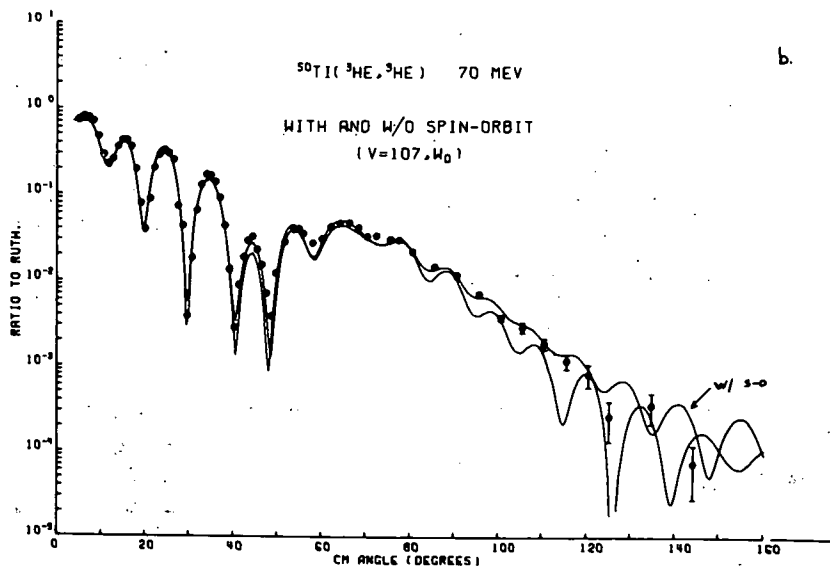


Fig. 2 Optical Model Calculations.

(a) Fits to  $^{51}\text{V}$  elastic scattering from different real well depths. Only the real well radius was held fixed in the search. Final parameters for the fits shown are given in the table.



(b) Fits to  $^{50}\text{Ti}$  elastic scattering with and without a spin-orbit potential. Starting parameter sets were otherwise the same. Only the real well radius was held fixed. Final parameters for the fits shown are given in the table.



The ( $^3\text{He},t$ ) charge exchange reaction has served in recent years as a valuable spectroscopic tool in determining spins and parities of states in many odd-odd nuclei. The density of levels in such nuclei and the low cross-sections encountered have not deterred experimentalists from making many measurements. As in other types of reactions the hope is that the level spins (or at least the angular momentum transfer) can be determined by the shapes of the angular distributions. In most instances for ( $^3\text{He},t$ ) this has been the case,<sup>1</sup> although, as brought out by work here in the past year, there are some notable exceptions to this surmise, that is, cases have been observed in which standard DWBA descriptions fall short of providing reasonable fits to the data and thus reliable spectroscopic information.

1. Transitions to  $0^+$  Antianalog States in  $^{64,66}\text{Ga}$  and  $^{40}\text{K}$ .

R.A. Hinrichs, R. Sherr,\* G.M. Crawley, and I. Proctor

The ( $^3\text{He},t$ ) reaction can populate both  $T_>$  (analog) and orthogonal  $T_<$  states (states of isospin one less than the target) that have the same spin and configuration as the analog state (antianalog states). If spin 0 states are selected for both the initial and final nuclei, then the interaction responsible for the transition, in usual microscopic terminology, is only the pure charge-exchange operator  $V_{\uparrow}(\vec{\tau}_1 \cdot \vec{\tau}_2)g(r)$ , with the transition proceeding via an L=0 angular momentum transfer. We have studied such  $0^+$  to  $0^+$  transitions to analog and antianalog states in  $^{40}\text{K}$  and  $^{64,66}\text{Ga}$ .<sup>2</sup> The  $0^+$   $T_<$  states in these nuclei are at 1.64, 0.0, and 0.0 MeV, respectively, and are well determined. Figure 1 shows angular distributions to these

states, as well as the  $0^+$  isobaric analog state. Also shown are macroscopic DWBA calculations. The analog state is fit very well in all cases by an allowed L=0 transfer but the antianalog state is shifted relative to the predicted angular distribution and is fit much better by the L=1 curve. Macroscopic calculations with several sets of optical model parameters; as well as microscopic calculations with different values of the range of the Yukawa interaction, failed to change the general shape of the L=0 curve. The spatial dependence of each excess neutron orbital contributing to the microscopic wave functions was also varied by changing the geometrical well parameters r and a, but the maxima and minima of the angular distributions remained at the same positions. Such observations have led to the conclusion that modifications need to be made in the conventional treatment of ( $^3\text{He},t$ ) reactions. Recent calculations by R. Schaeffer and G. Bertsch seem to show that two-step processes, for example those of the form ( $^3\text{He},\alpha$ )-( $\alpha,t$ ), are responsible for the observed anomalies.

2. The Reaction  $^{89}\text{Y}(^3\text{He},t)$  to  $T_<$  States

R.A. Hinrichs and G.F. Trentelman

In continuing the study of ( $^3\text{He},t$ ) reactions to antianalog and other  $T_<$  states, the target  $^{89}\text{Y}$  was selected.<sup>3</sup> The  $1/2^-$  (.59 MeV) and  $9/2^+$  (1.51 MeV) states in  $^{89}\text{Zr}$  are antianalog states. Other well-known  $T_<$  states nearby can also be observed. The transitions to these antianalog states can be expected to be complicated as more than one L value can contribute and the tensor term in the effective interaction is important. Figure 2 shows angular distributions to the isobaric analog (8.0 MeV) and antianalog (.59 MeV)  $1/2^-$  states in  $^{89}\text{Zr}$ . The microscopic DWBA calculations shown included a tensor term in the interaction; for the antianalog state they are out of phase with the data (as in the  $0^+$  to  $0^+$  transitions), which is fit better by a (macroscopic) L=1 transfer calculation.

Figure 3 shows angular distributions to the  $9/2^+$  excited antianalog state at 1.51 MeV and to the  $9/2^+$  ground state of  $^{89}\text{Zr}$ . The data in both cases is quite similar and shows more forward angle strength than the calculations would allow. The microscopic calculations, which emphasize the higher L transfer (L=5) with the inclusion of the tensor term, peak at a much larger angle than the data, which is fit better by an L=2 (macroscopic) calculation. Because of the similarity of the two  $9/2^+$  angular distributions, it appears that the anomaly noted in the last section is not dependent solely upon the uniqueness of the antianalog state. Shifts in the angular distributions for

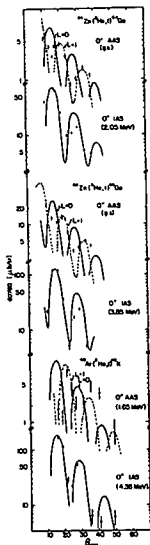


Fig. 1 Angular distributions for ( $^3\text{He},t$ ) transitions to the  $0^+$  analog (IAS) and anti-analog (AAS) states in  $^{64,66}\text{Ga}$  and  $^{40}\text{K}$ . The curves are macroscopic DWBA calculations (with the indicated L transfers) and normalized to the data.

$(^3\text{He},t)$  reactions to  $T_{<}$  states has been noted for other nuclei, especially for transitions involving high L transfers.<sup>4</sup> Our data for other  $T_{<}$  states in  $^{89}\text{Zr}$  show some shifts in angle from the calculated shapes, even for lower L transfers, but no trend seems to be apparent for such reactions. It should be noted that there are quite a few cases in which good fits to the data for  $T_{<}$  states do exist. The anomalous effects may thus be configuration dependent and so a determination of final state spins from the  $(^3\text{He},t)$  reaction, by either a comparison of the experimental shapes with transitions to known states or calculations with the present microscopic interaction, may be misleading. Two-step processes, as mentioned in the last section, may provide a firmer foundation for spectroscopy; however, additional modifications probably have to be added to explain the enhanced forward angle data seen in some of this work.

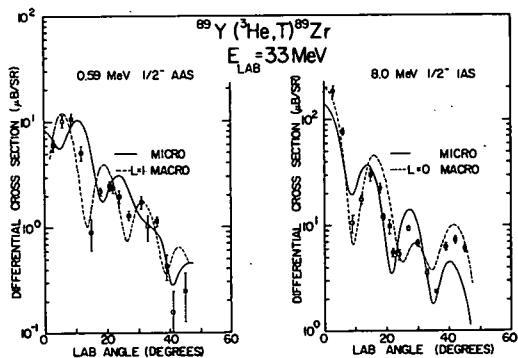


Fig. 2  $^{89}\text{Y}(^3\text{He},t)^{89}\text{Zr}$  angular distributions for transitions to the  $1/2^-$  analog (IAS) and anti-analog (AAS) states in  $^{89}\text{Zr}$ . The curves are DWBA calculations normalized to the data. The L transfers used in the macroscopic form factor are indicated.

Further studies (on the Sn isotopes) have begun to explore other examples of  $(^3\text{He},t)$  transitions with large L transfers.

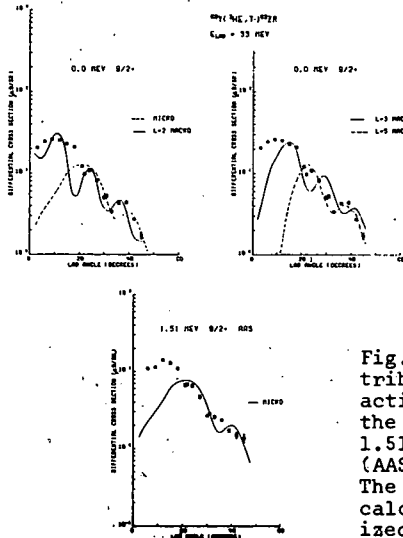


Fig. 3 Angular distributions for the reaction  $^{89}\text{Y}(^3\text{He},t)$  to the  $9/2^+$  ground and 1.51 MeV anti-analog (AAS) states in  $^{89}\text{Zr}$ . The curves are DWBA calculations normalized to the data.

### 3. Spectroscopy of $^{34}\text{Cl}$ via the $^3\text{S}(^3\text{He},t)$ Reaction

R.A. Hinrichs, B.H. Wildenthal, D. Show, and J.A. Rice.

The level structure of  $^{34}\text{Cl}$  has been investigated in a variety of different ways, including the reaction  $^{35}\text{Cl}(p,d)$  as found in this report. We have studied the levels of  $^{34}\text{Cl}$  below 5 MeV via the  $(^3\text{He},t)$  reaction on  $^{34}\text{S}$  at 35 MeV; this reaction selects proton-particle, neutron-hole excitations of the target ground state. Plates were exposed in the spectrograph and a resolution of 20-30 keV was obtained, with angular distributions taken between lab angles of  $3^\circ$  and  $45^\circ$ . Figure 4 shows the energy levels determined in this experiment for  $^{34}\text{Cl}$ . The energies agree quite well with those found in  $(p,\gamma)^5$  and  $(^3\text{He},d)^6$  studies. Previously unidentified states are observed at 4.21 and 5.00 MeV. The determination of the energies of the states above 4.3 MeV has not been completed. The spin assignments listed are those determined by other reactions and confirmed in this  $(^3\text{He},t)$  study—by comparison with angular distribution shapes for transitions to known levels or by DWBA calculations. If a discrepancy exists in the assignments, the present determinations are underlined.

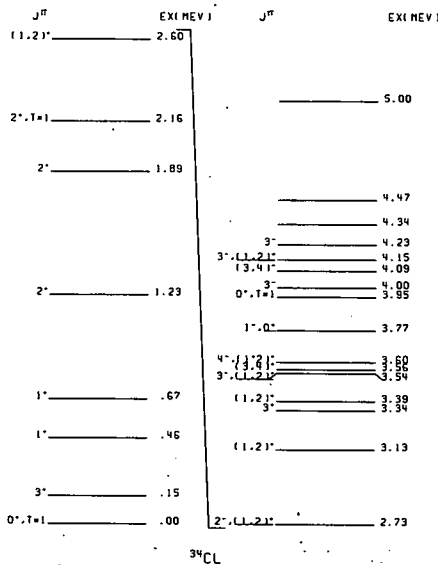


Figure 4

Three obvious discrepancies are noted in these assignments; the states at 2.72 and 3.60 MeV have been found in  $(^3\text{He},d)$  and  $(p,\gamma)$  studies to be  $2^-$  and  $4^-$  respectively, but our assignments indicate either  $1^+$  or  $2^+$ , based upon macroscopic DWBA calculations and comparisons with the shapes of other known  $1^+$  or  $2^+$  states. Some of these angular distributions with macroscopic DWBA calculations are shown in Fig. 5. The state at 3.77 MeV is very similar to the known  $0^+$ , T=1 state at 3.94 MeV, but its  $0^+$  assignment is doubtful as  $(p,\gamma)$  measurements indicate a  $1^-$  spin-parity and a strong transition to the  $0^+$  ground state for this level. One wonders whether these discrepancies could be

due to the shifts in angular distributions observed in the previous two subsections. In general though there is good agreement between expected spin-parity assignments and the theory.

References

1. See, e.g., J.J. Schwartz and B.A. Watson, Phys. Rev. Letters 24, 322(1970) and H.H. Duham, K. Pterseim, R. Seehars, R. Finlay and C. Detraz, and references cited therein.
2. R.A. Hinrichs, R. Sherr, G.M. Crawley, and I. Proctor, Phys. Rev. Letters 25, 829(1970).

3. R.A. Hinrichs and G.F. Trentelman, to be published.
4. J.R. Comfort, J.P. Schiffer, A. Richter, and M.M. Stantberg, Phys. Rev. Letters 26, 1338(1971).
5. A.K. Hyder and G.I. Harris, to be published.
6. J.R. Erskine, D.J. Crozier, J.P. Schiffer, and W.P. Alford, Phys. Rev. C3, 1976(1971).

\* On leave from Princeton University, Princeton, New Jersey.

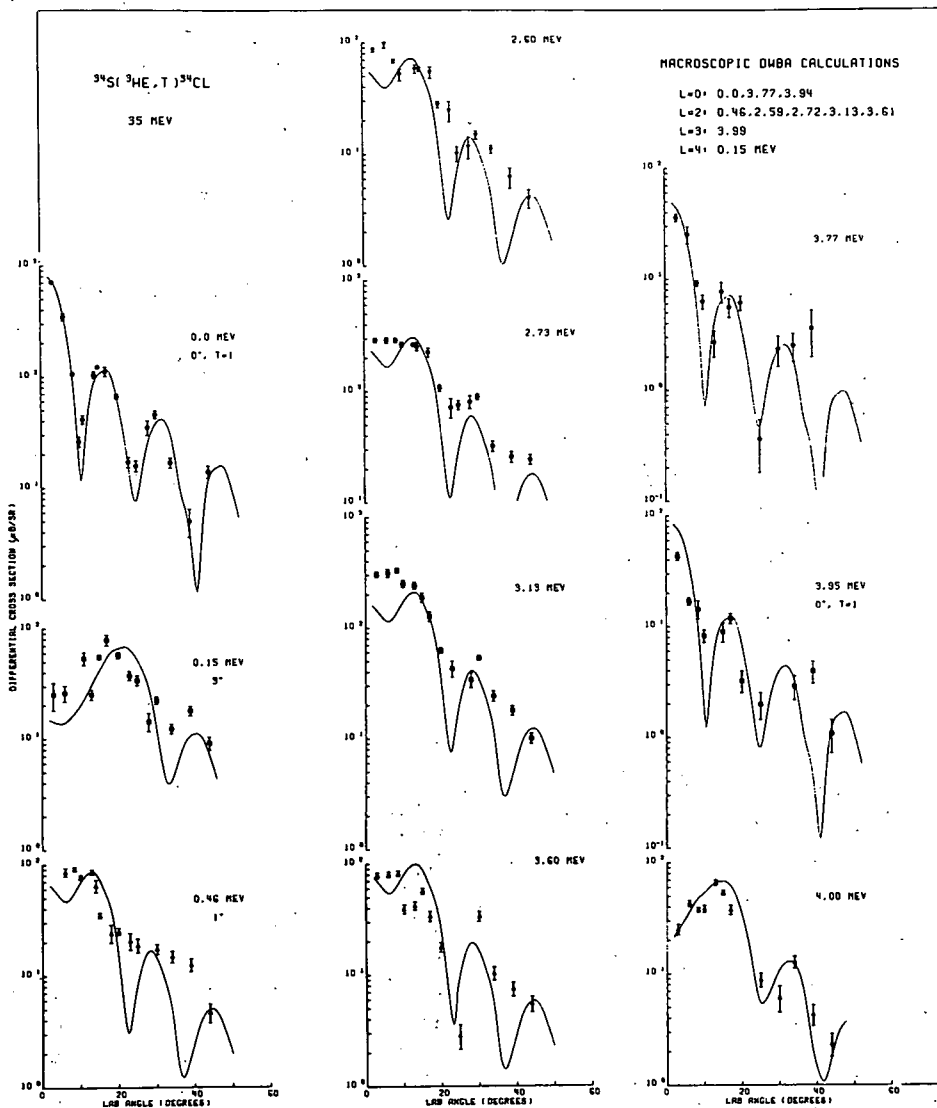


Fig. 5 Angular distributions for transitions to a multitude of representative states in  $^{34}\text{Cl}$  populated by the reaction  $^{34}\text{S}(^3\text{He},t)$ . The curves are macroscopic DWBA calculations (normalized to the data) with the L transfers as given in the right-hand corner.

The ( $^3\text{He}, ^6\text{He}$ ) reaction at 70 MeV is being used to measure ground state masses and to study proton-rich nuclei the level structure of which was previously completely unknown. The experimental method consists of using low-sensitivity photographic plates in the Enge split-pole spectrograph. Previous ( $^3\text{He}, ^6\text{He}$ ) measurements in this laboratory<sup>1,2,3</sup> have been of ground state masses of some of these nuclei and have made use of position sensitive solid state detectors on the focal plane of the spectrograph. Some of the advantages of plates over the counters are 1) larger energy bite, 2) better resolution, 3) better particle discrimination of weak  $^3\text{He}$  groups from background  $\alpha$ 's, and 4) insensitivity to neutrons and gammas.

Ilford Kminus 1 plates are used with absorbers stepped in thickness to give  $^6\text{He}$  energies between 20 and 25 MeV everywhere along the plate. This amount of absorber leaves the  $\alpha$ 's at the same focal plate position with typical energies of 50-60 MeV. The tracks left by the much more ionizing He's are readily distinguishable from the  $\alpha$ 's except at the peak of very intense  $\alpha$ -groups.

The kinematic compensation, dispersion matching and large solid angle of the spectrograph permit collection of  $^6\text{He}$  spectra in 4 to 12 hours. The energy resolution is limited by target thickness effects. The best resolution obtained was 25 keV for the  $^{28}\text{Si}(^3\text{He}, ^6\text{He})^{25}\text{Si}$  reaction at  $9^\circ$  and permitted resolving the ground-first excited state doublet. The presence of an excited state in  $^{25}\text{Si}$  at about 40 keV (shown in Fig. 1) means a re-adjustment of the  $^{25}\text{Si}$  mass downward by about 8 keV but does not effect the conclusions concerning the isobaric multiplet mass equation in Ref. 3. In addition to the 40 keV state, seven other states in  $^{25}\text{Si}$  were found as is shown by the spectrum

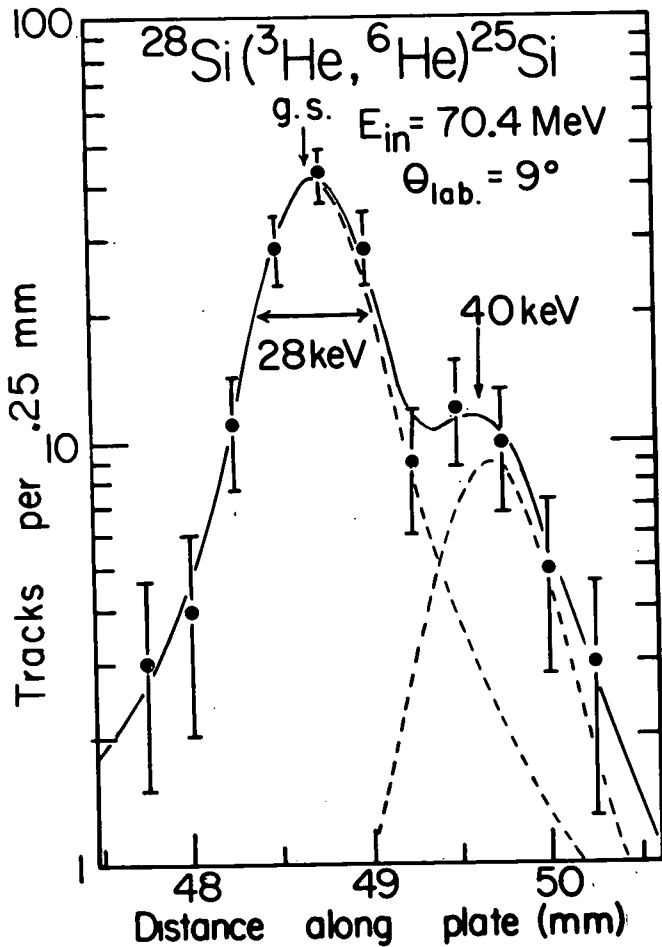


Figure 1

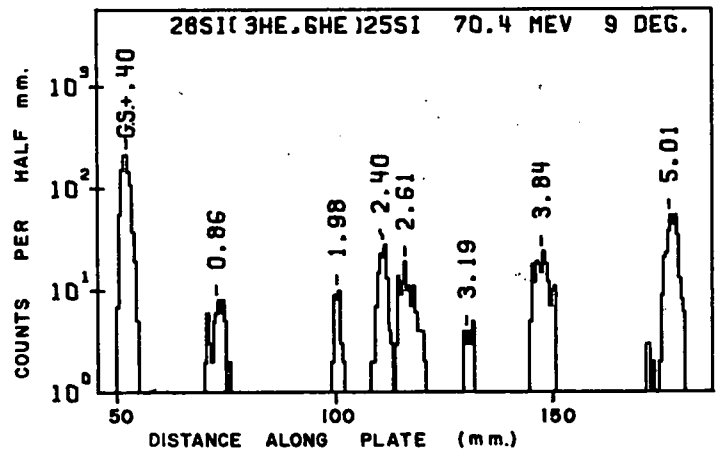


Figure 2

These levels line up well with the  $T=3/2$  levels in  $^{25}\text{Mg}$ ,  $^{25}\text{Al}$ , and  $^{25}\text{Si}$  as can be seen from the table.

Table 1

$^{25}\text{Na}$ $T_z=3/2$	$^{25}\text{Mg}$ $T_z=1/2$	$^{25}\text{Al}$ $T_z=-1/2$	$^{25}\text{Si}$ $T_z=-3/2$
0.0	0.0 ( $E_x=7.782$ )	0.0 ( $E_x=7.915$ )	0.0
0.090	0.081 <sup>x</sup>	0.072 <sup>x</sup>	0.040
1.068	1.009		0.86
2.201			1.98
2.417			2.40
2.788			2.61
2.914	2.836		
3.353			3.19
3.455			
3.685			
3.928	3.943		3.84
3.950	3.965		
3.995	3.993		
5.190	5.116		5.01

Except for the first excited state, at least one member of each quartet is still missing. Using the multiplet mass equation the missing energy level can be predicted accurately. The energies cited are preliminary. In addition to  $^{25}\text{Si}$ , the energy levels of  $^9\text{C}$ ,  $^{10}\text{C}$ , and  $^{21}\text{Mg}$  are being studied. In  $^9\text{C}$  only the ground state was observed.

and in  $^{10}\text{C}$  no states that were not previously observed<sup>5</sup> in  $^{12}\text{C}(p,t)$  were seen. Figure 3 shows a

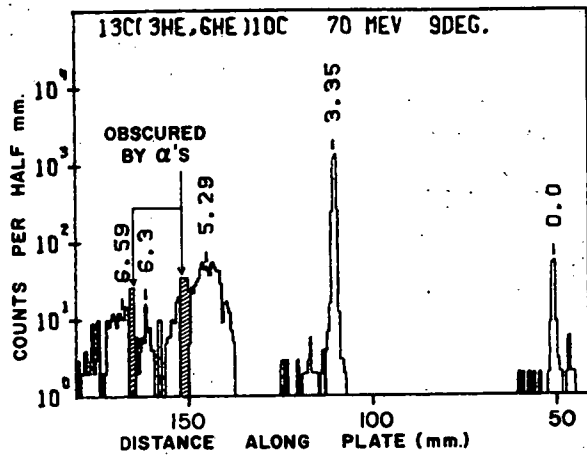


Figure 3

spectrum of  $^{13}\text{C}(^3\text{He},^6\text{He})$  at  $9^\circ$ . The location of very strong peaks from the  $^{13}\text{C}(^3\text{He},^4\text{He})^{12}\text{C}$  reaction is shown on the figure. In spite of the low sensitivity to  $\alpha$ 's it was not possible to scan right at the top of these peaks. Of interest in

the spectrum is the very strong yield to the  $2^+$  first excited state. In addition  $^9\text{C}$ ,  $^{10}\text{C}$ ,  $^{21}\text{Mg}$ , and  $^{25}\text{Si}$  work has begun on the masses and energy levels of  $^{37}\text{Ca}$ ,  $^{47}\text{Cr}$ ,  $^{51}\text{Fe}$ , and  $^{55}\text{Ni}$ . Other nuclei to be studied in the near future are  $^{13}\text{O}$ ,  $^{16}\text{F}$ ,  $^{24}\text{Al}$ ,  $^{29}\text{S}$ , and  $^{33}\text{Ar}$ .

#### References

1. G.F. Trentelman, B.M. Freedom, and E. Kashy, Phys. Rev. Letters **35**, 530(1970).
2. G.F. Trentelman, B.M. Freedom, and E. Kashy, Phys. Rev. **3C**, 2205(1971).
3. G.F. Trentelman and I.D. Proctor, Phys. Letters **35B**, 570(1971).
4. C. Detraz and R. Richter, Nucl. Phys. **A158**, 343(1970).
5. W. Benenson, G.M. Crawley, J.D. Dreisbach, and W.P. Johnson, Nucl. Phys. **A97**, 510(1967).

\* Visiting from the University of South Carolina.

In recent years interest has grown in the field of multinucleon transfer reactions. Due to the extreme complexity of such reactions, no satisfactory theory has yet been developed for them. The reaction mechanism appears to be simplest in the case of  $\alpha$ -transfer reactions. Because of the tight binding of the alpha particle, the four nucleons may, to some degree of approximation, be treated as an alpha cluster rather than four separate uncorrelated nucleons. Consequently, interest has been greatest in  $\alpha$ -transfer reactions. To date most work has been done with  $\alpha$ -stripping via the ( $^6\text{Li}, d$ )<sup>1</sup> ( $^7\text{Li}, t$ )<sup>2</sup> and ( $^{16}\text{O}, ^{12}\text{C}$ )<sup>3,4</sup> reactions. Very little study has been given to  $\alpha$ -pickup.

The present work is a study of the ( $^3\text{He}, ^7\text{Be}$ )  $\alpha$ -pickup reaction at 70 MeV incident beam energy. Earlier work on this reaction has been done at 30 MeV.<sup>5</sup> Preliminary data has been taken from  $^{12}\text{C}$ ,  $^{16}\text{O}$ ,  $^{24}\text{Mg}$ ,  $^{28}\text{Si}$ , and  $^{58}\text{Ni}$  targets. Figures 1 and 2 show spectra taken from the  $^{12}\text{C}$  and  $^{24}\text{Mg}$  target respectively. These data were taken in a 30-inch scattering chamber using silicon surface barrier detectors in an E- $\Delta E$  telescope arrangement. As can be noted from the spectra, each peak is a doublet since the  $^7\text{Be}$  nucleus may be ejected from the reaction in its particle-stable first excited state (432 keV) as well as the ground state.

Cross sections have been found to be small and they decrease systematically with increasing atomic number. For example,  $^{12}\text{C}(^3\text{He}, ^7\text{Be})^8\text{Be}$  (g.s.) has a maximum cross section of 80  $\mu\text{barn}/\text{str}$ . whereas  $^{58}\text{Ni}(^3\text{He}, ^7\text{Be})^{54}\text{Fe}$  (g.s.) has a cross-section of 2  $\mu\text{barn}/\text{str}$ . More detailed angular distributions for states in  $^8\text{Be}$  have been measured. The results for the  $0^+$  ground state and the  $2^+$ , 2.9 MeV first excited state are shown in Figs. 3 and 4. The doublet structure of each level was not resolved so the indicated cross sections are roughly twice the value for a single peak.

Because of the small cross sections and the need to resolve the doublet structure, the consequent counting rates make impractical a detailed study of a variety of targets using the detector telescope system. Therefore an effort has been made to develop a practical position sensitive detector system for use in the focal plane of the laboratory's split-pole broad range magnetic spectrograph. A larger solid angle becomes feasible because of the spectrograph's kinematic focusing property. Nuclear emulsions cannot be used to detect the  $^7\text{Be}$  particles since a variety of other ions would also strike the plate in the region of interest. Solid state position sensitive detectors are typically about 5 cm long, allowing one to collect data in only a

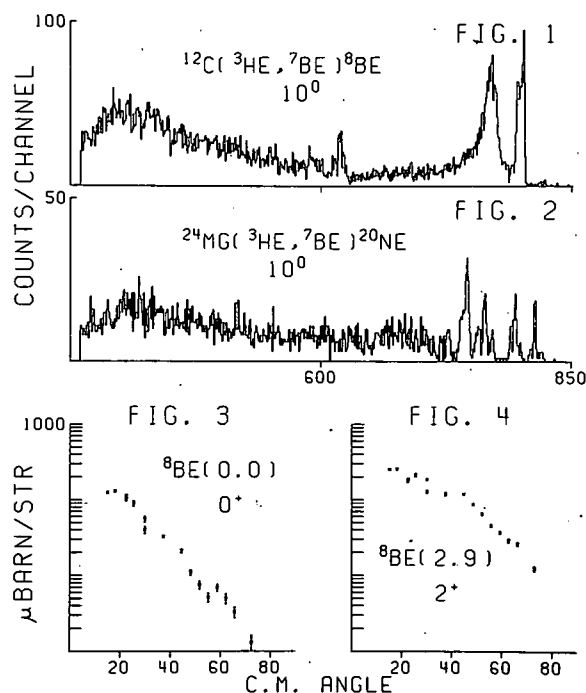
small region of a spectrum at one time.

For the present work, position sensitive gas proportional counters are well suited. They can be made sufficiently long, can identify particles, and are capable of adequate resolution. Test counters have been built and used to detect  $^7\text{Be}$  ions in the spectrograph. The tests show that indeed the gas counters are very suitable for detecting  $^7\text{Be}$  ions. Although the resolution of the initial counter was not optimum, it nevertheless produced better energy resolution (sufficient to resolve the  $^8\text{Be}$  g.s. doublet) than was obtained with the detector telescope arrangement.

Presently, improved position sensitive gas proportional counters are being designed. When available, they will be used for a detailed and comprehensive study of the ( $^3\text{He}, ^7\text{Be}$ ) reaction.

#### References

1. K. Meier-Ewert, K. Bethge and K.O. Pfeiffer, Nucl. Phys. A110, 142(1968).
2. R. Middleton, L.M. Polsky, C.H. Holbrow, and K. Bethge, Phys. Letters 21, 1398(1968).
3. A.M. Friedman, H.T. Fortune, G.C. Morrison, R.H. Siemssen, Proc. Int. Conf. Nuclear Reactions Induced by Heavy Ions, R. Bock, W. Hering eds. (North-Holland, Amsterdam), p. 171.
4. H. Faraggi, A. Jaffrin, M-C. Lemaire, M.C. Mermaz, J-C. Faivre, J. Gastebois, B.G. Harvey, J.M. Loiseaux, A Papineau, de-Shalit Memorial Volume (Annals of Physics 1971).
5. C. D ttraz, H.H. Duhm, H. Hafner, Nucl. Phys. A147, 488(1970).



The nuclide  ${}^6\text{Ge}$  has  $N=Z$  and is predicted<sup>1</sup> to be stable against  $\alpha$ - and proton emission. It is thus of considerable astrophysical interest as it would be the heaviest  $N=Z$  member of the  $\alpha$ -capture chain believed to be established in explosive nucleosynthesis. An accurate knowledge of its mass is needed in order to make predictions about the abundances of heavier nuclei.<sup>2</sup>

We are attempting to produce  ${}^6\text{Ge}$  by the  ${}^6\text{Zn}({}^3\text{He}, 3n){}^6\text{Ge}$  reaction at  $E_{{}^3\text{He}} \approx 45$  MeV. A 70 MeV He beam is degraded by an absorber and allowed to pass through a 10 mg/cm<sup>2</sup> target enriched to 99.66% in  ${}^6\text{Zn}$ . Recoil nuclei from the target are stopped (thermalized) in helium gas at 2 atm. and pumped at sonic speeds through a capillary to a low-background counting area, using the technique first described by Macfarlane *et al.*<sup>3</sup> and implemented here by Kosanke and Giesler.<sup>4</sup> The decays of reaction products are then observed with a Ge(Li) detector.

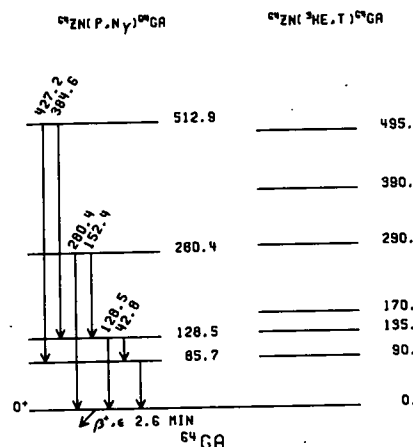
It is probable that the ground state of  ${}^6\text{Ga}$  is  $0^+$ , and therefore the isospin selection rule will require much of the beta-decay of  ${}^6\text{Ge}$  to lead to excited states in  ${}^6\text{Ga}$ . Since little is known about states in  ${}^6\text{Ga}$  a preliminary study of the  ${}^6\text{Zn}(p, n\gamma){}^6\text{Ga}$  reaction has been undertaken. The  $(p, n\gamma)$  reaction should reveal many of the  $\gamma$ -rays likely to follow the decay of  ${}^6\text{Ge}$ , since both will favor low-spin states.

A large number of low-energy  $\gamma$ -rays appear when the beam energy is raised well above 7.98 MeV, the threshold for  ${}^6\text{Zn}(p, n){}^6\text{Ga}$ . These are tabulated below, where an x signifies that a  $\gamma$ -ray has been observed clearly.

$E_\gamma$ (keV)	$E_p$ (MeV)						
	8.193	8.225	8.251	8.305	8.418	8.577	9.530
42.8		x	x	x	x	x	x
85.7		x	x	x	x	x	x
128.5		x	x	x	x	x	x
152.4						x	x
280.4						x	x
291.2							x
323.1						x	x
363.8						x	x
367.5							x
384.6							x
420.4							x
427.2						x	x
434.8							x
491.8							x
495.3							x
550.2							x
583.9							x
592.8							x
666.9							x
885.9							x

Based on energy sums a possible level scheme for  ${}^6\text{Ga}$  has been drawn up as shown. Some support for this scheme comes from earlier studies in this laboratory of the  ${}^6\text{Zn}({}^3\text{He}, t){}^6\text{Ga}$  reaction by Hinrichs.<sup>5</sup> However, the cross-sections in that

reaction are so low that the number of counts obtained was small, and the levels shown must be considered open to question.



Thus far, none of the above  $\gamma$ -rays has been observed in the thermalizer experiments, although  ${}^61\text{Cu}$ ,  ${}^61, 62, 63\text{Zn}$ ,  ${}^63, 64, 65\text{Ga}$  and possibly  ${}^65\text{Ge}$  activities have all been recognized. Present efforts are being directed towards reducing the background caused by long-lived activities, as it seems probable that the half-life of  ${}^6\text{Ge}$  will be quite short.

References

1. G.T. Garvey, W.J. Gerace, R.L. Jaffe, I. Talmi and I. Kelson, *Rev. Mod. Phys.* **41**, S1(1969).
2. W.D. Arnett, private communication (1971).
3. R.D. Macfarlane, R.A. Gough, N.S. Oakey, and D.F. Torgerson, *Nucl. Instr. and Methods* **73**, 285(1969).
4. K. Kosanke and G. Giesler, MSU report COO-1779-49(1970) p. 247.
5. R.A. Hinrichs, private communication (1971).



The bulk of the available information on the levels in  $^{40}\text{Ca}$  has been obtained through scattering experiments.<sup>1-5</sup> Although some earlier work on the  $^{40}\text{Sc}$  decay has been performed,<sup>6-8</sup> the rather short half-life of this isotope has hindered detailed  $\gamma$ -ray investigation of the levels in  $^{40}\text{Ca}$  populated by this decay. However, with the advent of slow-pulsing for the MSU Cyclotron, together with good on-line detection systems, it has now been possible to study the  $\gamma$  decay of  $^{40}\text{Sc}$  to obtain the levels in  $^{40}\text{Ca}$  with a relatively high degree of accuracy.

For these experiments, the beam pulsing and routing of the data was accomplished with a special timing module designed by Dr. P. Miller of this laboratory.<sup>9</sup> The beam was pulsed by modulation of the cyclotron RF. The timing module also provided adjustable routing outputs and an adjustable inhibition period after the beam burst. A typical period of modulation started with a 0.4-sec beam burst, during which data was stored in one 4096-channel spectrum, followed by a total beam-off period of 0.6 sec, divided into four additional 0.15-sec counting intervals. No inhibition period was used in these experiments.

Several kinds of targets were tried in attempts to reduce the background of unwanted  $\gamma$  rays. Slurries of  $\text{CaCO}_3$  (natural and isotopically enriched) were prepared in polystyrene or Duco-Cement binders on thin mylar. Good results, however, were not obtained until a 2-mg/cm<sup>2</sup>, 99.973% isotopically-enriched  $^{40}\text{Ca}$  foil, prepared at Oak Ridge National Laboratory, became available for this experiment. This foil was bombarded in a small chamber equipped with a vacuum-transfer port. A well-shielded Faraday cup was located about 2 m beyond the target. Background activity, induced by ions which suffered multiple scattering in the target, was minimized by removing all constrictions of less than 4-in. diameter between the target and Faraday cup. The target plane was inclined at 45° to the beam. At 90° to the beam, a 2.5%-efficient Ge(Li) detector was used to observe the  $\gamma$  rays following the  $\beta^+$  decay of  $^{40}\text{Sc}$ . This detector had a resolution of 2.1 keV and a peak-to-Compton ratio of 16.5:1. The  $^{40}\text{Sc}$  was produced by the  $^{40}\text{Ca}(p,n)^{40}\text{Sc}$  reaction, using a 24-MeV proton beam from the cyclotron.

The resulting  $\gamma$ -ray spectra were accumulated in the laboratory's Sigma-7 Computer.

Four beam-off routed spectra from this study are shown in Fig. 1. These resulted from a 32-hour accumulation of data in the slow-pulsing mode. From the half-lives, and comparison with scattering data, seven  $\gamma$  rays were found to belong in the  $^{40}\text{Ca}$  level scheme. The energies and intensities

of these  $\gamma$  rays are given in Table I. Although the intensities are in good agreement with most of the values reported by earlier workers,<sup>6-8</sup> the energies are not. The proposed decay scheme for  $^{40}\text{Sc}$  is shown in Fig. 2.

Table I  
 $\gamma$ -ray Energies and Intensities from the Decay of  $^{40}\text{Sc}$  to  $^{40}\text{Ca}$

Energy (keV)	Intensity
754.5±0.2	48±3
1121.4±0.6	13±2
1875.5±0.5	25±2
2043.6±0.3	27±3
3166.4±0.6	14±2
3736.9±0.7	100
3919.5±1.0	10±2

#### References

1. C.M. Braams, Phys. Rev. 101, 1764(1956).
2. P.M. Endt and C. Van Der Leun, Nucl. Phys. A105, 1(1967).
3. J.R. Erskine, Phys. Rev. 149, 854(1966).
4. W.S. Gray, R.A. Kenefick, and J.J. Kraushaar, Nucl. Phys. 67, 542(1965).
5. A. Springer and B.G. Harvey, Phys. Letters 14, 116(1965).
6. A.J. Armin, J.W. Sunier, and J.R. Richardson, Phys. Rev. 165, 1194(1968).
7. W.C. Anderson, L.T. Dillman, and J.J. Kraushaar, Nucl. Phys. 77, 401(1966).
8. E. Kashy and J.L. Snelgrove, Phys. Rev. 172, 1124(1968).
9. Nuclear Chemistry Annual Report, Michigan State University, 1970, p. 257.

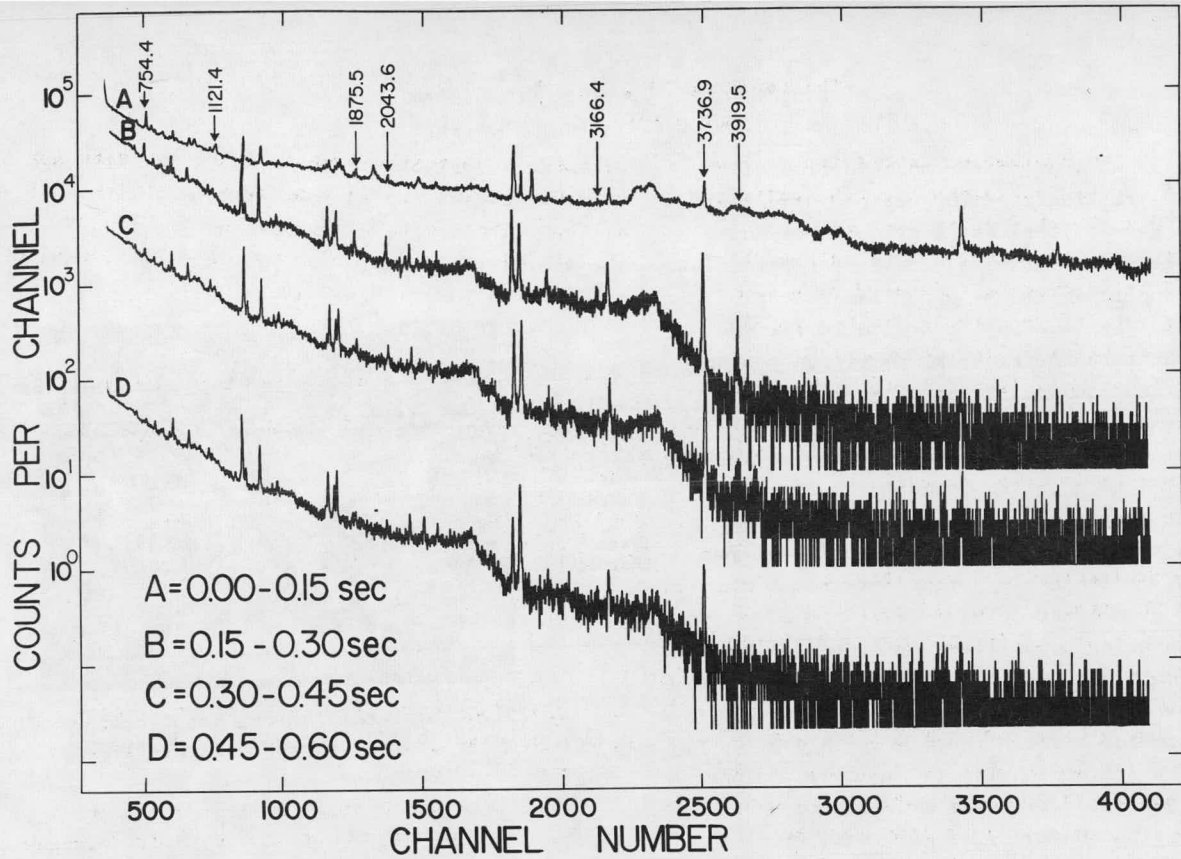


Fig. 1 Routed  $\gamma$ -ray spectra from the pulsed-beam study of  $^{40}\text{Sc}$ .

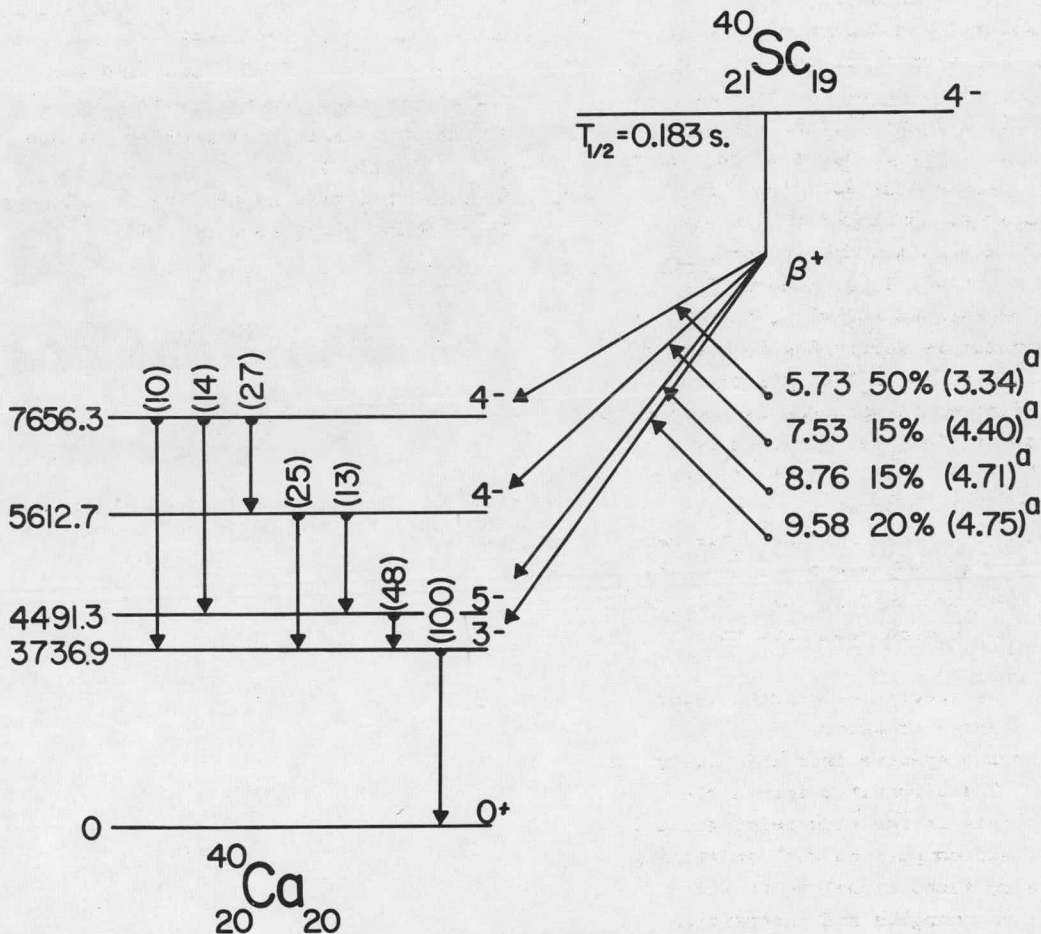


Fig. 2 The proposed  $\gamma$ -decay scheme for  $^{40}\text{Sc}$ .

<sup>a</sup>Values taken from Ref. 6.

Our initial motivation for construction of the He thermalizer-jet transport was its proposed use in an on-line mass filter (see Section 21 of this report). While this remains the case, the thermalizer-jet transport has become a popular research tool in itself. It is being used with increasing frequency for the rapid transport cyclotron produced activities to low background counting areas for conventional  $\gamma$  and  $\alpha$  counting experiments. To facilitate this use we have just completed a tape transport system to move the activity to successive detector locations after it is collected from the He-jet. We anticipate that the He thermalizer-jet transport will remain an important research tool in and of itself even after we have developed our on-line mass separation capability.

The thermalizer we constructed was patterned after that developed by R.D. Macfarlane<sup>1</sup> and we are grateful to him for his continued help in developing our system. We are continuing to use polyethylene capillary (0.034" ID) which was extended to about 60 feet in length. However, we will soon start using a larger diameter capillary in an attempt to reduce the recoil collection time by pumping a larger quantity of gas. The set up of the thermalizer shown in Fig. 1 is one in which three targets were used and the recoils collected at 90° to the cyclotron beam. Here the targets are staggered in the holder so that the He flow entering the teflon blocks from the right sweeps in front of each target successively. We have found the use of multiple targets to be a useful method of increasing the recoil yield in cases where the added time necessary to sweep the recoils from the larger volume into the capillary could be afforded. Further we have found collecting at 90° to the beam to be a more reliable technique than 0° (described in Ref. 1 and 2) for collecting and transporting the recoils. We do expect to use the 0° technique when working with extremely short lived activities.

References

1. R.D. Macfarlane, R.A. Gouch, N.S. Oakey, and D.F. Torgeson, ORO-3820-2 (1969); Nucl. Instr. and Methods 73, 285(1969).
2. K.L. Kosanke and G.C. Giesler. Michigan State University. Nuclear Chemistry Annual Report for 1970 (C00-1779-49) 247-50.

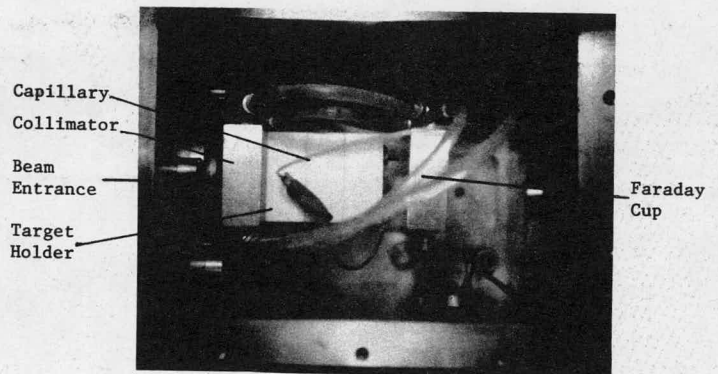


Fig. 1a Recoil thermalizer showing target holder-collector and Faraday Cup.

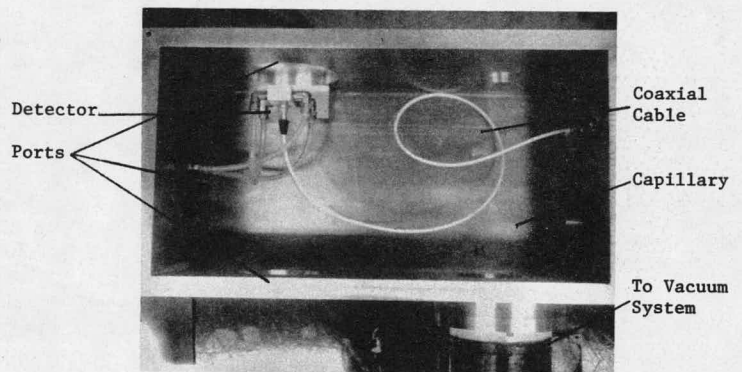


Fig. 1b Recoil counting chamber showing capillary and detector in cooled mount.

To date our work toward an on-line isotope separation has been directed at two areas of the overall system. First has been the development of our He thermalizer-jet transport (See next section of this report) with a tape transport that will later be used in our complete system. Second has been with our electric quadrupole mass filter. We have directed the initial work on our overall system to these areas because we felt they would each prove to be useful research tools in themselves and could be used before the complete system was constructed. The remaining work on the system will be the linking of these two pieces of hardware together.

The on-line mass separation system under construction and its operation are shown schematically in Fig. 1. A collimated cyclotron beam enters the apparatus, striking a thin target (or a series of thin targets if half-lives are sufficiently long) in an atmosphere of helium (1 to 3 atm. of pressure). Those nuclei near the back of the targets interacting with the beam will be recoiled out of the target into the helium. The recoils are then slowed to

thermal energies through collisions in the helium. Recent work by R.D. Macfarlane<sup>1</sup> suggests that the next step is the attachment of the recoils to large molecule collectors (with masses up to  $10^8$  amu) formed from impurities in the helium in the plasma generated by the cyclotron beam as it leaves the target passing through the helium atmosphere. The recoils then leave the thermalizer attached to these large molecular clusters through a polyethylene or teflon capillary<sup>2</sup> (0.02 to 0.06 in ID) accelerating to near the sonic velocity of He ( $\approx 3$ ft/msec). The capillary is run through concrete shielding to a low background area about 60 feet away. At the end of the capillary the helium will be skimmed off using a one or two stage skimmer. Quite efficient skimming of the helium should be possible<sup>1</sup> just by directing the flow from the capillary at a conical orifice. The molecular clusters with their horrendous masses are extremely well collimated and should be passed quite efficiently through the orifice whereas the helium will diverge and be largely pumped off. If our pumping capacity is not sufficient to reduce

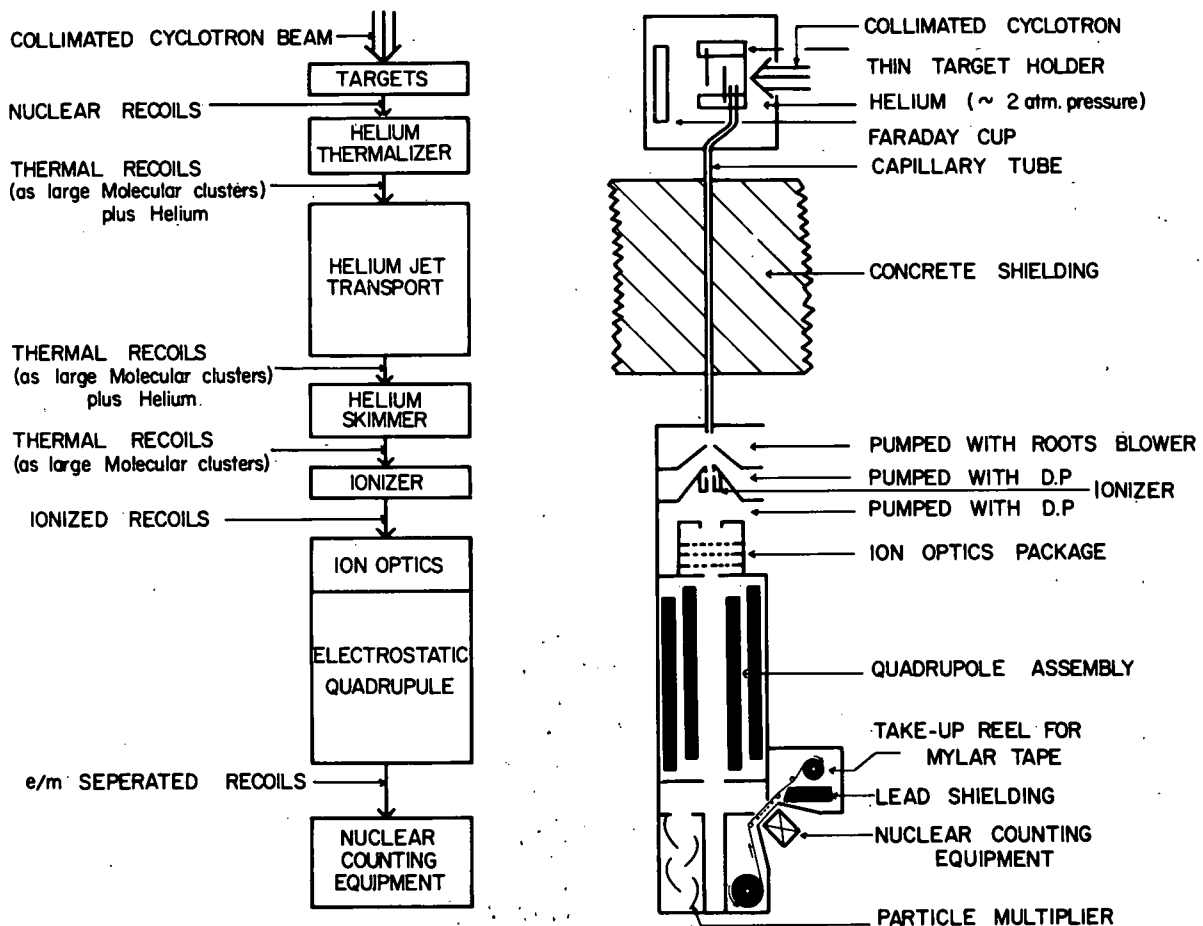


Fig. 1 Block and schematic diagrams of the on-line isotope separator.

the pressure to  $\sim 10^{-5}$  ton after the first skimming stage, a second stage will be added. The molecular clusters will be broken up and the recoils ionized in an RF or DC induced discharge setup in one of the skimming stages with the recoils directed into the ion optics associated with the electrostatic quadrupole.<sup>3</sup> With the quadrupole setup properly only selected masses are transmitted through it.<sup>4</sup> At the exit of the quadrupole the recoils will either be directed into an electron multiplier such that it is possible to obtain a mass scan or onto paper or aluminized mylar tape for conventional nuclear counting. A typical mass scan from the quadrupole is shown in Fig. 2.

#### References

1. H. Jungclas, R.D. MacFarlane, and Y. Fares, to be published.
2. K. Kosanke, G. Giesler, MSU Nuclear Chemistry Annual Report for 1970 (COO-1779-49) p. 247-50.
3. Electric quadrupole supplied by Extranuclear Labs. P.O. Box 11512, Pittsburgh, Penn.
4. For a theoretical description of the Electric Quadrupole sec: W. Paul, H.P. Reinhard, and U. von Zahn, Z. Phys. 152, 143(1958).

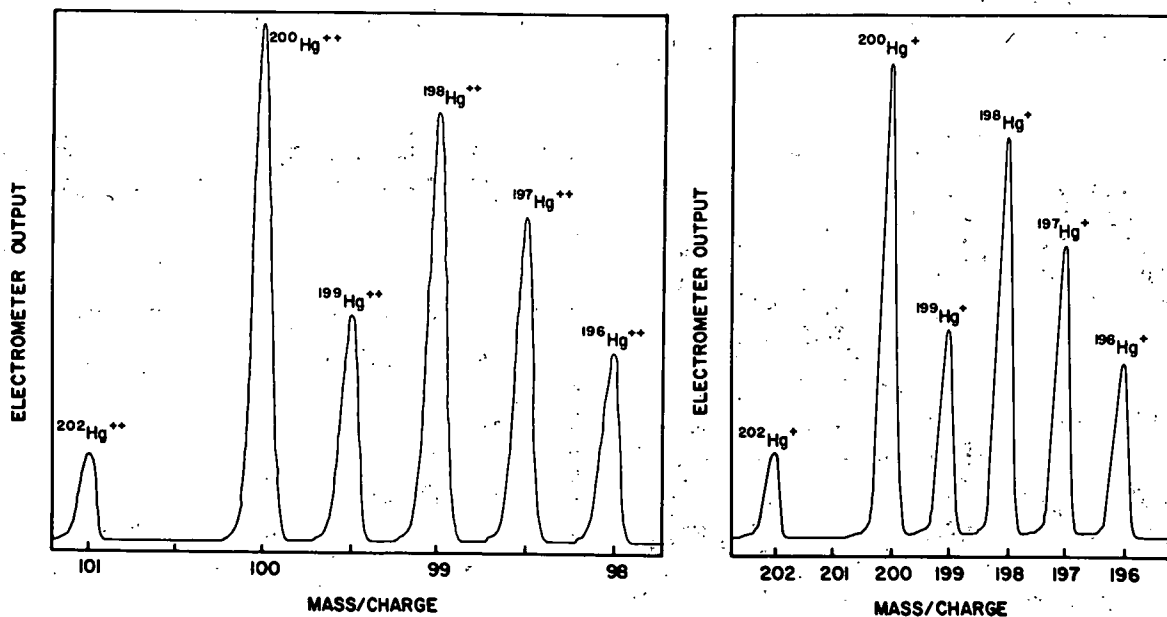


Fig. 2 Typical Hg mass spectra taken with the extranuclear electric quadrupole mass filter.

A pneumatic target system (rabbit) has been developed to aid in the study of moderately short-lived nuclides ( $t_{1/2} \sim 3$  seconds) and to make more efficient use of the cyclotron time in general. The functioning of the rabbit system is diagrammed in Fig. 1. The rabbit has proven so successful that for the past two years all sources prepared for off-line study by the Nuclear Chemistry and Physics groups here in the lab were made using the rabbit system.

Target holders (rabbits) and the terminals of the system (rabbit hutches) are shown in Fig. 2. Rabbits used for irradiation are 2 inches in diameter and 3 inches long, with target material and associated absorbers carried in the central region. The targets are air cooled directly and water cooled by conduction through the target holder. The rabbit can be reproducibly oriented ( $\pm 5^\circ$ ) with respect to the cyclotron beam. The mechanism used to orient the rabbit is to rotate it by directing a jet of air onto a set of fins near its base. The rotation is stopped by the attraction between a small permanent magnet mounted

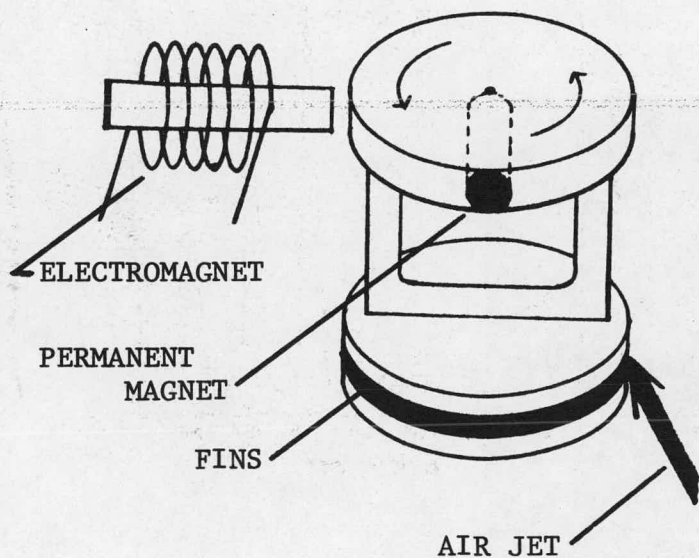


Figure 3

in the top portion of the rabbit and an electromagnet in the rabbit hutch. The rabbit shown with an exploded view of its sample container in Fig. 2 has been quite useful in preparation of multiple separated isotope targets. The central bolt-like piece contains one sample, and a series of sample containers and/or absorbers are stacked before it. In this way, we have prepared as many as four sources at once. The rabbit is constructed such that only the fraction of cyclotron beam that passes through the 5/16-inch diameter target

container reaches the Faraday cup, so only that portion of the beam passing through target material is monitored.

The rabbit is propelled through a cellulose acetate pipe (with bends made of poly-vinyl-chloride pipe) by setting up a pressure differential across the rabbit. We are now using 3psi pressure on one side of the rabbit and a partial vacuum, created by a commercial vacuum cleaner, on the other. At the end of its path the rabbit is stopped with an air cushion, initiated by a small unit attached to the rabbit pipe to sense the passage of the magnet mounted in the rabbit. Transit times for the rabbit are now usually  $\sim 5$  seconds. This is almost twice as long as previously reported. This is because we have lengthened rabbit line to about 250 ft. We felt the added transit time, allowing us to move to a more convenient location was acceptable in that our searches for shorter lived isotopes are now being conducted using our He thermalizer-ject transport (see another section of this report).

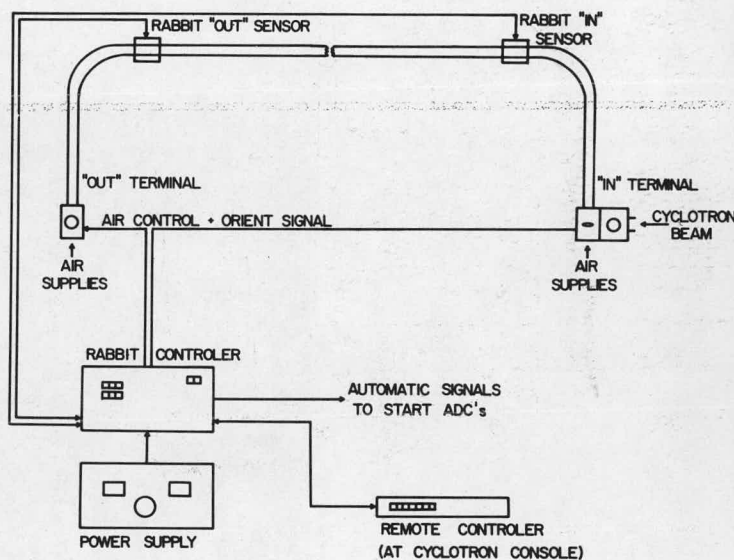


Fig. 1 Schematic lay-out of "Rabbit" system.

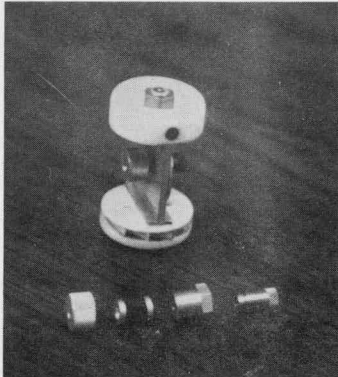
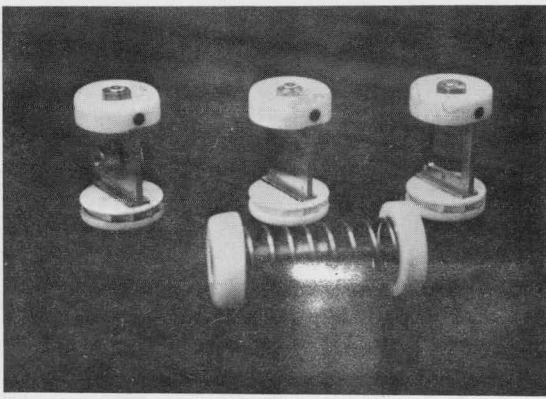


Fig. 2a "Rabbits" used in system.

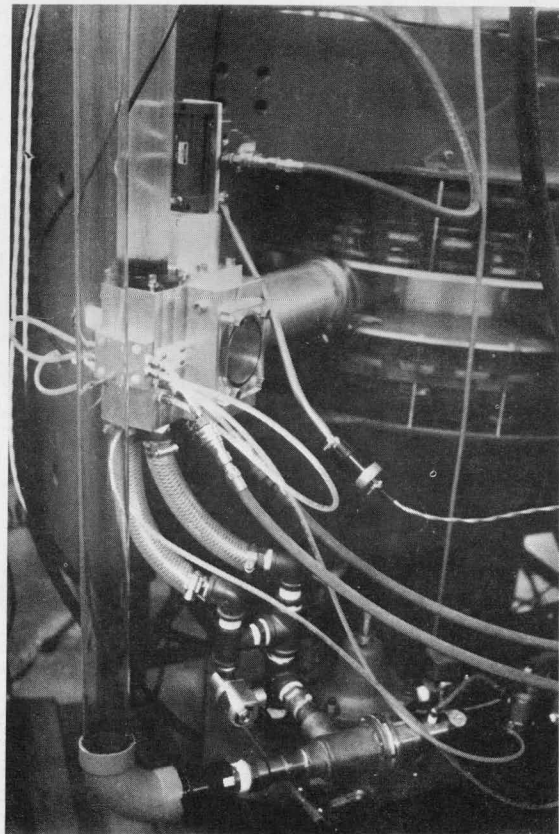


Fig. 2b "In-Terminal" of system.

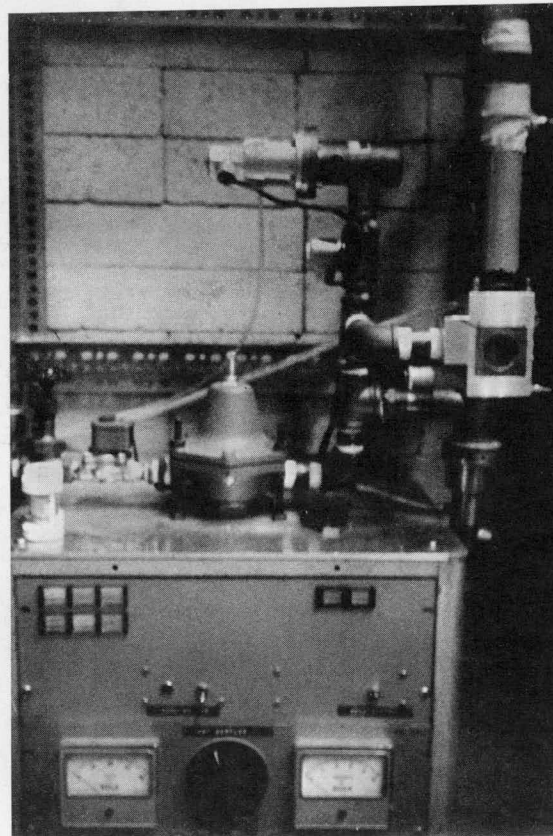


Fig. 2c "Out-Terminal" of system.

Our initial  $\gamma$  sources were prepared by bombarding natural Pb foils with 36 MeV protons to induce the  $^{20}\text{Pb}(p,4n)^{205}\text{Bi}$  reaction. The targets were aged from 6 to 10 weeks to optimize the  $15.3\text{d }^{205}\text{Bi}$  activity. Before counting, the  $^{205}\text{Bi}$  activity was chemically separated from the targets.<sup>1</sup> Additional  $\gamma$  sources were prepared by bombarding mass separated  $^{206}\text{Pb}$  with 19 MeV protons to induce the  $^{206}\text{Pb}(p,2n)^{205}\text{Bi}$  reaction and also by bombarding natural Tl with 37 MeV alphas to induce the  $^{205}\text{Tl}(^4\text{He},4n)^{205}\text{Bi}$  reaction. The primary detector used was a Ge(Li) detector with 3.6% efficiency relative to a 3"x3" NaI(Tl) detector and had a photopeak resolution (FWHM) of 2.1 keV at 1.332 MeV. In our  $\gamma$  singles experiment we identified and determined intensities for 97 definite and 15 possible transitions as belonging to the decay of  $^{205}\text{Bi}$ . Also we have placed upper intensity limits on 12 transitions reported by other investigators and not observed in this study.

The primary thrust of our study was the conduction of two megachannel Ge(Li) vs Ge(Li) coincidence experiments.<sup>2</sup> In the second run of the experiment >3.5 million coincidence events were recorded on magnetic tape. Detectors having 2.5% and 3.6% relative efficiencies and placed at  $\sim 75^\circ$  to each other with a graded level absorber between them were used to collect the coincidence events. Subsequent to collecting the coincidence events the tapes were played back having set various gates to be scanned on each pass. In addition to generating spectra by setting gates on peaks, backgrounds adjacent to peaks and normalized peak to background difference spectra could be generated. Accordingly using these 3 different types of coincidence spectra it was readily possible to make coincidence assignments. More than 300 different gates were set on 95 areas of interest in the spectrum. In a few cases where the coincidence results were ambiguous, the event tapes were played back in a sum coincidence mode<sup>3</sup> allowing a few additional coincidence assignments. On the basis of this coincidence study, we have placed 80 transitions in our first confidence decay scheme (see Fig. 1). Also, less conclusive coincidence data helped place 14 of 27 additional transitions included in our second confidence decay scheme.

Another area of investigation of the  $^{205}\text{Bi}$  decay was the  $\beta^+$  feedings to states in  $^{205}\text{Pb}$ . For this study we used a 2.5% Ge(Li) detector with a resolution (FWHM) of 2.3 keV at 1.33 MeV in conjunction with an 8"x8" NaI(Tl) split annulus having a resolution of  $\sim 10\%$  at 1.33 MeV. The Ge(Li) detector was located just outside the annulus with the source placed inside the annulus. The events analyzed required a triple coincidence between the Ge(Li) detector and the halves of the

annulus each gated on the 511 keV region and had a resolving time of  $\sim 150$  nsec. After correcting for chance energy sums, Compton events, and pair producing transitions a ratio of the triple coincidence to singles count rate was determined. Repeating the experiment using  $^{22}\text{Na}$  with a known  $\epsilon/\beta^+$  ratio we were able to report the following percent  $\beta^+$  feeding in  $^{205}\text{Bi}$ : 703.4-keV level 0.095  $\pm$  0.02%, 987.5-keV level 0.006  $\pm$  0.002%, 1043.7-keV level <0.002%.

The final area of investigation was the search for the n and o conversion of the 2.3-keV first excited to ground state transition.<sup>4</sup> This was accomplished using the Michigan State University  $\pi/Z$  beta spectrometer with a post accelerator which extended its range to <1 keV. Needless to say the chemistry involved in the source preparation required exceptional care to maintain the necessary parity. We observed definite  $n_{\text{II}}$  and  $n_{\text{III}}$  lines with the ratios,  $n_{\text{II}}/n_{\text{III}}=0.70 \pm 0.25$  and  $n_{\text{II}}+n_{\text{III}}/L_{\text{I}}(26.22 \text{ keV}) = 0.48^{+0.15}_{-0.05}$ .

## References

1. K.L. Kosanke, W.H. Kelly, Wm.C. McHarris, to be published in Phys. Rev.
2. Event Recorder/Recovery described in MSU Cyclotron Annual Report for 1969-70, pp. 107.
3. G.C. Giesler, K.L. Kosanke, R.A. Warner, Wm.C. McHarris, Nucl. Instr. and Methods, 93, 211(1971).
4. W.C. Johnston, W.H. Kelly, S.K. Haynes, K.L. Kosanke, Wm.C. McHarris, Phys. Rev. Letters 26, 1043(1971).



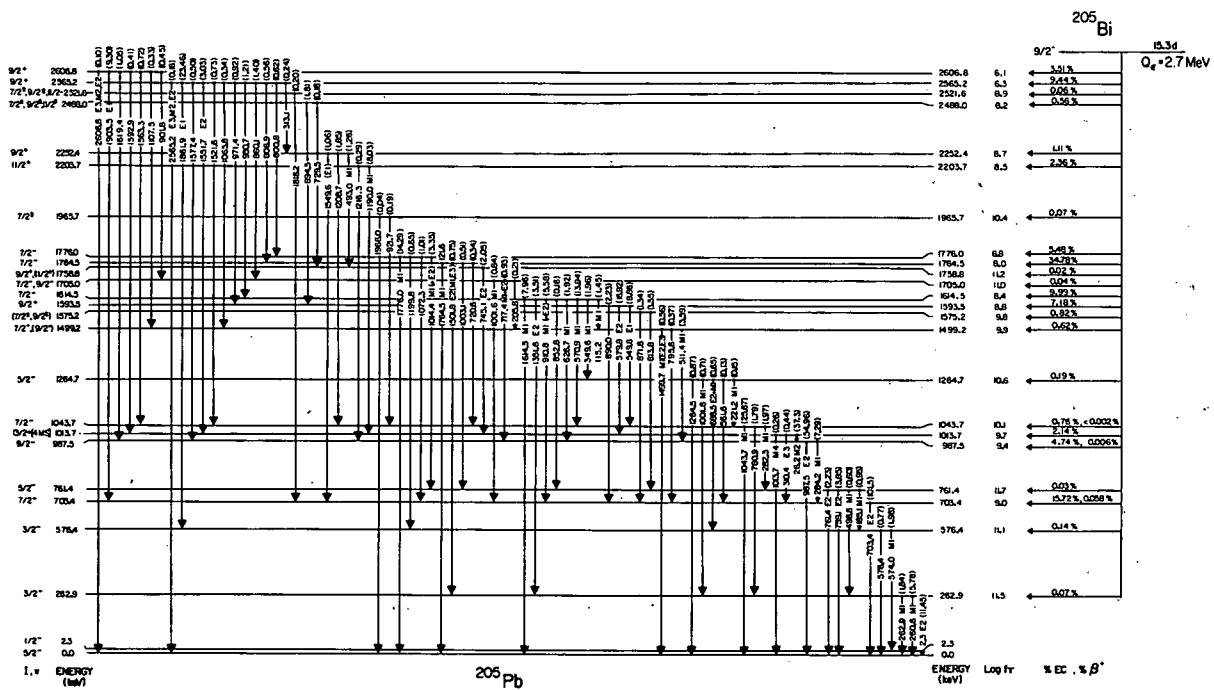


Fig. 1a  $^{205}\text{Bi}$  first confidence decay scheme.

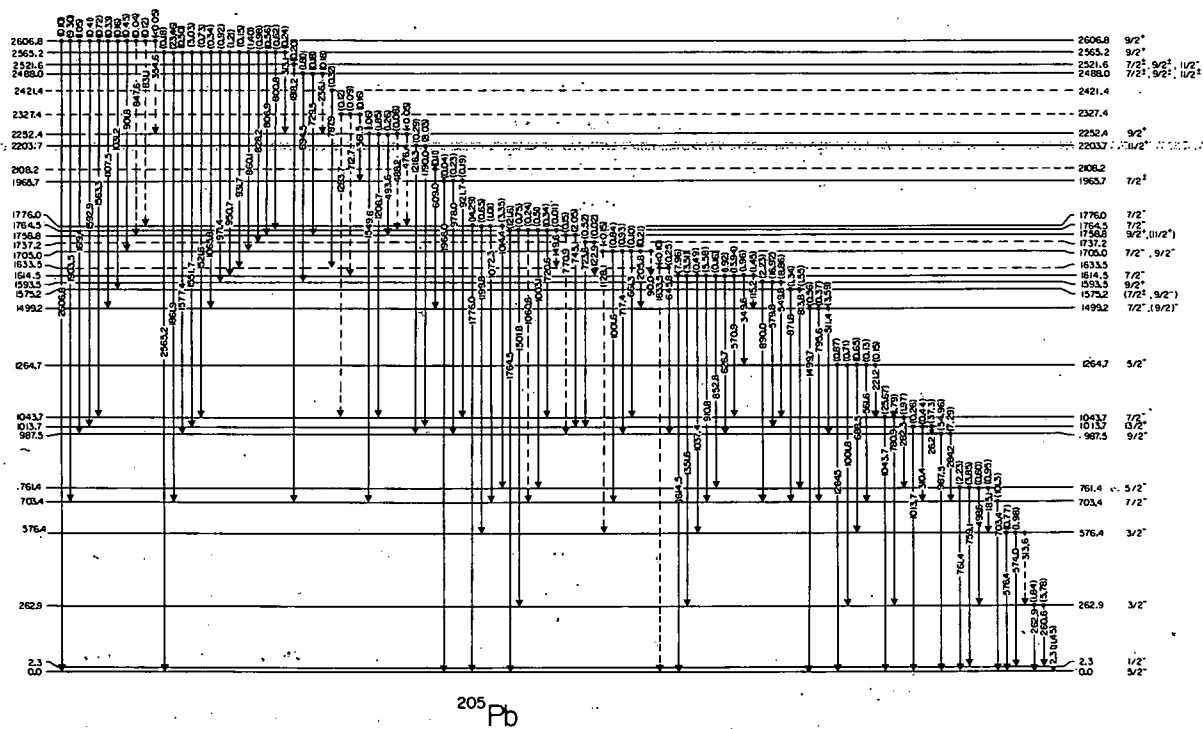


Fig. 1b  $^{205}\text{Bi}$  second confidence decay scheme.

Since the existence of an isomer associated with  $^{202}\text{Pb}$  was first reported<sup>1</sup> in 1954, the decay of  $^{202}\text{mPb}$  has been the object of several further studies.<sup>2-5</sup> The most extensive of these was conducted by McDonnell and co-workers.<sup>4</sup> Their investigation resulted in a decay scheme that has remained essentially unchanged until the present study.

Our renewed interest in this isomer was stimulated by work done in this laboratory on the decay of  $^{201}\text{Pb}$  in which accurate  $\gamma$ -ray intensities of several of the  $^{202}\text{mPb}$  transitions were needed in order to correct for their contributions to the  $^{201}\text{Pb}$  spectra. In our attempt to determine these intensities, several previously unreported  $\gamma$ -ray transitions with a 3- to 4-hour half-life were observed. It was, therefore, deemed worthwhile to conduct a more extensive investigation of  $^{202}\text{mPb}$  using the improved  $\gamma$ -ray spectroscopic techniques now available.

The  $^{202}\text{mPb}$  sources were prepared by bombarding natural thallium foils and enriched  $^{203}\text{Tl}$  (70%  $^{203}\text{Tl}$ , obtained from Oak Ridge National Laboratory) with a 16-MeV proton beam from the Michigan State University Cyclotron. The induced  $^{203}\text{Tl}(p,2n)^{202}\text{mPb}$  reaction produced the desired activity in good yield with a 7-10 min. bombardment at a beam current of 0.7  $\mu\text{A}$ . No chemical separation was deemed necessary, but sources were allowed to age for a period of 2 to 3 hours before counting in order to minimize contamination from shorter-lived isotopes.

The energies and intensities of the  $\gamma$ -rays emitted in the decay of  $^{202}\text{mPb}$  were studied using a Ge(Li) detector with a photopeak efficiency of 10.4% at 1332 keV (compared with the efficiency of a 3x3 in. NaI(Tl) detector having the source at a distance of 25 cm) and an optimum resolution of 2.1 keV at that same energy. A typical  $^{202}\text{mPb}$   $\gamma$ -ray singles spectrum is presented in Fig. 1. Seventeen

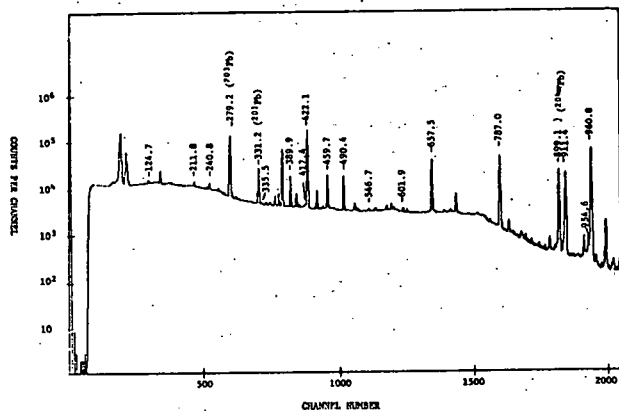


Fig. 1 A typical  $^{202}\text{mPb}$   $\gamma$ -ray singles spectrum.

$\gamma$ -rays with a half-life comparable to that of  $^{202}\text{mPb}$  were observed. Table I lists the energies and relative intensities of these  $\gamma$ -rays and compares our values with those obtained by McDonnell et al.<sup>4</sup> Of the transitions in this table, those

Table I

Energies and Relative Intensities of  $\gamma$ -rays and Conversion Electrons from the Decay of  $^{202}\text{mPb}$

Energy (keV)	Relative $\gamma$ -ray Intensity	Relative Conversion Line Intensity <sup>a</sup>
124.75±0.09	1.3 ±0.4	---
211.88±0.07	1.12±0.5	---
240.83±0.08 <sup>b</sup>	1.17±0.4	---
335.56±0.1	0.32±0.7	1.3±0.1
389.91±0.07	8.9 ±0.1	28. ±3.
417.44±0.1	0.68±0.08	---
422.13±0.06	128.1 ±0.3	66. ±5.
459.11±0.08	13.5 ±0.1	9. ±1. (EL)
490.44±0.07	14.9 ±0.2	1.7±0.2(EL)
546.7 ±0.5	0.25±0.1	1.1±0.1(EL)
601.95±0.09	1.05±0.08	---
657.48±0.06	60.6 ±0.3	4.4±0.4
787.00±0.06	100	100
954.62±0.09	1.9 ±0.2	---
960.77±0.3	194.8 ±0.4	13. ±1.
---	---	690. ±50. (EL)
---	---	17. ±3.
---	---	4.0±0.3
---	---	2.5±0.2

<sup>a</sup>From McDonnell et al. (Ref. 7). Relative intensities are for the K-conversion lines unless otherwise specified.

<sup>b</sup>In our measurements we were unable to delineate between the 240.3- and 241.1-keV  $\gamma$  rays emitted in the decay of  $^{202}\text{mPb}$ . The energy and relative intensity given here, are therefore due to the total unresolved doublet peak.

with energies of 124.75-, 211.88-, 417.44-, 601.95-, and 954.6-keV have not been previously reported. Among these, the 417.44-keV transition was seen to fit into the existing decay scheme between the 2041- and 1624-keV levels in  $^{202}\text{Pb}$ . The existence of a transition in this energy range was predicted by McDonnell et al.,<sup>4</sup> but no experimental verification was available at that time. Energy sums and differences indicated that the remaining four transitions could be incorporated into the decay scheme by adding two new energy levels: one at 1916.6 keV in  $^{202}\text{Pb}$  and one at 1552.1 keV in  $^{202}\text{Tl}$ . These levels have been included in the decay scheme given in Fig. 2.

To determine the cascade relationships in the decay of  $^{202}\text{mPb}$  and help test the consistency of these new assignments, a  $\gamma$ - $\gamma$  coincidence experiment was performed. For these measurements, the detector mentioned above was coupled with a 4.6% efficient Ge(Li) detector with an optimum resolution of 1.9 keV at the energy of 1332 keV. The addresses of coincidence events from both sides of the system were processed and listed on magnetic tapes, to be recovered later, off-line, as gated



The Decay of  $^{170}\text{Lu}$  to Levels in  $^{170}\text{Yb}$ <sup>\*</sup>  
 D.C. Camp<sup>\*\*</sup> and F.M. Bernthal

A detailed study of the complex decay of  $^{170}\text{Lu}$  to levels in  $^{170}\text{Yb}$  has recently been carried out at the Berkeley and Livermore Lawrence Radiation Laboratories and the MSU Cyclotron Laboratory.

The  $^{170}\text{Lu}$  activity was produced by irradiating  $\text{Tm}_2\text{O}_3$  with 40 MeV  $\alpha$ -particles at the Berkeley 88-inch cyclotron. Ge(Li) and Si(Li) detectors were employed to obtain  $\gamma$ -ray singles, conversion electron, and  $\gamma$ - $\gamma$  coincidence data. The  $\gamma$ -ray singles and pair-peak data were gathered with the Livermore anti-Compton spectrometer operated in the Compton-suppression and double-escape pair-peak modes simultaneously. Isotope-separated sources of  $^{170}\text{Lu}$  were obtained for counting the low-energy portion of the spectrum and for the Ge(Li)-Ge(Li)  $\gamma$ - $\gamma$  coincidence experiments. The conversion electron spectrum from 0-3 MeV was obtained with use of a 3-mm deep by 1cm<sup>2</sup> cooled Si(Li) detector.

A total of 550  $\gamma$ -ray transitions has been observed in the  $^{170}\text{Lu}$  decay spectrum, 217 of which are assigned to the  $^{170}\text{Yb}$  level scheme on the basis of 112  $\gamma$ - $\gamma$  coincidence spectra. An additional 118  $\gamma$ -ray transitions were placed in the level scheme on the basis of energy differences. The proposed  $^{170}\text{Yb}$  level scheme is shown in Fig. 1. Spin and parity assignments are proposed for some 48 levels. Not included in Fig. 1 are those  $\gamma$ -rays that could be assigned from energy differences.

One of the most unusual features of the  $^{170}\text{Yb}$  level scheme is the appearance of four low-lying  $0^+$  excitations, at 1069.4, 1228.9, 1479.9, and 1566.4 keV. The pairing energy gap  $2\Delta$  is thought to be about 1.7 MeV in this nucleus, so all four of the observed states lie within the gap and must be presumed to be influenced by collective interactions. Numerous explanations have been proposed to account for the presence of such multiple  $0^+$  excitations in doubly-even deformed nuclei.<sup>1</sup> None of these explanations has been very successful, however, and it appears that further progress in this area must await more detailed experimental data.

One useful property of the  $K=0^+$  excitations that may be extracted from decay data is the ratio of monopole to quadrupole decay into other  $0^+$  bands. This ratio is usually expressed as the X-parameter,  $\rho^2 e^2 R_0^2 / B(E2)$ .

Table 1 gives a summary of the X-parameters for the  $I\pi K=0+0$  and  $2+0$  excitations in  $^{170}\text{Yb}$ . Also shown in Table 1 are derived values for the nuclear monopole transition moment,  $\rho(E0)$  for cases where B(E2) data from the Coulomb excitation work of Riedinger, *et al.*<sup>2</sup> are available. The most evident conclusion that may be drawn from these data is that the 1228.9-keV  $0^+$  state seems to carry the bulk of

Table 1. Values of the Parameters

$$X = \frac{\rho^2 e^2 R_0^2}{B(E2)} \text{ for } ^{170}\text{Yb}$$

Level(keV)	$I\pi K$	X	$\rho^+$
1069.4	$0+0_1$	0.0049	$\leq 0.009$
1145.6	$2+0_1$	$\leq 0.032$	$\leq 0.01$
1228.9	$0+0_2$	0.080	0.13
1306.4	$2+0_2$	$\leq 0.14$	
1479.9	$0+0_3$	0.94	
1534.5	$2+0_3$	$\leq 1.2$	
1566.4	$0+0_4$	0.54	
1634.8	$2+0_4$	$\leq 0.50$	

<sup>+</sup>Values for  $\rho$  derived with use of preliminary data of Riedinger, *et al.*<sup>2</sup>

the quadrupole vibrational strength in  $^{170}\text{Yb}$ . The exact character of the other  $0^+$  states is still in question.

Also of interest in the  $^{170}\text{Yb}$  level scheme is the  $2+2$   $\gamma$ -vibrational state ostensibly at 1138.6 keV. The  $\gamma$ -ray branching data and Riedinger's B(E2) data indicate very strong mixing between this state and the  $2+0_1$  state.

It is also noteworthy that we are able to observe the E0 transitions between several of the excited  $0^+$  states in  $^{170}\text{Yb}$ . The E0 moment,  $\rho(E0)$ , between these states seems to be comparable to the moment to the ground state.

Finally, we are unable to identify in  $^{170}\text{Yb}$  a level at 2533.1 keV previously thought to be of the type  $I\pi K=1+0$ .<sup>3</sup> According to Gabrakov *et al.*<sup>4</sup> such a state would be predominantly  $\{5/2[5234]_{n\setminus} - 5/2[512+]_n\}$ , but would also exhibit a weak collectivity proposed to arise from oscillations of the spin part of the nuclear magnetic dipole moment.

Details of the  $^{170}\text{Yb}$  level scheme will be discussed further in a forthcoming publication.<sup>5</sup>

References

1. N.I. Pyatov, JINR Report P4-5422(1970); F.M. Bernthal, J.O. Rasmussen, and J.M. Hollander, *Bull. Am. Phys. Soc.* **15**, 523(1970).
2. L.L. Riedinger, private communication (1971).
3. N.A. Bonch-Osmolovskaya, H. Ballund, A. Plochocki, Z. Preibisz, and A. Zglinski, *Nucl. Phys.* **A162**, 305(1971).
4. S.I. Gabrakov, A.A. Kuliev, and N.I. Pyatov, *Sov. Journ. Nucl. Phys. (trans.)* **12**, 44(1971).
5. To be submitted to *Physical Review*.

<sup>\*</sup>This work was supported in part by the U.S. Atomic Energy Commission.

<sup>\*\*</sup>Lawrence Radiation Laboratory, Livermore, California 94550

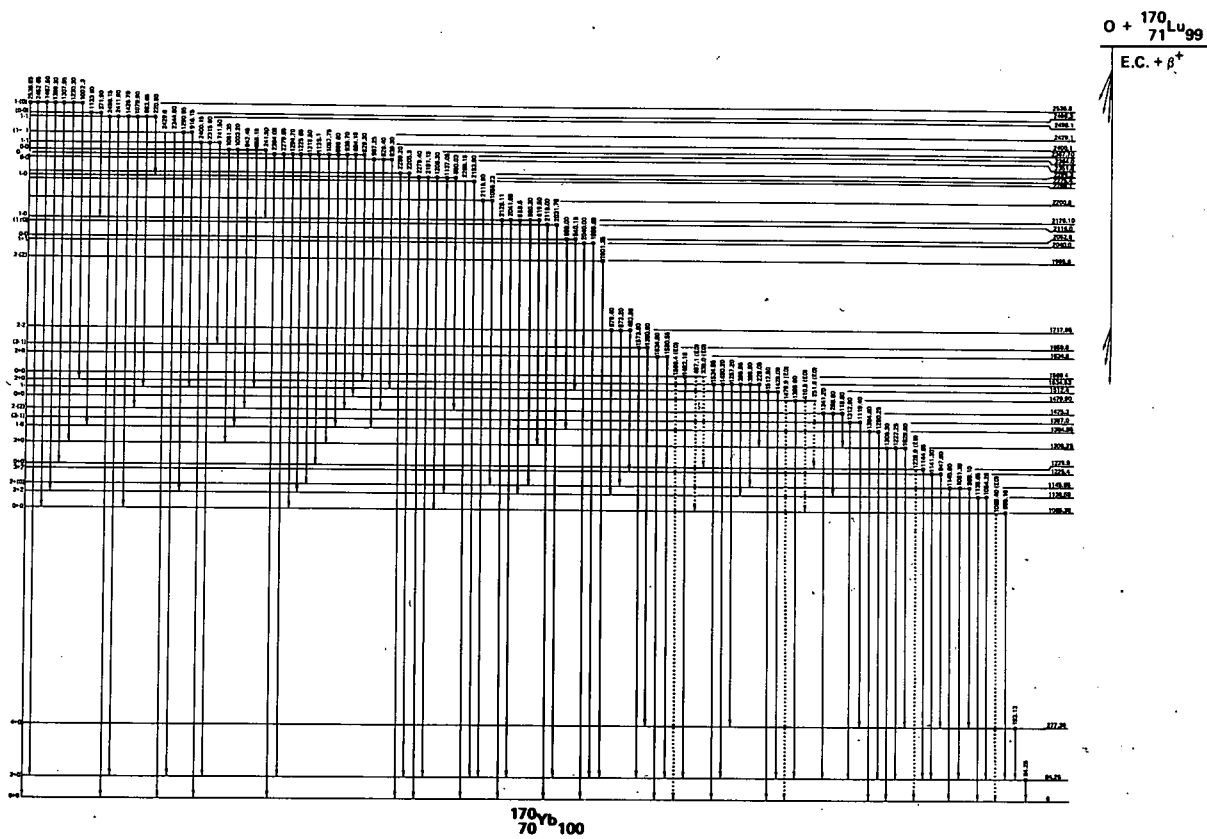


Fig. 1a Decay scheme for 0-2600 keV levels in  ${}^{170}\text{Yb}$  populated by EC- $\beta^+$  decay of  ${}^{170}\text{Lu}$ .

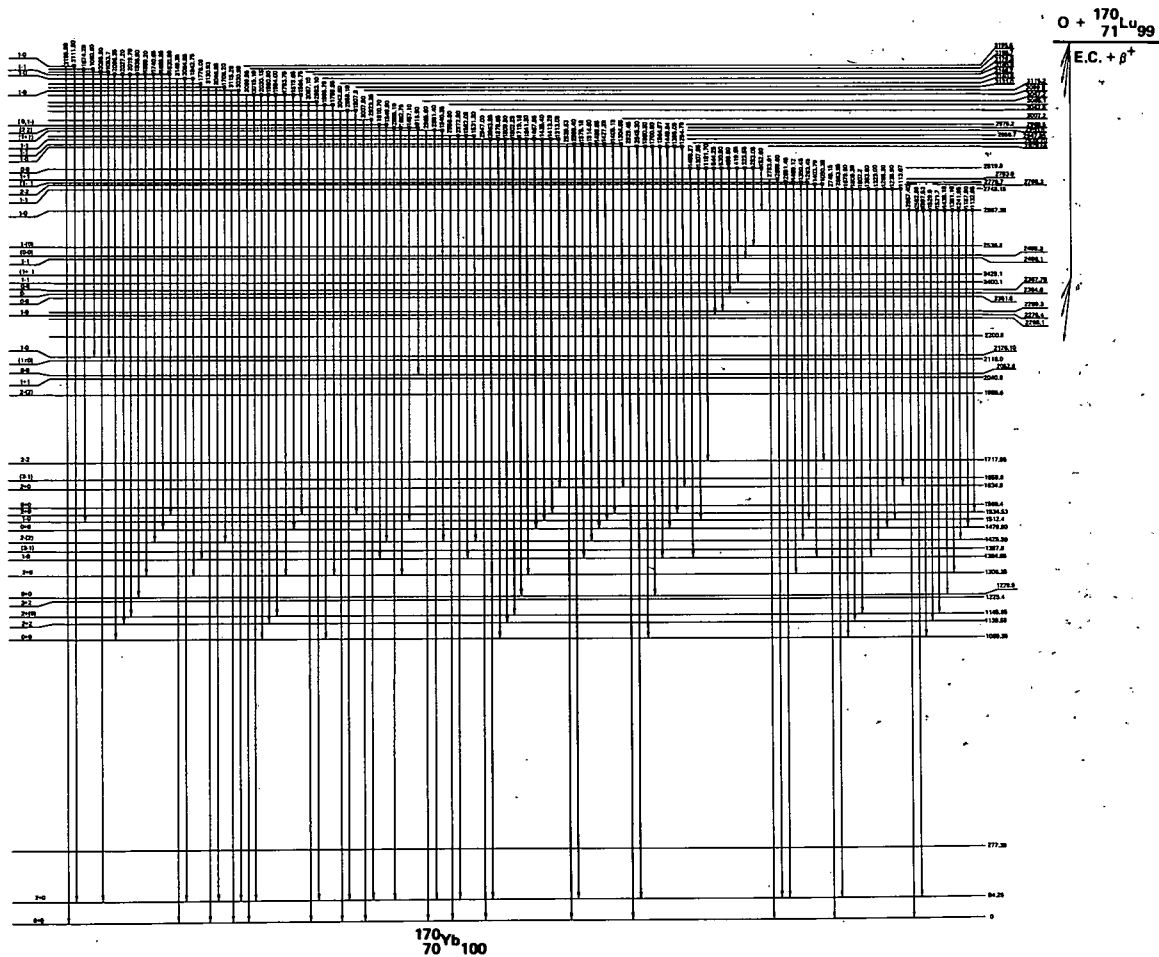


Fig. 1b Decay of 2600-3200 keV levels in  ${}^{170}\text{Yb}$  populated by EC- $\beta^+$  decay of  ${}^{170}\text{Lu}$ .

2

Study of Levels in Even-Even Deformed Nuclei  
by ( $^3\text{He},d$ ) and ( $^4\text{He},t$ ) Reaction Spectroscopy  
F.M. Bernthal and R.A. Warner

One of the most puzzling phenomena discovered in recent years in the "well-understood" doubly-even deformed nuclei has been the systematic occurrence of multiple low-lying excited  $0^+$  states. The energies of several of these states have commonly been found to lie within the pairing gap,  $2\Delta$ , a region once thought to be reserved for only  $0^+$  states of the simplest quadrupole-type  $\beta$ -vibrations, and more recently, perhaps, for pairing vibrations. In  $^{170}\text{Yb}$  for example,<sup>1</sup> no less than four  $0^+$  states are observed below 1600 keV.

It has proved difficult to account for this phenomenon in  $^{170}\text{Yb}$  as well as in other deformed nuclei. Though various explanations have been proposed,<sup>2</sup> none of them has been entirely satisfactory, and in the absence of detailed information on the structure of the multiple  $0^+$  states, it has proved difficult to test the various collective interactions thought to influence these states.

Decay work has successfully identified the locations of many of the  $0^+$  states, but details of their structure are perhaps best determined by other means. One such means is the use of single-particle and two-particle transfer reactions to deduce spectroscopic factors for populating the  $0^+$  states. We have begun a program of study at the MSU Cyclotron Laboratory designed to extract the information on  $0^+$  states that such transfer reactions can provide. Initial work has been carried out on levels in  $^{170}\text{Yb}$  and  $^{176}\text{Hf}$  by the  $^{169}\text{Tm}(\alpha,t)$ ,  $^{169}\text{Tm}(^3\text{He},d)$  and the  $^{176}\text{Lu}(\alpha,t)$  and  $^{175}\text{Lu}(^3\text{He},d)$  reactions. Multiple  $0^+$  excitations in both residual nuclei are well characterized from earlier work. The experiments have been carried out with 33-MeV  $\alpha$ -particles bombarding carbon-backed foils of the rare-earth metals. The outgoing particles were energy-analyzed in the MSU broad range Enge-type split-pole magnetic spectrograph and were collected on nuclear emulsion plates for counting.

To date, lower resolution studies ( $\sim 25$  keV FWHM for tritons) have revealed several qualitative features of the  $^{170}\text{Yb}$  and  $^{176}\text{Hf}$  nuclei in the region of interest, and it is already clear that there are wide variations in the proton-transfer cross-sections leading to the various  $0^+$  levels in these nuclei. Further experiments are planned which will employ thinner targets in an effort to enhance the resolution. Also planned are  $(p,t)$  reaction studies of the same residual nuclei to measure the possible influence of neutron pairing vibrations on the observed  $0^+$  states.

References

1. D.C. Camp and F.M. Bernthal, this report.
2. For an excellent review of current thinking on the subject, see N.I. Pyatov, JINR Report P4-5422(1970).

---

\*This work supported in part by the U.S. Atomic Energy Commission.

In-Beam ( $\alpha, xn\gamma$ ) and ( $^3\text{He}, xn\gamma$ ) Studies of Rotational Band Structure  
in Transitional Odd-Mass Deformed Nuclei\*

F.M. Bernthal and R.A. Warner

Studies of the rotational band structure in deformed odd-A nuclei have yielded a substantial amount of information on the interaction between collective and single-particle motion in such nuclei. Most thoroughly studied has been the rotational band mixing that results from the Coriolis interaction. It has become common practice to solve for the perturbed quasi-particle wavefunctions at increasing rotational angular momentum by making use of the experimentally observed energies of rotational band members and then diagonalizing the complete Coriolis interaction matrix. The Nilsson wave-functions are most commonly used as a basis set in this type of calculation.

Such a procedure has apparently been quite successful in accounting for the highly perturbed band structure of the so-called "parity-unique" Nilsson states emanating from the  $h_{11/2}$  and  $i_{13/2}$  shell-model states. The behavior of odd-A nuclei near the edges of deformation is still poorly documented, however, and it appears that a substantially different treatment of the coupling between rotational and particle motion may be required in such nuclei.<sup>1,2</sup>

One method of tracing the transition from deformed to spherical equilibrium shape is to observe the breakdown of rotational band structure as one moves away from the regions of stable deformation. We have embarked on a program of study to elucidate the structure of such transitional nuclei. The techniques of ( $\alpha, xn$ ) and ( $^3\text{He}, xn$ ) in-beam  $\gamma$ -ray spectroscopy are being employed. Because of the complex, poorly-ordered structure of these nuclei,  $\gamma$ - $\gamma$  coincidence data are required to deduce band structure. Initial difficulties with electronic interference from the cyclotron RF oscillator seem now to have been overcome and excellent in-beam Ge(Li)-Ge(Li) coincidence data have been obtained. Full-width at half maximum time resolution for a detector system comprised of two large-volume coaxial detectors has been less than 15 nsec with a 20:1 dynamic range.

Initial studies are focusing on the N=105 and 107 isotones in an attempt to follow the behavior of the  $9/2+[624]$  rotational band in the  $^{179}\text{W}$ ,  $^{181}\text{W}$ ,  $^{181}\text{Os}$ , and  $^{183}\text{Os}$  nuclei. This  $9/2+$  member of the  $i_{13/2}$  family of Nilsson states has previously been shown to be highly perturbed.<sup>3</sup> Similar studies are planned for the transitional Sm and Gd nuclei. Preliminary data have now been obtained on  $^{179}\text{W}$ ,  $^{183}\text{Os}$ , and  $^{151}\text{Gd}$ .

References

1. P. Vogel, Phys. Letters 33B, 400(1970).
2. I. Rezanka, J.O. Rasmussen, and R. Needham, Preprint (1971).

3. F.M. Bernthal and J.O. Rasmussen, Nucl. Phys. A101, 513(1967); F.M. Bernthal, (Thesis) UCRI-18651(1969).

---

\*This work supported in part by the U.S. Atomic Energy Commission.

The (p,t) reaction on  $^{141}\text{Pr}$ ,  $^{159}\text{Tb}$ ,  $^{165}\text{Ho}$  and  $^{169}\text{Tm}$  has been carried out for the purpose of studying the general systematics of the (p,t) reaction on rare earth nuclei.

#### $^{141}\text{Pr}(p,t)$ Experiment

In this study an  $\sim 800 \mu\text{g}/\text{cm}$  metallic target of  $^{141}\text{Pr}$  was bombarded with 40-MeV protons. An E- $\Delta$ E detector telescope consisting of two cooled Si surface barrier detectors was used to both identify and measure the energies of the outgoing scattered tritons. Triton spectra were collected between  $15^\circ$  and  $65^\circ$  at  $5^\circ$  intervals. Typical spectra taken at the lab angles of  $25^\circ$  and  $35^\circ$  are illustrated in Fig. 1. Overall experimental resolution for this study was 50 keV.

The experimental angular distributions obtained from this experiment together with distorted wave calculations<sup>1</sup> appear in Fig. 2. The  $5/2^+ + 5/2^+$  ground state transition clearly exhibits an angular distribution corresponding to a dominant  $(d_{3/2})^2_{\ell=0}$  transfer.

The five distributions appearing below the  $\ell=2$  designation in this figure all exhibit a characteristic  $(d_{3/2})^2_{\ell=2}$  angular shape. Moreover this result is consistent with the vibrational character previously ascribed to these states.<sup>2</sup>

The remaining states in this figure all exhibit odd- $\ell$  angular shapes. This implies transitions corresponding to either an octupole core excitation or an  $h_{11/2}$  neutron pickup. Both explanations eliminate the possibility of  $\ell=1$  assignments for the 1.62-MeV and 2.05-MeV states.

The results of this experiment clearly illustrate the collective strength associated with the (p,t) reaction. Beside the ground state, only states having a collective and possibly  $(\pi d_{5/2})^1 (v d_{3/2})^{-1} (v h_{11/2})^{-1}$  shell model origin were observed to be populated through this reaction.

#### $^{159}\text{Tb}(p,t)$ , $^{165}\text{Ho}(p,t)$ , and $^{169}\text{Tm}(p,t)$ Experiments

In these studies a  $\sim 300 \mu\text{g}/\text{cm}^2$  target of the metallic rare earth was bombarded with 30-MeV protons. The scattered tritons were analyzed with an Enge-split-pole magnetic spectrometer and were collected on photographic plates. A typical spectrum obtained from these studies appears in Fig. 3. Overall experimental resolution obtained in these studies was in the range of 10-12 keV. Resolution obtained in the angular distribution study of the  $^{159}\text{Tb}(p,t)$  reaction was in the 15-20 keV range.

In each of the deformed nuclei studied, a strong population of the ground state rotational band was observed with at least six band members being excited in each case. Moreover, a  $\beta$  vibrational band in  $^{159}\text{Tb}$  and  $\gamma$  vibrational bands in  $^{157}\text{Tb}$  and  $^{163}\text{Ho}$  were also found to be strongly excited through this reaction. In addition, the  $^{169}\text{Tm}(p,t)$

spectral results suggest the possible presence of a  $K=5/2$   $\gamma$  vibrational band at 1380 keV of excitation and the possibility of a  $K=1/2$   $\beta$  vibrational band at  $\sim 1200$  keV of excitation in  $^{167}\text{Tm}$ . All bands were identified on the basis of systematics, previous results, consistent band member energy spacings and the proven directness of the (p,t) reaction at the bombarding energies used in these studies. The results of these studies which are summarized in Tables 1-3 clearly illustrate the power of using this reaction as a tool of probing the collective properties of deformed nuclei.

Angular distributions of low energy states populated through the  $^{159}\text{Tb}(p,t)$  reaction were taken between  $10^\circ$  and  $75^\circ$  at  $5^\circ$  intervals and appear in Fig. 4 along with distorted wave predictions.<sup>1</sup> Of the members of the ground state rotational band populated through this reaction, only the ground state appears to be populated through a single dominant angular momentum transfer. The  $5/2$  and  $7/2$  members of this band appear to exhibit some  $\ell=2$  strength, although the poor agreement between experiment and theoretical  $\ell=2$  predictions make even this statement extremely uncertain.

The angular shapes exhibited by the first three members of the  $\gamma$  vibrational band are within statistical uncertainty identical, indicating a complete absence of  $\ell=0$  strength in the transition to the  $3/2$  member of this band. Moreover, the angular shapes exhibited by these three states as well as the remaining two members of this band indicate that these states are populated by a complex mixture of several allowed  $\ell$  values.

Unlike the  $\gamma$  vibrational band, the members of the  $\beta$  band appear to be populated through a single dominant angular momentum transfer. The overall shape and underlying strength of the  $3/2^+$  experimental curve undoubtedly express its dominant  $\ell=0$  character. The angular distributions of the remaining two members of this band both exhibit a characteristic  $\ell=2$  angular shape.

Angular distributions of two additional states of unknown origin were determined in the study and appear under the heading "Other States".

#### References

1. R.W. Goles, Ph.D. Thesis, Michigan State University (1971).
2. D.B. Beery, W.H. Kelly, and Wm.C. McHarris, Phys. Rev. **188**, 1851(1969).
3. G. Winter, L. Funke, K. Hohmuth, K.H. Kaun, P. Kemnitz, and H. Sodan, Nucl. Phys. **A151**, 337(1969).



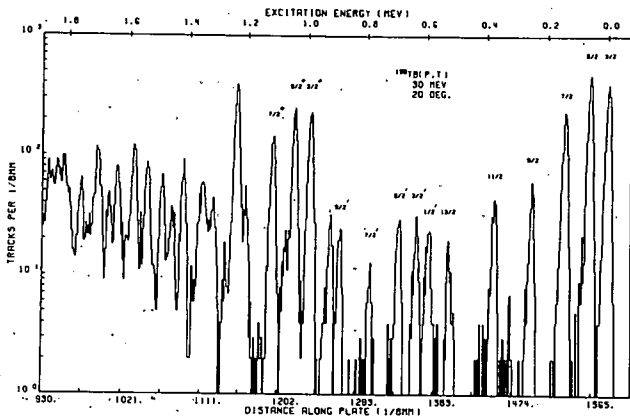


Fig. 3.  $^{159}\text{Tb}(p,t)$  spectrum obtained at the laboratory scattering angle of  $20^\circ$ .

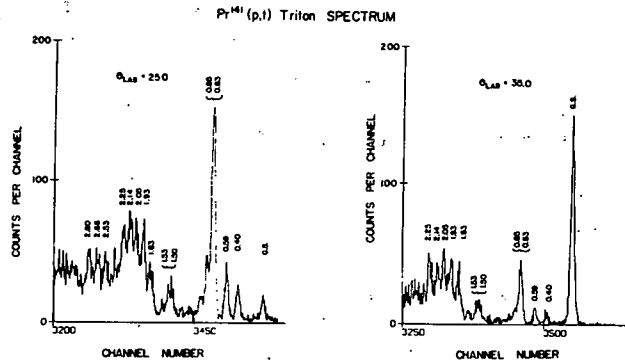


Fig. 1.  $^{141}\text{Pr}(p,t)$  triton spectra taken with an  $E_p \Delta E$  detector telescope.

Table 1. States Populated Through the  $^{159}\text{Tb}(p,t)$  Reaction.

Energy (keV)	Energy <sup>a</sup> (keV)	Theory (keV)	Assignment <sup>b</sup>	Energy (keV)	Energy <sup>a</sup> (keV)	Theory (keV)	Assignment <sup>b</sup>
G.S.	G.S.	---	$3/2^+$	1120	---	1124	$7/2^{++}$
61	60.8	---	$5/2^+$	1207	---	---	---
144	143.8	---	$7/2^+$	1238	---	1241	$(9/2)^{++}$
254	---	252	$9/2^+$	1276	---	---	---
325	---	---	---	1318	---	---	---
379	---	384	$11/2^+$	1352	---	---	---
527	---	539	$13/2^+$	1417	---	---	---
598	597.5	---	$1/2^{++}$	1454	---	---	---
640	637.5	---	$3/2^{++}$	1487	---	---	---
699	697.4	---	$5/2^{++}$	1535	---	---	---
795	---	797	$7/2^{++}$	1578	---	---	---
896	---	898	$9/2^{++}$	1602	---	---	---
927	---	923	$11/2^+$	1631	---	---	---
947	---	---	---	1659	---	---	---
994	992.6	---	$3/2^{++}$	1695	---	---	---
1048	1044.5	---	$5/2^{++}$	1749	---	---	---
1080	---	---	---	---	---	---	---

<sup>a</sup> P. B. Blichert-Toft, E. G. Funk, and J. V. Mihalich, Nucl. Phys. A100, (1967) 369-391.  
<sup>b</sup>  $+$  = number of ground state rotational band;  $++$  = number of K=2,  $\gamma$ -vibrational band.  
 $^{++}$  = number of K=2, 2-vibrational band.

Table 2. States Populated Through the  $^{141}\text{Pr}(p,t)$  Reaction.

Energy (keV)	Theory (keV)	Assignment <sup>a</sup>	Energy (keV)	Theory (keV)	Assignment <sup>a</sup>
G.S.	---	$7/2^+$	1117	---	---
100	---	$9/2^+$	1156	---	---
224	---	$11/2^+$	1175	---	---
369	367	$13/2^+$	1194	---	---
533	533	$15/2^+$	1232	---	---
560	---	$3/2^{++}$	1245	---	---
618	---	$5/2^{++}$	1259	1256	$15/2^{++}$
695	699	$7/2^{++}$	1286	---	---
720	722	$17/2^+$	1308	---	---
755	---	---	1345	---	---
791	---	---	1373	---	---
807	804	$9/2^{++}$	1419	---	---
826	---	---	1441	---	---
898	---	---	1457	---	---
912	---	---	1513	---	---
926	931	$11/2^{++}$	---	---	---
1060	---	---	---	---	---
1075	1082	$13/2^{++}$	---	---	---

<sup>a</sup>  $+$  = number of ground state rotational band;  $^{++}$  = number of K=2,  $\gamma$ -vibrational band

Table 3. States Populated Through the  $^{149}\text{Tb}(p,t)$  Reaction.

Energy (keV)	Energy <sup>a</sup> (keV)	Assignment <sup>b</sup>
10	G.S.	$1/2^+$
117	110.4	$3/2^+$
142	116.6	$5/2^+$
329	142.4	$7/2^+$
374	326.5	$9/2^+$
470	371.0	$11/2^+$
604	---	---
624	---	---
663	---	---
682	---	---
706	---	---
1010	---	---
1092	---	---
1134	---	---
1192 <sup>c</sup>	---	---
1210	---	---
1283	---	---
1320	---	---
1380	---	$5/2^{++}$
1404 <sup>c</sup>	---	$7/2^{++}$
1434	1435 <sup>c</sup>	$9/2^{++}$
1457	---	---
1486	---	---
1526	---	---
1574	---	---
1598	---	---
1625	---	---
1655	---	---

a) Ref. 3  
b)  $+$  and  $^{++}$  are members of the ground and  $\gamma$  vibrational bands respectively.  
c) Energy calculated from the first two members of this band.

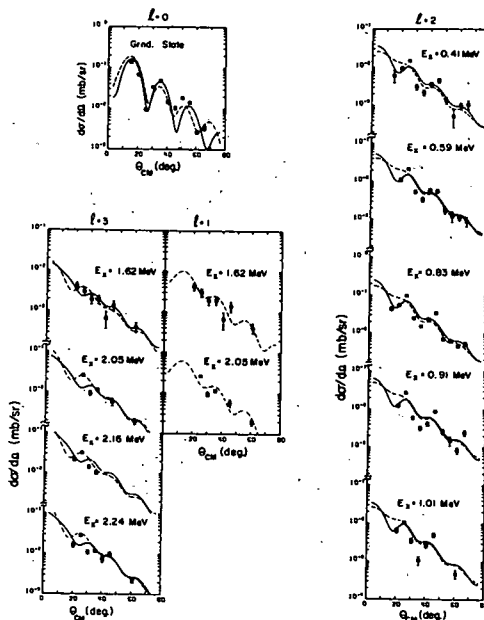


Fig. 2. Angular distributions of states populated through the  $^{141}\text{Pr}(p,t)$  reaction. Theoretical two neutron pick-up and cluster transfer calculations are represented by continuous and broken curves respectively. Relative cross sections have been normalized to reflect measured absolute values.

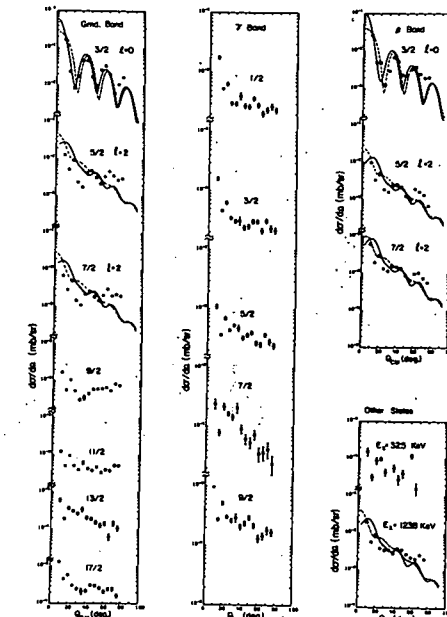


Fig. 4. Angular distributions of states populated through the  $^{159}\text{Tb}(p,t)$  reaction. Theoretical two neutron pick-up and cluster transfer calculations are represented by continuous and broken curves respectively. Relative cross sections have been normalized to reflect measured absolute values.

The  $\beta^+/\epsilon$  Decay of  $^{143}\text{Eu}$   
Richard B. Firestone

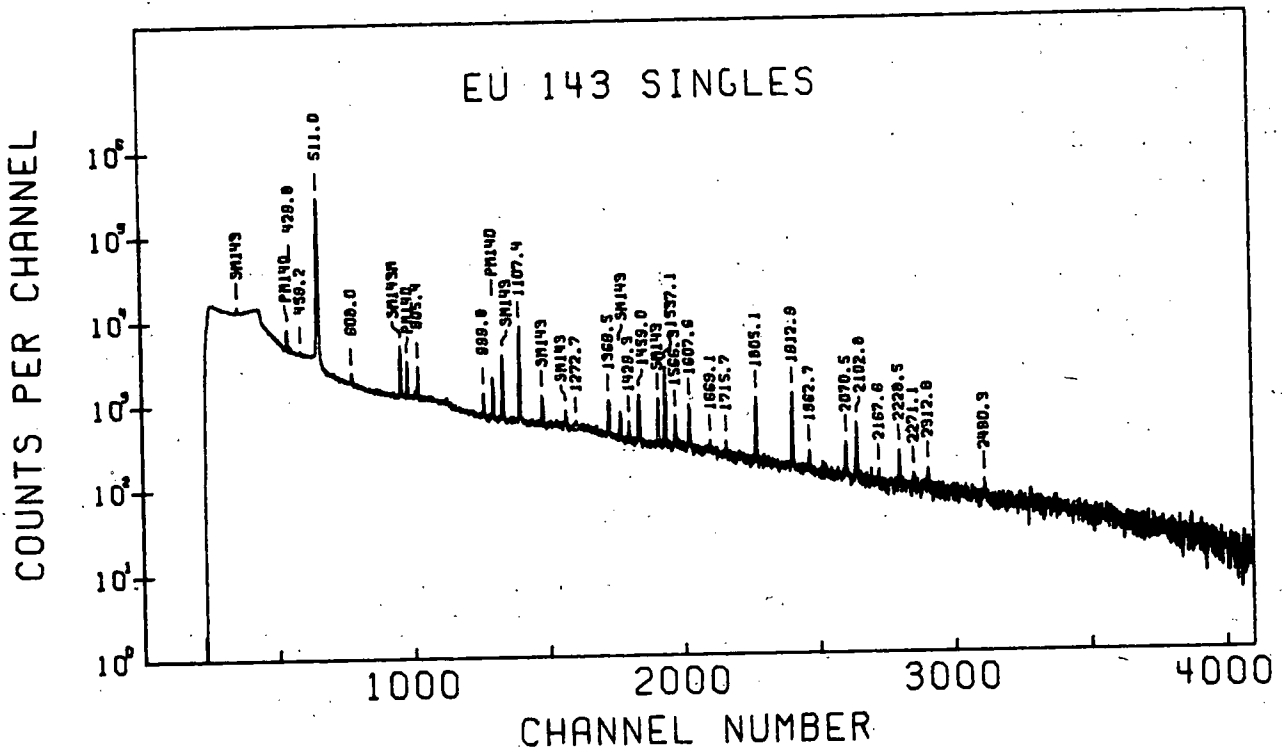
The decay of  $^{143}\text{Eu}$  was first studied by Kotajima and Malan,<sup>1,2</sup> who measured its half-life (2.6 min) and  $\beta$ -endpoint energy (4.0 MeV). No  $\gamma$ -ray decay schemes were reported, presumably because of the weak transitions and the interference of the short-lived  $^{143}\text{Sm}$  daughter decay.  $^{143}\text{Sm}$  has been part of a continuing study of N=81 isotones by the Nuclear Spectroscopy Group at Michigan State University, and the  $^{143}\text{Eu}$  decay scheme is a welcome by-product of this study.

$^{143}\text{Eu}$  was prepared by the reaction  $^{144}\text{Sm}(p,2n)^{143}\text{Eu}$  on a separated isotope target (95.10%  $^{144}\text{Sm}$ ), using 28-MeV protons from the Michigan State University Sector Focused Cyclotron. As the  $^{143}\text{Sm}$  daughter has a half-life of only 8.8 min, a series of 9 min spectra were taken so that the transitions arising from various decays could be separated by half-life. Figure 1 shows the first 9 min spectrum which was accumulated starting 2 min after bombardment to allow very short-lived activities to decay away. This spectrum was taken with a 10.4% Ge(Li) detector of 2.1-keV (FWHM) resolution at 1332 keV.

From the  $^{144}\text{Sm}(p,d)^{143}\text{Sm}$  reaction data of Jolly and Kashy,<sup>3</sup> levels in  $^{143}\text{Sm}$  were found at 0.110 MeV ( $1/2^+$ ), 0.76 MeV ( $11/2^-$ ), 1.11 MeV ( $5/2^+$ ), 1.36 MeV ( $7/2^+$ ), 1.53 MeV ( $5/2^+$ ), 1.72 MeV ( $5/2^+$ ), 1.95 MeV ( $1/2^+$ ), 2.06 MeV ( $5/2^+$ ), 2.06 MeV ( $5/2^+$ ), 2.16 MeV ( $7/2^+$ ), and 2.29 MeV ( $7/2^+$ ). Using this information, and energy sums and intensity balances for  $\gamma$  rays seen in the present study, a tentative decay scheme for  $^{143}\text{Eu}$  has been prepared, and is shown in Fig. 2. None of the energies and intensities or log ft values given in this decay scheme are to be taken as well-established, as more definitive experiments are still in progress.

References

1. K. Kotajima, K.W. Brockman, and G. Wolzak, Nucl. Phys. 65, 109(1965).
2. H.P. Malan, H. Munzel, and G. Pfenning, Radiochem. Acta. 5, 24(1966).
3. R.K. Jolly and E. Kashy, MSUCL-28, 1970.



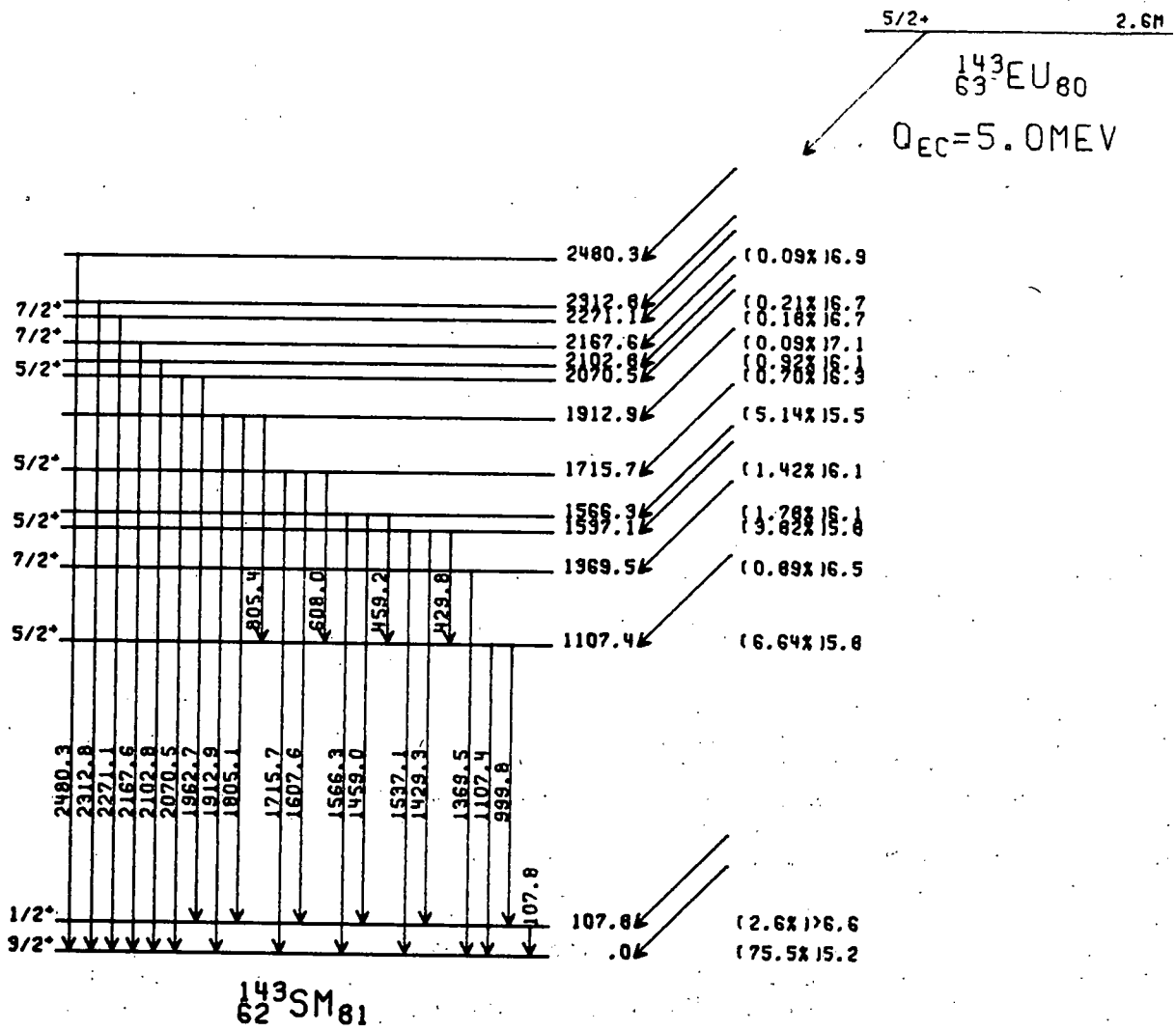


Fig. 2 Decay scheme for  $^{143}\text{Eu}$ .

The  $\beta^+/\epsilon$  Decay of  $^{143}\text{Sm}$

Richard B. Firestone

The decay of  $^{143}\text{Sm}$  has been studied most thoroughly by Frenne, Heyde, *et al.*<sup>1,2</sup> They produced  $^{143}\text{Sm}$  by the  $(\bar{\gamma}, n)$  reaction on natural  $\text{Sm}_2\text{O}_3$  (3.09%  $^{143}\text{Sm}$ ). A decay scheme was presented along with several log ft values.

The study of the  $^{143}\text{Sm}$  decay is of considerable interest in the light of previous work<sup>3,4</sup> on the neighboring odd Z, N=81 isotones,  $^{141}\text{Nd}$  and  $^{145}\text{Gd}$ . All three isotones have  $11/2^-$  metastable states at 720-756 keV with 60- to 85-sec half-lives. The  $^{143}\text{Sm}$  and  $^{145}\text{Gd}$  metastable states were found to have small  $\beta$  branches in their decays.

Of further interest are the  $7/2^+$  first-excited states in the daughters of all three isobars. These appear to be the  $1g_{7/2}$  quasiparticle states predicted for N=82 nuclei by Kisslinger and Sorenson.<sup>6</sup> These states occur at 145.4, 272.9, and 329.5 keV in  $^{141}\text{Pr}$ ,  $^{143}\text{Pm}$ , and  $^{145}\text{Eu}$ , respectively. The log ft values given for the  $7/2^+$  states in  $^{141}\text{Pr}$  and  $^{145}\text{Eu}$  were 8.8 and 7.5. Prior to this study, no value was reported for the log ft of the corresponding state in  $^{143}\text{Pm}$ , but since the transition to this state is from the  $3/2^+$  ground state of  $^{143}\text{Sm}$ , this second-forbidden transition might be expected to lie in the range  $10 \leq \log ft \leq 14$ . The transitions to the  $7/2^+$  states in the other two nuclei are also second forbidden however, suggesting that the  $^{143}\text{Sm}$  decay to the  $7/2^+$  state may also show an abnormally low log ft value.

In an attempt to measure this log ft, and to determine more precisely other properties of the decay scheme for  $^{143}\text{Sm}$ , the reaction  $^{142}\text{Nd}(^3\text{He}, 2n)^{143}\text{Sm}$  was first tried. This reaction proved unsatisfactory, as the rather loosely bound  $\alpha$  particles in

this region make the  $(^3\text{He}, ^4\text{He}, n)$  reaction more probable. The problem is compounded by the fact that  $^{143}\text{Sm}$  decay goes overwhelmingly to the ground state of  $^{143}\text{Pm}$ .

The reaction  $^{144}\text{Sm}(p, 2n)^{143}\text{Eu}$ , in which the 2.6-min  $^{143}\text{Eu}$  quickly decays to its  $^{143}\text{Sm}$  daughter, has been used with more success. The  $^{143}\text{Eu}$  decay is discussed in another section. Singles spectra of  $^{143}\text{Sm}$  have been taken using a 10.4% Ge(Li) detector with 2.1-keV (FWHM) resolution, and peak-to-Compton ratio of 38:1 at 1332 keV. To separate the  $^{143}\text{Eu}$  and  $^{143}\text{Sm}$  activities, a series of spectra at 9-min intervals were accumulated, starting 2 min after bombardment and continuing until all short-lived activity was unnoticeable. The fourth 9-min spectrum is shown in Fig. 1, and consists primarily of transitions originating from  $^{143}\text{Sm}$ . A tentative decay scheme for  $^{143}\text{Sm}$  is given in Fig. 2, based on the  $^{142}\text{Nd}(^3\text{He}, d)$  results of Wildenthal as well as the current study.

The log ft value for the second forbidden decay to the 272.9-keV level is seen to be 8.1, much lower than usual, but similar to those for the corresponding decays of  $^{145}\text{Gd}$  and  $^{141}\text{Nd}$ .

References

1. D. De Frenne, K. Heyde, L. Dorikens-Vanpraet, M. Dorikens, and J. Demuyneck, Nucl. Phys. A110, 273(1968).
2. D. De Frenne, E. Jacobs, and J. Demuyneck, Z. Physik 237, 327(1970).
3. D.B. Beery, W.H. Kelly, and Wm.C. McHarris, Phys. Rev. 171, 1283(1968).
4. R.E. Eppley, Ph.D. Thesis, Michigan State Univ. (1970).
5. J. Felsteiner and B. Rosner, Phys. Letters 31B, 12(1970).
6. K.S. Kisslinger and R.A. Sorenson, Revs. Mod. Phys. 35, 853(1963).
7. H.J. Bleyl, H. Munzel, and G. Pfennig, Radiochem. Acta, 9, 173(1968).

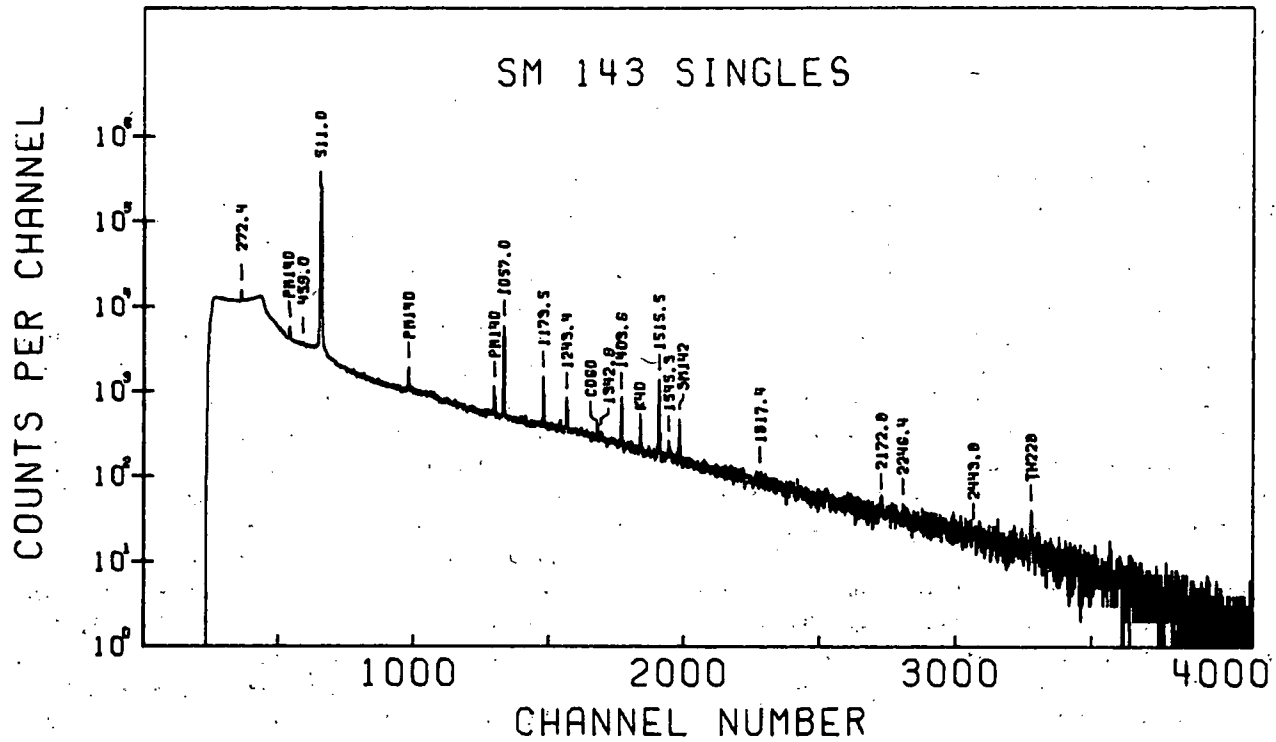


Fig. 1  $\gamma$ -ray singles spectrum for  $^{143}\text{Sm}$ .

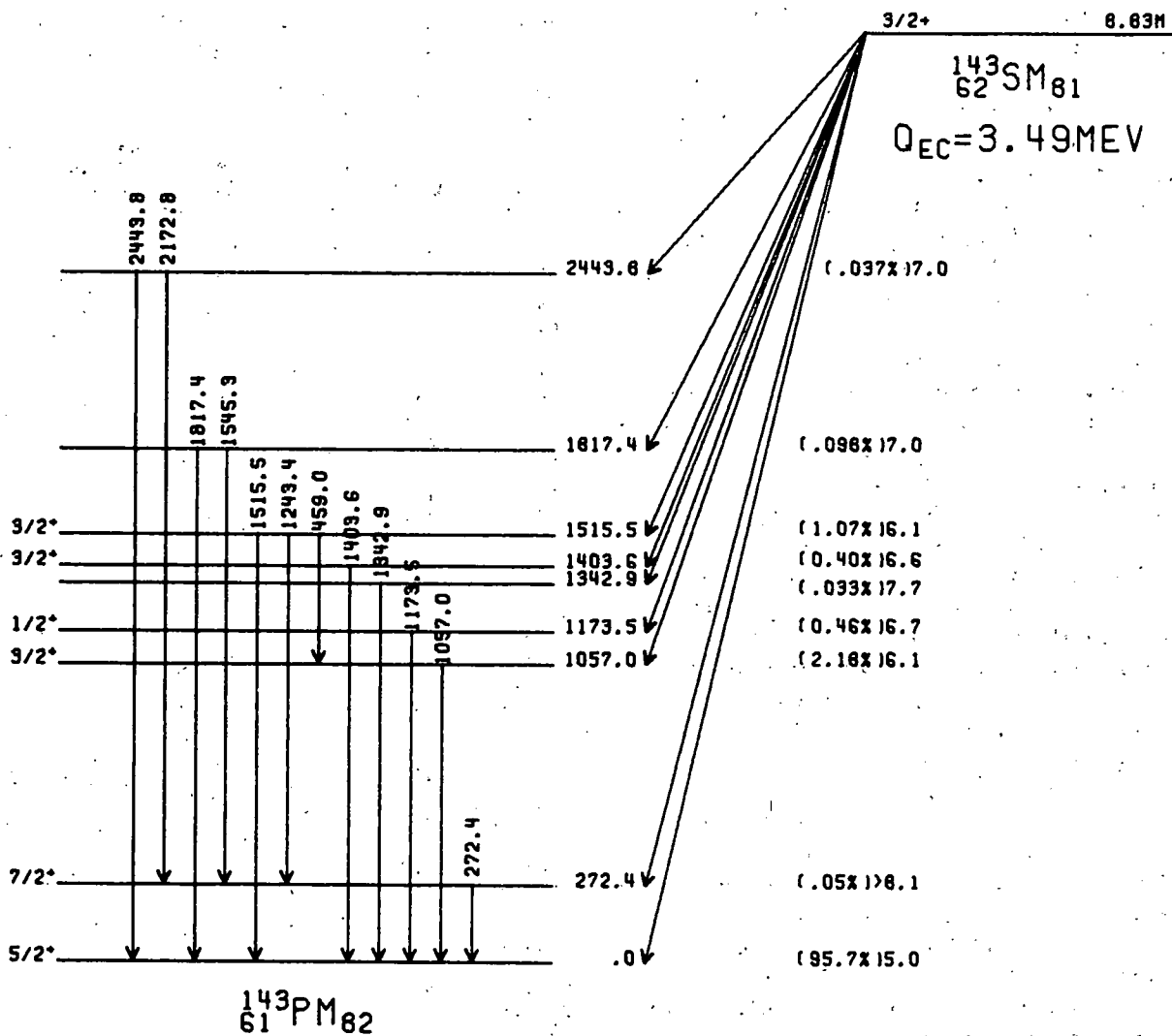


Fig. 2 Decay scheme for  $^{143}\text{Sm}$ .

$^{141}_{61}\text{Nd}_{81}$  is a link in the chain of nuclides near the N=82 closed shell, a region of the nuclidic chart which the nuclear  $\gamma$ -spectroscopy group is currently investigating. We have made measurements of the states of this isotope resulting from the  $\beta^+/\epsilon$  decay of  $^{141}_{61}\text{Pm}_{80}$ .

Our samples were prepared via the  $^{14}\text{Nd}(\text{p}, 2\text{n})^{141}\text{Pm}$  reaction. We bombarded the powdered oxide,  $\text{Nd}_2\text{O}_3$ , of the 99.9% pure separated isotope for typically 0.5-2 min with a 0.5-3  $\mu\text{A}$  25 MeV proton beam from the MSU cyclotron. Counting was usually started 5-10 min after bombardment after most of the suspected short-lived contaminants had decayed.

Unravelling the decay scheme required experiments of various configurations:  $\gamma$ -ray singles, two-dimensional "megachannel"  $\gamma$ - $\gamma$  coincidence, anticoincidence, and  $\gamma$ -511-511 keV coincidence. For our main runs we used at various times four Ge(Li) detectors of 1.0%, 2.5%, 4.5%, and 10.4% efficiency to record the high resolution  $\gamma$ -ray spectra, with resolutions typically ranging from 2.0 to 3.5 keV at the 1.33 MeV  $\gamma$ -ray of  $^{60}\text{Co}$ . An 8x8 inch NaI(Tl) split annulus was also used for the  $\gamma$ -511-511 keV coincidence and anticoincidence detection. Standard NIM electronics were employed for amplifying, gating, and timing, and the data were analyzed by one or more 4096-channel ADC's coupled to either the MSU Sigma-7 or the PDP-9 computer. Various in-house computer codes such as MOIRAE, EVENT RECOVERY, MOIRAE(EI) and SAMPO<sup>1</sup> were then used to help reduce the data to energies, intensities and log ft values necessary for the construction of the decay scheme.

Our results are presented in Table I, where we list the energies and relative intensities of the  $\gamma$ -rays observed in the various experiments. The  $\gamma$ -rays belonging to our decay scheme were identified on the basis of their half-lives. From the data we were able to deduce the decay scheme shown in Fig. 1. The transition and excited-state energies are given in keV, and the disintegration energy  $Q_\epsilon$  is taken to be the value measured by Charvet *et al.*<sup>2</sup> All the transition intensities are expressed in percent of the total  $^{141}\text{Pm}$  disintegrations, and the log ft values are calculated on the basis of a measured 20.6-min half-life for  $^{141}\text{Pm}$ . The possible spin and parity assignments are listed in Table II and were made from an examination of the log ft values, as well as the electromagnetic transition rates to levels of known spins and parities. Those assignments which are less probable are enclosed in parentheses. For comparison, we also list in the same table the spins and parities obtained by Jolly and Kashy<sup>3</sup> for corresponding levels from their deuteron angular distribution studies of the  $^{142}\text{Nd}(\text{p}, \text{d})^{141}\text{Nd}$  reaction.

In the main our decay scheme is in good agreement with that proposed by Charvet *et al.*,<sup>2</sup> but we have greatly extended the number of  $\gamma$ -ray transitions and the range of levels. There are a few noteworthy differences. The amounts of  $\beta$ -feeding to the various levels in  $^{141}\text{Nd}$  differ appreciably, especially in the ground state transition, where we obtain 88.6% feeding while they saw 95% feeding. We placed a new level at 1051.9 keV based on the existence of a  $\gamma$ -ray of that energy with the correct half-life, as well as its enhancement in the  $\gamma$ -511-511 keV coincidence experiment. The new level at 2066.4 keV rests on the observation of a  $\gamma$ -ray of that energy and another of 1872.6 keV in coincidence with the 193.8 keV  $\gamma$ -ray from the first excited state. The levels at 2246.6, 2303.4, 2354.4, 2388.4, 2620, and 2805 keV are supported by the results of our anticoincidence experiment. From the sums and differences of several observed  $\gamma$ -rays with the requisite half-life, as well as the anticoincidence results, we also place a level at 2506 keV. The remaining new levels are only tentative since they are based solely on their observed half-lives and relatively large energies.

Table I. Relative Intensities of  $\gamma$ -rays in the Decay of  $^{141}\text{Pm}$  in Various Experiments.

Energy (keV)	Singles	Anti-Coinc.	Integral Coinc.	194 keV Gated Coinc.	$\gamma$ -511-511 keV Coinc.
180.2	0.6				
193.8	34.9	26.4	574.1		7.5
289.4	3.6		39.6	1.9	
511.0	2385.	---	---	---	65.5
538.2	1.7		7.4		
544.7	1.4				
597.2	1.2		4.7		
622.2	18.9	7.3	58.7		4.6
647.2	1.3				
706.0	1.0				
886.3	52.5	20.5	114.3	3.3	4.2
901.2	1.1				
958.7	1.3		2.1		
966.3	2.0		3.4		
1022.8	2.8		4.7		
1029.9	7.8	1.9	17.3	6.9	5.3
1051.9	2.0				12.6
1080.7	1.0				
1223.3	100.0	56.1	100.0		100.0
1282.1	0.9				3.3
1345.8	27.6	9.0	39.3		8.6
1371.0	2.2		2.7	2.8	
1403.2	16.0	5.8	17.5	16.0	6.6
1564.8	17.9	13.9	6.5		16.9
1596.8	16.1	16.1	3.2		19.4
1626.7	5.8		7.1	5.8	
1703.8	1.2		0.7	0.6	
1820.4	1.6	2.0	1.0		
1872.6	0.5		0.8	1.3	
1879.9	6.9	3.8	4.2	6.0	
1897.1	1.1				
1967.6	3.6	3.4			
2052.8	2.6			2.5	
2066.2	1.3				
2073.7	13.4	16.0			1.8
2109.6	1.8	2.5			

Energy (keV)	Singles	Anti-Coinc.	Integral Coinc.	194 keV Gated Coinc.	$\gamma$ -511-511 keV Coinc.
2145.2	0.3				
2246.4	1.5	2.5			
2265.3	0.7				
2303.4	2.4	2.5			
2311.6	0.5				
2354.4	1.0	1.1			
2388.4	1.3	1.5			
2429.8	0.6	0.3			
2505.0	0.6	0.5			
2602.1	0.1				
2619.6	0.4	0.3			
2804.9	0.5	0.3			
2985.5	0.9				

<sup>a</sup>Not measured in total annihilation.

Table II. Spins and Parities of States in <sup>141</sup>Nd Obtained in this work and by Jolly and Kashy.

This Work		Jolly & Kashy	
E (keV)	J <sup><math>\pi</math></sup>	E (MeV)	J <sup><math>\pi</math></sup>
0	3/2 <sup>+</sup>	0	3/2 <sup>+</sup>
193.8	1/2 <sup>+</sup>	0.19	1/2 <sup>+</sup>
756.7	11/2 <sup>-</sup>	0.76	11/2 <sup>-</sup>
1051.9	3/2 <sup>-</sup> , 5/2 <sup>-</sup> , 7/2 <sup>-</sup>		
1223.3	5/2 <sup>+</sup> (-), 3/2 <sup>+</sup> (-)	1.20	5/2 <sup>+</sup>
1345.8	7/2 <sup>+</sup> (-)	1.33	(7/2 <sup>+</sup> )
1564.8	5/2 <sup>+</sup> , (3/2 <sup>+</sup> )	1.56	(5/2 <sup>+</sup> )
1596.8	3/2 <sup>±</sup> , (5/2 <sup>±</sup> )		
1820.4	5/2 <sup>+</sup> (-), (3/2 <sup>±</sup> )	1.80	(5/2 <sup>+</sup> )
1897.1	3/2 <sup>±</sup> , (5/2 <sup>±</sup> )	1.87	1/2 <sup>+</sup>
1968.0	7/2 <sup>±</sup> , (5/2 <sup>±</sup> ), (3/2 <sup>±</sup> )		
2066.4	3/2 <sup>±</sup> , (5/2 <sup>±</sup> )	2.06	(5/2 <sup>+</sup> )
2073.7	3/2 <sup>±</sup> , (5/2 <sup>±</sup> )		
2109.6	5/2 <sup>+</sup> , (3/2 <sup>+</sup> )	2.19	11/2 <sup>-</sup>
2145.2	3/2 <sup>-</sup> , 5/2 <sup>-</sup> , 7/2 <sup>-</sup>		
2246.6	3/2 <sup>+</sup> , 5/2 <sup>+</sup> , 7/2 <sup>+</sup>		
2265.3	3/2 <sup>±</sup> , 5/2 <sup>±</sup> , 7/2 <sup>±</sup>		
2303.4	5/2 <sup>+</sup> , 7/2 <sup>+</sup>	2.30	(7/2 <sup>+</sup> )
2354.4	3/2 <sup>±</sup> , 5/2 <sup>±</sup> , 7/2 <sup>±</sup>		
2388.4	3/2 <sup>±</sup> , 5/2 <sup>±</sup> , 7/2 <sup>±</sup>		
2430	3/2 <sup>±</sup> , 5/2 <sup>±</sup> , 7/2 <sup>±</sup>		
2506	3/2 <sup>+</sup> , 5/2 <sup>+</sup> , 7/2 <sup>+</sup>		
2620	3/2 <sup>±</sup> , 5/2 <sup>±</sup> , 7/2 <sup>±</sup>		
2805	3/2 <sup>±</sup> , 5/2 <sup>±</sup> , 7/2 <sup>±</sup>		
2986	3/2 <sup>±</sup> , 5/2 <sup>±</sup> , 7/2 <sup>±</sup>		

We are indebted to Dr. Henry Blosser and the clerical and computer staff of the MSU Cyclotron Laboratory for their assistance during various phases of this work. We also thank Dr. Dwight Beery and Messers Kenneth Kosanke, Clare Morgan, and William Chaffee for their helpful discussions and aid in data reduction.

### References

1. J.T. Routti and S.G. Prussin, Nucl. Instr. and Methods **72**, 125(1969).
2. A. Charvet, R. Duffait, A. Emsallem, and R. Chery, Journ. de Physique **31**, 737(1970).
3. R.K. Jolly and E. Kashy, Phys. Rev. (to be published, 1971).

\*NSF Summer Research Participant. Permanent address: Department of Physics, Wilson College, Chambersburg, Pa. 17201

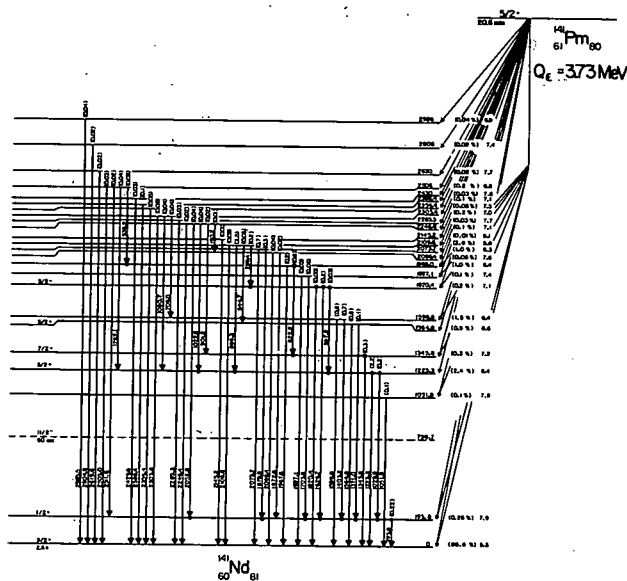


Fig. 1 The decay scheme of <sup>141</sup>Pm<sub>80</sub> deduced from the present study. Energies are given in keV and transition intensities are given in percent of the total <sup>141</sup>Pm disintegrations.

The Electron Capture Decay of  $^{56}\text{Ni}$   
L. Samuelson

The electron capture decay of  $^{56}\text{Ni}$  was used as part of a study of the levels of  $^{56}\text{Co}$  below 1.8 MeV of excitation. Singles  $\gamma$ -ray spectra and  $\gamma$ - $\gamma$  coincidence spectra using a Ge(Li)-Ge(Li) spectrometer were taken of the  $^{56}\text{Ni}$  electron capture decay. These two experiments yielded  $\gamma$ -ray energies and intensities and  $\gamma$ -ray placement in the  $^{56}\text{Ni}$  decay scheme.

The 6.1-day  $^{56}\text{Ni}$  activity was produced via the  $^{56}\text{Fe}(^3\text{He}, 3n)^{56}\text{Ni}$  reaction ( $Q = -16.3$  MeV) by bombarding a 0.001 inch iron foil with 70 MeV  $^3\text{He}$  particles (reduced to approximately 45 MeV with an aluminum absorber) from the M.S.U. cyclotron. After a 10-day wait to allow the 1.5-day  $^{57}\text{Ni}$  contaminant activity to die down, and an appropriate chemical separation, the source was dissolved in 15N HCl and placed in a plastic vial for counting.

Singles spectra were taken at two different source to detector distances (for identification of sum peaks) with both a 2.5%-efficient Ge(Li) detector and a 10.4%-efficient Ge(Li) detector. Fig. 1 shows a typical  $^{56}\text{Ni}$  singles spectrum. All singles spectra were analyzed using the peak-fitting computer code SAMPO.<sup>1</sup> After correcting the measured peak areas for the relative  $\gamma$ -ray detector efficiencies and averaging several runs, the  $^{56}\text{Ni}$   $\gamma$ -ray intensities were obtained and are listed in Table 1. The  $^{56}\text{Ni}$   $\gamma$ -ray energies were measured by counting several well-known  $\gamma$ -ray energy standards simultaneously with the  $^{56}\text{Ni}$  activity. A quadratic least-squares fit was then made to the resulting peak centroids and calibration energies in two energy regions (100-800 keV and 700-2000 keV). The  $^{56}\text{Ni}$   $\gamma$ -ray energies obtained are listed in Table 1.

Table 1. Energies and relative intensities of  $\gamma$ -rays from the electron capture decay of  $^{56}\text{Ni}$ .

Energy keV	Relative $\gamma$ -ray intensity
158.4 $\pm$ 0.1	100.
269.5 $\pm$ 0.1	36.0 $\pm$ 1.4
480.5 $\pm$ 0.1	36.0 $\pm$ 1.5
749.9 $\pm$ 0.1	50.5 $\pm$ 2.5
811.8 $\pm$ 0.1	88.5 $\pm$ 4.4
1562.0 $\pm$ 0.2	14.3 $\pm$ 1.4

The two parameter  $\gamma$ - $\gamma$  prompt coincidence experiment was performed with a 4.5%-efficient Ge(Li) detector and a 10.4%-efficient Ge(Li) detector placed in a 150° geometry with a graded lead absorber placed between them to prevent Compton scattering from one detector into the other. Coincident events (resolving time  $2t=100$  nsec) from both sides were processed and their addresses listed in pairs on magnetic tape using

the M.S.U. cyclotron Sigma-7 computer code EVENT.<sup>2</sup> This listing yielded a 4096x4096-channel array of prompt-coincidence events which were sorted off-line in gated slices including background subtraction, using the computer code EVENT RECOVERY.<sup>3</sup> The resulting any-coincidence and gated spectra are shown in Fig. 2 and the coincidence results are summarized in Table 2.

Table 2. Summary of  $\gamma$ - $\gamma$  prompt coincidence results.

		Coincidence relations						
Gamma ray		158	269	480	511( $\beta^+$ )	750	812	1562
158			yes	yes	no	yes	yes	yes
269	yes			yes	no	no	yes	no
480	yes	yes			no	no	yes	no
511( $\beta^+$ )	no	no	no			no	no	no
750	yes	no	no	no		yes		no
812	yes	yes	yes	no		yes		no
1562	yes	no	no	no		no		

Finally the resulting  $^{56}\text{Ni}$  electron capture decay scheme is presented in Fig. 3. Internal conversion corrections have been included using internal conversion coefficients measured by Jenkins and Meyerhof.<sup>4</sup> Decay intensities are normalized to 100 decays of the 158.4-keV first excited level. This decay scheme corroborates those presented elsewhere by Ohnuma,<sup>5</sup> et al., and Piluso,<sup>6</sup> et al.

References

1. J.T. Routti, S.G. Prussin, Nucl. Instr. and Meth., 72, 125(1969).
2. EVENT, computer code written by D. Bayer, unpublished.
3. EVENT RECOVERY, computer code written by D.B. Beery and G. Giesler, unpublished.
4. R.C. Jenkins, W.E. Meyerhof, Nucl. Phys. 58, 417(1964).
5. Hajime Ohnuma, Jospho Hashimoto, and Isao Tomita, Nucl. Phys. 66, 337(1965).
6. C.J. Piluso, D.O. Wells, and D.K. McDaniels, Nucl. Phys. 77, 193(1966).

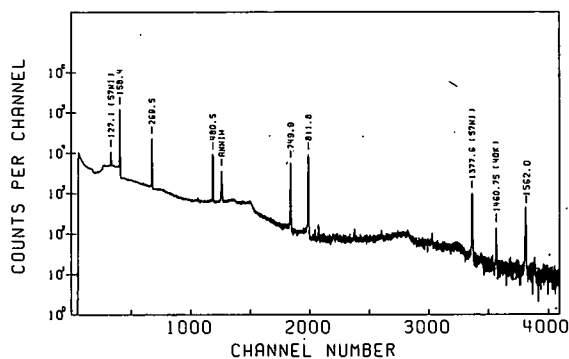


Fig. 1 Typical  $^{56}\text{Ni}$  singles spectrum.



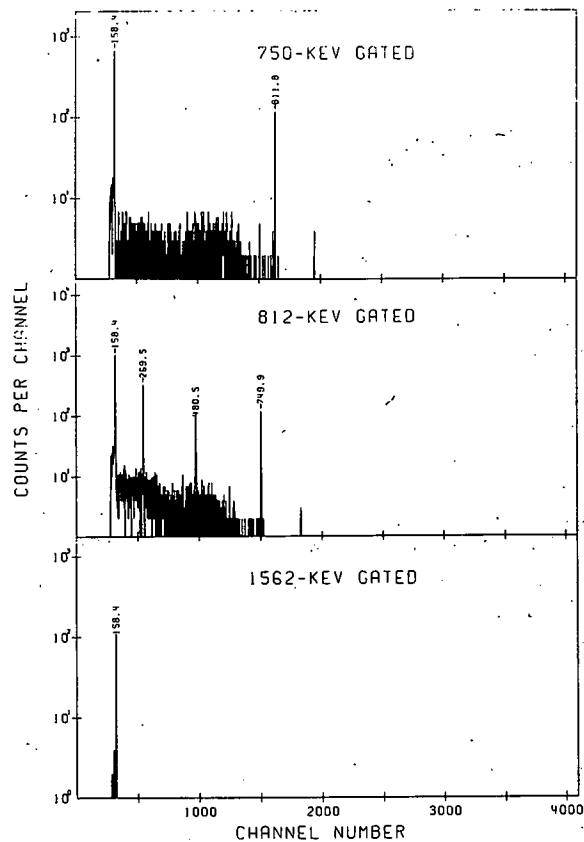
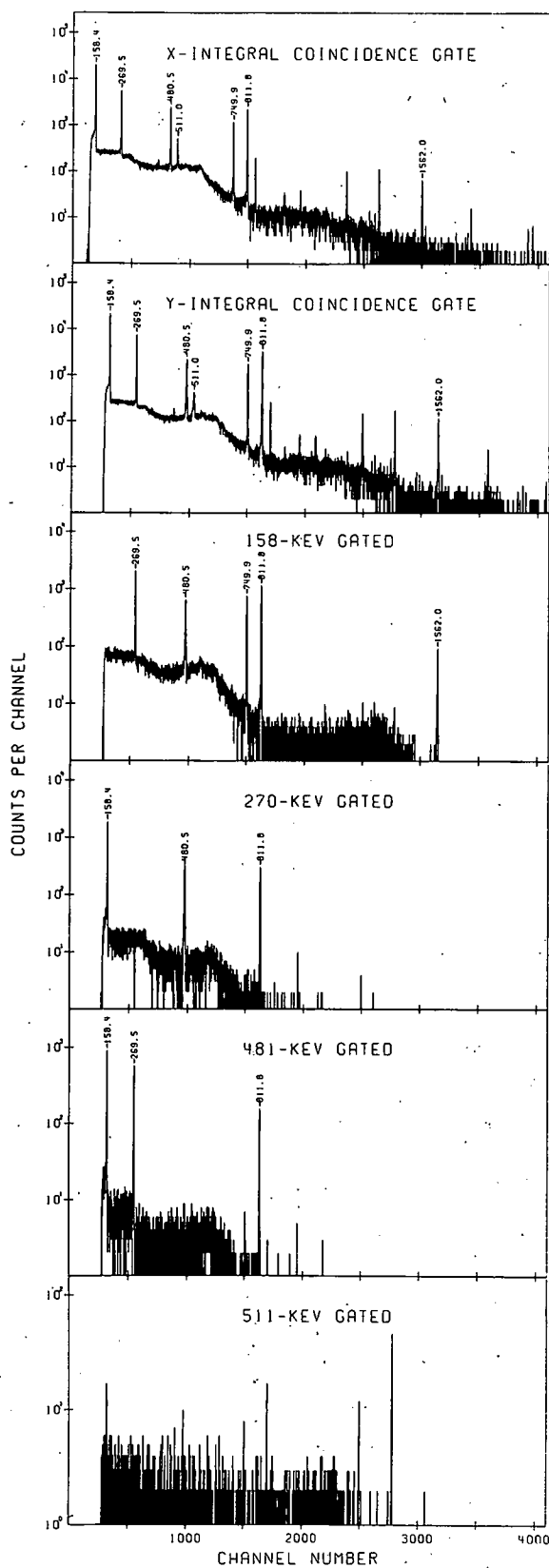


Fig. 2 Integral coincidence and gated spectra of the  $^{56}\text{Ni}$   $\gamma$ - $\gamma$  coincidence experiment. Unlabelled weak peaks in the gated spectra are either triple coincidences where two of the  $\gamma$  rays have been summed in one detector or chance coincidences with intense peaks.

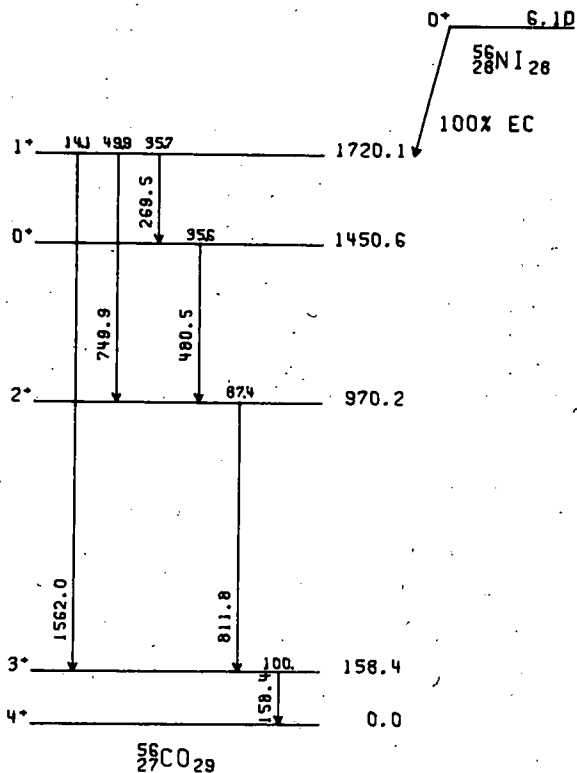


Fig. 3 Decay scheme of  $^{56}\text{Ni}$ . The labelled intensities are normalized to 100 decays of the 158-keV level.

Low-Lying States of  $^{56}\text{Co}$  from  $^{56}\text{Fe}(p, n\gamma)$   
 Thresholds and  $\gamma$ -ray Angular Distributions  
 L. Samuelson

The  $^{56}\text{Fe}(p, n\gamma)^{56}\text{Co}$  reaction was used to study the levels of  $^{56}\text{Co}$  below 1.8 MeV of excitation. Excitation functions,  $\gamma$ -ray angular distributions, and absolute  $(p, n)$  cross-sections (at  $E_p = 7.30$  MeV) were measured by detecting de-exciting  $\gamma$ -rays in a 2.5%-efficient Ge(Li) detector. Proton beams of 5.55 to 7.45 MeV in 100-keV steps were furnished for the excitation functions measurements by the Western Michigan University Tandem Van de Graaff while proton beams of 5.77, 6.65, 7.05, and 7.30 MeV were furnished for the  $\gamma$ -ray angular distribution and absolute cross-section measurements by the Michigan State University Cyclotron. The target was a 99.4% isotopically enriched  $^{56}\text{Fe}$  foil of 0.9 mg/cm<sup>2</sup> thickness (approximately 40 keV at the above beam energies). A least squares fit to the experimental  $\gamma$ -ray angular distributions using the computer code GADFIT<sup>1</sup> was made to the equation  $W(\theta) = A_0[1 + A_2^*P_2(\cos\theta) + A_4^*P_4(\cos\theta)]$ . The absolute level feedings and the  $\gamma$ -ray mixing-ratio dependent parameters  $A_2^* = A_2/A_0$  and  $A_4^* = A_4/A_0$  (i.e.  $\delta$ -ellipses) were calculated using the statistical CN computer code MANDY.<sup>2</sup> Energy-level spins and parities presented are those that are most consistent with the present experiment, with all previous work<sup>3</sup> done on  $^{56}\text{Co}$ , and with shell-model calculations<sup>3</sup> done on  $^{56}\text{Co}$ .

Table 1

Measured  $\gamma$ -ray Energies and Mixing Ratios

Energies keV	Mixing Ratio	Transition assumed
158.4	$-.04 \leq \delta \leq -.01$	3+ $\rightarrow$ 4+
576.5	$.04 \leq \delta \leq .07$	5+ $\rightarrow$ 4+
671.3	$.24 \leq \delta \leq .27$	4+ $\rightarrow$ 3+
829.6	$.05 \leq \delta \leq .85$	4+ $\rightarrow$ 4+
811.8	$.02 \leq \delta \leq .04$	2+ $\rightarrow$ 3+
1009.2	$.07 \leq \delta \leq .15$	5+ $\rightarrow$ 4+
284.8	$-.04 \leq \delta \leq .08$	3+ $\rightarrow$ 4+
1114.5	$-.10 \leq \delta \leq -.05$	3+ $\rightarrow$ 4+
480.5	0.0 = $\delta$	0+ $\rightarrow$ 2+
269.5	0.0 = $\delta$	1+ $\rightarrow$ 0+
749.9	$-.03 \leq \delta \leq .23$	1+ $\rightarrow$ 2+
1561.9	---	1+ $\rightarrow$ 3+

Table 2

Experimental and Theoretical  $^{56}\text{Fe}(p, n\gamma)^{56}\text{Co}$  Absolute and Relative (normalized to the 158 keV level) Cross-sections at  $E_p = 7.30$  MeV.

Level keV	$\sigma$ exp millibarns	$\sigma$ rel exp	$\sigma$ thy millibarns	$\sigma$ rel thy	Spin & Parity assumed
158	88.1	1.000	28.2	1.000	3+
577	15.3	.177	5.2	.173	5+
830	24.6	.356	8.6	.279	4+
970	72.4	.895	23.2	.822	2+
1009	9.3	.112	3.3	.106	5+
1115	41.33	.424	13.4	.469	3+
1451	19.7	.458	4.5	.224	0+
1720	19.0	.273	8.8	.216	1+

References

- GADFIT, computer code written by R. Warner, unpublished.
- E. Sheldon and R.M. Stang, Computer Physics Communications 1, 35(1969).
- M.J. Schneider and W.W. Daehnick, and Refs. cited therein, to be published.

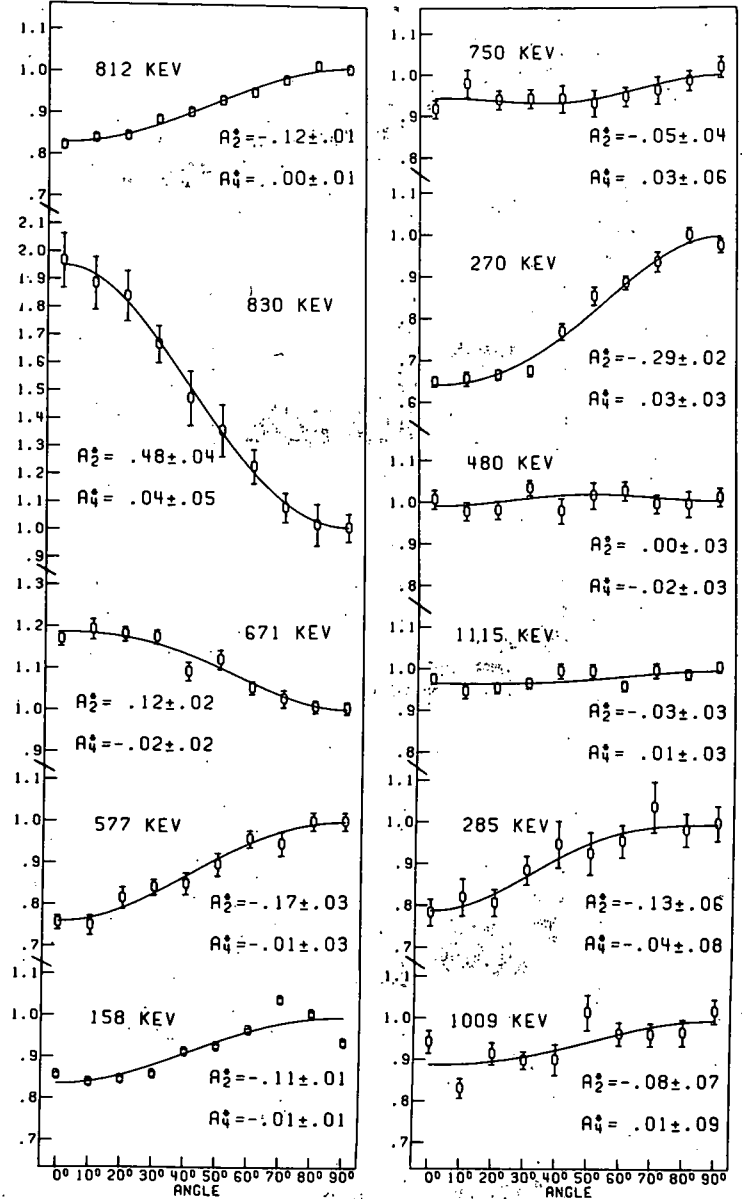


Fig. 1 Experimental  $\gamma$ -ray angular distributions. The solid lines represent least squares fits to the data using the equation for  $W(\theta)$  given in the text.

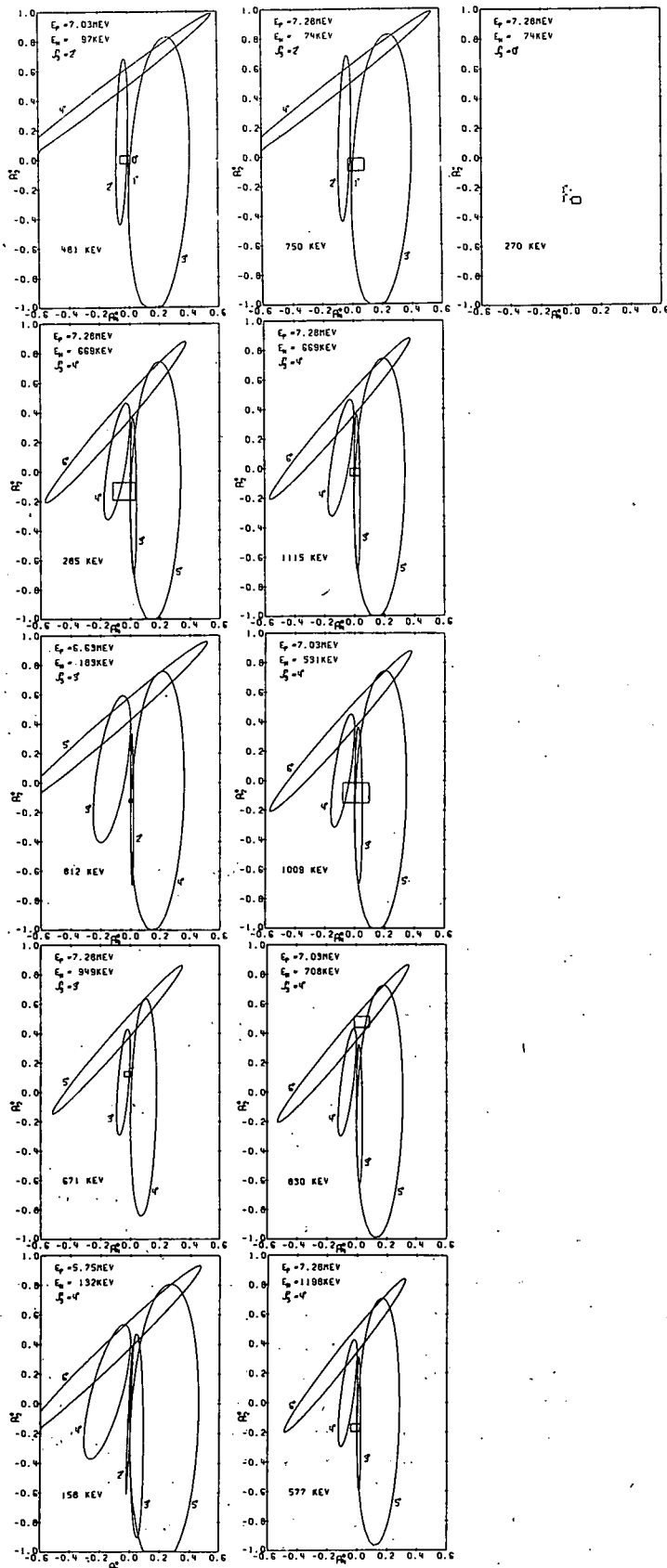


Fig. 2 Theoretical  $\gamma$ -ray  $\delta$ -ellipses. The boxes represent the experimental values of  $A_3^{\gamma}$  and  $A_4^{\gamma}$  and their associated errors. The possible initial-state spins and parities label the ellipses while the  $J_f^{\pi}$  value represents the spin and parity assumed for the final state.

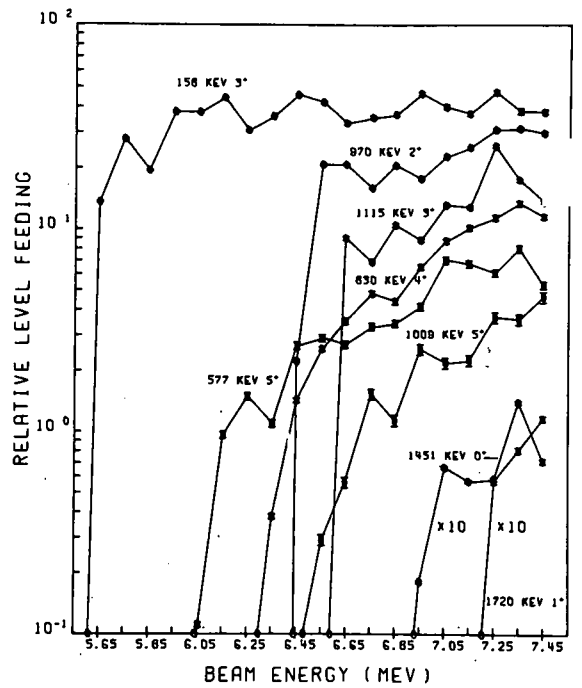


Fig. 3 Excitation functions for the eight energy levels of  $^{56}\text{Co}$  lying below 1.8 MeV of excitation. The data were taken at  $\theta=125^\circ$ , a zero of  $P_2(\cos\theta)$ . The appropriate intensities of de-exciting and feeding  $\gamma$ -rays have been added and subtracted to obtain the relative level feedings. The thresholds were calculated using  $Q=-5.36$  MeV.

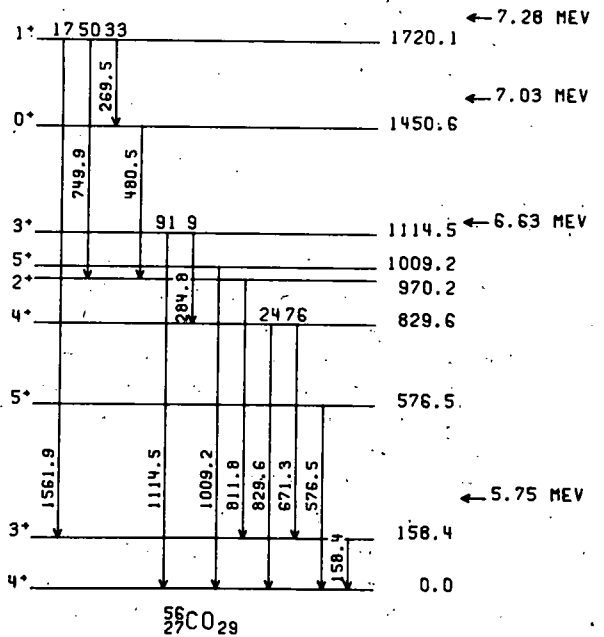


Fig. 4  $\gamma$ -ray decay scheme for excitations of  $^{56}\text{Co}$ . Where appropriate,  $\gamma$ -ray branching ratios are given. The arrows on the right indicate maximum possible excitation for the labeled incident proton energy.

As part of a search for  $\beta$ -delayed  $\alpha$  emission and an examination of the systematics of the light Zn and Cu isotopes, the  $\beta$  decays of  $^{63}\text{Ga}$  and its daughter  $^{63}\text{Zn}$  were examined. The possibility of  $\beta$ -delayed  $\alpha$  emission in the light Ga isotopes was proposed by Tangepera and Nurmi<sup>1</sup> along with their predictions for all nuclei with  $Z=82$  or less. A further discussion on these possibilities and the results of a search for  $\beta$ -delayed  $\alpha$  emission are given in another section of this report.

Nurmi and Fink<sup>2</sup> reported the discovery of 33-second  $^{63}\text{Ga}$  in 1965, but did not report any other information about the isotope. A further examination of this isotope was performed by Dulfer et al.<sup>3</sup> in which they reported the placement of nine  $\gamma$  rays with energies of 192.9, 247.8, 627.1, 637.1, 649.9, 768.2, 1065.1, 1395.5, and 1691.8 keV in a decay scheme containing levels at 0, 192.9, 247.8, 627.1, 637.1, 649.9, 1065.1, 1395.5, and 1691.8 keV. They also reported a half-life of 31.4 sec. Bernstein et al.<sup>4</sup> reported the results of the  $^{63}\text{Cu}(p,n\gamma)$  reaction used to examine the excited states of  $^{63}\text{Zn}$  up through the 1065-keV state. There is good agreement between the two sets of results.

For our work, a 4.6% efficient Ge(Li) detector with a resolution of 1.9 keV was used in a Ge(Li) time coincidence system to examine the decay of  $^{63}\text{Ga}$ . This system is used to obtain several successive, timed spectra from the decay of  $^{63}\text{Ga}$  by adding together the successive, timed spectra from each of many separate samples. A further description of this system is found in Ref. 5. These timed spectra were used to determine which of the many  $\gamma$  rays present decayed with a half-life corresponding to that of  $^{63}\text{Ga}$ . It was also used to measure the  $32.4 \pm 0.5$  sec half-life of  $^{63}\text{Ga}$ . Sixteen  $\gamma$  rays were assigned to the decay of  $^{63}\text{Ga}$ . A decay scheme summarizing our results is shown in Fig. 1. The total transition intensities, in percent of total  $^{63}\text{Ga}$  decays, are given in the decay scheme. The total  $\beta$  feedings to the levels and the log ft's based on them are given to the right of the levels. The spin and parity assignments deduced from the  $\beta$  and  $\gamma$  transitions and the charged particle scattering results are given on the left of the decay scheme.

The decay of  $^{63}\text{Zn}$  was first reported by Bothe et al.<sup>6</sup> in 1937. Since then many groups have studied the  $\beta$  decay of this isotope. Since the advent of Ge(Li) detectors, several authors have reported  $\gamma$ -ray results that are a great improvement over the earlier NaI(Tl) detector  $\gamma$ -ray results. Although numerous results from  $\gamma$ -ray studies are available, only one author<sup>7</sup> has reported any coincidence results, these being from a Ge(Li)-NaI(Tl) coincidence spectrometer. In addition to the  $\beta$ -de-

cay results, many different charged-particle reactions have been used to examine the excited states in  $^{63}\text{Cu}$ .

We studied the decay of  $^{63}\text{Zn}$  by  $\gamma$ - $\gamma$  megachannel, anti-, and 511-keV-511-keV- $\gamma$  coincidence experiments in addition to  $\gamma$ -ray singles experiments. In addition to Ge(Li) detectors our 20.3x20.3-cm NaI(Tl) split annulus and a 7.6x7.6-cm NaI(Tl) detector were utilized for the various coincidence experiments. Details of the various coincidence systems used are given in Ref. 5. The results of these various experiments were combined to place the forty-three  $\gamma$  transitions, including nine not reported by other authors, in a decay scheme containing twenty-four levels, shown in Fig. 2. The  $\beta^+$  feedings were obtained from the 511-511- $\gamma$  triple coincidence results while the total feedings to each level were obtained from the relative transition intensities and the feeding to the ground state. The percent  $\beta$  feedings and the log ft's based on them are given on the right. The spins and parities given on the left are based on our  $\gamma$ -ray results and the charged particle reactions results.

We observed several very interesting results during this study. One interesting result was the resolving of the 1392-keV  $\gamma$ -ray peak into a doublet of the 1389.5- and 1392.3-keV  $\gamma$  rays. All previous authors report it as a single  $\gamma$  ray. Since the 1389.5-keV  $\gamma$  ray is only about one-third the intensity of the 1392.3-keV  $\gamma$  ray, it appears only as a slight broadening on the low energy side of the 1392-keV peak. Using the computer program SAMPO,<sup>8</sup> we were able to reproducibly strip this peak into the doublet. Both  $\gamma$  transitions fit well into the decay scheme with the placement of the 1392.3-keV  $\gamma$  ray substantiated by the  $\gamma$ - $\gamma$  megachannel coincidence results.

Another interesting result is the placing of two levels in the 1965-keV region. All previous results including charged-particle scattering results, have reported only one level in this region. The  $\gamma$ -ray singles experiments show two resolved peaks at 1860.9 and 1865.7 keV. The relative intensities of the two have remained rather constant even though several different Ge(Li) detectors have been used and both chemically separated and unseparated sources have been used.

In the anticoincidence experiment results, these two have the same relative intensities as in the singles. Although they were not enhanced over their singles intensities, several other weak ground-state transitions in this region were also not enhanced. The possibility of either one being a double escape peak is removed since their intensities remain constant relative to each other while using several different detectors and; the

strongest known double-escape peak in the spectrum is several times weaker in intensity. Since both transitions appear to be of the same type, cascade or ground-state, we place them both as ground-state transitions based on the relative singles and anti-coincidence results.

Although the states in the neutron deficient  $A=63$  isotopes are known, both from  $\gamma$ -ray decay studies and charged particle reaction results, their interpretation has been somewhat neglected. Only the ground state and first three excited states of  $^{63}\text{Cu}$  have had any significant characterization. Since the systematics of this region just beyond the doubly closed shell at  $^{56}\text{Ni}$  are not well known, we are endeavoring to characterize these states and improve the systematics in this region.

### References

1. R. Taagepera and M. Nurmia, *Ann. Acad. Sci. Fenn. AVI*; 78(1961).
2. M. Nurmia and R.W. Fink, *Phys. Letters* **14**, 136(1965).
3. G. Dulfer, H. Beertema, and H. Berheul, *Nucl. Phys. A149*, 518(1970).
4. L. Birstein, M. Harchol, A. Jaffe, and A. Tsuksoritz, *Nucl. Phys.* **84**, 81(1966).
5. G.C. Giesler, Ph.D. Thesis, Michigan State University, C00-1779-55, 1971.
6. W. Bothe and W. Gentner, *Z. Physik* **106**, 236(1937).
7. I. Borchert, *Z. Physik* **223**, 473(1969).
8. J.T. Routi and S.G. Prussin, *Nucl. Instr. and Methods* **72**, 125(1969).

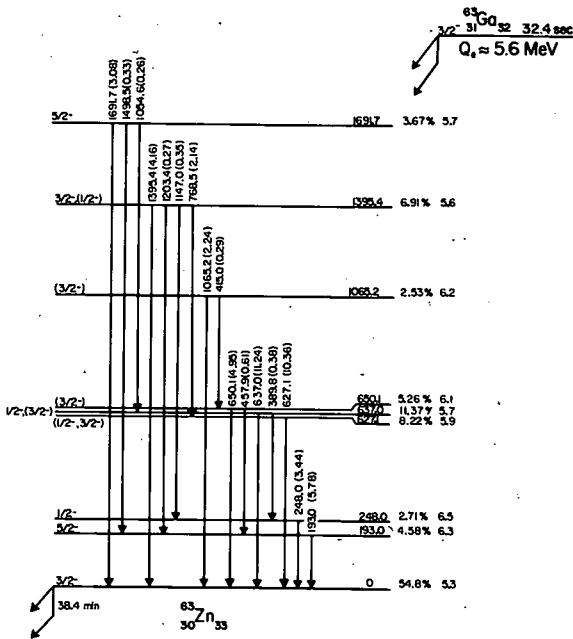


Fig. 1 The decay of  $^{63}\text{Ga}$ .

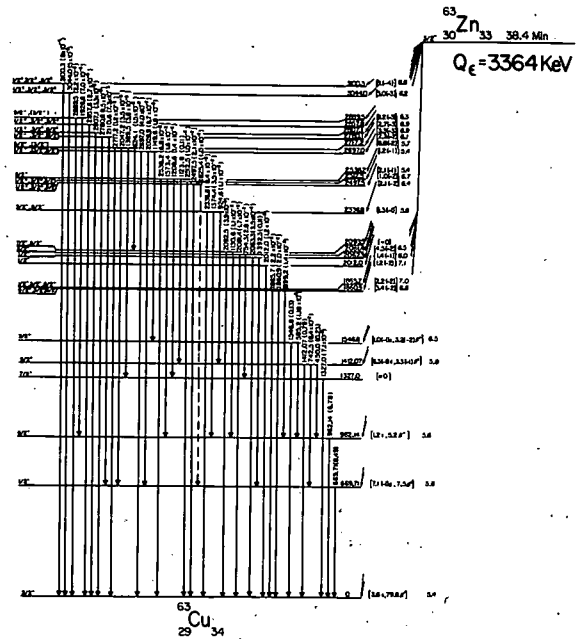


Fig. 2 The decay of  $^{63}\text{Zn}$ .

The examination of these nuclei was prompted by the possibility of  $\beta$ -delayed  $\alpha$  emission in the light Ga isotopes. In order to be able to identify  $\gamma$  transitions from the parent, the  $\gamma$  transitions of the daughter must be well known. Although there has been a flurry of activity in this region, with several authors studying the decay of  $^{62}\text{Zn}$  with Ge(Li) detectors, no  $\gamma$  transition was observed above 650 keV even though it has a  $Q_{\alpha} \approx 1620$  keV. Davidson *et al.*<sup>1</sup> used the results from the  $^{62}\text{Ni}(p,n\gamma)$  reaction to study the excited states in  $^{62}\text{Cu}$ . They reported  $\gamma$  transitions from levels through 916 keV.

For our examination, we used the largest Ge(Li) detectors we have available with relative efficiencies as large as 10.4%. All samples used were chemically separated to remove any possible contaminants. Six  $\gamma$  transitions above 650 keV were observed that had not been previously reported in  $\beta$  decay studies. Figure 1 shows these transitions placed in a decay scheme. The percent  $\beta$  feedings to the levels and the log ft's obtained from them, are shown on the right of the levels, and the spins and parities are given on the left. The placement of the transitions and the spins and parities of the levels below 920 keV are from Davidson *et al.*<sup>1</sup> and are consistent with the  $\beta$ -decay results. The remaining levels indicated on the right are from the  $^{61}\text{Ni}(r,d)$  reaction.<sup>2</sup>

The possibility of these  $\gamma$  rays being from the  $^{62}\text{Cu}$  daughter is ruled out based on the  $\beta$ -decay studies of Jongoma *et al.*<sup>3</sup> and the  $^{61}\text{Ni}(n,\gamma)$  results of Farger, *et al.*<sup>4</sup>

The possibility of  $\beta$ -delayed  $\alpha$  emission in the light Ga isotopes was first proposed by Taagepera and Nurmi.<sup>5</sup> Further calculations were performed by Fenges and Rupp<sup>6</sup> in which the predictions were given for all nuclei with  $Z < 85$  using the mass tables of Myers and Swiatecki.<sup>7</sup> Their results indicated  $^{64}\text{Ga}$  would be the heaviest possible  $\beta$ -delayed  $\alpha$  emitter for Ga. The heaviest known  $\beta$ -delayed emitter is 297-msec  $^{32}\text{Cl}$ .

In their reports of the discovery of  $^{63}\text{Ga}$ , Nurmi and Fink<sup>8</sup> reported their purpose was to look for delayed  $\alpha$ 's from  $^{62}\text{Ga}$ , but they did not observe any. We have extended their study and looked for delayed  $\alpha$  emission from isotopes as light as  $^{60}\text{Ga}$ . We bombarded natural Cu foils with 70 MeV  $\tau$  and examined the activated nuclei with both Si(Li)  $\alpha$  detectors and Ge(Li)  $\gamma$  detectors. Lower beam energies were obtained by using appropriate Al absorbers. The beam energies were chosen to maximize the production of  $^{60}\text{Ga}$ ,  $^{61}\text{Ga}$ , and  $^{62}\text{Ga}$ . The activated nuclei were removed from the activation area to a distant counting area by using the He-jet thermalizer described elsewhere in this report.

Figure 2, the  $\alpha$  spectra obtained are shown. The results of the experiments indicate the possibility of delayed  $\alpha$  emission from  $^{60}\text{Ga}$  although an upper limit of ten parts per million delayed  $\alpha$  branching has been placed on it by comparison of the  $\gamma$ -ray results with the  $\alpha$  spectra. Any delayed  $\alpha$  emission from the heavier Ga isotopes appears to have a smaller upper limit. The presence of the light Ga isotopes was determined by the observation of the decay of their Zn daughters. The Ga isotopes were not observed directly since their half-lives are expected to be seconds or less.

The non-observance of delayed  $\alpha$  emission could be from several different sources. The  $\alpha$  binding energies for the Zn isotopes are about 3 MeV, so in order to produce  $\beta$ -delayed  $\alpha$  emission from these isotopes, the Ga parents must decay to states in Zn above the  $\alpha$  binding energy. Even though the Ga ground states are calculated to be 10 MeV or more above their Zn daughters, the probability of their decaying to the higher lying states in the Zn daughters is small.

Several anomalies in these systematics are also noted. The  $^{61}\text{Ga}$  and  $^{61}\text{Zn}$  are mirror nuclei, and as such would permit super-allowed  $\beta$  decay from the  $^{61}\text{Ga}$  ground state to the  $^{61}\text{Zn}$  ground state. As a result the possibility of  $\beta$  feeding to the higher-lying excited states would be almost zero. A completely different case is presented by the  $^{60}\text{Zn}$  since it may be considered as a doubly magic  $^{56}\text{Ni}$  core with an  $\alpha$  particle bound to it. This would lead to a much lower binding energy for the  $\alpha$  particle and greatly increase the possibility of  $\beta$ -delayed  $\alpha$  emission. Experimental results indicate that there may be  $\beta$ -delayed  $\alpha$  emission from  $^{60}\text{Ga}$ .

Even if the  $\alpha$  binding energies are low enough to permit  $\beta$  feeding to levels above them, another problem enters. This problem is the Coulomb barrier which is about 7 MeV in this region. If the  $\alpha$  particles are to go over the barrier, they would have to come from states that are more than 8 MeV above the ground state if the  $\alpha$  binding were only 1 MeV. Obviously, the  $\beta$  feeding to these levels would be extremely small. If the  $\alpha$  particles with lower energy were to tunnel through the barrier, the  $\beta$  feeding to the states producing  $\alpha$  emission would be greater but the probability of the particle escaping the nucleus would be small. In either case the probability of  $\beta$ -delayed  $\alpha$  emission is very small.

Even with all these obstacles,  $\beta$ -delayed emission is possible but only to a very small extent. Further work is in progress, both to better define the limitations on  $\beta$ -delayed  $\alpha$  emission

and to determine the decay schemes of these light Ga isotopes.

References

1. W.F. Davidson, M.R. Najam, P.J. Dallimore, J. Hellström, and D.L. Powell, Nucl. Phys. A154, 539(1970).
2. G.C. Morrison, private communication.
3. H. W. Jonjmsa, B. Bengtsson, G.H. Dulfér, and H. Verheal, Phys. 42, 303(1969).
4. U. Fanger, D. Heck, W. Michaelis, H. Ottmar, H. Schmidt, and R. Gaeta, Nucl. Phys. A146, 549(1970).
5. R. Taagepera and M. Nurmia, Ann. Acad. Sci. Fenn. AVI, 78(1961).
6. T. Fengés and B. Rupp, ATOMKI Koylem. 10, 116(1968).
7. W. Myers and W. Sweatecki, UCRL-11980(1965).
8. M. Nurmia and R.W. Fink. Phys. Letters 14, 136(1965).

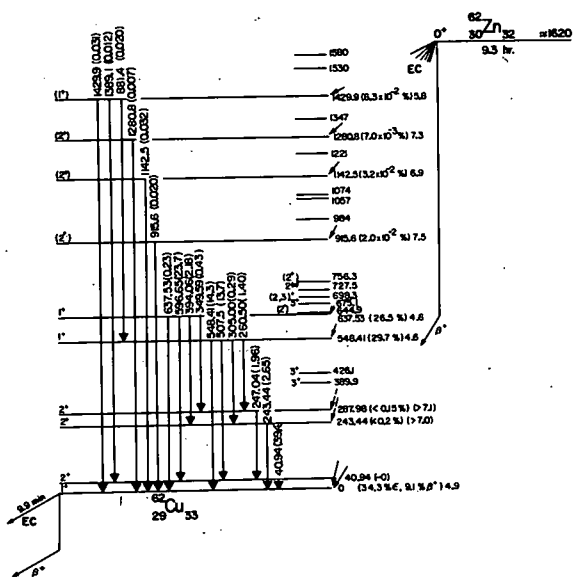


Fig. 1 <sup>62</sup>Zn decay scheme.

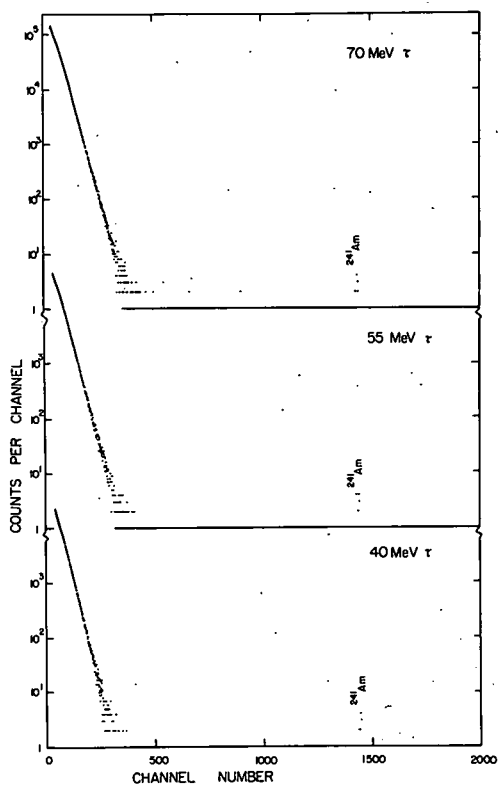


Fig. 2 A search for  $\beta$ -delayed  $\alpha$  emission in eight Ga isotopes.

The Search for Three-Particle  
Isomeric States in  ${}^4\text{Ti}$  and  ${}^4\text{Sc}$

J. Black

High-spin, three-particle states analogous to that discovered in  ${}^5\text{Fe}$  may exist in  ${}^4\text{Ti}$  and  ${}^4\text{Sc}$ . Preliminary experiments have been performed on these isotopes, but were limited to activities with half-lives greater than 15 sec.<sup>1</sup> From these experiments, no evidence was found to support the existence of such three-particle isomeric states in these isotopes. However, the large decay energy of  ${}^4\text{Ti}$  and the possibility of the decay of its  $19/2^-$  state by a super-allowed  $\beta^+$  transition to the  $19/2^-$  state of  ${}^4\text{Sc}$  implies that the half-life of the state is shorter than 1 sec. On the other hand, it is thought that the  $19/2^-$  state of  ${}^4\text{Sc}$  is very similar to the  ${}^5\text{Fe}$  case.

Thus far in the present investigation, we have attempted a number of different experiments in the search for these high-spin isomers. Due to the availability of target material, most of these experiments have utilized the  ${}^4\text{Sc}(p,3n){}^4\text{Ti}$  reaction, using 35 MeV protons from the MSU Cyclotron. This reaction affords both the possibility of observing  $\gamma$  rays from the de-excitation of  ${}^4\text{mTi}$  directly or from the de-excitation resulting after a super-allowed  $\beta^+$  transition to the analogous level in  ${}^4\text{mSc}$ .

The first experiments performed made use of the "slow-pulsing" technique to look for half-lives in the 10-1000 msec range. In these experiments, the cyclotron beam was pulsed by RF modulation, such that the activity was produced by beam bursts of about 2-sec duration; and then counted in 4 successive, routed, beam-off spectra of about 600 ns each. A spectrum of the beam-on period was also obtained.

Experiments were also conducted to look for half-lives in the nsec region. These were achieved by routing  $\gamma$  spectra in the time intervals between the microscopic structure of the cyclotron beam.

Direct examination of half-lives in the  $\mu\text{sec}$  range is normally available by the so-called, fast-pulsing technique—in which only one of a selected number of microscopic beam bursts is allowed to be accelerated. However, this method is temporarily unavailable to us, due to thermal stability problems with the deflection plate mechanism. Therefore, examination of this crucial half-life region, is confined to setting limits on levels as observed in the msec and nsec regions—e.g. a peak in this region would appear long-lived in the nsec experiments and short-lived in the msec ones.

Another type of experiment was performed in which a helium-jet thermalizer was used to look for  ${}^4\text{mSc}$ . A thin ( $\sim 0.5$  mg/cm<sup>2</sup>) layer of isotopically separated  ${}^4\text{Ca}$  was evaporated onto a tantalum backing and mounted in the thermalizer chamber. A beam of 24 MeV protons was used to

produce the  ${}^4\text{Sc}$  by the  ${}^4\text{Ca}_2, (p, 2n){}^4\text{Sc}_2$  reaction. The resulting recoils were thermalized in helium and transported through a polyethylene capillary to a collector and counting facility on the roof of the cyclotron vault. Due to the transit time in the capillary, this method was limited to half-lives greater than a few tens of msec.

All of the above experiments employed large high-resolution, Ge(Li) detectors having efficiencies of 2.5-10.4% compared with 3x3-NaI crystal at 25 cm.

While the analysis of our data is not complete, the results of preliminary experiments show the existence of many unidentified  $\gamma$  rays, some of which may belong in the  ${}^4\text{mSc}$  or  ${}^4\text{mTi}$  decay scheme. The positive assignment of a  $\gamma$  ray to one of these unknown schemes is rather tedious, due to the large number of side products from unwanted reactions and contaminants. It is hoped that improved half-life discrimination may be used to identify  $\gamma$  rays from these high-spin isomers.

The isomeric level in  ${}^4\text{Sc}$  has been tentatively identified by other workers. Iordachescu<sup>2</sup> reported the existence of two short-lived species in this region when performing a survey of  $\alpha$  particles of 17.2-20.0 MeV on a number of thick natural targets. With a potassium target, a  $\gamma$  activity with an energy of 154 keV and a half-life of 456  $\mu\text{sec}$  was reported. With a calcium target, a  $\gamma$  ray with an energy of 163 keV and half-life of 450  $\mu\text{sec}$  was found.

More recently Sawa and Bergström<sup>3</sup> have reported a decay scheme for  ${}^4\text{mSc}$  (Fig. 1). The isomeric transition they report is an E2 with an energy of 136 keV and half-life of 0.5  $\mu\text{sec}$ . Here it appears that the  $15/2^-$  state has crossed below the  $19/2^-$  level, resulting in a much shorter half-life than one would expect from comparison with the  ${}^5\text{mFe}$  conjugate configuration.

In our present study, we have observed all the  $\gamma$  rays reported by these workers, including the 136-keV transition. However, the assignment of these  $\gamma$  rays to a decay scheme for  ${}^4\text{mSc}$  has not been attempted, since a number of problems exist which are difficult to reconcile with our data. If the isomeric transition decays with a half-life of about 0.5  $\mu\text{sec}$ , then one would expect the  $\gamma$  rays in the resultant cascade to follow a similar half-life. However, our pulsed-beam measurements indicate a much longer ( $> 2$  sec) half-life for the 1157-keV, ( $15/2^- \rightarrow 11/2^-$ ) transition. Indeed, the assignment of this  $\gamma$  ray to the  ${}^4\text{mSc}$  decay scheme is difficult, since the reactions used to produce the  ${}^4\text{Sc}$  also produce  ${}^4\text{Sc}$ —whose decay contains a strong  $\gamma$  ray at almost the same energy (1156-keV). Using our method of bracketing



the half-life range, we have found several  $\gamma$  rays which follow the expected half-life—including the 135- and 1830-keV transitions. Because of the lack of energy sums and crossovers, it is not obvious that one can construct a completely unambiguous decay scheme for  $^{43m}\text{Sc}$ . The rather extensive study of the low-lying states in  $^{43}\text{Sc}$  by Ball, *et al.*<sup>4</sup> provides a few states which could belong to the isomer decay cascade (the 1157-keV problem also exists in this scheme). Nevertheless, it is quite difficult to assign  $\gamma$  rays to these and higher levels without very good half-life measurements.

#### References

1. K. Eskola, Phys. Letters 23, 471(1966); K. Eskola, Ann. Acad. Sci. Fenn. 261, 8(1967); I. Dernède, Zeit. Für Physik 216, 103(1968).
2. A Iordachescu, Rev. Roum. Phys. 13, 911(1968).
3. Z.P. Sawa and I. Bergström, Annual Report, Research Institute for Physics, 10405 Stockholm, Sweden (1970) p. 102.
4. G.C. Ball, J.S. Forster, F. Ingebretsen, and C.F. Monahan, Canadian Journal of Physics 48, 2735(1970).

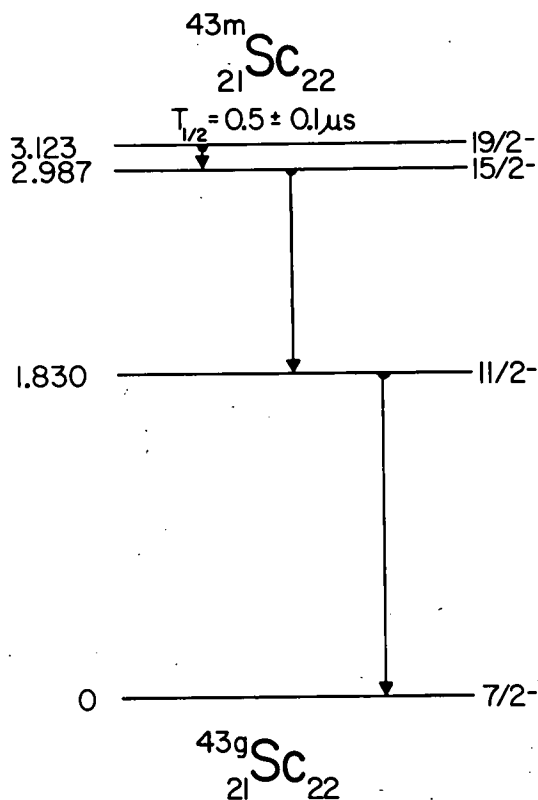


Fig. 1 The proposed decay scheme for  $^{43m}\text{Sc}$  from Ref. 3.

The discovery of a high-spin, three-particle isomer in the  $^{53}\text{Fe}$  nucleus has prompted the search for analogous isomers in nuclei having a similar configuration.<sup>1</sup> An early search for such isomers by Eskola yielded negative results for isomers having half-lives greater than 15 sec.

The isomer  $^{53}\text{MCo}$  is especially interesting, since its  $19/2^-$  state can decay by a super-allowed  $\beta^+$  transition to the isobaric analogue state in  $^{53}\text{MFe}$ —an isotope being studied in this laboratory. A search is continuing for a  $\gamma$ -decay branch of  $^{53}\text{MCo}$ . We are attempting to produce the  $^{53}\text{MCo}$  by a  $^{54}\text{Fe}(p, 2n)^{53}\text{MCo}$  reaction using 35-MeV protons from the MSU cyclotron. Although various oxide targets have been tried, we are presently using a self-supporting, isotopically-separated  $^{54}\text{Fe}$  foil. Two types of experiments have been carried out thus far. A series of experiments have been performed in which the beam was pulsed, with the beam on for about 1 sec and off for 1 sec. During the beam-off period, four 4096-channel spectra were routed in 0.25-sec intervals. A 2.5%-efficient Ge(Li) detector was used to observe the resulting  $\gamma$ -rays. The second type of experiment utilized a helium-jet thermalizer. The  $^{54}\text{Fe}$  foil was bombarded with 35-MeV protons, and the resulting recoils were thermalized in helium and piped up to a fixed collector on the roof of the cyclotron vault.

A 10.4%-efficient Ge(Li) detector was then used to observe the  $\gamma$  rays associated with the recoils. Since the mechanism for moving the collecting surface was not operational when these spectra were taken, they contain many peaks due to the buildup of longer-lived species on the fixed collector. Both of these series of experiments provided a relatively large number of unidentified  $\gamma$ -rays. The presence of  $^{53}\text{MFe}$   $\gamma$  rays was noted in all of these experiments. However, since the 13.6-MeV threshold for the  $^{54}\text{Fe}(p, pn)^{53}\text{M} + \text{gFe}$  reaction is lower than the threshold for the  $^{54}\text{Fe}(p, 2n)^{53}\text{g}(\text{+m})\text{Co}$  reaction (22.8 MeV), one cannot conclude merely from the observation of  $^{53}\text{MFe}$  gamma-rays that he has produced its  $^{53}\text{MCo}$  analogue.

There exist unidentified  $\gamma$  rays in the helium-jet data which can be fitted to a decay scheme very much like that of  $^{53}\text{MFe}$ . However, half-life determinations from the on-line experiments are still somewhat ambiguous. Thus, at this time, our data cannot attribute them positively to that nucleus.

Meanwhile, Cerny, *et al.*<sup>2,3</sup> have shown the existence of proton radioactivity from the  $^{53}\text{MCo}$  nucleus. Using  $^{40}\text{Ca}(^6\text{O}, 2n p)$  and  $^{54}\text{Fe}(p, 2n)$  reactions to produce the isomer, they have observed a  $1.57 \pm 0.03$  MeV proton activity with a  $242 \pm 15$ -msec

half-life. This half-life implies that the dominant mode of decay is by positron emission to  $^{53}\text{MFe}$ . The partial half-life for the Fermi component of the super allowed  $\beta^+$  decay was calculated to be 350 msec.<sup>4</sup> If one then uses the pure  $(f_{7/2})^{-3}$  configuration and includes the Gamow-Teller matrix element, the calculation yields a predicted  $\beta^+$  half-life of 200 msec— which agrees reasonably well with the experimental half-life.<sup>5</sup> The observed proton activity thus represents only a weak branch in the  $^{53}\text{MCo}$  decay. Using statistical model calculations, an order of magnitude estimate of 50 sec. was obtained for the proton partial lifetime.<sup>2</sup>

The facts currently known about the modes of decay of  $^{53}\text{MCo}$  are illustrated in Fig. 1. The search for a gamma branch in this decay is now in progress. Transitions in existing spectra are being examined, and an attempt is being made to assign them more concretely to levels in  $^{53}\text{MCo}$ . It is hoped that this study will establish the existence of  $\gamma$  rays corresponding to transitions from the  $19/2^-$  state of  $^{53}\text{MCo}$ , and thus extend the present knowledge of these three-particle isomer systematics.

#### References

1. K. Eskola, Phys. Letters 23, 471(1966); K. Eskola, Ann. Acad. Sci. Fenn. 261, 8(1967); I. Darnedde, Zeit. für Physik 216, 103(1968).
2. K. Jackson, C. Cardinal, H. Evans, N. Jelley and J. Cerny, UCRL-19963, preprint (1970).
3. J. Cerny, J. Esterl, R. Gough, and R. Sextro, UCRL-19973, preprint (1970).
4. J. Freeman, J. Jenkin, G. Murray, and W. Burcham, Phys. Rev. Letters 16, 959(1966).
5. A. de-Shalit and I. Talmi, Nuclear Shell Theory, Academic Press, 1963.

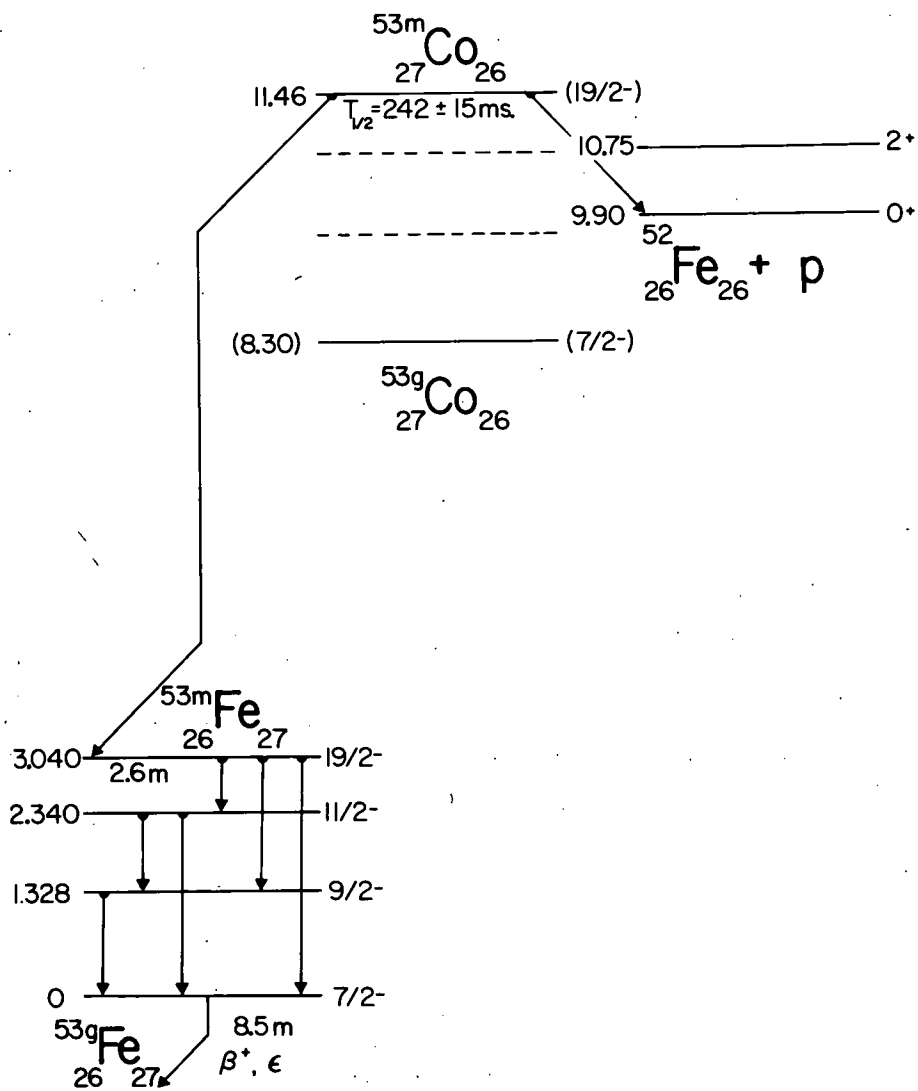


Fig. 1 The known modes of decay for  $^{53m}\text{Co}$ . (The dashed lines indicate levels that could be populated by a  $\gamma$ -decay branch.)

The remarkable process of cell differentiation in the human embryo was learned by most of us in our high-school years if not earlier. The process occurs in all the higher plants and animals and is responsible for their great diversity. Lacking, however, is an understanding of the mechanisms involved in the development of organisms and of the influence of environmental factors. Blue-green algae exhibit phenomena analogous to basic developmental processes encountered in the higher forms of life. In filamentous forms of blue-green algae, Fig. 1, special cells called heterocysts arise from the vegetative cells not at random but at rather regular intervals. Such algae may be to cell differentiation what p-p scattering is to nuclear physics. The function of the heterocysts was for many years considered a "botanical enigma". It has recently been suggested that the heterocyst is the sole site of nitrogen fixation in these algae. [On the practical side we note that rice agriculture depends upon atmospheric nitrogen fixed by various blue-green algae.] Evidence on this proposition is inconclusive in spite of great interest and much work on the subject. Destructive biochemical techniques such as centrifugation and sonication have not led to definitive experimental results.

Our approach is to obtain pictorial, in vivo, evidence from  $^{13}\text{N}$  autoradiography. Because of the short half-life (10 minutes) of  $^{13}\text{N}$ , it must be used where it is produced, and a cyclotron or similar accelerator is required for its production.

We use the  $^{16}\text{O}(p,\alpha)^{13}\text{N}$  reaction with 20 MeV protons incident on a 15 MeV thick target of  $\text{Li}_2\text{CO}_3$ . The chemical separation following production requires a small sample. We use 50 mg packed into a cylinder less than 4 mm in diameter. When the beam is properly focussed and aligned it penetrates the target to a Faraday cup where it is monitored throughout the bombardment. The target holder is shown in Fig. 2.

The production cross-section is energy dependent but averages around 20 mb. Hence, bombardment with a 1  $\mu\text{amp}$  beam produces  $^{13}\text{N}$  at the rate of  $10^9/\text{sec}$ . At the end of a saturation bombardment there are  $\sim 10^{12}$   $^{13}\text{N}$  atoms. This is  $2 \times 10^{-11}$  of the target atoms and equivalent to  $\sim 3 \times 10^{-8}$  atmospheric cc of  $\text{N}_2$  gas. To within our factor-of-two accuracy all of the calculated  $^{13}\text{N}$  activity is collected in gaseous form after chemical treatment with a commercial (Coleman) nitrogen analyzer utilizing mainly hot copper and hot copper oxide, a liquid nitrogen trap, and an alkaline permanganate wash to remove oxides of nitrogen. Further development of our chemical processing is underway to reduce below 0.01% nitrogen gases more rapidly fixed than  $\text{N}_2$ .

The activity collected in one run was counted until it had decayed by a factor of  $10^4$ . The decay curve was a single exponential with half-life-9.84 minutes. There was no trace of  $^{11}\text{C}$  (half-life 20 minutes). This is important because the algae assimilate  $\text{CO}_2$  more readily than  $\text{N}_2$ .

We have seen some tracks originating in algae and are presently working to improve our autoradiographic techniques. In comparison to  $^{14}\text{C}$  autoradiography, which has become routine,  $^{13}\text{N}$  autoradiography should be more difficult because of the paucity of low-energy, highly-ionizing positrons. Most of the positrons are near minimum ionizing. A reasonable solid angle for seeing minimum-ionizing tracks requires thick emulsions, which are more difficult to develop quickly and without distortion.  $^{32}\text{P}$ , which is more readily available than  $^{13}\text{N}$  and whose electron spectrum is similar to that of  $^{13}\text{N}$ , is being used as we improve our autoradiography. A track from  $^{32}\text{P}$  decay originating in a vegetative cell of an algae is visible in Fig. 3.

In addition to the present project, development of  $^{13}\text{N}$  autoradiography should be of value for future biological research.

\*MSU-AEC Plant Research Laboratory.

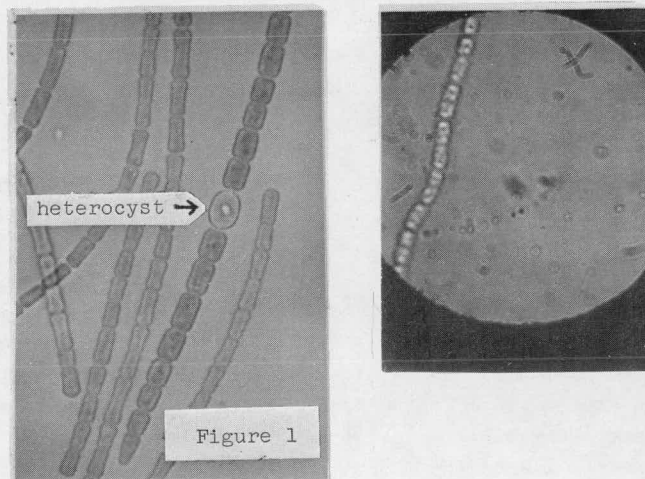


Figure 1

Target Holder

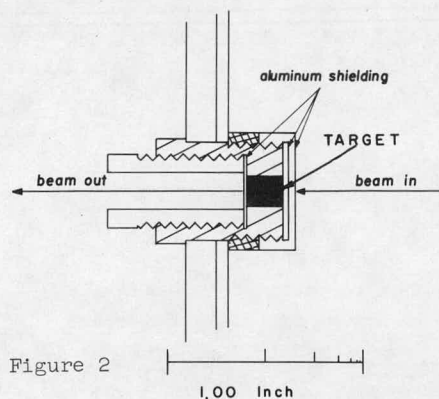


Figure 2

Neutron Yields From Proton  
Bombardment of Thick Targets  
T. Amos, A. Galonsky and R.K. Jolly

Stopping targets of natural C, Al, Cu, Ag, Ta and Pb have been bombarded by 22, 30 and 40 MeV protons. The resultant yield spectra of neutrons above 0.5 MeV were measured by the time-of-flight (TOF) technique at laboratory angles of 1, 30, 60, 90, 120, and 150 degrees.

The targets used were selected because they represent a reasonably wide mass sample of the known nuclides, and because they are commonly used in scientific instruments and applications where there are high energy protons present.

For each energy the targets were disc 2.54 cm in diameter with a thickness equal to the range plus range straggling of the incident protons. The TOF detector was a cylindrical glass encapsulated NE213 plastic scintillator 4.4 cm in diameter x 1.9 cm thick optically coupled to an RCA 8575 photomultiplier.

The dynamic range of neutron energies covered in the experiment was from 0.5 MeV to a maximum of about 40 MeV, or 80/l. Due to the non-linearity of the scintillator response as a function of neutron energy, this energy range corresponds to a range in pulse height in the photomultiplier output of approximately 600/l. The experimental electronics are incapable of handling such a large range of pulse heights with adequate resolution. Therefore the TOF spectra were taken in two parts: one spectrum gives accurately only neutrons between 0.5 and 4.5 MeV with a range in pulse height of approximately 35/l and flight path of 0.5 meter; the second spectrum corresponds to neutrons between 3.5 and 40 MeV with a range in pulse height of 25/l and a flight path of 1.5 meter.

The time of flight resolution as measured by the full width at half maximum of the target gamma peak was typically 0.5 nsec..

The high ambient flux of gamma rays from neutron capture events in the experimental room, plus the extremely large number of gamma rays from nuclear events inside the targets themselves required the use of pulse shape discrimination to separate neutrons from gamma rays. With the relatively small dynamic ranges noted above, gamma rejection ratios of better than 200/l were easily achieved.

Typical gamma and neutron TOF spectra are shown in Fig. 1. The neutron TOF spectra were converted to energy spectra, corrected for dead time losses and detection efficiency, and plotted with no other normalization factors as absolute yield spectra, two of which are shown in Fig. 2.

The data are currently being analyzed and will be treated to give yield spectra, angular distributions and angle- and energy- integrated total yields for all targets as a function of mass number and bombarding energy.

By subtracting corresponding thick target spectra taken at two different energies, "thin" target spectra may be obtained. These spectra will be compared with predictions of the statistical model to obtain nuclear temperature and level density parameters. In addition, such spectra will be used in an attempt to determine the individual yields of neutrons produced by direct and compound processes.

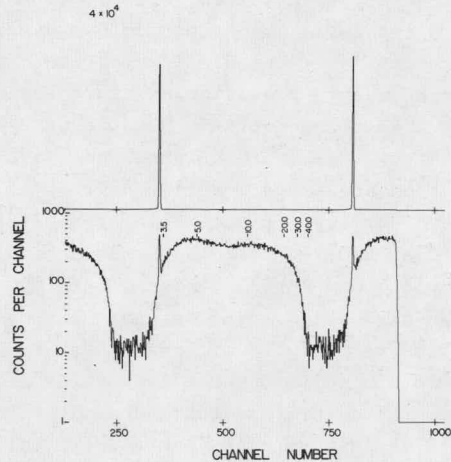


Fig. 1 Gamma-ray and neutron TOF spectra from bombardment of a thick lead target by 40 MeV protons, measured at 30° lab angle. The lower spectrum is that of neutrons above 3.5 MeV, with the energy scale of MeV at the top of the spectrum.

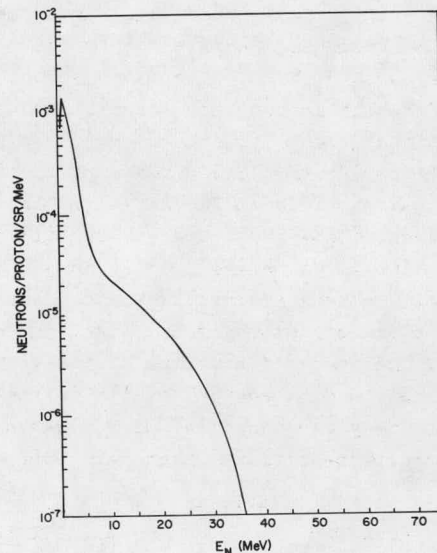


Fig. 2 The neutron yield spectrum corresponding to the TOF spectrum in Fig. 1, with the yield for neutrons between 0.5 and 3.5 MeV included to give the entire spectrum above 0.5 MeV.

Elemental Analysis by Elastic Scattering

R.K. Jolly and H.B. White

The object of the present study is to examine the nuclear scattering process, with a view to understanding the conditions that enable one to achieve maximum sensitivity and efficiency in its application to elemental analysis. In the following paragraphs it is shown that the chief value of the elastic scattering technique lies in the fact that, unlike conventional techniques, one can get information about all the elements in the sample in one good energy resolution measurement.

In the nuclear scattering technique, the sample to be analysed is bombarded by projectiles of mass  $m$  and energy  $E_{inc}$ . The energy loss  $\Delta E = E_{scatt} - E_{inc}$  which can be shown to be given by

$$\Delta E = \frac{2E_{inc}}{(1+A/m)} \quad (1)$$

for a scattering angle of  $90^\circ$  (chosen for simplicity).

Thus, for a given  $E_{inc}$  and  $m$  one can measure  $A$ , the mass of the target nucleus by measuring  $\Delta E$ , the energy lost in the scattering process. An element is identified by its characteristic isotopic abundance which serves as its signature (both in terms of the average atomic mass of the element and the relative abundance of its isotopes).

A plot of  $\frac{E_{scatt}}{E_{inc}}$  vs scattering angle both for protons ( $m=1$ ) and  $\alpha$ -particles ( $m=4$ ) is shown in Fig. 1 for various atomic masses. The rate of change of  $E_{scatt}$  with  $A$  and for scattering at  $90^\circ$  can be written as

$$\frac{\Delta E_{scatt}}{E_{inc}} = \frac{2m}{(A+m)^2} \quad (2)$$

Here  $\Delta E_{scatt}$  is the energy difference between particle scattered from two nuclei that differ by  $\Delta A=1$  mass unit.  $\Delta E_{scatt}$  is, therefore, the energy resolution required to separate two nuclei that differ by 1 mass unit. Table I gives some values of  $\Delta E_{scatt}$  for both protons and  $\alpha$ -particles of  $E_{inc}=20$  MeV. It is apparent that the energy resolution requirements for protons are three to four times as stringent as those for  $\alpha$ -particles of the same energy.

However, for  $\alpha$ -particles the specific energy loss,  $\frac{dE}{dx}$ , in all materials is  $\sim 10$  times that for protons of the same energy (20 MeV). This means that the thickness of the sample and, therefore, the yield will be lower by a factor of ten for  $\alpha$ -particles to maintain the same energy loss as in the case of protons. The yield, however, also depends on the scattering cross-sections which have been compared

Table 1

	PROTONS			$\alpha$ -PARTICLES		
	120°	80°	40°	120°	80°	40°
A= 25	83	48	14	236	160	54
A= 50	23	12	3.7	75	46	14
A=100	6	3.5	0.9	21	12	3.7
A=200	1.5	0.9	0.23	5.7	3.2	0.9

for 20 MeV  $\alpha$ -particles and protons in Table II for nuclei of masses  $A=60, 120, \text{ and } 208$ . It is highly unlikely that a typical sample will contain all the elements in the periodic table in equal abundance. Table III shows a more probable list of elements of comparable abundance in a given sample (only the most abundant isotopes in these elements have been tabulated). All the elements in such a sample can be easily resolved from one another at  $40^\circ$  with an energy resolution much poorer than that routinely achieved (10-15 keV) in several low energy nuclear

Table II

Differential Scattering Cross-sections (mb/sr) for 20 MeV  $\alpha$ -particles and Protons for  $^{60}\text{Ni}$ ,  $^{120}\text{Sn}$ , and  $^{208}\text{Pb}$

	$\theta=40^\circ$		$\theta=80^\circ$	
	$\alpha$ -particles	Protons	$\alpha$ -particles	Protons
$^{60}\text{Ni}$	366	130	5.9	20
$^{120}\text{Sn}$	2920	100	117	5.0
$^{208}\text{Pb}$	5800	500	470	40

physics laboratories. If several neighboring, very heavy, elements are present then the measurements have to be made at a larger angle like  $80^\circ$  to resolve these elements. At both of these angles the  $\alpha$ -particle scattering cross-sections for the heavy elements (Pb-Sn) are at least an order of magnitude greater (Table II) than the proton scattering cross-sections, so that the loss in yield due to a smaller target thickness is cancelled by the increase in yield due to the larger  $\alpha$ -scattering cross-sections. However, the advantages of greater mass resolution and the low inelastic scattering background due to the higher Coulomb barrier for  $\alpha$ -particles still remain.

For large solid angles, compensation of the larger kinematic broadening for  $\alpha$ -particles necessitates the use of magnetic spectrograph.<sup>1</sup>

Table III

Target Nucleus	$E_{scatt}$ (MeV) at $40^\circ$	$\Delta E$ (keV) at $40^\circ$
$^{207}\text{Pb}$	19.8193	89.8
$^{138}\text{Ba}$	19.7295	23.3
$^{127}\text{I}$	19.7062	19.6
$^{119}\text{Sn}$	19.6866	109.4
$^{88}\text{Sr}$	19.5772	72.4
$^{75}\text{As}$	19.5048	93.1
$^{63}\text{Cu}$	19.4117	72.4
$^{56}\text{Fe}$	19.3393	258.3
$^{40}\text{Ca}$	19.0810	23.1
$^{39}\text{K}$	19.0579	105.0

Table III con't.

$^{35}\text{Cl}$	18.9529	105.0
$^{32}\text{S}$	18.8573	95.6
$^{31}\text{P}$	18.8215	35.8
$^{23}\text{Na}$	18.4265	395.0
$^{16}\text{O}$	17.7705	656.0
$^{14}\text{N}$	17.4000	301.2
$^{12}\text{C}$	17.0705	398.8

Table V shows the number of counts/hr. for an organic target of thickness 100  $\mu\text{m}/\text{cm}$  and an impurity of mass=A and fractional atomic abundance  $10^{-6}$  for a 20 MeV, 1  $\mu\text{A}$   $\alpha$  beam and  $d\Omega=4\times 10^{-3}\text{sr}$

Table V

	$\theta_{\text{LAB}}=40^\circ$	$80^\circ$
A=60	$2.5\times 10^2$	5
A=120	$2\times 10^3$	$10^2$
A=208	$5\times 10^3$	$5\times 10^2$

It is apparent that for samples typified by Table III, atomic concentrations of various elements to the levels of  $10^{-6}$  to  $10^{-8}$  can be measured within an hour with 1  $\mu\text{A}$ . of beam intensity.

The first two spectra presented below were measured with a counter telescope while the last two measurements were made with a magnetic spectrograph.

i) Human Blood: A spectrum from human blood is shown in Fig. 2. Some of the carbon and oxygen in the spectrum is from the backing. Quite a few elements heavier than A=16 are seen. Most prominent are  $^{23}\text{Na}$ , Cl,  $^{31}\text{P}$ , Ca, Fe, and Pb.

A comparison between the relative abundance of the various elements seen in the blood of an average human (Ref. 2) and those observed in the present work in a single human blood specimen is shown in Fig. 3. The two sets of data are normalized to have equal abundance of K. Agreement is reasonably good in view of the large variance of the relative elemental abundance from one blood sample to another. The abundance measured in the present work is that of the prepared thin film sample used in the  $\alpha$ -scattering measurement and, therefore, has several possible sources of error.

ii) Milk: An  $\alpha$ -particle spectrum from a deposit of milk on Formvar is shown in Fig. 4. The most prominent peaks are those of C, N, O (an appreciable fraction of the C and O peaks are from Formvar) P, Cl and (K+Ca). But, in addition, there are also traces of F, Si, S, As and Pb(?). Both K and Ca are probably present in the spectrum in Fig. 5 as the (Ca+K) peak is broader than the Cl peak. The relative abundances of most elements in Fig. 4 qualitatively agree with those listed in Ref. 2.

iii) Whole Fish and the Composite (Au, Zn, and Mg)

#### Sample:

The focal plane orientation was adjusted as far as possible for simultaneous kinematic compensation for all elements from C to Pb. To obtain an "in situ" mass and/or energy calibration for the fish sample measurement, an exposure was also made with a composite thin target ( $\sim 20\ \mu\text{g}/\text{cm}^2$  each of Au, Zn, and Mg on Formvar) in place of the fish sample. The spectrum from the composite target is shown in Fig. 5 indicating the peaks from Au, Zn, and Mg in addition to those from the Formvar backing. The energy resolution for the heavy mass peaks is 11 keV (1/2 mm for 22 MeV  $\alpha$ -particles). Of particular interest is the elastic scattering from Zn where the elastically scattered  $\alpha$ -particles from the three even isotopes of Zn ( $^{64}\text{Zn}$  49%,  $^{66}\text{Zn}$  28%,  $^{68}\text{Zn}$  19%) are clearly separated.

The fish spectrum (Fig. 6) shows a fairly strong Hg peak in addition to those from K, Cl, P, Na, O, N, and C. There are also small peaks from Br, Sr, and Ba. The atomic concentration of Hg is estimated to be 0.2 ppm in the original fish specimen. The concentrations for Br and Sr are probably even greater because their scattering cross sections at  $70^\circ$  are 1% of the cross-section for Hg.<sup>3</sup> The light mass peaks are broad because complete kinematic compensation for these peaks could not be achieved because of the physical limitation of orienting the focal plane at the unusual angle required for the above purpose.

The main conclusions of the present work about the elastic scattering technique are as follows:

- i) The chief value of this technique lies in its ability to provide information on all the elements in a sample in one measurement at a suitably chosen angle.
- ii) The technique is particularly well suited for elemental analysis of biological samples (particularly in the areas of microbiology, pollution studies, and the role of heavy elements in the Biosphere).
- iii) Low energy  $\alpha$ -particle scattering offers better kinematic separation and possibly lower inelastic scattering background as compared to protons of the same energy without any loss of efficiency.
- iv) The sensitivity for detecting heavy elements in the presence of a bulk of light elements (e.g. Hg pollution of fish) is very high because of the practically non-existent background for the heavy elements. With the currently available intensities, concentrations of a few isolated heavy elements  $\sim 10^{-7}$ - $10^{-8}$  can be measured in a few tens of minutes. In favorable cases much higher sensitivities are achievable.

#### References

1. H.A. Enge, Nuclear Instr. and Methods 49, 181(1967).

3. R.K. Jolly and H.B. White (Elemental Analysis by Elastic Scattering, Nucl. Instr. and Methods (to be published).

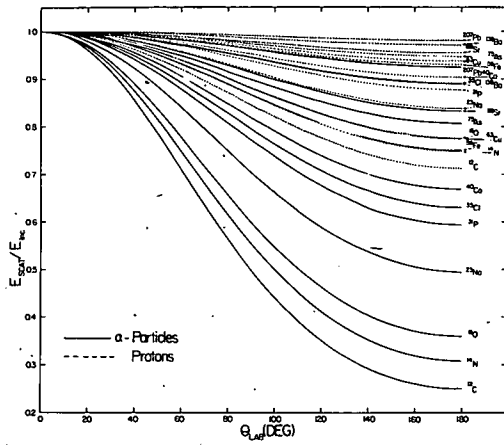


Figure 1

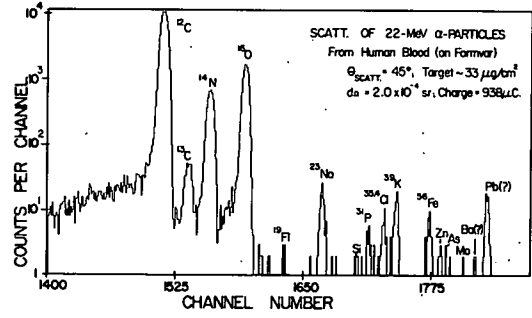


Figure 2

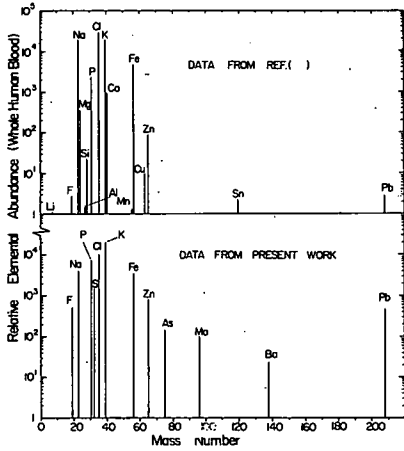


Figure 3

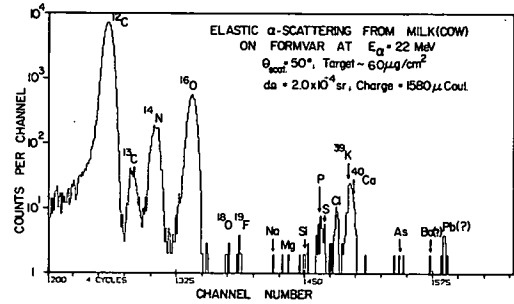


Figure 4

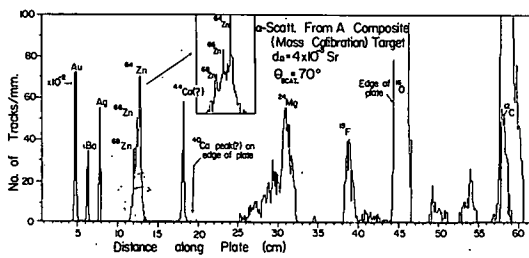


Figure 5

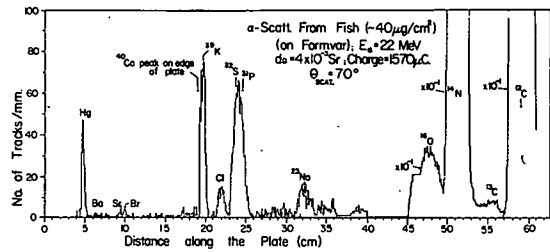


Figure 6



## New Computer Program for Field Trimming Calculations

M.M. Gordon and D.A. Johnson

A sector-focused cyclotron requires an efficient system for determining the multitude of "knob settings" necessary to produce a specific ion beam with a given energy. The MSU Cyclotron has been operating quite successfully for a long time with the use of a computer program "Set-Op" which provides these knob settings as output.<sup>1</sup> In order to achieve certain operational improvements, it was recently decided to rewrite the main part of this program which calculates the eight trim coil currents and the rf frequency. As a result, we have developed a completely new field trimming program "Fielder" which can determine the optimum values of these parameters under a wide variety of conditions.

Instead of trying to match the measured trim coil fields to a predetermined "ideal field", the Fielder program adjusts the parameters so as to obtain a least-square fit to a prescribed phase-energy curve  $\phi(E)$  for the central ray trajectory. Since  $\phi(E)=0$  corresponds to perfect isochronism, this prescription is usually employed, although the program is not limited to this choice. The program will accept as input any reasonable value for the initial phase  $\phi_0 = \phi(E=0)$ , and will automatically incorporate this choice into the fitting process. In the Set-Op program this quantity has the fixed value  $\phi_0=20^\circ$ , and while this choice has proved generally satisfactory, there is some recent evidence which indicates that a larger value may obtain in certain cases.

The least-square fitting routine in the new program contains a provision for imposing a set of linear constraints on the adjusted parameters within the fitting process. Several different types of constraints are available, some of which are always imposed, while others are optional. One optional constraint, for example, requires the  $\phi(E)$  curve to pass through a specified point. The number and type of constraints which are employed will differ from case to case depending on the circumstances.

For a separated turn cyclotron such as ours, a spread in initial phase  $\Delta\phi_0$  within the beam will produce a spread in final energy values  $\Delta E_f$ , and this energy spread must be minimized for optimum performance. The Fielder program carries out this minimization simply by imposing a suitable constraint within the fitting process. In the Set-Op program, however, this minimization was accomplished by an adjustment of the rf frequency after the completion of the field fitting, and this procedure sometimes yields an undesirable overall slope in the  $\phi(E)$  curve. The method used in the new program eliminates this difficulty entirely.

Small fluctuations in the magnetic field level (or rf frequency) will produce corresponding fluctuations in the final energy of the beam. By imposing another type of constraint on the fitting process, the Fielder program can also minimize this effect. (This capability is not available in the Set-Op program.) As a result of this minimization, and the one described above, the new program will produce a non-isochronous field with a resultant  $\phi(E)$  curve which possesses two very important properties of a perfectly isochronous field operating with  $\phi_0=0$ .

It is sometimes desirable to use the trim coils to produce a small change in the axial or radial focusing frequency,  $\nu_z$  or  $\nu_r$ , at certain energies. For example, if an isochronous field were to be employed for proton energies above 40 MeV, then the value of  $\nu_z$  would be too low (or even imaginary) in the energy region from 0.8 to 0.9 of the final energy. This difficulty was circumvented in the Set-Op program by use of a non-isochronous "ideal field" which provides adequate focusing together with tolerable phase excursions, but which required a rather tedious empirical process for its determination. The Fielder program handles this problem by providing an appropriate constraint within the fitting process whereby the value of  $\nu_z$  can be fixed to a specified value for a particular energy. This type of constraint can also be used to adjust the value of  $\nu_r$ . The cyclotron makes use of the  $\nu_r=1$  resonance to facilitate beam extraction, and a small  $\nu_r$  adjustment is sometimes needed in order to properly position this resonance.

The Fielder program operates in a cycle. In order to check the set of trim coil currents and rf frequency derived from the fitting process, the program calculates equilibrium orbit data (including focusing frequencies) for the resultant magnetic field, and then integrates the longitudinal motion equations to obtain the actual  $\phi(E)$  curve for this field and the given frequency. The program then uses these data to improve the fitting process. The entire cycle can be repeated as often as necessary to achieve convergence, although a single iteration has so far proved satisfactory. After examining the final data, the program user can alter the constraints as he sees fit and then extend the iteration process still further. In this way, the user can determine empirically the specific set of constraints which yield the optimum results under given operational conditions.

<sup>1</sup>R.E. Berg, MSUCP-24 (MSU, East Lansing, 1966).

Successful third harmonic operation (where the rf frequency is three times the orbital frequency) is essential for producing the most important heavy ion beams, as well as low energy protons and deuterons. Previous studies have clearly shown that third harmonic operation will be hampered by difficulties in obtaining well centered orbits. Since interest in heavy ion beams has increased substantially, it was decided that an intensive effort should be made to overcome these difficulties.

Well centered orbits are highly desirable since they avoid possible troubles with certain resonances, and since they generally improve the performance of the cyclotron. Accelerated orbits are driven off center by the electric gap crossing resonance which results from the interaction of the three sector magnet geometry with the two sector electric gap geometry. Moreover, when the orbits are off center, the resultant phase deviations produce an asymmetry in the gap voltages which tends to drive the orbits still further off center. Since this latter effect increases with harmonic number, the orbit centering problem will be most severe under third harmonic operational conditions.

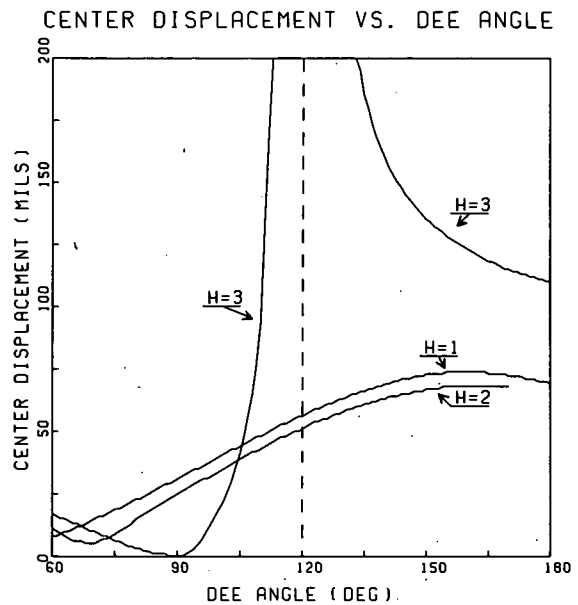
Orbit centering problems can be studied most easily with the use of a computer program "Disport" which calculates the displacement of the instantaneous equilibrium orbit resulting from the acceleration process.<sup>1</sup> Comparing the results obtained under typical first, second, and third harmonic operational conditions with our present dee geometry, we find that the third harmonic orbit center displacements are much larger in magnitude at all energies. In addition, these displacements make rather rapid changes in direction, which are quite contrary to the slow variations found for the lower harmonics. These studies verify that well centered orbits will be difficult to achieve under third harmonic operational conditions, at least for the present dee geometry.

In searching for a means to overcome this difficulty, it was decided to investigate the effect of reducing the dee angle from its present 138° down to 90°. When this change is simulated within the Disport program, the output reveals remarkably small center displacements for the accelerated orbits at all energies. This quite beneficial result can be attributed to the fact that when the electric gaps are all 90° apart, the resultant electric field then possesses fourfold rather than twofold symmetry.

In order to confirm this solution to the orbit centering problem, results were obtained from the Disport program for all dee angles from 60° to 180°. Part of these results are shown in

the figure below where the magnitude of the orbit center displacement (in mils.) is plotted against dee angle (in degrees) for one particular energy. The first harmonic curve (h=1) corresponds to 18 MeV protons, the second harmonic curve (h=2) to 9 MeV deuterons, and the third harmonic curve (h=3) to 24 MeV C<sup>4+</sup> ions; in each case, this energy is just one-half the final energy of the ions at extraction. All three curves represent an energy gain per turn  $\Delta E = E/60$  at the given energy E, and the dee voltage is adjusted to make  $\Delta E$  constant independent of dee angle. Under these conditions, the dee voltage would become infinite for h=3 when the dee angle approaches 120°, and also for h=2 when the dee angle approaches 180°; consequently, the corresponding two curves misbehave at these angles. Similar sets of curves obtained for different values of  $\Delta E$  or of E indicate that the displacements are roughly proportional to  $(\Delta E)/E$  at most energies. From the results of these studies it can be concluded that for three sector cyclotrons such as ours, the use of 90° dees will effectively eliminate orbit centering problems.

<sup>1</sup>M.M. Gordon, IEEE. Trans. Nuc. Sci. NS-13(4), 48(1966).



The phase of a beam packet  $\phi$  relative to the RF phase of a cyclotron is adequately described by the equation

$$V(\sin\phi - \sin\phi_0) = 2\pi[w_{rf} \int_0^E \frac{m(E)dE}{qB(r(E))} - E]$$

- where  $V$  = Peak RF voltage;
- $w_{rf}$  = RF frequency (radians/sec);
- $m(E)$  = Particle mass at energy  $E$ ;
- $q$  = Particle charge;
- $B$  = Magnetic field at particle radius  $r$ , which is in turn a function of  $E$ ;
- $\phi_0$  = Initial phase of beam packet.

Note that  $V$  appears as a gain factor when  $(\sin\phi - \sin\phi_0)$  makes small excursions about zero, and may, therefore, be considered unimportant if beam phase is to be stabilized by a device which holds  $(\sin\phi - \sin\phi_0)$  close to zero. Note that a small change in  $B$  the magnetic field is the only term on the right hand side which could cause a small phase change in a given mode of operation, since  $w_{rf}$  is orders of magnitude more stable than  $B$ . With this in mind, two devices for sensing beam phase are being tested. One device uses a photomultiplier to observe protons elastically scattered from a 100  $\mu\text{g}/\text{cm}^2$  carbon target which is mounted in the beam line external to the cyclotron. Timing pulses from the photomultiplier are compared in a time-to-amplitude converter (TAC) with the zero crossings of the RF. Thus far timing resolutions of 150 ps have been achieved. The significance of this number is revealed by noting that for 30 MeV protons a 100 ps change in phase represents a 5 ppm change in the Magnetic Field. The second device is a capacitive non-interfering probe. This probe has not yet been made insensitive to RF signals in the beam pipe, but if it can be made so, it would supply a simpler device than the photomultiplier.

Stabilization has been successfully achieved by electronic equipment which senses the beam phase indicated by the TAC output and generates an analog signal which can be fed into the Main Magnet regulator.

The stabilization scheme is illustrated in Fig. 1. The up/down counter together with the digital-to-analog converter insure a phase error signal

$$E_\phi = K \sum_{t=0}^t (W_1 - W_2),$$

that is the error signal is proportional to the difference between the number of TAC pulses which fall in window number 1 and those which fall in window number 2.

Figure 2 shows a typical spectrum measured by applying the TAC output to a multichannel analyzer.

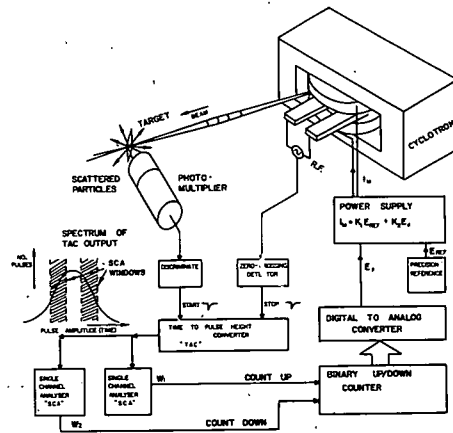


Figure 1

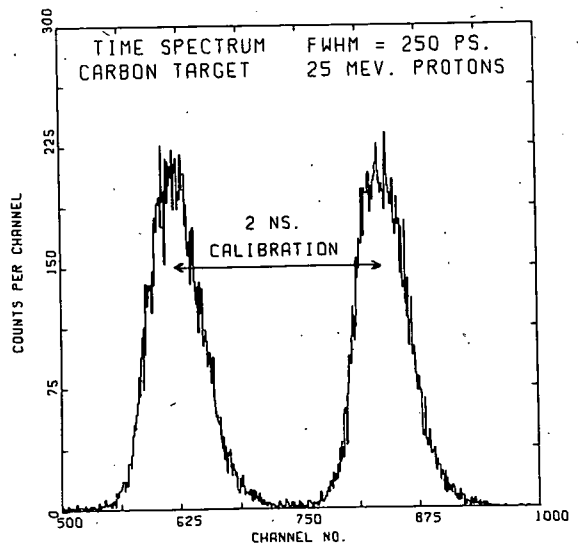


Figure 2

Abstract

A new servo control system, which allows computer as well as manual setup of the RF-system of the MSU Cyclotron has been built and tested. It features automatic switching to phase detectors when the desired positions are reached, in order to fine-tune the system if the RF drive goes on.

I. Introduction

The new RF-servo system allows simultaneous setup, either from thumbweelswitches on the console of the Cyclotron or from a computer.

Since the system contains seven tunable elements, this saves a considerable amount of time, since the old system required the operator to set each element to the desired position by a manual control switch. The operator no longer is required to pay any attention to the tuning process, though it still could be done manual if so desired. Separate two-speed clocks for each servo allow a high setting speed and a matched low speed for tuning from phase detectors or position indicators. The RF system has been described previously.<sup>1,2</sup>

The entire design of the control electronics is modular; the basic units are printed circuit boards which can be used in all servo loops. Since all threshold and speed adjustments are on front panels, modules of the same type can be exchanged without requiring recalibration. The basic units (PC-boards) are compatible with commercially available modules which allows us to use some XDS T-series modules and directly interface into our XDS Sigma-7 computer. Integrated circuits in dual in line packages are used throughout, diode-transistor-micrologic (DT $\mu$ L) for logical functions and microamplifiers ( $\mu$ A), for operational amplifiers and fast discriminators. For analog and signal switching, DT $\mu$ L-compatible miniature relays are used.

II. Description of the System

Figure 1 shows the seven different servo control loops. Some loops are in the same circuit, hence not operating independent. The DC stepping motors are controlled the following way:

Automatic setup (computer setup)

The program for setup checks whether the RF voltage is off and the servos operable, then five positions (12 bits BCD) are transferred into Digital-to-Analog Converters and strobed. Input buffers allow parallel setting, and when the devices have reached their appropriate positions, the system automatically switches over to phase detectors for fine tuning and flags this to the computer as well as to the operator.

Manual Setup

Thumbweelswitches on the main console allow setting of three decimal digits according to a run-sheet. Pushing a "manual set" button then

sets up the same way as the automatic setup, however, this does not require an operable computer.

Furthermore, using a manual control switch which overrides all other signals (except limits) one can position the devices by hand and read their positions on a Digital Voltmeter (DVM).

III. Description of a Typical Servo Loop

Figure 2 shows a block diagram of a typical servo loop. As mentioned above, setting can be done three different ways:

- 1) Computer
- 2) Thumbweelswitches on Console
- 3) Manual direction control switch on Console

The method to implement this is described now.

The manually controllable multiplexer switches inputs between computer and thumbweelswitch. The output of the multiplexer is fed into a Digital-to-Analog Converter (DAC) which has an output accuracy of  $\approx 0.01\%$  F.S.,  $\pm \frac{1}{2}$  LSB. Strobing (transfer of input register into output) of the DAC can only be done while RF voltage is off. This prevents erroneous detuning while the Cyclotron is operating.

The output of the DAC is the reference voltage in an analog feedback loop and is compared with a voltage proportional to the position of the tuning element.

An absolute value of the amplified error-signal is then used to determine "how far away" the real position is from the desired position and, if sufficiently small, switches the clock to low speed for fine tuning. An even smaller threshold is used to determine when the error signal is approximately zero and the input source control then switches on the phase detector and indicates this to the computer.

As soon as the computer has the confirmation that all servos are properly set, it can initiate the RF voltage control program, which turns on the RF drive and brings the RF voltage up to the desired value. Two voltage comparators (Zero Detector) then are used to determine the required sense of rotation of the stepping motor. The subsequent encoder and control unit transforms this information into pulse trains suitable for stepping motors. The encoder and control unit also contains lamp drivers for motion and limit indication lights on the main console. Furthermore, there are move and limit indication outputs available, as well as compatible inputs. With these, one system can be interconnected in a way as to inhibit another one while it is tuning. Or there occurs another case; if one servo (with a narrow tuning range) reaches a limit it starts another servo (with a wide tuning range) to move such that the first servo gets back within its tuning range. (Course and fine tuning, for example).

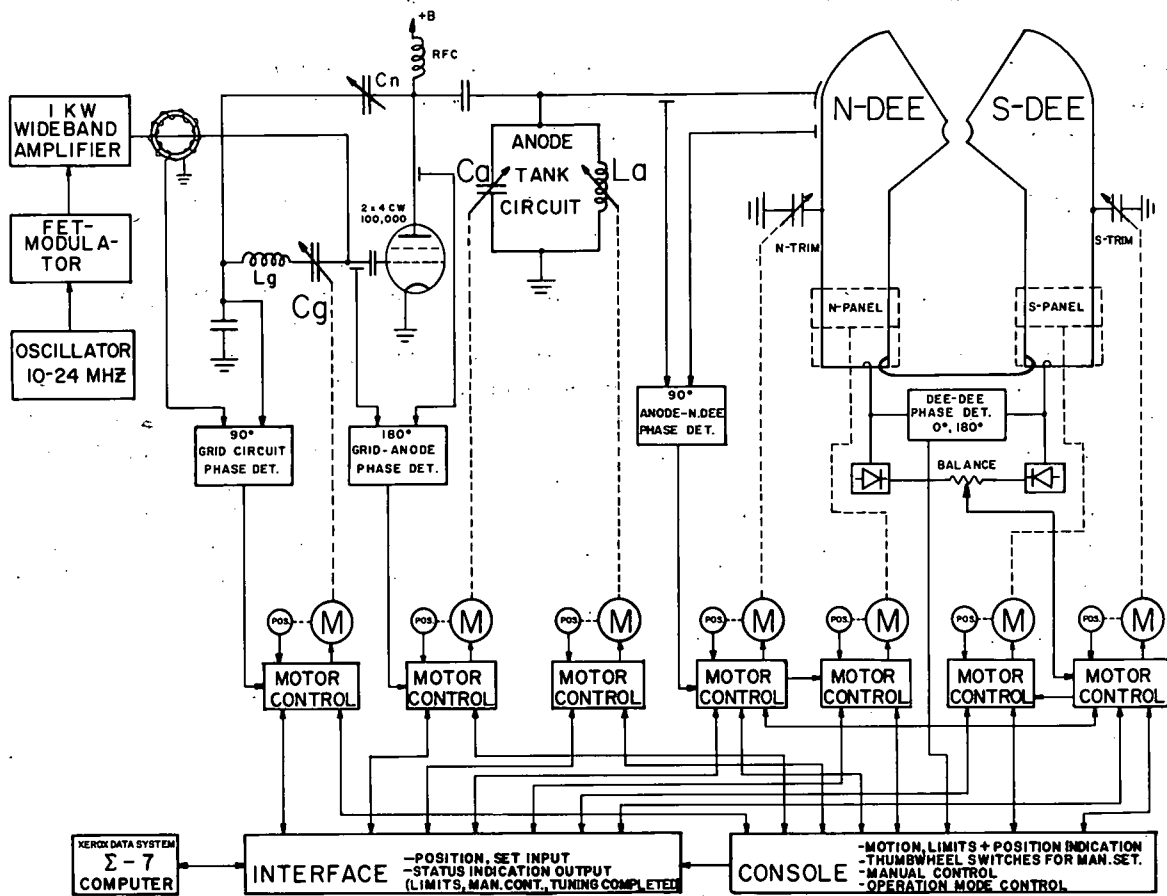


Figure 1

This shows why adjustable, independent tuning speeds are essential, because the two tuning speeds of two servo loops have to be adjusted such that the system always stays tuned during such a process.

References

1. W.P. Johnson, CERN Report 63-19, 279-285(1963).
2. W.P. Johnson, P. Sigg, IEEE Trans. on Nucl. Science, Vol. NS-16 #3 (1969).

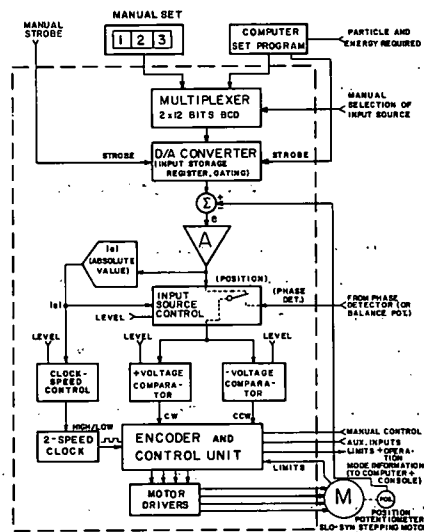


Figure 2.

The computer system is a unified data acquisition, analysis and control service unit. To improve and extend these services four major hardware and three software additions have been made, giving a marked improvement in the data analysis and acquisition areas. Each addition produced multiple improvements and, therefore, will be discussed in that context.

The addition of 16 words of CPU main core storage produced two results:

- (1) The data acquisition area was increased to double the number of data collection routines running concurrently.
- (2) The calculation overhead for large data analysis routines was reduced by a factor of ten and an increase in the number of concurrent routines was obtained.

A large (30"), high accuracy (.005") plotter was added to the computer system to reduce the backlog of plots and the resulting data analysis, acquisition conflicts caused by a single slow device. This produced the additional benefit of producing publication quality plots directly and thereby reducing the drafting load.

A small peripheral computer was acquired to perform four functions:

- (1) To relieve the main computer of the real-time scope display function and thereby gain about 10-20% in computational speed.
- (2) Provide for multi-low-cost remote interactive terminate stations for on-line data analysis via user FORTRAN routines. One of these terminals is to be used at the cyclotron console for machine control.
- (3) As a backup system to provide essential data acquisition and control functions (complex data analysis being lost) in the event of main computer failure.

The addition of a 25 mega-character diskpack storage unit was done for the following system improvements.

- (1) To provide user program storage for use during remote operation.
- (2) As data storage for faster analysis.
- (3) For raw data storage of multi-dimensional mega-channel analysers.
- (4) As a backup device to hold output for any device temporarily overloaded or inoperative.
- (5) To extend user file storage during stepwise computational runs.
- (6) And as a high speed "tape" unit to increase data search speed by about ten times.

The new software routines include a task for close-loop stabilization of the spectragraph and a task for high speed sequentially ordered data acquisition. A library of 500 FORTRAN scientific and numerical routines has been tested and are

available on-line. A number of new compilers have been added for users which include:

- (1) An extended FORTRAN to optimize code generation for increased execution efficiency.
- (2) A fast FORTRAN for quick compile and execution during the debugging process.
- (3) And additional compilers of SNOBOL, LISP, and BASIC to provide the remote user editing function, literature searches and report writing.

In summary the computer system has increased its data analysis service capacity by an order of magnitude by the addition of devices and software. The data acquisition service was doubled by the addition of core storage and extended into mega-channel analysers with the device additions. The system has proved it is capable of closed-loop control upon cyclotron equipment via the spectragraph.

In our program to measure proton induced spallation of the elements  $^{12}\text{C}$ ,  $^{14}\text{N}$ ,  $^{16}\text{O}$ , and  $^{20}\text{Ne}$  we were lead to consider gas targets for all except  $^{12}\text{C}$ . Usually the gas is confined in a gas cell which employs a foil or "window" through which the beam enters and reaction products leave to be detected outside the cell. A common foil used for gas cells is 1/2 mil thick Kapton. For the relatively heavy, low energy, reaction products to be detected in the spallation experiments this still implies a large and unacceptable energy loss. The gas cell described here permits exit particle areal densities in the range of 50-130  $\mu\text{g}/\text{cm}^2$ . The gas cell is shown in Fig. 1. The cell body is made of brass. The unique aspect of the cell is the shell sliding in the keyway. The shell end closest to the beam serves as defining slit and exit beam window support. The front end is tapered to allow close approach to the beam at forward angles. The geometry of the shell and its vacuum seal determine the minimum detection angle.

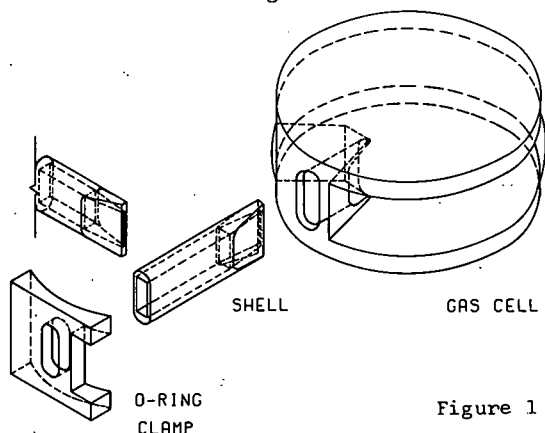


Figure 1

The angular range accessible with the cell is  $10^\circ$  to  $170^\circ$  provided the rotating table has a range of  $360^\circ$ .

The entrance beam window is 1/2 mil Kapton bonded to the cell structure with epoxy Ciba Araldite 502. For the exit beam window we selected formvar. The slit end of the shell is buffed so the lips of the slit are rounded and no sharp edges remain. A 2% solution of formvar in 1,2 Dichloroethane is prepared and films are produced by casting on water.<sup>2</sup> The film is picked up with a wire loop and transferred immediately to the shell. This is repeated until a formvar window of the desired thickness is build up. A 30  $\mu\text{g}/\text{cm}^2$  formvar window over a 40 mil slit sustains a pressure of 25 torr for many hours.

Reaction products lose energy not only in the formvar window but also in the gas they have to traverse. Depending on the detection angle the shell is positioned to minimize the gas traversed. For example for the nitrogen pressure, slit width, and formvar window mentioned above the average

total exit areal density can be  $\approx 50 \mu\text{g}/\text{cm}^2$  at  $90^\circ$  and  $\approx 130 \mu\text{g}/\text{cm}^2$  at  $15^\circ$  detection angle.

In our application we wanted to avoid repeated mechanical adjustments of the shell, but still wanted to minimize energy loss in the gas. We simply mounted the gas cell and slit system slightly off center on the scattering chamber table. As shown in Fig. 2 table rotations between  $15^\circ$  (or  $165^\circ$ ) and  $90^\circ$  can be carried out with one shell setting. The distance between the beam and the closest point of the shell is about constant and as a result a minimum in gas flight distance is achieved at all angles in this range.

In the present design the gas cell stays fixed with respect to the detector. This limits the incident beam intensity to about 1  $\mu\text{a}$  for protons since the cell cannot be vibrated to spread the beam over an effectively larger area of Kapton.

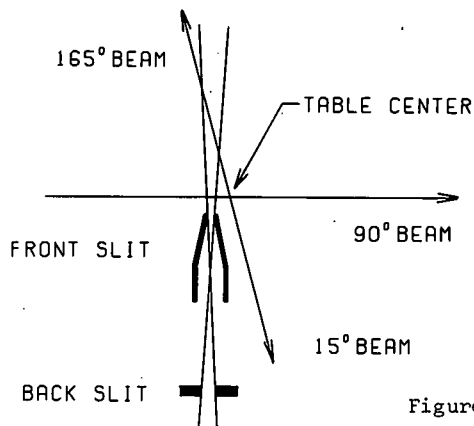


Figure 2

While in our experiment we were only interested in minimizing energy loss, the cell should be well adapted to yield good resolution energy spectra for heavier particles. The data in Table 1 was taken at  $15^\circ$  detection angle. The resolution of the detector for a 5.48 MeV calibration  $\alpha$  peak was  $\approx 35$  keV FWHM.

Table 1. Energy Resolution for Various Particles

Peak Energy in MeV	Particle	Resolution FWHM in keV
	$^{16}\text{O}+p$	
	$E_p = 42 \text{ MeV}$	
18.0	$^6\text{Li}$	50
14.9	$^7\text{Be}$	80
11.8	$^{14}\text{N}$	140
8.9	$^{16}\text{O}$	380

## References

1. Cary N. Davids, Helmut Laumer, and Sam M. Austin, Phys. Rev. **C1**, 270(1970).  
Also see topics on spallation in this report.
2. L. Yaffe, Ann. Rev. of Nucl. Sci., Vol. 12, 153(1962).

The cross-sections obtained by integrating the angular distributions are summarized in Fig. 3. The point at 17 MeV was obtained by degrading the 22 MeV beam with a thin aluminum plate.

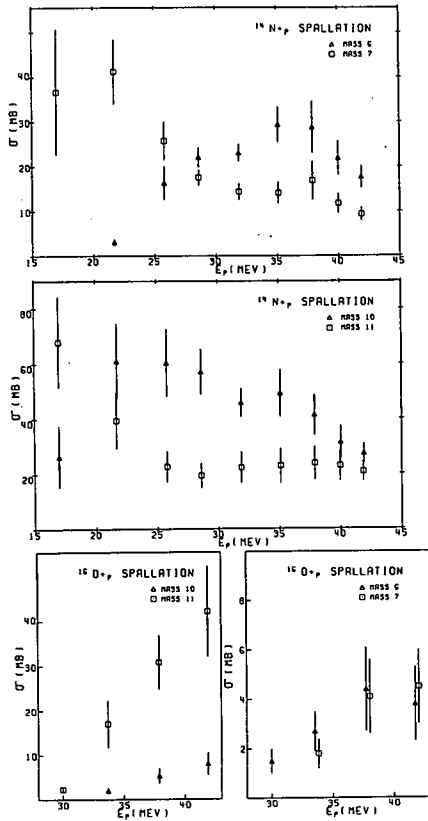


Figure 3

At 21.9 MeV the only mass-11 produced from  $^{14}\text{N}+p$  is  $^{11}\text{C}$  and the only mass-7 produced is  $^7\text{Be}$ . To check the reliability of our time-of-flight technique we performed an activation experiment to measure  $^{11}\text{C}$  and  $^7\text{Be}$  production. We counted .511 MeV  $\gamma$  rays from the  $\beta^+$  annihilation from  $^{11}\text{C}$  decay (half-life 20.5 min) and .4796 MeV  $\gamma$  rays (from the state in  $^7\text{Li}$  fed 10% of the time by the  $^7\text{Be}$  decay) with a Ge(Li) detector. Absolute detector efficiency was determined with a National Bureau of Standards 5% standard  $^{22}\text{Na}$  source. The  $^{11}\text{C}$  cross-section found is  $36 \pm 4$  mb; the  $^7\text{Be}$  cross-section is  $49 \pm 3.5$  mb. These numbers compare favorably with our other values  $39.5 \pm 10$  mb for  $^{11}\text{C}$  and  $41.2 \pm 7.2$  for  $^7\text{Be}$ . They also agree with recently published cross sections by Epherre et al.<sup>4</sup>

Various theories for the origin of the light elements have been developed. None of them are entirely satisfactory. A reliable calculation of the net contribution of various light element production mechanisms is at present not possible. A very interesting type of calculation with a better chance of yielding information is concerned with the precise and constant isotopic ratios  $^7\text{Li}/^6\text{Li}=12.5$  and  $^{11}\text{B}/^{10}\text{B}=4$  for earth and meteorite samples. We assume a source of protons with an energy spectrum

of the form  $E^{-\gamma}$  irradiating an isotopic mixture in the proportion C:N:O=3:1:5. Using all available cross-section data we perform the integration

$$I_{ij} = \int_{E_{\text{threshold}}}^{\infty} E^{-\gamma} \sigma_{ij}(E) dE; \text{ where } \sigma_{ij}(E) \text{ is the}$$

production cross-section of mass  $i$  from target nucleus  $j$  at proton energy  $E$ . Hence  $^7\text{Li}/^6\text{Li} = \frac{\sum I_{7j} n_j}{\sum I_{6j} n_j}$ ; where  $n_j$  is the relative abundance of the  $j$ th target nucleus quoted above.

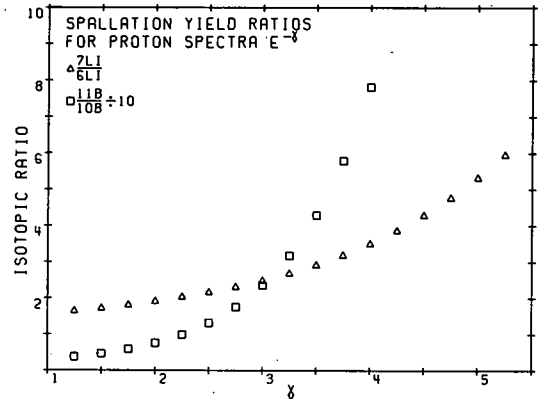


Figure 4

In Fig. 4 isotopic ratios are plotted as a function of  $\gamma$  for the region applicable to solar flare spectra. The  $^7\text{Li}/^6\text{Li}$  ratio is far below 12.5 over the range of  $\gamma$  considered.  $^{11}\text{B}/^{10}\text{B}=4$  only near  $\gamma=1.5$ ; and the ratio rises sharply for higher values of  $\gamma$ . This last result puts in doubt a theory by Fowler et al.<sup>5</sup> where the  $^{11}\text{B}/^{10}\text{B}$  ratio was assumed to be 1; and  $^{10}\text{B}$  depletion by a neutron flux was considered. From the low  $^7\text{Li}/^6\text{Li}$  ratio one may suspect that either there is a source of  $^7\text{Li}$  not due to proton spallation (big bang nucleosynthesis,<sup>6</sup> or  $\alpha\alpha$  in galactic cosmic rays<sup>7</sup>) or a  $^6\text{Li}$  preferential depletion mechanism is involved. The fact that  $^{11}\text{B}/^{10}\text{B}$  is only 4 may indicate a proton spectrum cutoff as inferred by Fowler<sup>7</sup> in his new theory of light element production by galactic cosmic rays. A mechanism to deplete  $^{11}\text{B}$  and  $^6\text{Li}$  simultaneously is not known.

#### References

1. Cary N. Davids, Helmut Laumer, and Sam M. Austin, Phys. Rev. C1, 270(1970).
2. Douglas L. Bayer, MSUCL-34 (MSU, East Lansing, Michigan, 1971).
3. R.M. Sternheimer, Methods of Experimental Physics, 5 Part B, Appendix 2.
4. E. Epherre and C. Seide, Phys. Rev. C3, 2167(1971).
5. W.A. Fowler, J.L. Greenstein, F. Hoyle, Geophys. JRAS 6, 148(1962).
6. R.V. Wagoner, W.A. Fowler, F. Hoyle, Ap. J. 148, 3(1967).
7. H. Reeves, W.A. Fowler, F. Hoyle, Nat. 226, 727(1970).



Preparation of Thin Film Deposits  
From Biological, Environmental and Other Matter  
R.K. Jolly and H.B. White

In the elemental analysis of materials employing nuclear reaction and scattering techniques,<sup>1,2,3</sup> it is necessary to prepare the sample in the form of a thin film (10-1000  $\mu\text{g}/\text{cm}^2$ ). Below we describe a technique that enables one to prepare thin film deposits from such diverse materials as mineral and rock samples, animal tissue, blood and soluble salts using relatively inexpensive equipment. In certain materials like a whole fish, the uniformity of the deposit depends on the uniformity and size of the particles in the colloidal suspension that is prepared.

Any material to be deposited must be first reduced to a solution or a suspension of microscopic particles (1-10  $\mu$ ) in an inert solvent. Table I gives a listing of the techniques used by the authors towards accomplishing this objective. The suspended or the dissolved material is placed in the container shown in the apparatus (called a Nebulizer<sup>5</sup>) in Fig. 1. The compressed gas (preferably inert) forces the liquid through a small hole in the form of a high speed spray which in turn impinges on an obstruction and thus breaks up into droplets of various sizes. The finest of these droplets are swept along by the gas escaping out of the nozzle. These droplets are so fine that they are not visible to the unaided eye. Illuminating the mouth of the nozzle reveals a cloudy mist but the individual droplets are still not seen. The nebulized mist is then allowed to deposit on a rotating substrate. By mounting the nebulizer bottle on a stand that performs a slow up and down (or sideways) oscillatory motion such that all parts of the substrate receive the mist for the same length of time, a very uniform deposit can be obtained. The microscopic size of these droplets is important for two reasons: i) The droplets evaporate immediately so that one does not get any streams of running fluid on the substrate and ii) Any one droplet brings such a small quantity of the suspended or dissolved matter with it that with a reasonably prolonged (30 minutes) period of deposition, a uniform layer of the dissolved or suspended matter is obtained. The heating coil in the figure is to inhibit condensation of the mist in the nozzle thus ensuring an unobstructed flow of the mist.

A microphotograph of the deposit from a sonicated whole fish (some skin removed) prepared in accordance with the procedure outlined in Table I is shown in Fig. 2. Particles of all sizes up to 5  $\mu$  are seen with the majority in the range of 0.2-2  $\mu$ . The larger particles are probably bone fragments and can perhaps be further broken down by using ultrasound of higher frequency and intensity or else eliminated by using a microfilter.

Examples of the use of thin (30-60  $\mu\text{g}/\text{cm}^2$ ) whole fish, blood and milk deposits on formvar in 22 MeV  $\alpha$ -particle scattering measurements are presented in another section by the authors.

REFERENCES

1. B.L. Cohen and R.A. Moyer, *Analytical Chem.* **43**, 123(1971).
2. R.K. Jolly, C.R. Gruhn, and C. Maggiore, *IEEE*, Vol. **NS-18**, No.1 p. 91(1971).
3. R.K. Jolly and H.B. White (Nuclear Inst. and Methods. To be published).
4. For example one marketed by McCrone Research Associates Ltd. 2 McCone Mews, LONDON NW3.
5. For example Nebulizer 180 commercially marketed by DeVilbiss Company of Somerset Pa

TABLE I

Reduction of Biological, Environmental and Other Matter to a Solution or Colloidal Suspension

Class of Materials	Technique for Reduction
I. <u>Animal Tissue, Plants etc.</u>	Slow freezing to rupture the cells followed by i) reduction to a liquidized form by a high speed blender (e.g. Waring Scientific Blender. 15,000 rpm model.) and ii) immersion of an ultrasonic probe in the liquidized sample for several minutes (length depending on the quantity and type of material).
II. <u>Blood, Milk etc.</u>	Sonication with an ultrasonic probe if necessary to break up the individual cells (25-50 $\mu$ ). In some applications (proton scattering, x-ray fluorescence) these substances may be deposited without any sonication.
III. <u>Rock, Dry Wood etc.</u>	Grinding in a tungsten carbide mortar and presle or a micro-nising mill <sup>b</sup> and subjecting a paste of the material to sonication (with an ultrasonic source) if necessary.
IV. <u>Beverages and Soluble Materials, etc.</u>	May be simply dissolved or diluted in pure water before deposition.

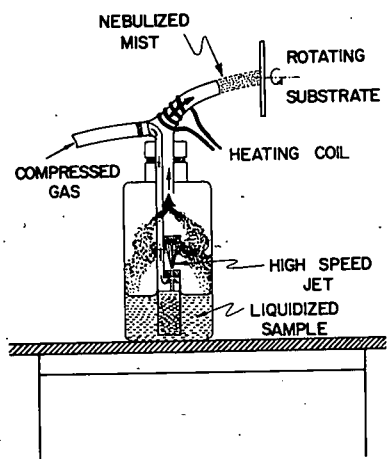


Figure 1

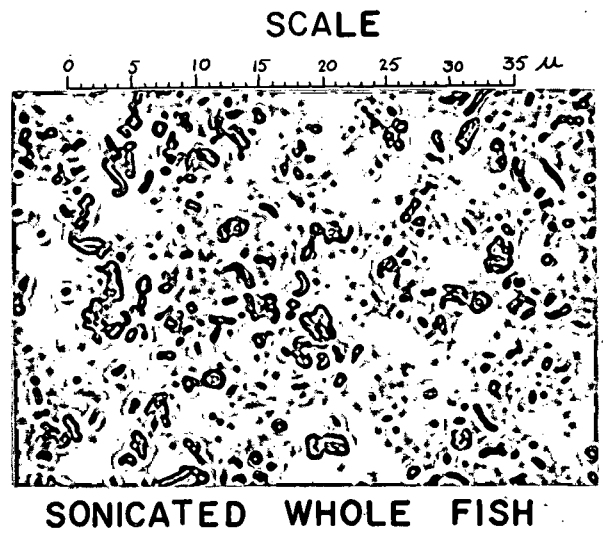


Figure 2

Section II

Abstracts of Talks at Meetings

July 1970-June 1971

American Phys. Soc. Houston Meeting, Oct. 1970

The Effects of Compton Scattering on Ge(Li)-Ge(Li) Coincidence Experiments.\* G.C. GIESLER, R.A. WARNER, W.C. MCHARRIS, and W.H. Kelly, Mich. State Univ.—In  $\gamma$ - $\gamma$  coincidence spectrometry, Compton scattering can become a nuisance by increasing the number of unwanted coincidence events and generally obscuring the weaker peaks. When gate and photopeak widths approach each other, "artificial photopeaks" can be generated. This was recognized as a serious limitation with NaI(Tl)-NaI(Tl) spectrometers. With Ge(Li)-NaI(Tl) coincidence system these "artificial peaks" are very broad and are not so serious because of the poor resolution of the scintillation detector. With the advent of large Ge(Li) detectors and Ge(Li)-Ge(Li) coincident spectrometers coming into general use, the presence of these artificial photopeaks can lead to the reporting of false transitions. We describe the results of a study of the effects of Compton scattering and narrow gates and methods that can be used to suppress these unwanted additions to the coincidence spectrum.

\*Work supported by the National Science Foundation and the U.S. Atomic Energy Commission.

American Phys. Soc. Houston Meeting, Oct. 1970

The Sum-Coincidence Method Applied to the Evaluation of Ge(Li)-Ge(Li) Coincidence Results.\* G.C. GIESLER, K.L. KOSANKE, R.A. WARNER, W.C. MCHARRIS, and W.H. KELLY, Mich. State Univ.—In 1958, Hoogenboom proposed a new method of measuring  $\gamma$ - $\gamma$  coincidence events. His "sum coincidence" method involves adding the coincidence signals from two NaI(Tl) detectors, then gating on this sum peak and looking at the output from one of the detectors. It reduces the Compton background in the displayed spectrum and improves the resolution of the peaks. With the advent of large Ge(Li) detectors and Ge(Li)-Ge(Li) multiparameter coincidence spectrometers, this method may be useful in unraveling complex decay schemes. We have applied this technique to the studies of the decay schemes of  $^{63}\text{Zn}$  and  $^{208}\text{Bi}$ . We will present some of the results obtained and will discuss the advantages and limitations of the sum coincidence method as compared to a conventional 2-dimensional megachannel coincidence system.

\*Work supported by the National Science Foundation and the U.S. Atomic Energy Commission.

<sup>1</sup>A.M. Hoogenboom, Nucl. Instr. and Methods 3, 57(1958).

American Phys. Soc. Houston Meeting, Oct. 1970

Energy of the Second Excited State of  $^{12}\text{C}$  and the  $3\alpha$  Reaction Rate.\* S.M. AUSTIN, Mich. State Univ. and the Niels Bohr Inst., G.F. TRENTLMAN and E. KASHY, Mich. State Univ.—The rate for the  $3\alpha$  reaction in helium burning stars depends critically on the excitation energy  $E_x$  of the second excited state of  $^{12}\text{C}$  near 7.6 MeV. We have measured  $E_x$  with an uncertainty of  $\pm 2.1$  keV to resolve an inconsistency in earlier results. In the present measurements,  $E_x$  was obtained by comparing the momentum of protons from the  $^{12}\text{C}(p,p')^{12}\text{C}(E_x, 7.6 \text{ MeV})$  reaction with the momenta of protons inelastically scattered from states of well known energy in  $^{12}\text{C}$  and  $^{16}\text{O}$ . We find  $E_x = 7.6562 \pm 0.0021$  MeV. This value of  $E_x$  leads to a change by a factor of  $\exp[-11.9/(86.17T_9)]$  of the  $3\alpha$  reaction rate of Fowler, Caughlan and Zimmerman. Implications for nucleosynthesis in helium burning stars will be discussed.

\*Research supported by the National Science Foundation.

<sup>1</sup>W.A. Fowler, G.R. Caughlan and B.A. Zimmerman, Ann. Review Ast. and Ap. 5, 525(1967).

American Phys. Soc. Houston Meeting, Oct. 1970

Neutron Yields from Proton Bombardment of Thick Targets.\* T. AMOS, A. GALONSKY, and R. JOLLY, Mich. State Univ.—Stopping targets of natural C, Al, Cu, Ta and Pb were bombarded by 30 and 40 MeV protons. The resultant neutron spectra were measured at laboratory angles of 0, 30, 60, 90, 120, and 150 degrees by a .7 nsec/meter neutron time-of-flight spectrometer for neutron energies above 2 MeV. Preliminary analysis of the data indicates the following results for the energy- and angle-integrated yields:

Target	Neutrons/Proton	
	30 MeV	40 MeV
C	.004	.02
Al	.02	.04
Cu	.035	.07
Ta	.02	.07
Pb	.025	.07

Neutron time-of-flight spectra, energy spectra, angular distributions and total yields will be presented and discussed.

\*Work supported by National Science Foundation.

American Phys. Soc. Houston Meeting, Oct. 1970

Ultra-High Resolution Spectrometer System for Charged Particle Studies of Nuclei.\* H.G. BLOSSER, G.M. CRAWLEY, R. deFOREST, E. KASHY, and B.H. WILDENTHAL, Mich. State Univ.—This paper describes an arrangement for introducing feedback into a charged particle magnetic analysis system for nuclear reaction studies. In initial tests of the system, a resolution of 5 keV has been obtained in (p,p') studies at 30 MeV with 70% of the cyclotron internal beam on target. This corresponds to a resolving power  $p/\Delta p$  of 12,000. Essential features of the system, in addition to the feedback, are a careful definition of the cyclotron source by means of internal slits and the use of dispersion matching<sup>1</sup> to cancel the effect of coherent on-target energy spread.

\*Work supported by the National Science Foundation.

<sup>1</sup>B.L. Cohen, Rev. Sci. Instr. 30, 415(1959).

American Phys. Soc. Houston Meeting, Oct. 1970

Proton Spin-Flip in (p,p') Reaction on  $^{120}\text{Sn}$  and  $^{124}\text{Sn}$ .\* R.H. HOWELL, R.R. DOERING, and A. GALONSKY, Mich. State Univ.—The angular distributions for proton spin-flip in the excitation of the first  $2^+$  state in  $^{120}\text{Sn}$  and  $^{124}\text{Sn}$  are being studied at 30 MeV. The technique requires measuring the p- $\gamma$  angular correlation function at 90° from the scattering plane. Coincidence particle-gamma spectra were stored in a live time, two parameter array with the single-particle spectrum stored separately by a computer. Measurements have been made from 30° to 150°. The angular distribution showed a typical shape with small forward-angle values and a peak at back angles. Values ranged from .04 $\pm$ .013 at 30° to .22 $\pm$ .04 at 150° for  $^{120}\text{Sn}$  and from .005 $\pm$ .004 at 30° to .26 $\pm$ .04 at 150° for  $^{124}\text{Sn}$ . These values do not include corrections ranging between -0.1 and -.02 for finite solid angles. The integrated spin-flip probability is (4.3 $\pm$ 1.3)% for  $^{120}\text{Sn}$  and (1.6 $\pm$ 0.8)% for  $^{124}\text{Sn}$ .

\*Supported by the National Science Foundation.

American Phys. Soc. Houston Meeting, Oct. 1970

$^{27}\text{Al}(p,n)^{27}\text{Si}$  at  $E_p=30$  MeV.\* R.K. JOLLY, T. AMOS, A. GALONSKY, and R. ST.ONGE, Mich. State Univ.—Neutron spectra from the  $^{27}\text{Al}(p,n)^{27}\text{Si}$  reaction have been measured using the MSU TOF facility. The ground state transition is observed to be the strongest except at very forward angles ( $<20^\circ$ ). Energy resolution in these measurements was limited to count rate considerations. Angular distribution for the ground state was measured from  $0^\circ$  to  $95^\circ$  and compared with i) DWBA calculations using a real derivative form factor for the t-T interaction ii) simple microscopic calculations (by F. Petrovich) involving charge exchange on a single  $1d_{5/2}$  proton hole in the  $^{28}\text{Si}$  core and using harmonic oscillator wave functions. Agreement of these calculations with the experimental angular distribution is quite good. The question of normalization still remains to be investigated.

\*Supported by the National Science Foundation.

American Phys. Soc. Houston Meeting, Oct. 1970

The Michigan State University Isochronous Cyclotron, Neutron Time-of-Flight Facility.\* R. ST.ONGE, T. AMOS, A. GALONSKY, and R. JOLLY, Mich. State Univ.—A description of the MSU Isochronous Cyclotron neutron time-of-flight facility (TOF) will be given. This will include: the cyclotron's time and energy resolutions, internal cyclotron beam pulser, beam line and dump, scintillation detector, electronic instrumentation, spectrum stabilizer, and the on-line data computer system. The proton beam time resolution is 0.2 ns and a resultant neutron spectrum [ $^{27}\text{Al}(p,n)^{27}\text{Si}$ ] has a time resolution of 0.3 ns and an energy resolution of 200 keV for 26 MeV neutrons. With 2-dimensional n- $\gamma$  pulse shape discrimination we achieve a figure of merit<sup>1</sup> "M" of 5 to 6. The TOF spectrum was stabilized by a zero level ADC stabilizer locked on the target gamma-ray peak.

\*Supported by the National Science Foundation.

<sup>1</sup>Nucl. Instr. & Methods 69, 25(1969).

American Phys. Soc. Houston Meeting, Oct. 1970

Electron Capture Decay Scheme of  $\text{Bi}^{203}$ .\* Wm.C. McHARRIS, J.B. CROSS, and W.H. KELLY, Mich. State Univ.—The  $\epsilon$  decay of 11.7-h  $\text{Bi}^{203}$  has been investigated using high-resolution Ge(Li) spectroscopy. The  $\text{Bi}^{203}$  sources were prepared by the  $\text{Pb}^{206}(p,4n)\text{Bi}^{203}$  reaction, using a 40 MeV proton beam from the MSU Sector-Focused Cyclotron and  $\text{Pb}^{206}$  separated isotope. A total of 147  $\gamma$ -ray were observed. Aided by coincidence and anti-coincidence data, including 2-dimensional Ge(Li)-Ge(Li) megachannel coincidence, we have placed 51  $\gamma$ -rays (accounting for  $>80\%$  of the  $\gamma$ -ray intensity) in a primary decay scheme having 26 levels. A secondary decay scheme with transitions placed solely on the basis of energy sums and weak coincidence data is also proposed. Spin and parity assignments of the nuclear states investigated are made on the basis of relative  $\gamma$  intensities to states of known spin and parity, transition multipolarities (for those transitions where internal conversion-electron intensities were available), and log ft values. A comparison with existing scattering data is presented, and intrinsic structures for some low-lying states will be suggested.

\*Supported in part by the U.S. Atomic Energy Commission and the National Science Foundation.

American Phys. Soc. Houston Meeting, Oct. 1970

Electron Capture Decay Scheme of  $\text{Bi}^{204}$ .\* J.B. CROSS, Wm.C. McHARRIS, and W.H. KELLY, Mich. State Univ.—The  $\epsilon$  decay of 11.2-h  $\text{Bi}^{204}$  has been investigated with high-resolution Ge(Li) detector systems. The  $\text{Bi}^{204}$  sources were prepared by the  $\text{Pb}^{206}(p,3n)\text{Bi}^{204}$  reaction, using a 30 MeV proton beam from the MSU Sector-Focused Cyclotron and  $\text{Pb}^{206}$  separated isotope. A total of 210  $\gamma$ -rays were observed. Utilizing a 2-dimensional megachannel coincidence system, 60  $\gamma$ -rays (accounting for  $>90\%$  of the  $\gamma$ -ray intensity) have been incorporated in a primary decay scheme having 31 states. A secondary decay scheme is proposed;  $\gamma$ -ray transitions in this decay scheme are placed solely on the basis of precise energy sums and weak coincidence data. Limits on spin and parity assignments of the nuclear states investigated are made on the basis of log ft values, relative  $\gamma$  intensities to states of known spin and parity, and transition multipolarities for those transitions where internal conversion-electron intensities were available. A comparison with previously reported scattering reaction data is presented.

\*Work supported in part by the U.S. Atomic Energy Commission and the National Science Foundation.

American Phys. Soc. Houston Meeting, Oct. 1970

The (p,t) Reaction on  $\text{Pr}^{141}$ .\* R.W. GOLES, Wm.C. McHARRIS, W.H. KELLY, and R.A. WARNER, Mich. State Univ.—40 MeV protons accelerated by the Michigan State University Isochronous Cyclotron were used to study this (p,t) reaction. Besides the ground state, 14 states ranging in energy up to 2.5 MeV were observed to be excited in the residual nucleus  $\text{Pr}^{139}$ . Angular distributions were taken between  $15^\circ$  and  $65^\circ$  using a  $\Delta E$ -E semiconductor counter telescope. Particle Identification was performed on-line with an XDS  $\Sigma$ -7 computer. Theoretical angular distributions for this reaction have been calculated using the DWBA code JULIE, and these predictions will be compared to the experimental results. A comparison will be made between the states populated by this reaction and those populated through the  $\beta^+/\epsilon$  decay of  $\text{Nd}^{139m}$  [1]. It is found that the (p,t) reaction on  $\text{Pr}^{141}$  strongly populates collective states of the residual nucleus  $\text{Pr}^{139}$ .

\*Work supported in part by the U.S. National Science Foundation and the U.S. Atomic Energy Commission.

[1] D.B. Beery, W.H. Kelly, and Wm.C. McHarris, Phys. Rev. 188, 1851(1969).

American Phys. Soc. Houston Meeting, Oct. 1970

E6 and M5 Gamma-Ray Transitions in the  $\text{Fe}^{53m}$  Decay.\* J.N. BLACK, Wm.C. McHARRIS, and W.H. KELLY, Mich. State Univ.—Evidence has been found for the existence of E6 and M5 transitions in  $\text{Fe}^{53m}$  decay. This 2.6-min isomer has been interpreted as being the highest spin state, J-19/2-, of the three-particle multiplet resulting from the configuration  $(\pi f7/2)^{-2}(\nu f7/2)^{-1}$ . This 19/2- state decays to an 11/2- state by a 701.1 keV E4 ( $\approx 100$ ), to a 9/2- state by a 1712.6 keV M5(0.7) and to the ground state by a 3040.6 keV E6(0.02). The isomer was prepared by the  $\text{Mn}^{55}(p,3n)\text{Fe}^{53m}$  reaction. Since single-particle estimates revealed E6/E4 and M5/E4 transition probability ratios of only 0.003 and 0.008 respectively, 3.6% Ge(Li) detector was used. Each experiment consisted of a continuous cycle of bombarding and counting such that a fresh source was counted every two minutes for a period of 24 hours. A series of experiments was designed which demonstrated that the observed transitions were not the result of summing effects. The result of this effort was the direct observation of  $\gamma$  rays corresponding to E6 and M5 transitions.

\*Work supported in part by the U.S. National Science Foundation and the U.S. Atomic Energy Commission.

American Phys. Soc. Houston Meeting, Oct. 1970

The  $^{34}\text{S}(^3\text{He},t)$  Reaction at 35 MeV.\* R.A. HINRICHS, B.H. WILDENTHAL, and J.A. RICE, Mich. State Univ.—Energy levels in  $^{34}\text{Cl}$  up to 5 MeV have been studied with the  $^{34}\text{S}(^3\text{He},t)$  reaction at 35 MeV. Angular distributions were taken between  $5^\circ$  and  $45^\circ$  using an Enge split-pole spectrograph with a resolution of 25 keV. Twenty-eight levels are observed. In addition to the well established low-lying levels, states at 2.61, 2.74, 3.16, 4.74, 4.94, and 5.14 MeV ( $\pm 30$  keV) are populated with significant intensity. Of particular interest are the transitions to the known  $1^+$  states at 460 and 667 keV. Their angular distributions are quite different. A comparison of the experimental angular distributions with microscopic DWBA calculations will be made.

\*Supported by the National Science Foundation.

American Phys. Soc. New York Meeting, Feb. 1971

Levels of  $^{56}\text{Co}$  Below 2 MeV Excitation from  $^{56}\text{Fe}(p,n)^{56}\text{Co}$  and  $^{56}\text{Ni}$  EC Decay.\* L.E. SAMUELSON, R.A. WARNER, W.H. KELLY, R.R. TODD, and W.C. MCHARRIS, Mich. State Univ.—Angular distributions have been measured for 11  $\gamma$ -rays depopulating 8 levels of  $^{56}\text{Co}$  excited by the  $^{56}\text{Fe}(p,n)^{56}\text{Co}$  reaction using proton beams of 5.77, 6.65, 7.03, and 7.30 MeV from the MSU Isochronous Cyclotron. Branching ratios and precise energies of  $\gamma$ -rays including 5  $\gamma$ -rays not observed in the  $^{56}\text{Ni}$  decay will be given. Spin and parity assignments of energy levels and multipolarity mixing ratios have been determined by comparing the experimental data with theoretical calculations using the code MANDY.<sup>1</sup> A  $0^+$  assignment is confirmed for the 1.4509 MeV level which is believed<sup>2</sup> to be the anti-analog of the  $^{56}\text{Fe}$   $0^+$  ground state.

\*Work supported in part by NSF and AEC.

<sup>1</sup>Eric Sheldon and R.M. Strang, *Computer Phys. Comm.* **1**, 35(1969); and Eric Sheldon and D.M. Van Patter, *Rev. Mod. Phys.* **38**, 143(1966).

<sup>2</sup>T.A. Belote, W.E. Dorenbuech, and J. Rapaport, *Nucl. Phys.* **A109**, 666(1968).

American Phys. Soc. New York Meeting, Feb. 1971

(p,t) Reaction on N=82 Nuclei at  $E_p=35$  MeV.\* R.K. JOLLY and E. KASHY, Mich. State Univ. Two nucleon pickup reactions have been studied on the closed neutron shell target nuclei of  $^{138}\text{Ba}$ ,  $^{140}\text{Ce}$ ,  $^{142}\text{Nd}$  and  $^{144}\text{Sm}$ . Angular distribution for 6-10 states in the first 2.5-3.5 MeV of excitation energy have been measured from  $12.5^\circ/15^\circ$  to  $90^\circ$  with an energy resolution of  $\sim 30$  keV. Absolute cross-sections were obtained by a simultaneous measurement of (p,p) and (p,t) cross at several angles. Spectroscopic analysis of these data using a direct one step reaction model in the DWBA approximation will be presented and compared with other analyses in the neighboring mass nuclei.

\*Supported by the U.S. National Science Foundation.

American Phys. Soc. New York Meeting, Feb. 1971

The (p,t) Spectra of  $\text{Tm}^{169}$ ,  $\text{Ho}^{165}$ , and  $\text{Tb}^{159}$ .\* R.W. GOLES, R.A. WARNER, Wm.C. MCHARRIS, and W.H. KELLY, Mich. State Univ.—Triton spectra resulting from the (p,t) reaction on  $\text{Tm}^{169}$ ,  $\text{Ho}^{165}$ , and  $\text{Tb}^{159}$  were measured at an incident proton energy of 36 MeV and lab observation angle of  $20^\circ$  using a broad-range magnetic spectrometer. The proton beam, accelerated from the MSU Sector Focused Cyclotron, was analyzed to give an energy spread of  $\sim 0.06\%$  and focused on  $\sim 800$   $\mu\text{g}/\text{cm}^2$  metallic foils of the above target material. The scattered tritons were detected using both a 3 cm Si position sensitive detector and photographic plates. The resulting spectra are all characterized by strong collective excitations of the residual nuclei. In particular, it is found that members of the ground state rotational band up to 6 spin units above the band head are strongly excited by this reaction.

\*Supported in part by the U.S. National Science Foundation and the U.S. Atomic Energy Commission.

American Phys. Soc. New York Meeting, Feb. 1971

Shell-Model Calculations for Nuclei with  $A=23-29$ . B.H. WILDENTHAL,\* Mich. State Univ. and J.B. MCGRORY,\*\* Oak Ridge Nat. Lab.—We have extended our previous calculations for  $A=18-22$ , made in the complete sd-shell configuration space, to  $^{23}\text{Na}$ ,  $^{23}\text{Ne}$ , and  $^{24}\text{Mg}$ . The approach has been to limit the population of the  $d_{3/2}$  orbit to no more than two particles, and to limit the number of  $d_{5/2}$  holes to no more than four. The Hamiltonian we have used in these calculations was obtained by empirically adjusting Kuo's two-body matrix elements so as to improve the agreement between model and observed level energies for  $A=18-22$ . The predictions obtained for  $A=23$  and  $24$  with this approach are very encouraging. Spectra and transition strengths will be presented. Analogous treatments of  $^{26}\text{Al}$  and  $^{28}\text{Si}$  are less successful. Further calculations for the  $A=26-29$  region will also be discussed.

\*Work supported by the National Science Foundation.

\*\*Work sponsored by US AEC under contract with Union Carbide Corp.

American Phys. Soc. New York Meeting, Feb. 1971

The Ghost Anomaly in the  $^9\text{Be}(p,d)^8\text{Be}$  (g.s.) Reaction.\* P.S. MILLER, G.M. CRAWLEY, W.F. STEELE, and F.C. BARKER, Mich. State Univ. The magnitude and spectral distribution of the ghost anomaly in  $^8\text{Be}$  can be useful in limiting the R-matrix parameters obtained from fitting  $\alpha$ - $\alpha$  scattering.<sup>1</sup> The ghost is observed in the present work at an incident laboratory energy of 40 MeV, where complications in the analysis due to compound nucleus effects presumably are negligible. The magnetic spectrograph detector system using position-sensitive solid state detectors yield an overall resolution of 50 keV FWHM. The results are compared with previous experiments, and implications for the R-matrix analysis are discussed.

\*Supported by the U.S. National Science Foundation.

<sup>1</sup>F.C. Barker, H.J. Hay and P.B. Treacy, *Aust. J. Phys.* **21**, 239(1968).

American Phys. Soc. New York Meeting, Feb. 1971

Isobaric Yields of Masses 6 to 11 from Proton Spallation of  $^{14}\text{N}$  in the Energy Range 17 to 42 MeV.\* H. LAUMER, C.N. DAVIDS,\*\* and S.M. AUSTIN, Mich. State Univ.—Time-of-flight methods were used to identify masses of reaction products stopped in a silicon surface-barrier detector. A gas cell with total exit area density 50-130  $\mu\text{g}/\text{cm}^2$  contained the  $^{14}\text{N}$ . Total cross-sections were obtained by integrating angular distributions. The ratio mass 7/mass 6 varies from 0.5 to 42 MeV to 10 at 21.7 MeV. Mass 10/mass 11 is 1.5 at 42 MeV, 3 at 28.6 MeV, and 0.25 at 17 MeV. The importance of these cross-sections to current models to the origin of the light elements Li, Be and B will be discussed.

\* Work supported by the U.S. National Science Foundation.

\*\* Present Address: Center for Nuclear Studies, University of Texas, Austin Texas 78712

American Phys. Soc. New York Meeting, Feb. 1971

Internal Conversion Studies of the 2.3 keV Transition from the Electron Capture Decay of  $\text{Bi}^{205}$ .\* W.C. JOHNSTON, K.L. KOSANKE, S.K. HAYNES, W.C. McHARRIS, and W.H. KELLY, Mich. State Univ. The internal conversion spectrum for the 2.3 keV transition in  $\text{Pb}^{205}$  has been measured using the MSU  $\pi/2$   $\beta$ -ray spectrometer. This transition had never been directly observed before although it was generally accepted to be an E2 transition from the first excited state to the ground state ( $1/2^- \rightarrow 5/2^-$ ). Internal conversion is energetically allowed for only the N and higher shells. The N conversion occurs near the threshold and should provide a good test for theoretical N shell ICC's. Our results for the relative intensity of the 2.3 keV transition, for the N and O conversion intensities and energies, and also for the M-Auger spectra for  $\text{Pb}^{205}$  and  $\text{Pb}^{206}$  will be presented.

\* Work supported in part by the U.S. National Science Foundation, and the U.S. Atomic Energy Commission.

American Phys. Soc. New York Meeting, Feb. 1971

Decay of  $\text{Sm}^{141\text{m}}$ .\* R.R. TODD, R.E. EPPLEY, W.H. KELLY, W.C. McHARRIS, and R.A. WARNER, Mich. State Univ.—The decay of  $\text{Sm}^{141\text{m}}$  ( $\approx 22.1\text{m}$  half-life) has been studied with Ge(Li) spectrometers using sources primarily prepared by the  $\text{Nd}^{142}(\text{He}, 4\text{n})\text{Sm}^{141\text{m}}$  reaction. The energies and relative intensities of 31  $\gamma$ -rays occurring in the decay have been determined. The level scheme has been established by means of  $\gamma$ - $\gamma$  coincidence experiments, resulting in the placement of 15 levels and the determination of a 628.6 keV delayed isomeric transition in the daughter  $\text{Pm}^{141}$ . We have identified 6, possibly 7 states belonging to a three quasi-particle multiplet of high spin states with low log ft values between 5.7 and 6.9. Some data will also be presented concerning the decay of  $\text{Sm}^{141\text{g}}$ .

\* Work supported in part by the U.S. National Science Foundation and the U.S. Atomic Energy Commission.

American Phys. Soc. Cleveland Meeting, March 1971

Study of Local Modes of Lithium and Boron in Silicon.\* E. DOUNCE, O.P. KATYAL, and C.R. GRUHN, Mich. State Univ.—Infrared studies of local vibrational modes of B doped Li compensated Si samples have been made. The temperature effects on-line width and centroid have been extended. Uniaxial stress was applied in an attempt to break up the local modes degeneracies, thereby, ascertaining to a greater degree the certainty of the  $522\text{ cm}^{-1}$  line thought to be a  $^7\text{Li}$  vibrational mode in a Li-B complex. So far, a search for the free interstitial Li local mode has turned out to be unproductive.

\* Work supported in part by NASA and NSF.

American Phys. Soc. Washington Meeting, Apr. 1971

$^3\text{He}$  Elastic Scattering at 70 MeV on  $^{50}\text{Ti}$  and  $^{51}\text{V}$ .\* R. A. HINRICHS, R.R. DOERING, and A. GALONSKY, Mich. State Univ.—We have begun a study of  $^3\text{He}$  elastic scattering on medium weight nuclei at 70 MeV by examining the nuclei  $^{50}\text{Ti}$  and  $^{51}\text{V}$ . Angular distributions were taken from  $3^\circ$  to  $170^\circ$  with detector telescopes. One particularly interesting aspect of the data in both cases was the rapid drop in cross-section (9 orders of magnitude) over this angular range. Optical model calculations were not able to fit this decrease at angles greater than  $100^\circ$  and good fits at angles less than this required a larger and more diffuse imaginary potential than used at substantially lower energies. The data for  $^{51}\text{V}(\text{spin } 7/2^-)$  for angles greater than  $50^\circ$  showed less structure than the corresponding  $^{50}\text{Ti}$  data, providing additional information on possible target spin dependences in  $^3\text{He}$  elastic scattering.<sup>1</sup>

\* Supported by the National Science Foundation.

<sup>1</sup>J.C. Hafele, C.B. Fulmer, and F.G. Kingston, Phys. Letters 31B, 17(1970).

American Phys. Soc. Washington Meeting, Apr. 1971

Inelastic Proton Scattering on N=82 Nuclei.\* D. LARSON, S.M. AUSTIN, B.H. WILDENTHAL, and S.H. FOX, Mich. State Univ.—High resolution spectra and angular distributions from  $10^\circ$  to  $80^\circ$  have been measured for  $^{138}\text{Ba}$  and  $^{144}\text{Sm}$ , as part of a study of proton inelastic scattering from nuclei with 82 neutrons. 30 MeV protons from the MSU Sector-Focused Cyclotron in conjunction with the Enge split-pole spectrograph and associated equipment<sup>1</sup> enable us to obtain resolutions of better than 10 keV FWHM routinely. This makes it possible to separate many of the multiplets previously unresolved in these nuclei. The  $(p, p')$  results will be compared with existing  $(\alpha, \alpha')$  and gamma-ray data and also with each other, the latter comparison in order to delineate the effects produced by the addition of six protons between Ba and Sm. Comments will be made as to the nature of the states excited viz a viz predictions of shell-model calculations.

\* Supported by the National Science Foundation.

<sup>1</sup>H.G. Blosser, et al. (to be published).

American Phys. Soc. Washington Meeting, Apr. 1971

Asymmetry in the Inelastic Scattering of 40.5 MeV Protons from  $^{16}\text{O}$  and  $^{12}\text{C}$ . W. BENENSON,\* and P.J. LOCARD ISN Grenoble, France and J.-L. ESCUDIE and J.M. MOSS, CEN Saclay, France—Polarized protons of 40.5 MeV from the Grenoble Cyclotron were used to study the asymmetry in inelastic scattering from  $^{16}\text{O}$  and  $^{12}\text{C}$ . The detection system consisted of a quadrupole triplet and a 1 cm lithium drifted silicon detector. Resolution of 50 keV permitted observation of the ground plus lowest  $3^-$ ,  $2^+$ ,  $1^-$  and  $2^-$  states in  $^{16}\text{O}$  and the ground plus lowest  $2^+$ ,  $0^+$ , and  $3^-$  states in  $^{12}\text{C}$  from 5 to  $120^\circ$  (Lab). Distorted wave calculations were made for  $^{16}\text{O}$  using UCLA optical model parameters. The small almost isotropic polarization of the unnatural parity  $2^-$  state is fairly well given by the microscopic model. For the  $1^-$  and  $3^-$  state the microscopic model fits poorly. The  $2^+$  states fit is good using a full Thomas form for the distorted spin orbit force.

\* Present Address: Mich. State Univ.

American Phys. Soc. Washington Meeting, Apr. 1971

Inelastic Proton Scattering from  $^{16}\text{O}$  at Bombarding Energies from 24.6 to 40.1 MeV.\* D.L. BAYER, I.D. PROCTOR, and F.L. PETROVICH, Mich. State Univ.—Position sensitive detectors on the focal plane of an Enge split pole spectrometer have been used to obtain angular distributions from  $10^\circ$  to  $100^\circ$  for the doublet of states at 6.05 MeV ( $0^+$ ) and 6.13 ( $3^-$ ) and the doublet of states at 6.92 MeV ( $2^+$ ) and 7.12 MeV ( $1^-$ ). The cross sections for exciting these four states have been analyzed within the framework of the macroscopic collective model and the microscopic model with realistic forces. In the microscopic calculations inelastic electron scattering data was used as a guide in constructing the necessary transition densities.

\* Supported by the National Science Foundation.

American Phys. Soc. Washington Meeting, Apr. 1971

Shapes of ( $^3\text{He},t$ ) Angular Distributions to T< States in  $^{89}\text{Zr}$ .\* R.A. HINRICHS, Mich. State Univ.—In most ( $^3\text{He},t$ ) reactions, while the magnitude of the calculated cross-section is dependent upon the form of the radial integral, the shape is primarily dominated by the angular momentum transfer L. In several cases the angular distributions to  $0^+$  anti-analog states have shown a non-allowed L=1 shape. We have studied the  $^{89}\text{Y}(^3\text{He},t)$  reaction to T< states in  $^{89}\text{Zr}$  to look for this effect when more than one L value is allowed. Angular distributions at 33 MeV were taken between  $3^\circ$  and  $40^\circ$  using an Enge split-pole spectrograph. The angular distributions to the  $1/2^-$  0.588 MeV state and possible  $1/2^-$  states at 1.740 and 1.866 MeV have predominately non-allowed L=1 shapes. The angular distributions for T< states with spins other than the spin of the target could not be fit with allowed L transfers and showed shapes composed of both even and odd L values.

\* Supported by the National Science Foundation.

<sup>1</sup>R.A. Hinrichs, R. Sherr, G.M. Crawley, and I. Proctor, Phys. Rev. Letters 25, 829(1970).

American Phys. Soc. Washington Meeting, Apr. 1971

Decay of  $\text{Pm}^{141}$ .\* F.Y. YAP† R.R. TODD, R.A. WARNER, W.H. KELLY, and Wm.C. MCHARRIS, Mich. State Univ.—The decay of  $\text{Pm}^{141}$  has been studied with Ge(Li) spectrometers using sources prepared by the reaction  $\text{Nd}^{142}(p,2n)\text{Pm}^{141}$ . Nearly 50 transitions belonging to the decay of  $\text{Pm}^{141}$  have been identified on the basis of half-life, and a level scheme is proposed incorporating more than 30 of these transitions. Various coincidence experiments have so far resulted in the placement of levels at 193.8, 756.7, 1223.3, 1345.8, 1564.8, 1596.8, 1967.6, 2073.7, 2109.6, 2246.6, 2505.0 keV. Spin assignments made from log ft values are compared with results from studies<sup>1</sup> of charged particle reactions populating states in  $\text{Nd}^{141}$ .

\* Supported in part by the U.S. National Science Foundation and U.S. Atomic Energy Commission.

† Present Address: Wilson College, Chambersburg, Pennsylvania.

<sup>1</sup>J.L. Foster, Jr., O. Dietzsch and D. Spalding, preprint; and R.K. Jolly and E. Kashy, Bull. Am. Phys. Soc. 16, 151(1971) and private comm.

Nucl. Sci. Applic. Symp. New York, Nov. 1970

Determination of Trace Elements in Samples by Nuclear Scattering and Reaction Techniques.\* R.K. JOLLY, C.R. GRUHN, and C. MAGGIORE, Mich. State Univ.—The feasibility of using low energy

(15-25 MeV)  $\alpha$ -particles scattering for detecting traces of heavy elements in a bulk of light elements as, for example, in biological and environmental matter is explored. These measurements can provide information on all elements in the sample simultaneously. Heavy elements require good energy resolution ( $\sim 10$  keV) for definite identification while light elements can be identified even with very poor energy resolution ( $\sim 100$  keV). Results of some measurements on a fish sample are presented.

Similarly sub-Coulomb (p,d)-reactions are explored for measuring traces of very light elements in a bulk of heavy elements. Suitable choice of bombarding energy almost completely suppresses the contribution from the heavy elements. Results of a measurement in a very pure Zr sample are presented.

\* Supported by the National Science Foundation.

Nucl. Struc. Symp., Jyvaskyla, Finland, Apr. 1970

Inelastic Scattering of Protons from  $^{16}\text{O}$  and the Effective Two-Body Interaction.\* S.M. AUSTIN, P.J. LOCARD, Mich. State Univ. S.N. BUNKER, J.M. CAMERON, J.R. RICHARDSON and J.W. VERBA, UCLA, W.T.H. VAN OERS, Univ. of Manitoba.—Cross sections for the  $^{16}\text{O}(p,p')^{16}\text{O}$  reaction leaving  $^{16}\text{O}$  in its  $2^-$  state at 8.88 MeV or the 6.05( $0^+$ )-6.13( $3^-$ ) doublet (dominated by  $3^-$ ) have been measured at 23.4, 24.5, 27.3, 30.1, 34.1, 36.8, 39.7, 43.1, and 46.1 MeV. Compound nucleus effects are evident below 30 MeV but the cross sections vary monotonically at higher energies. In the direct distorted wave approximation with central forces, the  $2^-$  transition can occur only through the term  $V_\sigma \vec{\sigma}_1 \cdot \vec{\sigma}_2$  in the effective interaction, while the  $3^-$  transition is dominated by the spin-isospin independent term  $V_0$ . Strengths of  $V_0$  and  $V_\sigma$  were obtained by fitting the cross sections with real interactions of the form  $V_\sigma \vec{\sigma}_1 \cdot \vec{\sigma}_2 e^{-r/r}$  and  $V_0 e^{-r/r}$ . We found  $V_\sigma = 23$  MeV,  $V_0 = 65$  MeV at  $E_p = 30.1$  MeV; and  $V_\sigma = 16$  MeV,  $V_0 = 51$  MeV at  $E_p = 46.1$  MeV. The data were also compared with the predictions of an impulse approximation. The impulse approximation underestimates the  $2^-$  cross section by a factor of about 4 at all energies, but predicts the  $3^-$  cross section within about 20%. The results for  $V_\sigma$  and  $V_0$  will be compared with available information on  $V_\sigma$  and  $V_0$ .



Section III

Abstracts of Papers in Press

August 1970

III. Abstracts of Papers in Press (August 1970)

Proton Scattering and the Optical Model Differences Between  $^{40}\text{Ca}$  and  $^{48}\text{Ca}$ \*

C.J. Maggiore\*\*, C.R. Gruhn, T.Y.T. Kuo, and B.M. Freedom\*\*\*

Department of Physics and Cyclotron Laboratory  
Michigan State University, East Lansing, Michigan

ABSTRACT

Elastic proton scattering from  $^{40}\text{Ca}$  and  $^{48}\text{Ca}$  has been measured at 25, 30, 35, and 40 MeV. The r.m.s. radius determined by the optical model is 0.15 fm larger for  $^{48}\text{Ca}$  than for  $^{40}\text{Ca}$ , consistent with the  $A^{1/3}$  law.

\* This work supported by the U.S. National Science Foundation.

\*\* Present Address: Department of Environmental Science, Mt. Sinai School of Medicine, New York, New York.

\*\*\* Present Address: Physics Department, University of South Carolina, Columbia, South Carolina 29208

Neutron Hole State Structure in N=81 Nuclei. I\*

$^{144}\text{Sm}$  and  $^{142}\text{Nd}(p,d)$

R.K. Jolly and E. Kashy

Cyclotron Laboratory, Michigan State University  
East Lansing, Michigan 48823

ABSTRACT

Angular distributions of deuterons from the (p,d) reaction (Energy Resolution  $\sim 35$  keV) on  $^{144}\text{Sm}$  and  $^{142}\text{Nd}$  at Ep=35 MeV have been measured and compared with Distorted Wave Born Approximation (DWBA) calculations. The DWBA calculations were performed both with and without the finite range and non-locality corrections. In some typical cases corrections were also included for the nuclear density dependence of the effective pn interaction. The DWBA cross sections for  $l=5$  show an enhanced sensitivity to the inclusion of these corrections. Calculations including both the non-locality and finite range corrections yield acceptable spectroscopic factors. Considerable fractionation of the  $(2d_{5/2})_v^{-1}$  and the  $(1g_{7/2})_v^{-1}$  states is observed. No measurable population of neutron states in the  $82 < N < 126$  major shell was observed. The neutron single hole energies (in MeV) are as follows:  $d_{3/2}-0.0$ ,  $s_{1/2}-0.45$ ,  $h_{11/2}-1.22$ ,  $d_{5/2}-1.52$ , and  $g_{7/2}-2.12$  for  $^{144}\text{Sm}$  and  $d_{3/2}-0.0$ ,  $s_{1/2}-0.43$ ,  $h_{11/2}-1.07$ ,  $d_{5/2}-1.47$  and  $g_{7/2}-2.20$  for  $^{142}\text{Nd}$ . Data on the systematics of splitting and movements of these single neutron hole states as a function of the proton number (Z) in  $^{143}\text{Sm}$ ,  $^{141}\text{Nd}$ ,  $^{139}\text{Ce}$ , and  $^{137}\text{Ba}$  shall be presented in a subsequent paper.

\* Supported by the National Science Foundation.

Neutron Hole State Structure in N=81 Nuclei\*.II

$^{140}\text{Ce}$  and  $^{138}\text{Ba}(p,d)$

R.K. Jolly and E. Kashy

Cyclotron Laboratory, Michigan State University  
East Lansing, Michigan 48823

ABSTRACT

In continuation of our program of neutron hole state studies in N=81 nuclei angular distributions of deuterons from (p,d) reactions (Energy resolution  $\sim 35$  keV) on  $^{140}\text{Ce}$  and  $^{138}\text{Ba}$  at Ep=35 MeV have been measured and compared with Distorted Wave Born Approximation (DWBA) calculations including finite range and non-locality corrections. These calculations yield acceptable spectroscopic factors and are in fair agreement with the shapes of the experimental angular distributions. The neutron single hole energies have been determined. These energies (in MeV) are  $d_{3/2}-0.0$ ,  $s_{1/2}-0.33$ ,  $h_{11/2}-1.07$ ,  $d_{5/2}-1.72$ , and  $g_{7/2}-2.90$  for  $^{140}\text{Ce}$  and  $d_{3/2}-0.0$ ,  $s_{1/2}-0.54$ ,  $h_{11/2}-1.07$ ,  $d_{5/2}-1.71$ , and  $g_{7/2}-2.93$  for  $^{138}\text{Ba}$ .

Considerable fractionation of the  $(2d_{5/2})_v^{-1}$  and the  $(1g_{7/2})_v^{-1}$  states is observed while the  $(3s_{1/2})_v^{-1}$  and the  $(1h_{11/2})_v^{-1}$  states are each observed to split mostly into two components. Systematics on the energies and strengths of the various neutron single hole states and their components is presented for all N=81 nuclei from  $^{137}\text{Ba}$  thru  $^{143}\text{Sm}$  and the significance of the systematics discussed. No measurable population of any neutron state in the  $82 < N < 126$  major shell has been observed.

\* Supported by the National Science Foundation.

The Mass of  $^{25}\text{Si}$  and the Isobaric Multiplet Mass Equation\*

G.F. Trentelman and I.D. Proctor

Cyclotron Laboratory, Michigan State University  
East Lansing, Michigan 48823

ABSTRACT

The mass excess of  $^{25}\text{Si}$  has been measured via determination of the Q-value for the  $^{28}\text{Si}(^3\text{He}, ^6\text{He})^{25}\text{Si}$  reaction. The results are used to test the isobaric multiplet mass equation for A=25.

\* Supported by the National Science Foundation.

Calculations with a  $1s, 0d$  Shell-Model for  $A=34-38$  Nuclei\*

B.H. Wildenthal

Michigan State University, East Lansing, Michigan  
and Oak Ridge National Laboratory, Oak Ridge, Tenn.

E.C. Halbert and J.B. McGrory

Oak Ridge National Laboratory, Oak Ridge, Tennessee

T.T.S. Kuo

Oak Ridge National Laboratory, Oak Ridge, Tennessee  
and State University of New York at Stony Brook,  
Stony Brook, L. I., New York

ABSTRACT

Results are presented of calculations made in the full space of  $sd$  shell-model wave functions for positive-parity states in the nuclei with  $A=34-38$ . We employed in this work several different effective Hamiltonians, some of which had two-body parts obtained by reaction matrix techniques from the Hamada-Johnston scattering potential. The observables calculated were energy level spectra, single-nucleon spectroscopic factors, and  $E2$  and  $M1$  moments and transition strengths. These calculations yield fair-to-good agreement with many of the observed nuclear structure data in this mass region.

\* Research jointly sponsored by the U.S. Atomic Energy Commission under contract with Union Carbide Corporation, and by the National Science Foundation.

Shapes of Angular Distributions in the  $^{89}\text{Y} (^3\text{He}, t)^{89}\text{Zr}$  Reaction to Antianalog and Other  $T_{\leq}$  States\*

R.A. Hinrichs and G.F. Trentelman

Cyclotron Laboratory, Michigan State University  
East Lansing, Michigan 48823

ABSTRACT

The  $^{89}\text{Y} (^3\text{He}, t)^{89}\text{Zr}$  reaction to  $T_{\leq}$  states in  $^{89}\text{Zr}$  shows the angular distributions to have shapes characteristics of non-allowed  $L$  transfers and not similar to microscopic predictions. The antianalog states appear not to be unique in possessing this feature.

\* Supported by the National Science Foundation.

The Structure of Nuclei with Masses  $A=30-35$ , as Calculated in the Shell-Model

B.H. Wildenthal

Cyclotron Laboratory, Michigan State University\*  
East Lansing, Michigan 48823

J.B. McGrory and E.C. Halbert

Oak Ridge National Laboratory, Oak Ridge, Tenn.\*\*

H.D. Graber

Cornell College, Mt. Vernon, Iowa 52314

ABSTRACT

Properties of positive-parity states of nuclei with  $A=30-35$  have been calculated in a shell-model space which encompasses all Pauli-allowed basis vectors of all configurations  $(0s)^4(0p)^{12}(0d_{5/2})^{n_1}(1s_{1/2})^{n_2}(0d_{3/2})^{n_3}$  for which  $n_1 \geq 10$ . Two different empirical Hamiltonians, one of a delta-function form, were used. Calculated energies and spectroscopic factors are in good agreement with an extensive body of experimental data. The model wave functions also yield satisfactory agreement with many available experimental data on electric quadrupole observables if effective charges of  $0.5e$  are added to the proton and neutron. The model predictions for magnetic dipole observables are generally in qualitative agreement with experimental observations, but inconsistencies between theory and experiment are more noticeable in this area.

\* Supported in part by the U.S. National Science Foundation.

\*\* Research supported in part by the U.S. Atomic Energy Commission under contract with Union Carbide Corporation.

Study of Charge-Exchange Coupling in Proton Induced Reactions on  $^{95,98,100}\text{Mo}$  and  $^{92,94}\text{Zr}$ \*

R.A. Hinrichs,\*\* G.W. Phillips,\*\*\* J.G. Cramer,  
and H. Wieman

Nuclear Physics Laboratory, University of Washington  
Seattle, Washington 98105

ABSTRACT

The presence of isospin coupling in the incident channel has been studied via proton induced reactions on  $^{95,98,100}\text{Mo}$  and  $^{92,94}\text{Zr}$ . Anomalous behavior in the excitation functions at backward angles was observed in deuteron and proton outgoing channels. In the deuteron channels these anomalies, located near the  $(p,n)$  threshold to the ground state analog were, for most all cases, similarly characterized as double dip in shape. Their strength is generally much weaker than the single minimums observed in  $(d,p)$  reactions near mass 90 and can be categorized by the proton decay energy from the analog state formed in the charge exchange process. The proton elastic excitation functions showed no structure near the  $(p,n)$  thresholds although the  $(p,p')$  curves did exhibit fluctuations.

\* Supported in part by the U.S. Atomic Energy Comm.  
\*\* Present Address: Cyclotron Laboratory, Michigan State University, East Lansing, Michigan 48823

\*\*\* Supported by the National Science Foundation.  
Present Address: Center for Nuclear Studies, Univ. of Texas, Austin, Texas.

The (p,t) Reaction on Even-Even N=Z Nuclei in the 2s<sub>1/2</sub> Shell\*

R.A. Paddock\*\*

Cyclotron Laboratory, Michigan State University  
East Lansing, Michigan 48823

ABSTRACT

The (p,t) reaction on the even-even N=Z nuclei in the 2s<sub>1/2</sub> shell has been used to study the energy level of <sup>18</sup>Ne, <sup>22</sup>Mg, <sup>26</sup>Si, <sup>30</sup>S, <sup>34</sup>Ar, and <sup>38</sup>Ca. The energies of the excited states observed are reported along with spin and parity assignments when possible. Two nucleon transfer distorted wave calculations were carried out. Comparisons are made with the shapes of the experimental angular distributions. It is found that the calculated shapes are primarily dependent upon the L-transfer and the optical model parameters. The magnitudes of the calculated cross-sections are found to depend strongly not only on the optical model parameters, but also the bound state parameters and the configuration mixing in the initial and final nuclear wave functions.

\* Work supported by the National Science Foundation.

\*\* Ph.D. Thesis, Present Address: Ripon College, Ripon, Wisconsin.

Preparation of Thin Film Deposits from Biological, Environmental and Other Matter\*

R.K. Jolly and H.B. White

Cyclotron Laboratory, Michigan State University  
East Lansing, Michigan 48823

ABSTRACT

A technique for preparing uniform thin film deposits (10-1000 μgm/cm<sup>2</sup>) of practically all materials of biological, environmental and nuclear physics interest is proposed. The technique involves preparing a solution or colloidal suspension of micron size particles of the substance of interest, generating a nebulized (practically invisible) mist from this liquid and condensing the mist on a rotating substrate. The cost in time and money for several materials is minimal.

\* Supported by the National Science Foundation.

Section IV

Reprints of Published Papers

July 1970-June 1971

## Inelastic Scattering of Protons from $^{16}\text{O}$ and the Spin-Dependent Part of the Effective Interaction

Sam M. Austin and P. J. Lócard\*†

*Department of Physics and Cyclotron Laboratory, Michigan State University, East Lansing, Michigan 48823*

and

S. N. Bunker,‡ J. M. Cameron,§ J. Reginald Richardson, and J. W. Verba||

*Department of Physics, University of California, Los Angeles, California 90024*

and

W. T. H. van Oers\*\*

*Department of Physics, University of Manitoba, Winnipeg, Canada*

(Received 23 April 1970; revised manuscript received 18 January 1971)

Angular distributions for the  $^{16}\text{O}(p,p')^{16}\text{O}$  reaction leading to the  $J^\pi=2^-$  state at 8.88 MeV and the doublet of states at 6.05 MeV ( $0^+$ ) and 6.13 MeV ( $3^-$ ) have been measured at 23.4, 24.5, 27.3, 30.1, 34.1, 36.8, 39.7, 43.1, and 46.1 MeV. In the distorted-wave approximation (DWA) with central forces, the transition to the unnatural-parity ( $2^-$ ) state can occur only through the spin-dependent part  $V_{10}=V_0 f(\mathbf{r})\vec{\sigma}_i \cdot \vec{\sigma}_p$  of the effective two-nucleon interaction. The experimental angular distributions were compared with DWA calculations assuming  $f(\mathbf{r})$  has a Yukawa shape with a range of 1.0 F. Normalization to the measured cross sections determined the strength  $V_0$ , which was found to decrease rapidly from a magnitude of 53 MeV to about 23 MeV between  $E_p=17.0$  MeV and  $E_p=30.1$  MeV, and then to decrease slowly to about 16 MeV at  $E_p=46.1$  MeV. The shape of the experimental angular distributions for the inelastic scattering to the  $2^-$  state are well represented by the DWA at the lower energies, but the agreement deteriorates as the energy increases. The forward peak in the higher-energy data occurs at larger angles than the DWA prediction. The cross section calculated using a pseudopotential derived from the impulse approximation is too small by a factor of about 4 at all energies. The possible contribution of other reaction mechanisms to the cross section for scattering to the  $2^-$  state is discussed. An analysis of the transition to the 6.1-MeV doublet is used to estimate the strength  $V_c$  of the spin-isospin-independent part  $V_{00}$  of the effective two-nucleon interaction. The experimental angular distributions for the 6.1-MeV doublet were also compared with the predictions of the impulse approximation.

### I. INTRODUCTION

The spin-dependent parts of the effective two-nucleon interaction can contribute to an inelastic proton scattering cross section whenever spin angular momentum  $S=1$  is transferred to the target nucleus. In terms of the transferred spin, isospin, orbital angular momentum, and total angular momentum,  $\vec{S}$ ,  $\vec{T}$ ,  $\vec{L}$ , and  $\vec{J}$ , the selection rules for inelastic nucleon scattering in the local distorted-wave approximation (DWA) are<sup>1</sup>

$$\begin{aligned}\vec{J} &= \vec{J}_f - \vec{J}_i, \\ \vec{S} &= \vec{J} - \vec{L}, \quad S=0, 1, \\ \vec{T} &= \vec{T}_f - \vec{T}_i, \quad T=0, 1, \\ \Delta\pi &= (-1)^L,\end{aligned}\tag{1}$$

where  $\Delta\pi$  denotes the change in parity. The symbols  $\vec{J}_i$ ,  $\vec{T}_i$  and  $\vec{J}_f$ ,  $\vec{T}_f$  denote the spin and isospin of the initial and final state, respectively. From these relations it is seen that  $S=1$  is allowed un-

less both the initial and final states have  $J=0$  and the same parity. Thus the spin-dependent part of the force contributes to most transitions and it must be understood before one can obtain accurate spectroscopic information from inelastic scattering.

Unfortunately, while  $V_{ST}=V_{11}$  is fairly well known,<sup>2-7</sup> only a few values of  $V_{ST}=V_{10}$  appear in the literature,<sup>8-13</sup> and these are at widely scattered energies. One can conclude only that  $V_{10}$  is fairly weak compared to the spin-isospin-independent component  $V_{00}$ .

The principal experimental measurements reported in this paper are angular distributions for inelastic proton scattering leading to the  $2^-$ ,  $T=0$  state at 8.88 MeV in  $^{16}\text{O}$  at nine proton energies between 23.4 and 46.1 MeV. This transition is exceptionally favorable for studies of  $V_{10}$ , since in the DWA the relations of Eq. (1) allow only  $S=1$  and  $T=0$ . Thus, for central forces, only  $V_{10}$  can contribute to the cross section. The differential cross sections for exciting the unresolved 6.05-

MeV ( $0^+$ )-6.13-MeV ( $3^-$ ) doublet are also reported. A preliminary analysis of these results is presented assuming the contribution of the  $0^+$  state can be neglected. The cross section for this transition is dominated by  $V_{00}$ .

If one wishes to determine the effective force by fitting the cross-section data, the reaction studied should satisfy at least two criteria. First, since the cross section depends on both the effective force and the wave functions of the nuclear states involved, these wave functions must be reasonably well known before information about the effective force can be obtained. The second criterion is that the reaction mechanism must be well described by the chosen model (the DWA). The first condition is satisfied, since random-phase-approximation (RPA) wave functions<sup>14</sup> are available for the states in  $^{16}\text{O}$  considered in this paper. Unfortunately, there is evidence that compound-nuclear<sup>15</sup> and possibly multiple-excitation<sup>16</sup> processes contribute to the cross section at the lower energies. Thus the DWA analysis performed here may be unreliable, particularly for incident proton energies ( $E_p$ ) smaller than 30 MeV, but these results represent the most detailed information about the energy dependence of  $V_{10}$  available at present, and the calculations should serve as a basis for more sophisticated analyses.

The experimental procedure and results are presented in Sec. II, while the DWA analysis to obtain  $V_{00}$  and  $V_{10}$  is given in Sec. III. In Sec. IV the calculated differential cross sections and the values of  $V_{00}$  and  $V_{10}$  are compared with previous work and with the predictions of an impulse-approximation (IA) pseudopotential. Possible contributions of other reaction mechanisms are also discussed.

## II. EXPERIMENT

### A. Experimental Method

The experimental part of this study was performed using the external beam facilities of the University of California, Los Angeles, sector-focused cyclotron. A detailed description of the experimental procedure used to study the elastic and inelastic scattering of protons from oxygen has been given previously,<sup>17</sup> and only a brief summary is included here.

A 10.75-in.-diam cylindrical cell with a 2.0-in.-high gap extending over  $330^\circ$  contained the oxygen gas. For laboratory angles greater than  $50^\circ$  the scattered particles were detected by an array of four scintillation detectors. The counting geometry for each of the detectors was defined by pairs of rectangular copper collimators mounted on the outside of an evacuated box. The collimators were 1.000 in. high, 0.500 in. wide, 0.156 in. thick and

were located 7.00 and 24.00 in. from the center of the gas cell. An antiscattering baffle 1.25 in. high and 1.00 in. wide was placed halfway between the defining apertures. For forward angles a single detector system with smaller angular acceptance was used to reduce the length of the gas path observed. For this arrangement the copper collimators were 0.500 in. high by 0.250 in. wide and their distances to the target center were 7.50 and 25.00 in., respectively.

The measurements were made with gas pressures in the range of 15–30 in. of mercury, except at the forward angles where lower gas pressures were used to diminish the effects of multiple scattering. The target gas was research-grade natural oxygen of 99.9% purity. Several flushings of the gas cell before each series of measurements insured that the total initial impurity of the gas was less than 0.3%. To prevent contamination buildup during the measurements the cylindrical gap of the gas cell was covered by two foils made of Kapton H film.<sup>18</sup> The outer foil was 0.002 in. thick and the inner foil was 0.001 in. thick. The volume between the two foils was maintained at a low pressure and acted as a buffer volume.

The scintillation detectors consisted of NaI(Tl) crystals (2 in. diam, 0.5 in. thick) optically coupled to RCA-8053 photomultiplier tubes. The amplified signals from the photomultiplier tubes were processed by an SDS 925 on-line computer operating in a  $4 \times 512$  channel, single-parameter mode. The over-all energy resolution was typically 1.5% for 46-MeV protons.

### B. Energy Spectra

A spectrum of protons scattered from the oxygen gas target is shown in Fig. 1 along with an energy level diagram.<sup>19</sup> The first two peaks below the elastic peak, which are not completely resolved, each contain contributions from two levels, 6.05 MeV ( $0^+$ ), 6.13 MeV ( $3^-$ ) and 6.92 MeV ( $2^+$ ), 7.12 MeV ( $1^-$ ), respectively. The clearly resolved 8.88-MeV ( $2^-$ ) state is relatively strongly excited at all energies studied. The next three levels, 9.61 MeV ( $1^-$ ), 9.85 MeV ( $2^+$ ), and 10.35 MeV ( $4^+$ ), are weakly excited. The group of levels between 10.95 and 11.63 MeV was strongly excited. A weakly excited level which corresponds to the 12.44-MeV ( $1^-$ ) or the 12.53-MeV ( $2^-$ ) state was observed at incident proton energies below 34.1 MeV. The data of Hornyak and Sherr<sup>20</sup> would indicate the latter to be the more probable choice. At least one of the four  $T=1$  levels between 12.80 and 13.26 MeV is strongly excited. Above  $E_p = 36.8$  MeV the strength in this region of excitation is noticeably decreased.

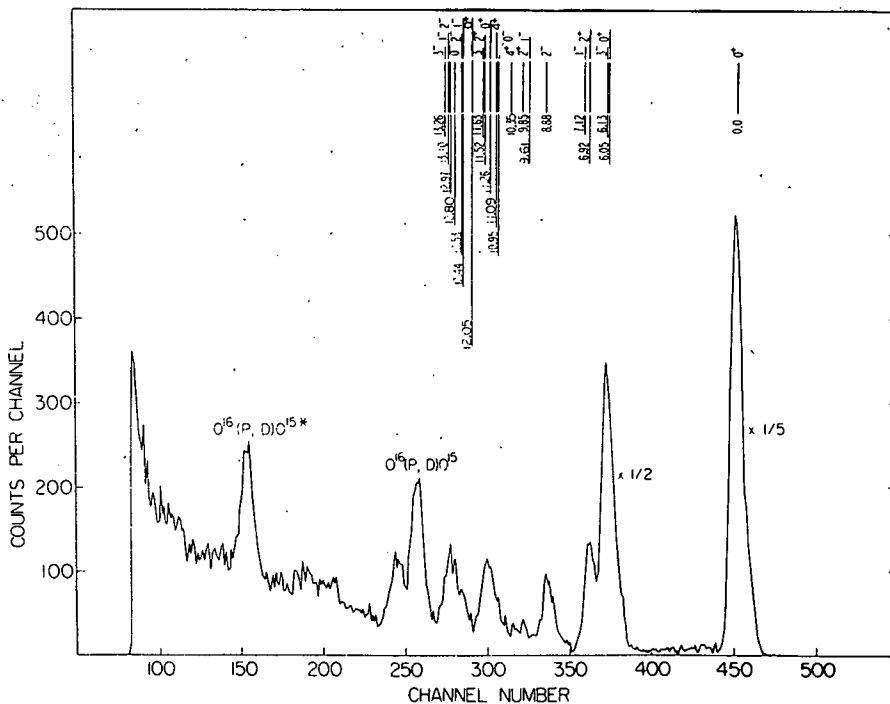


FIG. 1. Energy spectrum at  $E_p = 34.1$  MeV,  $\theta_{lab} = 40^\circ$ . The energy level diagram is taken from Ref. 19.

As can be seen in Fig. 1, the peaks sit on a continuous background which increases towards higher excitation energies. A nonnegligible contribution to the background stems from elastically scattered protons initiating nuclear reactions in the NaI(Tl) scintillation crystals.<sup>21</sup> In addition, the products of reactions having more than two bodies in the final state give rise to an increasing number of continua for increasing excitation energies. The highest energy end point is for the  $^{16}\text{O}(p, p\alpha)^{12}\text{C}$  reaction, which has a  $Q$  value of  $-7.16$  MeV.

### C. Data Reduction

The peak near 6.1 MeV of excitation is a doublet consisting of states at 6.05 and 6.13 MeV, and it partially overlaps with the 6.92-7.12-MeV doublet. Fortunately the 6.92-7.12-MeV peak was less than  $\frac{1}{4}$  the height of the 6.13-MeV peak at most angles, and it was possible to reliably extract the differential cross sections for the 6.05-6.13-MeV doublet. The 8.88-MeV peak was well resolved from other peaks and its analysis was straightforward.

To minimize subjective errors the spectra were analyzed using an automatic peak-stripping routine. The peaks were assumed to be of Gaussian form and the background function consisted of a combination of linear and exponential terms. The linear term was calculated by taking an average over a number of channels between the peaks corresponding to elastically scattered protons and protons scattered leaving the oxygen nucleus in its first excited state. The exponential and Gaussian func-

tions were varied to minimize the quantity  $\chi^2$ :

$$\chi^2 = \frac{1}{n-p} \sum_{i=1}^n \frac{(T_i - N_i)^2}{N_i},$$

where  $n$  is the number of data points and  $p$  is the number of free parameters. The number of events in the  $i$ th channel is denoted by  $N_i$ . The calculated number,  $T_i$ , is the sum of the contributions for the  $i$ th channel. In the analysis of the 8.88-MeV ( $2^-$ ) state one Gaussian was used and therefore  $p$  was five. In the case of the doublet at 6.1 MeV two Gaussians were used due to the partial overlap with the doublet centered at 7.0 MeV and thus  $p$  was eight. The values obtained for  $\chi^2$  were typically 0.5 to 1.5. When the program produced larger values of  $\chi^2$  the results were not included in the angular distributions.

The relative errors in the differential cross sections for the  $0^+ - 3^-$  doublet and the  $2^-$  state are typically 5% for angles greater than  $50^\circ$  increasing to 10% at smaller angles. The relative uncertainties are mostly due to counting statistics and possible errors introduced by the peak-fitting routine.

In addition to the relative errors, there is an uncertainty of  $\pm 2.5\%$  in the absolute scale. The largest contribution to this uncertainty is the fact that no corrections were made for protons which initiated nuclear reactions in the NaI(Tl) crystals. This correction varies as a function of proton energy and would increase the results of the measurements by less than 1.7% in this ener-



gy region.<sup>21</sup> The uncertainty due to finite geometry was estimated to be  $\pm 0.3\%$  using an extended version<sup>22</sup> of Silverstein's formalism in order to allow for a rectangular beam profile. The absolute calibration of the current integration is accurate to  $\pm 1.0\%$ . Other sources of relative and absolute error included in the above estimates are as discussed and evaluated in Ref. 17. The beam energy was determined to within  $\pm 0.2$  MeV by means of the crossover technique.<sup>23</sup>

#### D. Experimental Results

The experimental angular distributions for the  $^{16}\text{O}(p,p')^{16}\text{O}$  (8.88 MeV) reaction at 23.4, 24.5, 27.3, 30.1, 34.1, 36.8, 39.7, 43.1, and 46.1 MeV

are shown in Fig. 2. Also shown are angular distributions at 17.0 and 18.8 MeV from Daehnick.<sup>24</sup> The most striking feature of the angular distributions is the nonmonotonic variation with energy below 30 MeV. At 23.4 MeV the angular distribution is nearly flat as observed at 18.8 MeV by Daehnick<sup>24</sup> and at 17.5 MeV by Crawley and Garvey.<sup>25</sup> However, at 24.5 MeV a pronounced minimum appears at about  $115^\circ$  in the c.m. system. This minimum is present at all higher energies. The general shape of the curves then remains constant up to 30.1 MeV, but between 30.1 and 36.8 MeV the differential cross section at backward angles noticeably increases. As the incident energy is raised above 36.8 MeV, a second minimum begins to form at about  $90^\circ$  c.m. Above 30 MeV there is

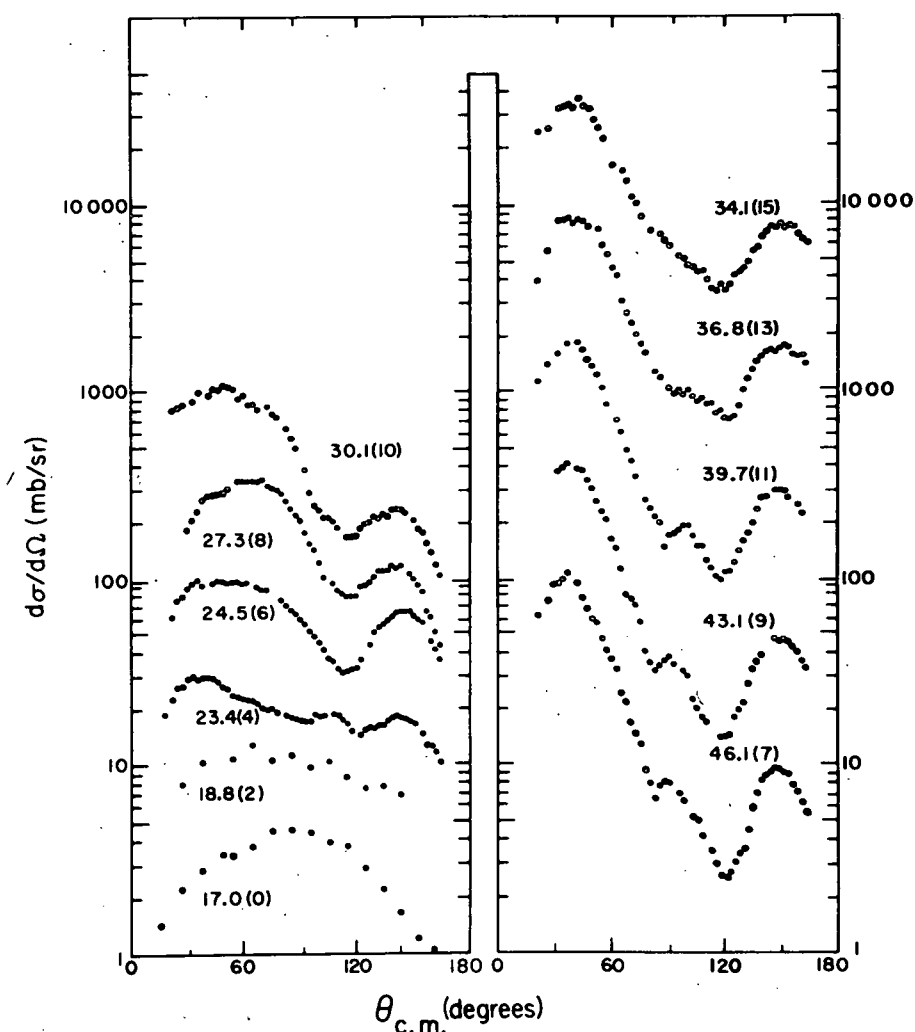


FIG. 2. Differential cross sections leading to the 8.88-MeV  $2^-$  state in  $^{16}\text{O}$ . The energies are given in MeV near each distribution. The number in parentheses following the energy is the power of 2 by which the plotted cross sections must be divided to obtain the true cross section. For example, the 30.1-MeV points must be divided by  $2^{10}=1024$ . The 17.0- and 18.8-MeV data are from Ref. 24 and the other data are the present work. Typical errors are  $\pm 10\%$  for  $\theta < 50^\circ$  and  $\pm 5\%$  for  $\theta > 50^\circ$ .

a smooth energy variation in the general shape.

Figure 3 shows the angular distributions of the 6.05-6.13-MeV doublet for the same incident proton energies. The ratio of the transitions to the 6.05-MeV state and the 6.13-MeV state is less than 1:8 between 20 and 90° at  $E_p = 17.5$  MeV.<sup>25</sup> Between 24 and 40 MeV this ratio is less than 1:10 between 20 and 100°.<sup>26</sup> For an incident proton energy of 150 MeV<sup>27</sup> the ratio at a laboratory angle of 15° is equal to 1:(14<sub>6</sub><sup>+21</sup>). Thus, at forward angles the angular distributions are essentially those for inelastic scattering to the 6.13-MeV ( $3^-$ ) state. The shape of the angular distributions does not vary appreciably over the range of incident proton energies 27-46 MeV. Furthermore, the differential cross section for angles below 50° c.m. is approximately constant.

The total cross section for each of the two tran-

sitions was obtained by extrapolating the cross sections linearly to  $\sigma(0^\circ) = 0$  from the last measured point at small  $\theta$  and to  $\sigma(180^\circ) = \sigma(\theta_{\max})$ , where  $\sigma(\theta_{\max})$  is the experimental cross section at the largest angle measured. The contribution from the extrapolated region was usually 3-7% except at 36.8 MeV where it was 13% for the 6.1-MeV transition, and at 43.1 MeV where it was 18% for the 8.88-MeV transition. The total cross sections are shown in Fig. 4. The errors shown are total errors and include an uncertainty of  $\frac{1}{2}$  the cross section in the extrapolated region.

Excitation functions for  $^{16}\text{O}(p, p')$  have been measured up to 40 MeV.<sup>15</sup> Relatively narrow peaks in the excitation functions were observed at backward angles up to about 27 MeV. Thus, compound-nucleus processes may be responsible for the rapid changes in the shape of the 8.88-MeV angular

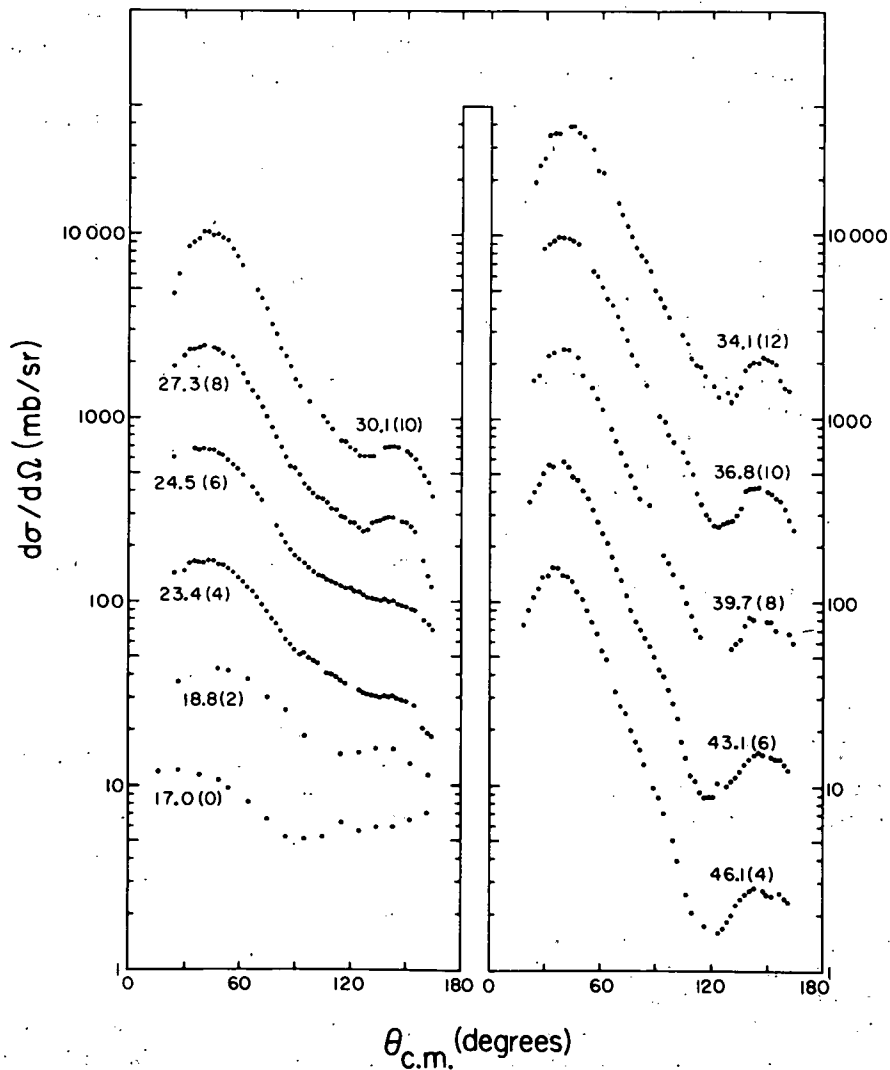


FIG. 3. Differential cross sections leading to the doublet of states near 6.1 MeV in  $^{16}\text{O}(6.05 \text{ MeV}, 0^+$  and 6.13 MeV,  $3^-$ ). For other details see the caption of Fig. 2.

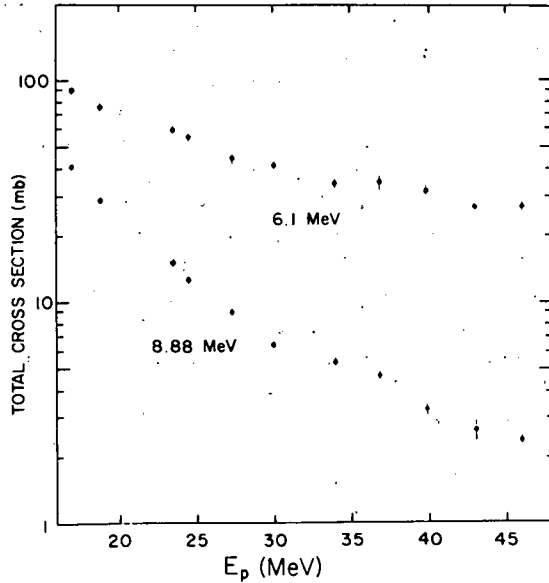


FIG. 4. Total cross sections for the 6.1- and 8.88-MeV transitions obtained by integrating over the differential cross sections shown in Figs. 2 and 3. See the text (Sec. II D) for details.

distributions for bombarding energies less than 25 MeV. The decreasing importance of compound-nucleus formation is presumably the reason for the rapid decrease observed in the total cross sections for both the 6.1- and 8.88-MeV transitions as the incident energy is increased towards 30 MeV. There is no clear evidence for nondirect processes at proton energies above 30 MeV. It should be noted that even above 30 MeV the total cross section for the 8.88-MeV transition decreases more rapidly than that for the 6.1-MeV transition. This behavior has been previously observed by Benenson and Crawley<sup>28</sup> in measurements of the deexcitation  $\gamma$  rays from these levels. A possible explanation of this effect will be discussed in Sec. IV.

### III. THEORETICAL ANALYSIS

#### A. Outline of the Theory

In the local DWA theory of inelastic scattering the transition amplitude can be written<sup>1</sup>

$$T_{fi} = \int \chi_f^{(-)*} \langle \psi_f | V_{\text{eff}} | \psi_i \rangle \chi_i^{(+)} d\vec{r}.$$

In this expression  $\chi_f$  and  $\chi_i$  are distorted waves generated from a phenomenological optical-model potential deduced by fitting the elastic scattering data. The form factor  $\langle \psi_f | V_{\text{eff}} | \psi_i \rangle$  contains all the nuclear-structure information. In a microscopic description of the reaction the wave functions  $\psi_f$  and  $\psi_i$  represent shell-model states. The effective interaction  $V_{\text{eff}}$  which causes transitions be-

tween these states is taken to be<sup>1</sup>

$$V_{\text{eff}} = \sum_i t_{ip},$$

where  $t_{ip}$  describes the scattering of the projectile  $p$  from the  $i$ th target nucleon and where the sum is over the nucleons of the target nucleus. If only central forces contribute to the interaction, one can approximate  $t_{ip}$  by

$$t_{ip} = V_{00} + V_{10} \vec{\sigma}_i \cdot \vec{\sigma}_p + V_{01} \vec{\tau}_i \cdot \vec{\tau}_p + V_{11} (\vec{\sigma}_i \cdot \vec{\sigma}_p) (\vec{\tau}_i \cdot \vec{\tau}_p). \quad (2)$$

Here  $\vec{\sigma}_i$  and  $\vec{\sigma}_p$  are the Pauli spin operators for the target nucleon and the projectile, respectively, and  $\vec{\tau}_i$  and  $\vec{\tau}_p$  are the analogous isospin operators. The subscripts on the  $V_{ST}$  are the transferred spin and isospin. For inelastic scattering to states of zero isospin in a self-conjugate nucleus, only the first two terms of the sum contribute. Possible effects of noncentral terms in  $t_{ip}$  will be discussed in Sec. IV.

#### B. Optical-Model Potentials

Cross-section and polarization angular distributions for the elastic scattering of protons from  $^{16}\text{O}$  had been obtained at all energies of this experiment.<sup>17,29</sup> The optical-model potentials derived by fitting both polarization and cross-section data have been published elsewhere.<sup>30</sup> The form of the optical model used in this analysis using the notation of Ref. 30 is given by

$$V(r) = V_c(r) - V \frac{1}{1+e^{x_1}} - iW \frac{1}{1+e^{x_2}} - iW_1 e^{-x_3^2} + (V_s + iW_s) \frac{4}{r} \frac{d}{dr} \frac{1}{1+e^{x_4}} (\vec{s} \cdot \vec{1}). \quad (3)$$

The  $x_i$  are related to the diffuseness and radius parameters according to

$$\begin{aligned} x_1 &= (r - r_0 A^{1/3})/a, & x_2 &= (r - r_1 A^{1/3})/a_1, \\ x_3 &= (r - r_2 A^{1/3})/b_1, & x_4 &= (r - r_s A^{1/3})/a_s. \end{aligned} \quad (4)$$

The relevant optical-model parameters for the DWA analysis are given in Table I.

One modification had to be introduced in the calculation of the distorted waves. The potential used in the DWA program contained a surface imaginary central potential of the derivative Woods-Saxon type

$$iW_D \times 4a_D \frac{d}{dr} \frac{1}{1+e^{x_5}}, \quad x_5 = \frac{r - r_1 A^{1/3}}{a_D}, \quad (5)$$

while that used in the optical-model analysis had a Gaussian shape [see Eq. (3)]. It was assumed that the derivative Woods-Saxon potential had the same strength and width at half maximum as the Gaussian potential: thus  $W_1 = W_D$ ,  $a_D = 0.472b_1$ .

TABLE I. UM-UCLA optical-model parameters. [See Ref. 30. The notation follows that of Eqs. (3) and (4).] The potential strengths are given in MeV.

$E_p$ (MeV)	$V^a$	$W$	$W_1$	$V_s$
23.4	47.25	0.00	7.06	-4.09
24.5	44.51	0.00	6.83	-5.41
27.3	48.43	0.00	7.28	-5.63
30.1	47.50	0.00	8.35	-6.82
34.1	47.02	2.31	6.52	-6.44
36.8	46.37	0.28	8.55	-7.98
39.7	46.58	2.25	7.65	-7.32
43.1	44.67	3.15	6.32	-6.20
46.1	42.13	4.44	4.64	-6.20

<sup>a</sup>The geometrical parameters are  $r_0 = 1.142$  F,  $r_1 = 1.268$  F,  $r_s = 1.114$  F,  $a = 0.726$  F,  $a_i = 0.676$  F,  $a_s = 0.585$  F, and  $b_i = 1.45$   $a_i$ .

As is common in light nuclei, it was not possible to obtain good simultaneous fits to the elastic scattering differential-cross-section and polarization data, although they could be fitted fairly well separately.<sup>30,31</sup> To estimate the effects of this ambiguity on the DWA calculations, distorted waves generated from optical-model potentials derived by Snelgrove and Kashy<sup>32</sup> from fits to their differential-cross-section data in this energy range were also used. These potentials are given in Table II.

The optical potentials for the exit channel were the same as those for the entrance channel, except that the real potential strength was determined using

$$V(\text{exit}) = V(\text{entrance}) + 0.33 \times \frac{17}{18} |Q|$$

to account for the energy dependence of the potential. The slope  $dV/dE = -0.33$  is consistent with the analysis of van Oers and Cameron<sup>30</sup> and Snelgrove and Kashy<sup>32</sup> in this energy range.

### C. Effective Interaction and Wave Functions

The radial dependence of the effective interaction was assumed to be Yukawan with an inverse range  $\alpha$  and was given by the relation

$$V_{10} = V_a \frac{e^{-\alpha r}}{\alpha r}, \quad V_{00} = V_c \frac{e^{-\alpha r}}{\alpha r}. \quad (6)$$

Earlier calculations<sup>8</sup> have shown that a range  $\alpha^{-1} = 1.0$  F is approximately correct for a Yukawan radial dependence, and this value for the range was used throughout the analysis except for a few test cases. The magnitude of the inelastic scattering cross section is proportional to  $V_a^2$  or  $V_c^2$  and these strengths can be determined by fitting the data.

The data were also compared with cross sec-

TABLE II. MSU optical-model parameters. [Obtained by extrapolation from the results of Ref. 32 at 25.46, 32.07, 35.20, 38.43, and 45.13 MeV. The notation follows that of Eqs. (3)–(5).] The potential strengths are given in MeV;  $r_i$  and  $a_D$  are given in F.

$E_p$ (MeV)	$V^a$	$W$	$W_D$	$V_s$	$r_i$	$a_D$
24.5	49.50	0.00	7.20	-7.00	1.155	0.560
27.3	47.55	0.00	6.20	-7.00	1.260	0.532
30.1	46.45	0.00	5.50	-7.00	1.365	0.505
39.7	43.80	2.30	5.45	-7.00	1.375	0.425
46.1	42.50	3.20	5.70	-7.00	1.250	0.415

<sup>a</sup>The geometrical parameters which were held constant are  $r_0 = 1.12$  F,  $r_s = r_0$ ,  $a = 0.69$  F, and  $a_s = a$ .

tions determined using an IA pseudopotential derived by Petrovich *et al.*<sup>33–36</sup> from the free two-nucleon interaction. This pseudopotential also has a Yukawan radial dependence, but it is complex and both the range and strength vary with energy. Typical values of the parameters are given in Table III.

The wave functions used in the calculations for the  $2^-$  and  $3^-$  states in  $^{16}\text{O}$  were those of the lowest-lying states of that spin and parity resulting from the calculations of Gillet and Vinh Mau.<sup>14</sup> Harmonic-oscillator radial wave functions were used with the oscillator parameter  $a = 1.76$  F, chosen to fit electron elastic scattering data.<sup>37</sup>

### D. Calculations for the 8.88-MeV ( $2^-$ ) State

The form factors were calculated and inserted into a DWA code which allows the use of spin-orbit coupling in the optical potentials.<sup>38</sup> The selection rules allow two amplitudes to contribute to the  $2^-$  transition. These amplitudes add coherently and correspond to transferred quantum numbers  $(LSJT) = (1120)$  and  $(3120)$ . Calculations including both amplitudes were performed at  $E_p = 30.1$  and  $46.1$  MeV, and it was found that the  $(3120)$  amplitude contributed less than 3.5% to the cross section at any angle. Therefore, all subsequent calculations included only the contribution of the  $(1120)$  amplitude.

The results of calculations at 27.3, 39.7, and 46.1 MeV are shown in Figs. 5–7. Each of these

TABLE III. Impulse-approximation values for  $V_{10}$ . (See Ref. 35. The form of  $V_{10}$  is  $V_{10}(r) = V_{OR} e^{-\beta r}/\beta r + iV_{OI} e^{-\gamma r}/\gamma r$ .)

$E_p$ (MeV)	$V_{OR}$ (MeV)	$\beta$ (F <sup>-1</sup> )	$V_{OI}$ (MeV)	$\gamma$ (F <sup>-1</sup> )
27.3	146	2.5	19	1.50
39.7	98	2.5	13	1.64
46.1	80	2.5	12	1.80

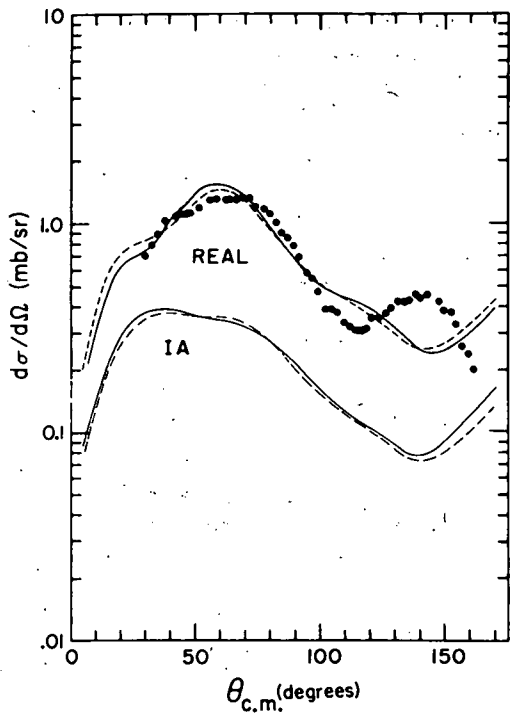


FIG. 5. Comparison of the 8.88-MeV angular distribution at  $E_p = 27.3$  MeV with DWA calculations. The upper two curves are for the real interaction of Eq. (6) with  $\alpha = 1.0 \text{ F}^{-1}$  and the lower two curves are for the impulse approximation of Refs. 34 and 35 as given in Table III. The dashed and solid curves were calculated with the MSU and UM-UCLA optical-model potentials, respectively. See the text (Secs. III B and III D) for details.

figures contains four curves. The lower two curves were calculated using the IA pseudopotential of Petrovich *et al.*,<sup>33-38</sup> which contains no adjustable parameters. The upper two curves were calculated using the real interaction of Eq. (6), with the strength of the interaction adjusted to make the calculated total cross section equal to the experimental total cross section shown in Fig. 4. The solid curves were calculated with the optical-model potentials of van Oers and Cameron<sup>30</sup> (UM-UCLA potentials) while the dashed curves were calculated with those of Snelgrove and Kashy<sup>32</sup> (MSU potentials).

The resulting values of  $V_0$  are shown in Fig. 8. The closed circles were obtained with the UM-UCLA potentials and the open circles were obtained with the MSU potentials. The points at low energy were calculated from the data of Crawley and Garvey<sup>25</sup> at 17.5 MeV and from the data of Daehnick<sup>24</sup> at 17.0 and 18.8 MeV using optical-model potentials derived from the elastic scattering cross sections at 17.5 MeV.<sup>39</sup> The points labeled impulse approximation, calculated using the UM-UCLA potentials, are the values of  $V_0$  for a

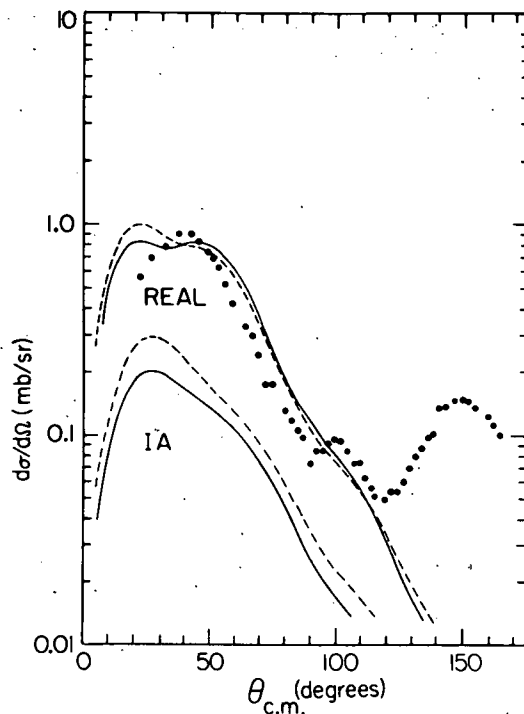


FIG. 6. Comparison of the  $E_p = 39.7$ -MeV angular distribution for the 8.88-MeV state with DWA calculations. See Fig. 5 for details.

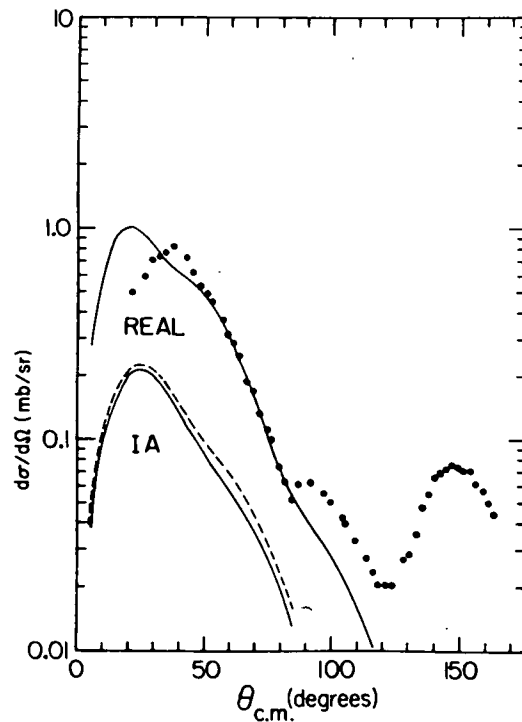


FIG. 7. Comparison of the  $E_p = 46.1$ -MeV angular distribution for the 8.88-MeV state with DWA calculations. See Fig. 5 for details. The calculations using the real interaction of Eq. (6) were indistinguishable for the MSU and UM-UCLA optical-model potentials.

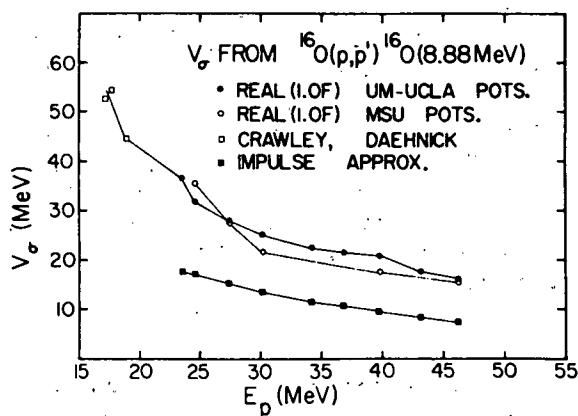


FIG. 8. The strength of the spin-dependent part of the two-nucleon interaction. For details see the text (Sec. III D).

real interaction of Yukawan shape with 1.0 F range which produces the same total cross section as the IA interaction.

#### E. Calculations for the 6.1-MeV Doublet

Calculations were performed at  $E_p = 30.1$  and 46.1 MeV using both the IA pseudopotential and a

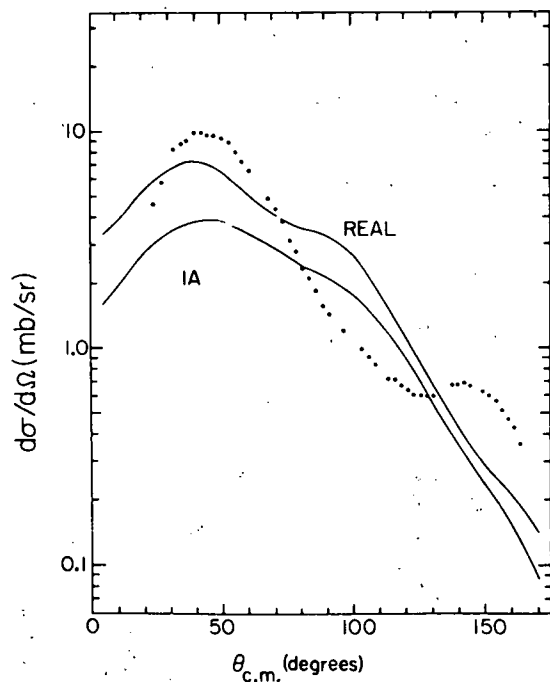


FIG. 9. Comparison of the  $E_p = 30.1$ -MeV angular distribution for the 6.1-MeV doublet with DWA calculations performed assuming only the 6.13-MeV  $3^-$  state has an appreciable cross section. The top curve is for the real interaction of Eq. (6) with  $\alpha = 1.0 \text{ F}^{-1}$  and the bottom curve is calculated with the impulse approximation of Refs. 34 and 35. The UM-UCLA optical-model potentials were used.

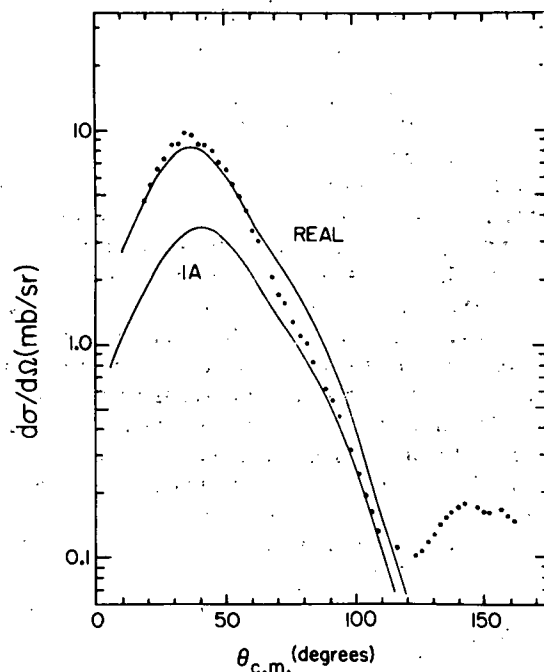


FIG. 10. Comparison of the  $E_p = 46.1$ -MeV angular distribution for the 6.1-MeV doublet with DWA calculations. For details see Fig. 9.

real interaction with the form of Eq. (6). Amplitudes with  $(LSJT) = (3030)$  and  $(3130)$  are allowed by the selection rules. While in principle these amplitudes can add coherently, they are in fact essentially incoherent.<sup>26</sup> The cross section for the  $(3130)$  amplitude was evaluated using the strengths  $V_\sigma$  shown in Fig. 8 and was only 1% of the experimental cross section at 30.1 and 46.1 MeV. The spin-flip amplitude was therefore neglected and the cross sections were calculated using the  $(3030)$  amplitude only. For the real interaction,  $V_C$  was determined by matching the calculated and experimental total cross sections, assuming that the entire experimental cross section was due to the 6.13-MeV  $(3^-)$  state. The results of the analysis are given in Figs. 9 and 10 and in columns 2 and 4 of Table IV.

TABLE IV. Values of  $V_C$  and  $V_{C,eq}$  obtained from the 6.13-MeV angular distributions.  $V_{C,eq}$  is a real potential which predicts the same total cross section as the impulse-approximation effective interaction.

$E_p$ (MeV)	$V_C^a$ (MeV)	$V_C^b$ , corrected (MeV)	$V_{C,eq}^a$ (MeV)
30.1	85	65	67
46.1	74	57	51

<sup>a</sup>For the potential of Eq. (6) with  $\alpha = 1.0 \text{ F}^{-1}$ .

<sup>b</sup>The values in column 3 were obtained by multiplying those of column 2 by  $(1/1.7)^{1/2}$ . See Sec. IV B.

## IV. DISCUSSION

A. 8.88-MeV ( $2^-$ ) Transition

Perhaps the most surprising aspect of the results shown in Figs. 5-8 is the amount by which the IA underestimates the total cross section. At all energies the ratio of the experimental cross section ( $\sigma_{\text{EXP}}$ ) to the IA prediction ( $\sigma_{\text{IA}}$ ) lies in the range  $\sigma_{\text{EXP}}/\sigma_{\text{IA}} = 4.0 \pm 0.7$ . Petrovich *et al.*<sup>34, 35</sup> have shown that the IA accounts for the strong  $S=0$ ,  $T=0$  transitions induced by  $V_{00}$  if one uses wave functions which properly describe the collective properties of the states involved. The IA also predicts the cross sections for transitions induced by  $V_{11}$  to within a factor of 2 at incident energies above 30 MeV.<sup>2</sup> Thus it is somewhat unexpected that the IA fails so badly in this case. In the present calculations space exchange has been neglected. This presumably does not affect the results of the IA calculations, since the IA pseudopotential was obtained<sup>34, 35</sup> from a nucleon-nucleon scattering amplitude which was calculated including exchange of the two nucleons. Petrovich<sup>35</sup> has shown that this treatment is approximately equivalent to using a potential which fits the nucleon-nucleon scattering and including exchange effects in the DWA calculation.

Another unexpected result is that the fits deteriorate at the higher energies where one would expect the DWA to reproduce more closely the experimental data. The predicted peak in the cross section occurs at smaller angles than the observed peak. In the next few paragraphs we discuss the sensitivity of the calculations to changes in the parameters of the model in an attempt to understand these discrepancies.

Since it is known<sup>14</sup> that the RPA wave functions used in the present calculations do not provide a particularly good description of the  $2^-$  state, we have investigated the sensitivity of the predictions to the less important configurations in the wave functions. Calculations were made at 30.1 MeV in which the wave functions of Gillet and Vinh Mau<sup>14</sup> were replaced by wave functions containing only the dominant configuration,  $(1p_{1/2}^{-1}, 1d_{5/2})$ . The resulting cross section is indistinguishable in shape from that calculated using the complete wave functions but is larger in magnitude by a factor of 1.42. This is in contrast to the case of  $S=T=0$  transitions which are strongly enhanced by the less important configurations in the wave function. If the same effect is assumed at all energies, the use of the simple wave functions defined above would reduce  $\sigma_{\text{EXP}}/\sigma_{\text{IA}}$  to  $2.8 \pm 0.5$  and reduce the values of  $V_0$  of Fig. 8 by a factor of  $1.42^{1/2}$ .

Calculations were performed with the range given

by  $\alpha^{-1} = 0.7 \text{ F}$  and  $\alpha^{-1} = 1.4 \text{ F}$  to compare with the standard calculations for which  $\alpha^{-1} = 1.0 \text{ F}$ . The results at 46.1 MeV are shown in Fig. 11. It is clear that reasonable changes in  $\alpha^{-1}$  cannot account for the observed behavior of the cross section. The results shown in Fig. 11, as well as a similar calculation at 27.3 MeV, permit a determination of a scaling relationship for  $V_0$  as a function of  $\alpha^{-1}$  in the range 0.7-1.4 F, which can be expressed as

$$V_0(\alpha)/V_0(\alpha') = (\alpha/\alpha')^{2.4}.$$

This result applies only to the reaction considered here.

Calculations were also performed at 30.1 MeV with the harmonic-oscillator parameter set equal to 2.13 and 1.49 F for comparison with the results for the canonical value of  $a = 1.76 \text{ F}$ . The angular distribution did not change significantly except that for a value of  $a = 2.13 \text{ F}$  a subsidiary peak developed near  $20^\circ$ . The total cross section at these extreme values of  $a$  changed by  $-11\%$  (2.13 F) and  $+15\%$  (1.49 F).

Finally, there are changes associated with different optical-model potentials. As can be seen from Figs. 5-8, the shapes of the angular distributions are weakly affected by changes in potentials which are consistent with the elastic scattering data. However, the total cross sections change by as much as 30%. Because the spin-orbit potentials are probably the least accurately de-

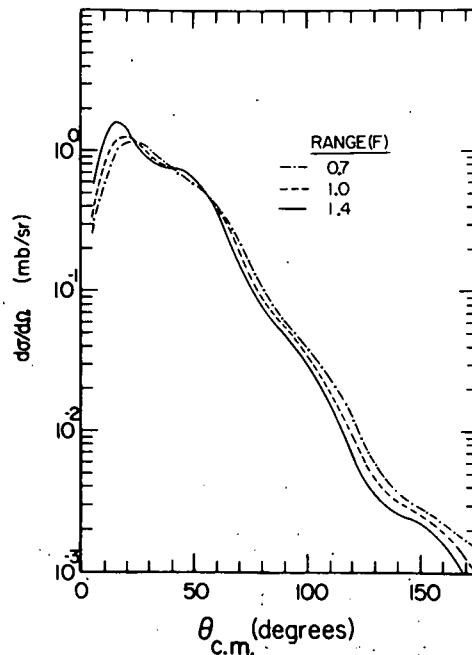


FIG. 11. DWA calculations for the 8.88-MeV state with several values of the range  $\alpha^{-1}$  of  $V_{10}$ .

TABLE V. Values of  $V_0$  from  $(p, p')$  reactions.

Target	Final state (MeV)	$E_p$ (MeV)	Interaction	$V_0^a$ (MeV)
$^{16}\text{O}^b$	$2^-, 8.88$	17.5	$V_0$	53
$^{32}\text{S}^b$	$1^+, 4.70$	17.5	$V_0$	53
$^{89}\text{Y}^c$	$\frac{3}{2}^-, 1.51$	24.5	$V_0 + V_{\sigma r}$	<23
$^{89}\text{Y}^d$	$\frac{3}{2}^+, 0.908$	61.2	$V_0 + V_{\sigma r}$	$\approx 7$
$^{89}\text{Y}^d$	$\frac{3}{2}^-, 1.51$	61.2	$V_0 + V_{\sigma r}$	<12
$^{208}\text{Pb}^e$	$4^-, 3.475$	61.2	$V_0 - V_{\sigma r}$	23.5
$1p$ shell <sup>f</sup>				15.6
$2s-1d$ shell <sup>f</sup>				23.3

<sup>a</sup>For  $\alpha^{-1} = 1.0$  F.

<sup>b</sup>Data of Ref. 25 as analyzed in Ref. 9.  $V_0$  was converted from the value for a 1.7-F Gaussian shape (Ref. 9) to a 1.0-F Yukawa shape by requiring that the volume integrals be equal.

<sup>c</sup>See Ref. 12.

<sup>d</sup>See Ref. 13.

<sup>e</sup>See Ref. 10.

<sup>f</sup>See Ref. 40.

terminated part of the optical-model potentials, calculations have been performed with  $V_s = 0.0$  MeV. At 46.1 MeV the shape is changed only slightly and the total cross section is decreased by 19%. One can conclude that reasonable changes in the parameters do not explain the discrepancy in either the shapes of the angular distributions at the higher energies or in the magnitude of the total cross section.

Other values of  $V_0$  from the literature are listed in Table V. In some of these cases the cross section is sensitive to  $V_{10} \pm V_{11}$ . To obtain the values of  $V_0$  shown in column 5, the strength of  $V_{11}$  ( $V_{\sigma r}$ ) is set equal to 13 MeV. The relative signs of  $V_{10}$  and  $V_{11}$  have not yet been fixed by experiment and the signs chosen here are the prediction of the IA.<sup>33-36</sup> The last two rows in the table contain results obtained by Schmittroth<sup>40</sup> from shell-model calculations for the  $1p$  and  $2s-1d$  shells.

#### B. 6.13-MeV ( $3^-$ ) Transition

The shapes of the calculated angular distributions match the data rather poorly at 30.1 MeV, but at 46.1 MeV the agreement is reasonably good. The agreement improves because of the change in the shape of the calculated angular distributions, since the shapes of the experimental angular distributions remain almost constant over this energy range.

The ratio  $\sigma_{\text{EXP}}/\sigma_{\text{IA}}$  equals 1.6 at 30.1 MeV and 2.1 at 46.1 MeV. At 46.1 MeV the shapes of the experimental and theoretical angular distributions agree well enough that a normalization to the peak in the differential cross section at  $35^\circ$  c.m. is reasonable [ $\sigma_{\text{EXP}}(\text{peak})/\sigma_{\text{IA}}(\text{peak}) = 2.7$ ]. Recently

Bergstrom *et al.*<sup>41</sup> have compared their inelastic electron scattering data for the 6.13-MeV state to differential cross sections obtained by Gillet and Melkanoff<sup>42</sup> with the same RPA wave functions as used in the present analysis. The measured cross sections exceed the predictions by a factor of about 1.7 for the entire range of momentum transfers ( $q$ ).

Since the discrepancy is independent of  $q$ , one can conclude that the radial transition density<sup>42</sup> is too small by a factor of  $(1.7)^{1/2}$ . The same transition density also appears in the expression for inelastic proton scattering<sup>35</sup> and contains all the important nuclear-structure information. Thus, one can correct for the inadequacy of the wave functions used in the present analysis by multiplying the DWA cross sections by 1.7.

Applying this correction to the IA prediction yields  $\sigma_{\text{EXP}}(\text{peak})/\sigma_{\text{IA}}(\text{peak}) = 1.6$ . Since the cross section is proportional to the square of the strength of the interaction, the IA gives the strength of the effective interaction to within 25% at  $E_p = 46.1$  MeV. If one compares total instead of peak cross sections, with this correction the strength of the IA effective interaction is correct within 11% at  $E_p = 30.1$  and 46.1 MeV. The values for the strength of the real interaction corrected in the same way are given in column 3 of Table IV.

As was noted above, space exchange is approximately included in the IA calculations, but it is neglected in the calculations with the real force of Eq. (6). It has been found<sup>33</sup> that the inclusion of exchange processes enhances the cross section for the  $^{12}\text{C}(p, p')^{12}\text{C}$  (9.64 MeV,  $3^-$ ) reaction at  $E_p = 45.5$  MeV by a factor of 4. A similar enhancement is expected in the present case, since the states have the same quantum numbers and roughly the same shell-model orbits. Thus it is likely that the strengths in Table IV would be reduced by about a factor of 2 if exchange were included in the DWA calculation.

#### C. Energy Dependence of Total Cross Sections

As previously noted the total cross section for the 8.88-MeV transition decreases much more rapidly with increasing incident proton energy than does the total cross section for the 6.13-MeV transition. Below 30 MeV it is reasonable to attribute this behavior to the decreasing importance of compound-nucleus formation. At the higher energies, however, direct-reaction processes predominate and a more attractive explanation is contained in the observation of Petrovich<sup>43</sup> that the cross section for a transition will decrease rapidly with increasing energy if the transition is mediated by a long-range force. An explanation of the observed



behavior is that  $V_{10}$  has a longer range than  $V_{00}$ . The spin-dependent part of the free nucleon-nucleon force also appears to have a long range, since  $V_{10}$  is the most rapidly varying part of the IA pseudopotential<sup>34</sup> which was derived from the Hamada-Johnston<sup>44</sup> potential (see Table III). This rapid energy dependence is evident in Fig. 8 where the IA prediction of  $V_{10}$ , while too small, decreases even more rapidly than the experimentally determined value of  $V_{10}$ .

It is the rapid decrease in the exchange part of the cross section which accounts for most of the decrease in the cross section with increasing energy.<sup>43</sup> Since the present calculation neglects exchange, one expects to find that  $V_0$  also decreases. This is consistent with the data shown in Fig. 8, but it is not clear how much of the observed decrease can be attributed to this effect.

#### D. Other Reaction Mechanisms

In the analysis of Sec. III it was assumed that the reaction was dominated by the direct spin-flip process. However, the  $^{16}\text{O}(\alpha, \alpha')^{16}\text{O}$  reaction is observed to populate the  $2^-$  state<sup>16</sup> and since spin-flip cannot occur for spin-zero particles, other reaction processes must exist which may contribute to the  $(p, p')$  cross sections discussed here. These processes can include<sup>16</sup> (i) processes induced by a tensor interaction or by a spin-orbit interaction between the orbital angular momentum of the incident particle and the spin of the valence nucleons of the target, (ii) space-exchange processes in which  $L$  need not satisfy the selection rule  $\Delta\pi = (-1)^L$ , (iii) compound-nucleus formation, and (iv) multiple-excitation processes in which the excitation proceeds through an intermediate state which is strongly excited by inelastic scattering [presumably the 6.13-MeV ( $3^-$ ) state for  $^{16}\text{O}$ ].

There are no calculations of the first two effects relevant to  $^{16}\text{O}$ , but it appears likely<sup>16, 40, 45</sup> that these effects do not strongly influence the cross section. Compound-nucleus formation is probably important in  $^{16}\text{O}(\alpha, \alpha')^{16}\text{O}$  (8.88 MeV,  $2^-$ ), since the cross section has rapid irregular variations in both shape and magnitude up to at least  $E_\alpha = 42$  MeV.<sup>46</sup> As has been noted above, compound-nuclear effects are not observed in  $^{16}\text{O}(p, p')$  above  $E_p = 30$  MeV.

It has been argued<sup>28, 47</sup> that if a cross section decreases rapidly with increasing energy as is observed for the 8.88-MeV transition, it is an indication that second-order processes are important. It was not possible to test this argument for  $^{16}\text{O}$ , since available coupled-channels codes assume a collective model for the wave functions of the nuclear states and such wave functions do not properly

describe the states involved. However, cross sections are available for the  $^{24}\text{Mg}(\alpha, \alpha')^{24}\text{Mg}$  (5.22 MeV,  $3^+$ ) reaction at  $E_\alpha = 50.0, 65.7, 81.0,$  and  $119.7$  MeV.<sup>48</sup> The cross sections leading to the  $3^+$  unnatural-parity state are well explained by a multiple-excitation process.<sup>48</sup> The differential cross sections for the 5.22-MeV transition and for the transition to the strongly excited  $2^+$  state at 1.369 MeV have been integrated and the ratio  $\sigma(5.22)/\sigma(1.369)$  decreases slightly less than a factor of 2 between 50.0 and 119.7 MeV. The ratio  $\sigma(8.88)/\sigma(6.13)$  for  $^{16}\text{O}$  decreases about four times more rapidly for proton energies between 30.1 and 46.1 MeV. Thus, it appears that multiple-excitation processes do not necessarily cause a rapidly decreasing cross section and in the case of  $^{16}\text{O}(p, p')$ - $^{16}\text{O}$  (8.88 MeV,  $2^-$ ) one may interpret the observed decrease as a further manifestation of the long range of  $V_{10}$ .

Evidence that different processes are responsible for the  $^{16}\text{O}(p, p')^{16}\text{O}$  (8.88-MeV,  $2^-$ ) cross section and the cross sections for  $(\alpha, \alpha')$  leading to unnatural-parity states in  $^{16}\text{O}$  (8.88 MeV,  $2^-$ ),  $^{20}\text{Ne}$  (4.97 MeV,  $2^-$ ), and  $^{24}\text{Mg}$  (5.22 MeV,  $3^+$ ) appears when one plots the cross sections as a function of momentum transfer. The  $(\alpha, \alpha')$  cross sections are found to vary irregularly as the energy is changed,<sup>48</sup> while the  $(p, p')$  cross sections have essentially identical shapes above 30.1 MeV as one expects for a direct process.

A possible experimental evaluation of the importance of processes which do not proceed through spin-flip would be recorded only those  $^{16}\text{O}(p, p')$ - $^{16}\text{O}$  ( $2^-, 8.88$ -MeV) events which are in coincidence with an 8.88-MeV deexcitation  $\gamma$  ray emitted at  $90^\circ$  to the reaction plane. Such events correspond to no-spin-flip in the total process,<sup>49</sup> so that if one could disentangle the spin-flipping effects of the optical-model potential, one would have a measure of the  $S = 0$  part of the cross section. Unfortunately, the  $\gamma$ -ray branch to the ground state is only about 7% of the total decays<sup>50</sup> so the experiment would be difficult.

#### V. SUMMARY

The cross sections for inelastic proton scattering to the 6.13-MeV ( $3^-$ ) and 8.88-MeV ( $2^-$ ) states of  $^{16}\text{O}$  have been measured at nine energies between 23.4 and 46.1 MeV. The measured cross sections have been compared with a microscopic model of the reaction using both IA and real interactions. The IA predictions are too small by a factor of about 4 for the spin-flip transition to the  $2^-$  state if RPA wave functions are used to describe the state. The cross sections for the RPA wave functions are smaller by a factor of 1.42 than

those calculated with a simple ( $1p_{1/2}^{-1}, 1d_{5/2}$ ) configuration. The strength of the real interaction with a 1.0-F range was obtained by normalizing to the experimental total cross sections and was found to decrease from 23 MeV at  $E_p = 30.1$  MeV to 16 MeV at  $E_p = 46.1$  MeV. The rapid decrease of the cross section for excitation of the  $2^-$  state with increasing energy was interpreted as an indication that the spin-dependent interaction  $V_{10}$  has a long range.

The shape of the angular distribution for the 6.13-MeV transition is fairly well described by the IA at 46.1 MeV but not at 30.1 MeV. However, at both energies the magnitude of the IA cross section is too small by about a factor of 2. Part of this discrepancy can be attributed to deficiencies in the RPA wave functions, since the predicted electron scattering cross sections are also too small. One can conclude that the IA pseudopotential describes the effective interaction within

10–25% depending on whether one fits the total or peak cross sections.

It is possible that small changes in the details of the calculation could improve the present somewhat unsatisfactory fits to the data. However, any interpretation must be tentative until a proper coupled-channels calculation is performed.

## VI. ACKNOWLEDGMENTS

We would like to thank D. C. Larson for performing some of the DWA calculations and F. Petrovich for illuminating discussions. The calculations involved in analyzing the experimental data were performed using the computing facilities of the University of California, Los Angeles, Campus Computer Network and the University of Manitoba Institute for Computer Studies. One of the authors (SMA) wishes to thank the Aspen Center for Physics for its hospitality.

\*Research supported in part by the National Science Foundation.

†Present address: Centre d'Études Nucléaires de Grenoble, Grenoble, France.

‡Present address: Department of Physics, University of Manitoba, Winnipeg, Canada.

§Present address: Department of Physics, University of Washington, Seattle, Washington 98105.

||Research supported in part by the U. S. Atomic Energy Commission, Contract No. AT(11-1)-GEN 10 P. A. 18.

\*\*Research supported in part by the Atomic Energy Control Board of Canada.

<sup>1</sup>G. R. Satchler, Nucl. Phys. **77**, 481 (1966); V. A. Madsen, *ibid.* **80**, 177 (1966); N. K. Glendenning and M. Veneroni, Phys. Rev. **144**, 839 (1966).

<sup>2</sup>S. M. Austin, P. J. Locard, W. Benenson, and G. M. Crawley, Phys. Rev. **176**, 1227 (1968).

<sup>3</sup>P. J. Locard, S. M. Austin, and W. Benenson, Phys. Rev. Letters **19**, 1141 (1967).

<sup>4</sup>J. D. Anderson, S. D. Bloom, C. Wong, W. F. Hornyak, and V. A. Madsen, Phys. Rev. **177**, 1416 (1969).

<sup>5</sup>G. C. Ball and J. Cerny, Phys. Rev. **177**, 1466 (1969).

<sup>6</sup>A. S. Clough, C. J. Batty, B. E. Bonner, C. Tschälar, L. E. Williams, and E. Friedman, Nucl. Phys. **A137**, 222 (1969).

<sup>7</sup>J. D. Anderson, C. Wong, and V. A. Madsen, private communication.

<sup>8</sup>G. R. Satchler, Nucl. Phys. **A95**, 1 (1967).

<sup>9</sup>R. Reif, J. Slotta, and J. Höhn, Phys. Letters **26B**, 484 (1968); and private communication.

<sup>10</sup>A. Scott, N. P. Mathur, and G. R. Satchler, to be published.

<sup>11</sup>Y. Awaya, J. Phys. Soc. Japan **23**, 673 (1967).

<sup>12</sup>W. Benenson, S. M. Austin, R. A. Paddock, and W. G. Love, Phys. Rev. **176**, 1268 (1968).

<sup>13</sup>A. Scott, M. L. Whiten, and W. G. Love, Nucl. Phys. **A137**, 445 (1969).

<sup>14</sup>V. Gillet and N. Vinh Mau, Nucl. Phys. **54**, 321 (1964).

<sup>15</sup>H. Appel, S. N. Bunker, J. M. Cameron, M. B. Epstein, J. R. Quinn, J. R. Richardson, and J. W. Verba, Bull. Am. Phys. Soc. **13**, 680 (1968); S. N. Bunker, H. Appel, J. M. Cameron, M. B. Epstein, J. R. Quinn, J. R. Richardson, and J. W. Verba, Bull. Am. Phys. Soc. **14**, 529 (1969); S. N. Bunker, Ph.D. thesis, University of California, Los Angeles, California, 1970 (unpublished).

<sup>16</sup>The strongest indication of the possibility of multiple-excitation processes is the excitation of the 8.88-MeV state by inelastic  $\alpha$  scattering; see, for example, W. W. Eidson and J. G. Cramer, Jr., Phys. Rev. Letters **9**, 497 (1962).

<sup>17</sup>J. M. Cameron, J. R. Richardson, W. T. H. van Oers, and J. W. Verba, Phys. Rev. **167**, 908 (1968).

<sup>18</sup>Kapton H film made by E. I. DuPont de Nemours, Wilmington, Delaware.

<sup>19</sup>T. Lauritsen and F. Ajzenberg-Selove, in *Nuclear Data Sheets*, compiled by K. Way *et al.* (Printing and Publishing Office, National Academy of Sciences - National Research Council, Washington, D. C., 1962), Sets 5 and 6; C. P. Browne and I. Michael, Phys. Rev. **134**, B133 (1964); J. D. Larson and T. A. Tombrello, Phys. Rev. **147**, 760 (1966).

<sup>20</sup>W. F. Hornyak and R. Sherr, Phys. Rev. **100**, 1409 (1955).

<sup>21</sup>L. H. Johnston, D. H. Service, and D. A. Swenson, IRE Trans. Nucl. Sci. **NS5**, 95 (1958); D. F. Measday, Nucl. Instr. Methods **34**, 353 (1965); D. F. Measday and C. Richard-Serre, *ibid.* **76**, 45 (1969); J. N. Palmieri and J. Wolfe, *ibid.* **76**, 55 (1969).

<sup>22</sup>E. A. Silverstein, Nucl. Instr. Methods **4**, 53 (1959).

<sup>23</sup>B. M. Bardin and M. E. Rickey, Rev. Sci. Instr. **35**, 902 (1964); R. Smythe, *ibid.* **35**, 1197 (1964).

<sup>24</sup>W. W. Daehnick, Phys. Rev. **135**, B1168 (1964).

<sup>25</sup>G. M. Crawley and G. T. Garvey, Phys. Rev. **160**,

981 (1967).

<sup>26</sup>D. C. Larson and D. Bayer, private communication.

<sup>27</sup>D. J. Rowe, A. B. Clegg, G. L. Salmon, and P. S. Fisher. Proc. Phys. Soc. (London) **80**, 1205 (1962).

<sup>28</sup>W. Benenson and G. M. Crawley, Bull. Am. Phys. Soc. **11**, 477 (1966).

<sup>29</sup>H. B. Eldridge, S. N. Bunker, J. M. Cameron, J. R. Richardson, and W. T. H. van Oers, Phys. Rev. **167**, 915 (1969); E. T. Boschitz, M. Chabré, H. E. Conzett, and R. J. Slobodrian, in *Proceedings of the Second International Symposium on the Polarization Phenomena of Nucleons, Karlsruhe, 1965*, edited by P. Huber and H. Schopper (Birkhäuser Verlag, Stuttgart, Germany, 1966), p. 331.

<sup>30</sup>W. T. H. van Oers and J. M. Cameron, Phys. Rev. **184**, 1061 (1969).

<sup>31</sup>G. R. Satchler, Nucl. Phys. **A100**, 497 (1967).

<sup>32</sup>J. L. Snelgrove and E. Kashy, Phys. Rev. **187**, 1246 (1969).

<sup>33</sup>F. Petrovich, H. McManus, V. A. Madsen, and J. Atkinson, Phys. Rev. Letters **22**, 895 (1969).

<sup>34</sup>F. Petrovich, D. Slanina, and H. McManus, Michigan State University Report No. MSPT-103, 1967 (unpublished).

<sup>35</sup>F. Petrovich, Ph.D. thesis, Michigan State University, 1970 (unpublished).

<sup>36</sup>F. Petrovich, H. McManus, and J. R. Borysowicz, to

be published.

<sup>37</sup>L. R. B. Elton, *Nuclear Sizes* (Oxford University Press, New York, 1961).

<sup>38</sup>This code was written by R. Haybron and T. Tamura and was modified for the Sigma 7 computer by J. J. Kollata.

<sup>39</sup>G. M. Crawley, private communication.

<sup>40</sup>F. A. Schmittroth, Ph.D. thesis, Oregon State University, 1969 (unpublished).

<sup>41</sup>J. C. Bergstrom, W. Bertozzi, S. Kowalski, X. K. Maruyama, J. W. Lightbody, Jr., S. P. Fivozinsky, and S. Penner, Phys. Rev. Letters **24**, 152 (1970).

<sup>42</sup>V. Gillet and M. A. Melkanoff, Phys. Rev. **133**, B1190 (1964).

<sup>43</sup>F. Petrovich, private communication.

<sup>44</sup>T. Hamada and I. D. Johnston, Nucl. Phys. **34**, 382 (1962).

<sup>45</sup>J. Atkinson and V. A. Madsen, Phys. Rev. C **1**, 1377 (1970).

<sup>46</sup>J. S. Blair, N. Cue, and D. Shreve, University of Washington Annual Report, 1965 (unpublished).

<sup>47</sup>H. McManus, private communication.

<sup>48</sup>M. Reed, Ph.D. thesis, University of California, Berkeley, Report No. UCRL-18414, 1968 (unpublished).

<sup>49</sup>A. Galonsky, private communication.

<sup>50</sup>F. Ajzenberg-Selove and T. Lauritsen, Nucl. Phys. **11**, 1 (1959).

DETERMINATION OF TRACE ELEMENTS IN SAMPLES \*  
BY NUCLEAR SCATTERING AND REACTION TECHNIQUES

R.K. Jolly, C.R. Gruhn, and C. Maggiore \*\*  
Cyclotron Laboratory, Michigan State University  
East Lansing, Michigan 48823

SUMMARY

The feasibility of using low energy (15-25 MeV)  $\alpha$ -particle scattering for detecting traces of heavy elements in a bulk of light elements as, for example, in biological and environmental matter is explored. These measurements can provide information on all the elements in the sample simultaneously. Heavy elements require good energy resolution ( $\sim 10$  keV) for definite identification while light elements can be identified even with very poor energy resolution ( $\sim 100$  keV). Results of some measurements on a fish sample are presented.

Similarly sub-Coulomb (p, $\alpha$ ) reactions are explored for measuring traces of very light elements in a bulk of heavy elements. Suitable choice of bombarding energy almost completely suppresses the contribution from the heavy element. Results of a measurement in a very pure Zr sample are presented.

INTRODUCTION

Nuclear scattering and reaction techniques are proposed to measure the detailed elemental composition of biological, environmental, geological and metallurgical materials. The scattering technique is particularly suited for measuring traces (from parts per million to parts per billion) of heavy elements like copper, arsenic, strontium, mercury, lead, etc. in biological and environmental matter. Unlike the conventional analytical techniques, a high resolution scattering experiment is capable of providing a simultaneous determination of all the elements (and even their isotopic composition) in a given sample. As a result the technique can also be of value in crime investigation, analysis of metallurgical, geological and mineral ore samples. Similarly sub-Coulomb (p, $\alpha$ ) reactions on samples composed largely of heavy mass nuclei are proposed to measure traces of ( $\sim 1$  part per million) light mass impurities in such samples. This technique is particularly suited for analysing metallurgical or solid state samples where the physical properties of solids can be appreciably altered by the presence of various light mass impurities.

A brief description of the proposed techniques, details of feasibility calculations, some preliminary measurements of mercury pollution in fish, of light mass impurities in an enriched zirconium sample and development of techniques of sample preparation and analysis are presented in the following sections.

\* Work supported by the National Science Foundation.

\*\* Present address: Mt. Sinai School of Medicine, New York, New York.

A. NUCLEAR SCATTERING

Nuclear scattering techniques have been used in the past to determine the elemental components of a sample.<sup>1</sup> However, with the current availability of high efficiency and energy resolution analysing magnets, it has become possible to perform these elemental analyses to a much greater precision and detail. With some development effort it is quite feasible to separately identify even the neighboring isotopes in the heaviest stable elements in the periodic table. With such a capability, it seems conceivable to identify and precisely measure any element in a given sample.

I. Some Basics of Nuclear Scattering Measurements

In the nuclear scattering process, the sample to be analysed is bombarded by projectiles of mass  $m$  and energy  $E_{inc}$ . After an elastic collision with an atomic nucleus of mass  $A$  in the sample, the energy of the particles scattered at  $90^\circ$  (chosen for the sake of simplicity) can be written as

$$\frac{E_{scatt}}{E_{inc}} = \frac{A-m}{A+m} \quad (1)$$

for non-relativistic particles. A plot of  $E_{scatt}/E_{inc}$  both for protons ( $m=1$ ) and  $\alpha$ -particles ( $m=4$ ) is shown in Fig. 1 for atomic nuclei of different masses and for different scattering angles. It is clear that  $E_{scatt}$  can be very different from  $E_{inc}$  particularly for  $\alpha$ -particles scattered from relatively light nuclei at large angles. A measure of the sensitivity of a nuclear scattering measurement for separating nuclei of different masses is the mass resolution. This can be defined as the rate of change of  $E_{scatt}$  with  $A$  and for scattering at  $90^\circ$  can be written as

$$\frac{\Delta E_{scatt}}{E_{inc}} = \frac{2m}{(A+m)^2} \quad (2)$$

Here  $\Delta E_{scatt}$  is the energy resolution required to distinguish between two nuclei that differ by  $dA=1$  mass unit. The following table gives values of  $dE_{scatt}$  for both protons and  $\alpha$ -particles of  $E_{inc}=20$  MeV for  $A=25, 50, 100,$  and  $200$  a.m.u. and at  $\theta=40^\circ, 80^\circ,$  and  $120^\circ$ .

TABLE I

Energy Resolution  $\Delta E$ (keV) required for 1 a.m.u. mass resolution for different  $A$  and  $E_{inc}=20$  MeV

	Protons			$\alpha$ -particles		
	120°	80°	40°	120°	80°	40°
A= 25	83	48	14	236	160	54
A= 50	23	12	3.7	75	46	14
A=100	6	3.5	0.9	21	12	3.7
A=200	1.5	0.9	0.23	5.7	3.2	0.9

It is apparent that the energy resolution requirements for protons are three to four times as stringent as those for  $\alpha$ -particles of the same energy. The energy resolution capabilities of modern low-energy nuclear scattering facilities are typically

$$\frac{1}{5 \times 10^3} \text{ which means } \Delta E = 4 \text{ keV for } 20 \text{ MeV}$$

particles. For  $\alpha$ -particles this is quite adequate for resolving neighboring isotopes at  $A=200$  and  $\theta > 120^\circ$  even after allowing  $\sim 5$  keV contribution to energy resolution from target thickness effects.

Another distinct advantage that  $\alpha$ -particles offer over protons is the virtual absence of any inelastic scattering even at large angles when measurements are made near or below the Coulomb barrier for any nucleus. 20 MeV  $\alpha$ -particles are below or near the Coulomb barrier for all elements of  $A > 160$ .

The disadvantage in the choice of  $\alpha$ -particles is that their specific energy loss,  $\frac{dE}{dx}$ , in all materials is  $\sim 10$  times that for protons of the same energy (20 MeV). (The situation is much worse in the case of heavier ions like  $^{16}\text{O}$ . This fact together with the lack of availability of heavy ion beams of sufficient intensity and techniques for detecting heavy ions with good energy resolution has led the authors to abandon the exploration of heavy ions for use in the present measurements.) This means that the thickness of the sample and therefore, the yield (purely for target thickness standpoint) will be smaller by a factor of ten to maintain the same energy loss as in the case of protons so that the overall energy resolution is the same in both cases. The yield, however, also depends on the scattering cross-sections which have been compared for  $\sim 20$  MeV  $\alpha$ -particles<sup>2</sup> and protons<sup>3</sup> in Table II for nuclei of masses  $A=60, 120, \text{ and } 208$ . For heavy elements (e.g.  $A=120$  and  $208$ ), measurements have to be made at large angles (e.g.  $\theta=80^\circ$  or  $120^\circ$ ) to resolve neighboring elements (see Table I). For lighter elements (e.g.  $A=60$ ) however measurements can be made at small angles (e.g.  $\theta=40^\circ$ ) without sacrificing the necessary mass resolution [(2) and Table I] in the light element mass region and with a considerable gain in the scattering cross-section (Table II). It is apparent from an examination of Table II that the  $\alpha$ -particle scattering cross-sections are considerably larger than those for protons in the measurement situations described above. In the circled cases in Table II appropriate to the discussion above, the loss in yield due to target thickness is more than compensated for by the gain in the scattering cross-section achieved by the use of  $\alpha$ -particles except in the case of  $A=60$  and  $\theta=40^\circ$  where the increase in cross-section does not quite offset the loss in yield due to target thickness.

TABLE II

Differential Scattering Cross-Sections (mb/sr) for 20 MeV  $\alpha$ -particles and Protons

	$\theta=40^\circ$		$\theta=80^\circ$		$\theta=120^\circ$	
	$\alpha$ -par- ticles	Pro- tons	$\alpha$ -par- ticles	Pro- tons	$\alpha$ -par- ticles	Pro- tons
A=60	366	130	5.9	20	0.9	5.0
A=120	2920	100	117	5.0	7.2	1.8
A=208	5800	500	470	40	99	4.0

From the above discussion a procedure that suggests itself for a routine analysis of samples is to first measure a mass spectrum at a small angle e.g.  $40^\circ$  for 20 MeV  $\alpha$ -particles, which will reveal mass components lighter than e.g.  $A=80$  well resolved and heavier components somewhat poorly resolved, and then make a second measurement at a large angle to resolve the heavy components seen in the small angle measurements.

Another factor that needs consideration in the choice of  $\alpha$ -particles is the kinematic broadening of monoenergetic  $\alpha$ -particle "lines" after scattering from a light atomic nucleus. This is due to the finite angular acceptance of the detection system. Thus, when large solid angles are to be used, some cancellation of kinematic broadening is necessary and is achieved by using a magnetic spectrometer.<sup>4</sup>

The largest solid angle that has been used with adequate kinematic compensation on the Enge split-pole spectrometer in the Michigan State University Cyclotron Laboratory is  $4 \times 10^{-3}$ sr. Table III shows the number of counts/hr. for an organic target of thickness  $40 \mu\text{g}/\text{cm}^2$  (compatible with the desired mass resolution of  $\Delta A=1$  at  $A=200$  for  $\theta=120^\circ$ ) and an impurity of mass= $A$  and fractional atomic abundance  $10^{-6}$ . The scattering cross-sections used are taken from Table II. A greater beam intensity will obviously speed up the rate of data acquisition (a fast rotating target<sup>5</sup> can withstand beam intensities  $\gg 1 \mu\text{A}$ ). Table I shows that for  $\Delta A=1$  at  $A=200$ ,  $\theta$  has to be  $> 120^\circ$ . This means that several heavy elements of abundance  $10^{-6}$  can be resolved and measured in a few hours. (This is on the assumption that depending on the number of dominant isotopes in an element, 10-50 events are required to identify an element from the natural abundance pattern of its isotopes.) If only a few isolated heavy mass impurities are present (as is usually the case, the requirement of  $\Delta A=1$  at  $A=200$  can be

TABLE III

Count Rate/hr for an Impurity of mass= $A$ , Abundance= $10^{-6}$  in an Organic Matter (Avg.  $A=10$ ) Target (Thickness= $40 \mu\text{g}/\text{cm}^2$ ) for 20 MeV  $^4\text{He}^{++}$  Beam; Intensity= $1.0 \mu\text{A}$ ; Solid Angle= $4 \times 10^{-3}$ sr.

	$\theta_{\text{LAB}}=40^\circ$	$80^\circ$	$120^\circ$
A=60	$10^2$	2	0.1
A=120	$8 \times 10^2$	40	1
A=208	$2 \times 10^3$	$2 \times 10^2$	16

relaxed, for example to  $\Delta A=1$  at  $A=75$  and measurements made at  $\theta=40^\circ$  where heavy mass abundances as low as  $10^{-8}$  can be measured in a few hours. Table I indicates that with  $\Delta E \sim 7$  keV a mass resolution of  $\Delta A=1$  at  $A=120$  is possible at  $\theta \sim 60^\circ$ . This result in conjunction

with Table III shows that the lower limit of measureability between  $A=60$  and  $120$  may be set at  $10^{-7}$  to  $10^{-8}$ . Our preliminary measurements show that abundances as low as  $10^{-6}$  can be measured without any detectable interference from the various possible sources of background. It remains to be determined as to how low the impurity abundances have to be before such background becomes a serious limitation. It should be mentioned that in the case of mono-isotopic elements, the limit of detectability may be lowered further by a factor of ten. Also several biological samples contain  $\sim 90\%$  or more water which gets lost upon sample processing, giving one a possible gain of another factor of ten in the lower limit of detectability. In summary, estimates of lower limit of detectability could be set at values between  $10^{-7}$  to  $10^{-10}$  assuming that various sources of background (including contamination or decontamination of the sample by its handling or processing) do not set limits different from those quoted above.

An example of a low mass resolution measurement using a solid state counter at a large angle is shown in Fig. 2. This is the elastic scattering spectrum from a fish target on a thin formvar backing. The low energy resolution in this data is largely due to lack of kinematic compensation and dispersion matching features that are normally available in a magnetic spectrograph. The mass spectrum in Fig. 2 shows several elements well resolved below  $A=40$ . It also shows appreciable impurities in the mass regions  $A=86-90$  and  $A=190-208$ . In this particular measurement we were looking for traces of mercury (avg.  $\Delta A$  200) in the fish sample. To ascertain whether mercury was seen or not in the solid state detector spectrum, a high resolution measurement with a position sensitive detector in an Enge split-pole spectrometer was made at  $\theta=90^\circ$ . A mass calibration was obtained by locating the very well separated elastic groups from  $^{197}\text{Au}$  and  $^{209}\text{Bi}$  from a composite calibration target. With this mass calibration, the fish target (on Formvar backing) was examined for its mercury content. As shown in Fig. 3 ten counts were observed spanning the range of masses for Hg isotopes with a  $20\mu\text{g}/\text{cm}^2$  fish target and a total accumulated charge of  $1500\mu\text{-Coulombs}$ . ( $d\Omega=1.5\times 10^{-3}\text{sr}$ ) [Ten counts in this measurement correspond to an atomic abundance of  $1.4\times 10^{-6}$  or  $0.4\times 10^{-9}\text{gm}$ . of Hg in the target used.] This measurement essentially demonstrates the capability of the scattering technique to measure traces of heavy elements in biological matter. To establish the presence of Hg in fish, carefully controlled measurements are necessary to ensure that Hg was not introduced into the sample accidentally or externally. For example, the Hg detected could be present in the Formvar backing. Such contributions to the elemental spectra from the backing material can be ruled out or subtracted out by measuring the elemental composition of the backing material beforehand. Obviously a more desirable solution is to use a backing material of extremely high purity.

## II. Sample Preparation

Use of  $\alpha$ -particles requires very thin and uniform samples ( $\sim 50\mu\text{g}/\text{cm}^2$ ) to achieve usable mass resolution ( $\Delta A=1-2$ ) at  $A=200$ . For metallurgical samples, techniques of making very

thin films by vacuum evaporation already exist. Similarly techniques for preparing thin targets for matter in a gaseous form have been in use in Nuclear Physics for several years. Biological (plants, animals) and liquid matter however needed a new technique for preparing thin targets for use in  $\alpha$ -scattering measurements. Such a technique has been recently developed in the Michigan State University Cyclotron Laboratory.<sup>6</sup> Targets of thickness much smaller than those needed in the present measurements have been made with this technique. Briefly, the process involves liquidizing the biological sample in a high speed ( $\sim 15,000$  rpm) Waring blender and further breaking down the size of suspended particles in the liquidized sample by immersing an ultrasonic probe in the liquid. Microscopic examination revealed particle sizes between  $5-10\times 10^{-7}\text{cm}$ . A very dilute suspension (in very pure water) of this sonicated sample is then sprayed onto a rotating substrate (e.g. Formvar  $\sim 5\mu\text{g}/\text{cm}^2$ ) by a device called a nebulizer. A nebulizer produces a mist from the diluted solution so fine that the microscopic droplets evaporate immediately upon deposition on the rotating substrate. It is thus possible to deposit a single-particle thickness layer of the suspended solid matter on the substrate. Further development work in this technique is needed to enable a greater reduction in the size of the particles and a greater uniformity thus contributing to an increase in the efficiency of the present scattering measurements without an appreciable loss of resolution.

## B. SUB-COULOMB ( $p,\alpha$ ) REACTIONS TO MEASURE LIGHT MASS IMPURITIES IN A BULK OF HEAVY MASS MATERIAL

### I. Introduction

The ( $p,\alpha$ ) reactions on most nuclei have  $Q$ -values that are either slightly negative or zero. If the incident proton energy is below the Coulomb barrier for the heaviest nuclei in a sample, then the  $\alpha$ -particles will emerge considerably below the Coulomb barrier for the same heavy nuclei. This leads to a practically vanishing cross-section for the heavy nuclei. However, if there are traces of light elements in the bulk of heavy nuclei, both protons and  $\alpha$ -particles may be close to or above the Coulomb barrier for those elements and therefore have their ( $p,\alpha$ ) cross-sections enhanced by several orders of magnitude relative to those for the heavy nuclei. This combined with the fact that in any reaction process (as opposed to the scattering process) the background can be made practically zero, the dynamic range between the lowest and the highest cross-sections may be  $\sim 10^6$  implying that light mass impurity concentrations of  $10^{-6}$  or lower can be measured by this technique with moderate proton beam intensities ( $\sim 1\mu\text{A}$ ). Once again measurement of still lower concentrations can be made possible by use of higher beam intensities and the use of large solid angle detection systems. The ( $p,\alpha$ ) reactions at sub-Coulomb energies for the heavy nuclei, will not detect light mass isotopes that have very large negative  $Q$ -values (e.g.  $^{16}\text{O}$ ). Such cases, however, are rather few and usually

have another isotope (generally of odd A e.g.  $^{170}$ ) with a favorable Q-value so that the amount of the element can be determined from that of the favorable Q-value isotope.

### Results on $^{90}\text{Zr}(p,\alpha)$

An example of such a measurement is shown in Fig. 4 where the (p, $\alpha$ ) spectrum from a 99.9% Zr target (thickness  $200\mu\text{g}/\text{cm}^2$ ;  $d\Omega \approx 5 \times 10^{-4}$  and charge  $-1400\mu\text{Coul.}$ ) containing 97.8%  $^{90}\text{Zr}$  was measured at  $E_p = 7.71\text{-MeV}$ , near the Coulomb barrier for  $^{90}\text{Zr}$  in the entrance channel and  $\approx 6\text{ MeV}$  below the barrier for the most energetic  $\alpha$ -particles from  $^{90}\text{Zr}(p,\alpha)$  in the exit channel. Measurements of (p, $\alpha$ ) spectra were made at  $40^\circ$  and  $90^\circ$  at four energies between 6.57 and 6.78-MeV and also at  $30^\circ$ ,  $60^\circ$  and  $90^\circ$  at 7.71-MeV. In none of the spectra, there is any definite evidence of  $\alpha$ -particles originating from  $^{90}\text{Zr}$  in the target thus indicating the strong inhibition of (p, $\alpha$ ) cross-sections below the Coulomb barrier for Zr or other heavy elements in the sample. But for lighter elements, (notably  $^{27}\text{Al}$ ) where the reaction takes place several MeV above the Coulomb barrier, the number of events is quite measurable despite the fact that these impurities occur in trace quantities ( $^{27}\text{Al} < 0.05\%$ ). Also notice that all four of the low-lying states in  $^{27}\text{Al}(p,\alpha)^{24}\text{Mg}$  have been observed. One can expect a similar situation to exist for the other light elements in the target. Presence of a large number of impurities, therefore, requires a library of low energy (p, $\alpha$ ) data and a large computer to do the complete elemental analysis. It is probably for this reason that the authors have not been able to identify the element(s) corresponding to at least a couple of prominent intensity groups in Fig. 4. In the absence of a library of (p, $\alpha$ ) data and a large computer, the present procedure is perhaps best suited for searching for a few pre-determined) light mass impurities with the aid of good calibration standards. Previously published  $^{27}\text{Al}(p,\alpha)^{24}\text{Mg}$  data<sup>7</sup> was compared with the appropriate intensity groups in Fig. 4 to confirm our assignment of  $^{27}\text{Al}$  as the source of these groups.

As in  $\alpha$ -scattering, measurements of sub-Coulomb (p, $\alpha$ ) reactions also require thin samples for good resolution if the number of light impurities is large. As is perhaps apparent by now, the applicability of this technique is limited to detecting light impurities in the presence of a bulk of heavy nuclei. The sensitivity of this technique decreases as the mass of the light impurity approaches that of the bulk of heavy nuclei.

### C. CONCLUSION

Reliable calibration and control techniques have to be explored before the procedures presented here can be routinely applied. Some examples of such future applications may be found in studies of pollution, crime investigation, geology and mineralogy, biology, metallurgy, solid state physics, etc.

### REFERENCES

1. B.L. Cohen and R.A. Moyer (private communication); also S. Rubin, T. Passel, and L. Bailey, *Anal. Chem.* **29**, 736(1957).
2. J.C. Correlli, E. Bleuler, and D.J. Tendam, *Phys. Rev.* **116**, 1184(1959).

3. C.B. Fulmer, *Phys. Rev.* **125**, 631(1962).
4. H.A. Enge, *Nucl. Instr. and Methods* **49**, 181(1967).
5. Details of the target rotator can be found in D.R. Maxon, R.K. Jolly, and K.C. Knox, *Nucl. Instr. and Methods* **62**, 276(1968).
6. R.K. Jolly (to be published).
7. K.L. Warsh, G.M. Temmer, and R.H. Blieden, *Nuc. Phys.* **44**, 329(1963).

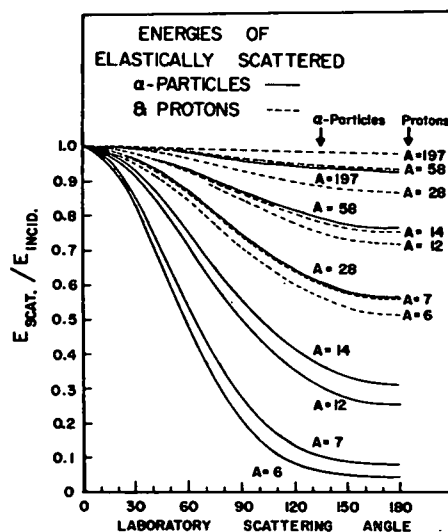


Fig. 1 Comparison of the kinematic energy loss suffered by  $\alpha$ -particles and protons upon scattering at different angles from nuclei of different masses.

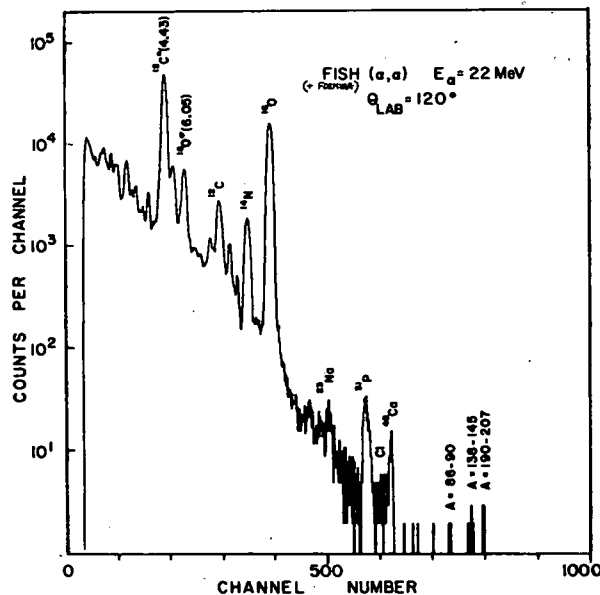


Fig. 2 A low resolution spectrum of 22 MeV  $\alpha$ -particles elastically (and in the case of lighter nuclei even inelastically) scattered from the various elemental constituents of a  $20\mu\text{g}/\text{cm}^2$  fish target on a Formvar backing. The resolution is adequate to resolve all masses below  $A=40$ .

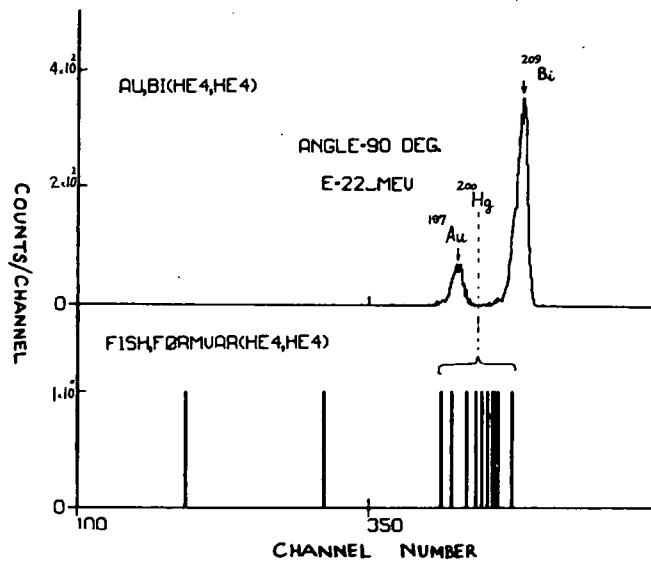


Fig. 3 A high resolution spectrum of elastically scattered  $\alpha$ -particles in the A=190-208 region of Fig. 2. The large intensity groups in the top part are from a composite Au-Bi mass calibration target. The few counts shown in the lower part of this figure are from the fish target used in Fig. 2 and these cover the range of masses for the various Hg isotopes.

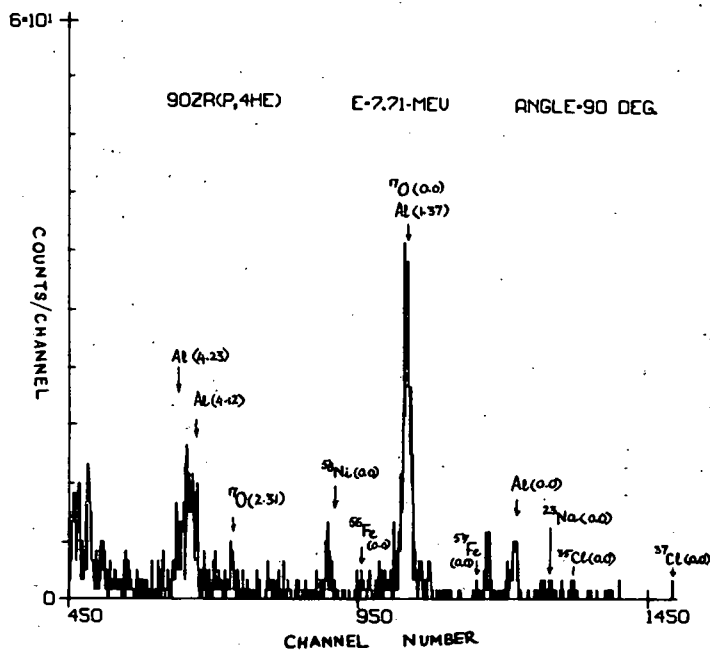


Fig. 4 An  $\alpha$ -particle spectrum from an enriched (97.8%)  $^{90}\text{Zr}$  foil. The names above the various intensity groups indicate the impurity in the sample leading to the ground state or an excited state (energy within parentheses) of the residual nucleus.

3



## SPURIOUS PEAKS PRODUCED BY COMPTON SCATTERING IN Ge(Li) - Ge(Li) COINCIDENCE GAMMA-RAY SPECTROMETER SYSTEMS

G. C. GIESLER, Wm. C. McHARRIS and R. A. WARNER

*Department of Chemistry\* and Cyclotron Laboratory†, Department of Physics, Michigan State University,  
East Lansing, Michigan, U.S.A.*

and

W. H. KELLY

*Cyclotron Laboratory†, Department of Physics, Michigan State University, East Lansing, Michigan, U.S.A.*

Received 17 July 1970

We present results from our investigations of Compton scattering between Ge(Li)  $\gamma$ -ray detectors in coincidence experiments. Such scattering can generate false peaks that can be mistaken for photopeaks. The effects of varying gate position, gate width,

background subtraction, and angle between detectors are discussed, and suggestions are made for recognizing and minimizing spurious effects.

### 1. Introduction

In  $\gamma$ - $\gamma$  coincidence spectrometry Compton scattering is often regarded as a benign nuisance, its worst effects being a wasteful increase in the number of spurious coincident events and an effective obscuring of the weaker peaks. When the gate and full-energy peak widths approach each other in magnitude, however, more insidious effects can set in, such as the generation of "artificial full-energy peaks". Thus, in the days when NaI(Tl)-NaI(Tl) coincidence spectrometers were standard, a number of such false  $\gamma$  rays found their way into the literature and a number of precautionary papers appeared to discuss ways of recognizing and avoiding such effects<sup>1</sup>).

With the advent of Ge(Li) detectors with their low efficiencies, a NaI(Tl) detector was retained more often than not as the gate detector in a coincidence system, and, because now the gates were much wider than even the widest photopeaks, such problems largely disappeared. But now that larger Ge(Li) detectors are available and Ge(Li)-Ge(Li) coincidence spectrometers are coming into general use, misleading Compton-generated  $\gamma$  rays are again making their appearance. The problem is especially acute for experiments with short-lived radioactivities for which repeated bombardments and/or source preparations are required in order to accumulate enough data to make the results statistically significant. The highest count rates possible are desired to minimize the number of necessary bombardments, and this often leads to the

use of close 180° geometry, which is very efficient but somewhat unfavorable with respect to Compton scattering.

The basic problem that can arise from the ability to gate on a region only a few keV wide in a Ge(Li)-Ge(Li) coincidence experiment is quite simple in concept. Each tiny region in a Compton distribution from one detector has a one-to-one correspondence, both with respect to energy and with respect to angle, with a specific region in the Compton distribution resulting from scattering from that detector into a second detector. And, at a fixed angle, if the gate from the first detector be made small enough, the corresponding coincident region from the second detector could also be quite small or narrow, narrow to the point of having the width of a full-energy peak. In a simple spectrum these are easy to spot, but in a complex spectrum one may confuse them with full-energy peaks if he is not wary of them. In some instances the spurious peaks may well fall at the very same energies as a real  $\gamma$  ray itself. Herein lies perhaps the greatest danger of all, for one could easily be misled by false coincidence results into placing the  $\gamma$  ray into an incorrect position in a decay scheme. Thus when we found ourselves on the verge of coming up with such "new" full-energy peaks in the <sup>63</sup>Zn experiment described below, we decided to make a thorough study of the effects of Compton scattering and narrow gates. This paper describes the interesting results and the methods that can be used to suppress these unwanted additions to the coincidence spectrum.

\* Work supported in part by the U.S. Atomic Energy Commission.

† Work supported in part by the U.S. National Science Foundation.

### 2. Experimental apparatus

Sources were counted with a two-parameter "mega-channel" system using two five-sided coaxial Ge(Li)

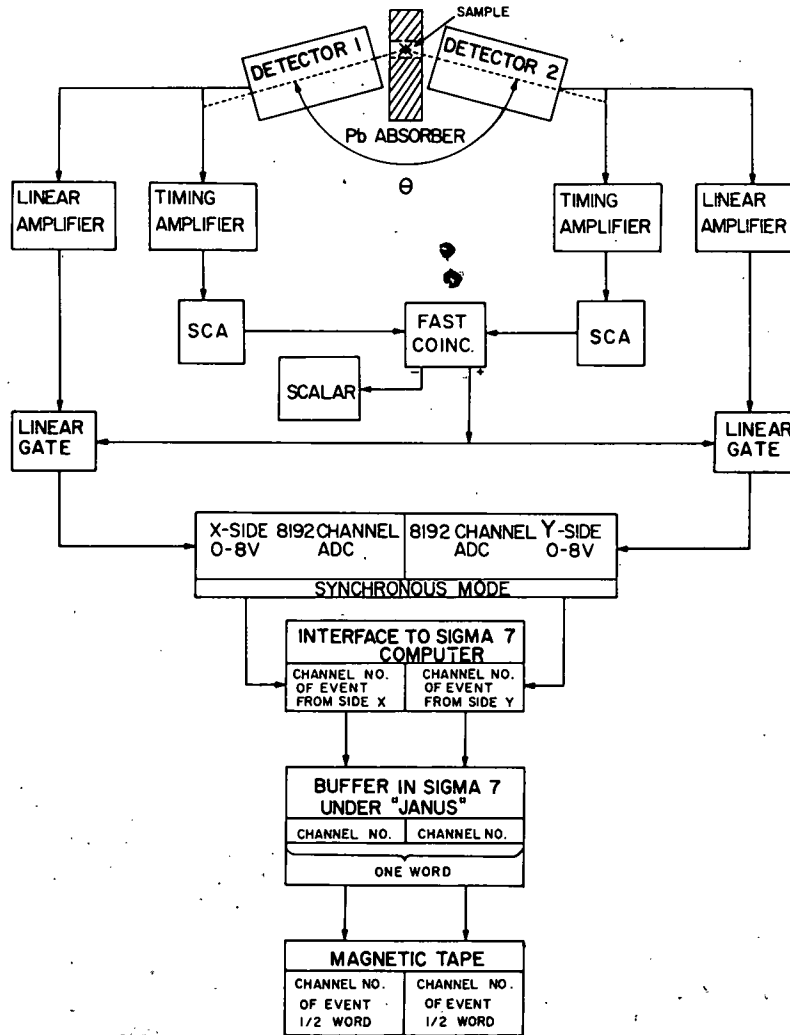
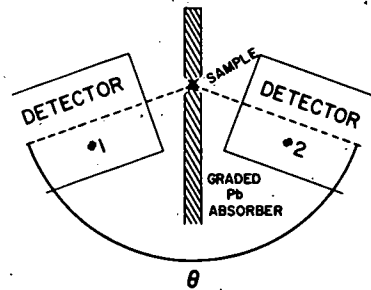


Fig. 1. Block diagram of the electronics used for the Ge(Li)-Ge(Li) "megachannel" coincidence experiments.

A) TOP VIEW



B) SIDE VIEW

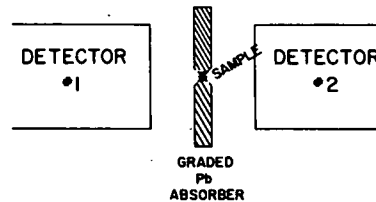


Fig. 2. Relative positioning of the Ge(Li) detectors for the coincidence experiments.

detectors obtained from Nuclear Diodes, one with a resolution of 2.2 keV fwhm for the 1.332-MeV  $\gamma$  from  $^{60}\text{Co}$  and an efficiency of 2.5% relative to a  $7.6 \times 7.6$ -cm NaI(Tl) detector, the other with a resolution of 3.4 keV and an efficiency of 2.0%. Both detectors used room-temperature FET preamplifiers (Nuclear Diodes type 101A and Canberra type 1408C) and the signals were then passed through Canberra type 1417 RC linear amplifiers, type 1435 timing single-channel analyzers, a type 1441 fast coincidence unit (resolving time,  $2\tau$ , set to  $\approx 100$  nsec), and type 1451 linear gates. The output

then passed into two Northern Scientific type NS-629 13-bit ADC's which were interfaced to the MSU Cyclotron Laboratory's time-sharing XDS Sigma-7 computer. A block diagram of the electronics is shown in fig. 1.

The experimental set-up is much like a conventional fast coincidence experiment, except that the analog outputs from both detectors are processed each time a fast coincident event is detected. The  $x$  and  $y$  addresses are stored in the two halves of a single (32-bit) computer word in a dedicated buffer. When the buffer is filled, events are collected in a second buffer while the contents of the first are written on magnetic tape.

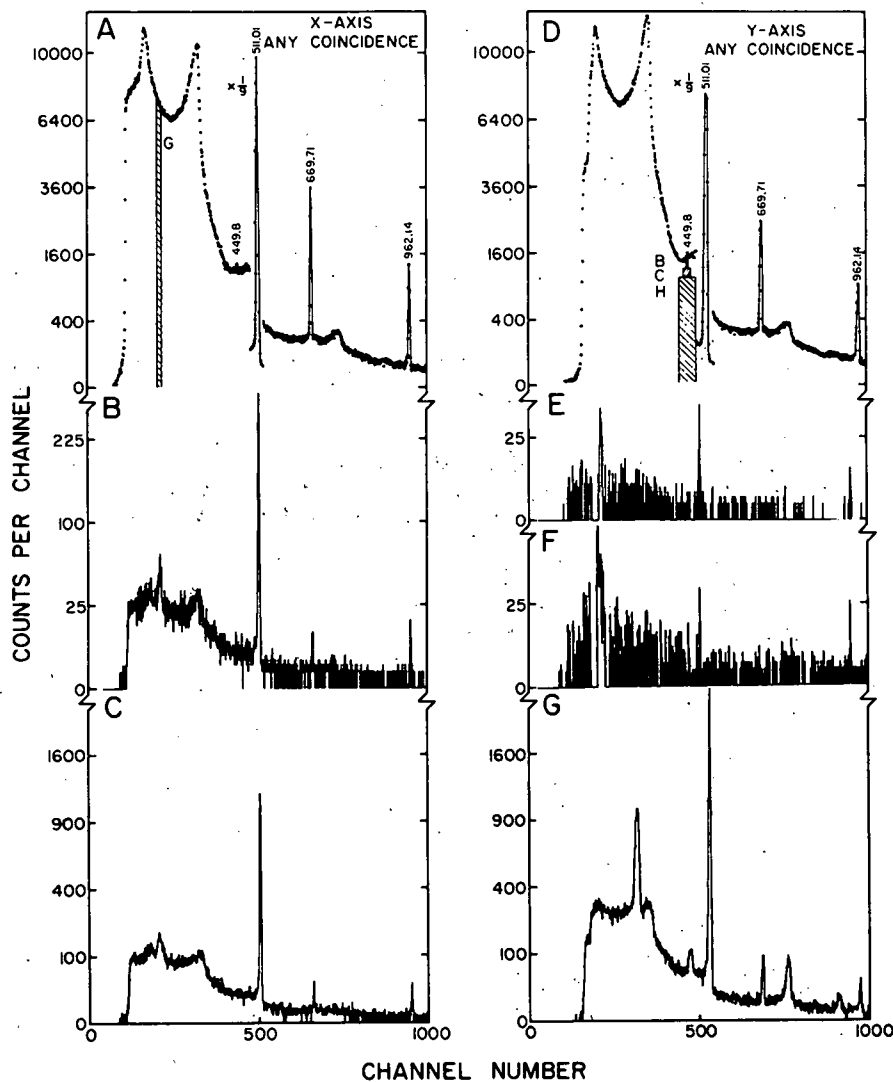


Fig. 3. Coincidence spectra for  $^{63}\text{Zn}$ . The integral coincidence spectra are shown in A and D. Gates were set on the spectrum in D as indicated by the bars, with the following results: B, narrow gate on the 449.8-keV peak; C, wider gate on the 449.8-keV peak; E and F, same as B and C except that the background indicated by bar H has been subtracted. Spectrum G was produced by gating on the spurious "220-keV" peak and produces "new" spurious peaks 220 keV lower than each major photopeak.

The spectra are recovered later off-line by a program<sup>2)</sup> that allows one to obtain gated "slices" with or without a linearly interpolated background subtraction.

Fig. 2 shows the relative positioning of the detectors. Since both detectors were mounted on right-angle dipstick cryostats, it was possible to adjust their relative angular positions to almost any angle. For some of the experiments a 1.27-cm thick graded Pb collimator was placed between the detectors. A small biconical hole,  $\approx 0.64\text{-cm}\varnothing$ , was drilled in an absorber and the source was placed at the center of this hole so that  $\gamma$  rays from the source itself would not be absorbed. The source was normally placed such that it was  $3.8 \pm 0.2$  cm from each detector and on a line with the axis of each detector. The various angles were measured from detector axis to detector axis, with the collimator, if used, bisecting the angle as closely as possible.

### 3. Results

#### 3.1. $^{63}\text{Zn}$ : A COMPLEX SPECTRUM

In fig. 3 we show a portion of the spectra obtained from a two-dimensional  $\gamma$ - $\gamma$  coincidence experiment on 38-min  $^{63}\text{Zn}$ . The detector angle was  $150^\circ$  and an absorber was placed between the detectors but only up to the source. The integral or "any" coincidence spectra taken with the 2.5% and 2.0% detectors are shown at the top in parts A and D, respectively. In these the various gates have been denoted. The only remarks that need be made here about the decay scheme<sup>3)</sup> are that the intense 669.71- and 962.14-keV  $\gamma$ 's are ground state transitions from the first and second excited states in  $^{63}\text{Cu}$  and that the weak 449.8-keV  $\gamma$  feeds the second excited state.

As part of the examination of the coincidence data, a very narrow gate as indicated by the bar B was set on the weak 449.8-keV peak, and the result is shown in part B. Since the 962.14-keV peak is more intense in this spectrum than the 669.71-keV peak but is much weaker in the singles and any coincidence spectra, the 962.14-keV  $\gamma$  is shown to be in coincidence with the 449.8-keV  $\gamma$ . A new peak also appears at 220 keV. There was never any sign of this peak in the singles spectra, so further gates were used.

Part C shows the results of a gate on the 449.8-keV peak with a width four times that of B. Here the entire spectrum increases in intensity, but the peak at 220 keV has also increased greatly in width and is now much wider than the three known photopeaks.

In parts E and F the results of background subtraction are shown. The background used was the region denoted by the bar H but excluding the regions in

gates B and C, respectively. Region H is 50 keV wide and centered on the 449.8-keV peak. In spectra E and F the 669.71-keV peak has disappeared, confirming our previous conclusion, but the  $\gamma^\pm$  and 962.14-keV peaks are weakly though definitely present. The 220-keV "peak", however, has increased greatly with respect to these and the regions on either side of it have gone to zero. This shows clearly that the Compton distribution in the gates was not only in coincidence with other regions of the spectrum in general, but also with this region in particular.

By gating on the 220-keV "peak", as shown in in spectrum G, new peaks appear at 290, 740, 895, and

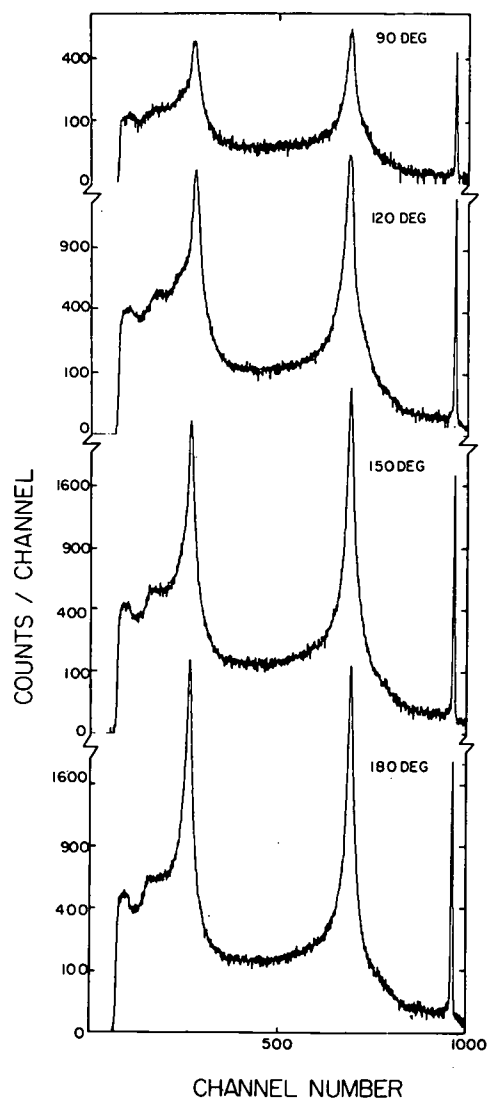


Fig. 4.  $^{137}\text{Cs}$  Compton-scattering coincidence spectra showing the effects of the angle between detectors. (Integral gates.)

180 keV in addition to the one at 450 keV. These energies are 220 keV less than the strong  $\gamma^\pm$ , 669.71-, 962.14-, 1115- ( $^{65}\text{Zn}$  contaminant), and 1412.1-keV peaks, corresponding to Compton-scattered  $\gamma$  rays from one detector being captured in the other detector.

3.2. ANGULAR DEPENDENCE

In order to insure that the effects observed came strictly from Compton scattering between the detectors, our further studies were performed with a  $^{137}\text{Cs}$  source.

The effects of variations in the angle between the detectors on Compton scattering can be seen in fig. 4. The full-energy chance-coincidence peak is noticeably narrower than the large Compton edge and back-

scatter peaks. As the detectors are moved from 90° geometry toward the unfavorable 180° geometry, the increase in the Compton edge and backscatter peaks is very apparent, indicating that the primary direction of the Compton-scattered photons is back toward the source of the incident radiation. Table 1 gives the total, chance, and true coincidence rates.

Calculations of these angular effects are well known. With  $E_\gamma$  as the energy of the incoming photon,  $E'_\gamma$  that of the scattered photon,  $E_0$  the electron rest energy, and  $\theta$  the scattering angle of the photon, one obtains

$$E_0 \left[ \frac{E_\gamma - E'_\gamma}{E'_\gamma E_\gamma} \right] = 1 - \cos \theta,$$

which has a maximum at  $\theta = 180^\circ$ ;  $E'_\gamma$  is related to  $E_\gamma$  and  $E_0$  by

$$E'_\gamma = \frac{E_0 E_\gamma}{2 E_\gamma + E_0}$$

For  $^{137}\text{Cs}$ ,  $E'_\gamma = 184.4$  keV, which is the energy of the backscatter peak observed at all angles; in these close geometries the angular acceptance of the detectors is large enough to wash out most of the predicted angular dependence.

When a graded Pb collimator, as shown in fig. 2, is placed between the detectors, we see the effects illustrated in fig. 5. At 90° the huge Compton edge and

TABLE 1

Coincidence counting rates as a function of angle and absorber.

Angle	Absorber	Total cps	Random cps ( $R_1 R_2 \tau$ )	Net cps
90°	no	2.74	2.55	0.19
90°	yes	1.51	1.33	0.18
120°	no	9.84	1.85	7.99
150°	no	10.95	2.21	8.74
180°	no	12.08	1.61	10.47
180°	yes	3.21	2.45	0.76

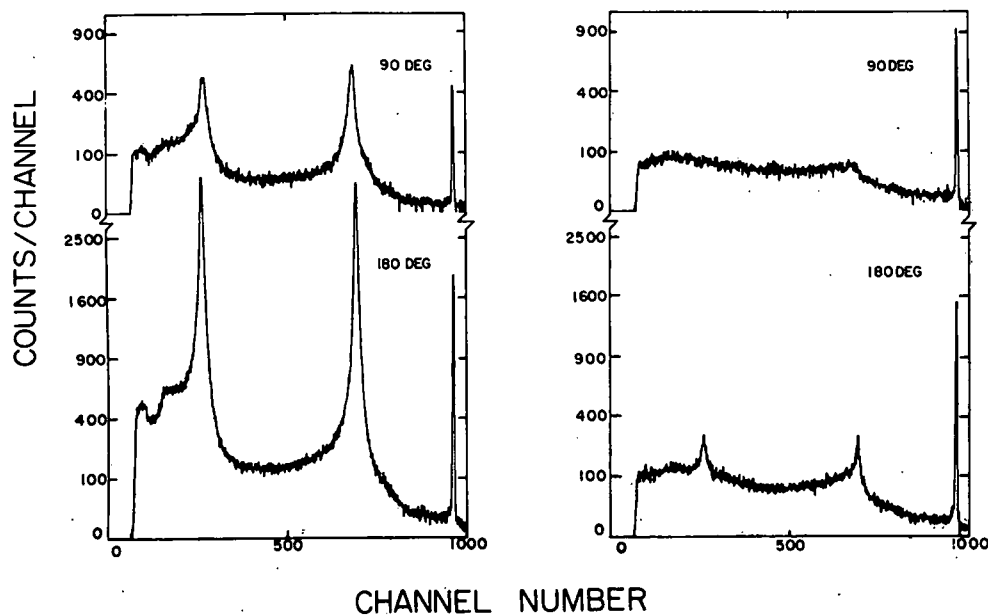


Fig. 5.  $^{137}\text{Cs}$  Compton-scattering coincidence spectra showing the effects of placing an absorber between the detectors. The spectra on the left were taken without a collimator; those on the right, with a 1.27-cm thick graded Pb absorber placed as shown in fig. 2. (Integral gates.)

backscatter peaks have been almost removed. At  $180^\circ$ , while not removed, they have been decreased to an almost reasonable level. This points up the fact that such collimators are all but essential for serious Ge(Li)-Ge(Li) coincidence experiments, but even they cannot insure completely valid results at close  $180^\circ$  geometry. These results are also included in table 1.

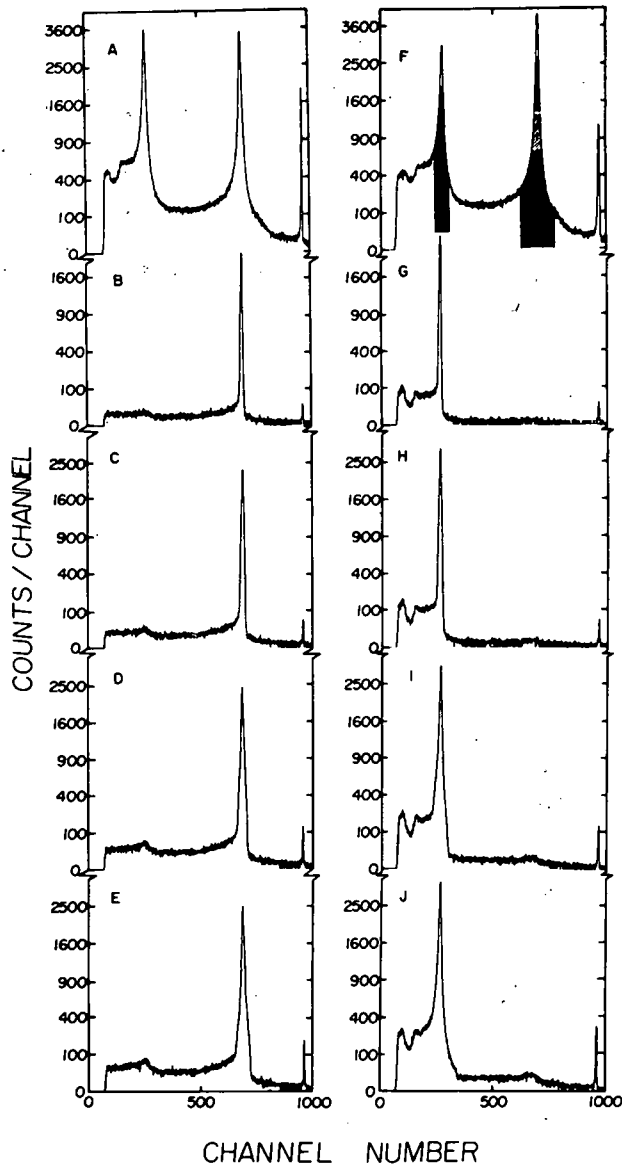


Fig. 6.  $^{137}\text{Cs}$  Compton-scattering coincidence spectra showing the effects of varying gate width. These spectra were taken at  $130^\circ$  geometry. The two integral coincidence spectra are shown at the top in A and F, and the gate widths are indicated in F. Spectra B, C, D, and E show the effects of increasing gate width on the backscatter peak, while G, H, I, and J show the effects of increasing gate width on the Compton edge.

### 3.3. GATE WIDTHS

Fig. 6 shows the effects of varying gate width on the coincident backscatter and Compton edge peaks. The display spectrum (from the 2.5% detector) is shown in part A, while the gates (from the 2.0% detector) are shown in part F. In parts B through E we see the effects, of the various widths of gates on the backscatter peak, as denoted by the four areas on this peak in part F. For the narrowest gate (in B) the Compton edge peak is about twice the width of the photopeak, and by decreasing the gate width even further, it could undoubtedly be made the same width as the photopeak. As the gate width is increased, the Compton edge peak broadens somewhat but does not increase in height. This is rather graphic evidence for the one-to-one correspondence between portions of the spectra resulting from Compton scattering between detectors.

A similar effect is seen by gating on the Compton edge and looking at the resulting spectra, G through J. Notice the dip that appears in the spectrum below the backscatter peak. We discuss this in the next section, where gates are applied on different regions of the Compton distribution.

In fig. 7 we show a plot of the full width at half and tenth maximum vs the gate width. Gating on the backscatter peak and on the Compton edge produced

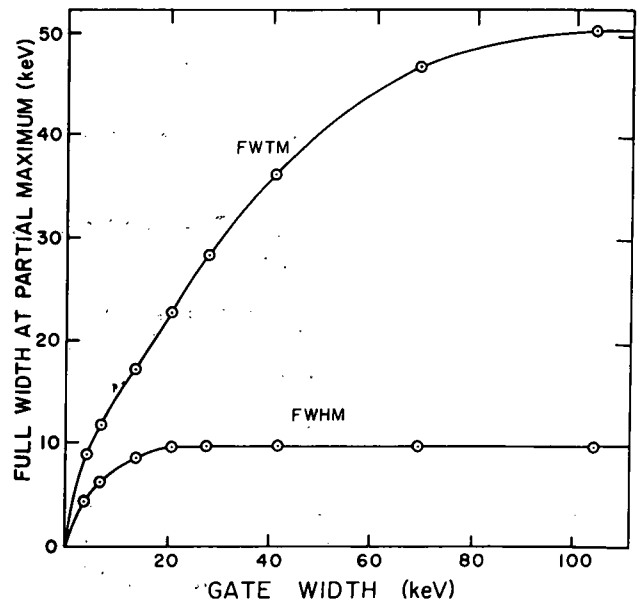


Fig. 7. Plot of the peak widths as a function of gate widths. Points for the spectra in fig. 6 and four additional  $^{137}\text{Cs}$  spectra are included. The results from gating on the Compton edge are essentially identical with those from gating on the backscatter peak, so both are included in each point in this figure.

identical results, so both are included in the points on the graph.

We could reproduce the flattening out of the fwhm curve fairly well by a very simple calculation. Two Gaussian-shaped peaks were used, a wider one for the gate (G) and a narrower one for the displayed peak (P) – this because customarily (but not always) one gates on the spectrum with the poorer resolution. For these Gaussians we used the experimental fwhm for our two detectors as found from the worst integral coincidence spectrum, the one at  $180^\circ$  with no absorber.

Each channel in G then corresponded to a complete peak P, the amplitude depending on the height of the channel in G. Thus, a particular gate width in G was represented by a sum of peaks P having shifted centroids and differing amplitudes. The results showed that, for this idealized case, the limiting value of the fwhm is twice that of the display peak in its integral coincidence

spectrum. This limiting value is reached at a gate width twice that of the fwhm of G, the same as was found experimentally in fig. 7. However, the calculated limiting value is about half that observed experimentally.

We are currently calculating the effects of the intrinsic resolution of the detectors on the peak width vs gate width and angle, but a discussion of the results is beyond the scope of this paper<sup>4</sup>.

### 3.4. GATE POSITION

In fig. 8 gates have been set on various regions of interest in the coincidence spectrum resulting from  $180^\circ$  geometry without using an absorber. Parts A and F show the 2.5% and 2.0% detector integral coincidence spectra, respectively. All gates were set as indicated in part F.

Gates B, C, and D study the region with energies less than the backscatter peak. In part B the large Compton

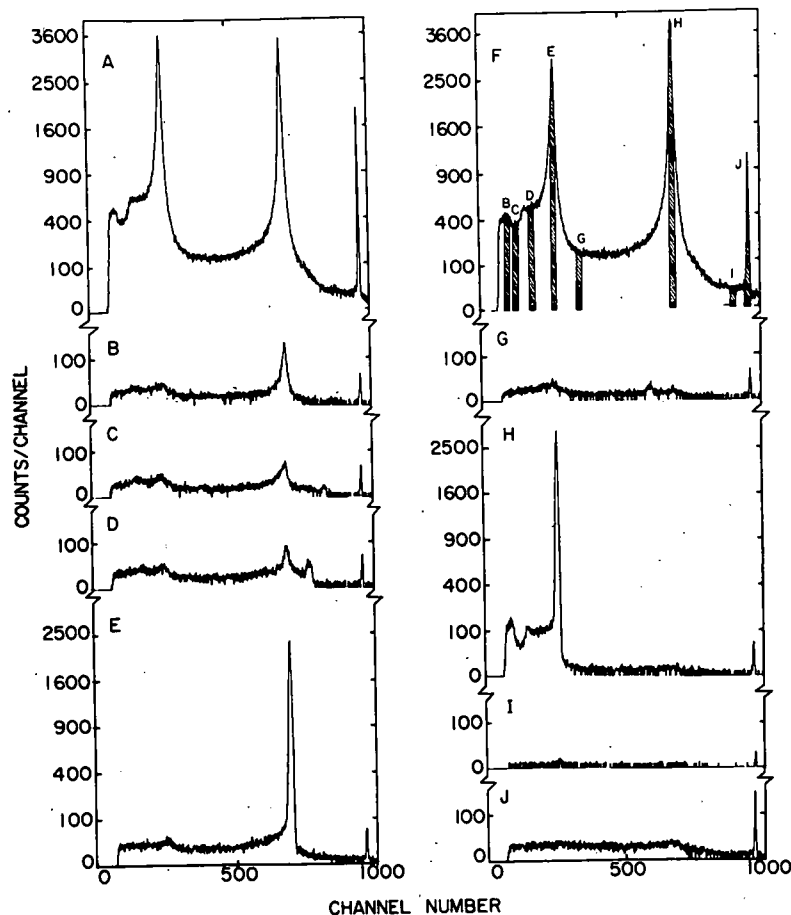


Fig. 8.  $^{137}\text{Cs}$  Compton-scattering coincidence spectrum showing the effects of gating at different positions. The display integral coincidence spectrum is shown in A, while the gate integral coincidence spectrum is shown in F. The other spectra correspond to their respective gates as indicated on F.

edge and the full-energy photopeak are seen on top of a rather typical Compton background. Part C shows the Compton edge broadening and with lower intensity and another broad, weak peak at about channel 820. By the time gate D is reached, the edge has again narrowed and the new peak has increased in intensity and has moved to a lower energy. The distance of this shift is the same as and in the opposite direction of the movement of the gate from C to D. Other gates show that as the gate is moved toward the backscatter peak, the new peak moves toward the Compton edge. In all cases the sum of the energy of the new peak and that of the gate equals that of the photopeak. That, plus the fact that the new peak appears in the Compton-forbidden region between the edge and the photopeak, indicates that this is the result of multiple Compton scattering. It arises when a photon is emitted from the source, then is Compton scattered in the first detector, rescattered in the second detector, and finally captured completely in the first detector. As a result, the Compton valley for the backscatter occurs at C instead of adjacent to the backscatter peak, at D.

Gate E is the center of the backscatter peak, and it is, as expected, mostly in coincidence with the Compton edge. In part G, in addition to the weak backscatter and Compton edge peaks and the full-energy peak, a broad peak is present at about channel 600. The centroid of this peak when added to that of gate G again equals the full-energy peak. This also is a Compton scattered photon in coincidence with a captured Compton scattered photon.

The backscatter peak plus the lower energy region are found in coincidence with gate H. In this gate the drop in the Compton background is even more prominent and is strong evidence for the double Compton scattering.

The gate I on the valley between the Compton edge and the photopeak shows the photopeak, a Compton background, and a weak peak at the backscatter position. Evidently these are mostly chance coincidences. Finally, in part J we see a coincidence spectrum

where the gate was on the photopeak. This appears as a normal  $^{137}\text{Cs}$  spectrum, resulting entirely from chance coincidences.

#### 4. Conclusions

Large, high-resolution Ge(Li) detectors present many exciting new possibilities for nuclear research; yet, along with all their advantages, several problems appear. Potentially one of the most troublesome is the Compton scattering between detectors in a coincidence experiment, which we have illustrated and discussed in this paper. In many cases it is possible to use a  $90^\circ$  geometry with a large graded Pb absorber between the detectors to eliminate the problem, but when working with short half-lives, more care must be used. An absorber of the type described in section 2 has been found useful, and using a geometry of  $150^\circ$  or so instead of  $180^\circ$  can be helpful. Most of all, however, one must simply be aware of the problems that now exist with such coincidence experiments. For without consideration of Compton scattering, newly found coincidence peaks may unknowingly be considered to arise from  $\gamma$  transitions in the nucleus under study, when in fact they are only Compton scattered photons.

We are indebted to Mrs. Carolee Merritt and the MSU Cyclotron computer staff for their assistance in the operation of the computer. We also thank Dr. C. R. Gruhn for his reading of the manuscript and very helpful discussions concerning the effects of Compton scattering.

#### References

- 1) For example, the problem is considered in P. R. Bell, in *Beta- and gamma-ray spectroscopy* (ed. K. Siegbahn; North-Holland Publ. Co., Amsterdam, 1955) p. 132.
- 2) D. Bayer, D. B. Beery and G. C. Giesler, EVENT RECOVERY, a FORTRAN program written for the MSU Cyclotron Laboratory Sigma-7 computer.
- 3) G. C. Giesler, Wm. C. McHarris and W. H. Kelly, to be published; summary available in Michigan State University Nuclear Chemistry Annual Report COO-1779-13 (1969) p. 103.
- 4) R. A. Warner, Wm. C. McHarris, G. C. Giesler and W. H. Kelly, unpublished results (1970).



# Study of the Level Structure of $N = 82$ Nuclei via Proton-Transfer Reactions\*

B. H. Wildenthal†

Michigan State University, East Lansing, Michigan‡ 48823  
and Oak Ridge National Laboratory, Oak Ridge, Tennessee 37830

and

E. Newman and R. L. Auble

Oak Ridge National Laboratory, Oak Ridge, Tennessee 37830

(Received 19 June 1970)

Measurements of the angular distributions of the ( $^3\text{He}, d$ ) and ( $d, ^3\text{He}$ ) reactions on the stable, even-mass  $N = 82$  isotones are presented and discussed. In each of the residual nuclei formed in these reactions,  $^{135}\text{I}$ ,  $^{137}\text{Cs}$ ,  $^{139}\text{La}$ ,  $^{141}\text{Pr}$ ,  $^{143}\text{Pm}$ , and  $^{145}\text{Eu}$ , the lowest two levels are populated with significant strength, one by  $l_p = 4$  transfer and one by  $l_p = 2$  transfer. Analysis indicates that these states result from coupling a  $1g_{7/2}$  or  $2d_{5/2}$  proton (or proton hole) to the respective  $J^\pi = 0^+$  target ground states. The relative energies of these states change as a function of mass, the  $\frac{5}{2}^+$  state lying 590 keV above the  $\frac{1}{2}^+$  state in  $^{135}\text{I}$ , and 330 keV below the  $\frac{1}{2}^+$  state in  $^{145}\text{Eu}$ . Spectroscopic factors extracted from the data with distorted-wave Born-approximation analysis indicate that the active particles in the target ground states predominantly occupy the  $1g_{7/2}$  and  $2d_{5/2}$  orbits, with the ratio of  $1g_{7/2}$  protons to  $2d_{5/2}$  protons varying from 3.5/0.5 for  $^{136}\text{Xe}$  to 6.3/3.6 for  $^{144}\text{Sm}$ . The pickup reactions reveal small admixtures of  $1h_{11/2}$ ,  $3s_{1/2}$ , and  $2d_{3/2}$  protons into the heavier target ground states. These orbits, together with the  $1g_{7/2}$  and  $2d_{5/2}$ , constitute the major shell which fills between  $Z = 50$  and 82. The stripping experiments locate the centroid energies of these higher three orbits relative to the  $\frac{5}{2}^+$  and  $\frac{1}{2}^+$  states. It is found that the centroids of the  $1h_{11/2}$ ,  $3s_{1/2}$ , and  $2d_{3/2}$  single-particle states relative to the ground states decrease monotonically from excitations of 1.9, 2.1, and 2.1 MeV, respectively, in  $^{137}\text{Cs}$  to excitations of 0.72, 0.81, and 1.1 MeV in  $^{145}\text{Eu}$ .

## I. INTRODUCTION

This paper reports the results of a comprehensive experimental study<sup>1-3</sup> of the low-energy level structure ( $\leq 3$  MeV) of odd-mass nuclei which have a neutron number of 82. The data to be discussed consist of the spectra of the ( $d, ^3\text{He}$ ) and ( $^3\text{He}, d$ ) reactions on  $^{136}\text{Xe}$ ,  $^{138}\text{Ba}$ ,  $^{140}\text{Ce}$ ,  $^{142}\text{Nd}$ , and  $^{144}\text{Sm}$ . From these spectra, energy levels are located in the residual nuclei  $^{135}\text{I}$ ,  $^{137}\text{Cs}$ ,  $^{139}\text{La}$ ,  $^{141}\text{Pr}$ ,  $^{143}\text{Pm}$ , and  $^{145}\text{Eu}$ . The measurements of the differential cross sections of the transitions to these levels are analyzed with the distorted-wave Born-approximation (DWBA) theory in order to extract the values of the orbital angular momenta ( $l_p$ ) of the protons transferred between the target and final states. From this information, the parities of the various final states are determined, and limits ( $J = l_p, \pm \frac{1}{2}$ ) placed on their spins. In addition, and of comparable importance, the DWBA analysis of the angular distributions yields the intrinsic strengths [spectroscopic factors  $S(nlj)$ ] of the various transitions. These strengths, which correspond to the expectation values of appropriate single-particle creation or annihilation operators between the initial and final states, relate the structure of the residual states to that of the tar-

get ground state. They also provide information about the occupation probabilities of the shell-model orbits which are actively involved in the structure of the low-lying energy levels.

The purpose of these experiments has been to obtain quantitative experimental information necessary for the initiation and evaluation of detailed theoretical studies of nuclear structure in this region. The most general tenets of the nuclear shell model<sup>4</sup> indicate that systems of 50 and 82 nucleons each constitute unusually tightly bound (and hence stable) aggregates. In this formulation the nucleons which are added as the proton or neutron number is increased from 51 to 82 occupy single-particle orbits in the average shell-model potential which are characterized by the quantum numbers  $1g_{7/2}$ ,  $2d_{5/2}$ ,  $2d_{3/2}$ ,  $3s_{1/2}$ , and  $1h_{11/2}$ . We shall in the future refer to these orbits as constituting the "gdhs" major shell. In the present experiments we are dealing with nuclei which have 82 neutrons and from 53 to 63 protons. The chart of the nuclides in this region is illustrated in Fig. 1. The ideas of the shell model thus suggest that the wave functions of the lowest-lying energy levels of these nuclei should have the following characteristics: (1) an effectively closed and inert core of 82 neutrons; (2) an effectively closed and inert core of

50 protons; and (3) essentially complete vacancy of the proton orbits lying above the *gdhs* shell. Characteristics (2) and (3), of course, imply that those protons in excess of  $Z = 50$ , and only those, occupy the *gdhs* shell.

The present investigation was directed initially at testing these general hypotheses about the  $N = 82$  nuclei. Assuming their validity, it is apparent that a major theoretical simplification results from being able to treat the characteristics of the levels occurring at low excitation energies as arising solely from the interactions among from 3 to 13 protons within one major shell. For this reason it would appear that the  $N = 82$  isotones are one of the most appropriate regions in the Periodic Table in which to apply the techniques of the nuclear shell model to the problem of explaining experimental structure phenomena. Despite their potential theoretical importance, however, relatively little experimental work had been done on these nuclei until the last two years.<sup>5,6</sup> In particu-

lar, proton-transfer data, essential in delineating the basic structural characteristics of the energy levels, were lacking. The measurements to be presented provide a significant improvement in

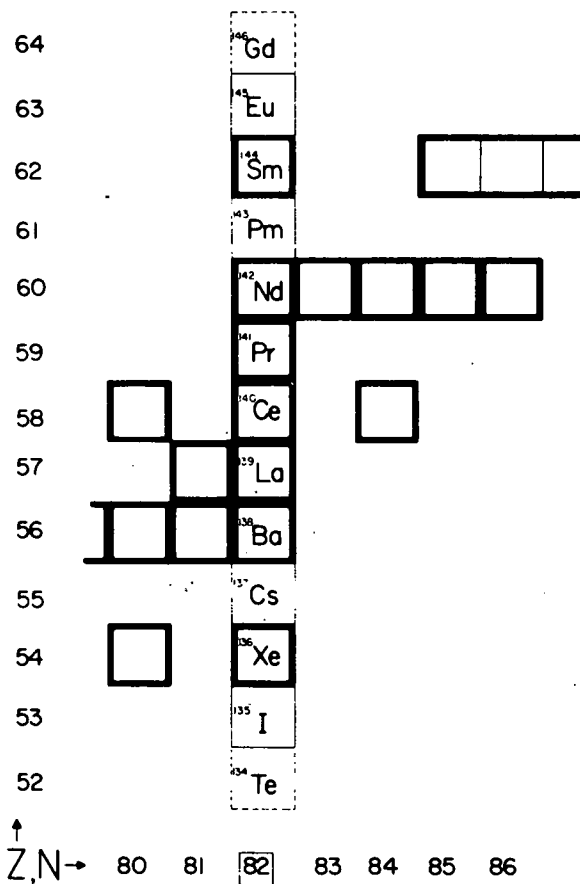


FIG. 1. Chart of the nuclides in the region of  $N = 82$ . Stable nuclei are heavily outlined, unstable nuclei whose properties have been studied are enclosed with thin solid lines, and nuclei as yet uninvestigated are outlined with dashed lines.

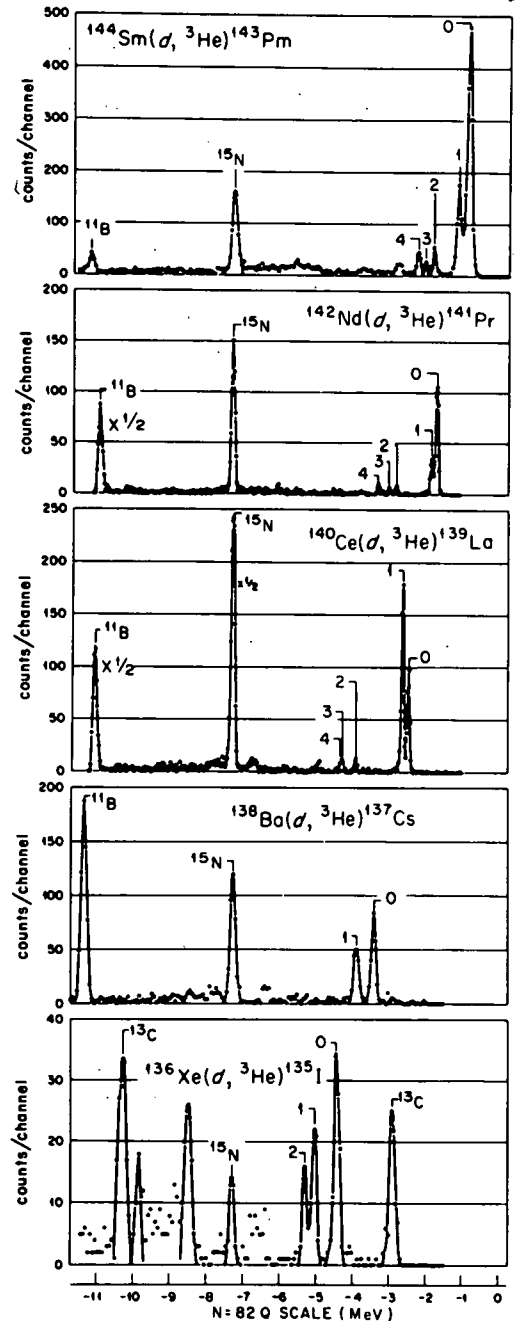


FIG. 2. Spectra of  $^3\text{He}$  particles detected at or near  $\theta_L = 20^\circ$  which result from deuteron bombardment of even-mass  $N = 82$  targets. The peaks of interest are denoted by numerals. The excitation energies of these states are listed, in their corresponding numerical order (0 = g.s., etc.), in the second column of Table III for each appropriate residual nucleus. Impurity peaks are specifically designated.

situation. In an associated article the relationships between the present data and specific model calculations will be studied.<sup>7,8</sup>

## II. EXPERIMENTAL PROCEDURE

The measurements reported here were performed with the Oak Ridge Isochronous Cyclotron. The  $^3\text{He}$  spectra resulting from the deuteron bombardments were obtained with a standard solid-state particle detector  $\Delta E$ - $\bar{E}$  telescope, combined with pulse-multiplier techniques. Typical energy resolution for the  $^3\text{He}$  particle groups was 90 keV, full width at half maximum (FWHM). The deuteron

bombarding energies were about 40 MeV. The spectra measured for each target near  $\theta_L = 20^\circ$  are shown in Fig. 2.

The deuteron spectra from the  $^3\text{He}$  bombardments were recorded in photographic emulsions placed in the focal plane of a broad-range magnetic spectrograph. Energy resolution for the particle groups in these spectra was about 35 keV FWHM. The spectra obtained for the various targets at about  $\theta_L = 20^\circ$  are shown in Fig. 3. The  $^3\text{He}$  bombardments were also at 40 MeV except for the case of the  $^{136}\text{Xe}$  target, where a 25-MeV beam was used. The use of the same energies for both the deuteron and  $^3\text{He}$  beams, and the relatively small range of the reaction  $Q$  values, produced a situation in which the incident channel for one set of reactions was very similar to the exit channels of the inverse set of reactions. Beam energies of 40 MeV were chosen in order to optimize the distinctiveness of the angular distributions of the various  $l_p$  transfers expected to be important in the "gdhs" shell.

The naturally occurring abundances of the  $N = 82$  isotopes of the target elements are listed in the second column of Table I. The target materials used in the present experiments were enriched in the  $N = 82$  isotopes to the values shown in the third column.<sup>9</sup> The  $Q$  values of the  $(d, ^3\text{He})$  and  $(^3\text{He}, d)$  reactions to the ground states of the respective  $(A - 1)$  and  $(A + 1)$  nuclei are listed in columns four and six of Table I, respectively. The  $^{136}\text{Xe}(d, ^3\text{He})$ - $^{135}\text{I}$  and the  $^{142}\text{Nd}(^3\text{He}, d)^{143}\text{Pm}$   $Q$  values were obtained from the present series of measurements. Other masses were known to within the accuracies attainable in the present experiments and the listed values are taken from the tables of Mattauch, Thiele, and Wapstra.<sup>10</sup> The  $Q$  values for the  $(d, ^3\text{He})$  and  $(^3\text{He}, d)$  reactions on  $^{16}\text{O}$  and  $^{12}\text{C}$ , the dominant contaminants in all of the targets except  $^{136}\text{Xe}$ , are also given in Table I. It can be seen that these contaminants do not pose a serious problem for most of the low-energy spectra of the residual  $N = 82$  nuclei. The specific bombarding energies used in the various experiments are listed in columns 5 and 7 of Table I.

The targets of  $^{138}\text{Ba}$ ,  $^{140}\text{Ce}$ , and  $^{142}\text{Nd}$  were each prepared by reducing the isotopically enriched carbonate to the oxide in a tantalum-tube furnace under vacuum. The oxides were then evaporated by electron bombardment from a carbon boat onto very thin carbon backings. Target thicknesses exclusive of the backings ranged between 50 and 300  $\mu\text{g}/\text{cm}^2$ . The  $^{144}\text{Sm}$  target was a self-supporting rolled foil of 500  $\mu\text{g}/\text{cm}^2$  areal density. The Xe gas was contained in a 3-in.-diam cell modeled after one designed by Jones and Mancusi.<sup>11</sup> Havar entrance and exit windows were 0.0001 in. thick

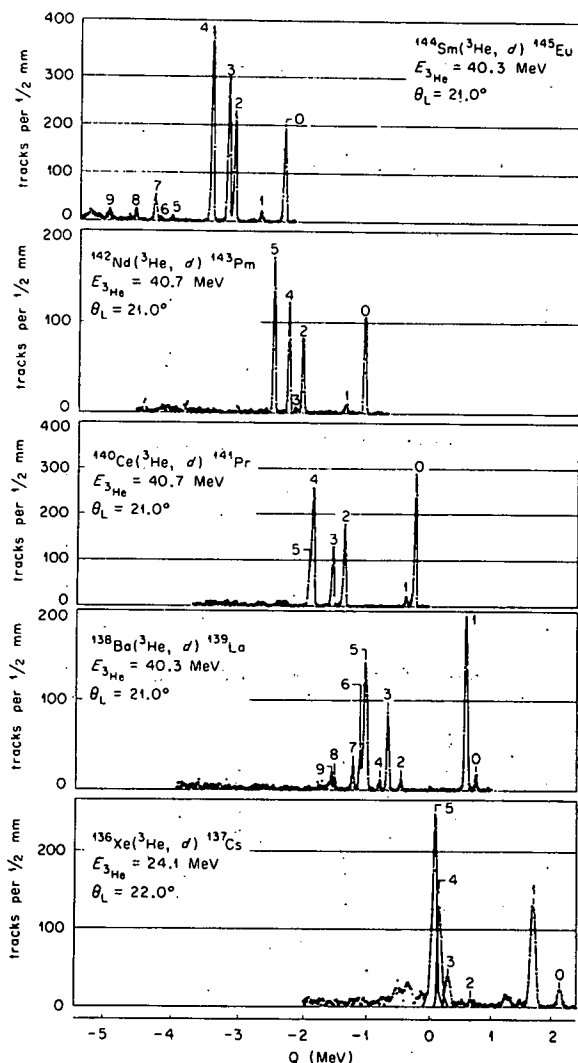


FIG. 3. Spectra of deuterons detected at or near  $\theta_L = 20^\circ$  which result from  $^3\text{He}$  bombardment of even-mass  $N = 82$  targets. The peaks of interest are denoted by numbers. The excitation energies of these states are listed in their corresponding numerical order (0 = g.s., 1 = first excited state, etc.), in the second column of Table III for each appropriate residual nucleus.

TABLE I. Target and reaction information.

Element	Natural (%)	Enriched (%)	$Q(d, {}^3\text{He})$ (MeV)	$E_d$ (MeV)	$Q({}^3\text{He}, d)$ (MeV)	$E_{{}^3\text{He}}$ (MeV)
${}^{136}\text{Xe}$	8.9	90 <sup>a</sup> -95 <sup>b</sup>	$-4.438 \pm 0.040$	40.3	$2.216 \pm 0.070$	24.1
${}^{138}\text{Ba}$	71.7	99.8	$-3.463 \pm 0.070$	40.3	$0.734 \pm 0.032$	40.3
${}^{140}\text{Ce}$	88.5	99.7	$-2.493 \pm 0.048$	40.3	$-0.258 \pm 0.010$	40.7
${}^{142}\text{Nd}$	27.1	97.7	$-1.732 \pm 0.010$	40.3	$-1.099 \pm 0.025$	40.7
${}^{144}\text{Sm}$	3.1	94.5	$-0.661 \pm 0.030$ <sup>c</sup>	40.3	$-2.203 \pm 0.050$	40.3
${}^{16}\text{O}$	...	...	$-6.632 \pm 0.001$	...	$-4.893 \pm 0.001$	...
${}^{12}\text{C}$	...	...	$-10.463 \pm 0.001$	...	$-3.550 \pm 0.001$	...

<sup>a</sup>For ( ${}^3\text{He}, d$ ).<sup>b</sup>For ( $d, {}^3\text{He}$ ).<sup>c</sup>Derived from  ${}^{142}\text{Nd}({}^3\text{He}, d){}^{143}\text{Pm}$  measurement.

and pressures of about  $\frac{1}{10}$  atmosphere were employed. These pressures, coupled with the slit system used, were equivalent to a target thickness of about  $100 \mu\text{g}/\text{cm}^2$ . The several types of targets and their different thicknesses produced spectra of varying quality.

Differential cross sections were usually measured to about  $40^\circ$ . The rapid decrease of reaction intensities as the angle to the beam increased made measurements at larger angles prohibitively time consuming. And, in any case, the data at large angles have essentially no bearing on the spectroscopic information of interest in the present study. The smallest angle at which data were taken was  $5^\circ$  for the ( ${}^3\text{He}, d$ ) experiments and  $11^\circ$  for the ( $d, {}^3\text{He}$ ) experiments. The high counting rates of elastically scattered deuterons in the solid-state detectors made taking ( $d, {}^3\text{He}$ ) data at smaller angles impractical even though such information would have been useful.

In the present work it was not feasible to make an absolute determination of the cross sections for a particular target to an accuracy of better than 25%. The cross sections for one target relative to another had the same sort of uncertainty. The procedure by which the experimental cross sections were related to the DWBA calculated cross sections is discussed in the next section.

### III. DISTORTED-WAVE ANALYSIS

#### A. Optical-Model Potentials and Predicted Angular Distributions

From the discussion in the Introduction, it is to be expected that the proton transfers occurring via the ( ${}^3\text{He}, d$ ) and ( $d, {}^3\text{He}$ ) reactions on  $N=82$  targets will involve  $l_p$  values of 4, 2, 5, and 0. The differential cross sections for these transfers were calculated in the local, zero-range (LZR) approximation of the DWBA with the code JULIE.<sup>12</sup> The choice of bombarding energies made a rigid consistency in the DWBA calculations possible. The same deuteron optical-model potential and the same  ${}^3\text{He}$  optical-model potential were used in all of the calculations. The deuteron parameters are those deduced by Newman *et al.*<sup>13</sup> from the analysis of 34-MeV deuteron elastic scattering data. The  ${}^3\text{He}$  parameters are based on those obtained by Gibson *et al.*<sup>14</sup> from the analysis of  ${}^3\text{He}$  elastic scattering on several medium-mass targets at energies in the 30-60-MeV range. All of the parameters which enter into the DWBA calculations are listed in Table II. The shapes and intrinsic magnitudes of the angular distributions calculated in the DWBA for the four values of  $l_p$  are shown in Fig. 4. The curves result from calculations which assume the ( ${}^3\text{He}, d$ ) reaction on

TABLE II. Optical-model potentials.

	$V$ (MeV)	$r_0$ (F)	$r_{0c}$ (F)	$a$ (F)	$W$ (MeV)	$r'_0$ (F)	$a'$ (F)	$W_D$ (MeV)
Deuteron	99.0	1.12	1.30	0.820	...	1.24	0.86	15.75
${}^3\text{He}$	175.0	1.14	1.40	0.723	17.5	1.60	0.86	...
Bound state (centroid)	(Separation energy prescription)	1.24	1.25	0.65	...	...	...	...
Bound state (spin-orbit)	( $\lambda=20$ )	1.14	...	0.65	...	...	...	...

$^{140}\text{Ce}$  with a  $Q$  value of 0.0 MeV. It can be seen that the curves for the various  $l_p$  transfers are quite distinctive from one another, and that each is uniquely identified by the portion of the curve

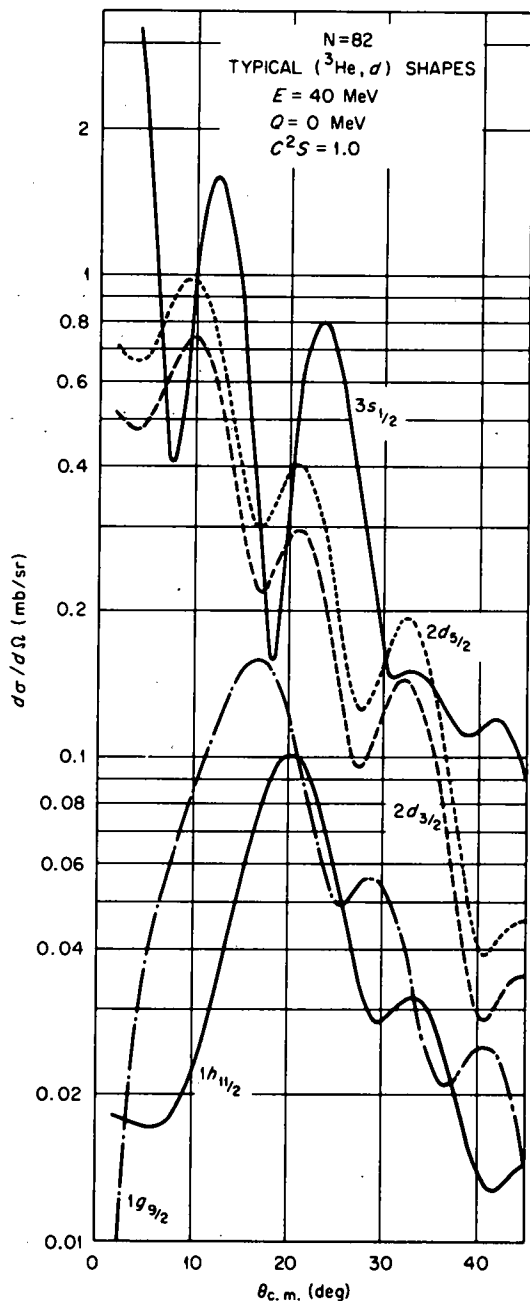


FIG. 4. Shapes of DWBA predictions for transitions involving the orbits which are filled between  $Z=51$  and  $82$ . The calculations assume  $(^3\text{He}, d)$  stripping at  $40$  MeV on  $^{140}\text{Ce}$  with a  $Q$  value of  $0.00$  MeV and the quantum numbers associated with the various curves. The absolute cross sections are plotted so as to reflect the relative intrinsic cross sections of the various  $l$  transfers. The values result from the standard version of the calculations.

between  $10$  and  $35^\circ$ . It follows that for the process of assigning  $l_p$  values to experimental angular distributions by matching them to the DWBA curves, experimental data in this angular range are sufficient. It can also be seen that to achieve the desired goal of matching theoretical to experimental cross sections at the angles of maximum cross section, data from  $5$  to  $10^\circ$  are desirable for the cases of  $l_p=2$  and, in particular,  $l_p=0$  transitions.

#### B. Predicted Cross Sections from the DWBA and Parameters of the "Bound-State Well"

The differential cross sections obtained from the DWBA calculations are interpreted as corresponding to the stripping (pickup) of a particle into (out of) a single-particle orbit ( $nlj$ ) under the condition that the other nucleons in the target nucleus (which are inequivalent to the transferred particle) from an inert core which is identical in the initial and final states. The bound-state wave function for the transferred nucleon is obtained by assuming the orbit to be an eigenfunction of a Woods-Saxon potential well with an energy eigenvalue equal to the experimentally observed separation energy for the nucleon in question. The form of the well is

$$V(r) = V_0(r) + V_{so}(r) + V_{Coul.}(r), \quad (1)$$

where

$$V_0(r) = -V_0 f(r); \quad (2a)$$

$$V_{so}(r) = -\lambda V_0 (\hbar/2M_p c)^2 \vec{l} \cdot \vec{\sigma} r^{-1} df(r)/dr; \quad (2b)$$

$$V_{Coul.}(r) = Ze^2(3 - r^2/R_0^2)/2R_0, \quad r < r_c A^{1/3}; \quad (2c)$$

$$= Ze^2/r, \quad r > r_c A^{1/3};$$

and

$$f(r) = \left[ 1 + \exp\left(\frac{r - r_0 A^{1/3}}{a_0}\right) \right]^{-1} \quad (3a)$$

$$f'(r) = \left[ 1 + \exp\left(\frac{r - r_{so} A^{1/3}}{a_{so}}\right) \right]^{-1} \quad (3b)$$

One aspect of the calculations which strongly affects the magnitude of the predicted cross sections, but only minimally affects the relative cross sections for different ( $nlj$ ) transfers, is the radius parameter,  $r_0$ , of the central part of the bound-state well. Changes of  $5\%$  in the bound-state radius for ( $d$ - $^3\text{He}$ ) transfer reactions can produce  $30\%$  changes in the predicted cross sections.<sup>15</sup> Increased radii correspond to larger expectation values for the transferred particle at the absorption surface and hence to larger cross sections. The value of  $r_0$  which, together with the "Bessel normalization"<sup>16</sup> of the ( $d$ - $^3\text{He}$ ) overlap, seems to give consistency between LZR DWBA analyses of

data and general sum-rule expectations is about 1.24 F.<sup>17</sup> Our results are, within the experimental uncertainties, consistent with the  $r_0 = 1.24$  F- "Bassel normalization" combination.

There is another, less well known, aspect of the DWBA calculations which is particularly important for the strongly surface-dominated ( $d$ - $^3\text{He}$ ) processes. This concerns the use of the spin-orbit term in the bound-state well of Eq. (1). For the same value of the transferred orbital angular momentum  $l$ , the spin-orbit term causes those transitions with  $j = l + \frac{1}{2}$  to have larger predicted cross sections than those with  $j = l - \frac{1}{2}$ . This results from the fact that the spin-orbit term is acting at the edge of the nucleus, pushing the wave function of the bound particle inwards for the  $j = l - \frac{1}{2}$  case and pulling it outward for the  $j = l + \frac{1}{2}$  case. In the traditional use of the DWBA, the geometrical parameters of the spin-orbit and central wells [Eqs. (2a) and (2b)] are constrained to the same values, i.e.,  $r_{so} = r_0$  and  $a_{so} = a_0$ .

A study of the single-particle states in  $^{209}\text{Bi}$  via the  $^{208}\text{Pb}(^3\text{He}, d)^{209}\text{Bi}$  reaction<sup>18</sup> has shown that the conventional prescription for introducing spin-orbit effects produces too large a difference between the cross sections of  $j = l + \frac{1}{2}$  and  $j = l - \frac{1}{2}$  transitions. The effect is, of course, strongly dependent upon  $l$  and hence showed up clearly in the  $l = 3, 5,$  and  $6$  transitions to  $^{209}\text{Bi}$ . Subsequent investigations<sup>19</sup> have shown that making the spin-orbit radius about 10% smaller than that of the central well radius ameliorates this problem. This prescription is suggested by and consistent with the findings of various recent nucleon-nucleus scattering studies.<sup>20</sup>

As may be expected, the  $l = 4, j = \frac{7}{2}$  cross sections of ( $^3\text{He}, d$ ) transitions in the  $N = 82$  region are quite sensitive to this effect. The cross section from the calculation with a reduced spin-orbit radius is a factor of  $\sim 1.20$  larger than that from the conventional calculation, all other aspects being held constant. The changes in the cross sections resulting from this modification in the DWBA calculations for the other transfers are as follows:  $2d_{5/2} \sim 0.93$ ,  $1h_{11/2} \sim 0.82$ , and  $2d_{3/2} \sim 1.11$ . Thus, the modified DWBA analysis produces significantly different results from the standard analysis. We will present results from both procedures.

### C. Spectroscopic Factors

The effects of the nuclear structure of the initial and final energy levels involved in a particular direct-reaction transition manifest themselves as a ratio of the experimentally measured differential cross sections to the pertinent intrinsic cross sections calculated in the DWBA. The experimentally

observed transition is identified as to  $l_p$  by finding a match between its angular distribution and the curves calculated for various values of  $l_p$ . The complete ( $nlj$ ) specification for the transition (if otherwise unknown) is then arrived at, if possible, by a combination of assumptions and deductions based on general shell-model ideas. An index of the structural details affecting the strength of the particular transition, called the spectroscopic factor  $S(nlj)$ , is then extracted on the basis of the following equations<sup>12</sup> for, respectively, ( $^3\text{He}, d$ ) and ( $d, ^3\text{He}$ ) reactions:

$$\frac{d\sigma(\theta)}{d\Omega}(nlj)_{\text{exp}} = \frac{2J_f + 1}{2J_i + 1} S(nlj) N(^3\text{He}, d) \frac{d\sigma(\theta)}{d\Omega}(nlj)_{\text{DW}} \quad (4)$$

and

$$\frac{d\sigma(\theta)}{d\Omega}(nlj)_{\text{exp}} = S(nlj) N(d, ^3\text{He}) \frac{d\sigma(\theta)}{d\Omega}(nlj)_{\text{DW}} \quad (5)$$

The factors " $N$ " account for the overlap and statistics of the ( $d$ - $^3\text{He}$ ) aspect of the reaction cross sections,<sup>16</sup> and  $J_i$  and  $J_f$  refer to the spins of the initial and final nuclear states.

The stripping spectroscopic factor corresponds theoretically to the expectation value between the initial and final wave functions of a particle-creation operator of the correct ( $nlj$ ) quantum numbers. The pickup spectroscopic factor corresponds to the analogous particle-destruction operator. As such, the spectroscopic factor yields a measure of the overlap of the final state with the wave function formed by coupling a single particle or hole to the initial state. Also, the sum of all  $S$ -factor strength for a particular ( $nlj$ ) provides a measure of the occupation (vacancy) probability of that orbit in the target ground state.<sup>21</sup>

The occupation probabilities for the various active orbits in the target states thus can be obtained either from the ( $d, ^3\text{He}$ ) experiments - measuring occupancies - or from the ( $^3\text{He}, d$ ) experiments - measuring the complementary vacancies. A consistent set of answers from the two approaches is a fundamental test of the internal consistency of the DWBA analysis. In this regard we will find that the DWBA calculations modified to use reduced spin-orbit radii are significantly better than the standard version. Inconsistency between stripping and pickup results manifests itself as follows. The usual analysis yields spectroscopic factors that are too small for  $j = l - \frac{1}{2}$  transitions (spectroscopic factors being inversely proportional to DWBA cross sections). Thus, for the  $1g_{7/2}$  orbit, the pick-up results would yield too small an occupation probability while the stripping results would indicate too small a vacancy, which corresponds to too large an occupation probability. The effects

propagate through the other orbits. Since we will be dealing with relative spectroscopic factors, this problem shows up, for example, as inconsistent ratios for the  $1g_{7/2}-2d_{5/2}$  occupation probabilities as determined via the complementary pick-up and stripping reactions on a given target. By reducing the effect of the spin-orbit potential on cross sections, the modified DWBA analysis produces results from stripping and pick-up reactions on a given target which are more consistent with each other.

Even under the best possible conditions, however, there are probably still uncertainties in relative spectroscopic factors of 15%. This sort of uncertainty can, in some cases, lead to much larger percentage errors in the extraction of occupation probabilities. For example, an important question in the present study concerns the occupation of the  $1h_{11/2}$  orbit in the target ground states. The  $(d, {}^3\text{He})$  spectroscopic factor for the  $\frac{11}{2}^-$  state in the various residual nuclei gives a direct value for this quantity. However, since the occupation probability is small and in addition the intrinsic cross section for  $l_p = 5$  is weak (see Fig. 4), the observed cross sections are small, and accurate values for the pick-up  $S$  factors are difficult to obtain for purely experimental reasons. Conversely, stripping into the  $1h_{11/2}$  vacancy yields much larger cross sections and the  $S$  factors can be extracted with good experimental accuracy. For  $(nlj) = (1, 5, \frac{11}{2})$ ,  $S = 0.9$ , the occupation probability,  $\langle 1h_{11/2} \rangle$ , is 1.2. Considering the 15% uncertainty inherent in  $S$ , however, we see that the value of  $\langle 1h_{11/2} \rangle$  could, in this example, legitimately range between 0 and 2.8. The ubiquity of this type of problem carries the implication that measurements of "small" effects of the sort illustrated will have inherent uncertainties of the order of a factor of 2.

#### D. Normalization of Spectroscopic Factors

As was mentioned, the absolute cross sections for a given reaction and target contained large uncertainties. It follows that individual absolute spectroscopic factors could not be extracted with good accuracy. We have chosen to normalize the  $S(nlj)$  so as to illuminate the *internal* consistency of the DWBA-extracted results. One of the most striking features of the  $({}^3\text{He}, d)$  spectra of Fig. 3 is the concentration of transition intensity into the low-lying states. It appears to be a secure assertion that the preponderance of the spectroscopic strength to the empty "gdhs" orbits is contained in the analyzed angular distributions. We assume here that all of the observed stripping transitions proceed to orbits of the "gdhs" shell and that all of the target protons in excess of 50 also occupy orbits of this shell. Under these conditions, a gen-

eral limitation on the sum of the stripping strength to "gdhs" states exists and has the form

$$\sum_{\substack{n,l,j \in \text{"gdhs"} \\ i \in \text{obs. states}}} (2j+1)S_i(nlj) \leq (32 - [Z - 50]), \quad (6)$$

where  $Z$  is the proton number of the  $N=82$  target nucleus. This sum rule expresses the fact that protons can be created and coupled to an  $N=82$  nuclear ground state only to the extent that its wave function has proton holes remaining in the "gdhs" shell. To the extent that the *observed* stripping strength corresponds to the total existing, the inequality (6) approaches equality.

For our purposes here we *assume* that all of the stripping transitions have been observed, and correspondingly choose a normalization for the  $({}^3\text{He}, d)$  spectroscopic factors on a given target such that the equality in formula (6) holds. By this procedure, we impose a normalization on the experimental  $({}^3\text{He}, d)$  results for each of the  $N=82$  targets, and the tabulated spectroscopic factors are based on these normalizations. Now if the DWBA analysis for a set of stripping transitions from a given target was completely consistent, no spectroscopic sum for a particular  $(nlj)$  would exceed unity. The cases in which this rule is violated thus yield an estimate of the minimum uncertainty of the DWBA analysis. There are a multiplicity of other criteria that could be used to choose a normalization, e.g., imposing the conditions just stated, that no orbit have a  $\sum_i S_i(n, l, j)$  greater than unity. We chose the one previously described because we felt it averaged over the various calculations and data best. However, in some cases the results lead to "supervacancy" for orbits that the complementary pickup reaction shows to be populated to some extent.

The  $(d, {}^3\text{He})$  spectroscopic factors were normalized to be consistent with the  $({}^3\text{He}, d)$  results for the same target nuclei. The sum of the pickup strength to the lowest  $\frac{7}{2}^+$  and  $\frac{5}{2}^+$  states was adjusted so as to yield a combined  $(1g_{7/2} - 2d_{5/2})$  occupation probability consistent with that deduced from the stripping measurements. Thus, from stripping,

$$\langle 1g_{7/2} + 2d_{5/2} \rangle = \sum_j (1 - \sum_i S_i(j))(2j+1), \quad (7)$$

and from pickup,

$$\langle 1g_{7/2} + 2d_{5/2} \rangle = \sum_{i,1} S_i(j), \quad (8)$$

where in each case "j" can equal  $\frac{7}{2}$  and  $\frac{5}{2}$  and "i" runs over all observed states of a particular "j". Hence, the pick-up spectroscopic factors were normalized to the stripping results by requiring equality between Eqs. (7) and (8). We emphasize

that the significant aspects of the spectroscopic factors to be presented lie in their values *relative* to one another.

#### IV. RESULTS AND DISCUSSIONS

##### A. General Remarks

The spectra of observed particles from the ( $d, {}^3\text{He}$ ) and ( ${}^3\text{He}, d$ ) reactions on the even  $N=82$  targets have been presented in Figs. 2 and 3, respectively. Each of the ( $d, {}^3\text{He}$ ) spectra in Fig. 2 shows evidence for only two transitions of major strength in the first 3 MeV of excitation. On the other hand, each of the ( ${}^3\text{He}, d$ ) spectra of Fig. 3 shows at least five transitions with significant intensity in the same region. As will be seen in the detailed exposition which follows, one of the two strong groups observed in each of the pick-up reactions has an  $l_p=2$  shape and the other an  $l_p=4$  shape. The ideas developed in the preceding sections lead to the following conclusions. The presence of only two kinds of transitions in the pick-up spectra (a first approximation) implies that only two active orbits in the target state have appreciable occupation probability. The ordering of single-particle states in the "shell-model" potential well then requires that the  $l_p=4$  transitions be associated with the  $1g_{7/2}$  orbit, since  $1g_{9/2}$  protons should be tightly bound in the  $Z=50$  core. Both  $2d_{5/2}$  and  $2d_{3/2}$  orbits occur in the  $gdhs$  shell, but if only one orbit is occupied, it should on all counts be that with  $j=l+\frac{1}{2}$ . Hence, the general conclusion to be drawn from the pick-up studies is that in the target ground states the protons outside  $Z=50$  occupy  $1g_{7/2}$  and  $2d_{5/2}$  orbits. This is in fact consistent with the more detailed predictions of the shell-model ordering schemes and with other experimental studies of the ground- and first excited-state spins of some of the odd-mass nuclei.<sup>5,6</sup>

The strong states observed in the stripping spectra have angular distributions characterized by  $l_p=0, 2, 4,$  and  $5$ . The lowest  $l_p=2$  transition corresponds to the  $l_p=2$  state seen in the pickup transition to the same nucleus. Hence, it follows that it must also correspond to transfer of a  $2d_{5/2}$  proton. Similarly, the  $l_p=4$  stripping transition populates the same states that is formed by  $l_p=4$  pick-up. In addition to these two states, each stripping spectrum has a single transition characterized by  $l_p=5$  and one each (or a set of fragments thereof) characterized by  $l_p=0$  and  $l_p=2$ . It is consistent with our previous discussion to assume that these higher states (or centroids in the cases of fragmentation) correspond to the remaining three single-particle orbits in the  $gdhs$  shell, namely  $1h_{11/2}$ ,  $2s_{1/2}$ , and  $2d_{3/2}$ .

Our simple expectations about the structure of

the levels of  $N=82$  nuclei at low excitation energies are confirmed by this initial inspection of the experimental results. Levels in the odd-mass nuclei whose wave functions might involve the proton orbits above  $Z=82$  would be characterized by stripping transitions of  $l_p=5, 3,$  and  $1$  (corresponding to the  $1h_{9/2}$ ,  $2f$ , and  $3p$  orbits). No transitions with  $l_p=1$  or  $3$  are observed. The single  $l_p=5$  transition observed for any one nucleus must logically be associated with the  $1h_{11/2}$  member of the  $gdhs$  shell rather than the  $1h_{9/2}$  member of the shell above  $Z=82$ , since the pickup results indicate neither "h" orbit is significantly occupied. Levels arising from configurations involving the excitation of protons out of the orbits below  $Z=50$  would be populated by pick-up transitions of  $l_p=4, 3,$  or  $1$ , corresponding to the  $1g_{9/2}$ ,  $1f$ , and  $2p$  orbits. Again, no  $l=3$  or  $1$  transitions are seen, and the single  $l_p=4$  transition must be associated with the  $1g_{7/2}$  orbit of the  $gdhs$  shell, since stripping indicates only one "g" orbit is unfilled, and this one must be the higher-lying,  $j=l-\frac{1}{2}$  member. Hence, the final states populated by ( ${}^3\text{He}, d$ ) or ( $d, {}^3\text{He}$ ) are all explicable in terms of  $gdhs$  configurations. The same general evidence can be used to conclude that the target ground states are also constructed from within the  $gdhs$  shell, with the  $Z \leq 50$  and  $Z \geq 82$  shells effectively completely full and completely empty, respectively.

The angular distributions of the ( $d, {}^3\text{He}$ ) reactions on the various even-mass  $N=82$  targets are shown in Figs. 6, 8, 10, 12, and 14, while the ( ${}^3\text{He}, d$ ) angular distributions for the same target nuclei are shown in Figs. 7, 9, 11, 13, and 15. The curves are the DWBA predictions for the individual transitions, and the fits of the calculated shapes to the data points are the basis of the assignments of  $l_p$ .

Table III lists the excitation energies of the various levels of the odd-mass  $N=82$  nuclei which are observed in the present experiments. Because of the better energy resolution and statistical accuracy of the ( ${}^3\text{He}, d$ ) data, the excitation energies are taken from the ( ${}^3\text{He}, d$ ) data except for  ${}^{135}\text{I}$ , where of course none were available. Also listed in this table are the assigned values of  $l_p$ , the assumed values of  $J$ , and the spectroscopic factors  $S(nlj)$  extracted from both the ( ${}^3\text{He}, d$ ) and ( $d, {}^3\text{He}$ ) angular distributions. Results from both the standard and the modified DWBA analyses are included.

##### B. Details of Results

###### 1. ${}^{136}\text{Xe}(d, {}^3\text{He}){}^{135}\text{I}$

Prior to the present experiment, the only definite information available about  ${}^{135}\text{I}$ , the lightest



TABLE III. Excitation energies,  $l_p$  values, and spectroscopic factors for levels of odd-mass  $N = 82$  nuclei excited by roton stripping and pick-up reactions. Uncertainties in measured excitation energies are 8 keV per MeV of excitation.

Residual nucleus	Measured excitation energy (MeV)	$l_p$	$J^\pi$ Assumed	$S(n, l, j)$ ( $^3\text{He}, d$ )		$S(n, l, j)$ ( $d, ^3\text{He}$ )	
				Mod.	Stand.	Mod.	Stand.
$^{135}\text{I}$	0.00	4	$\frac{7}{2}^+$			2.74	1.82
	$0.590 \pm 0.030$	2	$\frac{5}{2}^+$			0.34	0.17
	$0.860 \pm 0.040$	2	$\frac{5}{2}^+$			0.12	0.06
$^{137}\text{Cs}$	0.00	4	$\frac{7}{2}^+$	0.60	0.75	3.91	3.57
	0.455	2	$\frac{5}{2}^+$	1.02	0.99	1.01	0.71
	1.49	0	$\frac{1}{2}^+$	0.07	0.07		
	1.87	5	$\frac{11}{2}^-$	1.01	0.87		
	2.07	2	$\frac{3}{2}^+$	0.79	0.92		
	2.15	0	$\frac{1}{2}^+$	0.86	0.89		
$^{139}\text{La}$	0.00	4	$\frac{7}{2}^+$	0.43	0.54	6.21	6.07
	0.166	2	$\frac{5}{2}^+$	0.94	0.90	1.71	1.29
	1.21	0	$\frac{1}{2}^+$	0.09	0.10		
	1.42	5	$\frac{11}{2}^-$	0.84	0.71	0.7	0.6
	1.56	2	$\frac{3}{2}^+$	0.06	0.07		
	1.78	0	$\frac{1}{2}^+$	0.65	0.67		
	1.78	2	$\frac{3}{2}^+$	0.73	0.83		
	1.85	2	$\frac{3}{2}^+$	0.26	0.30		
	1.96	2	$\frac{3}{2}^+$	0.16	0.19		
	2.24	2	$\frac{3}{2}^+$	0.08	0.10		
2.31	0	$\frac{1}{2}^+$	0.13	0.13			
$^{141}\text{Pr}$	0.00	2	$\frac{5}{2}^+$	0.64	0.64	2.70	2.12
	0.145	4	$\frac{7}{2}^+$	0.28	0.35	6.06	6.20
	1.11	5	$\frac{11}{2}^-$	0.96	0.84	1.03	0.86
	1.30	0	$\frac{1}{2}^+$	0.61	0.65	0.09	0.09
	1.60	2	$\frac{3}{2}^+$	1.04	1.23		
	1.65	0	$\frac{1}{2}^+$	0.51	0.54		
$^{143}\text{Pm}$	0.00	2	$\frac{5}{2}^+$	0.54	0.52	3.80	3.20
	0.270	4	$\frac{7}{2}^+$	0.25	0.32	6.85	7.50
	0.96	5	$\frac{11}{2}^-$	0.82	0.71	1.65	1.40
	1.06	2	$\frac{3}{2}^+$	0.05	0.06		
	1.17	0	$\frac{1}{2}^+$	1.08	1.12	0.23	0.23
	1.40	2	$\frac{3}{2}^+$	1.13	1.31	0.48	0.53
$^{145}\text{Eu}$	0.00	2	$\frac{5}{2}^+$	0.33	0.33		
	0.329	4	$\frac{7}{2}^+$	0.17	0.22		
	0.716	5	$\frac{11}{2}^-$	0.83	0.72		
	0.808	0	$\frac{1}{2}^+$	1.00	1.05		

TABLE III (Continued)

Residual nucleus	Measured excitation energy (MeV)	$l_p$	$J^\pi$ Assumed	$S(n, l, j)$ ( $^3\text{He}, d$ )		$S(n, l, j)$ ( $d, ^3\text{He}$ )	
				Mod.	Stand.	Mod.	Stand.
	1.04	2	$\frac{3}{2}^+$	1.03	1.21		
	1.76	2	$\frac{3}{2}^+$	0.02	0.05		
	1.84	2	$\frac{3}{2}^+$	0.10	0.12		

$N=82$  nucleus that can be studied with current techniques, was that its ground state had  $J^\pi = \frac{7}{2}^+$ . The uncertainty in its mass was listed<sup>9</sup> as 1 MeV.

The ( $d, ^3\text{He}$ ) reaction cross sections on  $^{136}\text{Xe}$  are quite small. This results from the fact that there are only four active protons in the ground state and these predominantly occupy the  $1g_{7/2}$  orbit, for which the intrinsic transfer cross section is quite weak. Compounding the experimental problems for this reaction was the fact that energy resolution in the spectra was appreciably poorer than in the other ( $d, ^3\text{He}$ ) experiments because of straggling in the gas cell windows and in the gas. Data from the  $^{136}\text{Xe}(d, ^3\text{He})^{135}\text{I}$  reaction were accumulated over a period of three days, during which the target gas was left undisturbed. At least two spectra were accumulated at each angle at separate times, so as to provide information on possible contaminant accumulation. No change in the target gas could be detected.

A spectrum of the  $^3\text{He}$  events from the  $^{136}\text{Xe}$  target is shown in Fig. 5. The three labeled peaks are interpreted as corresponding to the ground, first excited and second excited states of  $^{135}\text{I}$ . The

angular distributions of the transitions to these levels are shown in Fig. 6. The ground-state distribution agrees with an  $l_p=4$  DWBA curve and the excited-state distributions are each in agreement with  $l_p=2$  curves. The energies of the excited states are listed in Table III. In order to establish the  $Q$  value for the ground-state transition without first-order dependence on beam energy and the thicknesses of the target gas, cell window, etc., the  $^{136}\text{Xe}$  target was deliberately contaminated with a charge of air at the end of the experiment. Spectra at several angles were accumulated with the particle groups from the  $^{14}\text{N}(d, ^3\text{He})^{13}\text{C}$  and  $^{16}\text{O}(d, ^3\text{He})^{15}\text{N}$  reactions superimposed upon the  $^{135}\text{I}$  spectrum. One of these spectra is shown in Fig. 2. Since all the particles had passed through the identical environment, the  $Q$  value for  $^{136}\text{Xe}(d, ^3\text{He})^{135}\text{I}$  was immediately established by reference to the known  $Q$  values of the reactions on  $^{16}\text{O}$  and  $^{14}\text{N}$  and the appropriate kinematic corrections. The new measured value is listed in Table I. As will be discussed later, both of the  $l_p=2$  transitions were assumed to correspond to pickup of  $2d_{5/2}$  protons, and the spectroscopic factors listed in Table III

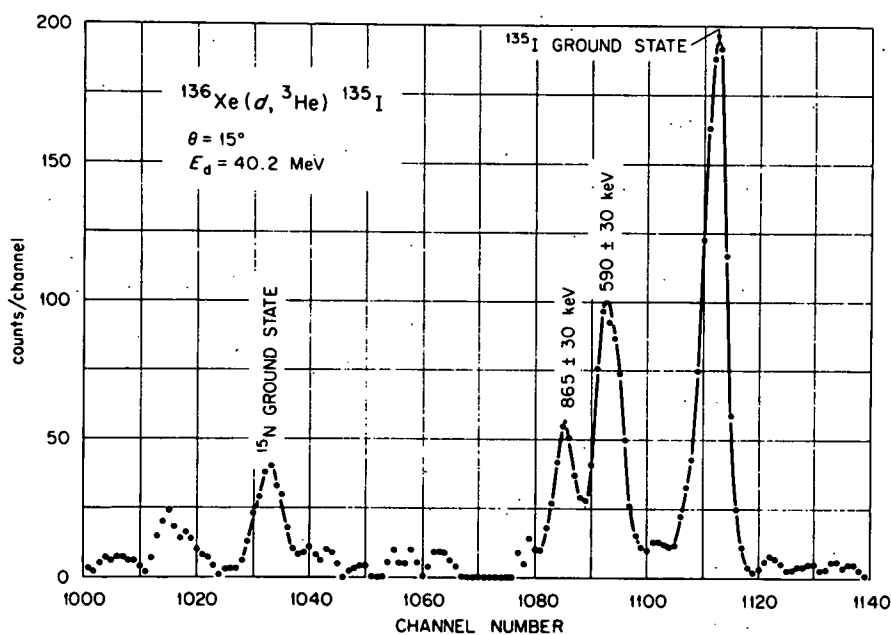


FIG. 5. Spectrum of  $^3\text{He}$  particles emitted in the  $^{136}\text{Xe}(d, ^3\text{He})^{135}\text{I}$  reaction.

were extracted on this basis.

### 2. $^{136}\text{Xe}(\text{}^3\text{He}, d)^{137}\text{Cs}$

The data for the  $(^3\text{He}, d)$  reaction on  $^{136}\text{Xe}$  were taken at a bombarding energy of 25 MeV rather than 40 MeV because of technical difficulty with the cyclotron beam during that particular experimental period. This had two effects, the first being that energy straggling in the windows and tar-

get gas was relatively more severe than would have been the case at 40 MeV and the second being that the extraction of spectroscopic factors with the 40-MeV families of optical-model parameters was subject to additional uncertainties compared to the other sets of experimental data.

A sample spectrum of the reaction is shown at the bottom of Fig. 3. The angular distributions of the six groups to which energies are assigned in Fig. 3 are shown in Fig. 7, together with the DWBA calculations. The ground-state transition is  $l_p = 4$  and the first excited state is  $l_p = 2$ . The spectroscopic factors are consistent with these two levels being formed by coupling  $1g_{7/2}$  and  $2d_{5/2}$  protons, respectively, to the  $^{136}\text{Xe}$  ground state. We will in the following discussion refer to this sort of level as a " $(nlj)$ -single-particle (hole) state." A weakly excited level at 1.49 MeV has an  $l_p = 0$  angular distribution, as does a much stronger transition to a level at 2.15 MeV. Levels at 1.87 and 2.07 MeV are populated by  $l_p = 5$  and 2 transitions, respectively. The spectroscopic factors suggest the assignment of  $J = \frac{3}{2}$ , and a  $2d_{3/2}$ -single-particle nature, for the 2.07-MeV state and  $1h_{11/2}$  and  $3s_{1/2}$  single-particle characters for the 1.87- and 2.15-MeV levels, respectively. It is possible that states in the vicinity of 800 keV are populated also, but the reaction events in this region which are observable in Fig. 3 cannot definitely be attributed to any one unique parent.

In a recent study<sup>22</sup> of the  $\gamma$  rays which follow the  $\beta$  decay of  $^{137}\text{Xe}$ , several levels in  $^{137}\text{Cs}$  between 800 and 2100 keV have been reported. Of these, the only one which appears to correspond to a level excited with the  $(^3\text{He}, d)$  reaction is one at 2071 keV, the energy of which is in good agreement with that of the strong  $l = 2$ ,  $J = \frac{3}{2}^+$  transition we see at an excitation of 2.07 MeV. Our  $l_p = 0$  and  $l_p = 5$  states would not be directly populated via the  $\beta$  decay and are unlikely to be observed in the  $\gamma$  spectra. The levels deduced to lie at 849- and 982-keV excitations on the basis of the  $\gamma$ -ray data are not in good enough energy agreement with the broad peak at  $\sim 800$  keV mentioned earlier to convince us of a relationship, but this possibility cannot be ruled out. A direct-reaction study,  $(^3\text{He}, d)$  or  $(d, n)$ , with higher resolution would be useful in resolving this question.

### 3. $^{138}\text{Ba}(d, ^3\text{He})^{137}\text{Cs}$

The  $^{137}\text{Cs}$  level structure was also investigated by proton pickup from  $^{138}\text{Ba}$ . The only two levels that are discernably excited with consistency are the ground and first excited states. The ground-state transition is  $l_p = 4$  and the first-excited-state transition is  $l_p = 2$ , as is shown in Fig. 8. As outlined previously, the occurrence of only two strong

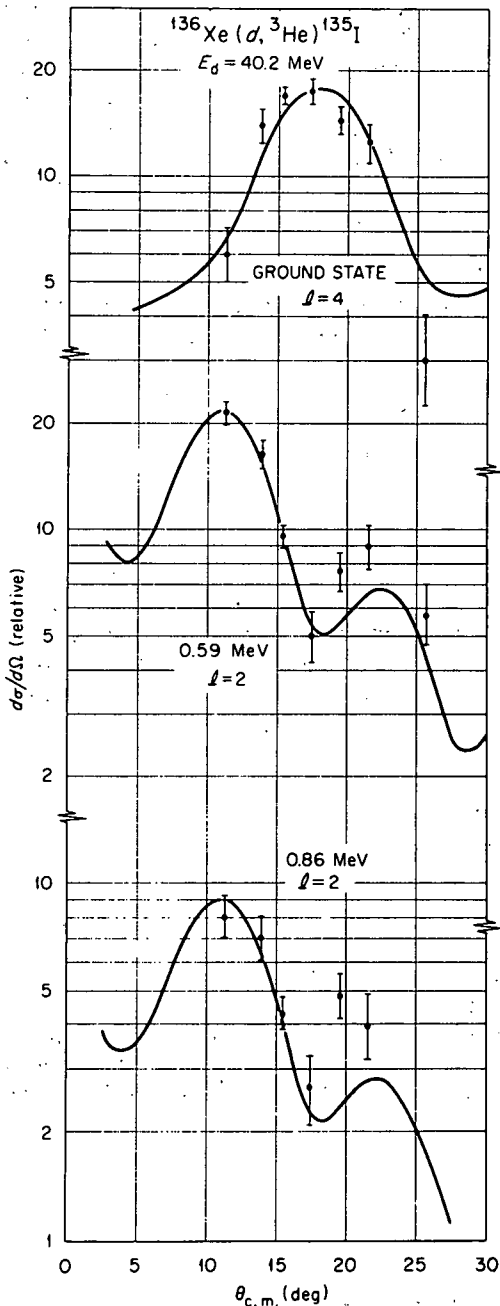


FIG. 6. Angular distributions of the first three transitions observed in the  $^{136}\text{Xe}(d, ^3\text{He})^{137}\text{Cs}$  reactions. The curves are DWBA predictions.

transitions is interpreted as indicating that only two orbits are appreciably occupied by the six active protons of the  $^{138}\text{Ba}$  ground state. It is from this premise that we deduce  $J^\pi = \frac{5}{2}^+$  for the first excited state, a point drawn upon in the prior discussion of the stripping transition to this same state. The strength of the pick-up transitions to these two levels indicate that they can be considered as single-hole states relative to  $^{138}\text{Ba}$ , as

well as single-particle states relative to  $^{136}\text{Xe}$ .

#### 4. $^{138}\text{Ba}(^3\text{He}, d)^{139}\text{La}$

The ground and first excited states of  $^{139}\text{La}$  are populated via proton stripping on  $^{138}\text{Ba}$  by  $l_p = 4$  and 2 transitions, respectively, as is shown in Fig. 9. Arguments similar to those made for  $^{137}\text{Cs}$  result in our assigning  $J^\pi = \frac{7}{2}^+$  and  $\frac{5}{2}^+$ , respectively, to these states. These are the  $1g_{7/2}$  and  $2d_{5/2}$  sin-

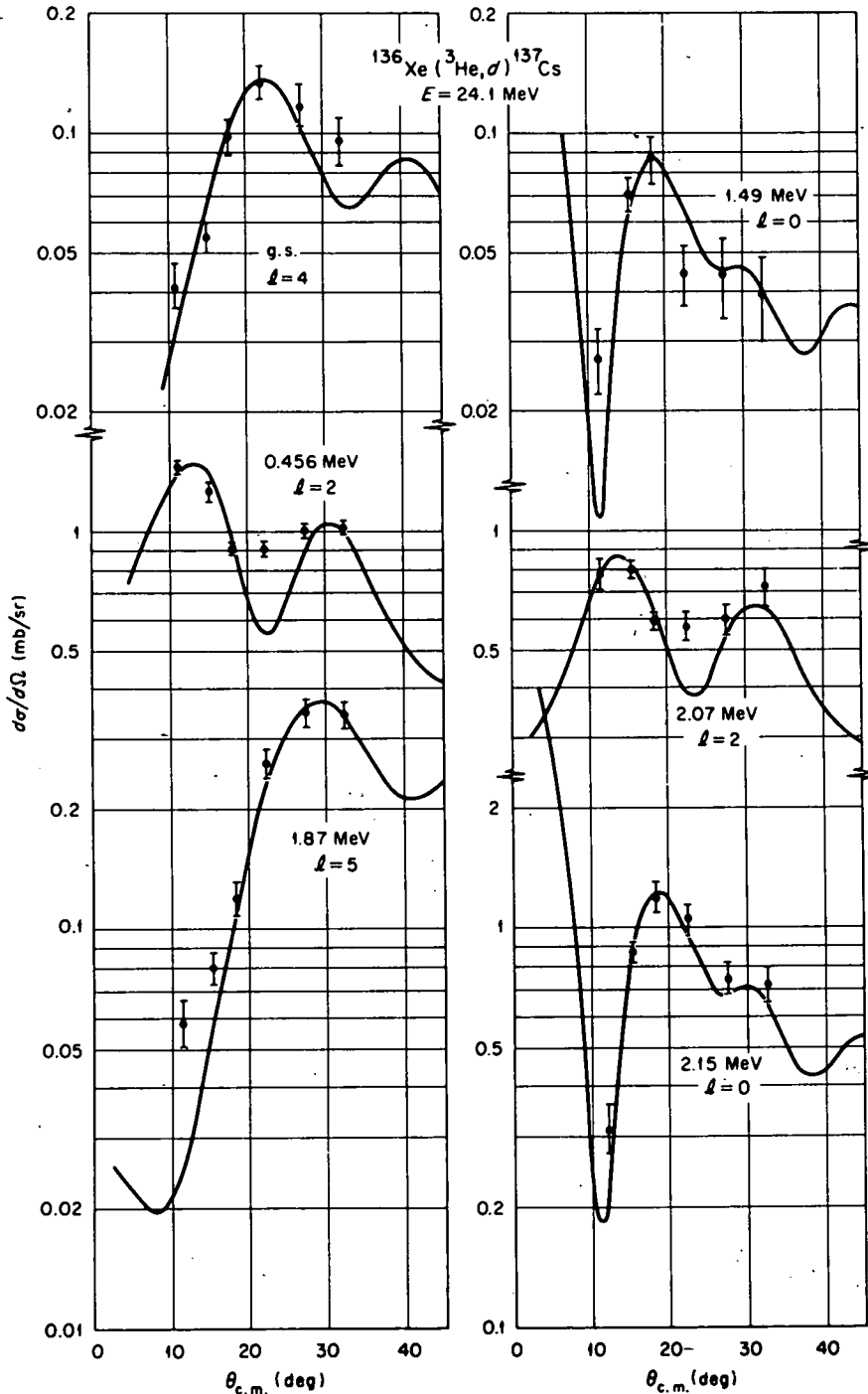


FIG. 7. Angular distributions of the observed transitions in the  $^{136}\text{Xe}(^3\text{He}, d)^{137}\text{Cs}$  reaction. The curves are DWBA predictions.

single-particle states relative to  $^{138}\text{Ba}$ . No other states are seen (Fig. 3) up to an excitation of 1207 keV. Between 1200- and 2400-keV excitation, several levels are identified and their angular distributions measured. The data and DWBA curves are also shown in Fig. 9, and the results of the analysis listed in Table III. The  $l_p = 5$  ( $J^\pi = \frac{11}{2}^-$ ) state has moved down in excitation energy from its position

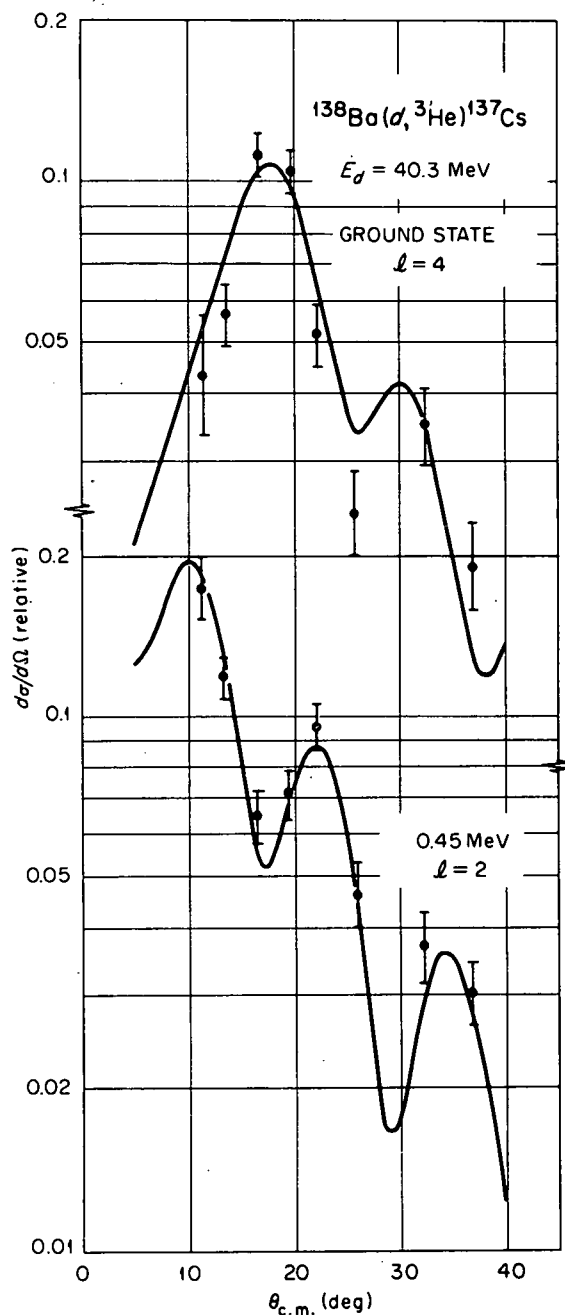


FIG. 8. Angular distributions of the transitions to the ground and first excited states of  $^{137}\text{Cs}$ , observed in the  $^{138}\text{Ba}(d, ^3\text{He})^{137}\text{Cs}$  reaction. The curves are DWBA predictions.

in  $^{137}\text{Cs}$ . The presence of several  $l_p = 0$  levels and several higher-lying  $l_p = 2$  levels indicates the partial fragmentation of the  $3s_{1/2}$  and  $2d_{3/2}$  single-particle states. The largest fragments of each lie at 1.78-MeV excitation and are not experimentally resolved in the spectra, a situation which creates an additional problem in extracting these important spectroscopic factors. It should be clearly noted that the employment of  $J^\pi = \frac{3}{2}^+$  for all of the higher  $l_p = 2$  transitions is an assumption of convenience only, since states with spectroscopic factors which are a small fraction of unity could be either  $\frac{3}{2}^+$  or  $\frac{5}{2}^+$ . Nonetheless, we tend to believe that they are all  $\frac{3}{2}^+$ .

In the interim since the first report of the  $(^3\text{He}, d)$  results<sup>1</sup> several investigators<sup>23-27</sup> have published level schemes of  $^{139}\text{La}$  obtained either through observation of the  $\gamma$ -ray decay of levels populated by  $\beta$  decay or by inelastic scattering of neutrons or  $\gamma$  rays. The results of older studies of the  $^{139}\text{La}$  level structure are generally suspect since they typically report levels in the 200-1100-keV region of excitation energy, where the consensus of later studies indicates no states at all. It appears that all of the states seen via  $(^3\text{He}, d)$  have been observed with one or more of the other experimental techniques. The high level density above 1400 keV makes an unambiguous rationalization of the various experimental results impractical for the present, however.

#### 5. $^{140}\text{Ce}(d, ^3\text{He})^{139}\text{La}$

The dominant pick-up transitions, (see Fig. 2) to  $^{139}\text{La}$  from  $^{140}\text{Ce}$  are to the ground state, with  $l_p = 4$ , and to the first excited state at 166 keV, with  $l_p = 2$ . These angular distributions are shown in Fig. 10. This leads to the assignments  $J^\pi = \frac{7}{2}^+$  and  $\frac{5}{2}^+$ , respectively, for these levels. They have  $1g_{7/2}$  and  $2d_{3/2}$  single-hole characters relative to  $^{140}\text{Ce}$ . A very weak transition can be detected to a level with energy corresponding to the level excited with  $l_p = 5$  in the  $^{139}\text{Ba}(^3\text{He}, d)^{139}\text{La}$  reaction. We assume that the state seen in pickup is the single-particle  $1h_{11/2}$  state and use the observed pickup intensity to set an upper limit for the occupation probability of  $1h_{11/2}$  in the ground state of  $^{140}\text{Ce}$ . The results are listed in Table III. The  $l = 0$  and  $l = 2$  spectroscopic factors which could be extracted from the small peak at 1.78 MeV are negligible.

#### 6. $^{140}\text{Ce}(^3\text{He}, d)^{141}\text{Pr}$

The ground state of  $^{141}\text{Pr}$  is populated in proton stripping with an  $l_p = 2$  transition, while an  $l_p = 4$  transition, which in the lighter nuclei is associated with the ground state, now populates the first

excited state at 145 keV. These two states are again associated with the addition of protons into the  $2d_{5/2}$  and  $1g_{7/2}$  orbits, respectively. This is consistent with the results of the  $(d, {}^3\text{He})$  reaction to  ${}^{141}\text{Pr}$  and with the previous<sup>5,6</sup> assignments of  $\frac{5}{2}^+$  and  $\frac{7}{2}^+$  to these levels based on atomic beam

and decay methods. The next state observed with the  $({}^3\text{He}, d)$  reaction lies at 1.11-MeV excitation and has an  $l_p = 5$  angular distribution. Levels at excitations of 1.30 and 1.65 MeV are populated with  $l_p = 0$  transitions and a level at 1.60 MeV is populated with  $l_p = 2$  transfer. Thus, making our

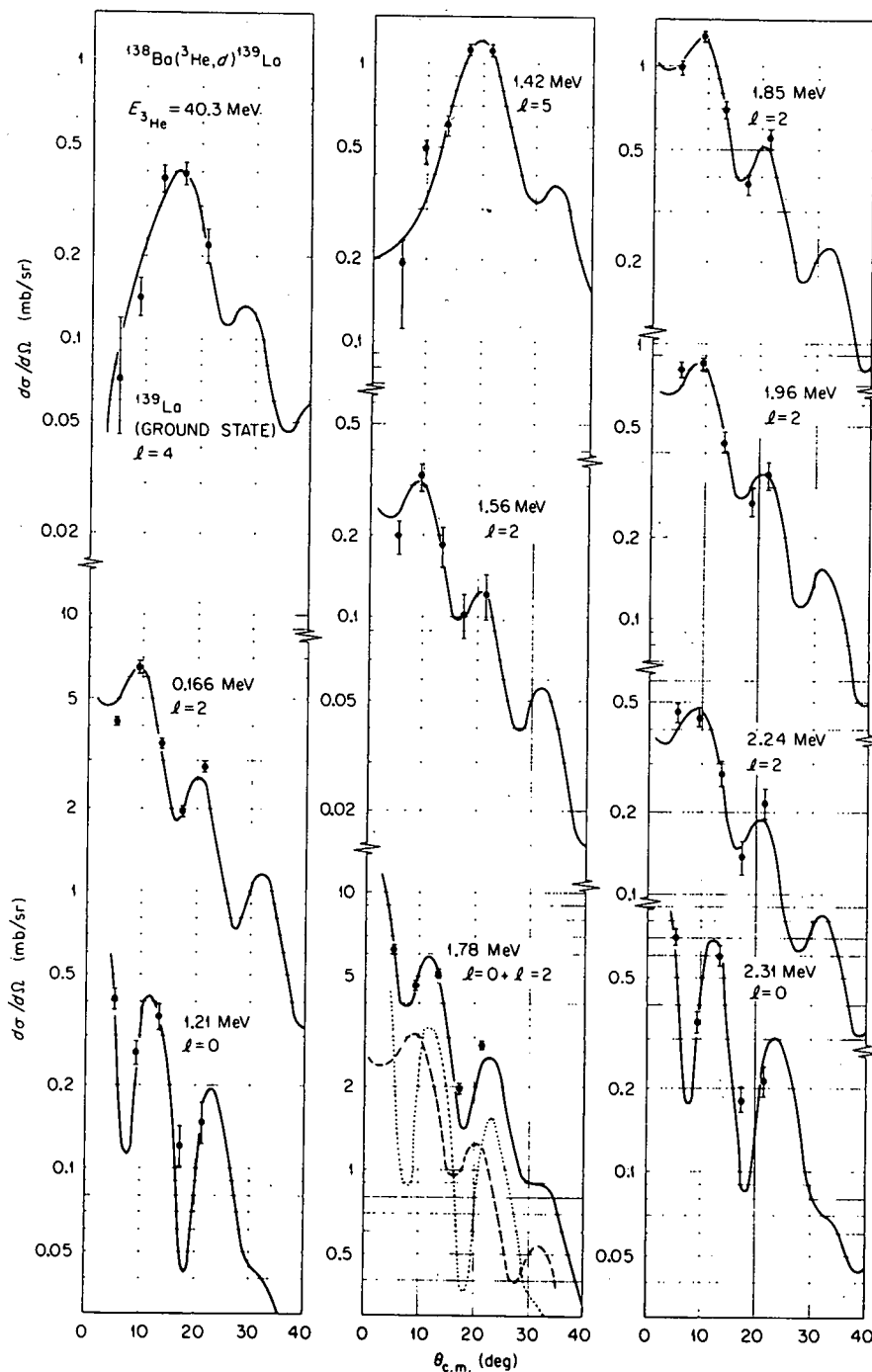


FIG. 9. Angular distributions of the observed transitions in the  ${}^{138}\text{Ba}({}^3\text{He}, d){}^{139}\text{La}$  reaction. The curves are DWBA predictions. The curve for the 1.78-MeV transition is a sum of  $l_p = 0$  and  $l_p = 2$  predictions.

usual assumption that strong stripping transitions to higher states represent population of the higher orbits of the  $gdhs$  shell, only one level each is observed for  $1h_{11/2}$  and  $2d_{3/2}$  while the  $3s_{1/2}$  strength is fairly evenly split between two levels. The angular distributions and DWBA curves are shown in Fig. 11.

As was the case for  $^{139}\text{La}$ , there have been numerous recent high-resolution studies of the  $^{141}\text{Pr}$  energy level spectrum in which  $\gamma$  decays are observed from levels excited by  $\beta^+$ -decay, inelastic

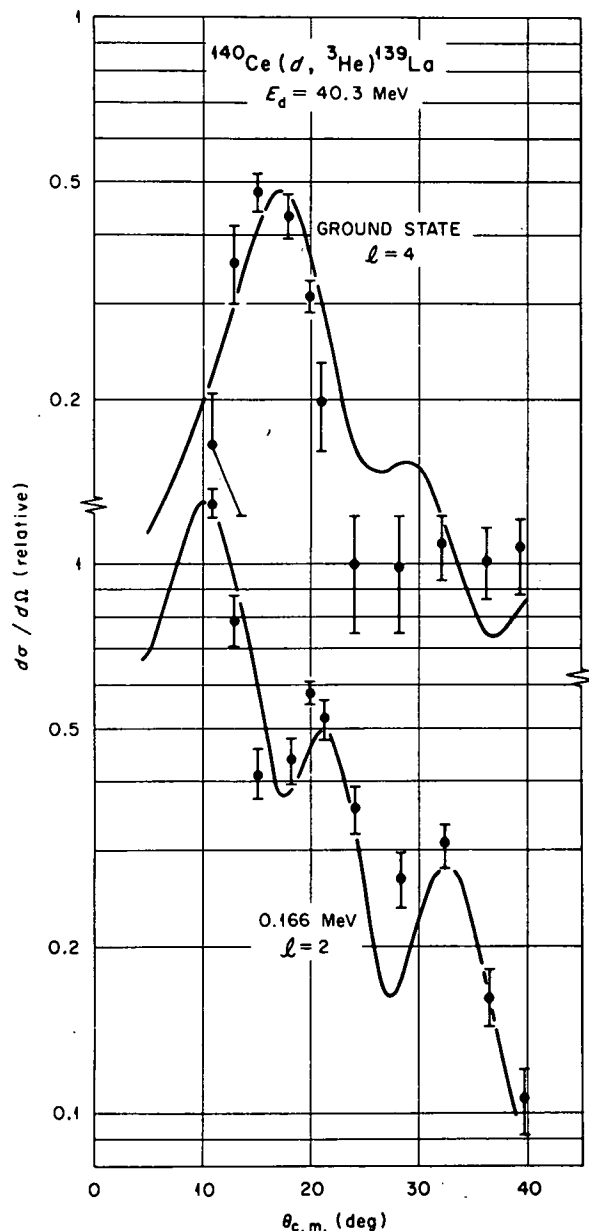


FIG. 10. Angular distributions of the transitions to the ground and first excited states of  $^{139}\text{La}$ , observed in the  $^{140}\text{Ce}(d, ^3\text{He})^{139}\text{La}$  reaction. The curves are DWBA predictions.

neutron, or  $\gamma$ -ray scattering.<sup>25-30</sup> In this instance it appears possible to make unambiguous correlations of the levels seen here with the consensus of level-energy assignments from the  $\gamma$ -ray data. The  $l_p = 5$  level at 1.11 MeV corresponds to the level seen in  $(n, n'\gamma)$  at 1.118 MeV. The  $l_p = 0$  level at 1.30 MeV corresponds to a level seen in both  $(\beta^+, \gamma)$  and  $(n, n'\gamma)$  at 1.299 MeV while the second  $\frac{1}{2}^+$  state at 1.65 MeV is listed at 1.650 MeV from  $(n, n'\gamma)$  and at 1.657 MeV from the  $(\beta^+, \gamma)$  work. The  $l_p = 2$  level at 1.60 MeV corresponds to the level seen at 1.607 MeV with both the  $(\beta^+, \gamma)$  and  $(n, n'\gamma)$  reactions. Numerous other states observed in the rather nonselective  $(n, n')$  reaction are not detectable in the  $(^3\text{He}, d)$  spectra, but this is to be expected.

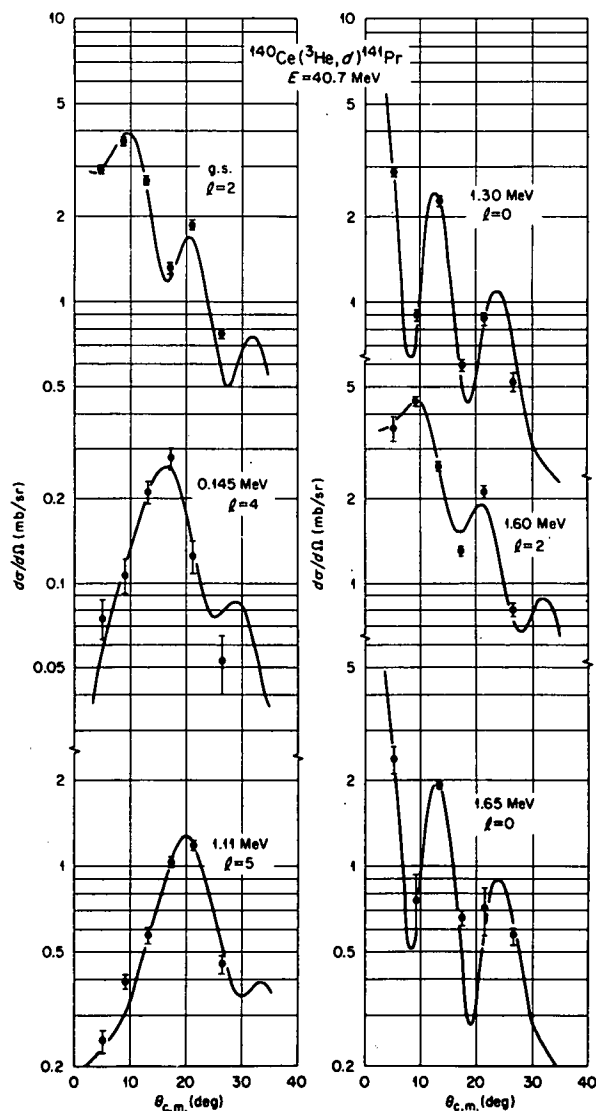


FIG. 11. Angular distributions of the transitions observed in the  $^{140}\text{Ce}(^3\text{He}, d)^{141}\text{Pr}$  reaction. The curves are DWBA predictions.

7.  $^{142}\text{Nd}(d, ^3\text{He})^{141}\text{Pr}$ 

The spectroscopic factors extracted from the  $l_p = 2$  and  $l_p = 4$  angular distributions (see Fig. 12) to, respectively, the ground and first excited states of  $^{141}\text{Pr}$  are large. Arguing as before, this leads to the inference of  $J = \frac{5}{2}^+$  and  $\frac{7}{2}^+$ , and  $2d_{5/2}$  and  $1g_{7/2}$  single-hole characters relative to  $^{142}\text{Nd}$ , for these levels.

There is evidence in the  $^3\text{He}$  spectra (see Fig. 2) for the population of levels at excitations of 1.11, 1.30, and 1.62 MeV, energies which correspond to the energies of the higher "gdhs" single-particle states observed with the  $(^3\text{He}, d)$  reaction to  $^{141}\text{Pr}$ . We assume the correspondence, even though the  $(d, ^3\text{He})$  data do not provide conclusive angular distributions for these levels. The small observed

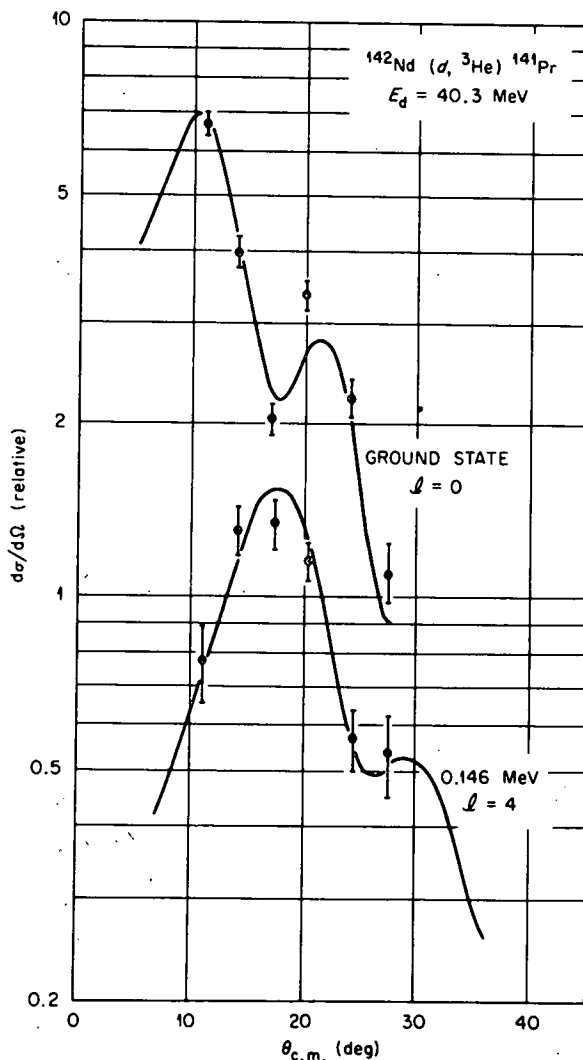


FIG. 12. Angular distributions of the transitions to the ground and first excited states of  $^{141}\text{Pr}$ , observed in the  $^{142}\text{Nd}(d, ^3\text{He})^{141}\text{Pr}$  reaction. The curves are DWBA predictions.

cross sections correspond to negligible spectroscopic strength for the  $3s_{1/2}$  and  $2d_{3/2}$  states but, as in the case of the  $^{140}\text{Ce}(d, ^3\text{He})^{139}\text{La}$  reaction, the upper limit on the  $1h_{11/2}$  spectroscopic factor is significant. Our conclusions are similar to those obtained by other workers with the same reaction.<sup>31</sup>

8.  $^{142}\text{Nd}(^3\text{He}, d)^{143}\text{Pm}$ 

The angular distributions to the levels of  $^{143}\text{Pm}$  noted in Fig. 3 are shown in Fig. 13. Comparing the levels of  $^{143}\text{Pm}$  to those of  $^{141}\text{Pr}$ , we find the following changes. There is a larger separation between the  $l_p = 4$  first-excited state and the  $l_p = 2$  ground state. The excitation energy of the  $1h_{11/2}$

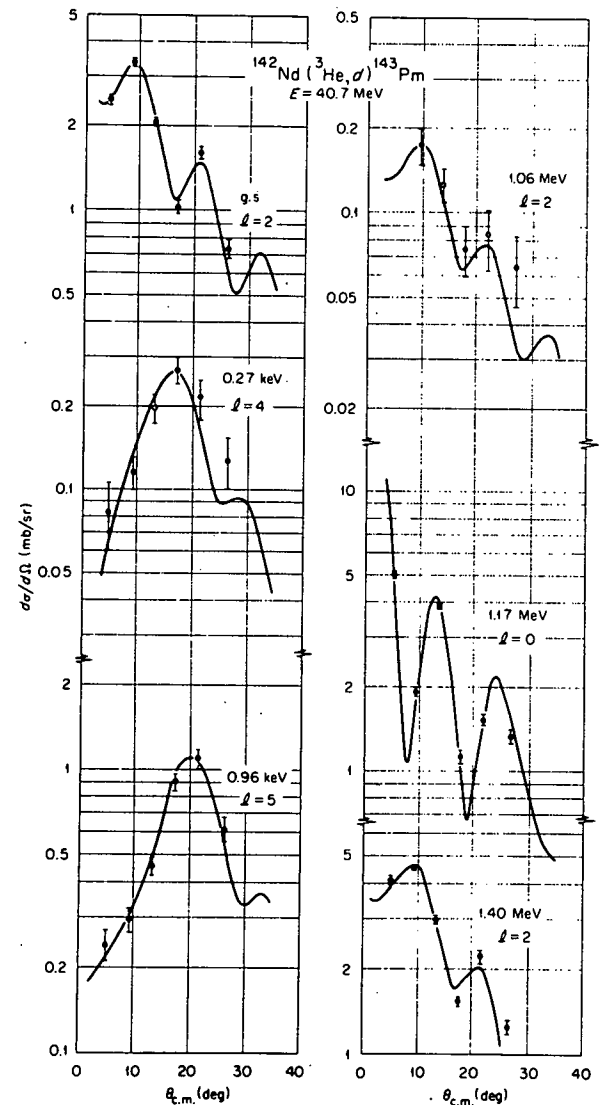


FIG. 13. Angular distributions of the transitions observed in the  $^{142}\text{Nd}(^3\text{He}, d)^{143}\text{Pm}$  reaction. The curves are DWBA predictions.



single-particle state has continued to decrease, and the  $l_p = 0$ ,  $3s_{1/2}$ , strength is now concentrated in one, not two final states. Most of the  $l_p = 2$ ,  $2d_{3/2}$ , strength is found in a state at 1.40-MeV excitation, but a weakly excited  $l_p = 2$  state is also seen at 1.04 MeV.

The  $Q$  value for this reaction had a listed<sup>10</sup> uncertainty of 300 keV. From our data we deduced the new value listed in Table I.

### 9. $^{144}\text{Sm}(d, ^3\text{He})^{143}\text{Pm}$

The increasing occupation probabilities in  $^{144}\text{Sm}$  of the higher  $g$  shells made it feasible to obtain definitive  $(d, ^3\text{He})$  angular distributions, shown in Fig. 14, for the five states of  $^{143}\text{Pm}$  excited with significant strength in  $(^3\text{He}, d)$  reaction. The  $(d, ^3\text{He})$  results are consistent with the conclusions drawn from the  $(^6\text{He}, d)$  data. Proton pickup has also been studied on  $^{144}\text{Sm}$  by the  $(t, \alpha)$  reaction<sup>32</sup> at 13-MeV bombarding energy. Although in that study the resulting angular distributions were not distinctive enough to permit definite  $l_p$  assignments to be made, the correct assumptions were made in each case, and the resulting spectroscop-

ic factors extracted for the various transitions are in reasonable agreement with those of Table III. In addition to the five transitions seen in  $(d, ^3\text{He})$ , the  $(t, \alpha)$  reaction also excited levels tentatively at 1.58 and 1.64 MeV and definitely at 1.85 and 1.97 MeV.

The information gained about the  $^{143}\text{Pm}$  energy level spectrum from the proton transfer reactions can be compared to the results of a study<sup>33</sup> of the decay of  $^{143}\text{Sm}$ . In this study, levels in  $^{143}\text{Pm}$  are found at 0.273, 1.057, 1.173, 1.341, 1.404, 1.516, 1.751, and 1.817 MeV. Of these, those at 1.057, 1.173, and 1.404 MeV should correspond to the  $l_p = 2, 0,$  and  $2$  states, respectively, seen in proton transfer at essentially the same energies. The conclusions drawn about the level structure of  $^{143}\text{Pm}$  on the basis of the decay work are in serious disagreement with the proton-transfer results, however. These conclusions were that the 1.057-MeV level was the  $3s_{1/2}$  single-particle state and that the 1.516-MeV level was the  $2d_{3/2}$  single-particle state. Furthermore, the three levels lying

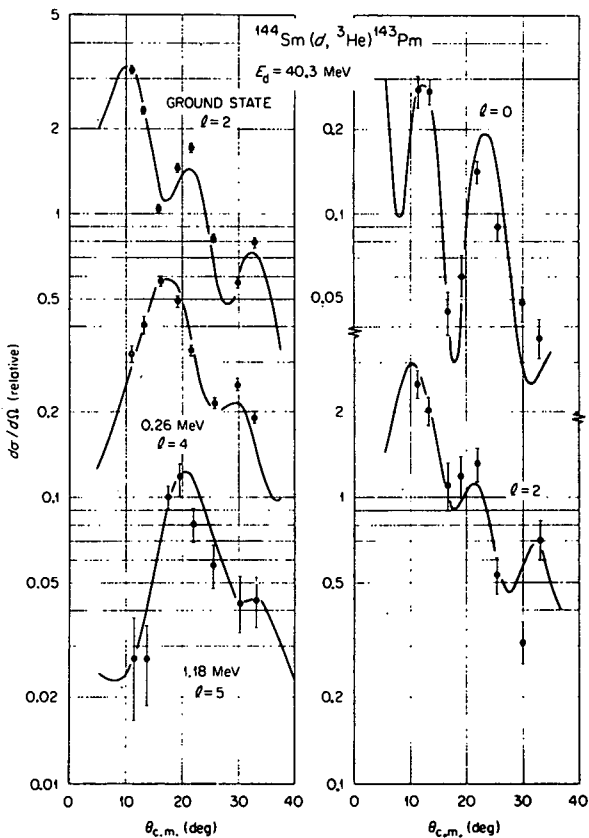


FIG. 14. Angular distributions of the transitions observed in the  $^{144}\text{Sm}(d, ^3\text{He})^{143}\text{Pm}$  reaction. The curves are DWBA predictions.

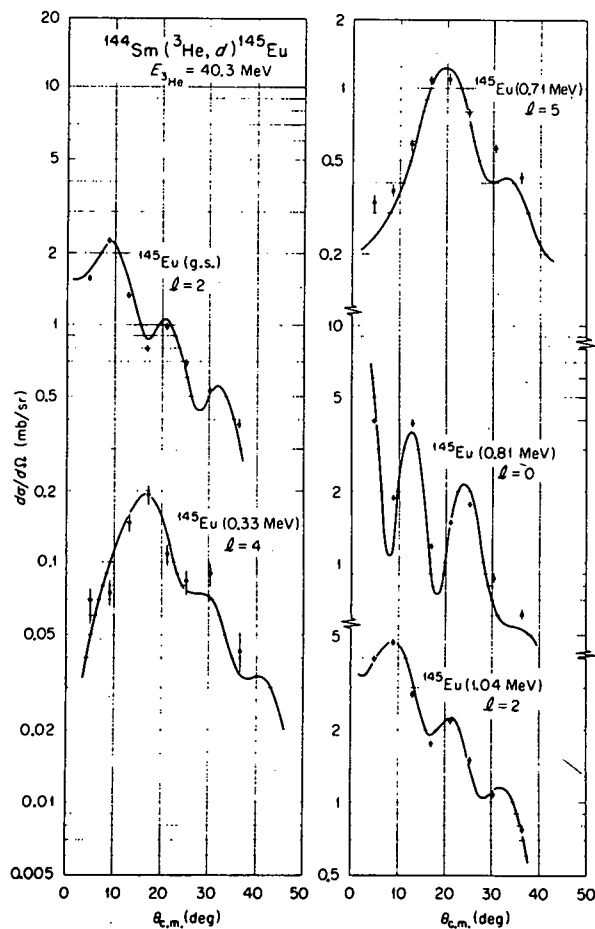


FIG. 15. Angular distributions of the transitions observed in the  $^{144}\text{Sm}(^3\text{He}, d)^{145}\text{Eu}$  reaction. The curves are DWBA predictions.

between these two were tentatively all assigned  $J = \frac{1}{2}$ . As mentioned, the stripping results indicate that the 1.057-MeV state is only weakly excited, and with an  $l_p = 2$  transfer which rules out  $J = \frac{1}{2}$ . The  $3s_{1/2}$  single-particle state corresponds, rather, to the level at 1.173 MeV. Finally, the  $2d_{3/2}$  state is the level seen at 1.404 MeV, not the one at 1.516 MeV, since the former is populated strongly with an  $l_p = 2$  ( $^3\text{He}, d$ ) transition while the latter is not measurably excited.

#### 10. $^{144}\text{Sm}(^3\text{He}, d)^{145}\text{Eu}$

The  $^{144}\text{Sm}(^3\text{He}, d)^{145}\text{Eu}$  reaction populates the ground state of  $^{145}\text{Eu}$  with an  $l_p = 2$  transition and populates excited states at 0.33-, 0.713-, 0.809- and 1.042-MeV excitation energies with transitions of  $l_p = 4, 5, 0,$  and  $2,$  respectively. The angular distributions and DWBA curves are presented in Fig. 15. These levels are taken to correspond to the coupling of  $2d_{3/2}, 1g_{7/2}, 1h_{11/2}, 3s_{1/2},$  and  $2d_{3/2}$  protons to a core consisting of the  $^{144}\text{Sm}$  ground state. The characteristics of these states are consistent with the trends established for the five *gdhs* single-particle states in the lighter nuclei. Detailed discussion of the  $^{145}\text{Eu}$  results have been presented elsewhere.<sup>3</sup>

### C. Commentary

#### 1. Energy Centroids of *gdhs* Orbits

The ( $^3\text{He}, d$ ) results provide a means of locating the energy centroids of the  $1h_{11/2}, 3s_{1/2},$  and  $2d_{3/2}$  proton orbits. In every target studied the total observed  $l_p = 5$  strength is found concentrated into a single final state. The  $2d_{3/2}$  and  $3s_{1/2}$  strengths are essentially concentrated into one state each

for the lightest and heaviest nuclei studied, but in  $^{141}\text{Pr}$  and  $^{139}\text{La}$  significant fragmentation is observed. Only one  $l_p = 4$  transition is observed for each target and we assume, with some justification, that only one  $2d_{3/2}$  state is populated.

The trends as a function of mass (or proton number) of the centroids of the higher three *gdhs* orbits relative to the low-lying  $\frac{7}{2}^+ - \frac{5}{2}^+$  doublets are displayed in Fig. 16. The trend lines are drawn through the centroids of the various orbits where several fragments exist. The length of the line corresponding to an observed energy level indicates the relative magnitude of its spectroscopic factor. We see that as protons are added in going from  $^{137}\text{Cs}$  to  $^{145}\text{Eu}$  [both the ( $d, ^3\text{He}$ ) and ( $^3\text{He}, d$ ) results indicate that the added protons are filling the  $1g_{7/2}$  and  $2d_{3/2}$  orbits predominantly] the excitation energies of the  $1h_{11/2}, 3s_{1/2},$  and  $2d_{3/2}$  states decrease smoothly. At the same time their energies relative to each other remain essentially constant.

#### 2. Evaluation of Differences Between the Standard and Modified DWBA Analyses

The results of the present measurements can be used to test the efficacy of the modified form of the standard DWBA analysis of transition intensities, outlined in a previous section, in which the radius of the spin-orbit term of the bound-state well is reduced by 10% relative to the radius of the central well.

If the normalization of the stripping results for a given target is assigned so as to satisfy the overall sum rule for the entire *gdhs* shell, then consistency demands that the sum rules for all individual orbits must be satisfied simultaneously.

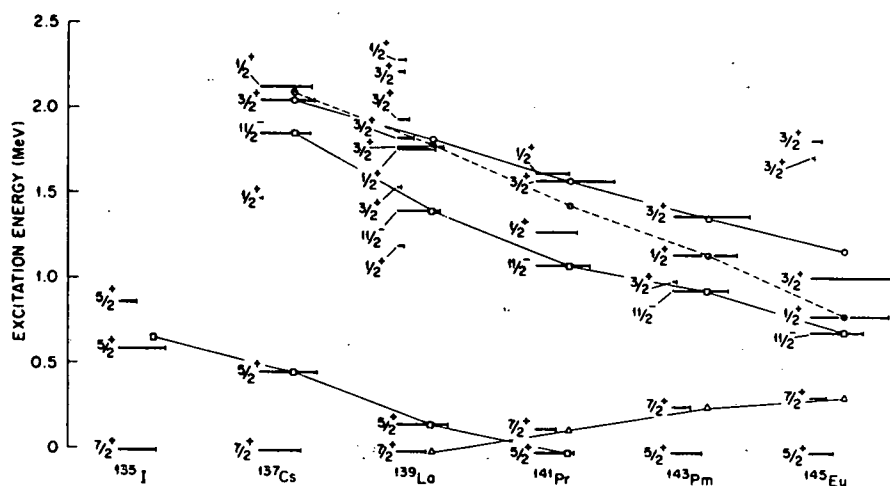


FIG. 16. Synopsis of ( $^3\text{He}, d$ ) results. All levels observed in the stripping studies are indicated. The excitation energies are noted by vertical positioning and the magnitudes of the spectroscopic factors indicated by the extent of the horizontal lines marking each level. The sloping lines trace the movements of the centroids of the various *gdhs* orbits. The pickup results to  $^{135}\text{I}$  are included in analogous fashion to the stripping results.

Thus, the sum of stripping spectroscopic factors for a particular  $J$  value in a given reaction must be less than or equal to 1.0. Violations of these limits are a measure of the internal inconsistencies in the way in which the DWBA analysis distributes the spectroscopic strength among the various transitions. This assumes of course, accurate experimental data and the proper normalization of the DWBA predictions to the experimental points.

Inspection of the numbers in Table III shows that for the transitions to  $^{139}\text{La}$ ,  $^{141}\text{Pr}$ ,  $^{143}\text{Pm}$ , and  $^{145}\text{Eu}$  the sum-rule limits on the  $2d_{3/2}$  transitions are violated to the extent of 25 to 35% in the standard DWBA analysis, while the modified analysis yields violations only of the order of 10–20%. The possibility that some of the higher  $l_p = 2$  transitions could correspond to the  $2d_{5/2}$  orbit rather than the  $2d_{3/2}$  does not significantly alter the conclusion to be drawn, since in most cases there is a single  $l_p = 2$  transition which by itself exceeds the limit on  $S(2, 2, \frac{3}{2})$ . In a similar fashion, it can be seen that the limits on the  $3s_{1/2}$  orbit are exceeded by about 15% in the standard analysis and to about half that in the modified results. We feel that dis-

crepancies of the order of 10% are to be expected from the uncertainties in the experimental statistics and curve-fitting procedures. Hence, the modified analysis appears to give relative value of the DWBA cross sections for different transferred orbital angular momenta which are consistent to within better than 10%.

A different kind of consistency check, also discussed in Sec. III, is available from a comparison of the pick-up and stripping results from the same target nucleus. The pick-up spectroscopic factors listed in Table III are in each case normalized so the sum of occupancy in the  $1g_{7/2}$  and  $2d_{5/2}$  orbits is equal to the occupancy implied for these two orbits by the analysis of the complementary stripping reaction. Thus, the occupation number for a particular orbit in a given target wave function should, ideally, be the same, whether extracted from the ( $d, ^3\text{He}$ ) or the ( $^3\text{He}, d$ ) data. The actual values are listed in Table IV.

The comparison is most meaningful for the heavier nuclei. For  $^{140}\text{Ce}$ ,  $^{142}\text{Nd}$ , and  $^{144}\text{Sm}$ , an inspection of Table IV shows that the corresponding occupation numbers deduced from stripping and pick-up data with the modified analysis are

TABLE IV. Occupation probabilities  $\langle nj \rangle$  for the proton orbits of the  $gdhs$  shell as obtained for the ground states of the even-mass  $N = 82$  nuclei from analysis of pick-up and stripping reactions.

Nucleus	Orbit	$\langle nj \rangle$				Best values and estimated uncertainties
		Mod. DWBA		Stand. DWBA		
		( $^3\text{He}, d$ )	( $d, ^3\text{He}$ )	( $^3\text{He}, d$ )	( $d, ^3\text{He}$ )	
$^{136}\text{Xe}$	$1g_{7/2}$	3.2	2.7	2.0	1.8	$3.5 \pm 0.4$
	$2d_{5/2}$	0	.4	.1	.2	$0.5 \pm 0.2$
	$2d_{3/2}$	0.7		0.3		$0.0 \pm 0.2$
	$3s_{1/2}$	0.1		0.1		$0.0 \pm 0.2$
	$1h_{11/2}$	0		1.6		$0.0 \pm 0.7$
$^{138}\text{Ba}$	$1g_{7/2}$	4.6	3.9	3.7	3.6	$4.3 \pm 0.4$
	$2d_{5/2}$	0.35	1.0	0.60	0.70	$0.7 \pm 0.3$
	$2d_{3/2}$	0		0		$0.0 \pm 0.2$
	$3s_{1/2}$	0.3		0.2		$0.0 \pm 0.2$
	$1h_{11/2}$	2.0		3.5		$1.0^{+1.0}_{-0.7}$
$^{140}\text{Ce}$	$1g_{7/2}$	5.8	6.2	5.2	6.1	$5.6 \pm 0.3$
	$2d_{5/2}$	2.2	1.7	2.2	1.3	$1.8 \pm 0.2$
	$2d_{3/2}$	0		0		$0.0 \pm 0.2$
	$3s_{1/2}$	0		0		$0.0 \pm 0.2$
	$1h_{11/2}$	0.5	0.7	2.0	0.6	$0.6^{+0.6}_{-0.2}$
$^{142}\text{Nd}$	$1g_{7/2}$	6.0	6.1	5.4	6.2	$5.7^{+0.2}_{-0.4}$
	$2d_{5/2}$	2.8	2.7	2.9	2.1	$2.6^{+0.3}_{-0.3}$
	$2d_{3/2}$	0	0	0	0	$0.2 \pm 0.1$
	$3s_{1/2}$	0	0.1	0	0.1	$0.2 \pm 0.1$
	$1h_{11/2}$	2.1	1.0	3.5	0.9	$1.3^{+0.6}_{-0.3}$
$^{144}\text{Sm}$	$1g_{7/2}$	6.6	6.8	6.2	7.5	$6.3 \pm 0.2$
	$2d_{5/2}$	4.0	3.8	4.0	3.2	$3.6^{+0.1}_{-0.2}$
	$2d_{3/2}$	0	0.5	0	0.5	$0.3 \pm 0.1$
	$3s_{1/2}$	0	0.2	0	0.2	$0.2 \pm 0.1$
	$1h_{11/2}$	2.0	1.6	3.3	1.4	$1.6 \pm 0.3$

clearly more consistent with each other than are those obtained with the standard analysis. For  $^{138}\text{Ba}$  and  $^{136}\text{Xe}$ , the conclusions are mixed. If only the  $1g_{7/2}$  and  $2d_{5/2}$  orbits are considered, then the "modified" results are less consistent than the "standard" results, but, if the  $1h_{11/2}$  state is considered, then the "modified" values are in better agreement. We feel that the major problem here is that the small occupancy of the  $2d_{5/2}$  orbit in the lightest targets, leading as it does to stripping  $S$  factors near to 1.0, make the occupation numbers extracted from stripping too sensitive to uncertainties of the order of 5% in the  $S$  factor, as was explained in Sec. III C.

Hence, we conclude in these examples also that the modified analysis leads to results which are internally more consistent than those which are obtained with the standard analysis. We will, accordingly, use the results of the modified analysis in the remaining discussion.

### 3. Configurations of Ground-State Wave Functions

(a)  $^{136}\text{Xe}$ . The  $(^3\text{He}, d)$  data indicate some vacancy for the  $2d_{3/2}$  orbit in the ground state of  $^{136}\text{Xe}$ . This is inconsistent with the conclusions drawn from the  $(^3\text{He}, d)$  data on the other nuclei and we believe that it is spurious, resulting from the failure to identify, detect, or correctly extract the remaining  $2d_{3/2}$ ,  $l_p = 2$  strength. The relatively low quality of the  $^{136}\text{Xe}(^3\text{He}, d)^{137}\text{Cs}$  spectra is consistent with the possibility that such strength could have been missed. There is no evidence in the stripping results for the occupancy of the  $1h_{11/2}$  or  $3s_{1/2}$  orbits and we conclude that, to the limit of the accuracy of the present study, the active protons in the wave function of the  $^{136}\text{Xe}$  ground state occupy only the  $1g_{7/2}$  and  $2d_{5/2}$  orbits. From the pickup results on  $^{136}\text{Xe}$ , we recall that two  $l_p = 2$  levels in  $^{135}\text{I}$  were excited with comparable strength, as opposed to only one in the heavier nuclei. This might be taken as evidence for significant occupation of the  $2d_{3/2}$  orbit in  $^{136}\text{Xe}$ , something just ruled out in rather *ad hoc* fashion. However, the energy of the second  $l_p = 2$  level seen in  $^{135}\text{I}$  is significantly below the empirically extrapolated energy of the " $2d_{3/2}$ "  $\frac{3}{2}^+$  state in  $^{135}\text{I}$ . We believe that both of the  $^{135}\text{I}$  levels excited with  $l_p = 2$  are  $J^\pi = \frac{3}{2}^+$  and that the pick-up strength is shared between them by virtue of the convergence of the excitation energy of the  $2d_{5/2}$  single-particle state and the pairing energy.<sup>8</sup> The ratio of occupancy of  $1g_{7/2}$  protons to  $2d_{5/2}$  protons is taken from the  $(d, ^3\text{He})$  results. The value is 85%  $1g_{7/2}$  to 15%  $2d_{5/2}$ , or  $\langle 1g_{7/2} \rangle = 3.5 \pm 0.4$ ,  $\langle 2d_{5/2} \rangle = 0.5 \pm 0.2$ .

(b)  $^{138}\text{Ba}$ . The  $(^3\text{He}, d)$  results indicate small occupancy of both the  $1h_{11/2}$  and  $3s_{1/2}$  orbits mixed

into the dominant  $1g_{7/2}$  and  $2d_{5/2}$  structure of the  $^{138}\text{Ba}$  ground state. The  $(d, ^3\text{He})$  data do not provide a check upon these  $1h_{11/2}$  and  $3s_{1/2}$  values. The  $3s_{1/2}$  value from stripping is not regarded as significant because of the difficulty in extracting the  $S$  factor from the  $l = 0 - l = 2$  doublet at 1.78 MeV in  $^{139}\text{La}$ . The occupation numbers we would choose for  $^{138}\text{Ba}$  are  $\langle 1g_{7/2} \rangle = 4.3 \pm 0.4$ ,  $\langle 2d_{5/2} \rangle = 0.7 \pm 0.3$ , and  $\langle 1h_{11/2} \rangle = 1.0_{-0.7}^{+1.0}$ .

(c)  $^{140}\text{Ce}$ . The results of the modified DWBA analysis of the  $(d, ^3\text{He})$  and  $(^3\text{He}, d)$  data for  $^{140}\text{Ce}$  are in good agreement with each other. The following occupation values follow directly from the analysis:  $\langle 1g_{7/2} \rangle = 5.6 \pm 0.3$ ,  $\langle 2d_{5/2} \rangle = 1.8 \pm 0.2$ ,  $\langle 1h_{11/2} \rangle = 0.6_{-0.2}^{+0.6}$ , and  $\langle 3s_{1/2} \rangle$  and  $\langle 2d_{3/2} \rangle \leq 0.2$ .

(d)  $^{142}\text{Nd}$ . The "modified" spectroscopic factors from the  $(d, ^3\text{He})$  and  $(^3\text{He}, d)$  experiments on  $^{142}\text{Nd}$ , when averaged and normalized, yield the following occupation numbers for the ground-state wave function:  $\langle 1g_{7/2} \rangle = 5.7_{-0.4}^{+0.2}$ ,  $\langle 2d_{5/2} \rangle = 2.6_{-0.3}^{+0.2}$ ,  $\langle 1h_{11/2} \rangle = 1.3_{-0.4}^{+0.6}$ , and  $\langle 3s_{1/2} \rangle$  and  $\langle 2d_{3/2} \rangle \leq 0.2$ . The increased lower limits on  $\langle 1g_{7/2} \rangle$  and  $\langle 2d_{5/2} \rangle$  reflect the uncertainty residing in undetermined occupancy of the  $2d_{3/2}$  and  $3s_{1/2}$  orbits.

(e)  $^{144}\text{Sm}$ . The  $(d, ^3\text{He})$  experiment on  $^{144}\text{Sm}$  yields unambiguous evidence for the occupancy of all of the *gdhs* orbits in the target ground state. Weighting these results with those from the  $(^3\text{He}, d)$  reaction and normalizing to 12 particles produces the following values:  $\langle 1g_{7/2} \rangle = 6.3 \pm 0.2$ ,  $\langle 2d_{5/2} \rangle = 3.6 \pm 0.2$ ,  $\langle 1h_{11/2} \rangle = 1.6 \pm 0.3$ ,  $\langle 2d_{3/2} \rangle = 0.3 \pm 0.1$ , and  $\langle 3s_{1/2} \rangle = 0.2 \pm 0.1$ .

To summarize, there is reasonably precise evidence for the occupation of the  $2d_{3/2}$  and  $3s_{1/2}$  orbits only in the ground state of  $^{144}\text{Sm}$ , where, together, they account for a strength of about 0.5 particle. About half this much strength appears to occur in the  $^{142}\text{Nd}$  ground state and negligible amounts in the lighter nuclei.

In the case of the  $1h_{11/2}$  orbit, there is consistent evidence for about a 1.5-particle occupancy in the  $^{144}\text{Sm}$  and  $^{142}\text{Nd}$  ground states. This seems to decrease for  $^{140}\text{Ce}$  to about 0.5 particle but, with less conclusive evidence, to return to about 1.0 for  $^{138}\text{Ba}$ . There is no evidence for occupancy of this orbital in  $^{136}\text{Xe}$ . Our opinion is that the apparent decrease in occupation at  $^{140}\text{Ce}$  is real and the apparent increase in  $^{138}\text{Ba}$  is not, and that the "true" occupation of  $1h_{11/2}$  in  $^{138}\text{Ba}$  is probably close to 0.5 protons. The data for  $^{136}\text{Xe}$  are, of course, consistent with an occupation of  $1h_{11/2}$  of the order of 0.2-0.4 also. Thus, we estimate that the amount of filling of the  $1h_{11/2}$  orbit changes from something less than 5% in the four-particle system to a value of approximately 14% in the 12-particle system.

The occupancy of the  $2d_{5/2}$  orbital changes most

markedly in the progression from 4 to 12 active particles. In the ground state of  $^{136}\text{Xe}$ , this orbit is only 8% filled and this percentage increases rather smoothly to a value of 60% (3.6 particles out of a possible 6) in the ground state of  $^{144}\text{Sm}$ . The  $1g_{7/2}$  orbit is the most tightly bound member of the *gdhs* shell. To lowest order in the shell-model scheme it should fill (to eight particles) at  $^{140}\text{Ce}$ . Actually, we see that this orbit is only 70% filled in the ground state of  $^{140}\text{Ce}$  and, in fact, its percentage occupancy remains essentially fixed at 70% from  $^{140}\text{Ce}$  through  $^{144}\text{Sm}$ .

### V. SUMMARY

The experimental results we have presented constitute evidence for a close and systematic relationship between the eleven  $N=82$  nuclei in the mass range  $A = 135-145$ . Complementary pickup and stripping reactions on the ground states of each of the even-mass nuclei indicate that the protons outside the  $Z = 50$ ,  $N=82$  core of these systems occupy the  $1g_{7/2}$  and  $2d_{5/2}$  orbits, predominantly, with the occupation of the  $1h_{11/2}$  orbit becoming appreciable towards  $A = 144$ .

Both the stripping and pickup reactions populate the lowest two levels in the odd-mass spectra, one level with  $l_p = 4$  and one with  $l_p = 2$ . The transitions are interpreted to involve transfer of  $1g_{7/2}$  and  $2d_{5/2}$  protons, respectively, and the spectroscopic factors are such as to indicate that the wave functions of these levels can be accurately approximated either as single particles coupled to the ground states of the stripping targets or as single holes coupled to the ground states of the pickup targets. Only one  $l_p = 4$  transition is observed in each different reaction, and only in the  $^{136}\text{Xe}(d, ^3\text{He})-^{135}\text{I}$  reaction is there probable evidence for more than one  $2d_{5/2}$  transition. With this exception, the single-particle (hole) strengths for these two orbits are always concentrated into single levels.

A similar situation is observed for the single-particle strength of the  $1h_{11/2}$  orbit. Only one  $l_p = 5$  transition is observed in each stripping reaction. The  $1h_{11/2}$  single-particle states located in the stripping experiments are weakly populated via pickup from the heavier targets. The evidence is that this orbit is not significantly occupied relative to its capacity in any of the target wave functions.

The single-particle strengths of the  $2d_{3/2}$  and  $3s_{1/2}$  orbits are observed, in general, to be fragmented over several states each. The fragmentation is most significant for the  $^{139}\text{La}$  and  $^{141}\text{Pr}$  nuclei, but even in these cases the total strength is well concentrated and the "single-particle" levels can typically be identified without ambiguity.

The large-scale aspects of the structure of these

nuclear systems that the present experiments delineate are the apparent validity of the hypothesis of a  $Z = 50$ ,  $N=82$  shell closure, the trends of the occupation probabilities of the five *gdhs* proton orbits as a function of proton number, and the energy orderings of the five *gdhs* "single-particle states," again as a function of mass. The finer details revealed include the quantitative ratios of occupation probabilities for the *gdhs* orbits, the quantum numbers and exact energies of the various observed levels, and the patterns of fragmentation of the single-particle strengths over these levels.

The comprehensive view of the  $N=82$  nuclei that is developed is one of consistent simplicity in terms of the shell model. The dominant features of the odd-mass level structures can be discussed in terms of a proton in one of the five *gdhs* orbits coupled to core consisting of closed shells of 82 neutrons and 50 protons plus  $(Z - 50)$  protons paired off in the  $1g_{7/2}$  and  $2d_{5/2}$  orbits. The deviations in detail from this simple picture which appear also seem uniformly to be explicable in terms of *gdhs* shell configurations. Thus it seems reasonable to hope that structure calculations which explicitly consider only protons in the *gdhs* orbits can account for the phenomena we have observed in the present experiments in a complete and unified way. Indeed, the ability of present theoretical techniques to explain these regular and, relatively speaking, transparent aspects of the structure of the  $N=82$  nuclei is a prerequisite if the same procedures are to reliably interpret the more complex phenomena observed in nuclei which lie off the shell closure. The extensive body of experimental information that is now available about the  $N=82$  band of nuclei should make possible definitive evaluations of the various theoretical approaches to nuclear structure in this region.

### ACKNOWLEDGMENTS

We are grateful to Jerry Nolan and Bill Horath for their essential assistance in fabricating the Ba, Ce, and Nd targets. Two of the authors (BHW and RLA) were supported by U. S. Atomic Energy Commission Postdoctoral Fellowships, administered by Oak Ridge Associated Universities, during the period when part of the work reported here was carried out. Some other aspects of the project were accomplished while one author (BHW) was in residence at the Cyclotron Institute, Texas A & M University, College Station, Texas.

\*Work supported in part by the U. S. Atomic Energy Commission under contract with the Union Carbide Corporation.

†Present address: Cyclotron Laboratory, Michigan State University, East Lansing, Michigan 48823.

‡Work supported in part by the National Science Foundation.

<sup>1</sup>B. H. Wildenthal, E. Newman, and R. L. Auble, *Phys. Letters* **27B**, 628 (1968).

<sup>2</sup>E. Newman, R. L. Auble, and B. H. Wildenthal, *Bull. Am. Phys. Soc.* **13**, 70, 658 (1968); **14**, 56 (1969); B. H. Wildenthal, R. L. Auble, and E. Newman, *Bull. Am. Phys. Soc.* **13**, 1430 (1968); **14**, 1239 (1969).

<sup>3</sup>E. Newman, K. S. Toth, R. L. Auble, R. M. Gaedke, M. F. Roche, and B. H. Wildenthal, *Phys. Rev. C* **1**, 1118 (1970).

<sup>4</sup>M. G. Mayer and J. H. D. Jensen, *Elementary Theory of Nuclear Shell Structure* (John Wiley & Sons, Inc., New York, 1955).

<sup>5</sup>*Nuclear Data Sheets*, compiled by K. Way *et al.* (Printing and Publishing Office, National Academy of Sciences - National Research Council, Washington, D.C.).

<sup>6</sup>C. M. Lederer, J. M. Hollander, and I. Perlman, *Table of Isotopes* (John Wiley & Sons, Inc., New York, 1968), 6th ed.

<sup>7</sup>B. H. Wildenthal, *Phys. Rev. Letters* **22**, 1118 (1969) and *Phys. Letters* **29B**, 274 (1969).

<sup>8</sup>B. H. Wildenthal, E. Newman, and J. B. McGrory, to be published.

<sup>9</sup>The enriched samples of <sup>134</sup>Ba, <sup>140</sup>Ce, <sup>142</sup>Nd, and <sup>144</sup>Sm were obtained from the Isotopes Division of Oak Ridge National Laboratory. The sample of <sup>136</sup>Xe was obtained from Mound Laboratories.

<sup>10</sup>J. H. E. Mattauch, W. Thiele, and A. H. Wapstra, *Nucl. Phys.* **67**, 1 (1965).

<sup>11</sup>C. M. Jones and M. Mancusi, private communication.

<sup>12</sup>R. H. Bassel, R. M. Drisko, and G. R. Satchler, Oak Ridge National Laboratory Report No. ORNL-3240 (unpublished).

<sup>13</sup>E. Newman, L. C. Becker, B. M. Freedom, and J. C. Hiebert, *Nucl. Phys.* **A100**, 225 (1967).

<sup>14</sup>E. F. Gibson, B. W. Ridley, J. J. Kraushaar, M. E. Rickey, and R. H. Bassel, *Phys. Rev.* **155**, 1194 (1967).

<sup>15</sup>B. M. Freedom, E. Newman, and J. C. Hiebert, *Phys. Rev.* **166**, 1156 (1968).

<sup>16</sup>R. H. Bassel, *Phys. Rev.* **149**, 791 (1966).

<sup>17</sup>M. Dost and W. R. Herring, *Phys. Letters* **19**, 488 (1965).

<sup>18</sup>B. H. Wildenthal, B. M. Freedom, E. Newman, and M. R. Cates, *Phys. Rev. Letters* **19**, 960 (1967).

<sup>19</sup>E. Newman and B. H. Wildenthal, *Bull. Am. Phys. Soc.* **13**, 1436 (1968); W. C. Parkinson, D. L. Hendrie, H. H. Duhm, J. Mahoney, J. Saudinos, and G. R. Satchler, *Phys. Rev.* **178**, 1976 (1969).

<sup>20</sup>M. P. Fricke, E. E. Gross, B. J. Morton, and A. Zucker, *Phys. Rev.* **156**, 1207 (1967); G. W. Greenlees and G. J. Pyle, *ibid.* **149**, 836 (1966).

<sup>21</sup>M. H. Macfarlane and J. B. French, *Rev. Mod. Phys.* **32**, 567 (1960).

<sup>22</sup>G. Holm, *Arkiv Fysik* **37**, 1 (1967).

<sup>23</sup>J. C. Hill and M. L. Wiedenbeck, *Nucl. Phys.* **A119**, 53 (1968).

<sup>24</sup>G. Berzins, M. E. Bunker, and J. W. Starner, *Nucl. Phys.* **A128**, 294 (1969).

<sup>25</sup>J. G. Malan, W. R. McMurray, P. van der Merwe, I. J. van Heerden, and C. A. Engelbrecht, *Nucl. Phys.* **A124**, 111 (1969).

<sup>26</sup>P. van der Merwe, I. J. van Heerden, W. R. McMurray, and J. G. Malan, *Nucl. Phys.* **A124**, 433 (1969).

<sup>27</sup>R. Moreh, private communication.

<sup>28</sup>R. Moreh and A. Nof, *Phys. Rev.* **178**, 1961 (1969).

<sup>29</sup>D. B. Beery, W. H. Kelly, and W. C. McHarris, *Phys. Rev.* **171**, 1283 (1968).

<sup>30</sup>V. R. Dave, J. A. Nelson, and R. M. Wilenzick, *Nucl. Phys.* **A142**, 619 (1970).

<sup>31</sup>H. W. Baer and J. Bardwick, *Nucl. Phys.* **A129**, 1 (1969).

<sup>32</sup>O. Hansen, O. Nathan, L. Vistisen, and R. Chapman, *Nucl. Phys.* **A113**, 75 (1968).

<sup>33</sup>D. DeFrenne, K. Heyde, L. Dorikens-Vanpret, M. Dorikens, and J. Demuyneck, *Nucl. Phys.* **A110**, 273 (1968).

ENERGY OF THE SECOND EXCITED STATE OF  $^{12}\text{C}$  AND THE  
RATE OF THE TRIPLE-ALPHA REACTION\*

SAM M. AUSTIN

Niels Bohr Institute, University of Copenhagen, and Cyclotron Laboratory,  
Physics Department, Michigan State University

AND

G. F. TRENTelman AND E. KASHY

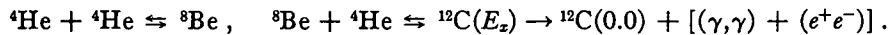
Cyclotron Laboratory, Physics Department, Michigan State University

Received 1970 November 16

ABSTRACT

The excitation energy of the second excited state of  $^{12}\text{C}$  has been measured to be  $E_x = 7.6562 \pm 0.0021$  MeV. This value of  $E_x$  leads to a factor of  $\exp(-0.138/T_9)$  change in the  $3\alpha$  reaction rate quoted by Fowler, Caughlan, and Zimmerman and a substantial change in the products of helium-burning nucleosynthesis.

During stellar helium burning,  $^4\text{He}$  is fused into  $^{12}\text{C}$  in a resonant two-stage process called the  $3\alpha$  process (Salpeter 1952; Burbidge *et al.* 1957):



In the first reaction the resonant state is the ground state of  $^8\text{Be}$  while the second excited state of  $^{12}\text{C}$  at an excitation energy  $E_x \simeq 7.6$  MeV is normally the relevant resonance for the second reaction. One can show (Burbidge *et al.* 1957) that the reaction rate  $P_{3\alpha}$  depends on  $E_x$  according to

$$P_{3\alpha} \propto \exp(-\chi/kT), \quad (1)$$

$$\chi = (M_{12} - 3M_\alpha)c^2 + E_x. \quad (2)$$

In these equations  $k$  is Boltzmann's constant,  $c$  is the velocity of light,  $T$  is the temperature, and  $M_{12}$  and  $M_\alpha$  are the atomic masses of  $^{12}\text{C}$  and  $^4\text{He}$ . Since  $kT \simeq 10$  keV for the temperatures of helium burning,  $T \sim 10^8$  °K, it is necessary to know  $E_x$  rather well if one wishes to predict  $P_{3\alpha}$  accurately.

In their recent compilation, Fowler, Caughlan, and Zimmerman (1967, hereafter referred to as FCZ) use  $\chi = 370 \pm 4$  keV which corresponds to  $E_x = 7.644 \pm 0.004$  MeV. This value is obtained from the measurement (Cook *et al.* 1957) of the  $Q$ -value for the breakup  $^{12}\text{C}(E_x) \rightarrow ^8\text{Be} + \alpha$  and is the most precise single measurement of  $E_x$ . However, it lies at the lower extreme of other available measurements (Ajzenberg-Selove and Lauritsen 1968). The weighted average of these, excluding the measurement of Cook *et al.* (1957), is  $7.6598 \pm 0.0045$ . The use of this number rather than 7.644 reduces the reaction rate by a factor of about 5 at  $kT = 10.0$  keV. Because of the extremely strong temperature dependence of  $P_{3\alpha}$  such a change is probably unimportant for most stellar properties, but it can substantially affect the products of helium burning and hence the succeeding stages of stellar evolution.

In this Letter we describe a resolution of the discrepancy noted above by a measurement of  $E_x$  with an accuracy of about 2 keV. The basic technique was a comparison of the momentum of protons inelastically scattered from  $^{12}\text{C}$  leaving the nucleus in its

\* Research supported in part by the National Science Foundation.

TABLE 1  
REACTIONS USED IN THE MEASUREMENT OF  $E_x$

Reaction	Excitation Energy of Residual Nucleus (MeV)	Reaction Number
$^{12}\text{C}(p,p)^{12}\text{C}$ .....	0.000	1
$^{12}\text{C}(p,p)^{12}\text{C}^*$ .....	$4.4398 \pm 0.0003^*$	2
$^{12}\text{C}(p,p)^{12}\text{C}^*$ .....	$E_x \approx 7.6$	3
$^{16}\text{O}(p,p)^{16}\text{O}^*$ .....	$6.1305 \pm 0.0004^\dagger$	4
$^{16}\text{O}(p,p)^{16}\text{O}^*$ .....	$8.8711 \pm 0.0011^\dagger$	5

\* Chasman *et al.* 1967.

† Throop 1969 and Bayer 1970.

† Marion 1967.

second excited state, with the momenta of protons produced in reactions whose  $Q$ -values are well known. These reactions are enumerated in Table 1.

The momentum measurements were carried out in a split-pole spectrograph (Spencer and Enge 1967) with a position-sensitive detector in the focal plane. The reactions  $^{16}\text{O}(p,d)^{15}\text{O}(0.0)^1$  and  $^{12}\text{C}(p,p')^{12}\text{C}(4.4398)$  were used in a momentum-matching procedure (Trentelman and Kashy 1970) to set the energy of the incident proton beam to  $22.744 \pm 0.004$  MeV. The laboratory scattering angle  $\theta_L$  was determined to be  $15^\circ 09' \pm 0^\circ 03'$  by measuring the momentum of protons from  $^1\text{H}(p,p)^1\text{H}$  scattering. Following a recycling procedure the magnetic field was increased to make protons from the reactions 5, 3, 4, 2 of Table 1 coincide in turn with a chosen point in the focal plane. The magnetic field, as measured by a nuclear-magnetic-resonance fluxmeter (NMR), was recorded at each coincidence. The entire procedure was repeated three times. The target used in these measurements was a Mylar foil 0.00025 inches thick which was rotated during the measurement to insure uniformity and to minimize target deterioration. An  $\alpha$ -source thickness gauge was used to measure the areal density of the foil.

The data thus obtained are shown in Figure 1. The results shown are the average over three runs, but each run was also analyzed separately in the same fashion. On the ordinate is plotted the ratio of the momentum  $p$  calculated for the assumed beam energy, scattering angle,  $Q$ -value, and target thickness to that deduced from the NMR reading. The ratio was normalized to 1.00000 at the momentum of protons from the  $^{12}\text{C}(p,p')^{12}\text{C}(4.4398)$  reaction as observed during the beam energy calibration procedure. The straight line is a fit to the three calibration points. The slope of this calibration line arises from an unknown combination of saturation effects in the magnet iron and uncertainty in the beam energy within the quoted limits, but since calibration points bracket the unknown it is unnecessary to understand this behavior in detail. The value of  $E_x$  was then determined by forcing the ratio for the  $^{12}\text{C}(p,p')^{12}\text{C}(E_x)$  reaction to fall on the calibration line.

A fourth independent measurement of  $E_x$  was made by using reactions 1-4 at a beam energy of  $24.64 \pm 0.01$  MeV (determined from the beam-analysis system and normalization to the previous data),  $\theta_L = 15^\circ 0$ , and using a  $63 \mu\text{g cm}^{-2}$  carbon foil as a target. The analysis was essentially the same as that described above. The results of the four measurements were 7.6557, 7.6557, 7.6575, and 7.6548 MeV. The weighted average of these results is 7.6562 MeV, and the unweighted standard deviation of the mean based on the results themselves is  $\pm 0.0006$  MeV. Allowing for uncertainties in the calibration energies, beam energy, and target thickness, we obtain finally

$$E_x = 7.6562 \pm 0.0021 \text{ MeV}.$$

<sup>1</sup> The numbers in the parentheses represent the excitation energy in MeV of the residual nucleus.



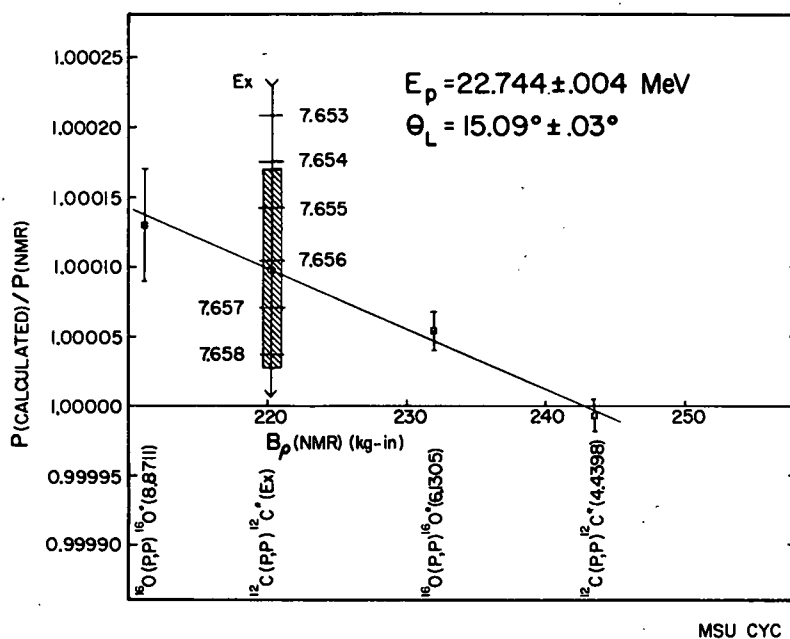


FIG. 1.—Average of three measurements of  $E_x$ . The points denoted by filled squares are from the calibrating reactions while the point denoted by a filled circle has been forced to lie on the calibration line by adjustment of  $E_x$ . The values of the ratio for other values of  $E_x$  are shown as horizontal bars. The errors shown on the calibration points include an allowance for uncertainty in the beam energy and for the reproducibility of the data. The height of the crosshatched area corresponds to the assigned error of  $\pm 0.0021$  MeV.

This result is in agreement with the earlier, less precise measurements but is not consistent with the result of Cook *et al.* (1957). A possible explanation of the discrepancy is that the analysis of Cook *et al.* (1957) assumed a  $\beta$ - $\nu$  angular correlation for the  $\beta$ -decay of  $^{12}\text{B}$  which was characteristic of tensor coupling. It is now known that axial-vector coupling dominates such transitions, but it is not obvious what effect the use of the correct angular correlation would have had on the result.

A value of  $E_x = 7.6562 \pm 0.0021$  in equation (2) leads to  $\chi = 381.9 \pm 2.4$  keV which differs by 11.9 keV from the value of 370 keV adopted by FCZ. The corresponding terms in equations (87), (87'), and (89) of FCZ must therefore be multiplied by the factor  $F$ , where

$$F = \exp\left(-\frac{11.9}{86.17T_9}\right) = \exp(-0.138/T_9).$$

The ratio  $R = (\text{number of } ^{12}\text{C})/(\text{number of } ^{16}\text{O})$  in the products of helium burning depends primarily on the competition between the  $3\alpha$  process and the  $^{12}\text{C}(\alpha, \gamma)^{16}\text{O}$  reaction. Since the rates of these reactions depend on the density  $\rho$  and temperature  $T$  which change during stellar evolution, an accurate evaluation of the effect on  $R$  of the decrease in  $P_{3\alpha}$  can be obtained only by a full stellar-model calculation.

We have estimated the effects to be expected in a  $5 M_{\odot}$  star by integrating the differential equations describing the nucleosynthesis (Clayton 1968) using constant values of the reaction rates evaluated at  $\rho = 7370$  g cm $^{-3}$  and  $T = 1.47 \times 10^8$  K. These values occur at a helium mass fraction of 0.32 in the model calculations of Iben

(1966), and with Iben's reaction rates they reproduce the value of  $R$  found in these calculations. Calculations were also performed by using FCZ rates and MSU rates which were obtained from the FCZ rates by multiplying  $P_{3\alpha}$  by  $F$ . The reactions  $3\alpha$ ,  $^{12}\text{C}(\alpha, \gamma)^{16}\text{O}$ , and  $^{16}\text{O}(\alpha, \gamma)^{20}\text{Ne}$  were included in the integrations, but the last reaction was found to have a negligible effect on the nucleosynthesis of  $^{12}\text{C}$  and  $^{16}\text{O}$ . The results were

$$R(\text{Iben rates}) = 1.56, \quad R(\text{FCZ rates}) = 1.81, \quad R(\text{MSU rates}) = 0.86.$$

Thus we see that the results of the present experiment imply a substantial change in the products of helium-burning nucleosynthesis.

It is perhaps worth remarking at this point that while the  $3\alpha$  reaction rate is now sufficiently well known for estimates of nucleosynthesis, the rate of the  $^{12}\text{C}(\alpha, \gamma)^{16}\text{O}$  reaction is much less certain. It has been assumed (Fowler *et al.* 1967) that for  $T \leq 6 \times 10^9$  °K, this reaction is dominated by the tail of the bound  $1^-$  state at an excitation energy of 7.12 MeV in  $^{16}\text{O}$ , and that the effect of this level could be parametrized by a dimensionless reduced  $\alpha$ -width of about 0.1. However, recent measurements (Pühlhofer *et al.* 1970) and analyses (Barker 1970; Weisser, Morgan, and Thompson 1970) have cast doubt on both these assumptions.

One of the authors (S. M. A.) wishes to thank the Niels Bohr Institute for its hospitality and the Alfred P. Sloan Foundation for support while on leave from Michigan State University.

#### REFERENCES

- Ajzenberg-Selove, F., and Lauritsen, T. 1968, *Nucl. Phys.*, **A114**, 1.  
 Barker, F. C. 1970, private communication.  
 Bayer, D. 1970, private communication.  
 Burbidge, E. M., Burbidge, G. R., Fowler, W. A., and Hoyle, F. 1957, *Rev. Mod. Phys.*, **29**, 547.  
 Chasman, C., Jones, K. W., Ristinen, R. A., and Alburger, D. E. 1967, *Phys. Rev.*, **159**, 830.  
 Clayton, D. D. 1968, *Principles of Stellar Evolution and Nucleosynthesis* (New York: McGraw-Hill Book Co.), p. 420.  
 Cook, C. W., Fowler, W. A., Lauritsen, C. C., and Lauritsen, T. 1957, *Phys. Rev.*, **107**, 508.  
 Fowler, W. A., Caughlan, G. R., and Zimmerman, B. A. 1967, *Ann. Review Astr. and Ap.*, **5**, 525.  
 Iben, I., Jr. 1966, *Ap. J.*, **143**, 483.  
 Marion, J. B. 1967, Univ. Maryland Tech. Rept. ORO-2098-58.  
 Pühlhofer, F., Ritter, H. G., Bock, R., Brommundt, G., Schmidt, H., and Bethge, K. 1970, *Nucl. Phys.*, **A147**, 258.  
 Salpeter, E. E. 1952, *Ap. J.*, **115**, 326.  
 Spencer, J. E. and Engé, H. A. 1967, *Nucl. Instr. and Meth.*, **49**, 181.  
 Throop, M. J. 1969, *Phys. Rev.*, **179**, 1011.  
 Trentelman, G. F., and Kashy, E. 1970, *Nucl. Instr. and Meth.*, **82**, 304.  
 Weisser, D. C., Morgan, J. F., and Thompson, D. R. 1970, *Bull. Am. Phys. Soc.*, **15**, 805.

*E6 and M5 Transitions Observed in Fe<sup>53m</sup> Decay*

J. N. Black and Wm. C. McHarris

*Department of Chemistry,\* and Cyclotron Laboratory,† Department of Physics,  
Michigan State University, East Lansing, Michigan 48823*

and

W. H. Kelly

*Cyclotron Laboratory,† Department of Physics, Michigan State University, East Lansing, Michigan 48823  
(Received 10 December 1970)*

Photons corresponding to 3040.6-keV *E6* and 1712.6-keV *M5* transitions have been observed from the decay of 2.6-min Fe<sup>53m</sup>. They have intensities of  $2 \times 10^{-4}$  and  $7 \times 10^{-3}$ , respectively, compared with the 701.1-keV *E4* isomeric transition that is primarily responsible for depopulating Fe<sup>53m</sup>. These correspond to retardations of 650 and 43 over simple single-particle estimates.

Opportunities for observing  $\gamma$ -ray transitions of very high multipolarity are extremely rare. The existence of *M5*, *E6*, and higher multiplicities has never been substantiated by experimental fact except for their presence as small admixtures occasionally being invoked to explain small discrepancies in experiments such as angular correlations. However, the recent discovery<sup>1</sup> of a high-energy, high-spin, three-quasiparticle isomer in the nuclide  ${}_{26}\text{Fe}_{27}^{53}$  has now provided an opportunity for the direct observation of such transitions and the calculation of their transition probabilities with reasonable precision. In this Letter we report our observation of photons corresponding to 3040.6-keV *E6* and 1712.6-keV *M5* isomeric transitions from this nucleus.

The isomer Fe<sup>53m</sup> has a half-life of 2.6 min and an excitation energy of 3040.6 keV.<sup>1-3</sup> It has been interpreted, primarily through isomer preparation ratios<sup>1</sup> and the reduced transition probability of the isomeric transition, apparently of *E4* multipolarity, as having a spin and parity of  $(19/2)^-$ . This corresponds to the highest spin state that can result from the three-quasiparticle configuration,  $[(\pi f_{7/2})^{-2}]_{6+}(\nu f_{7/2})^{-1}$ . Our findings are quite consistent with these assignments, and we present the decay scheme, including our newly found transitions, in Fig. 1.

We prepared sources of Fe<sup>53m</sup> by the reaction  $\text{Mn}^{55}(p, 3n)\text{Fe}^{53m+\epsilon}$ , using a 40-MeV proton beam from the Michigan State University sector-focused cyclotron. Bombardment time, beam energy, and all other parameters were adjusted to optimize the production of the metastable state. Typically, 0.5-g targets of powdered Mn metal (99.94% pure) were bombarded with a 2- $\mu$  beam for 1 min. To expedite handling of the

short-lived Fe<sup>53m</sup>, a pneumatic rabbit system was used to transport the target from the beam to the counting area with a transit time of  $\approx 2$  sec. Detachable aluminum packets were used to fix the Mn powder to the rabbit. Transfer of the powder to a plastic counting vial was accomplished merely by punching a hole in the packet and draining the radioactive powder into the vial. The total elapsed time between the end of a bom-

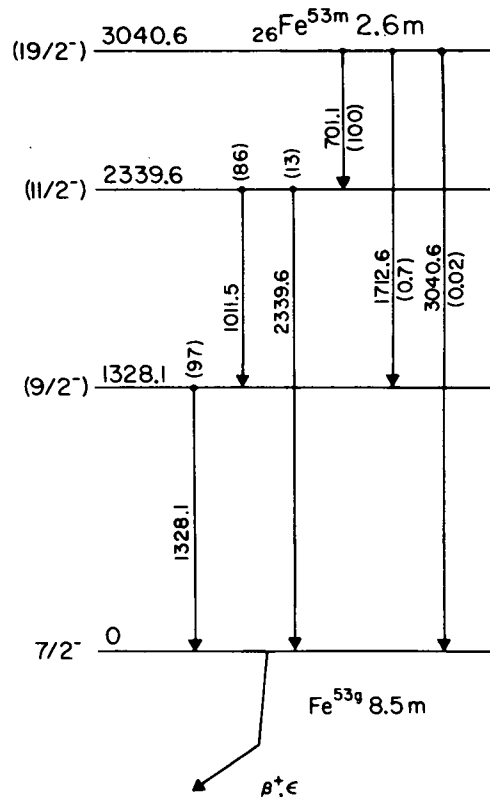


FIG. 1. Decay scheme of Fe<sup>53m</sup>, including the new *E6* (3040.6 keV) and *M5* (1712.6 keV) transitions observed in this work.

bardment and the beginning of counting was typically  $\approx 10$  sec.

$\gamma$  rays were detected with a 3.6%-efficient [for the  $\text{Co}^{60}$  1332.48-keV  $\gamma$ , measured relative to a  $3 \times 3$ -in.<sup>2</sup> NaI(Tl) detector at 25 cm], true-coaxial Ge(Li) detector having a resolution of 2.0 keV full width at half-maximum for the  $\text{Co}^{60}$  1332.48-keV  $\gamma$ . The remainder of the system consisted of an amplifier having high-rate baseline restoration and a 50-MHz analog-to-digital converter interfaced to a Sigma-7 computer. Graded lead absorbers having a combined thickness of  $\approx 3$  cm were used between the source and the detector to attenuate the lower-energy  $\gamma$  rays. Even so, counting rates as high as possible without appreciable deterioration of resolution were maintained throughout the experiments, with an average count rate of about 6700 counts/sec. This combination of isomer optimization, detector efficiency and resolution, and high-count-rate electronics was deemed absolutely necessary in order to obtain the number of events necessary for direct observation of the weak  $E6$  and  $M5$  transitions.

Various spectra were taken at different times and with different geometries and produced con-

sistent results. In Fig. 2 we show the spectrum resulting from a 24-h accumulation of data and front-end detector geometry. During this time a continuous cycle of bombarding and counting was maintained such that a fresh source was counted every 2 min. Definite peaks exist in this spectrum at the energies of 1712.6 and 3040.6 keV, where the  $M5$  and  $E6$  transitions are expected to occur. After careful energy and intensity analysis,<sup>4</sup> these peaks were found to correspond to transitions having intensities of  $7 \times 10^{-3}$  and  $2 \times 10^{-4}$  as compared with the 701.1-keV transition. Recent experiments using a large 10.5%-efficient Ge(Li) detector have shown that these peaks decay with the 2.6-min half-life of  $\text{Fe}^{53m}$  and are the only peaks in the spectrum (other than the four well-known, intense  $\text{Fe}^{53m}$  peaks) that decay with this half-life.

Having shown that these peaks are present, one is obligated to demonstrate that they are indeed true peaks and not merely the resultant sum peaks of two or more known constituents. Such sum peaks are known to occur in large-volume detectors under high-count-rate conditions. These can originate from two different physical conditions. First, if the source is suf-

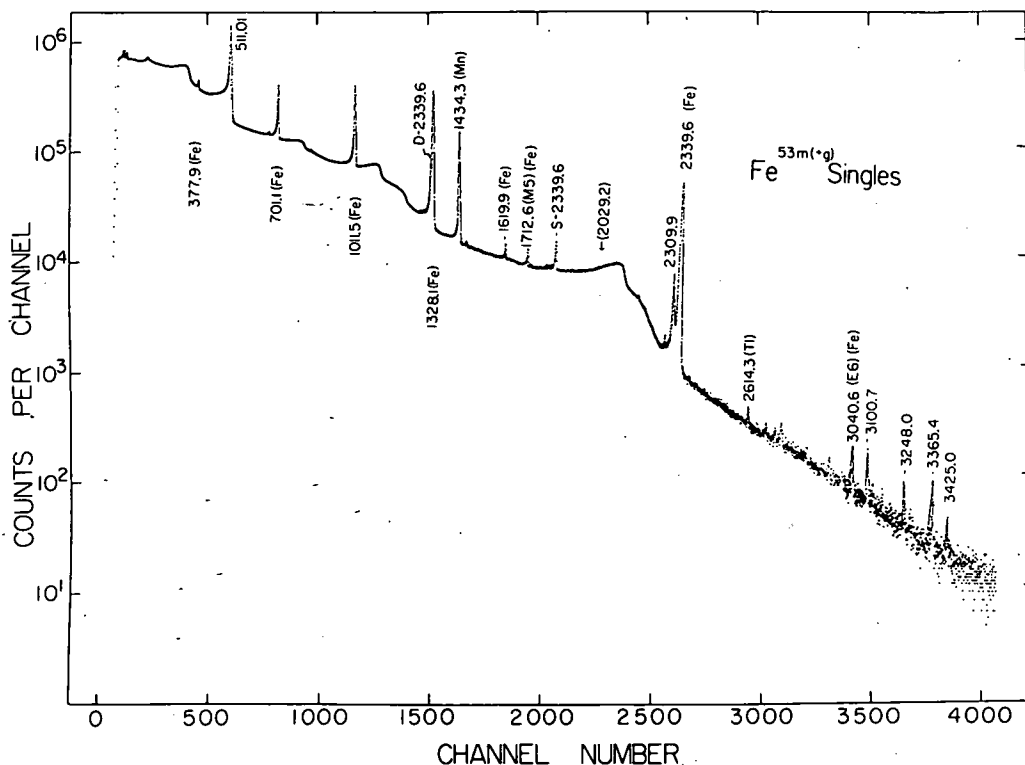


FIG. 2.  $\gamma$ -ray spectrum of  $\text{Fe}^{53m(+g)}$  taken with a 3.6% Ge(Li) detector. This spectrum represents a 24-h accumulation of data. The  $E6$  and  $M5$  peaks are so labeled, and the arrow (at 2029.2 keV) shows where a sum peak between the 701.1- and 1328.1-keV transitions would appear.

ciently close to the detector so that the detector presents a large solid angle, summing of events in the same  $\gamma$ -ray cascade can occur. Second, if the source is strong, accidental summing of events from the same or different  $\gamma$ -ray cascades can occur. With our  $\text{Fe}^{53m}$  experiments one needs to worry about both effects in turn.

This summing problem was examined both in light of the data themselves and also from additional experiments designed to elucidate the summing phenomenon. Considering the  $\text{Fe}^{53m}$  data alone, we can formulate several interesting arguments. Examination of the established decay scheme (Fig. 1) reveals that the two most intense transitions, at 701.1 and 1328.1 keV, are in a cascade connected by the 1011.5-keV transition, the third most intense. If indeed cascade-type summing were to occur to an appreciable extent during an experiment such as that recorded in Fig. 2, one would conclude that these two most intense transitions should give rise to a sum peak at 2029.2 keV. Examination of the spectrum, however, shows no evidence for a  $\gamma$ -ray peak at this energy. This absence was reproducible from experiment to experiment with widely varying count rates and source-detector distances. One can estimate for this spectrum, for example, that the contributions of summing to the  $M5$  and  $E6$  peaks would be considerably less than 0.1% and 10%, respectively, and come almost entirely from chance coincidences. Also, although the 511.01-keV  $\gamma^{\pm}$  peak was the most intense peak in the spectrum, no evidence was found for  $\gamma^{\pm}$  summing to give a 1022-keV peak or of their summing with any of the stronger  $\gamma$  rays in the spectrum. This in-

dicates that chance type summing was not a significant factor in these experiments except for a small possible contribution to the weak  $E6$  peak. A third consideration is the peak width. In general, sum peaks or peaks containing significant summing components tend to be wider than their true counterparts. However, here one finds the peaks corresponding to the  $M5$  and  $E6$  transitions to be of normal width, providing further evidence for the fact that they are true peaks. Finally, the  $E6$  and  $M5$  decay with the same half-life as the  $E4$  isomeric transition, and one would expect to measure a different half-life if there were a substantial contribution from chance-coincidence summing.

To check the internal data, a series of experiments was performed in which  $\text{Co}^{60}$  spectra were taken with various source-detector geometries at a constant count rate. The degree of summing to form a 2505.71-keV sum peak was observed as a function of geometry. Then using the same count rates and geometries, an analogous set of  $\text{Fe}^{53m}$  spectra was taken. The resulting intensity variations of the  $M5$  and  $E6$  peaks as a function of geometry were compared with the variations of the  $\text{Co}^{60}$  spectra. This method corroborated the fact that the 1712.6- and 3040.6-keV peaks are not sum peaks but do indeed reflect true transitions in the  $\text{Fe}^{53}$  nucleus.

In Table I we summarize the results for the  $\gamma$  rays from  $\text{Fe}^{53m}$ , including a comparison of the  $E4$ ,  $M5$ , and  $E6$  half-lives with simple single-particle estimates.<sup>5</sup> The  $E6$  appears to be retarded by a factor of 650 and the  $M5$  and  $E4$  by factors of 43 and 41, respectively, over the single-particle estimate. The retardation of the  $E6$ ,

Table I.  $\text{Fe}^{53m}$   $\gamma$  rays.

$E_{\gamma}$ (keV)	Multipolarity	Photon intensity	Partial (photon) $t_{1/2}$ (sec)		Retardation expt/calc
			Expt <sup>a</sup>	Calc <sup>b</sup>	
701.0 $\pm$ 0.1	$E4$	$\approx 100$	$1.57 \times 10^3$	$3.8 \times 10^1$	41
1011.5 $\pm$ 0.1	$M1$	$86 \pm 9$	...	...	...
1328.1 $\pm$ 0.1	$M1$	$97 \pm 10$	...	...	...
1712.6 $\pm$ 0.3	$M5$	$0.7 \pm 0.1$	$2.2 \times 10^5$	$5.2 \times 10^3$	43
2339.6 $\pm$ 0.1	$E2$	$13 \pm 2$	...	...	...
3040.6 $\pm$ 0.5	$E6$	$0.02 \pm 0.005$	$7.8 \times 10^6$	$1.2 \times 10^4$	650

<sup>a</sup>The 701.1-keV transition was corrected for conversion using a value of  $\alpha_K = 0.003$ , which we obtained by a linear extrapolation from the tables of R. S. Hager and E. C. Seltzer, Nucl. Data, Sec. A 4, 1 (1968). The conversion coefficients for the other transitions were small enough to be negligible.

<sup>b</sup>Ref. 5.

although large, should not be too surprising since it involves a recoupling in taking a state with seniority 3 to one primarily of seniority 1 ( $\approx 60\%$ ).<sup>6</sup> The very similar retardations for the  $M5$  and  $E4$  very likely arise because these involve transitions between seniority-3 states. A more extensive treatment of the transition rates is given in a paper to be published elsewhere.<sup>7</sup>

We are grateful for the assistance in data taking provided by G. C. Giesler and Dr. R. A. Warner. We also thank H. Hilbert and Dr. H. G. Blosser for their aid in operating the Michigan State University cyclotron.

---

\*Work supported in part by the U. S. Atomic Energy Commission.

†Work supported in part by the National Science Foundation.

<sup>1</sup>K. Eskola, Ann. Acad. Sci. Fenn., Ser. A6 261, 1 (1967).

<sup>2</sup>I. Dervedde, Z. Phys. 216, 103 (1968).

<sup>3</sup>K. Eskola, Phys. Lett. 23, 471 (1966).

<sup>4</sup>For a more complete description of the types of data-reduction methods used, see, e.g., R. E. Eppley, W. C. McHarris, and W. H. Kelly, Phys. Rev. 2, 1077 (1970).

<sup>5</sup>S. A. Moszkowski, in *Alpha-, Beta- and Gamma-Ray Spectroscopy*, edited by K. Siegbahn (North-Holland, Amsterdam, 1965), and Phys. Rev. 89, 474 (1953).

<sup>6</sup>J. D. McCullen, B. F. Bayman, and L. Zamick, Phys. Rev. 134, B515 (1964).

<sup>7</sup>J. N. Black, W. C. McHarris, and W. H. Kelly, to be published.

PROTON SCATTERING AND THE OPTICAL MODEL DIFFERENCES  
BETWEEN  $^{40}\text{Ca}$  AND  $^{48}\text{Ca}$  \*

C. J. MAGGIORE \*\*, C. R. GRUHN, T. Y. T. KUO and B. M. FREEDOM \*\*\*

*Department of Physics and Cyclotron Laboratory  
Michigan State University, East Lansing, Michigan 48823, USA*

Received 9 November 1970

Elastic proton scattering from  $^{48}\text{Ca}$  and  $^{40}\text{Ca}$  has been measured at 25, 30, 35 and 40 MeV. The rms radius determined by the optical model is 0.15 fm larger for  $^{48}\text{Ca}$  than for  $^{40}\text{Ca}$ , consistent with the  $A^{1/3}$  law.

Electromagnetic studies of the relative charge distributions of the calcium isotopes indicate that for  $^{48}\text{Ca}$  relative to  $^{40}\text{Ca}$ , the half-density point of the charge distribution increases by 0.15 fm and the surface diffusivity decreases by 12% [1]. Recent optical model analyses of 30 MeV elastic  $\alpha$ -particle scattering from these nuclei by Bernstein et al. [2] indicate that  $\Delta R_{\text{op}} = R_{\text{op}}(^{48}\text{Ca}) - R_{\text{op}}(^{40}\text{Ca}) = 0.15$  fm and that the surface diffusivity is essentially unchanged. A strong absorption radius for 42 MeV elastic  $\alpha$ -particle scattering has been calculated by Fernandex and Blair [3] and they also find  $\Delta R \approx 0.15$  fm with the diffusivity being a constant. The present experiment is an attempt to determine what differences are observed by proton scattering.

The differential cross sections of elastically scattered protons from  $^{48}\text{Ca}$  and  $^{40}\text{Ca}$  have been measured and the data have been analysed with the optical model in an analogous manner to the analysis of Bernstein et al. The experiment was performed with the proton beam of the MSU Sector Focused Cyclotron at four energies, 25, 30, 35 and 40 MeV. The targets were isotopically enriched (96.25%  $^{48}\text{Ca}$  and 99.97%  $^{40}\text{Ca}$ ) self-supporting metal foils (1.08 mg/cm<sup>2</sup>  $^{40}\text{Ca}$  and 2 g/cm<sup>2</sup>  $^{40}\text{Ca}$ ). The scattered protons were detected with Ge(Li) proton counters fabricated at this laboratory [4]. The angles were checked in each spectrum by comparing the positions of the

H and  $^{12}\text{C}$  contaminant peaks relative to the Ga ground state and found to be accurate to within 0.1°. The energy of the incident proton determined by measuring the fields of the energy analysing magnets with NMR probes is accurate to within 0.1% [5]. Data were taken every five degrees from 12° to 97°. The  $^{40}\text{Ca}$  absolute cross sections were found to be in agreement with previous results [6] to within 5%. The  $^{48}\text{Ca}$  data were normalized with respect to the  $^{40}\text{Ca}$  data by using the known ratio of isotopic abundances in the  $^{48}\text{Ca}$  target. This agreed with the normalization based on target thickness and integrated charge to within 10%. The uncertainty in absolute normalization of the  $^{48}\text{Ca}$  cross sections is taken to be approximately 10%.

If one assumes that the matter distribution is related to the geometry of the optical potential used to fit the elastic scattering, then one may be able to determine differences in the matter distribution by looking at differences in the optical potential. We have therefore used the optical model to fit the  $^{40}\text{Ca}$  data and to fix the potential well depths at each energy. The  $^{48}\text{Ca}$  data are then fit by using the potential strengths obtained from the  $^{40}\text{Ca}$  analysis and by performing a search which grids the parameters determining the geometry of the optical model. Such a grid search was performed so that sensitivity of the fit to the radius and diffusivity would be determined.

The same optical model potential form used by the authors of ref. [2] in their  $\alpha$ -particle analysis except that a surface absorption term was replaced by a volume absorption term was used in this study. The procedure was to fix the geometry for the  $^{40}\text{Ca}$  analysis ( $r_0 = 1.25$  fm,  $a = 0.65$  fm) and search on  $V_R$  and  $W_D$  to obtain the

\* This work supported by the U.S. National Science Foundation.

\*\* Present address: Department of Environmental Science, Mt. Sinai School of Medicine, New York, New York.

\*\*\* Present address: Physics Department, University of South Carolina, Columbia, South Carolina 29208.

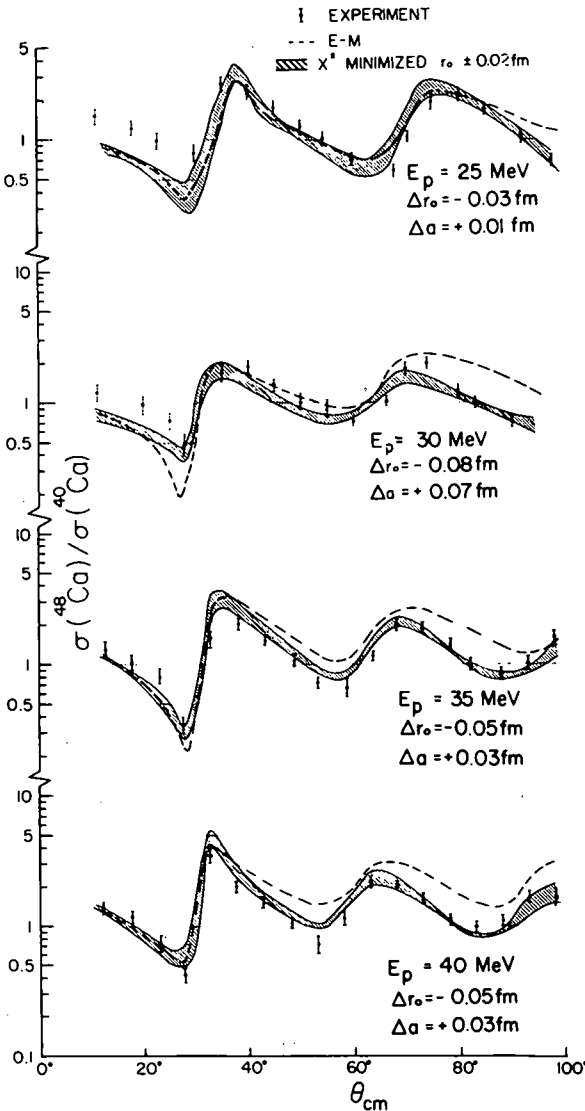


Fig. 1. Plot of the ratio of cross sections at each energy with real and imaginary geometries equal and  $U_{\text{SYM}} = 4.4$  MeV.

best fit at each energy. Then a "geometric" analysis of the  $^{48}\text{Ca}$  data was made by holding  $V_R$  and  $W_D$  the same for both isotopes and performing a grid search on  $r_0$  and  $a$ . A grid search was also performed for the  $^{48}\text{Ca}$  data where  $V_R(^{48}\text{Ca}) = V_R(^{40}\text{Ca}) + V_{\text{SYM}}(N-Z)/A$  [7]. The value of  $V_{\text{SYM}}$  used was 26.4 MeV [8] which added 4.4 MeV to the real well depth of  $^{40}\text{Ca}$ . The results of the grid search on  $r_0$  and  $a$  showed that the inclusion of the symmetry term had

little effect on the difference in rms radius. The same calculations were performed for volume absorption only and for a combination of volume and surface absorption. The geometry parameters yielding a best fit in each case were, however, approximately independent of the form of the imaginary potential at each energy.

The sensitivity of the results to the requirement that the real and imaginary geometries be equal was investigated by using the geometry parameters of Fricke et al. [6] for the  $^{40}\text{Ca}$  data. The cases where the radii and diffusivities were changed by the same absolute amounts and by the same percentage amounts were found to differ negligibly. The results at each energy were in reasonable agreement with the results obtained by holding the real and imaginary geometries equal.

Fig. 1 shows the ratio  $\sigma(^{48}\text{Ca})/\sigma(^{40}\text{Ca})$  versus the center-of-mass scattering angle for each energy. It is indicative of how well the ratio of cross sections is fit with the geometric search procedure and the optical model having equal real and imaginary geometries. The results obtained using the differences in the proton distributions determined by electron scattering are also shown. The electromagnetic differences do not fit the data, particularly at higher energies.

It has been pointed out by Greenlees, Pyle and Tang [9,10] that the geometric quantity which is best determined by the optical model is the rms radius. Our results are in good agreement with this fact if one neglects the results for the 25 MeV data. One can justify neglecting this 25 MeV data because the minimum in  $\chi^2$  space for  $r$  and  $a$  is not well defined at this energy, but consists of a broad trough, the minimum of which does not correspond to a line of constant rms radius.

The results indicate that the half-density point of the radius and the diffusivity are not uniquely determined by the present optical model analysis. The sign and the magnitude of the differences depend on the energy of the incident protons and on whether or not a symmetry term is added to the real potential. The average difference in the rms radii of  $^{48}\text{Ca}$  and  $^{40}\text{Ca}$  observed by this optical model analysis is 0.15 fm which equals the difference in the rms radii predicted by the  $A^{1/3}$  law. This result is not in agreement with the elastic  $\alpha$ -particle scattering data.

If one assumes that the rms radius of the matter distribution is related to the rms radius of the optical potential via a constant interaction distance, then the difference in the optical model rms radii equals the difference in the rms



matter radii. If one further assumes that the rms radius of the proton distribution is given by the rms radius of the charge distribution determined by electron scattering, then our results, in conjunction with the electron scattering results\*, indicate that the  $^{48}\text{Ca}$  nucleus has an excess neutron density in the surface region. This agrees with the conclusions based on Coulomb energy differences [11], shell model calculations [12], and Hartree-Fock calculations [13].

We wish to acknowledge the contribution of J. Anderson who helped to run the many optical model cases on the computer.

\* By Frosch et al. it has been found that the rms charge radius of  $^{48}\text{Ca}$  is 0.01 fm smaller than of  $^{40}\text{Ca}$  [1].

#### References

- [1] R. F. Frosch et al., Phys. Rev. 174 (1968) 1380.
- [2] A. M. Bernstein, M. Duffy and E. P. Lippincott, Phys. Letters 30B (1969) 20.
- [3] B. Fernandex and J. S. Blair, Phys. Rev. C1 (1970) 523.
- [4] C. R. Gruhn et al., IEEE Transactions on Nucl. Science NS-15 (1968) 337.
- [5] J. L. Snelgrove and E. Kashy, Nucl. Instr. 52 (1967) 163.
- [6] L. N. Blumberg et al., Phys. Rev. 147 (1966) 812.
- [7] D. Slanina and H. McManus, Nucl. Phys. A116 (1968) 271.
- [8] M. P. Fricke, E. E. Gross, B. J. Morton and A. Zucker, Phys. Rev. 156 (1967) 1207.
- [9] G. W. Greenlees, G. J. Pyle and Y. C. Tang, Phys. Rev. 171 (1968) 1115.
- [10] G. W. Greenlees, G. J. Pyle and Y. C. Tang, Phys. Letters 26B (1968) 658.
- [11] J. A. Nolen, J. P. Schiffer and N. Williams, Phys. Letters 27B (1968) 1.
- [12] L. R. B. Elton, Phys. Rev. 158 (1967) 970.
- [13] R. M. Tarbuton and K. T. R. Davies, Nucl. Phys. A120 (1968) 1.

\* \* \* \* \*

## Static Quadrupole Moments in $A = 18-38$ Nuclei as Predicted in the Shell Model

B. H. Wildenthal\*

*Michigan State University, East Lansing, Michigan 48823*

and

J. B. McGrory†

*Oak Ridge National Laboratory, Oak Ridge, Tennessee 37830*

and

P. W. M. Glaudemans

*Rijksuniversiteit, Utrecht, The Netherlands*

(Received 5 November 1970)

The static electric quadrupole moments of the ground and first excited states of nuclei in the  $sd$  shell are calculated from shell-model wave functions. The relative values of experimentally known moments of ground states are well reproduced by the calculations as are the relative values of the measured moments of  $J^\pi = 2^+$  first excited states. However, the absolute experimental values of the ground-state and excited-state moments cannot be reproduced simultaneously with a single choice of effective charge.

The exploitation of new experimental techniques<sup>1</sup> has recently led to the measurements of the static electric quadrupole moments of the  $J^\pi = 2^+$  first excited states of several even-even nuclei in the  $sd$  shell.<sup>2-7</sup> Such measurements are especially important because they yield the signs as well as magnitudes of the moments of these states, and hence give information about the intrinsic shapes of these nuclei. Moreover, any quadrupole moment measurement provides a direct test of the wave function of a single state, rather than a test of the overlap of two different states as provided by transition rate measurements. In this Letter we discuss predictions of static electric quadrupole moments obtained from shell-model calculations in the region  $A = 18-38$ . We treat the ground states (and some excited states) of even-odd and odd-odd nuclei and the  $2^+$  first excited states of the even-even systems.

The wave functions from which we derive our predictions have been obtained in a series of conventional shell-model calculations in each of which a different configuration space is used. Together, these calculations predict the low-lying structure of nuclei with all masses in the range  $A = 17-39$ . Five different calculations are involved. Their essential characteristics are as follows. Calculations I and V were made in the full space of  $sd$ -shell configurations and used "realistic" effective interactions. Calculations III and IV were made in truncated  $sd$ -shell bases which allowed active particles in all three  $sd$  orbits. The effective Hamiltonians were of the "surface delta interaction" type. Calculation II

was made in the  $d_{5/2}-s_{1/2}$  space and used an empirically adjusted "free parameter" effective interaction. More detailed and general accounts of these investigations are, or will be, available in the literature.<sup>8-12</sup>

We would stress here two points. The first is that the only experimental data used to determine the effective Hamiltonians in the cases for which these were empirically derived were the spins and excitation energies of observed states. In no case was a Hamiltonian affected by observed quadrupole moment values. The second point is that in several instances shell-model calculations were made for the same nucleus in more than one model space, and in these cases the qualitative features (i.e., signs and relative sizes from one nucleus to another) of the calculated moments are very similar in each of the models used. This gives us some degree of confidence in the calculations for nuclei in the mass regions where only the more truncated models can be applied.

In all of our calculations of the matrix elements of the quadrupole operator we use harmonic-oscillator radial functions for the single-particle nuclear wave functions. The oscillator size parameter was determined from the relation  $\hbar\omega = 41A^{-1/3}$ . In all of the calculations with three active shell-model orbits, (calculations I, III, IV, and V) effective charges of  $e_n = 0.5e$  and  $e_p = 1.5e$  were assumed for the neutron and proton, respectively. In calculation II, in which only two orbits are active, the effective charges were increased to  $e_n = 0.7e$  and  $e_p = 1.7e$ . These values of the effective charges have been suggested by

previous investigators as appropriate for calculations of  $B(E2)$  values and have been used by us in all of our work in the  $sd$  shell. The results of our calculations for static quadrupole moments are presented in Table I. A comparison of the predictions for nuclei in the mass regions where two different shell-model calculations were made substantiates our statement that the qualitative features are not too sensitive to the model space, and indicates that truncation effects in the two-shell calculation for these observables can be adequately compensated for simply by changing the effective charge.

The first significant point to note in Table I is the generally good agreement between the predicted quadrupole moments and the observed values for the ground-state moments (i.e., all cases except for even-even nuclei). In all cases the predicted and observed shapes (signs) are in agreement. The magnitudes of the calculated moments for nuclei with  $A < 28$  are in agreement with experiment to within roughly 10-20%. For the heavier nuclei the moments are smaller in magnitude, and the percentage deviations are larger. However, the absolute discrepancies are still reasonably small.

The agreement between our predictions and the observed values of the quadrupole moments of the  $J^\pi = 2^+$  first excited states of even-even nuclei is not as good as that obtained for the ground-state moments. In all cases the experimentally determined shapes are correctly predicted. However, with the exception of  $^{28}\text{Si}$ , all of the magnitudes of the measured moments for these excited states are larger than our predictions by a factor of about 1.7. One could, of course, obtain good agreement between the theoretical results and the data on excited states by using a larger effective charge in the calculations. The point we would emphasize however is that it is not possible to account for the experimental values for ground-state moments and the experimental values for excited-state moments simultaneously with a single choice for the effective charge.

The origins of this discrepancy could be either in our calculations or in one or the other set of experimental values. In the calculations it is conceivable that there is a fairly strong state dependence of the effective quadrupole operator so that the use of a fixed effective charge in the calculation of the matrix elements between all states is inadequate. It is also possible that the spaces adequate to describe the ground states are significantly different from the spaces adequate to de-

scribe the excited states, and that the spaces we use are more appropriate for the ground states. However, the properties of many of the levels in the even-even nuclei in this region have been rather well described in terms of states projected from one intrinsic state. If the members of ground-state bands of these even-even nuclei are related in this way, one would not expect a great difference in the space required to describe the ground state and the first excited state.

There are also reasons to suspect problems originating in the analysis of the experimental data. All of the experimental values<sup>13,14</sup> for ground-state moments have been determined in hyperfine splitting measurements. The extraction of quadrupole moment values from this kind of data depends upon a knowledge of the value at the nucleus of the gradient of the electric field of the atomic electrons.<sup>15</sup> It is still uncertain just how accurately this factor is known. It was partially to circumvent this difficulty that Breit and co-workers<sup>16</sup> proposed the Coulomb excitation-reorientation effect technique for measuring electric quadrupole moments. All of the excited-state moments referenced here have been obtained recently with this reorientation-effect method. It is possible that there are still unrecognized problems in the quantitative analysis of these newer experiments which are comparable with the uncertainties inherent in the ground-state values.

There already exists a disconcerting problem in the relationship of the measured  $B(E2)$  value for the  $2^+ - 0^+$  transition in  $^{20}\text{Ne}$ , and the quadrupole moment for the  $2^+$  state as measured by the "reorientation" techniques.<sup>4</sup> The intrinsic quadrupole moment of the ground-state band of  $^{20}\text{Ne}$  as extracted from the static quadrupole moment is 30% larger than the same moment as extracted from the measured  $B(E2)$  values via the usual rotational-model prescription. This same sort of problem exists for  $^{24}\text{Mg}$ .<sup>6</sup> These results can be interpreted as implying a breakdown of the common view, previously mentioned, which pictures the various members of a rotational band as projections from a single intrinsic state. If the details of the intrinsic state change from one member of the band to the next, then the  $B(E2)$ 's could be damped relative to the quadrupole moments. On the other hand, our calculations, which certainly allow some freedom in this respect (although they do not allow major-shell mixing), give no indication that the single-intrinsic-state picture is incorrect. We think that in

Table I. Existing experimental values for static electric quadrupole moments in the *sd* shell and the predictions of *sd*-shell model calculations for these observables.

Nucleus	J <sub>n</sub>	E <sub>expt.</sub> (MeV)	Static Electric Quadrupole Moment (eF <sup>2</sup> )					
			Expt.	I	II	Calc. III	IV	V
<sup>17</sup> O	5/2 <sub>1</sub> <sup>+</sup>	0.00	-2.7 <sup>±</sup> 0.3 <sup>a</sup>	-2.6				
<sup>18</sup> O	2 <sub>1</sub> <sup>+</sup>	1.98		-2.0				
<sup>18</sup> F	1 <sub>1</sub> <sup>+</sup>	0.00		-1.2				
<sup>19</sup> O	5/2 <sub>1</sub> <sup>+</sup>	0.00		-0.1				
<sup>19</sup> F	5/2 <sub>1</sub> <sup>+</sup>	0.20	+11.0 <sup>±</sup> 2.0 <sup>a</sup>	-9.2				
<sup>20</sup> F	2 <sub>1</sub> <sup>+</sup>	0.00		+7.6				
<sup>20</sup> Ne	2 <sub>1</sub> <sup>+</sup>	1.63	-24 <sup>±</sup> 3 <sup>b</sup> , -27 <sup>±</sup> 11 <sup>c</sup>	-14.3	-12.1			
<sup>21</sup> F	5/2 <sub>1</sub> <sup>+</sup>	0.00		-10.9	-12.4			
<sup>21</sup> Ne	3/2 <sub>1</sub> <sup>+</sup>	0.00	+9.3 <sup>±</sup> 1.0 <sup>a</sup>	+10.3	+9.9			
<sup>22</sup> Ne	2 <sub>1</sub> <sup>+</sup>	1.28	-21 <sup>±</sup> 4 <sup>b</sup> , -21 <sup>±</sup> 6 <sup>c</sup>	-13.6	-14.1			
<sup>22</sup> Na	3 <sub>1</sub> <sup>+</sup>	0.00		+22.1	+22.2			
<sup>23</sup> Ne	5/2 <sub>1</sub> <sup>+</sup>	0.00			+14.4			
<sup>23</sup> Na	3/2 <sub>1</sub> <sup>+</sup>	0.00	+11 <sup>h</sup>	---	+11.5			
<sup>24</sup> Na	4 <sub>1</sub> <sup>+</sup>	0.00			+25.2			
<sup>24</sup> Mg	2 <sub>1</sub> <sup>+</sup>	1.37	-24 <sup>±</sup> 4 <sup>d</sup> , -26 <sup>±</sup> 8 <sup>e</sup>	---	-15.0			
<sup>25</sup> Mg	5/2 <sup>+</sup>	0.00	+22 <sup>h</sup>	---	+17.8			
<sup>26</sup> Mg	2 <sup>+</sup>	1.81			+0.4			
<sup>27</sup> Al	5/2 <sup>+</sup>	0.00	+15 <sup>h</sup>	---	+13.4	+13.8		
<sup>28</sup> Si	2 <sub>1</sub> <sup>+</sup>	1.78	+11 <sup>±</sup> 5 <sup>f</sup> , +17 <sup>±</sup> 5 <sup>g</sup>	---	+16.0	+14.3		
<sup>30</sup> Si	2 <sub>1</sub> <sup>+</sup>	2.23					-6.6	
<sup>30</sup> P	1 <sub>1</sub> <sup>+</sup>	0.00					+3.2	
<sup>31</sup> Si	3/2 <sub>1</sub> <sup>+</sup>	0.00					-7.4	
<sup>32</sup> S	2 <sub>1</sub> <sup>+</sup>	2.24	-20 <sup>±</sup> 6 <sup>f</sup>	---	---	---	-13.6	
<sup>32</sup> P	1 <sup>+</sup>	0.00					-4.5	
<sup>33</sup> S	3/2 <sub>1</sub> <sup>+</sup>	0.00	-5.5 <sup>h</sup>	---	---	---	-7.1	
<sup>34</sup> S	2 <sub>1</sub> <sup>+</sup>	2.13					+6.7	
<sup>34</sup> Cl	3 <sub>1</sub> <sup>+</sup>	0.15					-17.0	
<sup>35</sup> S	3/2 <sub>1</sub> <sup>+</sup>	0.00	+4 <sup>h</sup>	---	---	---	+5.8	+7.5
<sup>35</sup> Cl	3/2 <sub>1</sub> <sup>+</sup>	0.00	-7.9 <sup>h</sup>	---	---	---	-9.0	-9.0
<sup>36</sup> Cl	2 <sub>1</sub> <sup>+</sup>	0.00	-1.7 <sup>h</sup>	---	---	---		-0.9
<sup>36</sup> Ar	2 <sub>1</sub> <sup>+</sup>	1.97						+14.3
<sup>37</sup> Cl	3/2 <sub>1</sub> <sup>+</sup>	0.00	-6.2 <sup>h</sup>	---	---	---	---	-8.4
<sup>37</sup> Ar	3/2 <sub>1</sub> <sup>+</sup>	0.00						+8.7
<sup>38</sup> Ar	2 <sub>1</sub> <sup>+</sup>	2.17						+1.3
<sup>38</sup> K	3 <sub>1</sub> <sup>+</sup>	0.00						+10.9

<sup>a</sup>Ref. 13.

<sup>b</sup>Ref. 4.

<sup>c</sup>Ref. 3.

<sup>d</sup>Ref. 6.

<sup>e</sup>Ref. 2.

<sup>f</sup>Ref. 5.

<sup>g</sup>Ref. 7.

<sup>h</sup>Ref. 14.

attempting to account for these discrepancies attention should be paid to attaining a more complete understanding of the reorientation effect, and of the experiments which take advantage of the effect, as well as to the theory of the details of the nuclear structure of the states involved.

In Table I we have listed a number of calculated quadrupole moments for which there are no measured values presently available. In particular, the quadrupole moments of the  $J^\pi = 2^+$  states of  $^{26}\text{Mg}$ ,  $^{30}\text{Si}$ ,  $^{34}\text{S}$ ,  $^{36}\text{Ar}$ , and  $^{38}\text{Ar}$  can all be measured, in principle. Our shell models predict a quite small value for the moment in  $^{26}\text{Mg}$ , and significant variations as a function of mass in the magnitudes and signs of the moments of the other nuclei. The experimental values for these quadrupole moments would provide a sensitive test for the shell model, as well as various other microscopic and collective models of the nuclei in this mass region. In particular, the calculated results for the signs of these moments appear to be essentially invariant under a number of alterations in the two-body Hamiltonians which we have made in the course of this investigation. Any experimental contradiction to the predicted signs shown in Table I would thus present a major challenge to the shell model.

We thank Edith Halbert for her many contributions to the studies from which those ideas were developed.

\*Work supported in part by the National Science Foundation.

†Work supported by U. S. Atomic Energy Commission

under contract with the Union Carbide Corporation.

<sup>1</sup>J. de Boer and J. Eichler, in *Advances in Nuclear Physics*, edited by M. Baranger and E. Vogt (Plenum, New York, 1968), Vol. I.

<sup>2</sup>A. Bamberger, P. G. Bizzeti, and B. Povh, *Phys. Rev. Lett.* **21**, 1599 (1968).

<sup>3</sup>D. Schwalm and B. Povh, *Phys. Lett.* **29B**, 103 (1969).

<sup>4</sup>K. Nakai, F. S. Stephens, and R. M. Diamond, *Nucl. Phys.* **A150**, 114 (1970).

<sup>5</sup>K. Nakai, J. L. Quebert, F. S. Stephens, and R. M. Diamond, *Phys. Rev. Lett.* **24**, 903 (1970).

<sup>6</sup>O. Häusser, B. W. Hooton, D. Pelte, T. K. Alexander, and H. C. Evans, *Can. J. Phys.* **48**, 35 (1970), and *Phys. Rev. Lett.* **22**, 359 (1969).

<sup>7</sup>O. Häusser, T. K. Alexander, D. Pelte, B. W. Hooton, and H. C. Evans, *Phys. Rev. Lett.* **23**, 320 (1969).

<sup>8</sup>E. C. Halbert, J. B. McGrory, B. H. Wildenthal, and S. P. Pandya, "Advances in Nuclear Physics" (Plenum, New York, to be published), Vol. IV.

<sup>9</sup>B. H. Wildenthal, J. B. McGrory, E. C. Halbert, and P. W. M. Glaudemans, *Phys. Lett.* **26B**, 692 (1968).

<sup>10</sup>B. H. Wildenthal, unpublished.

<sup>11</sup>B. H. Wildenthal, J. B. McGrory, E. C. Halbert, and P. W. M. Glaudemans, *Phys. Lett.* **27B**, 611 (1968).

<sup>12</sup>B. H. Wildenthal, E. C. Halbert, J. B. McGrory, and T. T. S. Kuo, *Phys. Lett.* **32B**, 339 (1970).

<sup>13</sup>V. S. Shirley, in *Hyperfine Structure and Nuclear Radiations*, edited by E. Matthias and D. A. Shirley (North-Holland, Amsterdam, 1968).

<sup>14</sup>G. H. Fuller and V. W. Cohen, in *Nuclear Data Sheets*, compiled by K. Way *et al.* (Printing and Publishing Office, National Academy of Sciences—National Research Council, Washington, D. C.), Appendix 1.

<sup>15</sup>H. Kopfermann, *Nuclear Moments* (Academic, New York, 1958).

<sup>16</sup>G. Breit and J. P. Lazarus, *Phys. Rev. Lett.* **100**, 942 (1955); G. Breit, R. L. Gluckstern, and J. E. Russell, *Phys. Rev. Lett.* **103**, 727 (1956).

ANOMALOUS  $L=1$  SHAPES OF ANGULAR DISTRIBUTIONS FOR  $({}^3\text{He}, t)$  TRANSITIONS  
TO  $0^+$  ANTIANALOG STATES IN  ${}^{64,66}\text{Ga}$  AND  ${}^{40}\text{K}^\dagger$

R. A. Hinrichs, R. Sherr,\* G. M. Crawley, and I. Proctor

*Cyclotron Laboratory, Michigan State University, East Lansing, Michigan 48823*

(Received 27 July 1970)

The  $({}^3\text{He}, t)$  reaction on  ${}^{64,66}\text{Zn}$  and  ${}^{40}\text{Ar}$  to the  $0^+$  analog and antianalog states has been studied at 35 MeV. The angular distributions for the  $T_< 0^+$  states show an  $L=1$  shape, implying a need for modifications in the conventional description of  $({}^3\text{He}, t)$  reactions.

The  $({}^3\text{He}, t)$  reaction on light- and medium-weight nuclei has recently been the subject of many studies with the extraction of significant spectroscopic information.<sup>1</sup> Such charge-exchange reactions can populate both  $T_>$  (analog) and orthogonal  $T_<$  states (states of isospin one less than the target nucleus) that have the same spin and configuration as the analog state (antianalog states). If spin-0 states for both the initial and final nucleus are selected, then the interaction responsible for the transition, in usual microscopic terminology, is only the pure charge-exchange operator  $V_r(t \cdot \vec{\tau}_i)g(r)$ , summed over the target nucleons  $i$ . If one assumes that the radial integrals (form factors) for all of the active nucleons that contribute to this sum are the same, then the excitation of  $0^+$  states other than the analog state is a measure of the amount of the analog-state wave function in those states, the cross section for exciting such states being 0 in the case of no isospin mixing. However, as French and MacFarlane<sup>2</sup> have pointed out, if there is a neutron excess in the target nucleus that spans more than one subshell, then  $T_< 0^+$  states can be excited if the radial integrals of the contributing neutron orbitals are different.

To see this we separate the isospin operator  $V_r \hat{t} \cdot \vec{\tau}$  into a part for each subshell (assuming two orbitals 1 and 2 with separate isospins  $T_1$  and  $T_2$ ). The matrix element for monopole transitions (with  $T_i = T_1 + T_2$  being the isospin of the initial state and  $T_f$  that of the final state) is then<sup>2</sup>

$$\langle 3C \rangle^2 (T_f = T_i - 1) = (T_1 T_2 / 2T_i) [V_1(r) - V_2(r)]^2,$$

$$\langle 3C \rangle^2 (T_f = T_i) = (1/2T_i) [V_1(r)T_1 + V_2(r)T_2]^2.$$

$V_j(r)$  is the radial integral of the form  $\int u_j^2(r)g(r, R)r^2 dr$ , where  $u_j$  is the radial wave function of the nucleon in orbital  $j$  and  $g(r, R)$  is the radial part of the effective projectile-nucleon interaction. From these expressions it is seen that a transition to the  $0^+ T_<$  state can proceed only if the radial integral for each subshell is different, and so a measure of the population of such  $0^+$  states can provide a measure of the dependence

of the interaction on the orbits involved.

Investigations of such transitions have been reported by Goodman and Roos for  ${}^{88}\text{Sr}$ <sup>3</sup> and  ${}^{56}\text{Fe}$ <sup>4</sup> targets. They conclude in the first case that they see the effect of the inequality of the radial integrals in  ${}^{88}\text{Y}$  in the large excitation of a low-lying  $0^+$  state. For the  ${}^{56}\text{Fe}$  case an  $L=1$  angular distribution is observed for a state at 1.453 MeV. Belote, Dorenbusch, and Rapaport<sup>5</sup> have assigned a  $0^+$  state at this energy from the reaction  ${}^{54}\text{Fe}({}^3\text{He}, p)$ , while Ohnuma, Hashimoto, and Tomita<sup>6</sup> suggest a  $1^-$  state at 1.451 MeV. Goodman and Roos conclude that it is likely that both a  $0^+$  and  $1^-$  state occur within a few keV of each other and that the latter is excited in their  $({}^3\text{He}, t)$  studies.

To study the population of  $0^+$  antianalog states, we selected the nuclei  ${}^{64}\text{Zn}$ ,  ${}^{66}\text{Zn}$ , and  ${}^{40}\text{Ar}$  since the positions of the  $0^+ T_<$  states are reasonably well established in the residual nuclei. In the  ${}^{64,66}\text{Ga}$  isotopes, these states are the ground states. The  $0^+$  assignment for  ${}^{66}\text{Ga}$  has been established for some time,<sup>7</sup> while  $\beta$ - $\gamma$  correlation measurements<sup>8</sup> strongly suggest a  $0^+$  assignment for the  ${}^{64}\text{Ga}$  ground state, a spin-1 assignment being possible only with the inclusion of a very large Coulomb matrix element. (These locations are consistent with the isospin splitting relationship,  $\Delta E_{T \rightarrow T-1} = \alpha T$ , where  $\alpha$  is found to be between 1 and 2 MeV; the analogs of the  ${}^{64,66}\text{Zn}$  ground states in  ${}^{64,66}\text{Ga}$  are at 2.05 and 3.84 MeV, respectively.) For the case of  ${}^{40}\text{K}$ , the state at 1.644 MeV is most likely a  $0^+$  state. Recent  ${}^{40}\text{Ar}(p, n)$  angular distributions at 5.5 MeV<sup>9</sup> indicate that this state has spin 0; a negative-parity assignment is unlikely because of the requirement of a large  $M3$  enhancement factor. Also, recent  ${}^{42}\text{Ca}(p, {}^3\text{He})$  studies by Kolata, Shapiro, and August<sup>10</sup> have shown a characteristic  $L=0$  shape for this transition and have confirmed the  $0^+$  assignment. This contradicts earlier  ${}^{39}\text{K}(d, p)$  work<sup>11</sup> which required an  $L=1$  angular momentum transfer for a very weakly excited state at  $1.639 \pm 0.013$  MeV. A  $({}^3\text{He}, t)$  study by Wesolowski, Hansen, and Stelts<sup>12</sup> at

7.9 MeV found an  $L=1$  shape for the angular distribution for the 1.65-MeV state which they felt was consistent with the  $^{39}\text{K}(d,p)$  results. In the light of the more recent  $0^+$  assignments for this state, it was of interest to investigate this  $(^3\text{He},t)$  reaction at a higher bombarding energy.

$(^3\text{He},t)$  angular distributions between  $10^\circ$  and  $35^\circ$  were taken with 35-MeV  $^3\text{He}$  ions from the Michigan State University sector-focused cyclotron. For  $^{40}\text{Ar}$  a detector telescope for particle identification was used to detect the outgoing tritons while for the Zn isotopes an Engle split-pole spectrograph with position-sensitive detectors was used. The resolution obtained in these latter measurements was 25 keV, adequate to separate the ground states from the first excited states at 160 and 44 keV in  $^{64}\text{Ga}$  and  $^{66}\text{Ga}$ , respectively.

The angular distributions for these three reactions to the  $0^+$   $T_+$  and  $T_-$  states are shown in Fig. 1. The fits shown are distorted-wave Born-approximation (DWBA) calculations for a macroscopic model using the code JULIE. A surface-peaked form factor with geometrical parameters equal to those of the imaginary optical well was used; the distorted waves for both the entrance and exit channels were calculated with optical-model parameters as determined by Gibson<sup>13</sup> for  $^3\text{He}$  elastic scattering on  $^{58}\text{Ni}$  and  $^{40}\text{Ca}$  at 37.7 MeV. For transitions to the analog state, the fits in all three cases are good. However, the fits for the  $0^+$   $T_-$  states with an  $L=0$  transfer are significantly out of phase with the experimental angular distributions for all three isotopes studied. Such  $0^+$  to  $0^+$  transitions should proceed by an  $L=0$  transfer but an  $L=1$  calculation, as shown, provides a very good fit to the data. These results for  $^{40}\text{Ar}$  are consistent with the lower-energy data. They are also similar to those seen in  $^{56}\text{Fe}$  if the state excited at 1.453 MeV has a  $0^+$  spin.

Microscopic calculations for the transition  $^{40}\text{Ar}(^3\text{He},t)^{40}\text{K}(1.65\text{ MeV})$  were carried out using a simple  $(f_{7/2})^2 - (d_{3/2})^2$  configuration for the state. Woods-Saxon wave functions were used for the radial wave functions and a Yukawa form was taken for the interaction. To try to fit the data for this transition, the spatial dependence

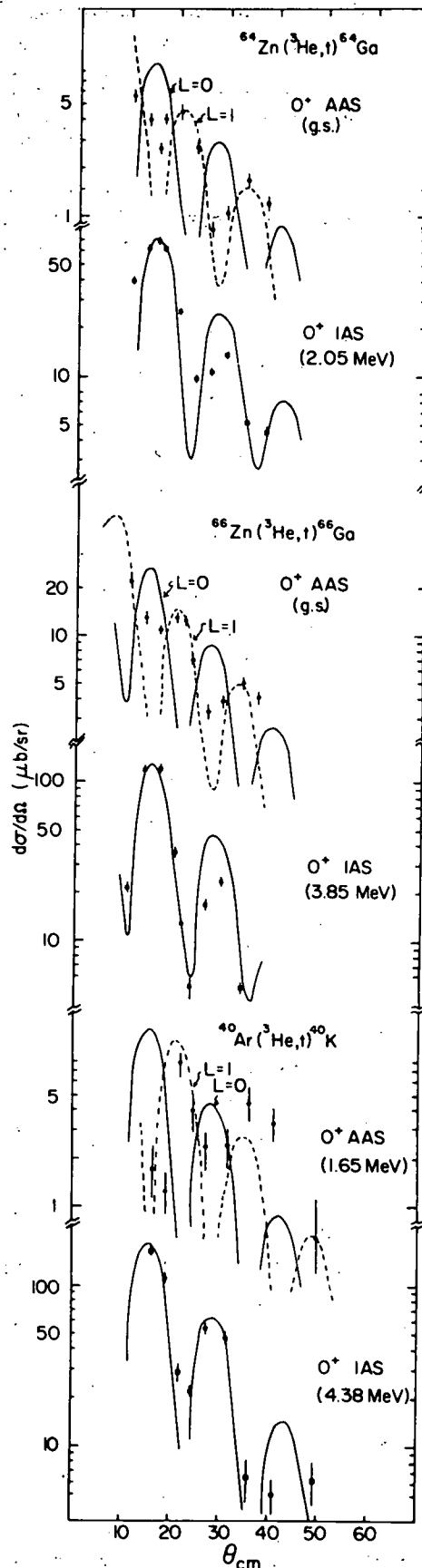


FIG. 1. Angular distributions for  $(^3\text{He},t)$  reactions at 35 MeV on  $^{64}\text{Zn}$ ,  $^{66}\text{Zn}$ , and  $^{40}\text{Ar}$  proceeding to the analog and antianalog states. The lines shown are WBA calculations using a surface-peaked form factor with  $L=0$  or  $L=1$  angular momentum transfers.

of each excess neutron orbital was varied over a wide range by changing the geometrical well parameters  $r_0$  and  $a$ , but a maximum in the angular distribution remained at  $15^\circ$ . (Variations in the range of the Yukawa interaction between 0.7 and 1.4 F also did not yield the desired changes.) For all cases, changes in the optical-model parameters did not alter the shape at forward angles. The ratios of the  $0^+$  analog to antianalog integrated cross sections were 11 for  $^{64}\text{Ga}$ , 4 for  $^{66}\text{Ga}$ , and 16 for  $^{40}\text{K}$ .

The two-body effective interaction currently used in charge exchange is<sup>14</sup>

$$V_{\text{eff}} = \vec{t} \cdot \vec{\tau}_i \{ (V_\tau + V_{\sigma\tau} \vec{\sigma}_0 \cdot \vec{\sigma}_i) g(r) + V_{\text{tensor}} S_{0i} h(r) \},$$

where  $V_\tau$ ,  $V_{\sigma\tau}$ ,  $V_{\text{tensor}}$  are the strengths of the charge-exchange, spin-flip, and tensor interactions. With this interaction only the  $V_\tau$  term contributes for  $0^+ \rightarrow 0^+$  transitions so that an  $L=1$  transfer is not allowed. Yet the experimental evidence shows that in the three cases discussed, the antianalog  $0^+$  states show an  $L=1$  transfer. Since the configurations of the three nuclei differ widely, it would appear that this effect is not configuration dependent, but rather that it is due to other terms in  $V_{\text{eff}}$  or to other modifications in the conventional description of the ( $^3\text{He}, t$ ) reaction.

We wish to acknowledge interesting discussions with R. Schaeffer on the possible interpretations of our results. Recent discussions with P. G. Roos and C. D. Goodman revealed that they have independently come to the same conclusions as

ours (based on their work on  $^{56}\text{Fe}$  and  $^{88}\text{Sr}$ ).

†Research supported in part by the National Science Foundation.

\*On leave from Princeton University, Princeton, N. J.

<sup>1</sup>See, e.g., J. J. Schwartz and B. A. Watson, Phys. Rev. Lett. **24**, 322 (1970), and references cited therein.

<sup>2</sup>J. B. French and M. H. MacFarlane, Phys. Lett. **2**, 255 (1962).

<sup>3</sup>C. D. Goodman and P. G. Roos, Bull. Amer. Phys. Soc. **14**, 121 (1969).

<sup>4</sup>P. G. Roos and C. D. Goodman, in *Nuclear Isospin*, edited by J. D. Anderson, S. D. Bloom, J. Cerny, and W. W. True (Academic, New York, 1969), p. 297.

<sup>5</sup>T. A. Belote, W. E. Dorenbusch, and J. Rapaport, Nucl. Phys. **A109**, 666 (1968).

<sup>6</sup>H. Ohnuma, Y. Hashimoto, and I. Tomita, Nucl. Phys. **66**, 337 (1965).

<sup>7</sup>J. C. Hubbs, W. A. Nierenberg, H. A. Shugart, and J. L. Worcester, Phys. Rev. **105**, 1928 (1957).

<sup>8</sup>L. G. Mann, K. G. Tirsell, and S. D. Bloom, Nucl. Phys. **A97**, 425 (1967).

<sup>9</sup>P. J. Twin, W. C. Olsen, and E. Wong, Phys. Lett. **29B**, 570 (1969).

<sup>10</sup>J. J. Kolata, P. Shapiro, and L. S. August, Phys. Lett. **32B**, 277 (1970).

<sup>11</sup>H. A. Enge, E. J. Irwin, and D. H. Weaner, Phys. Rev. **115**, 949 (1959).

<sup>12</sup>J. J. Wesolowski, L. F. Hansen, and M. L. Stelts, Phys. Rev. **172**, 1072 (1968).

<sup>13</sup>E. F. Gibson, B. W. Ridley, J. J. Kraushaar, M. E. Rickey, and R. H. Bassel, Phys. Rev. **155**, 1194 (1967).

<sup>14</sup>E. Rost and P. D. Kunz, Phys. Lett. **30B**, 231 (1969).



## Experimental Studies of Neutron-Deficient Gadolinium Isotopes.

### I. The Electron-Capture Decay of $Gd^{149}$

R. E. Eppley and Wm. C. McHarris

*Department of Chemistry\* and Cyclotron Laboratory, † Department of Physics, Michigan State University, East Lansing, Michigan 48823*  
and

W. H. Kelly

*Cyclotron Laboratory, † Department of Physics, Michigan State University, East Lansing, Michigan 48823*  
(Received 16 March 1970)

$\gamma$  rays emitted in 9.4-day  $Gd^{149}$  have been studied with Ge(Li) and NaI(Tl) detectors. 25  $\gamma$  rays have been attributed to the decay of  $Gd^{149}$  with energies and relative intensities of 149.6 (233), 214.5 (0.81), 252.3 (1.1), 260.5 (5.8), 272.0 (15), 298.5 (127), 346.5 ( $\approx 100$ ), 405.5 (3.7), 430 (0.33), 459.9 (2.4), 478.7 (0.95), 496.4 (7.2), 516.4 (11), 534.2 (13), 645.2 (5.9), 663.3 (1.1), 666.2 (3.9), 748.2 (35), 788.6 (30), 812.4 (0.55), 863 (0.32), 875.8 (0.90), 933.3 (2.2), 939.1 (9.0), and 947.7 keV (3.7). On the basis of coincidence and anticoincidence experiments, relative intensities, and energy sums, states in  $Eu^{149}$  have been placed at 0, 149.6, 459.9, 496.2, 534.2, 666.0, 748.2, 794.8, 812.4, 875.8, 933.3, 939.1, and 1097.3 keV. The  $Eu^{149}$  x-ray intensity has also been measured. From our  $\gamma$ -transition intensities and published conversion-electron intensities, conversion coefficients were obtained for most of the electromagnetic transitions, thus allowing multipolarity assignments to be made for these transitions. These assignments, together with the  $\log ft$  values, were then used for the placement of limits on the spins of the deduced levels. Our proposed decay scheme is compared with previously published decay schemes and is discussed in terms of current models.

#### I. INTRODUCTION

Neutron-deficient Gd isotopes lie in a region of interest for the testing of nuclear models.

They and their Eu daughters range from nuclei that have large quadrupole moments, suggesting permanently deformed nuclei, through closed-shell nuclei that can be described by an extreme single-

particle shell model. The heavier isotopes ( $N \geq 90$ ) are permanently deformed and exhibit well-developed rotational bands and other features that have been described successfully by the Bohr-Mottelson unified model. Spherical nuclei appear as one approaches the closed neutron shell at  $N=82$ . It would be of considerable interest to be able to correlate the nuclear levels, especially in the odd-mass nuclei where single-particle states are most easily observed, as one moves from the spheroidal region into the spherical region, and we have embarked on a program to do this, primarily through the study of the radioactive decay of neutron-deficient Gd isotopes. As Gd<sup>152</sup>, Gd<sup>154</sup> through Gd<sup>158</sup>, and Gd<sup>160</sup> are stable (Gd<sup>152</sup> is slightly  $\alpha$  active), Gd<sup>153</sup> is the isotope nearest stability which permits the study of Eu states. And, because the decay schemes of Gd<sup>153</sup> and Gd<sup>151</sup> are fairly well characterized,<sup>1,2</sup> the logical place to begin the experimental investigation was with Gd<sup>149</sup>.

9.4-day Gd<sup>149</sup> was first discovered in 1951 by Hoff, Rasmussen, and Thompson,<sup>3</sup> who produced the isotope by the reactions,  $\text{Eu}^{151}(p, 3n)\text{Gd}^{149}$  and  $\text{Sm}^{147}(\alpha, 2n)\text{Gd}^{149}$ . Since that beginning, several papers have been published on its partial decay scheme. Because of the complexity of the  $\gamma$ -ray spectrum, however, the earlier investigations<sup>3-5</sup> that used NaI(Tl) detectors did not observe a number of the weaker and/or more closely spaced lines, because of the inherently poor resolution of these detectors.

However, even in more recent investigations, in which Ge(Li) detectors<sup>6,7</sup> and conversion-electron detectors<sup>8-11</sup> were employed, discrepancies remain as to many of the Eu<sup>149</sup> energy levels and also even with respect to which transitions properly follow Gd<sup>149</sup> decay. In particular, there has been disagreement in the placement of transitions appearing at 993, 1013, and 1082 keV in the  $\gamma$ -ray spectrum. We undertook the present investigation to try to eliminate some of these uncertainties.

Gd<sup>149</sup> decays almost exclusively by electron capture, although a small  $\alpha$  branch of  $4.6 \pm 1.5 \times 10^{-6}$  and an energy of  $3.01 \pm 0.02$  MeV has been reported.<sup>12</sup> We have been able to put an upper limit of  $10^{-3}(\beta^+/K)$  on the positron branch (cf. Sec. IV). This means that the electromagnetic transitions become the exclusive tool for its study. Very good conversion-electron data already existed, so we made use of these and have concentrated on the photon spectra and coincidence and anticoincidence experiments.

## II. SOURCE PREPARATION

Gd<sup>149</sup> was prepared by the reaction  $\text{Eu}^{151}(p, 3n)\text{Gd}^{149}$ . Both natural europium oxide (47.82% Eu<sup>151</sup>,

52.18% Eu<sup>153</sup>) and separated isotope (96.83% Eu 3.17% Eu<sup>153</sup>) obtained from the Isotopes Division, Oak Ridge National Laboratory, were used in the proton bombardments. The proton beam was furnished by the Michigan State University sector-focused cyclotron, using a beam energy of 28 MeV with a typical current of 2  $\mu\text{A}$ . Typically, 100-mg targets were bombarded for periods of 1-2 h.

For the first few hours after the bombardments several short-lived peaks were evident in the spectra. However, after these disappeared, essentially pure Gd<sup>149</sup> remained. This happy circumstance results because other ( $p, xn$ ) reactions that should be possible have product nuclei with long half-lives. Activity resulting from the decay of the daughter Eu<sup>149</sup> ( $t_{1/2} = 106$  day) did not show up for several days. However, some spectra (particularly for the anticoincidence runs and for the study of the 993-, 1013-, and 1082-keV peaks) were obtained after chemical separation of Gd from the target material. Two different methods of chemical separation were employed.

The first method was the utilization of Zn-HCl reduction.<sup>13</sup> Owing to a semistable Eu<sup>++</sup> state, Eu can be separated from the reduction mixture by precipitation with H<sub>2</sub>SO<sub>4</sub>. This technique, carried out two successive times on the target material, yields quite pure (as to the radioactive components) Gd<sup>149</sup>. For  $\gamma$ -ray analysis this was the only step necessary. When the source must be essentially "mass free," as for an electron source, the Zn<sup>++</sup> must be removed. This can be accomplished by extraction of the Zn<sup>++</sup> from the mixture with methylisobutyl ketone (hexone).

The second method of separation used was cation exchange.<sup>14,15</sup> The resin beds were composed of Dowex 50  $\times$  8 resin (200-400 mesh) and were 4-5 cm in length and 2 mm in diameter. An isopropyl alcohol bath was used to maintain the column temperature at 83°C during the separation. The eluting agent was 0.4 M  $\alpha$ -hydroxy-isobutyric acid with the pH adjusted to approximately 3.8 by the addition of NH<sub>3</sub> solution.

## III. Gd<sup>149</sup> SPECTRA

### A. Singles Spectra

Two Ge(Li) detectors, both of which were manufactured in this laboratory, were used for all spectra. One was a 7-cm<sup>3</sup> five-sided coaxial detector, the other a 3-cm<sup>3</sup> planar detector. Both were mounted in dipstick cryostats having aluminum housings 0.16 cm thick. The detectors were used with low-noise room-temperature field-effect transistor preamplifiers, RC linear amplifiers having pole-zero compensation, and 1024- and 4096-channel analyzers.

The  $Gd^{149}$  sources were usually counted after being aged several days, but spectra were obtained at times varying from immediately after bombardment to several weeks after bombardment. This technique, together with the chemical separations, enabled us to identify impurity  $\gamma$  rays.

The  $\gamma$ -ray energies were determined by comparison with the standards listed in Table I. The larger peaks were first determined by counting the  $Gd^{149}$  sources simultaneously with these standards. The weaker peaks, which would be obscured by the standards, were later determined by using the then well-determined stronger  $Gd^{149}$  peaks as internal standards. The centroids of the standard peaks were determined by using a computer program<sup>16</sup> that first subtracts the background by performing a cubic least-squares fit to several channels on each side of the peak. The channels included in the peak are fit to a quadratic curve to determine the centroid, and the centroids of the peaks are fit to a least-squares  $n$ th degree curve, which becomes the calibration curve. This calibration curve, in turn, is used to determine the energies of the unknown peaks by a similar process.

The relative peak intensities were determined from the peak areas with the use of relative-peak-efficiency curves for both Ge(Li) detectors. The curves were obtained by the use of a set of standard  $\gamma$ -ray sources whose relative intensities have been carefully measured repeatedly with a NaI(Tl) detector.

We have identified 25  $\gamma$  rays as resulting from the  $\epsilon$  decay of  $Gd^{149}$ . Singles spectra are shown in Fig. 1 (separated  $Eu^{151}$  target) and Fig. 2 (natural Eu target). A list of the  $\gamma$ -ray energies and intensities is given in Table II. These energies and intensities are average values from many runs in which various counting geometries, both detectors, and different combinations of associated electronics were used. The listed errors are the over-all experimental errors determined as one half of the range of the values obtained for all the runs included for each average value.

The  $K$  x-ray intensity was obtained by a direct comparison with  $Ce^{141}$ , of which 70% decays to the 145.4-keV state of  $Pr^{141}$ . The ratio of  $K$  x rays to 145.4-keV  $\gamma$  rays has been measured<sup>17</sup> to be  $0.341 \pm 0.010$ . The area ratio [ $K$  x ray/149.6-keV  $\gamma$ ] for  $Gd^{149}$  was measured to be 2.45. When corrected for efficiency by the  $Ce^{141}$  ratio, this becomes 2.01. The errors involved should be quite small even through the efficiency curves are changing rapidly in this region, because the energies of the  $Gd^{149}$  and  $Ce^{141}$  x rays and  $\gamma$  rays are so similar.

As can be seen from the singles spectrum result from the bombardment of separated  $Eu^{151}$  (Fig. 1) peaks are present at 963, 993, and 1013 keV

TABLE I.  $\gamma$ -ray energy standards.

Nuclide	$\gamma$ -ray energies (keV)	Reference
$Am^{241}$	$50.545 \pm 0.031$	a
$Ce^{141}$	$145.43 \pm 0.02$	b
$Cm^{243}$	$209.85 \pm 0.06$	c
	$228.28 \pm 0.08$	c
	$277.64 \pm 0.02$	c
$Cs^{137}$	$661.595 \pm 0.076$	d
$Mn^{54}$	$834.85 \pm 0.10$	e
$Co^{60}$	$1173.226 \pm 0.040$	f
	$1332.483 \pm 0.046$	f
$Co^{56}$	$846.4 \pm 0.5$	g
	$1038.9 \pm 1.0$	g
	$1238.2 \pm 0.5$	g
	$1771.2 \pm 1.0$	g
	$D2598.5 \pm 0.5$	g

<sup>a</sup>J. L. Wolfson, Can. J. Phys. 42, 1387 (1964).

<sup>b</sup>J. S. Geiger, R. L. Graham, I. Bergström, and F. Brown, Nucl. Phys. 68, 352 (1965).

<sup>c</sup>R. E. Eppley, unpublished results, 1969.

<sup>d</sup>D. H. White and D. J. Groves, Nucl. Phys. A91, 453 (1967).

<sup>e</sup>W. W. Black and R. L. Heath, Nucl. Phys. A90, 650 (1967).

<sup>f</sup>G. Murray, R. L. Graham, and J. S. Geiger, Nucl. Phys. 63, 353 (1965).

<sup>g</sup>R. L. Auble, Wm. C. McHarris, and W. H. Kelly, Nucl. Phys. A91, 225 (1967).

in addition to those at lower energies. These three "high-energy" peaks were also seen in many of the bombardments using natural Eu, and they have been reported previously<sup>8</sup> as belonging to the decay of  $Gd^{149}$ . We questioned this because, as can be seen in Fig. 2, a spectrum taken from an older source (in this case using natural Eu target) no longer contains these transitions. An excitation function was run using a natural europium oxide target with proton beams from 10 to 35 MeV at 5-MeV intervals. The characteristic  $Gd^{149}$  peaks first appeared in the 20-MeV spectrum as expected ( $Q = -16.9$  MeV) and had all but vanished by 35 MeV, thus exhibiting an excitation function with a width typical of a compound-nuclear reaction. Of the three peaks (961, 993, and 1013 keV) only the 961-keV peak was in evidence in any of these runs. However, it first appeared in the 10-MeV spectrum and continued to be present in all of the higher-energy spectra. It was accompanied by peaks at 121 and 841 keV, these three transitions being characteristic of the decay of the 9.3-h isomeric level of  $Eu^{152}$ . This activity could easily be made by the  $Eu^{151}(n, \gamma)Eu^{152m}$  reaction. The peaks at 993 and 1013 keV did not appear in any of the excitation-

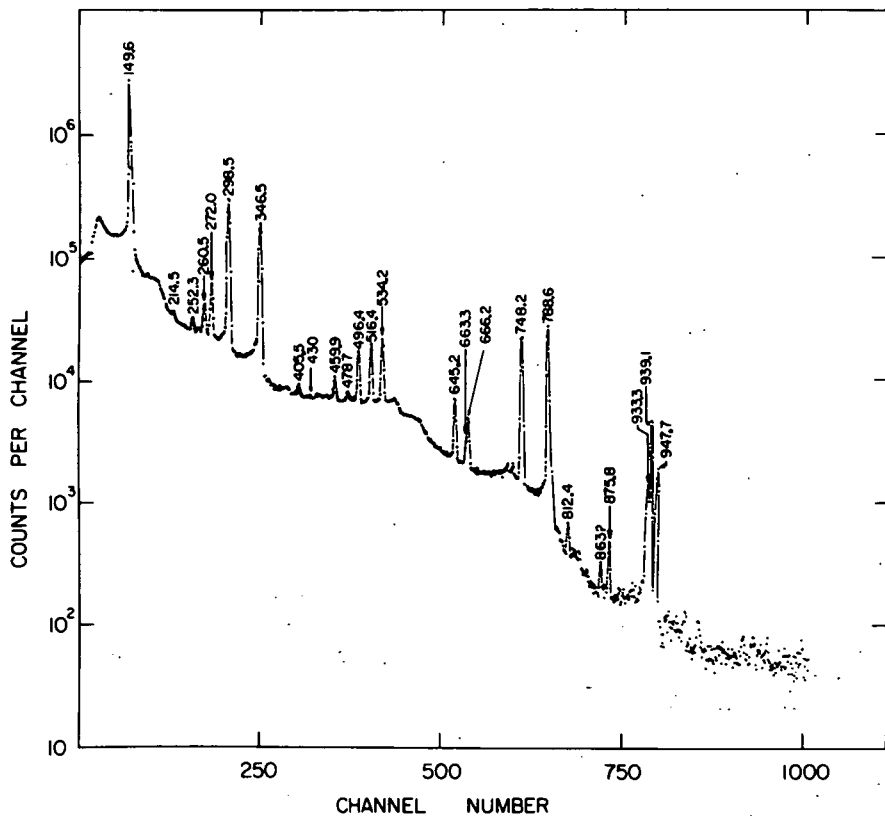
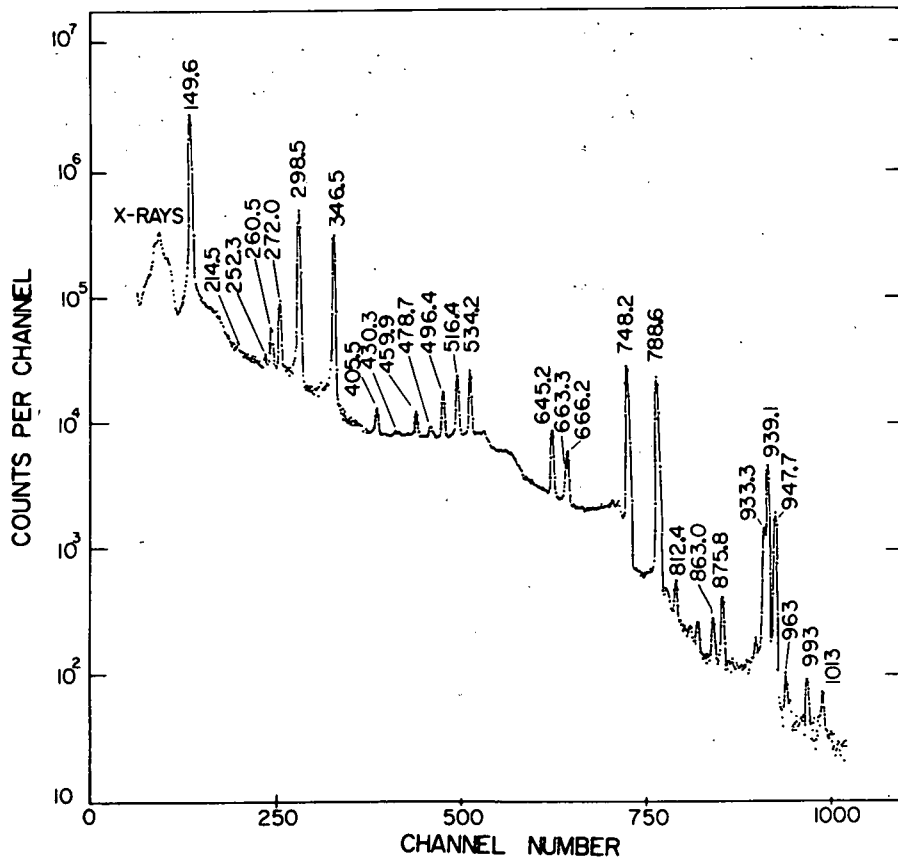


TABLE II. Energies and relative intensities of  $\gamma$  rays from the decay of  $Gd^{149}$ .

This work		Jaklevic, Funk, and Mihelich <sup>a</sup>		Adam, Toth, and Meyer <sup>b</sup>	
Energy (keV)	Intensity	Energy (keV)	Intensity	Energy (keV)	Intensity <sup>c</sup>
<i>K</i> x rays	468 $\pm$ 100	<i>K</i> x rays	487 $\pm$ 35	...	...
149.6 $\pm$ 0.2	233 $\pm$ 10	150.0 $\pm$ 0.5	197 $\pm$ 20	149.8	258.9 $\pm$ 20.0
...	...	...	...	184.8	0.23 $\pm$ 0.12
214.5 $\pm$ 0.6	0.81 $\pm$ 0.10	216.0 $\pm$ 0.5	1.6 $\pm$ 0.8	216	0.91 $\pm$ 0.40
...	...	...	...	230.4	0.65 $\pm$ 0.31
...	...	...	...	235.1	0.14 $\pm$ 0.07
252.3 $\pm$ 0.7	1.08 $\pm$ 0.25	...	...	252.5	0.54 $\pm$ 0.15
260.5 $\pm$ 0.3	5.80 $\pm$ 0.4	262.0 $\pm$ 0.5	7.0 $\pm$ 0.7	260.9	4.70 $\pm$ 0.80
...	...	...	...	264.6	...
...	...	...	...	267.8	0.061 $\pm$ 0.015
...	...	...	...	268.6	...
272.0 $\pm$ 0.2	14.6 $\pm$ 0.6	272.0 $\pm$ 0.5	16.1 $\pm$ 2	272.6	11.6 $\pm$ 1.0
298.5 $\pm$ 0.2	126 $\pm$ 10	298.5 $\pm$ 0.5	106 $\pm$ 10	298.7	114.8 $\pm$ 4.9
346.5 $\pm$ 0.3	$\equiv$ 100	347.0 $\pm$ 0.5	100 $\pm$ 10	346.8	100.0 $\pm$ 4.9
405.5 $\pm$ 0.7	3.7 $\pm$ 1.5	...	...	404.0	0.70 $\pm$ 0.30
430 $\pm$ 1 <sup>d</sup>	0.33 $\pm$ 0.05	...	...	...	...
459.9 $\pm$ 0.3	2.4 $\pm$ 0.2	461 $\pm$ 1	2.3 $\pm$ 0.3	460.3	1.81 $\pm$ 0.30
478.7 $\pm$ 0.3	0.95 $\pm$ 0.10	480 $\pm$ 1	0.4 $\pm$ 0.1	478.3	1.80 $\pm$ 0.51
496.4 $\pm$ 0.3	7.2 $\pm$ 0.4	497.0 $\pm$ 0.5	7.2 $\pm$ 0.7	496.6	6.61 $\pm$ 1.00
516.4 $\pm$ 0.3	11.1 $\pm$ 1.5	517.0 $\pm$ 0.5	10.7 $\pm$ 1	516.8	10.30 $\pm$ 1.00
534.2 $\pm$ 0.3	13.2 $\pm$ 0.6	534.0 $\pm$ 0.5	12.5 $\pm$ 1.3	534.4	13.50 $\pm$ 1.00
645.2 $\pm$ 0.3	5.9 $\pm$ 0.5	646.5 $\pm$ 0.5	7.0 $\pm$ 0.7	645.2	6.20 $\pm$ 0.59
663.3 $\pm$ 0.7	1.1 $\pm$ 0.2	...	...	663.4	...
666.2 $\pm$ 0.7	3.9 $\pm$ 0.6	666.5 $\pm$ 0.5	6.0 $\pm$ 0.6	666.6	4.51 $\pm$ 0.49
748.2 $\pm$ 0.3	34.6 $\pm$ 4.0	749.5 $\pm$ 0.5	37.0 $\pm$ 4	749.1	34.1 $\pm$ 4.0
788.6 $\pm$ 0.3	29.6 $\pm$ 3.0	790.5 $\pm$ 0.5	34.8 $\pm$ 4	789.3	31.2 $\pm$ 4.0
812.4 $\pm$ 0.5	0.55 $\pm$ 0.31	813 $\pm$ 1	0.7 $\pm$ 1	813.0	0.642 $\pm$ 0.149
863 $\pm$ 1 ?	0.32 $\pm$ 0.10	865 $\pm$ 1	0.3 $\pm$ 0.05	...	...
875.8 $\pm$ 0.4	0.90 $\pm$ 0.11	878 $\pm$ 1	0.7 $\pm$ 0.1	876.2	0.980 $\pm$ 0.201
933.3 $\pm$ 0.5	2.2 $\pm$ 0.5	934 $\pm$ 1	2.8 $\pm$ 0.3	934	2.41 $\pm$ 0.30
939.1 $\pm$ 0.4	9.0 $\pm$ 1.4	939.0 $\pm$ 0.5	12.1 $\pm$ 2	939.0	11.2 $\pm$ 2.0
947.7 $\pm$ 0.5	3.7 $\pm$ 0.6	949.0 $\pm$ 0.5	4.8 $\pm$ 0.5	948.0	3.70 $\pm$ 0.70
...	...	993 $\pm$ 1	1.5 $\pm$ 0.2	...	...
...	...	1013 $\pm$ 1	1.3 $\pm$ 0.1	...	...
...	...	1082 $\pm$ 1	0.8 $\pm$ 0.1	...	...

<sup>a</sup>See Ref. 6.<sup>b</sup>See Ref. 7.<sup>c</sup>These intensities were obtained by normalizing the intensity (891  $\pm$  44) for the 346.5-keV  $\gamma$  as given in Ref. 7 to 100, always retaining the original number of significant figures.<sup>d</sup>This transition was not seen in the singles spectra but only in the 600-keV region gated spectrum (Fig. 8).

function spectra; however, the statistics were such that very weak peaks at these energies would not be observed. When observed in other singles spectra these two peaks do appear to decay with a half-life similar to, but less than, that of  $Gd^{149}$ , although no specific half-life determination has been made. It should be noted that, when present, these peaks do remain with the Gd fraction after separation in an ion-exchange process.

#### B. Prompt Coincidence Spectra

Both prompt and delayed spectra were obtained with a variety of methods. The 7-cm<sup>3</sup> Ge(Li) detec-

tor was normally used for recording spectra, with a 3 $\times$ 3-in. NaI(Tl) detector setting the gates. For some of the spectra, however, the Ge(Li) detector was placed at one end inside the tunnel of an 8 $\times$ 8-in. NaI(Tl) split annulus.<sup>18</sup> The source was placed on top of the Ge(Li) detector inside the annulus. For an anticoincidence spectrum a 3 $\times$ 3-in. NaI(Tl) detector was placed at the other end of the annulus tunnel in order to subtend a greater solid angle from the source, thereby further reducing the Compton background, in particular the Compton edges resulting from backscattering from the Ge(Li) detector. For all of the coincidence ex-

periments a standard fast-slow coincidence circuit was used and the lower discriminators of the single-channel analyzers were adjusted to accept only pulses with energies greater than those of the K x rays. For the coincidence runs the resolving time ( $2\tau$ ) of the fast coincidence unit was  $\approx 100$  nsec, while for the anticoincidence run it was  $\approx 200$  nsec.

The anticoincidence and integral- or "any-" coincidence spectra are shown in Figs. 3 and 4. These spectra complement each other in helping to elucidate the decay scheme. The enhancement of a peak in the anticoincidence spectrum implies a ground-state transition either from a level fed primarily by direct  $\epsilon$  decay or from a level with a half-life long compared with the resolving time; examples are the 748.2- and 496.4-keV  $\gamma$ 's. In the integral-coincidence spectrum such transitions should be either absent or reduced in intensity. The integral-coincidence spectrum also confirms much of the information gained from the individually gated spectra below. The relative intensities of peaks in the coincidence runs are given in Table III, and a summary of our inferences from them is given in Table IV.

Other useful coincidence spectra were obtained by gating on the 149.6-, 346.5-, and 534.2-keV peaks and on the 600- and 900-keV regions. These are shown in order in Figs. 5-9. Tables III and IV again summarize the relevant information from these spectra, but we defer any detailed discussion until Sec. V, where points essential to our construction of the decay scheme will be covered.

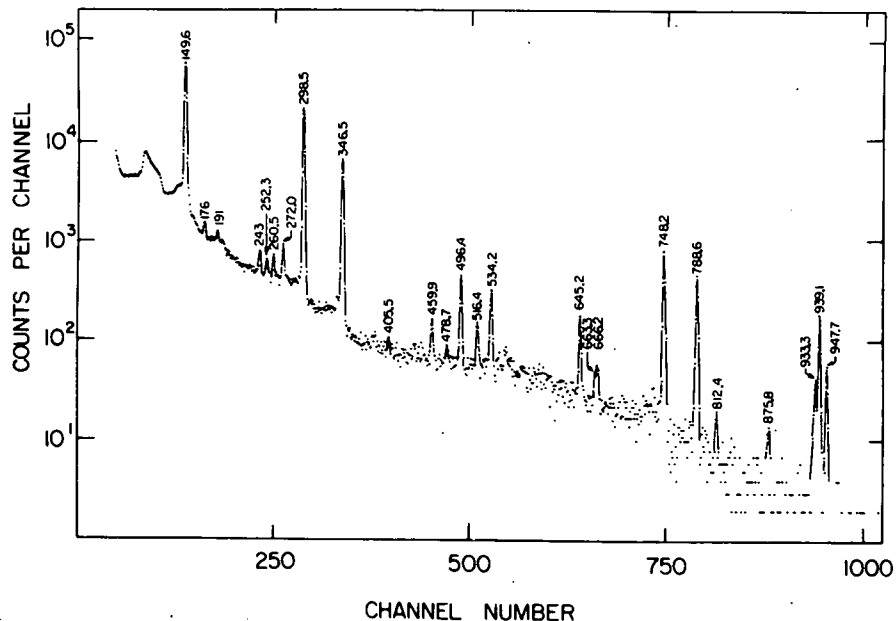


FIG. 3. Anticoincidence spectrum of  $Gd^{149}$  recorded by the 7-cm<sup>3</sup> Ge(Li) detector when placed inside the tunnel of 8  $\times$  8-in. NaI(Tl) split annulus, with a 3  $\times$  3-in. NaI(Tl) detector at the other end of the tunnel.

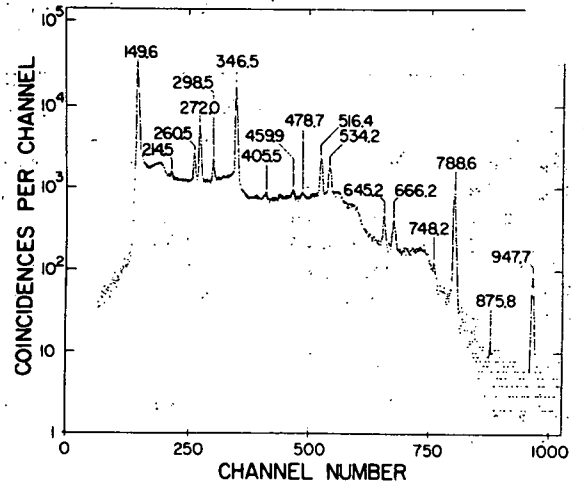


FIG. 4. Integral-coincidence spectrum of  $Gd^{149}$  taken with the 7-cm<sup>3</sup> Ge(Li) detector using the 8  $\times$  8-in. splitting annulus for the gating signals. The fast-coincidence resolving time was  $\approx 100$  nsec.

### C. Delayed Coincidence Studies

Many nuclei in this region have an  $h_{11/2}$  isomeric state, and  $Eu^{149}$  is no exception. The 496.4-keV state was first suggested to be isomeric by Shirley, Smith, and Rasmussen,<sup>4</sup> who assigned the 346.5-keV transition as  $M2$  on the basis of its conversion ratios. The half-life of the state was later measured by Berlovich *et al.*,<sup>19</sup> to be  $2.48 \pm 0.05 \times 10^{-6}$  sec. In several previous studies<sup>5,6</sup> delayed-coincidence experiments were performed to determine the feeding of the 346.5-keV state from above, but

TABLE III. Intensities of  $Gd^{149}$   $\gamma$  rays in coincidence experiments.

$E_\gamma$ (keV)	Singles	Anticoincidence	Relative intensity					900-keV gate
			Integral coincidence	149.6-keV gate	346.5-keV gate <sup>a</sup>	534.5-keV gate	600-keV gate	
149.6±0.2	233 ±10	...	48.4	...	≅233	1.10	5.02	Ref. b
214.5±0.6	0.81±0.10	1.37	0.78	...	...	0.68	...	...
252.3±0.7	1.08±0.25	1.30	...	...	...	...	...	...
260.5±0.3	5.80±0.40	1.43	5.03	2.88	6.03	≅5.80	0.79	...
272.0±0.2	14.6 ±0.6	2.78	18.1	33.3	14.5	6.21	≅14.6	...
298.5±0.2	126.7 ±10	109	4.71	15.7	25.9	0.43	...	...
346.5±0.3	≅100	63.7	≅100	272	4.93	0.21	...	...
405.5±0.7	3.7 ±1.5	...	1.67	...	...	0.87	0.12	...
430 ±1	...	...	...	...	...	...	0.33	...
459.9±0.3	2.4 ±0.2	1.41	2.80	...	...	0.38	0.11	...
478.7±0.3	0.95±0.10	...	1.63	...	...	...	0.089	...
496.4±0.3	7.2 ±0.4	≅7.2	...	...	...	...	...	...
516.4±0.3	11.1 ±1.5	1.89	23.0	≅11.1	14.1	0.054	0.19	...
534.2±0.3	13.2 ±0.6	6.53	14.9	2.36	5.82	0.062	0.13	...
645.2±0.3	5.9 ±0.5	3.83	6.1	6.22	...	...	...	...
663.3±0.7	1.1 ±0.2	1.81	6.34	1.11	...	...	...	...
666.2±0.7	3.9 ±0.6							
748.2±0.3	34.6 ±4.0	31.1	0.35	...	...	0.048	...	...
788.6±0.3	29.6 ±3.0	18.7	28.1	16.3	...	...	...	...
812.4±0.5	0.55±0.13	0.46	...	...	...	...	...	...
863.1±1.0	0.32±0.10	...	...	...	...	...	...	...
875.8±0.4	0.90±0.11	...	...	...	...	...	...	...
933.3±0.4	2.2 ±0.5	2.55	...	...	...	...	...	...
939.1±0.6	9.0 ±1.4	9.90	...	...	...	...	...	...
947.7±0.5	3.7 ±0.6	2.41	...	...	...	...	...	...

<sup>a</sup>Nothing appears to be in prompt coincidence with the 346.5-keV  $\gamma$  except the 149.6-keV  $\gamma$ , and its intensity should be diminished in this spectrum because it is fed by many other  $\gamma$  rays in addition to the 346.5-keV  $\gamma$ . Thus, all the intensities in this column should be regarded as upper limits originating from chance or instrumental effects.

<sup>b</sup>Only peak in spectrum.

TABLE IV. Summary of coincidence data.

Gate energy (keV)	Peaks in coincidence (keV)	Figure No.
Integral gate	149.6, 214.5, 260.5, 272.0, 346.5, 405.5, 459.9, 478.7, 516.4, 534.2, 645.2, 663.3, 666.2, 788.6, 947.7	4
149.6	272.0, 346.5, 516.4, 645.2, 663.3, 788.6, 947.7	5
346.5	149.6	6
534.2	214.5, 260.5, 405.5	7
600 region	149.6, 272.0, 430.3	8
900 region	149.6	9
149.6 delayed coincidence	252.3, 298.5	10

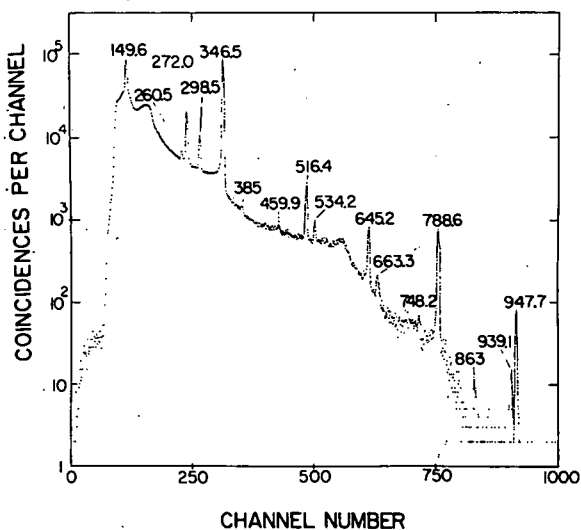


FIG. 5. Spectrum of  $\gamma$  rays from  $Gd^{149}$  decay observed in coincidence with the 149.6-keV transition. The spectrum was taken with the 7-cm<sup>3</sup> Ge(Li) detector using a 3×3-in. NaI(Tl) detector to provide the gating signals.

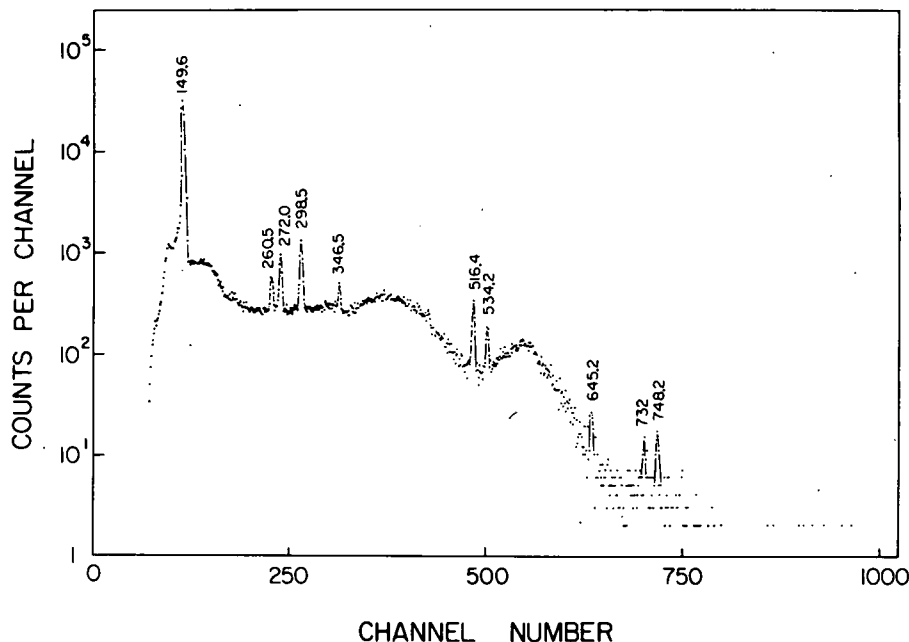


FIG. 6.  $Gd^{149}$  coincidence spectrum taken with a prompt gate on the 346.5-keV transitions. Only the 149.6-keV transition is in coincidence with the 346.5-keV transition. The remainder of the peaks actually arise from chance.

we obtain somewhat different results from these.

We used a  $3 \times 3$ -in. NaI(Tl) detector to gate on the 346.5-keV  $\gamma$  and on the 149.6-keV  $\gamma$  that is in coincidence with it (cf. the decay scheme in Fig. 13 below). The  $7\text{-cm}^3$  Ge(Li) detector signal was delayed relative to these gates by inserting passive delays ranging from 0.25 to 0.50  $\mu\text{sec}$ , depending on the particular run. The fast resolving time ( $2\tau$ ) again was set at  $\approx 100$  nsec. The spectrum resulting from the 149.6-keV delayed gate is shown in

Fig. 10, and the intensities of peaks in this spectrum are compared with their intensities in the corresponding prompt spectrum in Table V. A summary of the conclusions is also included in Table IV. The spectrum resulting from the 346.5-keV gate produced essentially the same results, so it is not shown.

In all the delayed spectra the 298.5-keV  $\gamma$  was enhanced, indicating that it does indeed feed the 496.4-keV level. There was also some evidence

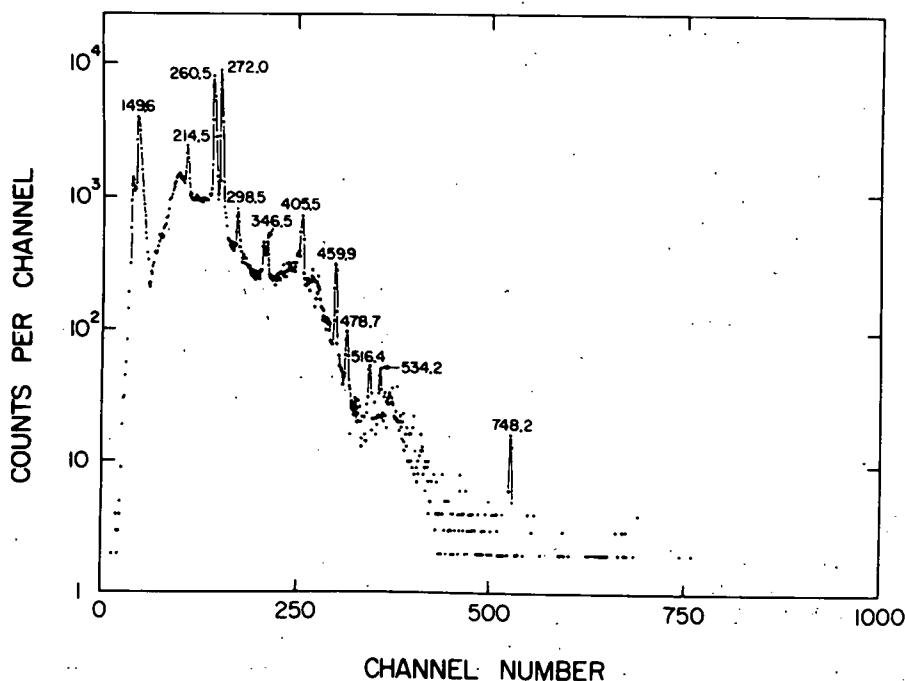


FIG. 7. Coincidence spectrum of  $Gd^{149}$  with the gate on the 534.2-keV transitions. The  $7\text{-cm}^3$  Ge(Li) detector was used for the spectrum, with the  $8 \times 8$ -in. split-ring annulus being used for the gating signals.



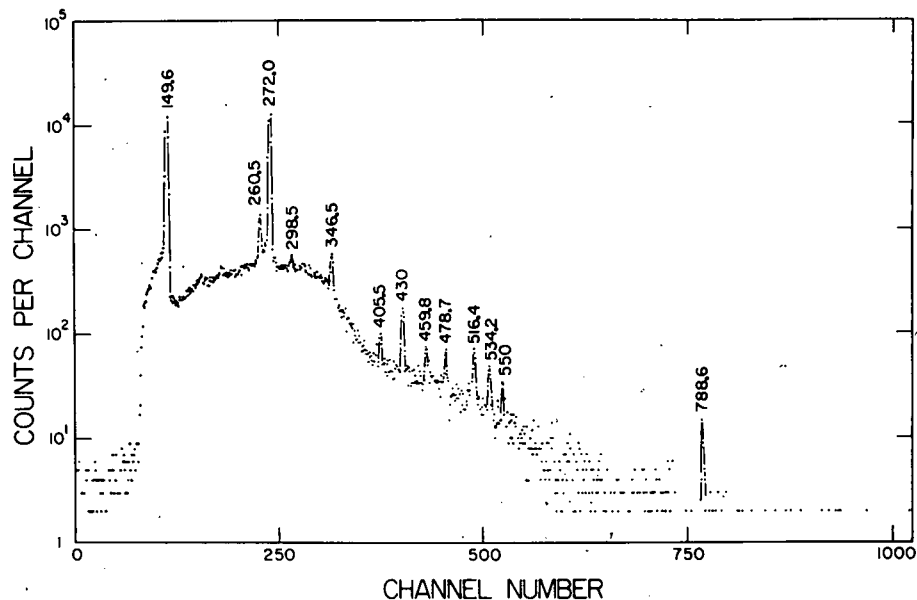


FIG. 8.  $Gd^{149}$  coincidence spectrum with the gate set on the 600-keV region. The 7-cm<sup>3</sup> detector was again used for the spectrum, with the 8×8-in. annulus used to provide the gating signals. This is the only spectrum in which the peak at 430 keV is enhanced.

for enhancement of the 252.3-keV  $\gamma$ . However, the 459.9-keV  $\gamma$ , which had previously been reported<sup>5,6</sup> as feeding the 496.4-keV level, is completely missing from Fig. 10. This, and other evidence which will be discussed in Sec. V, leads us to the conclusion that the 459.9-keV  $\gamma$  does not proceed to the 496.4-keV level but instead depopulates a newly proposed 459.9-keV level.

#### D. Internal-Conversion Coefficients

For the determination of internal-conversion coefficients we used the electron intensities reported by Harmatz and Handley,<sup>11</sup> who reported extensive values for  $K$  electrons along with some values for  $L_1$  and  $M_1$  electrons. These values were obtained with flat-field permanent-magnet spectrographs using photographic plates and have reported uncertainties of  $\approx 15\%$  for the most prominent lines. For

purposes of normalization we assumed the 346.5-keV transition to be pure  $M2$  and used the theoretical value of  $\alpha_K$  from Hager and Seltzer.<sup>20</sup>

Multipolarities or possible multipolarities were assigned for all transitions where  $K$ -electron intensities were available. We compared the experimental  $\alpha_K$ 's with the theoretical  $\alpha_K$ 's of Hager and Seltzer.<sup>20</sup> Where necessary, (logarithmic) quadratic interpolation was made between the tabular theoretical values. As our lowest energy was 149.6 keV, this method yielded satisfactory results. These theoretical values were used to construct the smooth curves in Fig. 11, upon which we have superimposed the experimental points

TABLE V. Intensities of  $Gd^{149}$   $\gamma$  rays in delayed and prompt coincidence.

$E_\gamma$ (keV)	Relative intensity (normalized to singles intensity)	
	149.6-keV delayed	149.6-keV prompt
149.6±0.2	4.78	...
252.3±0.7	0.85	...
260.5±0.3	0.86	2.88
272.0±0.2	2.08	33.3
298.5±0.2	$\approx 126$	15.7
346.5±0.3	18.2	272
496.4±0.3	1.17	...
516.4±0.3	1.51	$\approx 11.1$
534.2±0.3	2.73	2.36
645.2±0.3	...	6.22
663.3±0.7	...	1.11
666.2±0.7	...	...
748.2±0.3	5.37	...
788.6±0.3	5.68	16.3

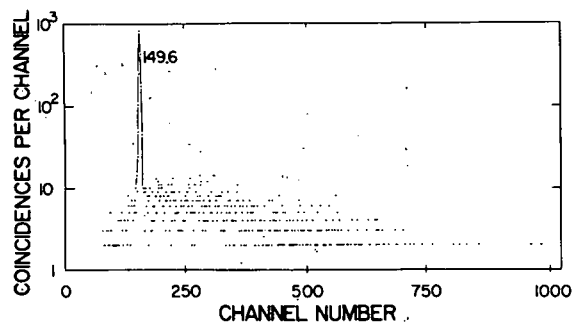


FIG. 9.  $Gd^{149}$  coincidence spectrum with the gate set on the 900-keV region. This spectrum, used in conjunction with the 149.6-keV gated spectrum, shows that, of peaks in the 900-keV region, only the peak at 947.7 keV is in coincidence, it being in coincidence with the 346.5-keV level.

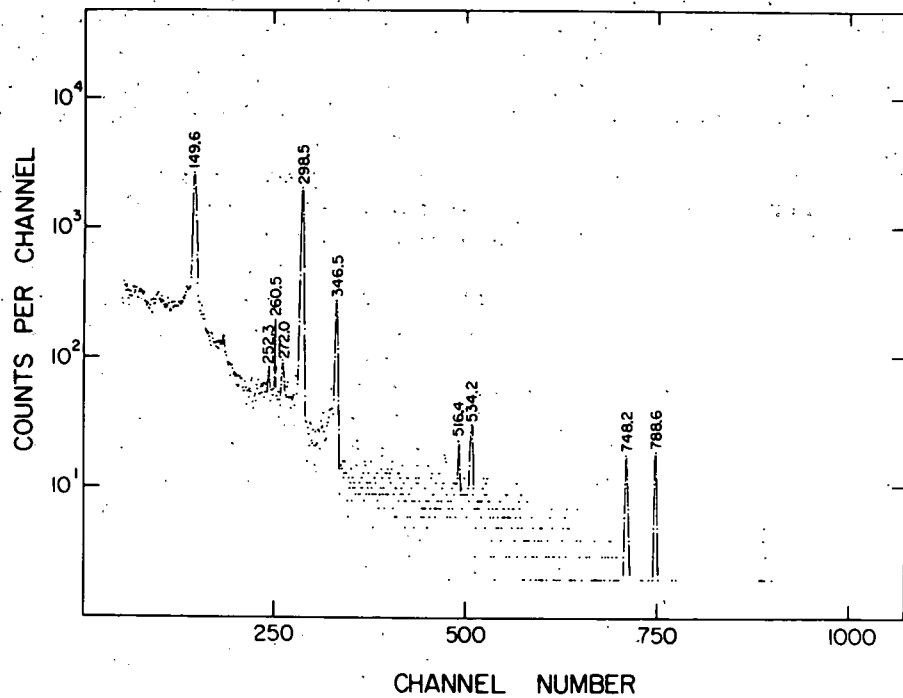


FIG. 10.  $Gd^{149}$  delayed-coincidence spectrum. The spectrum signal was delayed relative to the gate by adding a 0.5- $\mu$ sec passive delay to the Ge(Li) detector side before it entered the fast-coincidence unit ( $2\tau \approx 100$  nsec). In this manner, the resulting spectrum shows only those transitions feeding the 496.4-keV isomeric level.

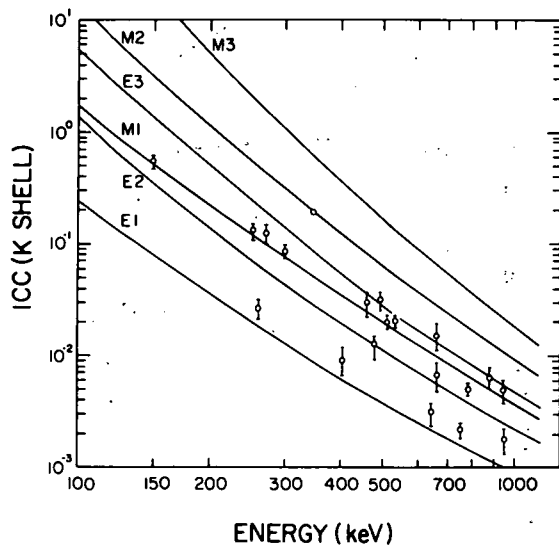


FIG. 11. Experimental and theoretical conversion coefficients for the transitions in  $Eu^{149}$  following the decay of  $Gd^{149}$ . These values are also listed in Table VI. The smooth curves were drawn by using values interpolated from the tables of Hager and Seltzer (Ref. 20). The error bars placed on the experimental values are only crude estimates, since no precise error values were available for the conversion-electron intensities.

along with their estimated errors (ranging between 15 and 30%).

Some of the multipolarity assignments were corroborated by  $K/L_1$  or  $K/M_1$  ratios, although these are less sensitive indicators than the  $K$ -conversion coefficients. The interested reader is referred to Harmatz and Handley<sup>11</sup> for their  $L_1$  and  $M_1$  intensity values.

#### IV. ELECTRON-CAPTURE ENERGY

Because there is no measurable  $\beta^+$  emission from the decay of  $Gd^{149}$ , a direct measurement of its decay energy is not possible. Various estimates of  $Q_e$  range all the way from 1.220<sup>21</sup> to 2.275 MeV.<sup>22</sup> As an alternative to an arbitrary adoption of one of the several published values, we made a graphical estimate of  $Q_e$ , using a method similar to that suggested by Way and Wood<sup>23</sup> and previously used by Grover.<sup>24</sup>

A plot (Fig. 12) was made of all experimentally known decay energies versus  $Z$  for pairs of nuclei having the same neutron numbers as the pair for which the decay energy is to be determined. Both electron-capture and  $\beta^-$  decay pairs were plotted, and for our particular graph, as  $Q_e$  is chosen to be positive and  $Q_\beta^-$  negative, the abscissa for the former is  $Z_{parent}$ , and for the latter,  $Z_{daughter}$ .

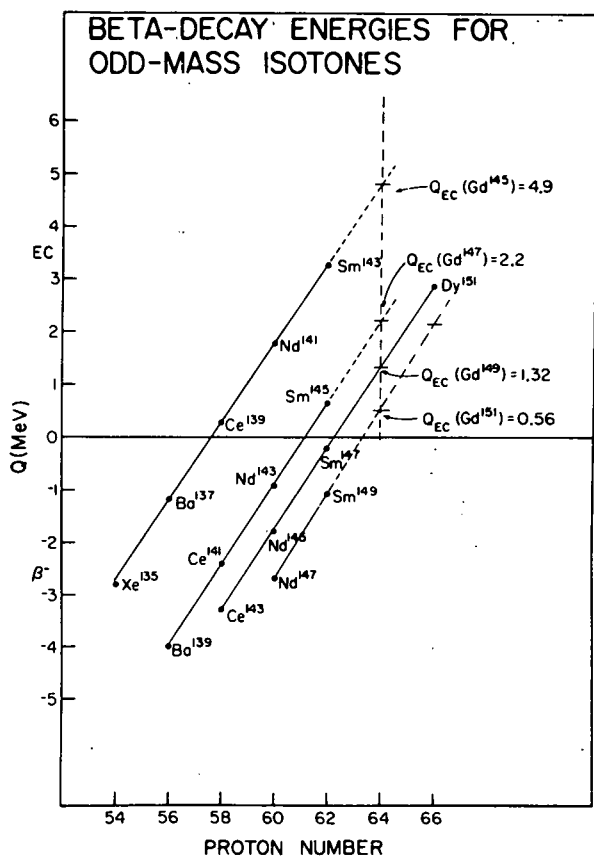


FIG. 12. Graphical estimates for the electron-capture decay energies for several odd-mass Gd isotopes, including Gd<sup>149</sup>. For example, the decay energy for Gd<sup>149</sup> is estimated by plotting all known decay energies versus the proton number (for both  $\beta^+$  and  $\beta^-$  decay) which involve nuclear pairs having a neutron change of 85  $\rightarrow$  86 or 86  $\rightarrow$  85. The resulting straight line allows the value of 1.32 MeV to be interpolated for the decay of Gd<sup>149</sup>.

For example, in estimating  $Q_\epsilon$  for Gd<sup>149</sup>, the experimental decay energies of all pairs with  $N = 85 - 86$  or  $N = 86 - 85$  were plotted. As can be seen from Fig. 12, these points all fall on a straight line, and  $Q_\epsilon$  for Gd<sup>149</sup> can be read from the same line. Using this method we estimate  $Q_\epsilon$  as 1.320 MeV. The plots for Gd<sup>145</sup>, Gd<sup>147</sup>, and Gd<sup>151</sup> have also been included for reference. As read from the graph,  $Q_\epsilon$  for these isotopes is 4.9, 2.2, and 0.56 MeV, respectively. These compare with previous estimates of 5,<sup>24</sup> 1.8,<sup>25</sup> and 0.4 MeV.<sup>25</sup>

In essence, this method involves taking the difference between two parabolas cutting across the mass surface and assumes that there are no appreciable bumps or ridges to distort the surface in the region involved. Had we chosen to make a similar plot based on proton pairs rather than neutron pairs, it is easy to see that the  $N = 82$  shell would have introduced a serious distortion. Al-

though there is no formal justification for the plot we did make, the fact that no major proton shells or subshells are likely to be encountered means that such estimates for  $Q_\epsilon$  should be reasonably reliable.

## V. PROPOSED DECAY SCHEME

On the basis of the foregoing coincidence, delayed-coincidence, and anticoincidence spectra, aided by energy sums and intensity balances, we have placed excited states in Eu<sup>149</sup> as indicated by our decay scheme, which is presented in Fig. 13. The results of our  $\gamma$ -ray energy and intensity measurements, conversion coefficients, and assigned transition multiplicities are summarized in Table VI. Unfortunately, as we have intimated earlier, the preparation of clean Gd<sup>149</sup> sources free from subtle contaminants is not a trivial task, and many incorrect transitions and states have accrued in the literature. Thus, we have included in our decay scheme only those states that were actually indicated by experiments in our laboratory. To ameliorate this inflexible position somewhat, we have included in Fig. 13, to the side of our decay scheme, some placements that we could neither confirm nor deny and which appear to be reasonable. For the most part these originate from the conversion-electron work of Harmatz and Handley,<sup>11</sup> who observed a number of transitions too weak to be detectable in  $\gamma$ -ray spectra.

Specific evidence for our placing of each level and its associated transitions follows:

**149.6-keV level.** The 149.6-keV peak is by far the most intense transition in the  $\gamma$ -ray spectrum. If this were not a ground-state transition, we should see other transitions of comparable intensity that would deexcite the level fed by the strong 149.6-keV transition. Therefore, in agreement with all previous workers, we place the first excited state near 150 keV, specifically, at 149.6 keV. This is also consistent with an overwhelming mass of systematics showing that odd-proton nuclei with  $51 \leq Z \leq 63$  have  $\frac{3}{2}^+$  or  $\frac{1}{2}^+$  ground states or first excited states separated by an energy rarely greater than 150 keV.

The coincidence experiment having its gate on the 149.6-keV peak (Fig. 5) showed enhanced peaks at 272.0, 346.5, 516.4, 645.2, 663.3, 788.6, and 947.7 keV. These results agree with those of Jaklevic, Funk, and Mihelich,<sup>6</sup> with the exception of the 663.3-keV peak, which they did not see in a coincidence spectrum. All of these transitions can thus be considered as feeding the 149.6-keV level, and it will be shown later that, with the exception of the 272.0-keV  $\gamma$ , all feed it directly.

The 149.6-keV coincidence spectrum, in conjunc-

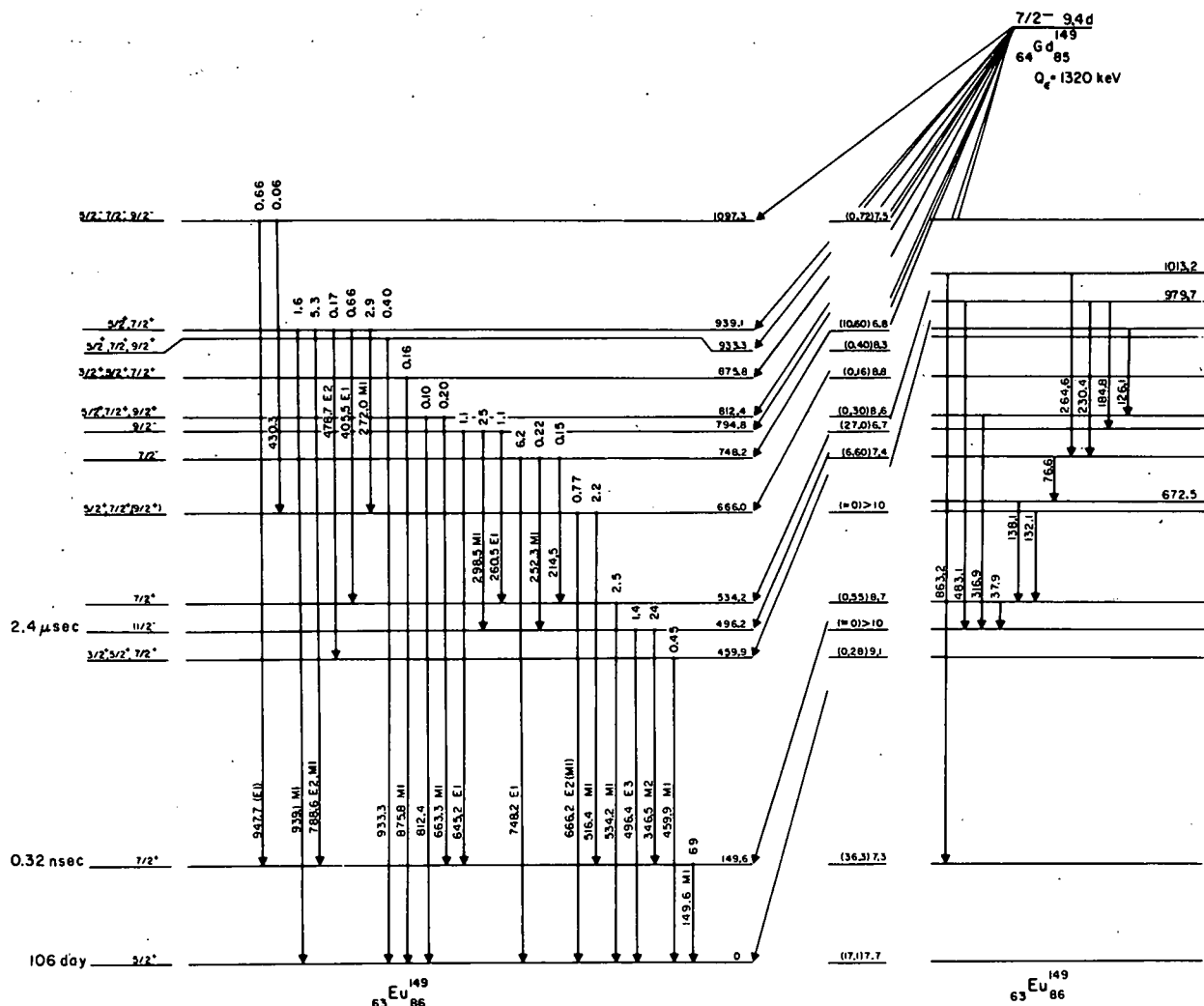


FIG. 13. Decay scheme of  $Gd^{149}$ . The scheme shown at the left is our proposed decay scheme. All energies are given in keV and (total) transition intensities are given in percent of the disintegrations of  $Gd^{149}$ . The percent decay to each level (in parenthesis) and the  $\log t$  values are listed at the right side of the level scheme. The skeletal scheme shown at the right of the figure shows the same levels as at the left, with the addition of three levels and the addition of electromagnetic transitions for which electrons have been reported but for which no  $\gamma$  rays have been observed. These extra levels and transitions are those reported by Harmatz and Handley (Ref. 11). All of their electron transitions that are compatible with our proposed scheme have been included.

tion with the singles spectra, made it possible to determine the energies of the peaks in the 663.3-666.2-keV doublet more precisely than before. As only the 663.3-keV  $\gamma$  was in coincidence with the 149.6-keV  $\gamma$ , its energy and intensity could be determined directly from the coincidence spectrum. These values were then used to subtract the 663.3-keV peak from the singles doublet, leaving the 666.2-keV peak quite well determined by the difference.

**459.9-keV level.** Owing to the results of the delayed coincidence spectra (Fig. 10), the 459.9-keV  $\gamma$  can no longer be considered to be feeding the 496.4-keV level, as had been concluded by pre-

vious workers.<sup>5-7</sup> Also, as seen in Fig. 3 and Table III, this  $\gamma$  ray is enhanced in the anticoincidence spectrum but is absent from most of the prompt-coincidence spectra. From this evidence, we place the 459.9-keV  $\gamma$  as emanating from a level of this same energy.

On the basis of energy sums, the 478.7-keV  $\gamma$  could be placed connecting the 459.9-keV level with the well-established 939.1-keV level (see below). Other evidence for this placement comes from the 534-keV gated spectrum (Fig. 7). While the 459.9-keV peak is less intense than in the singles spectra, it is still present—most likely due to some of the 478.7-keV  $\gamma$  in the relatively wide

TABLE VI. Transition data for Gd<sup>149</sup>

Energy	Photon intensity	K-conversion intensity <sup>a-c</sup>	Total intensity <sup>d</sup>	Experimental $\alpha_K$	Multipole order
K x rays	468 ± 100	...	...	...	...
149.6±0.2	233 ± 10.0	124.9	377	0.54	M1
214.5±0.6	0.81± 0.1	...	0.84	...	...
252.3±0.7	1.1 ± 0.2	0.14	1.23	0.13	M1
260.5±0.3	5.8 ± 0.4	0.15	5.92	2.6×10 <sup>-2</sup>	E1
272.0±0.2	14.6 ± 0.6	1.75	16.3	1.2×10 <sup>-1</sup>	M1
298.5±0.2	127 ± 10	10.75	138	8.5	M1
346.5±0.3	≡100	20.0	123	0.20	M2
405.5±0.7	3.7 ± 1.5	0.033	3.7	9.0×10 <sup>-3</sup>	E1
430	0.33± 0.05	...	0.33	...	...
459.9±0.3	2.4 ± 0.19	0.073	2.49	3.0×10 <sup>-2</sup>	M1
478.7±0.3	1.0 ± 0.1	0.011	0.96	1.2×10 <sup>-2</sup>	E2
496.4±0.3	7.2 ± 0.35	0.238	7.49	3.3×10 <sup>-2</sup>	E3
516.4±0.3	11.1 ± 1.5	0.213	11.3	1.9×10 <sup>-2</sup>	M1
534.2±0.3	13.2 ± 0.55	0.256	13.5	1.9×10 <sup>-2</sup>	M1
645.2±0.3	5.9 ± 0.5	0.018	5.9	3.0×10 <sup>-3</sup>	E1
663.3±0.7	1.1 ± 0.2	0.016	1.10	1.5×10 <sup>-2</sup>	M1
666.2±0.7	3.9 ± 0.6	0.026	4.0	6.6×10 <sup>-3</sup>	E2
748.2±0.3	34.6 ± 4.0	0.071	34.7	2.0×10 <sup>-3</sup>	E1
788.6±0.3	29.6 ± 3.0	0.15	29.8	5.1×10 <sup>-3</sup>	M1+E2
812.4±0.5	0.55± 0.1	...	0.55	...	...
863 <sup>e</sup> ?	0.32± 0.1	weak	...	...	...
875.8±0.4	0.90± 0.1	0.0041	0.91	4.6×10 <sup>-3</sup>	M1
933.3±0.	2.2 ± 0.5	...	2.2	...	...
939.1±0.	9.0 ± 1.4	0.044	9.0	4.9×10 <sup>-3</sup>	M1
947.7±0.5	3.7 ± 0.6	0.0062	3.7	1.7×10 <sup>-3</sup>	(E1)

<sup>a</sup> Intensities are from Ref. 11.

<sup>b</sup> Intensities are renormalized such that the  $\alpha_K(346.5 \text{ keV}) \equiv 0.20$ .

<sup>c</sup> Errors in the relative intensities are reported as being 15% for the most-intense peaks and increasing for the weaker ones.

<sup>d</sup> For the purpose of arriving at total intensity values, theoretical *L* and *M* conversion coefficients were used for the indicated multiplicities. Interpolated values are from Hager and Seltzer (Ref. 20).

<sup>e</sup> Not included in decay scheme.

NaI(Tl) gate. The fact that it is present to more than a very small extent implies that it does not feed the 496.4-keV level, which has a half-life of 2.48  $\mu\text{sec}$ . In Fig. 7 the 459.9- and 478.7-keV  $\gamma$  rays have the same intensity relative to each other as they do in the singles spectra, suggesting again that they are related as above.

**496.2-keV level.** This is the relatively well-known  $\frac{11}{2}^-$  isomeric state, again a characteristic of odd-*Z* nuclei in this region. Its half-life has been measured<sup>19</sup> to be  $2.48 \pm 0.05 \mu\text{sec}$ . As a result of this half-life, the transitions to and from this level must be studied by means of delayed-coincidence techniques. From the results of such experiments (Sec. III D, Fig. 10, Table V), only the 252.3- and 298.5-keV  $\gamma$  rays are placed as proceeding to the 496.2-keV level. It is depopulated by the 496.4-keV  $\gamma$  to the ground state (cf. Fig. 3) and by the 346.5-keV  $\gamma$  to the 149.6-keV level (Fig. 1 and Sec. III D). The adopted energy, as for all of the excited states to be discussed, is a weighted

average of these  $\gamma$  rays.

**534.2-keV level.** In the 534-keV gated coincidence spectrum (Fig. 7) the 214.5- and 260.5-keV peaks are most obviously enhanced. Other relatively intense peaks are those at 272.0, 405.5, 459.9, and 478.7 keV, all of which are more intense than can be ascribed to chance coincidences. We have already dealt with the 459.9- and 478.7-keV peaks, and the 272.0-keV peak can be explained by the 516.4-keV  $\gamma$  falling within the gate. This leaves the 405.5-keV  $\gamma$  as feeding the 534.2-keV level, although its coincidence intensity is somewhat less than expected. This coincidence spectrum does not rule out its feeding the 748.2-keV level, which in turn feeds the 534.2-keV level. From energy sums and differences, however, it is one of five  $\gamma$  rays that depopulate the 939.1-keV state, and this is the only placement consistent with our proposed decay scheme.

**666.0-keV level.** The three primary peaks included in the gate for the "600-keV region" coin-

cidence spectrum (Fig. 8) lie at 645.2, 663.3, and 666.2 keV. We have already discussed how the 666.2-keV  $\gamma$  appears to be a ground-state transition (above, in the section on the 149.6-keV level), implying the existence of a level at this energy. The peaks in Fig. 8 are those at 149.6, 272.0, 430.3, and perhaps 516.4 keV (crossover timing jitter cut down on the intensity of the latter). That these transitions are involved in cascades is corroborated by the integral-coincidence spectrum. The 149.6-keV coincidence spectrum shows the 516.4-keV  $\gamma$  feeding the 149.6-keV level; if we try to place it as feeding this level indirectly through some higher level we obtain no consistency whatever with the remainder of the decay scheme and very quickly exceed the available decay energy. Thus, it depopulates the 666.0-keV level.

The 272.0- and 430.3-keV  $\gamma$ 's feed into the 666.0-keV level from the 933.3- and 1097.3-keV levels, respectively. These placements are the only ones supported by energy sums.

*748.2- and 812.4-keV levels.* The 748.2- and 812.4-keV  $\gamma$ 's were indicated to be ground-state transitions by the anticoincidence spectrum. In addition, the 534.2-keV coincidence (Fig. 7) and the delayed coincidence (Fig. 10) spectra indicated our placement of the 214.5- and 252.3-keV  $\gamma$ 's, making the level at 748.2 keV reasonably certain. Similarly, the enhancement of the 663.3-keV  $\gamma$  in the 149.6-keV gated spectrum adds confidence to the placement of a level at 812.4 keV, which had not been adduced by previous workers (the 812.4-keV  $\gamma$  had been variously assigned).

*794.8-keV level.* There are no transitions to the ground state from this level, probably because of the proposed high spin of the state. However, each of the transitions leading from it was enhanced in the appropriate coincidence spectrum - 260.5 keV in Figs. 4 and 7, 298.5 keV in Fig. 10, and 645.2 keV in Figs. 4 and 5.

*875.8-keV level.* Perhaps the least certain level in our decay scheme, this placement rests solely on the enhancement of the 875.8-keV  $\gamma$  in the anticoincidence spectrum and its suppression in all of the coincidence experiments. Also, there is no other position consistent with the remainder of the decay scheme in which to put it.

*933.3-, 939.1-, and 1097.3-keV levels.* In the "900-keV-region" gated coincidence spectrum (Fig. 9), the only peak present is the one at 149.6 keV. From the integral-, 149.6-keV-gated, and anticoincidence spectra, it is evident that the 947.7-keV  $\gamma$  is the only one in coincidence. It indicates a level at 1097.3 keV, which is corroborated by the enhancement of the 430.3-keV  $\gamma$  to the 666.0-keV level, as discussed above. The 933.3-keV level is placed on the basis of its sole transition to the

ground state. The 939.1-keV level, on the other hand, depopulates by five  $\gamma$  rays, all of which are confirmed by coincidence spectra, as discussed above under the sections concerning the levels to which each feeds.

## VI. DISCUSSION

${}_{86}^{149}\text{Eu}$ , with four neutrons above the  $N=82$  closed shell, must have its structure interpreted cautiously. Although the closed shell is only four neutrons away in one direction, well-defined rotational structure makes its appearance<sup>26</sup> at  $\text{Eu}^{153}$ , only four neutrons in the other direction. This means that when discussing states in  $\text{Eu}^{149}$  one must be careful not to draw arbitrary conclusions from the spherical shell model and must be prepared to accept collective effects and the fractionation of single-particle strengths over many states.

That  $\text{Eu}^{149}$  should be very soft toward vibrational deformations is borne out by the fact that  $\text{Sm}^{148}$ , its even-even core, has a  $2^+$  one-phonon vibrational state<sup>27</sup> at only 551 keV, a  $3^-$  (octupole?) state at 1162 keV, and a  $4^+$  (from the two-phonon vibrational triplet?) at 1181 keV.

The simple shell model predicts that above  $Z=50$  the available proton orbits are  $g_{7/2}$  and  $d_{5/2}$  lying close together, then, after a gap of a few hundred keV,  $h_{11/2}$ ,  $s_{1/2}$ , and  $d_{3/2}$ . The parent,  $\text{Gd}^{149}$ , should have eight  $g_{7/2}$  and six  $d_{5/2}$  protons (or some distribution of proton pairs in these nearly degenerate orbits) outside the  $Z=50$  closed shell. Its last three neutrons should lie in  $h_{9/2}$  and/or  $f_{7/2}$  orbits, the unpaired neutron being in the  $f_{7/2}$  orbit, similar to many other  $I^\pi = \frac{7}{2}^-$  nuclei above  $N=82$ . (This neutron assignment involves somewhat circular logic connected with the  $\text{Gd}^{149}$   $\epsilon$ -decay properties, but no other assignment gives any sort of consistent picture.)

Similarly, the ground state of  $\text{Eu}^{149}$  can be characterized as  $(g_{7/2})^8(d_{5/2})^5$  protons above  $Z=50$  and  $(h_{9/2})^4$  or  $(f_{7/2})^4$  (or some combination) neutrons above  $N=82$ . This  $\frac{5}{2}^+$  configuration is well established from its  $\epsilon$  decay<sup>28</sup> and again is consistent with many odd- $Z$  nuclei in this region. The first excited state undoubtedly has a  $g_{7/2}$  proton hole as a major component in its configuration, i.e.,  $(g_{7/2})^7(d_{5/2})^6$ , again in agreement with many other odd- $Z$  nuclei in the region. These assignments are consistent with the 0.32-nsec half-life<sup>29</sup> of the 149.6-keV state, a half-life quite in line with  $l$ -forbidden  $M1$  transitions between  $g_{7/2}$  and  $d_{5/2}$  states.

The  $\epsilon$  decay to the ground and 149.6-keV states demonstrates quite clearly that they are separate single-particle states and not members of a  $K=\frac{5}{2}$  rotational band. From our above assignments the  $\epsilon$  decay can be pictured as  $\pi d_{5/2} - \nu f_{7/2}$  for the

ground state and  $\pi g_{7/2} - \nu f_{7/2}$  for the 149.6-keV state. The observed branchings (and  $\log ft$ 's), 17.1% (7.7) and 36.3% (7.3), are perfectly consistent with such transitions. On the other hand, if the 149.6-keV state were the  $\frac{7}{2}^+$  member of a  $K = \frac{5}{2}$  rotational band, the relative  $\epsilon$  population should be predictable by the ratio of the squares of the following vector-coupling coefficients:

$$\frac{\langle I_i K_i | (K_f - K_i) | I_i I_i K_f \rangle^2_{\text{excited}}}{\langle I_i K_i | (K_f - K_i) | I_i I_i K_f \rangle^2_{\text{ground}}} = \frac{\langle \frac{7}{2} \frac{7}{2} 1 - 1 | \frac{7}{2} 1 \frac{7}{2} \frac{5}{2} \rangle^2}{\langle \frac{7}{2} \frac{7}{2} 1 - 1 | \frac{7}{2} 1 \frac{5}{2} \frac{5}{2} \rangle^2} = \frac{1}{3}.$$

This is clearly in the wrong direction even before the energy dependence has been included.

The only other simple single-particle state that can be clearly identified is the  $h_{11/2}$  state at 496.2 keV. The measured  $M2$  and  $E3$  multipolarities of the 346.5- and 496.4-keV transitions indicate the  $\frac{11}{2}^-$  assignment, as does the  $2.48 \pm 0.05$ - $\mu\text{sec}$  half-life of the state. Single-particle estimates<sup>30</sup> for the half-lives of the  $M2$  and  $E3$  are  $3.8 \times 10^{-8}$  and  $8.2 \times 10^{-5}$  sec, respectively, to be compared with the measured partial half-lives of  $2.7 \times 10^{-6}$  and  $3.6 \times 10^{-5}$  sec. The  $M2$  is retarded by a factor of approximately 70, but then,  $M2$ 's are commonly retarded by such factors. More surprising, the  $E3$  is enhanced by a factor of about 2.3 over its single-particle estimate, and most  $E3$ 's are also retarded. However, there are three other known enhanced  $E3$  transitions,<sup>31,32</sup> in  $\text{La}^{137}$ ,  $\text{Pr}^{139}$ , and  $\text{Eu}^{147}$ , all nuclei just above or below  $N = 82$  and all involving an  $h_{11/2}$  state. A cursory attempt<sup>32</sup> has been made to explain the enhancements on the basis of octupole-coupled admixtures of the ground states in the  $h_{11/2}$  states, but at this point meaningful quantitative calculations cannot be made. However, the assignment of the 496.2-keV state as an  $h_{11/2}$  state is warranted, and its receiving no direct  $\epsilon$  population from  $\text{Gd}^{149}$  is consistent with this assignment.

A number of spin and parity assignments can be made for the other states, but deciding much about their internal structures is quite difficult. Many of the states are undoubtedly core coupled, e.g., the 459.9- and 534.2-keV states, but most conclusions at this point would be somewhat arbitrary. Unfortunately, theoretical studies of this region are all but nonexistent, and even useful experimental systematics are scarce. We are currently studying other nearby Gd isotopes and hope to be able to say more about the structures of states in the various nuclei in this region at the conclusion of these studies. Meanwhile, in this paper we confine ourselves to a more or less straightforward discussion of the spins and parities *per se*, as they can be deduced from the  $\gamma$  transitions. The  $\epsilon$  decay

itself yields little information, for most of the  $\log ft$  values lie in the range which indicates either first-forbidden or allowed transitions, and it will be necessary to know more about the internal structures of the states before drawing serious conclusions from these values.

The 459.9-keV state can be assigned  $\frac{3}{2}^+$ ,  $\frac{5}{2}^+$ , or  $\frac{7}{2}^+$  because of the  $M1$  character of its ground-state  $\gamma$ -ray transition. The  $\log ft$  value of 9.1 seems to imply a first-forbidden unique transition. However, if one considers this state as arising from core coupling to the one-phonon 551-keV state in  $\text{Sm}^{148}$ , the  $\log ft$  value would be expected to be larger than normal. With this in mind, the  $\epsilon$  decay could in fact be a normal first-forbidden transition. Consequently, the spin assignment for the 459.9-keV state cannot be narrowed down from the above. And if the  $d_{5/2}$  ground state were the single-particle component of the core-coupled state, this could easily explain the absence of a transition to the 149.6-keV state.

The 534.2-keV state can also be assigned  $\frac{3}{2}^+$ ,  $\frac{5}{2}^+$ , or  $\frac{7}{2}^+$  because of the  $M1$  character of its ground-state transition. It is also tempting to think of this state as the  $d_{5/2}$  ground state coupled to the  $2^+$  quadrupole vibrational state. We shall see below that the assignment for the 534.2-keV state can be narrowed down to  $\frac{7}{2}^+$ .

The 666.0-keV state is limited to  $\frac{5}{2}^+$ ,  $\frac{7}{2}^+$ , or  $\frac{9}{2}^+$  by the  $M1$  transition to the 149.6-keV state. If, as it appears, the 666.2-keV transition to the ground state does have appreciable  $M1$  admixing in its  $E2$  character, the  $\frac{9}{2}^+$  possibility is eliminated.

Assignments for the next two states, at 748.2 and 794.8 keV, can be much more specific because of the many  $\gamma$ -ray branches proceeding from them. The 748.2-keV  $E1$   $\gamma$  implies a spin of  $\frac{3}{2}^-$ ,  $\frac{5}{2}^-$ , or  $\frac{7}{2}^-$  for the 748.2-keV state. The 252.3-keV  $\gamma$  to the  $\frac{11}{2}^-$  state appears to be an  $M1$ , which is inconsistent with the 748.2-keV  $\gamma$  being an  $E1$ . However, assuming the 252.3-keV  $\gamma$  to be really an  $E2$  narrows the choice for the 748.2-keV state to  $\frac{7}{2}^-$ . The  $\log ft$  of 7.4 is somewhat high for an allowed transition, but remembering that the 748.2-keV state undoubtedly has a complex structure, one would expect a  $\beta$  transition to it to be hindered. With a  $\frac{7}{2}^-$  assignment, the 214.5-keV  $\gamma$  to the 534.2-keV state allows the narrowing of assignments for the latter down to  $\frac{5}{2}^+$  or  $\frac{7}{2}^+$ .

The strong 298.5-keV  $M1$  transition from the 794.8-keV state to the 496.4-keV state suggests the possibilities  $\frac{9}{2}^-$ ,  $\frac{11}{2}^-$ , or  $\frac{13}{2}^-$  for the upper state. The 645.2-keV  $E1$  transition to the 149.6-keV state limits the choice to  $\frac{9}{2}^-$ . The  $\log ft$  for  $\epsilon$  decay to this state is the lowest for decay to any state, implying that this transition, if any, is allowed, again consistent only with the  $\frac{9}{2}^-$  assignment. The 260.5-

keV  $E1$   $\gamma$  then allows the assignment for the 534.2-keV state to be narrowed further to  $\frac{7}{2}^+$ .

If we may be forgiven a little speculation at this point, a word about one component of the wave function of the 794.8-keV state might perhaps be in order. Consider the two facts: (1) A relatively simple mechanism must exist for populating the state so readily from  $Gd^{149}$ , and (2) the abnormally large intensity of the transition to the 496.4-keV state indicates a similarity to that state. Now, there is ample indication<sup>33-35</sup> that, below  $N=82$  at least, there is appreciable  $h_{11/2}$  character in the proton pairs of the Gd isotopes, and this should also be true here. Any  $\epsilon$  transitions from  $Gd^{149}$  involving  $g_{7/2}$  or  $d_{5/2}$  protons would not be expected to proceed at all rapidly to the available final neutron states, nor would they lead to  $\frac{3}{2}^-$  over-all final states. On the other hand, a  $\pi h_{11/2} - \nu h_{9/2}$  transition not only would proceed relatively quickly, but also it would lead to the final configuration,  $(\pi h_{11/2})(\nu h_{9/2})(\nu f_{7/2})$ , which could furnish a  $\frac{3}{2}^-$  state among its couplings. Similar cases, resulting in three-particle final states are known<sup>31, 36</sup> in the  $N=82$  region, although the three-particle states lie considerably higher than 794.8 keV. Thus, although we do not suggest this as the primary component of the 794.8-keV state, such an admixture would account satisfactorily for the  $\epsilon$  decay.

The state at 812.4 keV is assigned  $\frac{5}{2}^+$ ,  $\frac{7}{2}^+$ , or  $\frac{9}{2}^+$  on the basis of its ground-state  $\gamma$  transition and the 663.3-keV  $M1$  transition to the 149.6-keV state. A possible  $\frac{3}{2}^+$  assignment for this state is ruled out on the argument that the large  $\log ft$  is probably a result of internal complexities in the state necessitating multiparticle rearrangement during the  $\epsilon$  decay rather than the  $\epsilon$  decay being first-forbidden unique.

The single  $\gamma$  transition of 875.8 keV emanating

from the state of this energy is assigned an  $M1$  multipolarity. This limits the state spin to  $\frac{3}{2}^+$ ,  $\frac{5}{2}^+$ , or  $\frac{7}{2}^+$ , assignments that are compatible with the  $\epsilon$  decay to this state.

Harmatz and Handley<sup>11</sup> do not report conversion-electron intensity values for the 933.3-keV transition. Therefore, we cannot make a definite spin assignment to the 933.3-keV state on the basis of this transition. From the  $\log ft$  value of 8.3, assuming this again to be a hindered first-forbidden transition, the spin could be  $\frac{5}{2}^+$ ,  $\frac{7}{2}^+$ , or  $\frac{9}{2}^+$ .

The 939.1-keV  $M1$  ground-state transition suggests  $\frac{3}{2}^+$ ,  $\frac{5}{2}^+$ , or  $\frac{7}{2}^+$  for the 939.1-keV state. The 788.6-keV transition (if it really contains an appreciable  $M1$  admixture) eliminates the  $\frac{3}{2}^+$  possibility, as does the relatively low  $\log ft$  value of 6.8. Neither the 478.7- nor the 272.0-keV  $\gamma$ 's allow this to be narrowed further. It should be noted that an  $E1$  multipolarity for the 405.5-keV transition, while experimentally indicated, is incompatible with the other assignments. A three-particle final-state component can also be invoked here to explain the  $\epsilon$  decay, this time a  $\pi g_{7/2} - \nu h_{9/2}$  transition resulting in  $(\pi g_{7/2})^{-1}(\nu h_{9/2})(\nu f_{7/2})$  as a component of the final state.

The 947.7-keV  $E1$  transition implies  $\frac{5}{2}^-$ ,  $\frac{7}{2}^-$ , or  $\frac{9}{2}^-$  for the 1097.3-keV state. The  $\log ft$  is compatible with any of these possibilities, but other than this, little can be deduced about the state.

#### ACKNOWLEDGMENTS

We are indebted to H. Hilbert for his aid in the operation of the Michigan State University cyclotron. We also wish to thank Dr. D. Beery for his assistance with the setup of some of the electronic equipment, as well as his help in the acquisition of data. Finally, we wish to thank Mrs. I. Samra for her excellent typing of this manuscript.

\*Work supported in part by the U. S. Atomic Energy Commission.

†Work supported in part by the U. S. National Science Foundation.

<sup>1</sup>P. Alexander, Phys. Rev. **134**, B499 (1964); T. Cretzu, K. Holmuth, and G. Winter, Nucl. Phys. **56**, 415 (1964).

<sup>2</sup>V. S. Shirley and J. O. Rasmussen, Phys. Rev. **109**, 2092 (1958); E. Steichele and P. Kienle, Z. Physik **175**, 405 (1963).

<sup>3</sup>R. W. Hoff, J. O. Rasmussen, and S. G. Thompson, Phys. Rev. **83**, 1068 (1951).

<sup>4</sup>V. S. Shirley, W. G. Smith, and J. O. Rasmussen, Nucl. Phys. **4**, 395 (1957).

<sup>5</sup>H. J. Prask, J. J. Reidy, E. G. Funk, and J. W. Mihelich, Nucl. Phys. **36**, 441 (1962).

<sup>6</sup>J. M. Jaklevic, E. G. Funk, and J. W. Mihelich, Nucl. Phys. **84**, 618 (1966).

<sup>7</sup>I. Adam, K. S. Toth, and R. A. Meyer, Nucl. Phys. **A106**, 275 (1968).

<sup>8</sup>N. M. Anton'eva, A. A. Bashilov, B. S. Dzhelepov, and B. K. Preobrazhenskii, Izv. Akad. Nauk SSSR Ser. Fiz. **22**, 895 (1958) [transl.: Bull. Acad. Sci. USSR, Phys. Ser. **22**, 889 (1958)].

<sup>9</sup>V. K. Adamchuk, A. A. Bashilov, and B. K. Preobrazhenskii, Izv. Akad. Nauk SSSR Ser. Fiz. **22**, 919 (1958) [transl.: Bull. Acad. Sci. USSR, Phys. Ser. **22**, 911 (1958)].

<sup>10</sup>B. S. Dzhelepov, B. K. Preobrazhenskii, and V. A. Sergienko, Izv. Akad. Nauk SSSR, Ser. Fiz. **23**, 219 (1959) [transl.: Bull. Acad. Sci. USSR, Phys. Ser. **23**, 211 (1959)].

<sup>11</sup>B. Harmatz and T. H. Handley, Nucl. Phys. **81**, 481 (1966).

<sup>12</sup>A. Siivola and G. Graeffe, Nucl. Phys. **64**, 161 (1965).



- R. N. Keller, reported in P. C. Stephenson and W. E. Lovik, Radiochemistry of the Rare Earths, Scandium, Cerium, and Actinium, "Nuclear Science Series," Nuclear Research Council, Committee on Nuclear Science, Report No. NAS-NS 3020, 1961 (unpublished).
- <sup>14</sup>G. R. Choppin, B. G. Harvey, and S. G. Thompson, *J. Inorg. Nucl. Chem.* **2**, 66 (1956).
- <sup>15</sup>S. G. Thompson, B. G. Harvey, G. R. Choppin, and G. T. Seaborg, *J. Am. Chem. Soc.* **76**, 6229 (1954).
- <sup>16</sup>MOIRAE, an oscilloscope code developed primarily by R. Au and G. Berzins for use on the Michigan State University Sigma 7 computer in the Cyclotron Laboratory.
- <sup>17</sup>L. Nemet, *Izv. Akad. Nauk SSSR Ser. Fiz.* **25**, 68 (1961) [transl.: *Bull. Acad. Sci. USSR, Phys. Ser.* **25**, 68 (1961)].
- <sup>18</sup>R. L. Auble, D. B. Beery, G. Berzins, L. M. Beyer, R. C. Etherton, W. H. Kelly, and Wm. C. McHarris, *Nucl. Instr. Methods* **51**, 61 (1967).
- <sup>19</sup>E. E. Berlovich, V. N. Klementyev, L. V. Krasnov, M. K. Nikitin, and I. Yursik, *Nucl. Phys.* **23**, 481 (1961).
- <sup>20</sup>R. S. Hager and E. C. Seltzer, *Nucl. Data* **4A**, 1 (1968).
- <sup>21</sup>M. P. Avotina, as quoted in Ref. 7.
- <sup>22</sup>Reference 11, using the results of P. A. Seeger, *Nucl. Phys.* **25**, 1 (1961).
- <sup>23</sup>K. Way and M. Wood, *Phys. Rev.* **94**, 119 (1954).
- <sup>24</sup>J. R. Grover, *Phys. Rev.* **116**, 406 (1959).
- <sup>25</sup>J. H. E. Matlauch, W. Thiele, and A. H. Wapstra, *Nucl. Phys.* **67**, 1, 32, 73 (1965).
- <sup>26</sup>P. Alexander, F. Boehm, and E. Kankeleit, *Phys. Rev.* **133**, B284 (1964).
- <sup>27</sup>C. V. K. Baba, G. T. Ewan, and J. F. Suárez, *Nucl. Phys.* **43**, 264, 285 (1963).
- <sup>28</sup>B. Harmatz, T. H. Handley, and J. W. Mihelich, *Phys. Rev.* **123**, 1758 (1961).
- <sup>29</sup>E. E. Berlovich, Yu. K. Gusev, V. V. Ilin, V. V. Nikitin, and M. K. Nikitin, *Zh. Eksperim. i Teor. Fiz.* **42**, 967 (1962) [transl.: *Soviet Phys.-JETP* **15**, 667 (1962)].
- <sup>30</sup>S. A. Moszkowski, in *Alpha-, Beta-, and Gamma-Ray Spectroscopy*, edited by K. Siegbahn (North-Holland Publishing Company, Amsterdam, The Netherlands, 1965); S. A. Moszkowski, *Phys. Rev.* **89**, 474 (1953).
- <sup>31</sup>D. B. Beery, W. H. Kelly, and Wm. C. McHarris, *Phys. Rev.* **188**, 1851 (1969).
- <sup>32</sup>J. R. Van Hise, G. Chilosi, and N. J. Stone, *Phys. Rev.* **161**, 1254 (1967).
- <sup>33</sup>R. E. Eppley, Wm. C. McHarris, and W. H. Kelly, to be published; also in Michigan State University Report No. COO-1779-13, 1969 (unpublished), p. 55.
- <sup>34</sup>J. Felsteiner and B. Rosner, *Phys. Letters* **31B**, 12 (1970).
- <sup>35</sup>B. H. Wildenthal, Michigan State University, private communication.
- <sup>36</sup>Wm. C. McHarris, D. B. Beery, and W. H. Kelly, *Phys. Rev. Letters* **22**, 1191 (1969).

## Properties of the $^{209}\text{Bi}$ Ground-State Analog in $^{209}\text{Po}^\dagger$

G. M. Crawley, W. Benenson, P. S. Miller, D. L. Bayer, and R. St. Onge  
*Cyclotron Laboratory, Michigan State University, East Lansing, Michigan 48823*  
 and

A. Kromminga  
*Calvin College, Grand Rapids, Michigan 49506*

(Received 16 February 1970)

The analog of the ground state of  $^{208}\text{Bi}$  was investigated by both the  $^{209}\text{Bi}(p,n)^{209}\text{Po}$  and the  $^{209}\text{Bi}(p,n\bar{p})^{208}\text{Bi}$  reactions. The Coulomb energy difference  $^{208}\text{Po}-^{208}\text{Bi}$  was determined as  $18.92 \pm 0.03$  MeV, and the relative partial widths for proton decay into the  $p_{1/2}$ ,  $f_{5/2}$ , and  $p_{3/2}$  channels were determined. The total width of the analog state was found to be  $380 \pm 80$  keV.

### 1. INTRODUCTION

The nuclei near the magic numbers  $Z = 82$  and  $N = 126$  have been the subject of numerous shell-model studies, and it is generally concluded that the low-lying states can be described by fairly simple configurations. For example, various stripping reactions have shown that  $^{207}\text{Pb}$  has a number of pure hole states in the  $^{208}\text{Pb}$  core.<sup>1</sup> The low-lying levels of  $^{208}\text{Bi}$  have also been treated as quite pure particle-hole configurations.<sup>2</sup> Both the positions of the levels, and stripping and pickup reactions<sup>3,4</sup> are consistent with small admixtures between various multiplets.

In addition, the analog of the ground states of many of the nuclei in this mass region have been observed as resonances in proton elastic and inelastic scattering, and their positions and widths have been extracted.<sup>5-8</sup> Information on the  $T = T_z + 1$  analog of the ground state of  $^{208}\text{Pb}$  has also been obtained recently from the reaction  $^{208}\text{Pb}(p, n\bar{p})$ .<sup>9</sup>

The experiment described in this paper exploits the  $(p, n\bar{p})$  reaction<sup>10-12</sup> to study the analog of the  $^{208}\text{Bi}$  ground state in the nucleus  $^{209}\text{Po}$ . This particular state cannot be readily studied by a resonance method, since the  $^{208}\text{Bi}$  target is unstable, with a half-life of  $3.7 \times 10^5$  yr. Since the  $\bar{p}$  spectrum contains a number of peaks due to the multiplet structure of  $^{208}\text{Bi}$ , the direct  $(p, n)$  measurement of the analog state was also undertaken to check its position and width. Additional information on the partial widths for proton decay of the analog state was also obtained.

### 2. EXPERIMENT

The  $^{209}\text{Bi}(p, n\bar{p})$  experiment was carried out using the extracted beam from the Michigan State University isochronous cyclotron at proton energies from 24 to 30 MeV. The protons were detected in a counter telescope of cooled silicon surface-barri-

er detectors. Protons were separated from other reaction products using the program TOOTSIE<sup>13</sup> in an XDS Sigma 7 computer. Spectra were taken at 90, 120, and 160° to check the kinematic effects on the line shape of the protons emitted from the analog state and to check the isotropy of the emitted protons. Isotropy is expected if the  $(p, n)$  reaction goes by simple charge exchange, since the isospin lowering operator  $T^-$  does not affect the population of magnetic substates in the nucleus.

A spectrum taken at 160° and at 24.7-MeV bombarding energy is shown in Fig. 1. The striking feature of this spectrum is the three peaks observed at a proton energy of about 11 MeV. These peaks were shown to remain at about the same absolute energy for a number of bombarding energies between 24 and 30 MeV.

The energy scale of the detector was calibrated using the inelastically scattered protons from a thin carbon foil. Calibration runs were made before and after each  $\bar{p}$  run. While the energy of the protons from the decay of the analog state is independent of the bombarding energy, the absolute calibration of the detector depends upon the calibration of the energy-analysis magnets in the beam transport system. This uncertainty is believed to be less than 50 keV<sup>14</sup> for 25-MeV protons.

The target thickness also contributes to the uncertainty in the position of the  $\bar{p}$  peak. Fortunately this could be calculated, since  $^{209}\text{Bi}(p, d)^{208}\text{Bi}$  spectra were taken at the same time as the  $\bar{p}$  runs and so from the width of the deuteron peaks (which was essentially due to target thickness), the target thickness for the protons could be calculated to within  $\pm 10$  keV.

The kinematic corrections are more difficult to establish since the distribution of the velocities of the  $^{209}\text{Po}$  recoil nuclei following the  $(p, n)$  reaction gives rise to both a shift and a broadening of the  $\bar{p}$  spectrum. The magnitudes of these effects depend

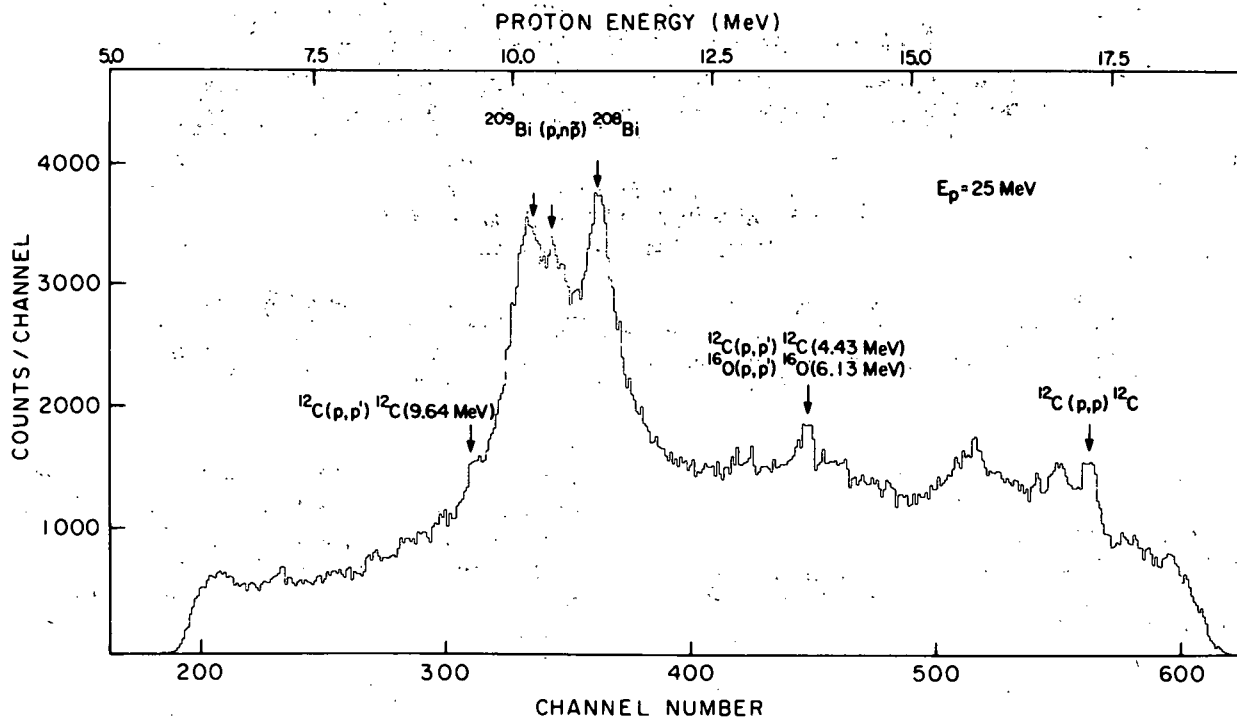


FIG. 1. Spectrum of protons scattered from  $^{209}\text{Bi}$  at a laboratory angle of  $160^\circ$ . The suppression of the spectrum below channel 200 and above channel 600 is instrumental, corresponding to the detector thickness used.

upon the angular distribution of the neutrons and the  $\bar{p}$  detection angle. There is an additional constant energy shift in the lab system because of the recoil caused by proton emission.

A summary of these effects, assuming three different neutron distributions (labeled 1, 2, and 3), is shown in Fig. 2. When the protons are detected at  $90^\circ$ , the centroid of the  $\bar{p}$  peak is the same as  $E_C$ , the lab energy obtained if the  $^{209}\text{Po}$  nucleus decayed at rest, regardless of the neutron angular distribution. The decay energy was therefore calculated from the spectra measured at  $90^\circ$ . The observed difference in energy between the  $90$  and  $160^\circ$  spectra, shown also in Fig. 2 implies that the  $(p, n)$  angular distribution for the analog state is forward peaked, although the detailed distribution cannot be uniquely determined.

Figure 3 gives a comparison of the calculated  $\bar{p}$  line shapes at  $90$  and  $160^\circ$  for the three  $(p, n)$  angular distributions shown in Fig. 2. The curves are normalized to have the same area. A very narrow intrinsic width for the analog state of 10 keV was chosen in the calculation so that the details of the line shape could be seen. The extreme distributions 1 and 3 give line shapes with essentially the same width at both angles. Distribution 2, which resembles most measured angular distributions, gives a full width at half maximum of 80 keV at  $90^\circ$  and 35 keV at  $160^\circ$ . The width is a maximum near

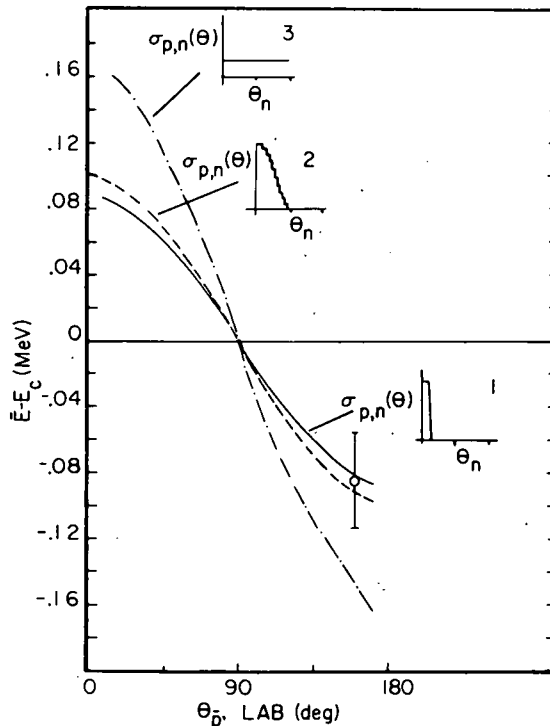


FIG. 2. Dependence of the proton centroid energy  $\bar{E}$  on the detection angle calculated for the three  $(p, n)$  angular distributions shown.  $E_C = 208/209 E_p$  (c.m.), where  $E_p$  (c.m.) is defined in Eq. (1).

$90^\circ$  for any moderately forward-peaked distribution. However, the magnitude of the effect is small compared to the observed width of the peaks, and only introduces a small error in the width of the analog state.

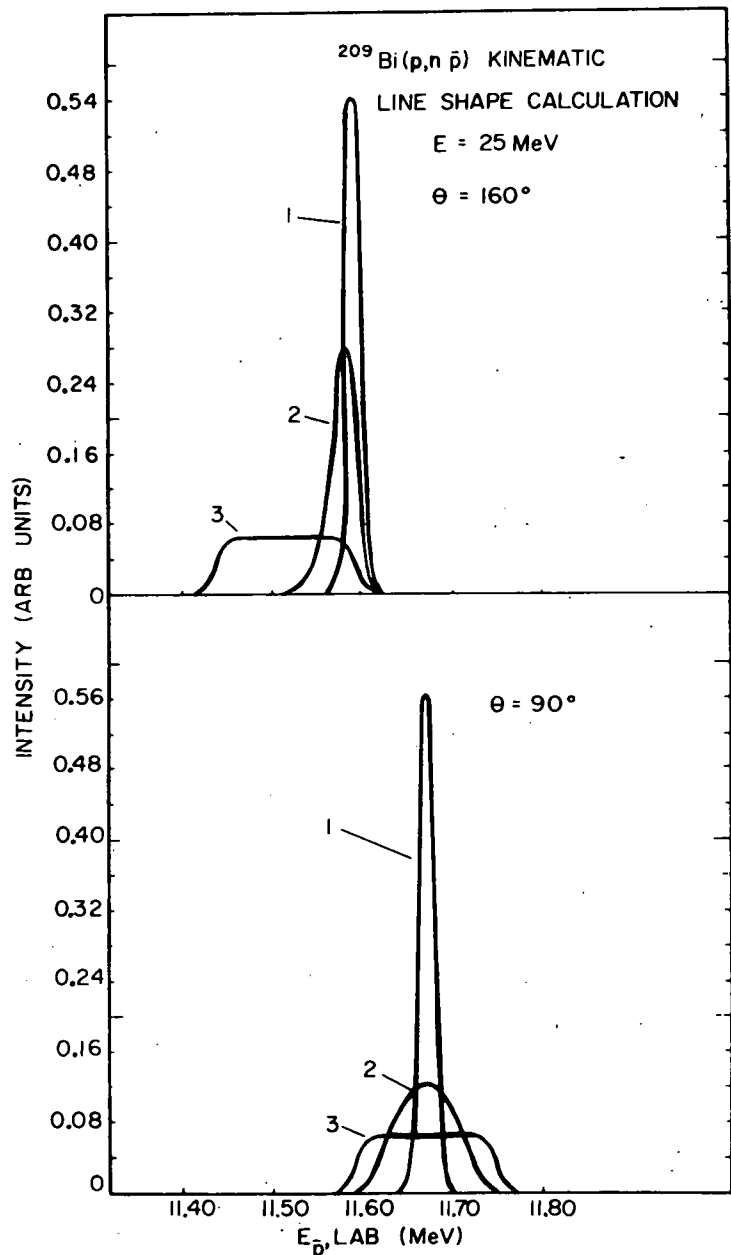
It should be noted that the curves in Fig. 3 were calculated for a Coulomb energy difference of 19.18 MeV, which is higher than the value observed. These curves therefore peak at correspondingly higher energies than the experimental spectra.

The determination of the energy of the analog state is further complicated by the fact that the proton decay proceeds to closely spaced multiplets in  $^{208}\text{Bi}$ . Even the ground-state multiplet

consists of two states 60 keV apart.<sup>2</sup> Therefore, as an independent check on the position and width of the analog state, the direct ( $p, n$ ) measurement was made.

Neutrons were detected in a 5-in. plastic scintillator about 5 m from the Bi target.  $\gamma$ -ray discrimination was improved by displaying the pulse-shape-discriminator output versus light output as a two-dimensional display in the Sigma 7 computer and using the program TOOTSIE<sup>13</sup> to allow for curvature in the  $\gamma$ -ray and neutron lines. The neutron time-of-flight spectrum was taken using a time-to-amplitude converter. The intrinsic time resolution of the system was 1.5 nsec. The  $^{209}\text{Bi}(p, n)$

FIG. 3. Calculation of line shapes at lab angles of  $90^\circ$  and  $160^\circ$  for various ( $p, n$ ) angular distributions. Note that the intrinsic line-width is assumed to be 10 keV to illustrate the effects clearly.



spectrum showed only one large neutron peak at the energy of the analog state. The energy calibration was obtained from the  $^{12}\text{C}(p, n)^{12}\text{N}$  reaction. The results were quite consistent with the  $\bar{p}$  data.

### 3. COULOMB ENERGY DIFFERENCES

The energy of the delayed protons to the ground state of  $^{208}\text{Bi}$  was determined as 11.409 MeV with an error of 30 keV due to the finite width of the state and the effect of the 60-keV doublet in  $^{208}\text{Bi}$ . The Coulomb energy difference between  $^{209}\text{Po}$  and  $^{209}\text{Bi}$  is then obtained from the equation

$$\Delta E_C = E_p(\text{c.m.}) + B_n(^{209}\text{Bi}), \quad (1)$$

where  $B_n$  is the binding energy of the last neutron in  $^{209}\text{Bi}$ .<sup>15</sup> After making the c.m. correction, the Coulomb energy difference was obtained as 18.917 MeV  $\pm$  33 keV. While this is the first measurement of the Po-Bi Coulomb energy difference, it is interesting to compare it with the  $^{209}\text{Bi}$ - $^{209}\text{Pb}$  values obtained previously. These results are shown in Table I. Although the effect of the extra proton is to increase the Coulomb energy by 110  $\pm$  40 keV, one might have expected an increase of nearly 300 keV from the formula<sup>16</sup>

$$\Delta E_C = 1.443 \bar{Z}/A^{1/3} - 1.12 \text{ MeV}. \quad (2)$$

However, even a simple model of the states which includes the Coulomb interaction of particles in shells outside the  $^{208}\text{Pd}$  core indicates that this value could easily be much smaller than 300 keV. A discussion of the many effects which arise in a more accurate calculation has been given by Auerbach *et al.*<sup>17</sup>

### 4. THEORY AND DISCUSSION

The low-lying states in  $^{208}\text{Bi}$  arise from particle-hole couplings which form closely spaced multiplets, and it is assumed that there are no admix-

TABLE I. Coulomb energy differences for  $A = 209$  in keV.

		Present
Po-Bi	18.917 $\pm$ 33	b
Bi-Pb	18.841 $\pm$ 10 <sup>a</sup>	b
	18.84 $\pm$ 20	c
	18.789 $\pm$ 7	d
	18.80 $\pm$ 20	e

<sup>a</sup>A previous result from Rutgers [D. J. Brendin, O. Hausen, G. Lenz, and G. M. Temmer, *Phys. Letters* **21**, 677 (1966)] gave a value of 18.98 MeV, but it is assumed that the more recent value is more accurate.

<sup>b</sup>G. H. Lenz and G. M. Temmer, *Nucl. Phys.* **A112**, 625 (1968).

<sup>c</sup>See Ref. 6.

<sup>d</sup>See Ref. 18.

<sup>e</sup>See Ref. 7.

tures between multiplets.<sup>2,4</sup> If such possible admixtures are neglected, the wave functions for the  $^{208}\text{Bi}$  states of interest here may be written as

$$\Psi^{l'j'} = (\pi l' j', \nu l j^{-1})_J |c\rangle, \quad (3)$$

where  $l'j'$  refers to the  $h_{9/2}$  proton, and  $lj$  to the various neutron hole states, and  $|c\rangle$  refers to the  $^{208}\text{Pb}$  core. Similarly, if the ground state of  $^{209}\text{Bi}$  is taken as a  $h_{9/2}$  proton outside the  $^{208}\text{Pb}$  core, its analog in  $^{209}\text{Po}$  is

$$\Psi^{\text{IAS}} = \sum_{j=9/2} \left( \frac{2j+1}{43} \right)^{1/2} (\pi l j, \nu l j^{-1})_0 \pi h_{9/2} |c\rangle + \delta_{j,9/2} \left( \frac{9}{43} \right)^{1/2} (\pi l \frac{9}{2}, \nu l \frac{9}{2}^{-1})_0 \pi h_{9/2} |c\rangle. \quad (4)$$

According to a simple resonance theory of the nuclear reaction, the other nucleons are not affected by the emission of a proton from the analog resonance. The partial width for the decay of the analog resonance to a given excited state is expressed as a sum of terms, each being the product of a spectroscopic factor and a single-particle width for the emitted proton. The single-particle width is strongly dependent on the energy and angular momentum of the outgoing proton, because of the Coulomb and centrifugal barriers.

An analysis based on this theory has been used to obtain structure information in the lead region.<sup>18</sup> The single-particle widths were extracted from elastic and inelastic proton scattering from  $^{207}\text{Pb}$ .<sup>19,20</sup> If the  $^{208}\text{Pb}$  ground state is a doubly closed shell, and the low-lying states  $(l, j)$  in  $^{207}\text{Pb}$  are single-neutron holes in the  $(l, j)$  orbit, the observed partial widths are given by

$$\Gamma_{lj} = (2j+1/44) \Gamma_{lj}^{\text{sp}}. \quad (5)$$

In the experiment reported here the simple shell-model estimates of the partial widths are

$$\Gamma_{l'j'}^{l'j} = \frac{2j+1}{43(2j'+1)} \Gamma_{lj}^{\text{sp}} \delta_{j'9/2}. \quad (6)$$

The  $\bar{p}$  cross section was then calculated using the expression

$$\frac{d\sigma}{d\Omega}(E\bar{p}) \propto \sum_i \frac{\Gamma_i}{(E - E_i)^2 + \frac{1}{4} \Gamma_i^2}, \quad (7)$$

where the sum extends over all states in the multiplets  $(\nu p_{1/2})^{-1} \pi h_{9/2}$ ,  $(\nu f_{5/2})^{-1} \pi h_{9/2}$ , and  $(\nu p_{1/2})^{-1} \pi h_{9/2}$ . The energies and spins of the states in  $^{208}\text{Bi}$  are taken from the  $^{209}\text{Bi}(d, t)$  experiment.<sup>2</sup>

In order to make the extracted single-particle

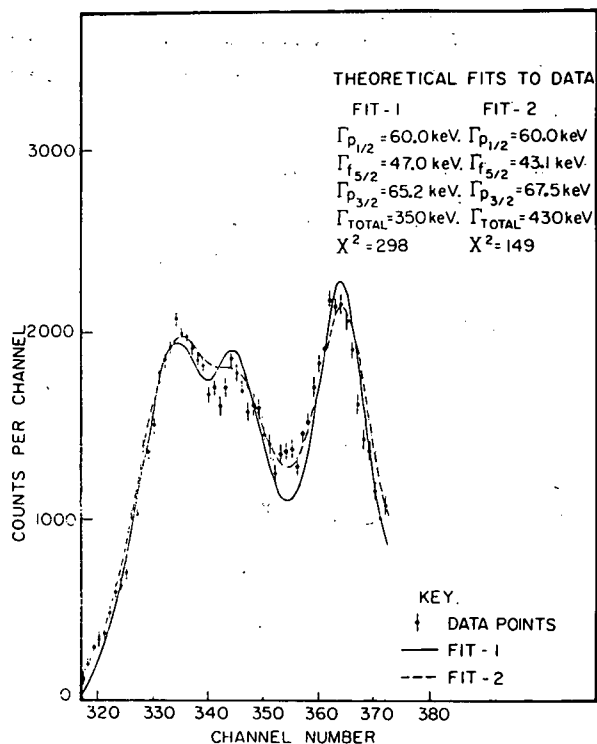


FIG. 4. A comparison of the theoretical fits to the data with background subtracted. Two curves calculated with different total widths are shown to illustrate the stability of the relative partial widths extracted.

widths directly comparable to the single-particle widths from the  $^{207}\text{Pb}$  proton scattering experiment, penetrability corrections have been made to the  $\Gamma_i$ 's appearing in Eq. (7). We replace  $\Gamma_i$  by  $\Gamma_i [P(E)/P(E_i)]$ , where  $E_i$  is the energy of the outgoing proton in the  $^{207}\text{Pb}$  (in) elastic scattering experiment at resonance, and  $P(E)$  is the penetrability calculated in the WKB approximation.

The procedure then was to subtract a smooth background from the experimental spectrum and do a least-squares fit to the remaining peaks,

TABLE II. Proton single-particle widths  $\Gamma_{ij}$  (keV).

	Present	$^{208}\text{Pb}(p, n\bar{p})^b$	$^{207}\text{Pb}(p, p)^c$	$^{207}\text{Pb}(p, p)^d$
$p_{1/2}$	60 <sup>a</sup>	60.5 ± 3.0	61 ± 15	66
$f_{5/2}$	43 ± 5	21 ± 2.4	17 ± 4	19
$p_{3/2}$	67 ± 5	69.2 ± 2.1	50 ± 11	44

<sup>a</sup>Normalized to 60 keV.

<sup>b</sup>See Ref. 9.

<sup>c</sup>G. M. Temmer, G. H. Lenz, and G. T. Garvey, in *Proceedings of International Conference on Nuclear Physics, Gattingburg Tennessee, 12-17 September, 1966*, edited by R. L. Beeker and A. Zucker (Academic Press Inc., New York, 1967), p. 225.

<sup>d</sup>See Ref. 19.

varying the relative partial widths and gridding on the total width. The final widths were then obtained by normalizing  $\Gamma_{p_{1/2}}^{\text{SP}}$  to 60 keV. Acceptable fits to the data for two different total widths are shown in Fig. 4. The relative partial widths are quite stable for different backgrounds and for a variation of the total width of up to 100 keV. However, for total widths smaller than 350 keV there is an excess of  $\bar{p}$  strength between the ground ( $h_{9/2}, p_{1/2}^{-1}$ ) and the ( $h_{9/2}, f_{5/2}^{-1}$ ) multiplet. The values for the proton widths extracted are shown in Table II. The errors quoted reflect the uncertainties associated with background subtraction and with the fitting procedure. The total width is not determined as accurately and, allowing for kinematic broadening, is given as  $380 \pm 80$  keV.

The relative widths extracted for the  $p_{1/2}$  and  $p_{3/2}$  channels agree reasonably well with the previous values obtained from other nuclei in this region, as shown in Table II. However the width for the  $f_{5/2}$  channel is considerably larger than previously observed.<sup>21</sup> Our results seem quite unambiguous, and in fact, a comparison with the  $\bar{p}$  spectrum from  $^{208}\text{Pb}(p, n\bar{p})$  shows that the  $f_{5/2}$  peak shown here is much stronger than the one extracted by Igo *et al.*<sup>9</sup> However, a recent preliminary result<sup>22</sup> on  $^{208}\text{Pb}(p, n\bar{p})$  confirms the larger  $f_{5/2}$  width. The value of the total width of the analog state is also larger for  $^{209}\text{Bi}$  than for  $^{208}\text{Pb}$ , but this may only reflect a difference in the mixing with the background levels.

A calculation is currently in progress taking into account the effect of the residual interaction on the partial widths.<sup>23</sup>

## 5. $^{209}\text{Bi}(p, d)^{208}\text{Bi}$

The  $^{209}\text{Bi}(p, d)^{208}\text{Bi}$  reaction was measured simultaneously with the ( $p, n\bar{p}$ ) experiment, and it also reaches the same final states in  $^{208}\text{Bi}$ . The thick-target spectrum shown in Fig. 5 shows the multiplet structure extending up to the ( $h_{9/2}, h_{9/2}^{-1}$ ) multiplet. A thin-target spectrum with good resolution is also shown in Fig. 5. The angular distributions are in good agreement with the  $l$  assignments from the ( $d, t$ ) reaction.<sup>2</sup>

## 6. CONCLUSIONS

The proton reduced widths extracted from the  $^{209}\text{Bi}(p, n\bar{p})$  experiment agree with the values extracted both from resonance experiments and the  $^{208}\text{Pb}(p, n\bar{p})$  experiment for the  $p_{1/2}$  and  $p_{3/2}$  shells. However, there is a marked disagreement for the  $f_{5/2}$  shell. A total width of 380 keV was also obtained for the analog state, and the  $^{209}\text{Pb}$ - $^{209}\text{Bi}$  Coulomb energy difference was  $18.92 \pm 0.03$  MeV.

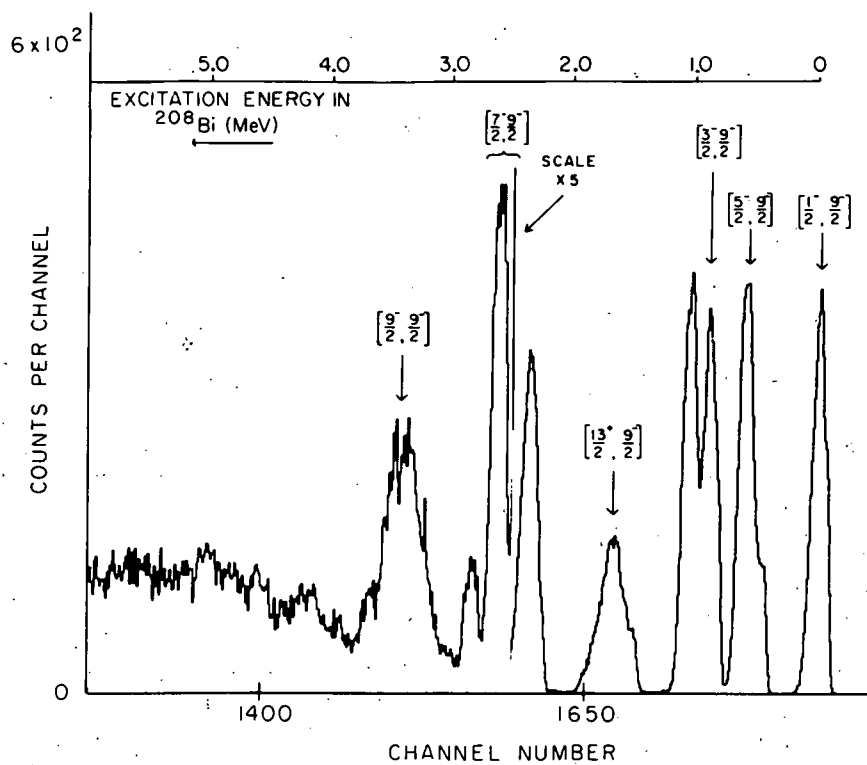
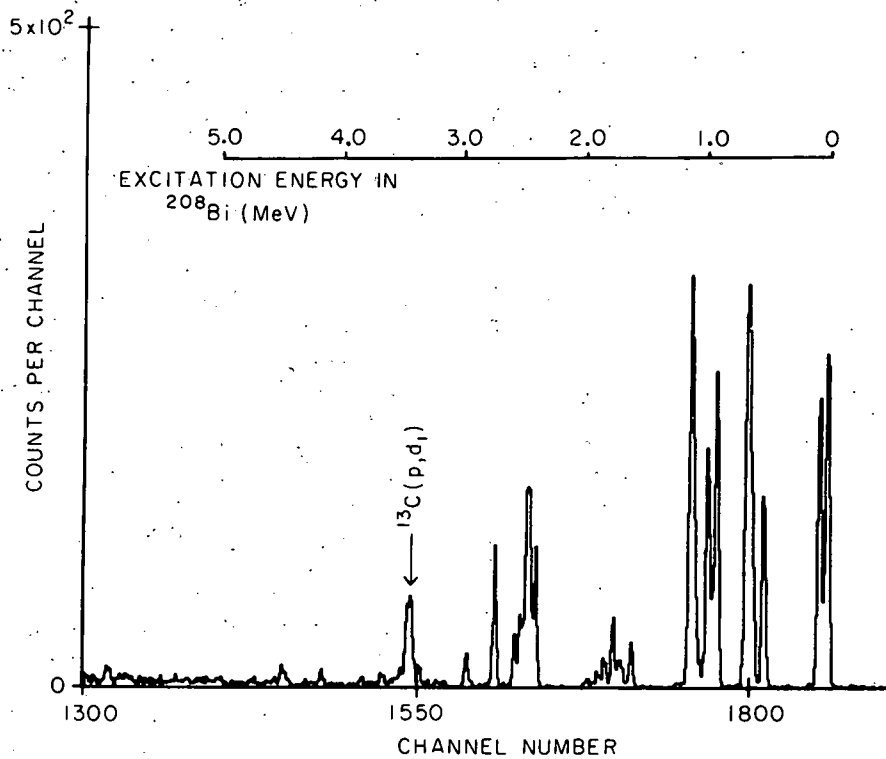


FIG. 5. (a)  $^{209}\text{Bi}(p, d)^{208}\text{Bi}$  spectrum with a thin target and (b)  $^{209}\text{Bi}(p, d)^{208}\text{Bi}$  with a thick target. The close multiplet structure of  $^{208}\text{Bi}$  up to  $(h_{9/2}h_{9/2}^-)$  is clearly seen in the thick-target spectrum.

†Research supported in part by the National Science Foundation.

<sup>1</sup>G. Muehlehner, A. S. Poltorak, W. C. Parkinson, and R. H. Bassel, *Phys. Rev.* **159**, 1039 (1967); W. P. Alford and D. G. Burke, *Phys. Rev.* **185**, 1560 (1969); G. R. Satchler, W. C. Parkinson, and D. L. Hendrie, *Phys. Rev.* **187**, 1491 (1969).

<sup>2</sup>Y. E. Kim and J. O. Rasmussen, *Phys. Rev.* **135**, B44 (1964).

<sup>3</sup>J. R. Erskine, *Phys. Rev.* **135**, B110 (1964).

<sup>4</sup>W. P. Alford, J. P. Schiffer, and J. J. Schwartz, *Phys. Rev. Letters* **21**, 156 (1968); W. P. Alford, private communication.

<sup>5</sup>P. Richard, W. G. Weitkamp, W. Wharton, H. Wieman, and P. von Brentano, *Phys. Letters* **26B**, 8 (1967).

<sup>6</sup>C. D. Kavaloski, J. S. Lilley, P. Richard, and N. Stein, *Phys. Rev. Letters* **16**, 807 (1966).

<sup>7</sup>C. F. Moore, L. J. Parish, P. von Brentano, and S. A. A. Zaidi, *Phys. Letters* **22**, 616 (1966).

<sup>8</sup>G. Ballois, J. Saudinos, O. Beer, M. Gendrot, and P. Lopato, *Phys. Letters* **22**, 659 (1966).

<sup>9</sup>G. J. Igo, C. A. Whitten, Jr., Lean-Luc Perreoud, J. W. Verba, T. J. Woods, J. C. Young, and L. Welch, *Phys. Rev. Letters* **22**, 724 (1969).

<sup>10</sup>A. I. Yavin, R. A. Hoffswell, L. H. Jones, and T. M. Noweir, *Phys. Rev. Letters* **16**, 1049 (1966).

<sup>11</sup>P. S. Miller, Princeton University Technical Report

No. PUC-937-339, 1968 (unpublished).

<sup>12</sup>P. S. Miller and G. T. Garvey, to be published.

<sup>13</sup>D. L. Bayer and W. Benenson, *Bull. Am. Phys. Soc.* **14**, 1243 (1969).

<sup>14</sup>E. Kashy, MSUCL Internal Report, 1969 (unpublished).

<sup>15</sup>C. Maples, G. W. Goth, and J. Cerny, University of California Lawrence Radiation Laboratory Report No. UCRL-16964 (unpublished).

<sup>16</sup>J. D. Anderson, C. Wong, and J. W. McClure, *Phys. Rev.* **138**, B165 (1965).

<sup>17</sup>N. Auerbach, J. Hufner, A. K. Kerman, and C. M. Shakin, *Phys. Rev. Letters* **23**, 484 (1969).

<sup>18</sup>W. R. Wharton, P. von Brentano, W. K. Dawson, and P. Richard, *Phys. Rev.* **176**, 1424 (1968).

<sup>19</sup>B. L. Anderson, J. P. Bondorf, and B. S. Madsen, *Phys. Letters* **22**, 651 (1966).

<sup>20</sup>C. J. Batty, B. Bommer, E. Freidman, C. T. Schaler, A. S. Cloagh, J. B. Hunt, and L. E. Williams, *Nucl. Phys.* **A116**, 643 (1968).

<sup>21</sup>P. Richard, in *Nuclear Isospin*, edited by J. D. Anderson, S. D. Bloom, J. Cerny, and W. W. True (Academic Press Inc., New York, 1969), p. 547 and Refs. therein.

<sup>22</sup>G. M. Crawley, P. S. Miller, and D. L. Bayer, *Bull. Am. Phys. Soc.* **15**, 626 (1970).

<sup>23</sup>S. A. A. Zaidi and P. Dyer, *Phys. Rev.* **185**, 1332 (1969).



SHELL-MODEL STRUCTURE OF  $^{35}\text{Cl}$ - $^{35}\text{Ar}$  \*

B. H. WILDENTHAL

*Michigan State University, East Lansing, Michigan 48823, USA\*\*  
and Oak Ridge National Laboratory, Oak Ridge, Tennessee 37830, USA*

E. C. HALBERT, J. B. McGRORY

*Oak Ridge National Laboratory, Oak Ridge, Tennessee 37830, USA*

and

T. T. S. KUO

*Oak Ridge National Laboratory, Oak Ridge, Tennessee 37830, USA  
and State University of New York, Stony Brook, N.Y. 11790, USA\*\**

Received 15 May 1970

Energy levels, E2 and M1 observables, and spectroscopic factors are calculated for  $^{35}\text{Cl}$ - $^{35}\text{Ar}$ , and compared with experimental data. The theoretical results are obtained by computations in a full  $(0s)^4(0p)^{12}(1s, 0d)^{A-16}$  shell-model vector space. Two alternative "realistic" interactions are used.

Examples of both "rotational" and "vibrational" phenomena can be found in sd-shell nuclei. The region of most obvious rotational structure is  $A = 19 - 25$ . In  $^{20}\text{Ne}$  for instance, members of a  $K = 0$  ground-state rotational band have been observed [1] up through  $J^\pi = 8^+$ . In  $^{21}\text{Ne}$ , members of a  $K = 3/2$  ground-state band seem to be identifiable [2] up through  $J^\pi = 13/2^+$ . On the other hand,  $^{36}\text{Ar}$  shows vibrational features, in that instead of the  $J(J+1)$ -like level spacing seen for  $^{20}\text{Ne}$ , the spectrum of  $^{36}\text{Ar}$  shows a closely spaced  $0^+$ ,  $2^+$ ,  $4^+$  triad at approximately twice the excitation energy of the  $2^+$  first-excited state [3]. The level structure of the adjacent nucleus  $^{35}\text{Cl}$  has been interpreted in terms of an intermediate-coupling vibrational model [4], and alternatively, in terms of a band-mixed rotational model [5].

In earlier reports [6] we have shown that many experimentally observed features of the nuclei  $A = 18 - 22$  (in particular features of their ground-state rotational bands) can be described successfully by shell-model calculations in a

full  $(0s)^4(0p)^{12}(1s, 0d)^{A-16}$  vector space, with a "realistic" effective Hamiltonian that was derived [7] for  $A = 18$  from the Hamada-Johnston potential. As a natural extension of this  $A = 18 - 22$  work we have carried out similar calculations for nuclei in the mass range  $A = 34 - 38$ . We again use the full sd-shell vector space. For  $A = 34 - 38$  we have tried a variety of realistic Hamiltonians having essentially the same character as the one we used for the light sd-shell region †. In this note we present as a sample of these  $A = 34 - 38$  calculations results obtained for  $A = 35$ ,  $T = 1/2$ . We include results from two different Hamiltonians in order to give some indication of the sensitivity of the various calculated observables to the details of the assumed two-body interaction and single-particle energies.

For both of the effective Hamiltonians to be

† In fact, an arithmetic error in the original calculation of the bare  $G$ -matrix element part of the "realistic" Hamiltonian has been discovered. In the treatment of the tensor force, the separation method should lead to a value of about 440 MeV for  $E_{\text{eff}}$ , the effective energy denominator, rather than a value of about 220 MeV as was used in the  $A = 18 - 22$  and present calculations. It has been found, however, that a more accurate overall treatment [8] of the tensor force results in values for the tensor-force matrix elements which differ from the ones used here by only about 10%.

\* Research jointly sponsored by the U.S. Atomic Energy Commission under contract with the Union Carbide Corporation and by the U.S. National Science Foundation.

\*\* Present addresses.

discussed, the two-body interactions were derived from the Hamada-Johnston potential in a similar way to that used in generating the  $A = 18 - 22$  Hamiltonian mentioned above. For the first Hamiltonian considered here, the principal difference from the  $A = 18 - 22$  interaction is that the harmonic oscillator parameter was taken to be  $\hbar\omega = 12.5$  MeV, instead of 14.0 MeV. This change was made because of a presumed increase in nuclear size between  $A \approx 18$  and  $A \approx 36$ . The important points of similarity between this  $A = 34 - 38$  Hamiltonian and the one used for  $A = 18 - 22$  are that: (a) the second-order  $2\hbar\omega$  corrections were calculated in particle formalism, and effective three-body interactions were neglected; and (b) the single-particle energies were taken directly from the observed spectrum of  $^{17}\text{O}$ . Thus, no direct adjustments towards fitting multi-particle level-structure data were made in either the two-body interaction or the single-particle energies. The diagrams which are included in the second-order  $2\hbar\omega$  corrections are shown in fig. 1. We note that in the treatment of the core-polarization terms, the nucleus  $^{16}\text{O}$  was treated as the core. We will refer to this first  $A = 34 - 38$  (1+2)-body Hamiltonian as  $12.5\text{ p} + ^{17}\text{O}$ .

The second Hamiltonian to be discussed here will be referred to as  $11.0\text{ h} + \text{aSPE}$ . The two-body part of this Hamiltonian was calculated with  $\hbar\omega = 11.0$  MeV. Other features which distinguish  $11.0\text{ h} + \text{aSPE}$  from  $12.5\text{ p} + ^{17}\text{O}$  are that (a) the second-order  $2\hbar\omega$  corrections in  $11.0\text{ h} + \text{aSPE}$  were calculated in hole formalism, and three-

hole interactions were neglected; and (b) the single particle-energies were adjusted so as to give a least-square fit to 23 measured excitation energies in the mass region  $A = 35 - 39^*$ . The diagrams which are included in the second-order  $2\hbar\omega$  corrections for the second Hamiltonian are identical to those shown in fig. 1 except that the external particle lines are replaced with hole lines. We note that in this case the nucleus  $^{40}\text{Ca}$  was treated as the core in the calculation of the corepolarization contribution.

The experimental data relevant to our study of the level structure of  $A = 35$ ,  $T = 1/2$  are presented in tables 1 and 2. Below 3.90 MeV in  $^{35}\text{Cl}$ , the total number of energy levels, and their spins and parities, seem securely established. As table 1 shows, the six observed positive-parity levels in this region have obvious counterparts in each of the two theoretical spectra. Above 3.90 MeV the experimental situation is not so clear. At 4.0 MeV there is definite evidence for levels of  $J^\pi = 9/2^+$  and  $1/2^+$ , and indeed the seventh and eighth states in both model spectra are  $9/2^+$  and  $1/2^+$ . Apart from these two levels, the number and identity of positive-parity levels at higher excitation energies is not clearly established. Measurements of the  $^{36}\text{Ar}(p, d)^{35}\text{Ar}$  reaction do indicate a possible  $1/2^+$  level at 4.7 MeV, and two strong  $l = 2$  levels above 5 MeV. The large  $l = 2$  pickup strength observed in the 5-6 MeV region is nicely consistent with the model predictions for the locations of  $d_{5/2}$ -hole strength. However, it is not clear whether the observed 4.7 MeV level, if indeed it is valid, should be taken as the second  $1/2^+$  state in the spectrum, or the third. No levels in this region of excitation energy are observed with the  $^{34}\text{S}(^3\text{He}, d)^{35}\text{Cl}$  reaction. For reasons such as these, detailed comparison between experiment and theory in the 4-6 MeV region must await more experimental work.

We conclude from inspection of table 1 that the experimental positions of the first eight positive-parity levels in  $A = 35$ ,  $T = 1/2$  are satisfactorily reproduced by both the shell model spectra, and that there are no clear inconsistencies in level structure up to  $\approx 6$  MeV of excitation. Furthermore, table 1 shows that the distribution of single-particle and single-hole strength over the model levels agrees reasonably well with the information which can be extracted

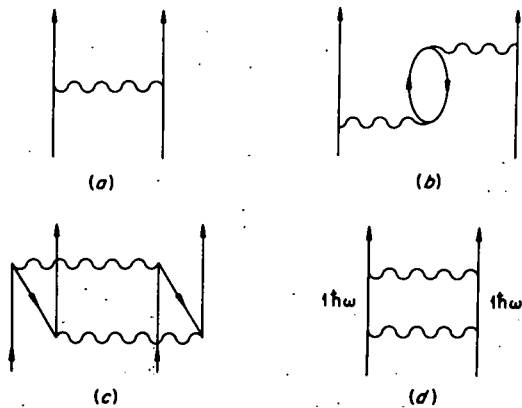


Fig. 1. Diagrams included in the effective interactions. Diagram a is the bare reaction matrix and the rest are second order  $2\hbar\omega$  corrections. In case d, each of the two intermediate-state particles lies  $1\hbar\omega$  above the active shells.

\* The adjusted  $d_{3/2}-s_{1/2}$  splitting is 2.2 MeV, rather than the 4.2 MeV observed in  $^{17}\text{O}$ . The  $d_{3/2}-d_{5/2}$  splitting of the adjusted single-particle energies is the same as in  $^{17}\text{O}$ .

Table 1  
Excitation energies and one-nucleon transfer spectroscopic factors for states of  $^{35}\text{Cl}^{35}\text{Ar}$ .

$J^\pi$	$E_{\text{exp}}$	$E_{\text{calc}}^*$		$S(\text{stripping})_{\text{exp}}$ ref.				$S(\text{stripping})_{\text{calc}}$				$S(\text{pickup})_{\text{exp}}$ ref.				$S(\text{pickup})_{\text{calc}}$			
		12.5p+ $^{17}\text{O}$	11.0h+aSPE	[11]	[12]	12.5p+ $^{17}\text{O}$	11.0h+aSPE	[15]	[13]	[14]	12.5p+ $^{17}\text{O}$	11.0h+aSPE	[15]	[13]	[14]	12.5p+ $^{17}\text{O}$	11.0h+aSPE		
3/2 <sup>+</sup>	0.00 [3]	0.00	0.00	1.08	1.3	0.73	0.64	3.4	3.5	2.9	4.33	4.30							
1/2 <sup>+</sup>	1.22 [3]	1.11	0.51	0.19	0.28	0.12	0.27	1.4	2.1	2.5	1.94	2.56							
5/2 <sup>+</sup>	1.76 [3]	1.70	1.68			0.01	0.00	≤ 0.2	0.2		0.02	0.03							
7/2 <sup>+</sup>	2.65 [9]	2.40	2.87			0	0				0	0							
3/2 <sup>+</sup>	2.69 [9]	2.17	1.86	0.02		0.03	0.06	~ 0.5	0.6		0.83	0.63							
5/2 <sup>+</sup>	3.00 [9]	2.43	2.65	0.04	0.04	0.13	0.13	2.6	3.1	2.5	4.83	3.55							
9/2 <sup>+</sup>	3.94 [10]	3.19	3.98			0	0				0	0							
1/2 <sup>+</sup>	3.96 [11,12]	4.01	4.17	0.02	0.06	0.05	0.04		?	?	0.64	0.30							
7/2 <sup>+</sup>		4.08	4.34			0	0				0	0							
1/2 <sup>+</sup>	(4.70) [13,14]	5.83	5.77			0.00	0.01	(0.08)	(0.17)		0.77	0.12							
3/2 <sup>+</sup>		5.09	4.98			0.01	0.01				0.07	0.06							
5/2 <sup>+</sup>	(5.57) [13,14]	5.59	5.44			0.00	0.01	2.5	2.4		0.93	3.31							
5/2 <sup>+</sup>	(6.01) [13,14]	5.82	6.06			0.02	0.01	1.6	1.3		2.92	1.52							

\* All states calculated to come below 5.2 MeV excitation are included.

Table 2  
Electric quadrupole and magnetic dipole transition strengths between states of  $^{35}\text{Cl}$ .

Initial state ( $J$ ) <sub>n</sub>	Final state ( $J$ ) <sub>n</sub>	$B(E2)$ in $e^2F^4$			$B(M1)$ in ( $\mu_N^2 \times 10^2$ )		
		Exp.	12.5p+ $^{17}\text{O}$	11.0h+aSPE	Exp.	12.5p+ $^{17}\text{O}$	11.0h+aSPE
(1/2) <sub>1</sub>	(3/2) <sub>1</sub>	16 ± 2 [16,10]	6.6	10.2	19 ± 6 [16]	27	16
(5/2) <sub>1</sub>	(3/2) <sub>1</sub>	78 ± 2 [16,10]	77.5	74.4	0.20 ± 0.06 [16]	1.2	0.0
"	(1/2) <sub>1</sub>		18.5	29.2		0	0
(7/2) <sub>1</sub>	(3/2) <sub>1</sub>	20 ± 7 [10,17]	30.7	29.7		0	0
"	(5/2) <sub>1</sub>	23 ± 10 [10,17]	34.4	23.6	2 ± 1 [10,17]	9.5	4.3
(3/2) <sub>2</sub>	(3/2) <sub>1</sub>	≥ 8 [17,9] ≤ 72 [18]	23.3	21.1	≥ 7 [17,9] ≤ 4 [18]	30	17
"	(1/2) <sub>1</sub>	≥ 32 [17,9] ≤ 130 [18]	67.5	63.9	≥ 1.7 [17,9] ≤ 2.1 [18]	23	11
"	(5/2) <sub>1</sub>	≥ 20 [17,9]	7.5	16.5	≥ 34 [17,9] ≤ 16 [18]	39	45
(5/2) <sub>2</sub>	(3/2) <sub>1</sub>	≥ 0.13 [17,9] 0.7 [18]	4.9	11.3	≥ 3.6 [17,9] 6.6 [18]	27	17
"	(1/2) <sub>1</sub>	≥ 40 [17,9] 43 [18]	51.2	36.4		0	0
"	(5/2) <sub>1</sub>		0.2	2.3		9	
(1/2) <sub>2</sub>	(3/2) <sub>1</sub>		11.8	13.2		11	12
"	(1/2) <sub>1</sub>		0	0		75	74
"	(5/2) <sub>1</sub>		0.4	2.7		0	0
(9/2) <sub>1</sub>	(5/2) <sub>1</sub>	46 ± 12 [10]	52.0	63.1		0	0
"	(7/2) <sub>1</sub>	18 ± 7 [10]	29.2	34.0	0.25 ± 0.14 [10]	0.01	0.3

from stripping and pickup experiments. The details are given in the last nine columns of table 1, which list experimental and calculated spectroscopic factors for  $0d_{5/2}$ ,  $1s_{1/2}$ , and  $0d_{3/2}$  single-nucleon transfer connecting  $^{35}\text{Cl}$ - $^{35}\text{Ar}$  to  $^{34}\text{S}$  and  $^{36}\text{Ar}$ . The numbers are given in the isotopic spin formalism.

Other aspects of the model wave functions can be examined by comparing calculated and measured values of electromagnetic observables. Electric quadrupole moments and  $B(E2)$  transition strengths were calculated from the model wave functions with the assumption of an effective charge  $\tilde{e}_p = 1.5e$  for each proton and an effective charge  $\tilde{e}_n = 0.5e$  for each neutron. The

single-particle matrix elements  $\langle r^2 \rangle$  were set equal to values given by single-particle harmonic-oscillator states for  $\hbar\omega = 41 A^{-1/3}$  MeV. In calculating magnetic dipole moments and  $B(M1)$  strengths, we used the free-nucleon gyromagnetic ratios. These are the same effective charges,  $\langle r^2 \rangle$  assumptions, and gyromagnetic ratios that we used in the  $A = 18 - 22$  calculations.

With these assumptions, the 12.5p +  $^{17}\text{O}$  and 11.0h + aSPE values for the ground-state quadrupole moment of  $^{35}\text{Cl}$  are  $-9.0 eF^2$  and  $-9.2 eF^2$ , respectively. The experimental value [3] is  $-7.9 eF^2$ . For the ground-state magnetic moment, the two theoretical values are  $+0.72$  and  $0.68 \mu_N$ , and the measured value [3] is  $0.82 \mu_N$ .

Table 2 lists  $B(E2)$  and  $B(M1)$  values for transitions among the low-lying states of  $^{35}\text{Cl}$ . As can be seen there, the agreement between these predictions and experimental data is generally satisfactory.

Insofar as the somewhat less complete experimental picture for the remainder of the  $A = 34 - 38$  region permits evaluation, the type of model-experimental agreement illustrated here for  $A = 35$ ,  $T = 1/2$  is typical for the  $A = 34 - 38$  region. In summary, then, we find in the  $A = 34 - 38$  region, as in the  $A = 18 - 22$  region, that most of the experimentally observed properties of the positive-parity states can be reproduced with reasonable accuracy by a  $(0s)^4(0p)^{12}(1s, 0d)^{A-16}$  shell model which incorporates "realistic" two-body interactions. Thus the identical approach can account simultaneously for the rotational features which are observed in nuclei near the lower end of the s-d shell and for the less easily classified features which are observed in nuclei near the upper end of the shell.

#### References

- [1] J. A. Kuehner and R. W. Ollerhead, *Phys. Letters* 20 (1966) 301.
- [2] C. Rolfs et al., *Bull. Am. Phys. Soc.* 15 (1970) 543.
- [3] P. M. Endt and C. van der Leun, *Nucl. Phys.* A105 (1967) 1.
- [4] B. Castel and K. W. C. Stewart, *Contributions - Int. Conf. on Properties of nuclear states, Montreal* (1969) 45.
- [5] B. W. Hooton, *Bull. Am. Phys. Soc.* 14 (1969) 626.
- [6] E. C. Halbert, J. B. McGrory and B. H. Wildenthal, *Phys. Rev. Letters* 20 (1968) 1112; E. C. Halbert, in *Third Symposium on the Structure of low-medium mass nuclei*; E. C. Halbert, J. B. McGrory, B. H. Wildenthal and S. P. Pandya, to be published.
- [7] T. T. S. Kuo, *Nucl. Phys.* A103 (1967) 71.
- [8] T. T. S. Kuo, to be published.
- [9] P. Taras and J. Matas, *Can. J. Phys.* 48 (1970) 603.
- [10] F. Ingebretsen, C. Broude and J. S. Forster, *Phys. Letters* 31B (1970) 297.
- [11] A. Graue et al., *Nucl. Phys.* A136 (1969) 577.
- [12] R. A. Morrison, *Nucl. Phys.* A140 (1970) 97.
- [13] R. L. Kozub, *Phys. Rev.* 172 (1968) 1078.
- [14] R. R. Johnston and R. J. Griffiths, *Nucl. Phys.* A108 (1968) 113.
- [15] C. A. Whitten Jr., M. C. Mermaz and D. A. Bromley, *Phys. Rev.* (in press).
- [16] O. Häusser et al., *Can. J. Phys.* 47 (1969) 1065.
- [17] F. Ingebretsen et al., *Can. J. Phys.* 47 (1969) 1295.
- [18] D. D. Duncan et al., *Phys. Rev.* 185 (1969) 1515.

\* \* \* \* \*

MEASUREMENT OF  $T_z = -\frac{3}{2}$  MASSES AND THE ISOBARIC MULTIPLET MASS EQUATION.\*

G. F. Trentelman, B. M. Freedom,† and E. Kashy

Cyclotron Laboratory, Michigan State University, East Lansing, Michigan 48823

(Received 18 June 1970)

Precise measurements of the masses of  $^9\text{C}$ ,  $^{13}\text{O}$ , and  $^{21}\text{Mg}$  have been made using a magnetic spectrograph. The results are used to test the isobaric multiplet mass equation.

One of few simply calculable model-independent expressions in nuclear physics is the isobaric multiplet mass equation,

$$M(\beta, T, T_z) = a(\beta, T) + b(\beta, T)T_z + c(\beta, T)T_z^2,$$

where  $\beta$  represents all necessary quantum numbers in addition to the isospin. The derivation of this equation treats charge-dependent forces as a first-order perturbation to a charge-independent nuclear Hamiltonian.<sup>1,2</sup>

Testing the validity of this equation requires knowing the masses of all members of at least isospin  $T = \frac{3}{2}$  quartets. At present the members of eight such multiplets ( $A = 7$  through 37) have been measured and reported,<sup>2,3</sup> but until recently the experimental uncertainties associated with the  $T_z = -\frac{3}{2}$  masses have been substantially larger than those of the other multiplet members.

Two recent measurements<sup>4,5</sup> of the  $^9\text{C}$  mass

excess to a precision  $\pm 4$  keV have been reported, and this uncertainty is commensurate with that of other members of the  $A = 9$ ,  $T = \frac{3}{2}$  quartet  $\pm 5$  keV. Application of the mass equation to this quartet indicates that a term in  $T_z^3$  with a coefficient of  $9.2 \pm 3.7$  keV may be added to the mass equation, at least for  $A = 9$ . It is of importance then to measure other of the  $T_z = -\frac{3}{2}$  masses with minimal experimental uncertainty not only to check the general precision of the quadratic mass equation but also to see if the occurrence of cubic terms persists in the other multiplets.

This Letter reports the measurement of the masses of  $^9\text{C}$ ,  $^{13}\text{O}$ , and  $^{21}\text{Mg}$  using ( $^3\text{He}$ ,  $^6\text{He}$ ) reactions on  $^{12}\text{C}$ ,  $^{16}\text{O}$ , and  $^{24}\text{Mg}$ , respectively. The  $^3\text{He}$  beam from the sector-focused Michigan State University cyclotron was used at various energies between 68 and 70 MeV and the  $^6\text{He}$  reaction products were detected in an Enge split-

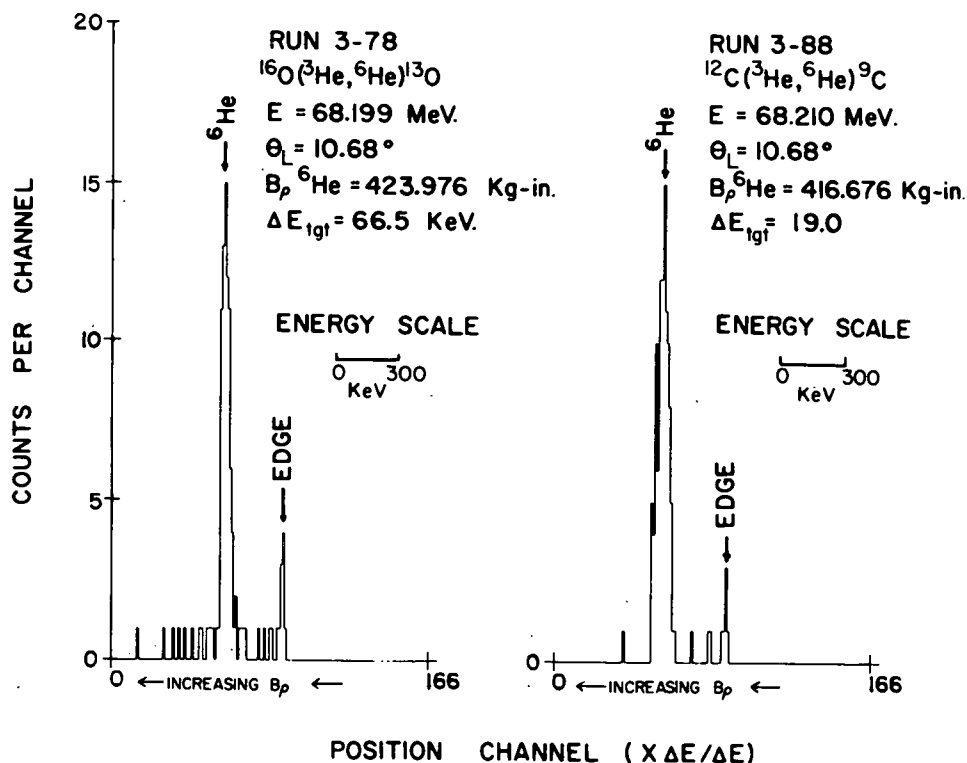


FIG. 1. Typical position spectra for  $^{16}\text{O}(^3\text{He}, ^6\text{He})^{13}\text{O}$  and  $^{12}\text{C}(^3\text{He}, ^6\text{He})^9\text{C}$ . The  $\Delta E_{\text{tgt}}$  represents energy correction to the  $Q$  value due to target effects. The peak marked "EDGE" indicates the end of the counter.

Table I. Reaction  $Q$  values and mass excesses for the  $T_z = -\frac{3}{2}$  nuclei  ${}^9\text{C}$ ,  ${}^{13}\text{O}$ , and  ${}^{21}\text{Mg}$ .

Element	Reaction	$Q$ Value (MeV)	Mass excess (MeV)	Mass excess previously reported (MeV)
${}^9\text{C}$	${}^{12}\text{C}({}^3\text{He}, {}^6\text{He}){}^9\text{C}$	$-31.578 \pm 0.008$	$28.911 \pm 0.009$	$28.906 \pm 0.004^a$
${}^{13}\text{O}$	${}^{16}\text{O}({}^3\text{He}, {}^6\text{He}){}^{13}\text{O}$	$-30.506 \pm 0.013$	$23.103 \pm 0.014$	$23.11 \pm 0.070^b$
${}^{21}\text{Mg}$	${}^{24}\text{Mg}({}^3\text{He}, {}^6\text{He}){}^{21}\text{Mg}$	$-27.512 \pm 0.018$	$10.912 \pm 0.018$	$10.95 \pm 0.120^c$

<sup>a</sup>See Ref. 4.<sup>b</sup>See Ref. 3.<sup>c</sup>See Ref. 2.

pole magnetic spectrograph. The spectrograph compensates for the energy spread due to the reaction kinematics and thus allows a large-solid-angle (1.2-msr) entrance aperture to be used. This is a definite advantage as the cross sections for the ( ${}^3\text{He}$ ,  ${}^6\text{He}$ ) reactions are small ( $\sim 1 \mu\text{b}$ ), and they also decrease with increasing target mass.

The magnetic rigidity of the particles was precisely calibrated for a particular orbital path in the spectrograph from 280 to 470 kG in. with a momentum-matching technique developed in this laboratory.<sup>6</sup> This technique requires, for example, the simultaneous detection at the same position on the focal plane of both protons and deuterons from a pair of reactions such as  ${}^{12}\text{C}(p, p){}^{12}\text{C}$  and  ${}^{12}\text{C}(p, d){}^{11}\text{C}$ . This condition is met at a given laboratory scattering angle only for a unique beam energy such that the magnetic rigidities of the outgoing protons and deuterons are equal. For these reactions at a laboratory scattering angle of  $15.0^\circ$ , the momentum matching yields  $E_p(\text{beam}) = 33.691 \pm 0.0022$  MeV and  $B\rho$  (spectrograph) = 332.256 kG in. The 2.2-keV uncertainty represents the limit of the accuracy in determining the beam energy by this method and reflects the uncertainty in the mass of  ${}^{11}\text{C}$ . This uncertainty, however, contributes only a small amount of the error in the determination of the absolute value of the masses presented below.

The energy of the  ${}^3\text{He}$  beam for each run was determined by elastic scattering from  ${}^{12}\text{C}$  and  ${}^{16}\text{O}$  in the calibrated spectrograph described above. The laboratory scattering angle for the  ${}^3\text{He}$ -induced reactions was sensitively measured with  ${}^1\text{H}({}^3\text{He}, {}^3\text{He}){}^1\text{H}$  scattering. Particle detection and identification for all reactions was made with a 300- $\mu\text{m}$  position-sensitive silicon surface-barrier detector on line with an XDS Sigma-7 computer. Figure 1 shows typical position spectra and experimental parameters for the reactions  ${}^{12}\text{C}({}^3\text{He}, {}^6\text{He}){}^9\text{C}$  and  ${}^{16}\text{O}({}^3\text{He}, {}^6\text{He}){}^{13}\text{O}$ . Eight such spectra were obtained for  ${}^9\text{C}$ , nine for  ${}^{13}\text{O}$ , and four for  ${}^{21}\text{Mg}$ . A more detailed account of the experimental procedures and their intrinsic uncertainties will be reported later.

Table I lists the reactions, their measured  $Q$  values and resulting mass excesses, as well as the latest published values of these masses for comparison. A principal source of error in the data shown in this table is the uncertainty in the energy loss in the targets. Other numerous contributions to the uncertainties arise from sources such as calibration of the spectrograph, statistical uncertainty in the centroids, scattering-angle determination, etc. A detailed analysis of these errors will be presented in a later paper.

Table II displays the coefficients  $a(\beta, T)$ ,  $b(\beta, T)$ , and  $c(\beta, T)$  of the quadratic mass equation obtained from a weighted least-squares fit of the

Table II. Empirically determined coefficients for the mass equation  $M = a + bT_z + cT_z^2$  using the latest  $T_z = -\frac{3}{2}$  mass excess values.<sup>a</sup> The last column indicates the coefficient of a  $T_z^3$  term assuming the equation to have the form  $M = a + bT_z + cT_z^2 + dT_z^3$ . The coefficients were determined from a weighted least-squares fit, and the  $\chi^2$  for the fit with the quadratic equation is indicated.

Mass	$a(\beta, T)$ (MeV)	$b(\beta, T)$ (MeV)	$c(\beta, T)$ (MeV)	$\chi^2$	$d(\beta, T)$ (MeV)
9	$26.343 \pm 0.004$	$-1.3185 \pm 0.003$	$0.266 \pm 0.003$	4.0	$0.0083 \pm 0.0039$
13	$19.257 \pm 0.0027$	$-2.1802 \pm 0.0035$	$0.256 \pm 0.003$	0.002	$-0.0002 \pm 0.0035$
21	$4.8987 \pm 0.0046$	$-3.6573 \pm 0.005$	$0.240 \pm 0.0048$	1.28	$0.0057 \pm 0.0051$

<sup>a</sup>For mass excesses of  $T_z = \frac{3}{2}, -\frac{1}{2}$ ; for  $T = \frac{3}{2}$  multiplet members, see Table I in Ref. 2.

masses -9, -13, and -12 quartets using the  $T_z = -\frac{3}{2}$  masses measured here and the masses taken from Ref. 2 for the  $T_z = \frac{3}{2}, \frac{1}{2},$  and  $-\frac{1}{2}$  members. The value of  $\chi^2$  was calculated from the equation

$$\chi^2 = \sum_i \left[ \frac{M(\text{calc}) - M(\text{expt})}{\sigma_M(\text{expt})} \right]^2$$

The deviation of the data from the quadratic fit is shown in Fig. 2. It is seen that the quadratic mass dependence predicts the mass values within their measured errors for  $A = 13$  and 21 and slightly misses two of the values for  $A = 9$ .

As has been pointed out, one may expect cubic terms in the isobaric multiplet mass equation to arise from a more exact treatment of charge-dependent forces.<sup>3</sup> Adding a term  $d(\beta T)T_z^3$  to the quadratic equation above and fitting to the data as before, one obtained the values of  $d$  presented in Table II. The uncertainty shown for  $d$  is determined as much by the errors in the  $T_z = \frac{1}{2}$  members of the quartet as by the present values of the  $T_z = -\frac{3}{2}$  members although the latter actually have larger errors. Only the  $A = 9$  quartet shows some justification for a cubic term. If such a cubic term does indeed exist, its magnitude has been estimated to be of the order of  $c\alpha Z_{av}$ , where  $c$  is the coefficient of the quadratic term,  $Z_{av}$  is the average charge of the isobaric multiplet, and  $\alpha$  is the fine-structure constant.<sup>2</sup> For  $A = 9$  this value is approximately 9 keV and the value of  $d = 8.3 \pm 3.9$  keV obtained here is not inconsistent with that estimate. Pursuing this topic further, measurements of the masses from <sup>25</sup>Si to <sup>37</sup>Ca are in progress using the same experimental techniques presented here.

It is clear that measurements of improved accuracy are required for all members of the isobaric multiplets if one hopes to use the mass equation to obtain more definite conclusions concerning the role of charge-dependent forces in nuclei. In the meantime, in view of the present results, one can use the quadratic isobaric multiplet mass equation to extrapolate to unknown masses with a high degree of confidence.

This work would not have been possible without the continuing effort of the Michigan State University cyclotron staff. We are also indebted

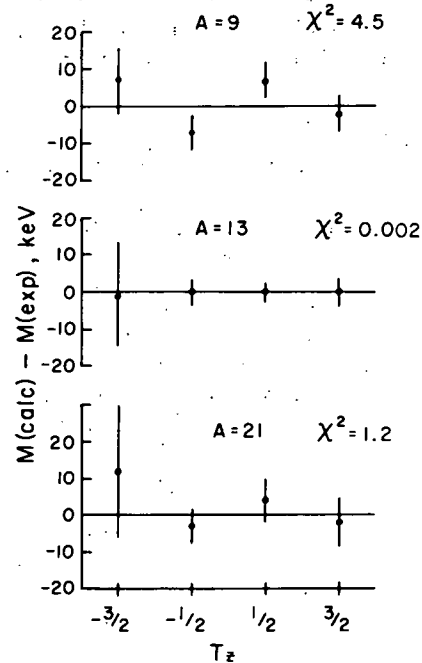


FIG. 2. Deviation of experimental  $T = \frac{3}{2}$  multiplet members from quadratic mass equation using the coefficients of Table II.

to Professor R. Sherr for many stimulating discussions on the importance of testing the mass equation.

\*Work supported by the National Science Foundation.

†Present address: Physics Department, University of South Carolina, Columbia, S. C.

<sup>1</sup>D. H. Wilkinson, Phys. Rev. Lett. **13**, 571 (1964), and Phys. Lett. **11**, 243 (1964).

<sup>2</sup>G. T. Garvey, in *Proceedings of the Second Conference on Nuclear Isospin, Asilomar-Pacific Grove, California, 13-15 March 1969*, edited by J. D. Anderson, S. D. Bloom, J. Cerny, and W. W. True (Academic, New York, 1969), p. 703.

<sup>3</sup>J. Cerny, Annu. Rev. Nucl. Sci. **18**, 27 (1968).

<sup>4</sup>C. A. Barnes, E. G. Adelberger, D. C. Hensley, and A. B. McDonald, in *Nuclear Physics: An International Conference*, edited by R. L. Becker, C. D. Goodman, P. H. Stelson, and A. Zucker (Academic, New York, 1967), p. 261.

<sup>5</sup>J. M. Mosher, R. W. Kavanagh, and T. A. Tombrillo, Bull. Amer. Phys. Soc. **14**, 1167 (1969).

<sup>6</sup>G. F. Trentelman and E. Kashy, to be published.

## USE OF THIN SEMICONDUCTOR POSITION SENSITIVE DETECTORS IN MAGNETIC SPECTROGRAPHS\*

R. K. JOLLY, G. F. TRENTELMAN and E. KASHY

*Cyclotron Laboratory, Michigan State University, East Lansing, Michigan 48823, U.S.A.*

Received 22 June 1970

Thin position sensitive silicon surface-barrier detectors in a magnetic-spectrograph have been found to yield good position resolution and a high degree of discrimination between various particles.

Solid state position sensitive detectors have become increasingly popular for detection of charged particles in magnetic spectrometers despite their high cost. These devices offer good position resolution and a high count rate capability in addition to highly discriminating particle identification.

A plot of the energy loss  $\Delta E$ , and straggling of the particles in silicon detectors as a function of their magnetic rigidity is shown in fig. 1. There are three sets of curves for three different detector thicknesses. The energy loss and straggling calculations were made using a computer code "Target"<sup>1</sup>). This code numerically integrates the Bethe-Bloch expression for  $dE/dx^2$  over the thickness of the detector. Calculations such as those of fig. 1 are essential in making a proper choice of thickness of these relatively costly devices. Two considerations are to be kept in mind. First, for counters where the energy loss is small, the position resolution may be significantly limited by noise. Second, for detectors such as the 425 $\mu$  of fig. 1 the separation of  $^3\text{H}$  from  $^3\text{He}$  does not pose great difficulty as these particles are seldom produced in that particular ratio of energies where their energy losses are the same.

The variable energy cyclotron at Michigan State University is capable of accelerating protons from 5-13 MeV and also 20-50 MeV, deuterons from 12-25 MeV,  $^3\text{He}^{++}$  from 17-40 MeV and 60-70 MeV, and  $\alpha$ -particles from 23-50 MeV. On the basis of the considerations above 425 $\mu$  (300 $\mu$  with the particles incident at 45°) was chosen as an optimum thickness for the detectors to be usable for the greatest number of experiments. Examples of particle separation achieved with a detector of this thickness are shown in figs. 2 and 3. Fig. 2 shows a group of  $^6\text{He}$  particles along with deuterons, tritons and  $\alpha$ -particles from the reactions  $^{12}\text{C}(^3\text{He},x)$ . Fig. 3 shows the separation between protons, deuterons, tritons and  $\alpha$ -particles which according to fig. 1 should be in the ratio 1.5, 5.4, 9.7 and 27. The

data shown in fig. 3 is in agreement with the calculations shown in fig. 1. One does not see any  $^3\text{He}$  particles since these are energetically forbidden.

These detectors have been used in various reactions

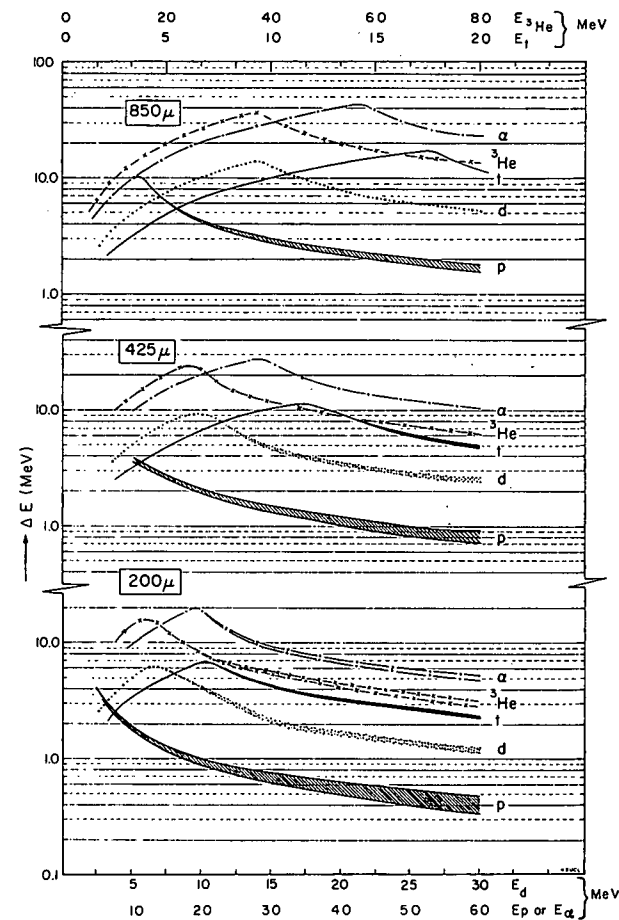


Fig. 1. A plot of the energy loss  $E$  and straggling of various particles in silicon detectors (thickness shown in boxes). The energies of protons, deuterons, tritons,  $^3\text{He}$  and  $\alpha$ -particles in MeV are shown along the abscissa and correspond to equal values of magnetic rigidity.

\* Work supported by the National Science Foundation.



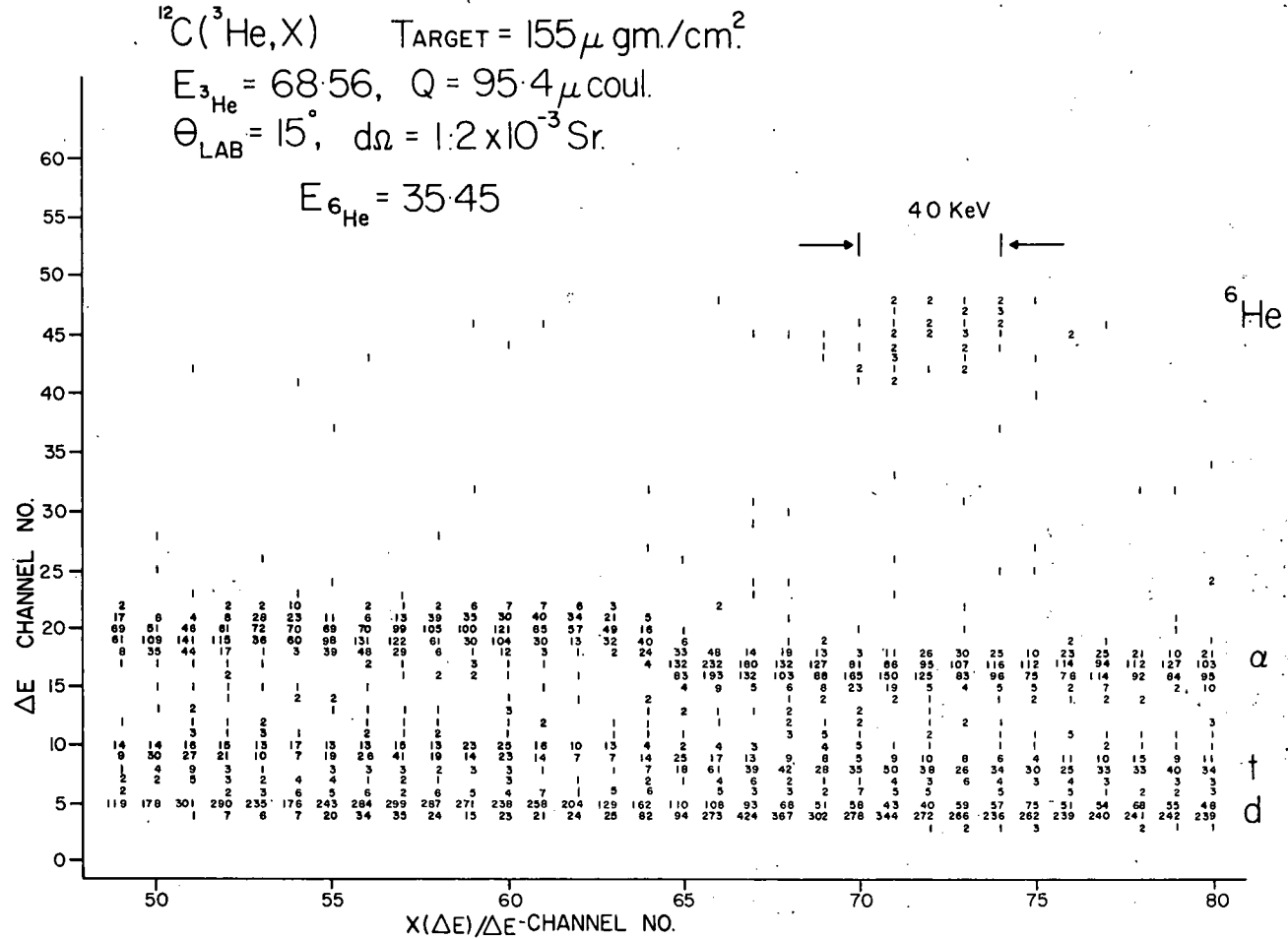


Fig. 2. A 2-D display of energy loss of deuterons, tritons,  $\alpha$ -particles and  $^6\text{He}^{++}$  particles as a function of position along the detector. The step shaped deviation in the energy loss (most apparent for  $\alpha$ -particles) is due to non-uniformity of the depletion layer and was cured by overbiasing the detector (fig. 3).

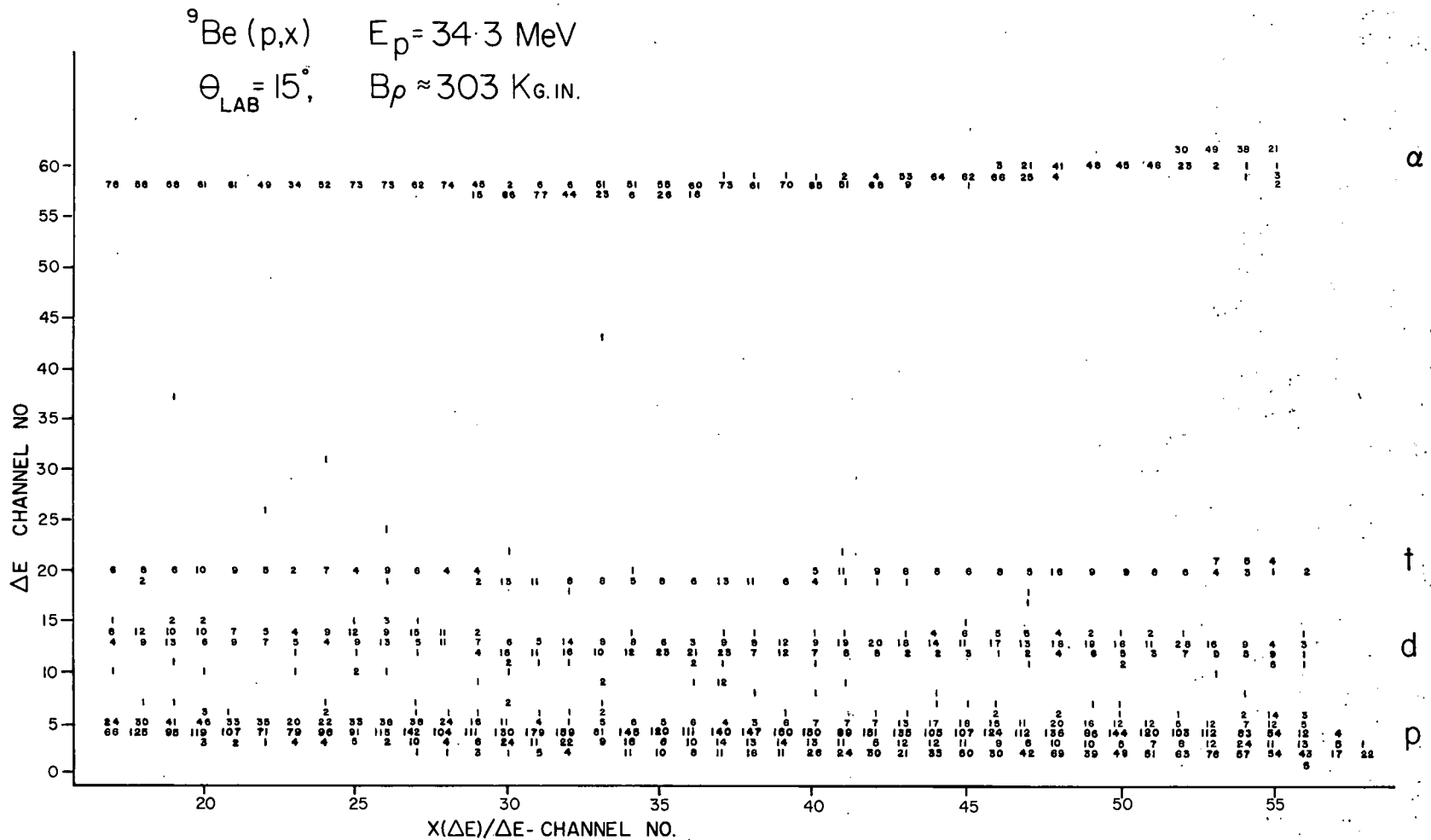


Fig. 3. A 2-D display of energy loss of protons, deuterons, tritons, and  $\alpha$ -particles on an expanded  $\Delta E$  scale to show the separation between the less ionizing particles more clearly than in fig. 2.

and the overall resolution obtained is typified by the following examples:

1. 10 keV (0.4 mm) for 25 MeV deuterons from the reaction  $^{144}\text{Sm}(p,d)$  with 35 MeV protons;

2. 40 keV (noise limited) for 33.6 MeV protons scattered from  $^{16}\text{O}$ ;

3. 9 keV for 10 MeV tritons in the  $^{58}\text{Ni}(p,t)$  with 34 MeV protons.

The contribution to the above numbers from beam energy spread and the aberrations in the spectrometer

was small. This was determined in another measurement of 30 MeV protons elastically scattered from a Bi target where a resolution of  $\sim 5$  keV (fwhm) was achieved using nuclear emulsions<sup>3</sup>.

#### References

- 1) J. J. Kolata, Michigan State University, Cyclotron Laboratory, Sigma-7 Computer Library Code 0022.
- 2) R. D. Evans, *The atomic nucleus* (McGraw-Hill Book Co., New York) p. 638.
- 3) H. Blosser et al., to be published.

## Experimental Studies of Neutron-Deficient Gadolinium Isotopes. III. The Strange Case of Gd<sup>145g</sup>

R. E. Eppley and Wm. C. McHarris

*Department of Chemistry\* and Cyclotron Laboratory,† Department of Physics, Michigan State University,  
East Lansing, Michigan 48823*

and

W. H. Kelly

*Cyclotron Laboratory,† Department of Physics, Michigan State University, East Lansing, Michigan 48823*

(Received 20 August 1970)

The  $\gamma$  rays emitted following the decay of 21.8-min Gd<sup>145g</sup> have been studied using Ge(Li) and NaI(Tl) detectors in a variety of singles, anticoincidence, pair-coincidence, and two-dimensional ("megachannel") coincidence experiments. Of the 38  $\gamma$  rays attributed to this decay, 27 (accounting for >97% of the intensity) have been placed in a consistent decay scheme that includes 20 states in Eu<sup>145</sup>. All of the single-proton states between  $Z=50$  and 82 are seen (including the  $h_{11/2}$  state populated directly by the decay of Gd<sup>145m</sup>), and the associated  $\beta$  and  $\gamma$  transitions are accounted for quite well using simple shell-model arguments. In addition, we propose an explanation for the abrupt change in decay properties of the  $N=81$  isotones that occurs at Gd<sup>145g</sup>, viz., the lack of observable population directly to the Eu<sup>145</sup> ground state but 72.6% of its decay going to states at 1757.8 and 1880.6 keV. With a  $(\nu s_{1/2})^{-1}$  ground state for Gd<sup>145</sup>, these "fast"  $\beta$  transitions can be represented as

$$(\pi h_{11/2})^{2n}(\nu s_{1/2})^{-1} - (\pi h_{11/2})^{2n-1}(\nu h_{9/2})(\nu s_{1/2})^{-1},$$

making the final states another example of three-quasiparticle states being populated by the  $\beta^+/\epsilon$  decay of nuclei below  $N=82$ .

### I. INTRODUCTION

This investigation continues our over-all studies of the neutron-deficient Gd isotopes, the decay<sup>1</sup> of Gd<sup>149</sup> and the characterization<sup>2</sup> of the isomer, Gd<sup>145m</sup>, having been reported previously.

Although several earlier papers speculated on Gd<sup>145</sup>, Grover<sup>3</sup> in 1959 seems to have been the first to characterize this nuclide to any degree of clarity. It was also reported at about the same time by Olkowsky *et al.*<sup>4</sup> Both sets of results, having been obtained with NaI(Tl) detectors, were incomplete. A good example is the fact that the two intense  $\gamma$ -ray transitions at 1757.8 and 1880.6 keV were unresolved. The NaI(Tl) data showed these as a composite peak reported to have an energy of 1.75 MeV,<sup>3</sup> although with some insight Grover decided that there were two transitions, but he did not elucidate further.

As far as we have been able to determine, no conversion-electron studies have ever been made on Gd<sup>145g</sup> decay, and, indeed its short half-life (21.8 min; cf. Sec. III D below) and the high energies of its stronger transitions make such experiments impracticable. And until the recent paper by Newman *et al.*,<sup>5</sup> no high-resolution [i.e., Ge(Li)]  $\gamma$ -ray studies had been reported. The lack, now and in the foreseeable future, of electron data cripples one in trying to assemble a com-

plete decay scheme, for he has to work without direct information on the multipolarities of the transitions. However, the spins and parities of a number of the lower-lying states in the daughter Eu<sup>145</sup> were determined by Newman *et al.*<sup>5</sup> through an analysis of the Sm<sup>144</sup>( $\tau, d$ )Eu<sup>145</sup> reaction. This reaction tends to discriminate against complex states, and, as will be seen later in this paper, we have reason to believe that the primary states populated by the decay of Gd<sup>145g</sup> are complex. Our work has proceeded in parallel with the work of Newman *et al.*, and there has been exchange of information between the groups.<sup>6</sup> They concentrated on the ( $\tau, d$ ) studies, however, taking only singles  $\gamma$ -ray spectra, whereas we have concentrated on  $\gamma$ -ray studies, using various coincidence and anticoincidence techniques. Their experiments thus excite and explain many of the more straightforward lower-lying states that we see only weakly or not at all. On the other hand, we see evidence of a number of higher-lying states populated or depopulated by weak  $\gamma$  rays, and we think that we can explain what we call the "strange case" of Gd<sup>145g</sup> decaying overwhelmingly to the two states at 1757.8 and 1880.6 keV in Eu<sup>145</sup>. Here, then, is an excellent case where  $\beta$ - $\gamma$  spectroscopy from one laboratory and reactions spectroscopy from another laboratory supplement and complement each other.

By the "strange case" we mean the abrupt break

in the decay properties of the odd-mass  $N=81$  isomer pairs<sup>2</sup> that occurs at  $Gd^{145g}$ . By now there is a well-known series of seven  $N=81$  isomer pairs, the ground state in each case presumably being a single  $d_{3/2}$  neutron hole in the  $N=82$  closed shell, and the metastable state being a single  $h_{11/2}$  neutron hole in the same shell. The metastable states decay exclusively to the ground states via an  $M4$  transition in the lighter-mass isotones, although recently some direct branching has been observed from  $Sm^{143m}$  decay<sup>7</sup> and  $Gd^{145m}$  decay<sup>2</sup> to the  $h_{11/2}$  states in  $Pm^{143}$  and  $Eu^{145}$ . More germane to the present work, on the neutron-deficient side of the series the  $(\nu d_{3/2})^{-1}$  ground states of  $_{58}Ce^{139}$ ,  $_{60}Nd^{141}$ , and  $_{62}Sm^{143}$  (Geiger *et al.*,<sup>8</sup> Beery, Kelly, and McHarris,<sup>9</sup> and DeFreene,<sup>10</sup> respectively) all decay in a very straightforward fashion to the  $\pi d_{5/2}$  states in their daughter nuclei. *A priori* there was no reason to expect the decay of  $_{64}Gd^{145g}$  to behave otherwise, yet it was soon discovered there there is essentially no decay to the  $\pi d_{5/2}$  ground state of  $Eu^{145}$  – its unhindered decay populates the two aforementioned high-lying states. We now think we have a reasonable explanation for this, involving: (1) a crossing of the  $\nu d_{3/2}$  and  $\nu s_{1/2}$  orbits such that the ground state of  $Gd^{145}$  is really  $(\nu s_{1/2})^{-1}$ , coupled with (2) a shift downward in energy of the  $\pi h_{11/2}$  orbits, allowing an appreciable  $(\pi h_{11/2})^{2n}$  component in the  $Gd^{145}$  wave function. There is now indirect evidence<sup>2,5</sup> for both of these, and if they be true, the decay of  $Gd^{145}$  can be described as a “straightforward decay” into high-lying three-quasiparticle states, somewhat analogous to the decay<sup>11</sup> of  $Nd^{139m}$ . This will be discussed in some detail below.

## II. SOURCE PREPARATION

$Gd^{145g}$  sources were prepared primarily by the  $Sm^{144}(\tau, 2n)Gd^{145}$  reaction, which has a  $Q$  value of  $-10.6$  MeV.<sup>12</sup> Beams of  $\tau$  particles at 20 MeV (the threshold for  $Gd^{144}$  production), furnished by the Michigan State University (MSU) sector-focused cyclotron, were used to bombard enriched targets of  $Sm^{144}_2O_3$  (95.10%  $Sm^{144}$ , obtained from the Isotopes Division, Oak Ridge National Laboratory). Typically, 25-mg targets were bombarded for 1–2 min with  $0.5 \mu A$  of beam current. We also used the  $Sm^{144}(\alpha, 3n)Gd^{145}$  reaction ( $Q = -30.9$  MeV) to prepare a few sources, bombarding similar targets with 40-MeV  $\alpha$  particles from the MSU cyclotron.

It is interesting to note the competing reactions that can accompany  $(\tau, xn)$  reactions. After a bombardment at MSU to produce  $Gd^{143}$  by the  $Sm^{144}(\tau, 4n)Gd^{143}$  reaction ( $Q = -31.2$  MeV) using 40-MeV  $\tau$ 's, we found that we had produced quite a pure source<sup>13</sup> of  $Sm^{141m+g}$ , most likely by a  $Sm^{144}(\tau, \alpha 2n)Sm^{141}$  reaction ( $Q = -9.8$  MeV). Also, on attempting to produce  $Dy^{147}$  by the  $Nd^{142}(C^{12}, 7n)Dy^{147}$  reaction ( $Q = -74.9$  MeV) using 70–120-MeV  $C^{12}$  beams from the Yale University heavy-ion accelerator, we found a sizable amount of  $Gd^{145}$  to be present, presumably through the competing  $Nd^{142}(C^{12}, \alpha 5n)Gd^{145}$  reaction ( $Q = -56.2$  MeV). And, as a climax we found we were also able to produce  $Gd^{145}$  by the  $Sm^{144}(C^{12}, 2\alpha 3n)Gd^{145}$  reaction ( $Q = -38.4$  MeV), which has an unexpectedly large cross section. It must proceed by a combination of cluster stripping and compound-nucleus formation. The low binding energies of  $\alpha$  particles in these neutron-deficient nuclei below  $N=82$  and the fact that  $\alpha$  particles can efficiently carry away large amounts of angular momentum make for large cross sections for evaporating  $\alpha$  particles as well as neutrons. Not only does this cause a large number of different nuclides to be made in most bombardments, thus complicating the task of analysis, but also it may set a practical limit on the use of standard bombarding techniques for the production of nuclei farther from stability in this region.

Our bombardments with the 20-MeV  $\tau$  beam did, however, produce quite pure sources of  $Gd^{145g}$ . Here, apparently, the bombarding energy was too low for any competing  $(\tau, \alpha xn)$  reactions. The next higher-mass nuclide,  $Gd^{146}$ , which should still have an appreciable formation cross section at this energy has a half-life of 48 days and thus posed no problem. In addition,  $Eu^{145}$  has a half-life of 5.9 days and a well-worked-out decay scheme,<sup>14</sup> so we did not have to worry about contamination of the spectra by daughter transitions.

Each source was counted within 2–3 min of the end of the bombardment and counted for varying intervals of time up to a maximum of 80 min, approximately four half-lives. The  $\gamma$  rays attributed to  $Gd^{145}$  decay all retained their constant relative intensities over this period.

## III. EXPERIMENTAL DATA

### A. Singles $\gamma$ -Ray Spectra

Two separate Ge(Li) detectors were used to obtain the  $Gd^{145g}$   $\gamma$ -ray spectra. One has a 7-cm<sup>3</sup>-active-volume five-sided coaxial detector [ $\approx 0.5\%$  efficient for the  $Co^{60}$  1333-keV  $\gamma$  ray, compared with a 3×3-in. NaI(Tl) detector at 25 cm] manufactured in this laboratory, the other a 2.6% efficient detector manufactured by Nuclear Diodes, Inc. The best resolution we obtained was 2.3 keV full width at half maximum for the  $Co^{60}$  1333-keV peak. Both detectors were used with room-temperature field-effect transistor preamplifiers, linear amplifiers having near-Gaussian pulse

shaping and pole-zero compensation, and 4096-channel analyzers or analog-to-digital converters (ADC) interfaced to computers.

The  $\gamma$ -ray energies were determined by counting the spectra simultaneously with the standards listed in Table I of Ref. 1. The larger peaks in the spectrum were first calibrated by use of the standards. These calibrated peaks, in turn, were used to determine the energies of the weaker peaks in spectra taken without the standards. The centroids and net peak areas were determined with the aid of the computer code SAMPO.<sup>15</sup> The backgrounds were first subtracted and the centroids then determined by fitting the peaks to Gaussian functions having exponential tails on both the upper and lower sides of the peaks. The specific peak shapes were determined by comparisons with reference peaks specified at intervals throughout the spectrum. The energies were then determined by fitting the centroids to a quadratic calibration equation. Peak areas were then converted to  $\gamma$ -ray intensities through curves previously determined in this laboratory<sup>16</sup> for each detector. These

curves were obtained by using a set of standard  $\gamma$ -ray sources whose relative intensities had been carefully measured with a 3 $\times$ 3-in. NaI(Tl) detector.

A word about the energies of the higher-energy  $\gamma$  rays ( $E_\gamma > 1880.6$  keV): Because of the weakness of these peaks it was not possible to observe them in spectra when standards were counted simultaneously. Thus, we had to resort to an extrapolation of our calibration curves up into this region. Various polynomial extrapolations were tried and discarded, for we found that a linear extrapolation gave the best agreement between the energies of the photopeak and those determined from double-escape peaks falling within our well-calibrated energy range. One should be somewhat wary, however, of systematic errors in the energies of these  $\gamma$  rays.

After taking spectra from and following the decay of at least 15 different Gd<sup>145g</sup> sources prepared at widely differing times, we have identified 38  $\gamma$  rays as resulting from the  $\beta^+/\epsilon$  decay of Gd<sup>145g</sup>. A singles spectrum taken with the 7-cm<sup>3</sup>

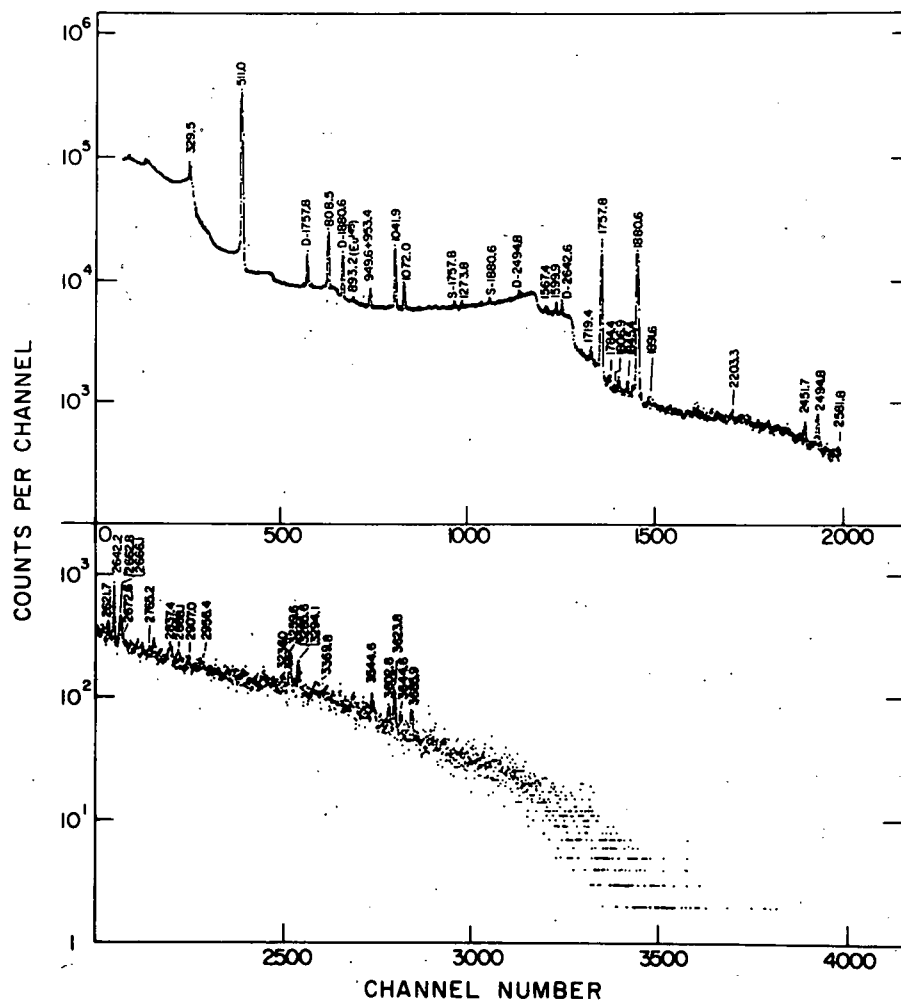


FIG. 1. Gd<sup>145g</sup> singles  $\gamma$ -ray spectrum taken with a 7-cm<sup>3</sup> Ge(Li) detector.

detector is shown in Fig. 1. A list of these  $\gamma$  rays and their relative intensities is given in Table I, where they are compared with the results of Newman *et al.*<sup>5</sup> All values from our work are the averages from many determinations, with the quoted errors reflecting the statistical fluctuations found among the different runs and the quoted errors on the standards used.

### B. Coincidence Spectra

1. *Anticoincidence spectra.* One of the most convenient "first steps" in elucidating a complex decay scheme such as that of  $\text{Gd}^{145g}$  is to determine which transitions are ground-state transitions, especially primarily  $\epsilon$ -fed ground-state transitions. To obtain such information we performed an anticoincidence experiment between the 7-cm<sup>3</sup> Ge(Li) detector and an 8×8-in. NaI(Tl) split annulus. This setup has been described in detail elsewhere,<sup>17</sup> but in brief it works as follows: The Ge(Li) detector is placed inside one end of the annulus tunnel and a 3×3-in. NaI(Tl) detector is used to plug the other end. The Ge(Li) detector is operated in an anticoincidence mode (resolving time,  $2\tau \approx 200$  nsec) with either (optically isolated) half of the annulus or the 3×3-in. detector. Thus, the system serves both as a Compton-suppression and, more important, as a cascade-suppression spectrometer. An anticoincidence spectrum is shown in Fig. 2, and the relative intensities of the  $\gamma$  rays in this spectrum are compared with those in the singles spectra in Table II.

2. *Megachannel coincidence spectra.* Our two-dimensional "megachannel" coincidence experiment utilized two Ge(Li) detectors, the Nuclear Diodes 2.5% detector and an ORTEC 3.6% detector. A block diagram of the electronics is shown in Fig. 3. The experiment was much like a standard fast-slow coincidence experiment, except that both the  $x$  and  $y$  events were processed each time a fast-coincident event was detected. The  $x$  and  $y$  addresses were stored in the two halves of a single (32-bit) word in a dedicated buffer in the MSU Cyclotron Laboratory Sigma-7 computer. When the buffer was filled, events were collected in a second, similar buffer while the contents of the first were written on magnetic tape. The spectra were recovered later off-line by a program that allowed one to obtain gated "slices" with or without a linearly interpolated background subtraction.<sup>18</sup>

The short half-life of  $\text{Gd}^{145g}$ , coupled with the fact that there just are not too many coincidences associated with its decay, makes it difficult to obtain "pretty" coincidence spectra. In order to record as many coincidence events as possible during a limited counting time, we used a 180° geome-

TABLE I. Energies and relative intensities of  $\gamma$  rays from the decay of  $\text{Gd}^{145g}$

This work		Ref. 5	
Energy (keV)	Intensity <sup>a</sup>	Energy (keV)	Intensity <sup>b</sup>
329.5±0.2	30.8±2.0	330.1	31
808.5±0.2	≅100	808.4	≅100
949.6±0.3	8.6±0.3	949.4	5.9
953.4±0.3	15.8±0.3	953.7	11.8
1041.9±0.2	112±4.0	1041.9	107
1072.0±0.4	31±1.0	1072.2	17.6
1567.4±0.2	10.4±0.2	1567.5	10.2
1599.9±0.2	20±0.4	1599.9	19.6
1719.4±0.2	13.3±0.1	1719.5	11.8
1757.8±0.3	380±10	1757.9	392
1784.4±0.4	4.8±0.2		
1806.9±1.0 <sup>c</sup>	2.7±0.3		
1845.4±0.4	6.3±0.1	1844.7	4.7
1880.6±0.5	364±10	1880.6	384
1891.6±0.3	4.9±0.2		
2203.3±0.2	2.2±0.1	2202.8	7.1
2451.7±0.5	3.6±0.2		
2494.8±0.5	14.5±0.5	2494.3	15.3
2581.8±0.4	3.0±0.2		
2642.2±0.5	21.6±0.2	2642.9	25.9
2662.8±0.4 <sup>c</sup>	6.7±0.7	2663.2	3.5
2666.1±0.4 <sup>c</sup>	7.2±0.1		
2672.6±0.9	1.8±0.2	2674.0 <sup>d</sup>	2.4
2765.2±1.5	1.9±0.1		
2837.4±0.3	4.6±0.4	2837.7	9.8
2868.1±0.7	1.3±0.1		
2907.0±0.4	1.2±0.1		
2956.4±0.2 <sup>c</sup>	1.5 <sup>d</sup>		
3236.0±0.5	1.6±0.2		
3259.6±0.6	2.2±0.2		
3285.6±0.5	1.7±0.1		
3294.1±0.5 <sup>c</sup>	1.4 <sup>d</sup>		
3369.8±0.5 <sup>c</sup>	0.8 <sup>d</sup>		
3544.6±0.5 <sup>c</sup>	1.6 <sup>d</sup>		
3602.8±0.5 <sup>c</sup>	1.0 <sup>d</sup>		
3623.8±0.5 <sup>c</sup>	2.1 <sup>d</sup>		
3644.6±0.5 <sup>c</sup>	0.9 <sup>d</sup>		
3685.9±1.6 <sup>c</sup>	1.4 <sup>d</sup>		
		781.3 <sup>e</sup>	3.1
		914.6 <sup>e</sup>	2.7
		1070.2 <sup>e</sup>	9.8
		1781.9 <sup>e</sup>	7.1

<sup>a</sup>The errors given on the intensities reflect only the statistical scatter about the average over many runs. The absolute uncertainties will be larger, perhaps ±10% for the more intense peaks and correspondingly greater for the less intense peaks.

<sup>b</sup>The intensities given in Ref. 5 were renormalized so that the 808.4-keV  $\gamma \equiv 100$ .

<sup>c</sup>These  $\gamma$  rays show up only weakly (but consistently) in the spectra, so we place them only *tentatively* as originating from  $\text{Gd}^{145g}$  decay.

<sup>d</sup>These intensities may well be off by as much as a factor of 2.

<sup>e</sup>Transitions reported in Ref. 5 for which we found no corresponding transitions. See the text for a discussion of these transitions.

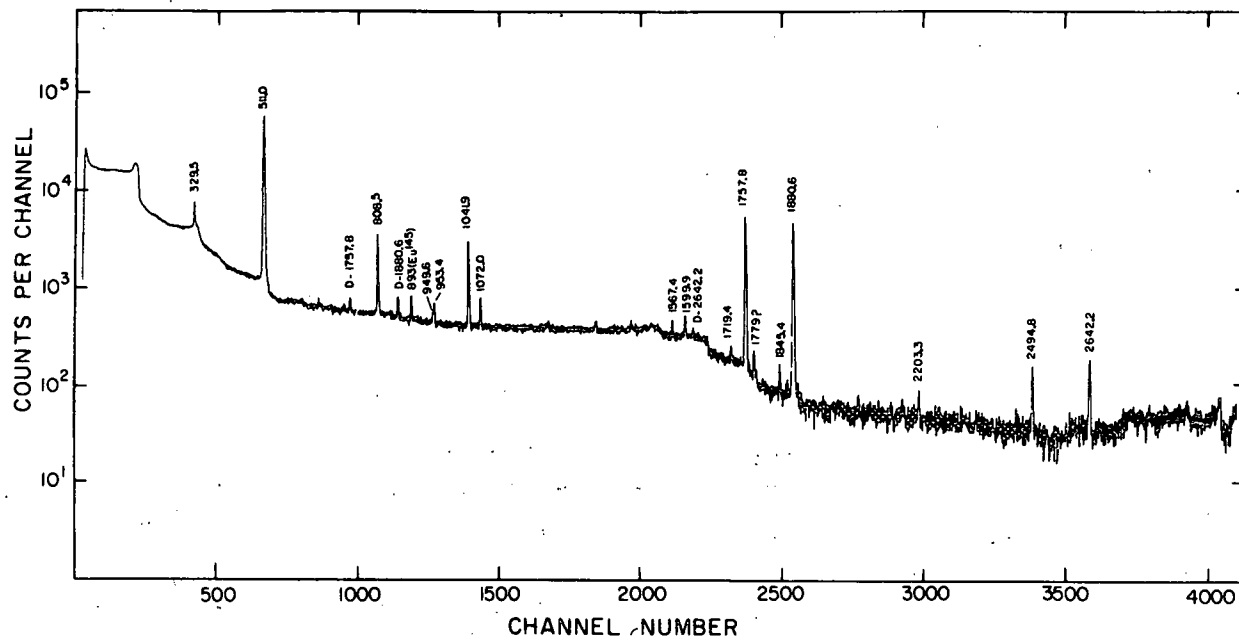


FIG. 2.  $Gd^{145g}$  anticoincidence  $\gamma$ -ray spectrum. This spectrum was recorded with a 7-cm<sup>3</sup> Ge(Li) detector placed in one end and operated in anticoincidence with an 8×8-in. NaI(Tl) split annulus. An additional 3×3-in. NaI(Tl) detector, also operated in anticoincidence with the Ge(Li) detector, blocked the other end of the tunnel.

try for the detectors, although this can cause serious complications because of Compton scattering between the detectors.<sup>19</sup> With repeated bombardments during a 1-day period we were able to collect  $1.8 \times 10^8$  coincidence events, which were then

analyzed. The integral coincidence spectra for the  $x$  (2.5%) and  $y$  (3.6%) detectors are shown at the top of Fig. 4(a), and six gated spectra (gates on  $x$ , display from  $y$ ), including background subtraction, are shown in the remainder of Fig. 4(a)

TABLE II. Relative intensities of  $Gd^{145g}$   $\gamma$  rays in coincidence experiments.

Energy <sup>a</sup> (keV)	Relative intensities			
	Singles	Integral coincidence	511-511- $\gamma$ -ray coincidence	Anti- coincidence
329.5	30.8	60		24
808.5	≅100	≅100	≅100	86
949.6	8.6	18.4		5.5
953.4	15.8	19.3		11
1041.9	112	85.6	28.0	112
1072.0	31	35.6		21
1567.4	10.4			11
1599.9	20		0.64	21
1719.4	13.3	13.5		6.6
1757.8	380	214	100	507
1784.4	4.8			
1806.9	2.7			
1845.4	6.3			7.9
1880.6	364	171	86.8	497
1891.6	4.9			
2203.3	4.4			5.6
2451.7	3.6			
2494.8	14.5		1.5	20
2581.8	3.0		1.1	
2642.2 <sup>b</sup>	21.6			30

<sup>a</sup>The errors for these  $\gamma$ -ray energies are given in Table I.

<sup>b</sup>No coincidence information was obtained above this energy.



and in Fig. 4(b). Of the slices taken, these were the only ones that contained substantially useful information. Relative intensities from the integral coincidence spectra are included in Table II, and the results of the megachannel coincidence experiment are summarized in Table III.

An important gate that is missing from Fig. 4 is the one on the 329.5-keV  $\gamma$  ray, which depopulates the first excited state in  $\text{Eu}^{145}$ . Because of its position atop the intense  $\gamma^{\pm}$  Compton edge, coincidence spectra gated on it, with or without intricate or nonintricate background subtraction, could not be "unconfused" from spectra indicating  $\beta^+$  feeding. Unfortunately, this has ramifications on the construction of the decay scheme, as will be shown in Sec. IV.

3. *Pair spectra.* The two halves of the  $8 \times 8$ -in.

$\text{NaI(Tl)}$  split annulus were used in conjunction with the  $7\text{-cm}^3$   $\text{Ge(Li)}$  detector to determine the relative amounts of  $\beta^+$  feeding to the various levels in  $\text{Eu}^{145}$ . Each half of the annulus was gated on the 511-keV  $\gamma^{\pm}$  peak and a triple coincidence (resolving time,  $2\tau \approx 100$  nsec) was required among these and the  $\text{Ge(Li)}$  detector. A resulting spectrum is shown in Fig. 5. Note that double-escape peaks are also enhanced in this spectrum. A discussion of the  $\beta^+$  feedings extracted from this experiment is deferred until Sec. V, where they are presented in Table IV.

C. Half-Life Determination for  $\text{Gd}^{145g}$

The half-life of  $\text{Gd}^{145g}$  was determined by following the net peak areas of the 1757.8- and 1880.6-

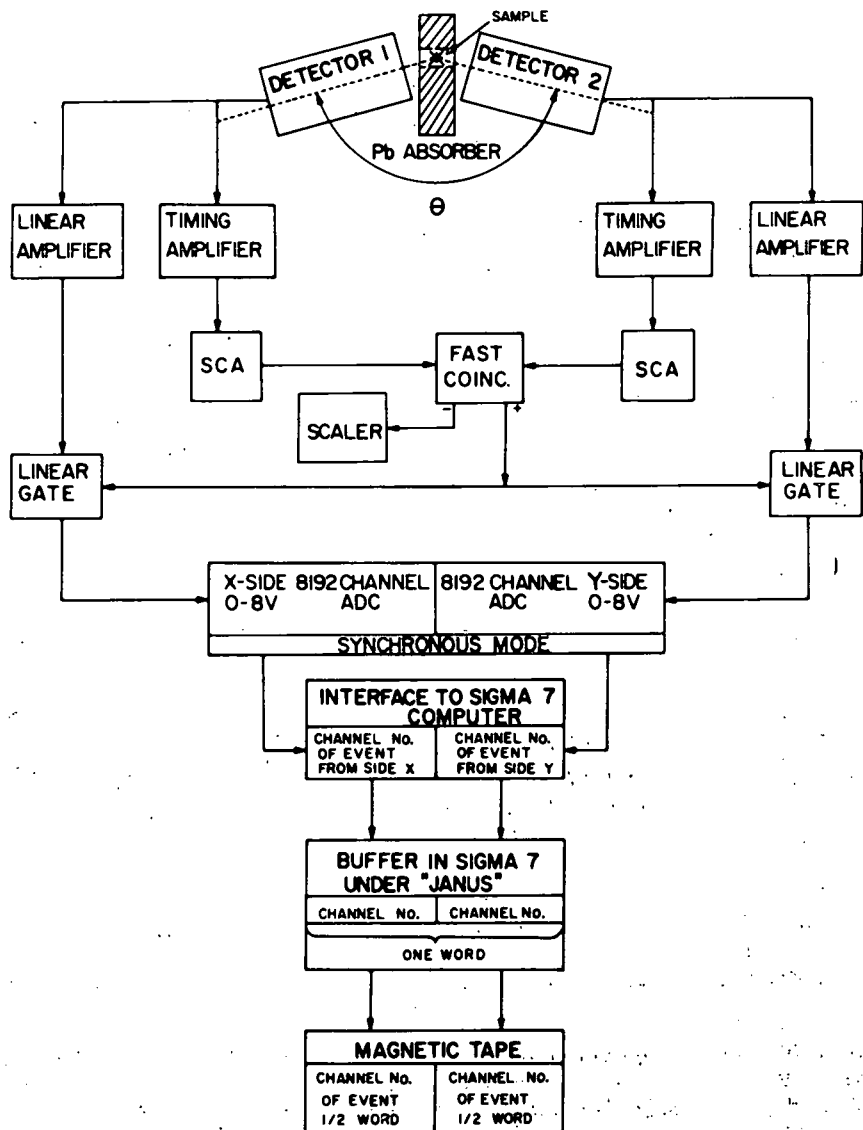


FIG. 3. Schematic diagram of the megachannel two-dimensional apparatus.

keV peaks as a function of time. We used a 50-MHz ADC interfaced to the MSU Cyclotron Laboratory Sigma-7 computer for this experiment. A code called GEORGE<sup>20</sup> allowed us to take data, have a live display on an 11-in. scope, and dump the displayed data onto the computer disk at precise inter-

vals that were determined at the beginning of the run. The sequence of events: Count for the predetermined length of time, stop the counting, dump the spectrum onto the disk, erase the memory, and begin counting again. The entire dumping process takes significantly less than 1 sec. The

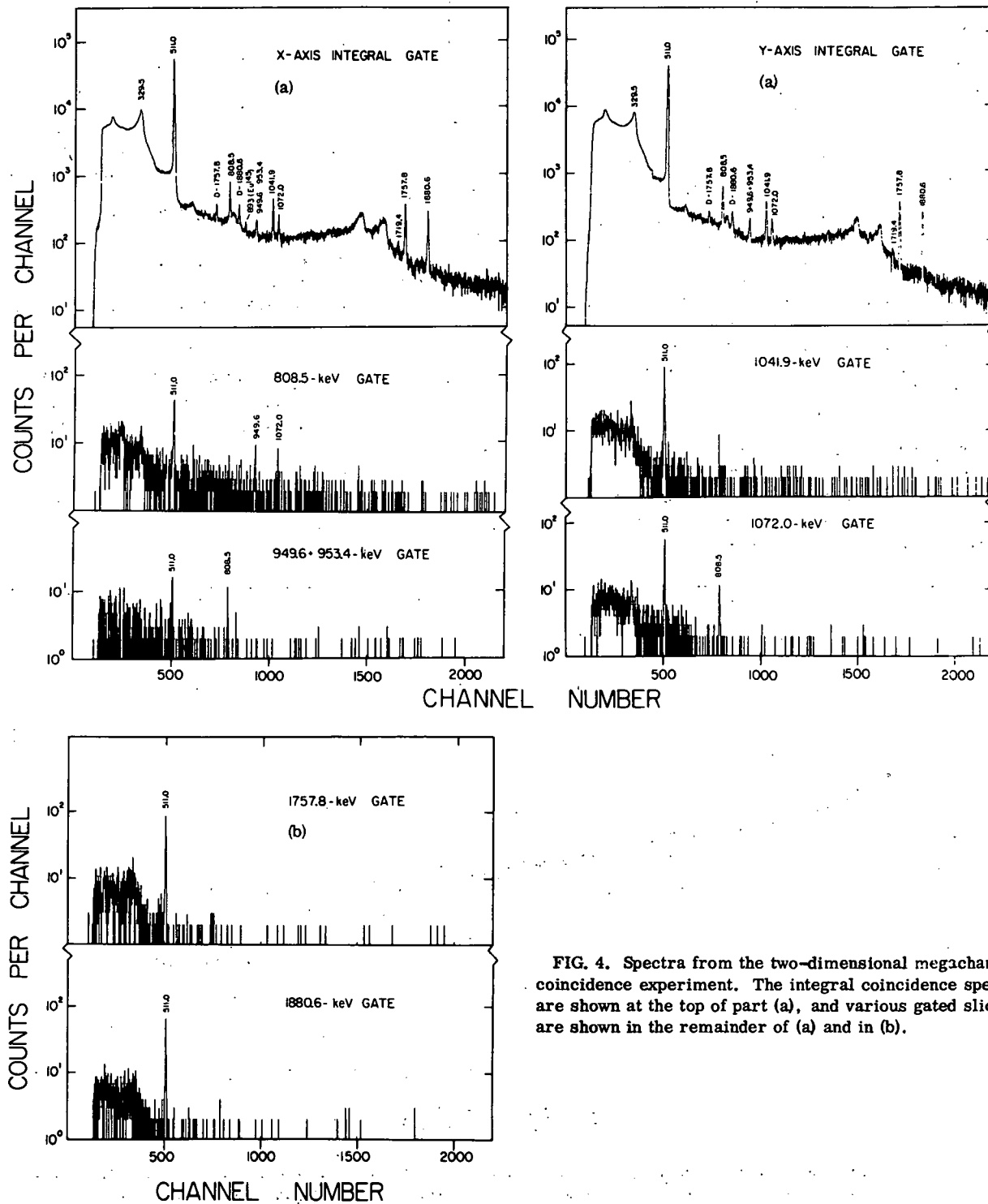


FIG. 4. Spectra from the two-dimensional megachannel coincidence experiment. The integral coincidence spectra are shown at the top of part (a), and various gated slices are shown in the remainder of (a) and in (b).

TABLE III. Summary of  $\gamma$ -ray coincidence in  $Gd^{145g}$ .

Gate energy (keV)	$\gamma$ rays enhanced (keV)
Integral	329.5, 808.5, 949.6, 953.4, (1041.9), <sup>a</sup> 1072.0, 1719.4
808.5	949.6, 1072.0
949.6	808.5
953.4	
1041.9	(329.5), <sup>b</sup> (893.2) <sup>c</sup>
1072.0	(329.5), <sup>b</sup> 808.5
1757.8	$\gamma^\pm$
1880.6	$\gamma^\pm$
511-511	808.5, 1041.9, 1757.8, 1880.6, 2494.8, <sup>d</sup> 2642.2 <sup>d</sup>
Anti	1041.9, 1567.4, 1599.9, 1757.8, 1845.4, 1880.6, 2203.3, 2494.8, 2642.2

<sup>a</sup>As seen in Table II, the intensity for this transition is less than in singles. This is reasonable since it is only weakly fed by two  $\gamma$  transitions and  $\beta^+$ .

<sup>b</sup>This transition appears weakly in the gated spectrum.

<sup>c</sup>From  $Eu^{145}$  decay.

<sup>d</sup>This peak is very weak in the 511-511-keV spectrum.

spectra can be punched on cards later as they are removed from the disk, thereby making the start and stop times of data acquisition independent of the card punching time. A pulser peak was included in each spectrum so that dead-time correc-

TABLE IV. Comparison of experimental and theoretical  $\epsilon(\text{tot})/\beta^+$  ratios for decay to states in  $Eu^{145}$ .

Energy <sup>a</sup> (keV)	$\epsilon(\text{tot})/\beta^+$	
	Experimental	Theoretical <sup>b</sup>
808.5	11	0.36
1041.9	1.6	0.65
1599.9	19	1.2
1757.8	$\approx 1.4$ <sup>c</sup>	1.4
1880.6	1.7	1.7
2494.8	5.0	5.0
2642.2	12	7.1

<sup>a</sup>These are the only states in  $Eu^{145}$  that are measurably fed by  $\beta^+$ , as determined from the  $\gamma^\pm$  gated coincidence spectrum.

<sup>b</sup>These values are only as precise as can be read from the graphs in Ref. 22.

<sup>c</sup>The experimental ratios were normalized to the theoretical ratios by assuming that the transition to the 1757.8-keV states is allowed and unhindered, presumably yielding the expected ratio.

tions could be properly applied to the data. In this manner the half-life can be measured independently for any or all of the peaks in the entire spectrum.

Forty consecutive spectra were obtained for each of the two peaks at 1757.8 and 1880.6 keV, each one representing a 2-min time span. After background subtraction and dead-time corrections

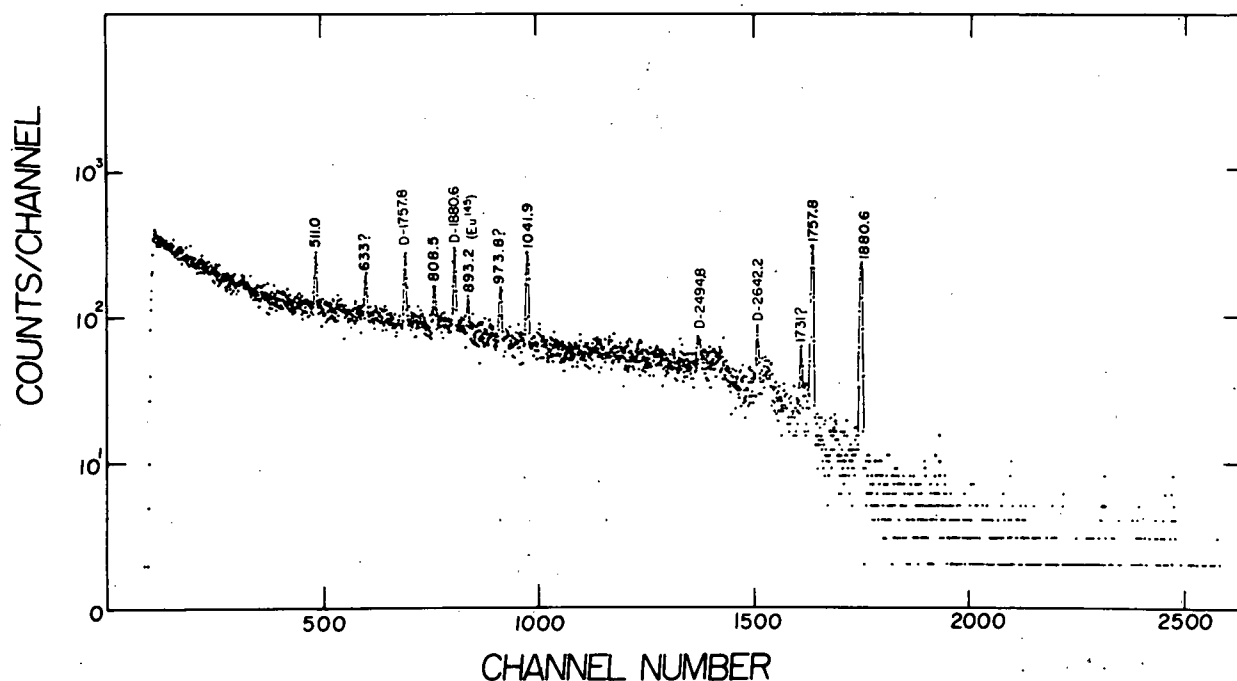


FIG. 5. Pair-coincidence spectrum showing the  $\beta^+$  feedings from  $Gd^{145g}$  decay. This spectrum was recorded with a 7-cm<sup>3</sup> Ge(Li) detector operated in triple coincidence with the two halves of an 8  $\times$  8-in. NaI(Tl) split annulus, each half of which was gated on the 511-keV region.

the points were least-squares-fitted with straight lines (semilog). From an average of these calculations we determined the half-life of  $Gd^{145g}$  to be  $21.8 \pm 0.6$  min, to be compared with the less precise value of 25 min obtained by Grover.<sup>3</sup> (Examples of these spectra and half-life curves can be found in Eppley.<sup>21</sup>)

IV. PROPOSED DECAY SCHEME

Our proposed decay scheme for  $Gd^{145g}$  is shown in Fig. 6. It is largely in agreement with the level scheme proposed by Newman *et al.*,<sup>5</sup> the main differences being our omission of their proposed levels at 2112.0, 2662.5, and 3167.2 keV and our addition of nine new levels at 953.4, 1567.3, 2203.3, 2642.2, 3236.0, 3259.6, 3285.6, 3623.8, and 4411.3 keV. Of the 38  $\gamma$  rays listed in Table I, 28 have been placed in the decay scheme, accounting

for over 97% of the total  $\gamma$ -ray intensity. It is entirely possible that many of the remaining  $\gamma$  rays proceed from levels that decay via a single transition. These  $\gamma$  rays were all too weak to have been seen in any of our coincidence work, so, with no further evidence for their placement, we have omitted them entirely.

The assigned spins and parities, discussed in Sec. V, represent a combination of deductions from our work and also the conclusions of Newman *et al.* for the states observed via the  $Sm^{144}(\tau, d)Eu^{145}$  reaction. The results of the two studies are in good agreement for most states. We calculated<sup>12</sup> the total  $\epsilon$ -decay energy to be  $\approx 5$  MeV. The  $\beta^+/\epsilon$  ratios displayed on Fig. 6 are all calculated values using the methods of Zweifel.<sup>22</sup> We shall see later (cf. Table IV) that our experimentally deduced ratios for some of the more hindered

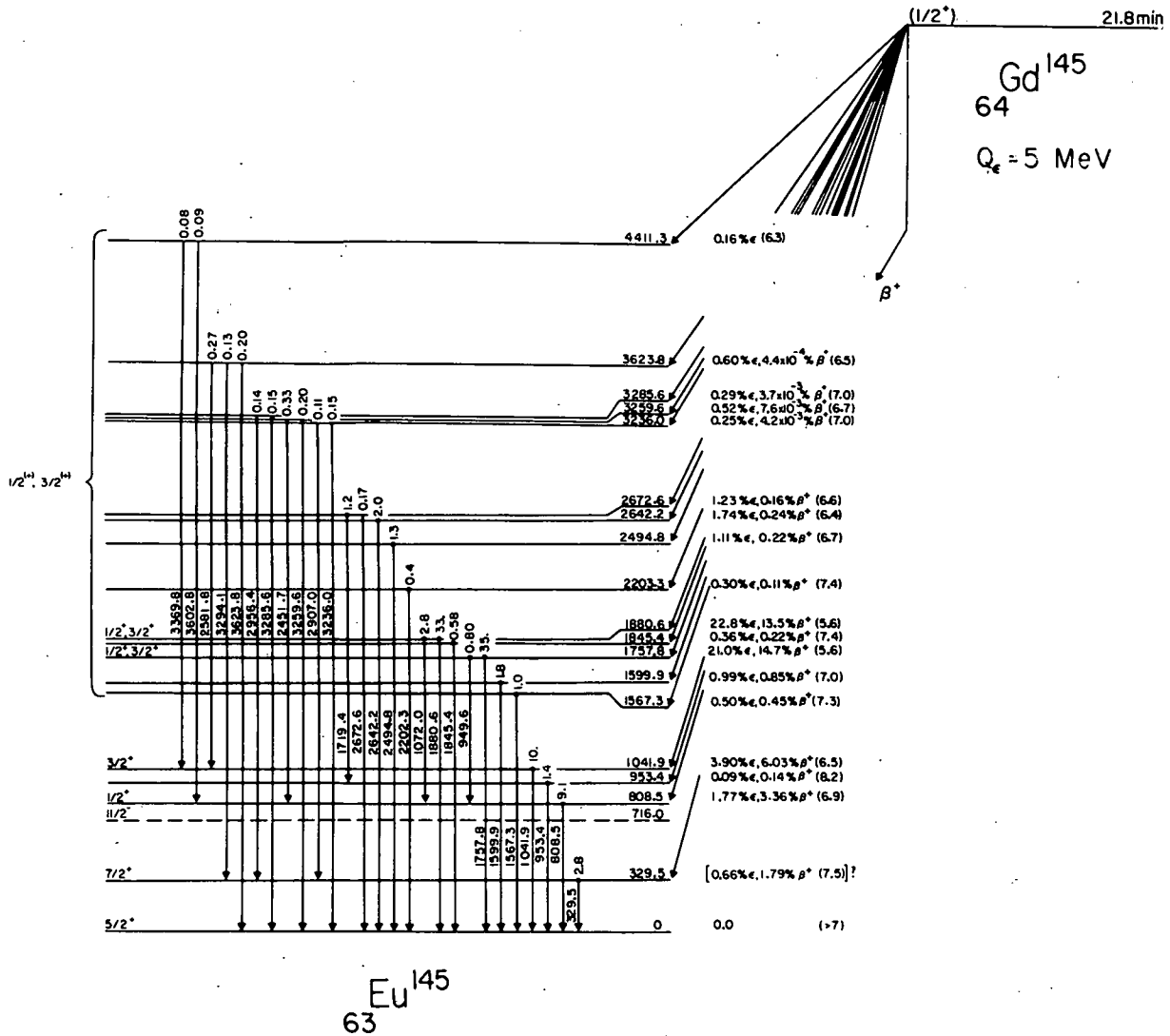


FIG. 6. Decay scheme of  $Gd^{145g}$ .

transitions do not agree with these values. However, we do not have experimental values for many of the states, and to be consistent we have used the calculated values. This does not alter any significant conclusions presented on the decay scheme.

The relative  $\gamma$ -ray intensities listed in Table I were based on a value of 100 for the 808.5-keV  $\gamma$  ray. The relative x-ray intensity was not measured. Thus, the intensities given on the decay scheme are based on the assumption that there is no direct  $\beta$  decay to the  $\text{Eu}^{145}(d_{5/2})$  ground state. This seems to be a good assumption in several respects. First, in light of good evidence<sup>2,5</sup> for the ground state of  $\text{Gd}^{145}$  being predominantly an  $s_{1/2}$  state, a direct transition to the  $\text{Eu}^{145}$  ground state would be a second-forbidden transition. Also, Newman *et al.* determined that the  $\approx 25$ -min component of the  $\gamma^{\pm}$  could be accounted for by assuming no  $\beta^+$  decay to the ground state, based on the  $\beta^+/K$  x-ray value of 0.6 obtained by Grover.<sup>3</sup> (Note, however, that one has to be cautious here, for there does appear to be some decay to the 329.5-keV state that we cannot explain away.)

Specific evidence for the placement of levels and transitions in the decay scheme is given as follows:

*Ground, 329.5-, 716.0-, 808.5-, and 1041.9-keV states.*

These states were all populated strongly by the  $\text{Sm}^{144}(\tau, d)$  reaction and appear to be essentially single-particle states, viz., the  $d_{5/2}$ ,  $g_{7/2}$ ,  $h_{11/2}$ ,  $s_{1/2}$ , and  $d_{3/2}$  in that order. We, too, see specific evidence for the 329.5-, 808.5-, and 1041.9-keV levels. The 716.0-keV state is the  $\pi h_{11/2}$  isomeric state, which is not populated by the decay of  $\text{Gd}^{145g}$  but is populated by the decay<sup>2</sup> of  $\text{Gd}^{145m}$ .

As seen in the integral coincidence spectra of Fig. 4(a), the  $\gamma^{\pm}$  Compton background peaks near the 329.5-keV  $\gamma$  ray, so no reliable information can be obtained from a gate on this  $\gamma$  ray. That it is indeed involved in cascades is indicated by the anticoincidence spectrum (Fig. 2), where its intensity is diminished. The four transitions into the 329.5-keV state were placed strictly on the basis of energy differences. From the intensity balances, we deduce that the 329.5-keV state receives 0.55%  $\epsilon$  and 1.5%  $\beta^+$  feeding. Also, the  $\gamma^{\pm}$  coincidence spectrum (Fig. 5) shows the 329.5-keV  $\gamma$  ray. However, this much  $\beta^+/\epsilon$  feeding implies a  $\log ft$  of 7.5, which is much lower than reasonable considering that the transition to this state would most likely be a  $\frac{1}{2}^+ - \frac{1}{2}^+$ , i.e., second-forbidden, transition. And, although the 329.5 lies in a particularly bad place for a precise intensity determination, we do not think that our intensity value (or that of Newman *et al.*) can be wrong enough to give us this low  $\log ft$  value artificially. In addition, although we could have missed placing sever-

al  $\gamma$  rays that feed into the 329.5-keV level from above, the over-all intensity of the unplaced  $\gamma$  rays is rather small, so it would be difficult to alter the intensity balance by placing them. We are left with a  $\beta^+/\epsilon$  feeding that we do not believe and cannot explain away easily.

The placement of the 808.5-keV  $\gamma$  ray as proceeding from a level of the same energy is consistent with our coincidence and anticoincidence data. The 949.6- and 1072.0-keV  $\gamma$  rays can be seen to be in coincidence with the 808.5-keV  $\gamma$  ray in Fig. 4(a). The 2451.7- and 3602.8-keV  $\gamma$  rays are too weak to be picked up in our coincidence spectra and were placed purely by energy differences. As we shall see in Sec. V, the 808.5-keV state is a  $\frac{1}{2}^+$  state, which is consistent with its depopulating only to the ground state. The  $\log ft$  of 6.9 is somewhat high for an allowed transition, but it falls within a reasonable range, and we shall see that the transition involves a multiparticle rearrangement, so it would be expected to be slow.

The 1041.9-keV  $\gamma$  ray can also be seen to be a ground-state transition, as it is enhanced in the anticoincidence spectrum. There are no strong coincidences in the 1041.9-keV gated spectrum (Fig. 4), again suggesting direct decay to the ground state. The 2581.8- and 3369.8-keV  $\gamma$  rays, too weak to be seen in our coincidence spectra, were placed solely on the basis of energy difference. The  $\log ft$  for  $\beta^+/\epsilon$  population of the 1041.9-keV state is quite in line with an allowed transition, consistent with the assignment of this state as  $\frac{3}{2}^+$  by Newman *et al.*

*1757.8- and 1880.6-keV states.* The two intense  $\gamma$  rays at 1757.8 and 1880.6 keV dominate the entire  $\text{Gd}^{145g}$   $\gamma$ -ray spectrum. They are enhanced in the anticoincidence spectrum and depressed in the integral coincidence spectra, and the spectra gated on them [Fig. 4(b)] show nothing other than  $\gamma^{\pm}$ . Thus, they are well established as ground-state transitions from levels having the same energies. Further, the 808.5-keV gated spectrum showed that each of these two states decays additionally through the 808.5-keV level. Together, these two states receive 72.6% of the total  $\beta^+/\epsilon$  population from  $\text{Gd}^{145g}$ . The low  $\log ft$  values (5.6 for each) certainly suggest allowed transitions, and, assuming the  $\frac{1}{2}^+$  assignment for  $\text{Gd}^{145g}$ , this means that the states are  $\frac{1}{2}^+$  or  $\frac{3}{2}^+$ . This is consistent both with their decaying directly to the ground state and through the  $\frac{1}{2}^+$  808.5-keV state. The 1757.8-keV state appears to be excited only slightly in the  $\text{Sm}^{144}(\tau, d)$  reaction<sup>5</sup> and it is not clear whether the 1880.6-keV state is excited or not (it falls too close to the peak from the 1843-keV state). Needless to say, neither state appears to be simple in structure, and we shall explain both of them as

three-quasiparticle states in the next section.

*953.4- and 2672.6-keV levels.* These levels were placed on the basis of moderately convincing, although by no means airtight, coincidence results. Both the 953.4- and the 1719.4-keV  $\gamma$  rays were enhanced in the integral coincidence spectra, neither was enhanced in the anticoincidence spectrum, and neither could be detected in the pair spectrum, implying that  $\beta^+$  feeding could not account for their appearance in the coincidence spectra. Unfortunately, both are weak enough that the gated spectrum on the 949.6–953.4-keV region proved inconclusive. Additionally, the sum, 953.4 + 1719.4 = 2672.8 keV, so we place levels at 953.4 and 2672.6 keV, the order of the 953.4- and 1719.4-keV  $\gamma$  rays being chosen because of their relative intensities.

*1567.3-, 1599.9-, 1845.4-, 2203.3-, 2494.8-, and 2642.2-keV levels.* These levels were placed on the basis of their respective ground-state transitions being enhanced in the anticoincidence spectrum. Newman *et al.* also observed states at 1843 and 2480 (doublet) keV excited by the  $(\tau, d)$  reaction.

*The remaining levels: 3236.0, 3259.6, 3285.6, 3263.8, and 4411.3 keV.* Because of the weakness of the  $\gamma$  rays, no coincidence data of any significance could be obtained above the line at 2642.2 keV. Thus, these four levels had to be placed solely on the basis of sums and must be considered as tentative. Under "normal" circumstances we would not venture to suggest levels on just this basis, but here there are mitigating circumstances. First, the precision on the sums is quite good, considering the energies and intensities involved: 0.5, 0.6, 0.3, 0.2, and 0.5 keV for the five levels, respectively. Second, the states are spaced rather widely apart in this nucleus with the  $\gamma$  rays having reasonably disparate energies. Such would tend to make accidental agreements less probable than under normal circumstances; yet it must be remembered that these are by no means random numbers, and there may be some subtle, insidious relations not recognized.

## V. DISCUSSION

Some 20 states have now been placed, with varying degrees of confidence, in  $\text{Eu}^{145}$ . In some respects, then, this nucleus finds itself among the better known members of the  $N=82$  series. All five major proton orbits between  $Z=50$  and 82 lie reasonably close together, resulting in relatively low-lying single-particle states that are not so fragmented as some in the lighter  $N=82$  isotones. Also, the peculiar decay properties of  $\text{Gd}^{145g}$  give us some information about what appear to be three-

quasiparticle states.

### A. Single-Particle States

The five states at 0, 329.5, 716.0, 808.5, and 1041.9 keV comprise the major components of all of the single-proton orbits between  $Z=50$  and 82, viz.,  $d_{5/2}$ ,  $g_{7/2}$ ,  $h_{11/2}$ ,  $s_{1/2}$ , and  $d_{3/2}$ , respectively. This was amply demonstrated by Newman *et al.*<sup>5</sup> in their  $(\tau, d)$  scattering, where the spectroscopic factors indicated precisely the occupations expected for adding a proton to a  $Z=62$  nucleus.

The  $\frac{5}{2}^+$  nature of the ground state is also corroborated by the decay properties<sup>14</sup> of  $\text{Eu}^{145}$  itself. The primary component of its wave function appears to be just what one might expect from a simple shell-model picture,  $(\pi g_{7/2})^8 (\pi d_{5/2})^5$  above the closed  $Z=50$  shell. Note, now, that there is little or no  $\beta^+/\epsilon$  decay ( $\log ft \geq 7$ ) from  $\text{Gd}^{145g}$  to this  $\pi d_{5/2}$  ground state. Herein lies the first portion of the  $\text{Gd}^{145g}$  "strange case," for both  $\text{Nd}^{141g}$  and  $\text{Sm}^{143g}$  decay<sup>9,10</sup> quite readily ( $\log ft \approx 5.3$ ) to the  $\pi d_{5/2}$  ground states of their respective daughters, in simple shell-model terms these decays being  $(\pi g_{7/2})^8 (\pi d_{5/2})^2 (v d_{3/2})^{-1} - (\pi g_{7/2})^8 (\pi d_{5/2})$  and  $(\pi g_{7/2})^8 (\pi d_{5/2})^4 (v d_{3/2})^{-1} - (\pi g_{7/2})^8 (\pi d_{5/2})^3$ . There are many ways in which one could explain away a milder retardation of the  $\text{Gd}^{145g}$  decay to the  $\text{Eu}^{145}$  ground state, but the only reasonable explanation that we find for the experimental facts (hindered by at least a factor of 100 and probably much greater) is that the ground state of  $\text{Gd}^{145}$  is not a  $(v d_{3/2})^{-1}$  state but instead a  $(v s_{1/2})^{-1}$  state. Newman *et al.* also come to this conclusion. Some reasonable indirect evidence for this is available, viz., the  $(v s_{1/2})^{-1}$  state does progress to lower and lower energies with increasing  $Z$  in the  $N=81$  nuclei: It lies at 281 keV<sup>23</sup> in  $\text{Ba}^{137}$ , at 250 keV<sup>23,24</sup> in  $\text{Ce}^{139}$ , and at 195 keV<sup>25</sup> in  $\text{Nd}^{141}$ . Thus, it might be expected to have replaced the  $(v d_{3/2})^{-1}$  state by the time  $\text{Gd}^{145}$  is reached. However, in our study<sup>2</sup> of  $\text{Gd}^{145m}$  we were neither able to confirm nor to deny this, so it must be admitted that the evidence is only indirect for this  $s_{1/2}$  assignment. More will be said about it in the next section.

The  $(\pi g_{7/2})^{-1}$  state [actually a  $(\pi g_{7/2})^7 (\pi d_{5/2})^{2n} \dots$  state – in the next section we shall see that the pairing force has undoubtedly removed some occupation from this orbit] at 329.5 keV is well established, but, quite surprisingly, it may receive a small amount of  $\beta^+/\epsilon$  population, the  $\log ft$  being  $\approx 7.5$ . Actually, we do not believe this, and, considering the uncertainty in the intensity of the 329.5-keV  $\gamma$  ray because of its position in the spectrum, perhaps most of the feeding can be attributed to experimental difficulties. The results, however, are duly recorded on Fig. 6.

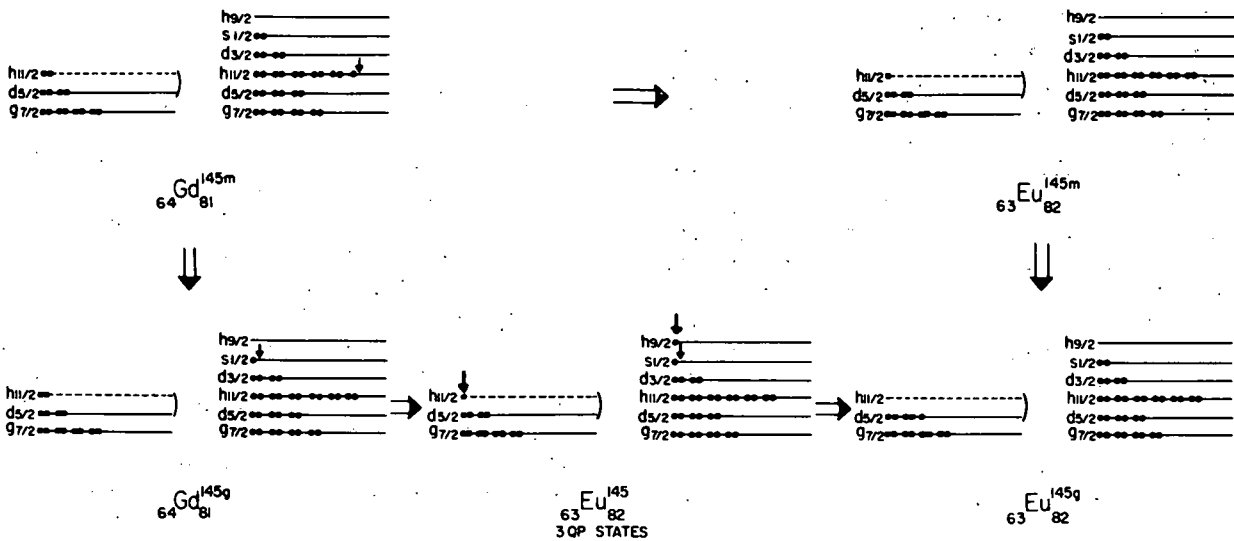


FIG. 7. Stylized representation of some important transitions in the  $Gd^{145}$ - $Eu^{145}$  system. Protons are represented by squares and neutrons by circles. The arrows point out the particles or holes of particular interest for a given state.

As expected, the  $h_{11/2}$  state at 716.0 keV is not populated by  $Gd^{145g}$  decay, although we noted<sup>2</sup> its being populated directly by 4.7% of the  $Gd^{145m}$  decay. The  $\log ft$  was found there to be 6.2. The fact that such a direct decay takes place implies some occupation of the  $h_{11/2}$  orbit by proton pairs in  $Gd^{145}$ . This is the second clue toward explaining the "strange case" of  $Gd^{145g}$ .

The  $\beta^+/\epsilon$  decays to the  $s_{1/2}$  808.5- and  $d_{3/2}$  1041.9-keV states, with respective  $\log ft$ 's of 6.9 and 6.5, appear to be allowed transitions. However, note that these are somewhat higher  $\log ft$  values than those for unhindered allowed transitions in this nuclear region. This is dramatically illustrated by comparing them with the  $\log ft$ 's for the transitions to the 1757.8- and 1880.6-keV states. The implication could be that the former transitions are not completely straightforward. Also, as can be seen in Table IV, the  $\epsilon(\text{tot})/\beta^+$  ratios for decay to the 808.5- and 1041.9-keV states are large compared with the predicted<sup>22</sup> ratios for straightforward allowed transitions. Often such squelching of the  $\beta^+$  branch is also an indication of complexities in the decay process. This is the third clue.

### B. Three-Quasiparticle States

The fourth and most obvious clue, of course, is the strong decay of  $Gd^{145g}$  to the states at 1757.8 and 1880.6 keV. These two states account for 72% of the  $Gd^{145g}$  decay, and the low  $\log ft$ 's, both 5.6, clearly indicate unhindered allowed transitions. Now, the state at  $\approx 1757$  keV populated by an  $l=2$  transfer (implying  $I^\pi = \frac{3}{2}^+$ ) in the  $(\tau, d)$  experiment

of Newman *et al.* may or may not be the same as the 1757.8-keV state populated by  $Gd^{145g}$  decay. In any event, the extracted spectroscopic factor ( $C^2S$ ) was only 0.02, indicating the structure of that state to be more complicated (or at least different) than what could be attained by a simple dropping of a proton into a vacant or semivacant  $Sm^{144}$  orbit. The 1880.6-keV state may or may not have been populated<sup>26</sup> (cf. Fig. 3 of Ref. 5) in the  $(\tau, d)$  experiment, but if populated at all it was only to a very slight extent. Also, in their shell-model calculations using a truncated basis set (which considered only proton states and which did not allow more than a single particle to be excited from the  $g_{7/2}$ - $d_{5/2}$  subspace into the higher orbits), Newman *et al.* were unable to construct states corresponding to the 1757.8- and 1880.6-keV states. Our inference here is that perhaps these states involved the promotion of more than one proton into the  $h_{11/2}$ ,  $s_{1/2}$ , and  $d_{3/2}$  region or, considering that the states lie well above the pairing gap, they involve broken neutron pairs.

We have arrived at a simple shell-model picture that, qualitatively at least, explains all four clues, or effects, quite well: (1) no  $\beta^+/\epsilon$  feeding to the  $Eu^{145}$  ground state, (2) some direct feeding of the 716.0-keV state by  $Gd^{145m}$ , (3) hindered transitions to the  $s_{1/2}$  and  $d_{3/2}$  states, and (4) fast transitions to the 1757.8- and 1880.6-keV states - meaning that these last go by major components of the wave functions and not by minor admixtures. Our model is outlined in stylized form in Fig. 7 and involves two assumptions: (1) The ground state of  $Gd^{145}$  is indeed a  $(\nu s_{1/2})^{-1}$  state, and (2) there is appreciable occupation of the  $h_{11/2}$  orbit by proton pairs in both

$Gd^{145g}$  and  $Gd^{145m}$ . Both assumptions have already been discussed implicitly, and (2) has been directly demonstrated by the population of the 716.0-keV  $h_{11/2}$  state by  $Gd^{145m}$  (cf. the appropriate transition in Fig. 7). (Also, compare the rapid drop in position of the  $h_{11/2}$  orbit from 1.1 MeV in  $Pr^{141}$  to 716.0 keV in  $Eu^{145}$ . It should lie even lower in  $Gd^{145}$ , and the pairing force should insure its partial occupation simply by virtue of its large degeneracy.)

Now, there are well-documented cases of  $\beta^+/\epsilon$  decay into high-lying three-quasiparticle states from the nearby nuclei  $Nd^{149m}$  (Ref. 9 and McHarris, Beery, and Kelly<sup>27</sup>) and  $Sm^{141m}$  (Ref. 13), both of which follow quite straightforwardly from simple shell-model considerations. Looking about for an analogous set of transitions, one is immediately struck by the availability of the  $\nu h_{9/2}$  orbit — by a crude extrapolation down from the lead-bismuth region we would predict it to lie somewhere between 1 and 2 MeV higher than the  $s_{1/2}$  or  $d_{3/2}$  orbits. Thus, the primary decay of  $Gd^{145g}$  can be represented as  $\pi h_{11/2} - \nu h_{9/2}$ , or more completely,  $(\pi h_{11/2})^{2n} (\nu s_{1/2})^{-1} - (\pi h_{11/2})^{2n-1} (\nu h_{9/2}) (\nu s_{1/2})^{-1}$ . This would make the 1757.8- and 1880.6-keV states three-quasiparticle states having the primary configuration  $(\pi h_{11/2}) (\nu h_{9/2}) (\nu s_{1/2})^{-1}$ .

This model also explains the hindrance of the  $\beta^+/\epsilon$  decay to the 808.5- and 1041.9-keV states. Each would require, in addition to the unfavorable transformation of an existing (high-spin) proton into an  $s_{1/2}$  neutron, a promotion of the remaining proton from that pair into a higher orbit. Thus, the observed transitions probably proceed primarily through admixtures.

Appealing though it be, this explanation must at this time remain a hypothesis, for we have no direct proof of (1) the  $(\nu s_{1/2})^{-1}$  nature of  $Gd^{145g}$  and (2) the fact that it is specifically the  $\nu h_{9/2}$  orbit that participates in the three-quasiparticle states. Information would be useful concerning  $Dy^{147m+g}$ , the next member of the series, but it is far enough from stability to present formidable production difficulties. The same is true for  $Tb^{145}$ , which could populate states in  $Gd^{145}$ . Perhaps most promising is the study of  $Gd^{145}$  states via the  $Sm^{144}(\tau, 2n\gamma)$  reaction.

#### C. Remaining States

Relatively little can be deduced about the remain-

ing states at this time. The 953.4-keV state is anybody's guess. Although placed by reasonably convincing coincidence data, we have no clues as to its structure. The remaining states are all populated by transitions having  $\log ft$ 's variously in the allowed or fast first-forbidden range. Thus, they are all probably  $\frac{1}{2}$  or  $\frac{3}{2}$  states, with the majority having even parity. One word about the 1599.9-keV state: We observe its being populated by the  $Gd^{145g}$  decay, which implies a  $\frac{1}{2}$  or  $\frac{3}{2}$  assignment. This is incompatible with the  $\frac{7}{2}^+$  assignment by Newman *et al.*, but they<sup>28</sup> consider the statistics in their angular distribution for this state to be poor enough to make that assignment somewhat questionable anyway.

#### D. $\epsilon/\beta^+$ Ratios

From our  $\gamma^+$  gated spectrum (Fig. 5) we obtained the relative  $\beta^+$  feedings to seven of the  $Eu^{145}$  states. The deduced  $\epsilon/\beta^+$  ratios for the transitions to these states are listed in Table IV, where they are compared with the theoretical ratios calculated by Zweifel's methods.<sup>22</sup> We normalized the experimental values to the theoretical values with the transition to the 1757.8-keV state, which we consider to be one of the two most straightforward transitions in the entire decay scheme. (If one normalizes to, say, the 808.5-keV state, then the  $\beta^+$  feeding to the other states quickly exceeds 100%.) It can be seen that the  $\epsilon/\beta^+$  ratio appears to be a fairly sensitive indicator of the degree of hindrance of a transition, for it does not take much to depress the  $\beta^+$  branch. Unfortunately, the entire theoretical consideration of  $\epsilon/\beta^+$  ratios versus forbiddenness or hindrance needs serious overhauling now, so little can be said in a quantitative sense.

#### ACKNOWLEDGMENTS

We thank H. Hilbert and Dr. H. Blosser for their aid and instruction in the operation of the MSU cyclotron. We also thank R. Todd for his aid in the acquisition of some of the data, and Dr. B. H. Widental for very helpful discussions on the nature of nuclear states near  $N=82$  and for his critical reading of the manuscript.

\*Work supported in part by the U. S. Atomic Energy Commission.

†Work supported in part by the U. S. National Science Foundation.

<sup>1</sup>R. E. Eppley, Wm. C. McHarris, and W. H. Kelly, *Phys. Rev. C* **2**, 1077 (1970).

<sup>2</sup>R. E. Eppley, Wm. C. McHarris, and W. H. Kelly, *Phys. Rev. C*, **2**, 1929 (1970).



- <sup>3</sup>J. R. Grover, *Phys. Rev.* **116**, 406 (1959).
- <sup>4</sup>J. Olkowsky, M. LePape, I. Gratot, and L. Cohen, *J. Phys. Radium* **20**, 549 (1959).
- <sup>5</sup>E. Newman, K. S. Toth, R. L. Auble, R. M. Gaedke, M. F. Roche, and B. H. Wildenthal, *Phys. Rev. C* **1**, 1118 (1970).
- <sup>6</sup>See, e.g., K. S. Toth, E. Newman, B. H. Wildenthal, R. L. Auble, R. M. Gaedke, and M. F. Roche, in *Proceedings of the International Conference on Radioactivity in Nuclear Spectroscopy*, Vanderbilt University, Nashville, Tennessee, 11-15 August 1969 (Gordon and Breach, Science Publishers, Inc., New York, to be published), and the comments following.
- <sup>7</sup>J. Felsteiner and B. Rosner, *Phys. Letters* **31B**, 12 (1970).
- <sup>8</sup>J. S. Geiger, R. L. Graham, I. Bergström, and F. Brown, *Nucl. Phys.* **68**, 352 (1965).
- <sup>9</sup>D. B. Beery, W. H. Kelly, and Wm. C. McHarris, *Phys. Rev.* **171**, 1283 (1968).
- <sup>10</sup>D. DeFrenne, K. Heyde, L. Dorikens-Vanpraet, M. Dorikens, and J. Demuynck, *Nucl. Phys.* **A110**, 273 (1968).
- <sup>11</sup>D. B. Beery, W. H. Kelly, and Wm. C. McHarris, *Phys. Rev.* **188**, 1851 (1969).
- <sup>12</sup>W. D. Myers and W. J. Swiatecki, University of California Lawrence Radiation Laboratory Report No. UCRL-11980, 1965 (unpublished).
- <sup>13</sup>For the properties of  $\text{Sm}^{141m+g}$ , see R. E. Eppley, R. R. Todd, R. A. Warner, Wm. C. McHarris, and W. H. Kelly, to be published; partially summarized by R. E. Eppley, Michigan State University Nuclear Chemistry Annual Report for 1969, No. COO-1779-13 (unpublished).
- <sup>14</sup>I. Adam, K. S. Toth, and M. F. Roche, *Nucl. Phys.* **A121**, 289 (1968).
- <sup>15</sup>J. T. Routti and S. G. Prussin, *Nucl. Instr. Methods* **72**, 125 (1969). We used a variant of this code adapted for the MSU Cyclotron Laboratory Sigma-7 computer by T. Arnette, C. Merritt, and W. H. Kelly.
- <sup>16</sup>R. E. Doebler, G. C. Giesler, and K. L. Kosanke, unpublished.
- <sup>17</sup>R. L. Auble, D. B. Beery, G. Berzins, L. M. Beyer, R. C. Etherton, W. H. Kelly, and Wm. C. McHarris, *Nucl. Instr. Methods* **51**, 61 (1967).
- <sup>18</sup>EVENT RECOVERY, a program written for the MSU Cyclotron Laboratory Sigma-7 computer by D. Bayer, D. B. Beery, and G. C. Giesler.
- <sup>19</sup>G. C. Giesler, Wm. C. McHarris, R. A. Warner, and W. H. Kelly, to be published.
- <sup>20</sup>GEORGE, a data-taking code with live oscilloscope display developed by P. Plauger.
- <sup>21</sup>R. E. Eppley, Ph. D. thesis, Michigan State University, 1970 (unpublished).
- <sup>22</sup>P. F. Zweifel, *Phys. Rev.* **96**, 1572 (1954); **107**, 329 (1957); and presented graphically in C. M. Lederer, J. M. Hollander, and I. Perlman, *Table of Isotopes* (John Wiley & Sons, New York, 1967) 6th ed., p. 575.
- <sup>23</sup>R. H. Fulmer, A. L. McCarthy, and B. L. Cohen, *Phys. Rev.* **128**, 1302 (1962).
- <sup>24</sup>E. I. Biryukov, V. T. Novikov, and N. S. Shimanskaya, *Izv. Akad. Nauk SSSR, Ser. Fiz.* **27**, 1408 (1963) [transl.: *Bull. Acad. Sci. USSR, Phys. Ser.* **27**, 1383 (1963)].
- <sup>25</sup>F. Yap, R. R. Todd, W. H. Kelly, and Wm. C. McHarris, to be published.
- <sup>26</sup>B. H. Wildenthal, Michigan State University, private communication.
- <sup>27</sup>Wm. C. McHarris, D. B. Beery, and W. H. Kelly, *Phys. Rev. Letters* **22**, 1191 (1969).

## (p, d) REACTION IN THE TITANIUM ISOTOPES

P. J. PLAUGER † and E. KASHY

*Cyclotron Laboratory, Michigan State University ††, East Lansing, Michigan 48823*

Received 4 May 1970

**Abstract:** Angular distributions for the  $^{48}\text{Ti}(p, d)^{47}\text{Ti}$  reaction were obtained for  $E_p = 25\text{--}45$  MeV to study the energy dependence of various methods of extracting spectroscopic factors. In the DWBA analysis for the principal  $l_n = 1, 2$  and 3 transitions, it was found that correcting for finite-range and non-locality in the interaction eliminated the energy dependence observed in spectroscopic factors obtained with local zero-range calculations. On the basis of these results, spectroscopic factors were measured for the  $^{46, 48, 50}\text{Ti}(p, d)^{45, 47, 49}\text{Ti}$  reactions and compared to the sum-rule predictions of French and Macfarlane. Most of the disagreement observed is attributed to incorrect treatment of  $Q$ -dependence in the calculations.

E NUCLEAR REACTIONS  $^{50, 48, 46}\text{Ti}(p, d)$ ,  $E = 25\text{--}45$  MeV; measured  $\sigma(E; E_d, \theta)$ .  
 $^{45, 47, 49}\text{Ti}$  deduced levels,  $l_n, J, \pi$ , spectroscopic factors. Enriched targets.

### 1. Introduction

The study of (p, d) reactions in the titanium isotopes provides useful information about both the reaction mechanism and the nuclei themselves. Stable titanium nuclei have  $Z = 22$ ,  $N = 24\text{--}28$ , and so each may be treated as a  $^{40}\text{Ca}$  core plus particles mainly in the  $1f_{7/2}$  shell. The (p, d) reaction consists principally of picking up a neutron from one of the outer shells of the target, with a minimum of configuration rearrangement. Therefore one would expect to observe at least one strong  $l = 3$  transition, corresponding to the pickup of a  $1f_{7/2}$  neutron, and some  $l = 1$  strength due to the admixture of the next higher subshell,  $2p_{3/2}$ . Even  $l$ -transfers, pickup from the filled  $2s\text{--}1d$  shell, are also expected.

The strength of these transfer reactions is a very direct measure of the overlap of the final state and target ground state wave functions. Since the shape of the angular distribution strongly depends on the  $l$ -transfer, the principal transitions can be sorted fairly well according to the orbital from which they originate. Given a theory of the reaction mechanism, one can then determine the occupation probabilities of the various shell-model orbitals. Such a theory is the distorted wave Born approximation, embodied in the Oak-Ridge computer code JULIE<sup>1</sup>). Spectroscopic factors are obtained from measured transition strengths by comparing experimental cross sections to DWBA predictions.

† Present address: Bell Telephone Laboratories, Holmdel, New Jersey.

†† Work supported in part by the National Science Foundation.

Consistency checks exist for these factors. Since the sum of all spectroscopic factors for picking up a neutron from a shell gives its total occupancy, the sum has a rigorous upper bound within the assumed nuclear structure model. One expects inner shells to be essentially filled, closely defining their sums. Still other sum rules exist for other constraints, as will be seen later. There exist also the calculations, by McCullen, Bayman and Zamick<sup>2)</sup>, of the wave functions of  $(1f_{7/2})^n$  configuration states. These provide a basis for predicting spectroscopic factors and other nuclear properties of the titanium isotopes.

Such considerations raised questions about the results obtained from  $^{46-50}\text{Ti}(p, d)$ ,  $^{45-49}\text{Ti}$  studies at 17.5 MeV by Kashy and Conlon<sup>3)</sup>. DWBA calculations using the zero-range approximation consistently indicated less than one neutron in the  $1d_{3/2}$  shell and, in  $^{48}\text{Ti}$ , almost two neutrons in the  $2p_{3/2}$  shell.

Still other difficulties were reported by Sherr *et al.*<sup>4)</sup> in a study performed at 28 MeV which included  $^{48,50}\text{Ti}(p, d)^{47,49}\text{Ti}$ . These experiments also excited high-lying isobaric analog states – states having a total isotopic spin of one greater than the low-lying states and configurations analogous to the low-lying states in their scandium isobars. Applying the sum rules developed by French and Macfarlane<sup>5)</sup> to the different isospin states, Sherr *et al.* were able to study the dependence of DWBA predictions on the reaction  $Q$ -value. Using the normal procedures they found too large a  $Q$ -dependence for  $l = 3$  transfers and were led to an effective binding prescription to improve agreement with the sum rules. Unfortunately, this procedure forces the nuclear overlap to have an incorrect asymptotic form.

Some hope for improving this state of affairs was raised by Snelgrove and Kashy<sup>6)</sup> in a study of  $^{16}\text{O}(p, d)^{15}\text{O}$  over an energy range of 21 to 45 MeV. They discovered strong energy dependence in the extraction of spectroscopic factors up to a deuteron exit energy of about 20 MeV. Consequently, it was decided to extend this energy dependence investigation to  $^{48}\text{Ti}$  in the hope of better understanding the mechanics of extracting spectroscopic factors. At the same time  $^{46,50}\text{Ti}(p, d)^{45,49}\text{Ti}$  measurements were made, each at one energy, to explore the systematics of the  $(p, d)$  reaction across the titanium isotopes and to apply the knowledge gained from the energy investigation.

## 2. Procedure

Proton beams for these experiments were accelerated in the Michigan State University sector-focused cyclotron<sup>7)</sup>. The enriched target foils used are described in table 1. Charged particles scattered from the target were detected with a counter telescope containing commercial silicon surface barrier detectors. Charge summing across a 5 M resistor in the telescope was used to obtain the total energy pulse, and an FET pulse multiplier<sup>8)</sup> provided the  $E\Delta E$  pulse which contained the mass and charge information. Particle identification and data acquisition were performed on-line to the lab XDS Sigma 7 computer, using the code TOOTSIE<sup>9)</sup>.

TABLE 1  
Isotopic analysis of targets by atomic per cent

Target	(mg/cm <sup>2</sup> )	<sup>46</sup> Ti	<sup>47</sup> Ti	<sup>48</sup> Ti	<sup>49</sup> Ti	<sup>50</sup> Ti
<sup>46</sup> Ti	1.054	86.1	1.6	10.6	0.8	1.0
<sup>48</sup> Ti	0.923	0.17	0.2	99.36	0.17	0.11
<sup>50</sup> Ti	1.090	3.1	2.39	22.8	2.02	69.7

The overall energy resolution was 50-60 keV. The energy scale was established from the analog excitation energies measured in <sup>45,47,49</sup>Ti by Rosner and Pullen<sup>10</sup>). Uncertainties in the excitations reported here are estimated at 15-25 keV, depending on the transition strengths. Absolute cross sections are believed to be accurate to 6% excluding statistical errors which are reflected in the error bars shown.

Theoretical cross sections were computed in the DWBA by the Oak Ridge FORT-RAN-IV code JULIE<sup>1</sup>). The distorted waves were determined by the optical potentials used to reproduce elastic scattering data at the appropriate energies. In all cases the nuclear overlap, or form factor, was taken to be the wave function of a neutron, in the appropriate orbital, bound to the residual nucleus. The bound state well geometry was the same as for the real well in the proton elastic channel, with the depth adjusted to produce the correct neutron separation energy.

TABLE 2  
Proton optical-model parameters

$V^a)$	$r_0$	$a$	$r_c$	$W$	$W_D$
46.8 MeV	1.16 fm	0.75 fm	1.25 fm	3 MeV	4 MeV
$r_{01}$	$a_1$	$V_{s.o.}$	$r_s$	$a_s$	
1.37 fm	0.63 fm	6.04 MeV	1.064 fm	0.738 fm	

<sup>a</sup>)  $V$  is given for <sup>48</sup>Ti at 35 MeV. In general:  $V = 49.9 - 0.22E + 0.4Z/A + 26.4(N-Z)/A$  MeV.

Proton optical-model parameters were taken from the 30-40 MeV study of Fricke [ref. <sup>11</sup>)] and are listed in table 2. The potential used is

$$U_C - Vf(r, r_0, a) + i(-W + 4W_D d/dx_1)f(r, r_{01}, a_1) + (\hbar/m_\pi c)^2 V_{s.o.}(1/r)(d/dr)f(r, r_s, a_s)(l \cdot s), \quad (1)$$

where  $m_\pi$  is the pion mass,

$$f(r, r_0, a) = 1/[e^x + 1], \quad (2)$$

$$x = (r - r_0 A^{1/3})/a, \quad (3)$$

$$U_C = ZZ'e^2/r, \quad r \geq R_C = r_c A^{1/3}, \quad (4)$$

$$= (ZZ'e^2/2r)[3 - (r/R_C)^2], \quad r \leq R_C. \quad (5)$$

Deuteron parameters were obtained by averaging over the 2.5-10 MeV set of Wilhjelm *et al.* <sup>12)</sup>, the 11.8 and 21.4 MeV sets of Perey and Perey <sup>13)</sup> and the 34.4 MeV set of Newman *et al.* <sup>14)</sup>. Table 3 shows the parameters used.

TABLE 3  
Deuteron optical-model parameters

$V^a)$	$r_0$	$a$	$r_c$	$W_D$
101 MeV	1.065 MeV	0.81 fm	1.30 fm	10 MeV
$r_{01}$	$a_1$	$V_{s.o.}$	$r_s$	$a_s$
1.41 fm	0.75 fm	7 MeV	1.065 fm	0.81 fm

<sup>a)</sup>  $V$  is given at 25 MeV. In general:  $V = 117 - 0.627E_d$  MeV.

The theoretical cross section for (p, d) is taken as <sup>1, 15)</sup>:

$$\sigma_{lsj}^{th}(\theta) = \frac{2s_d + 1}{2s_p + 1} S(1.5) \sigma_{lsj}^{DWBA}(\theta) \quad (6)$$

$$= 2.25 S \sigma_{lsj}^{DWBA}(\theta), \quad (7)$$

where  $S$  is the spectroscopic factor. Multiplying by 1.5 is equivalent to using the Hulthén wave function for the deuteron.

Corrections to the local zero-range DWBA calculations were made for finite-range and non-local effects using the local energy approximation. These corrections were applied to the form factor used in the zero-range as a radial damping function, computed by the Oak Ridge code WAVDAM <sup>16)</sup>. The range of the interaction was taken as 1.5 fm and the non-locality parameters were 0.85 fm for the proton and neutron and 0.54 fm for the deuteron.

TABLE 4  
Per cent increase in peak (p, d) cross section for 10% increase in parameters of DWBA calculation

Parameter	Change in cross section (%)	Parameter	Change in cross section (%)	Parameter	Change in cross section (%)
$r_0$	28	$V$	20	$V$	-47
$a$	neutron BSW 8	$r_0$	incident 20	$r_0$	outgoing -49
$r_c$	0	$a$	proton -2	$a$	deuteron 5
		$r_c$	0	$r_c$	3
		$W$	0	$W_D$	-12
		$W_D$	-2	$r_{01}$	-21
		$r_{01}$	-15	$a_1$	-17
		$a_1$	-3	$V_{s.o.}$	0
		$V_{s.o.}$	0		
		$r_s$	0		
		$a_s$	0		

To investigate the sensitivity of the DWBA calculations to changes in the optical parameters, test cases were computed, each with one of the parameters increased by 10%. Table 4 shows the results of this study for an  $l = 3$  transfer at 25 MeV. The first three entries are for the neutron bound state well. As expected, the dominant effects are caused by varying the real well depths and radii, but the cross section is surprisingly sensitive to the parameters of the deuteron real well. Uncertainties on the order of 20% in extracted spectroscopic factors, then, are to be expected just due to the uncertainties in the parameters.

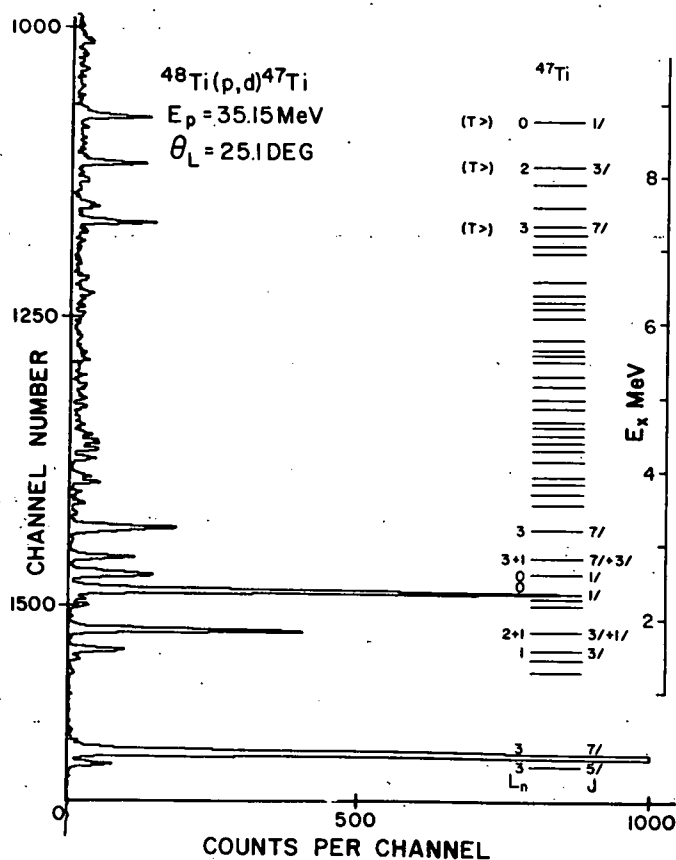


Fig. 1. Deuteron spectrum from the  $^{48}\text{Ti}(p, d)^{47}\text{Ti}$  reaction, aligned with the energy level diagram. The total spin  $J$  is in units of  $\frac{1}{2}\hbar$ .

### 3. Energy dependence of $^{48}\text{Ti}(p, d)^{47}\text{Ti}$

Angular distributions of  $^{48}\text{Ti}(p, d)^{47}\text{Ti}$  transitions have been measured over an angular range of 8 to 90° in the lab at 24.80, 29.82, 35.15, 39.97 and 45.05 MeV incident energies. Fig. 1 shows a typical spectrum, aligned with the observed energy

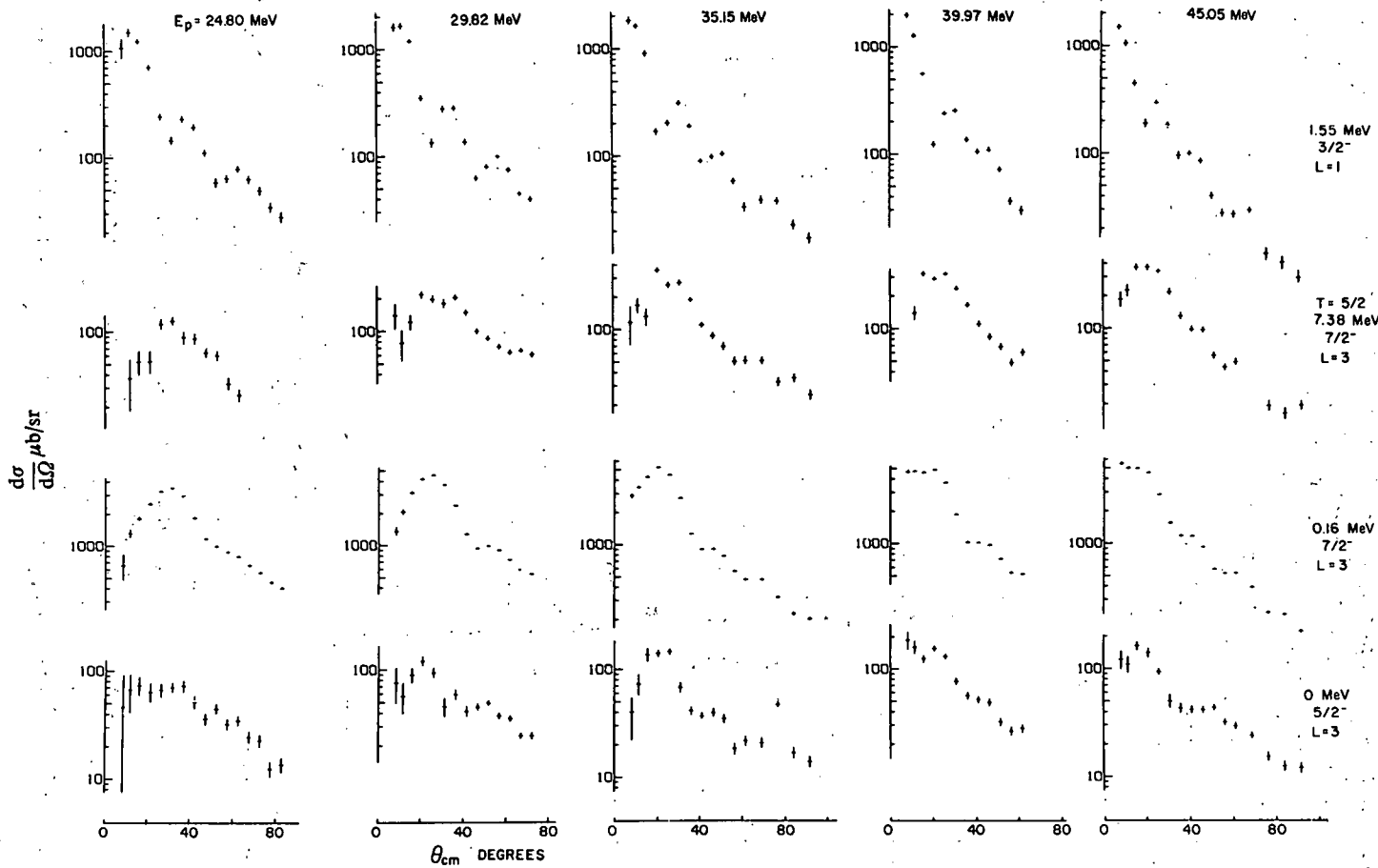


Fig. 2. Energy dependence of the cross sections of odd-*l* transitions in  $^{48}\text{Ti}(d, p)^{47}\text{Ti}$ .

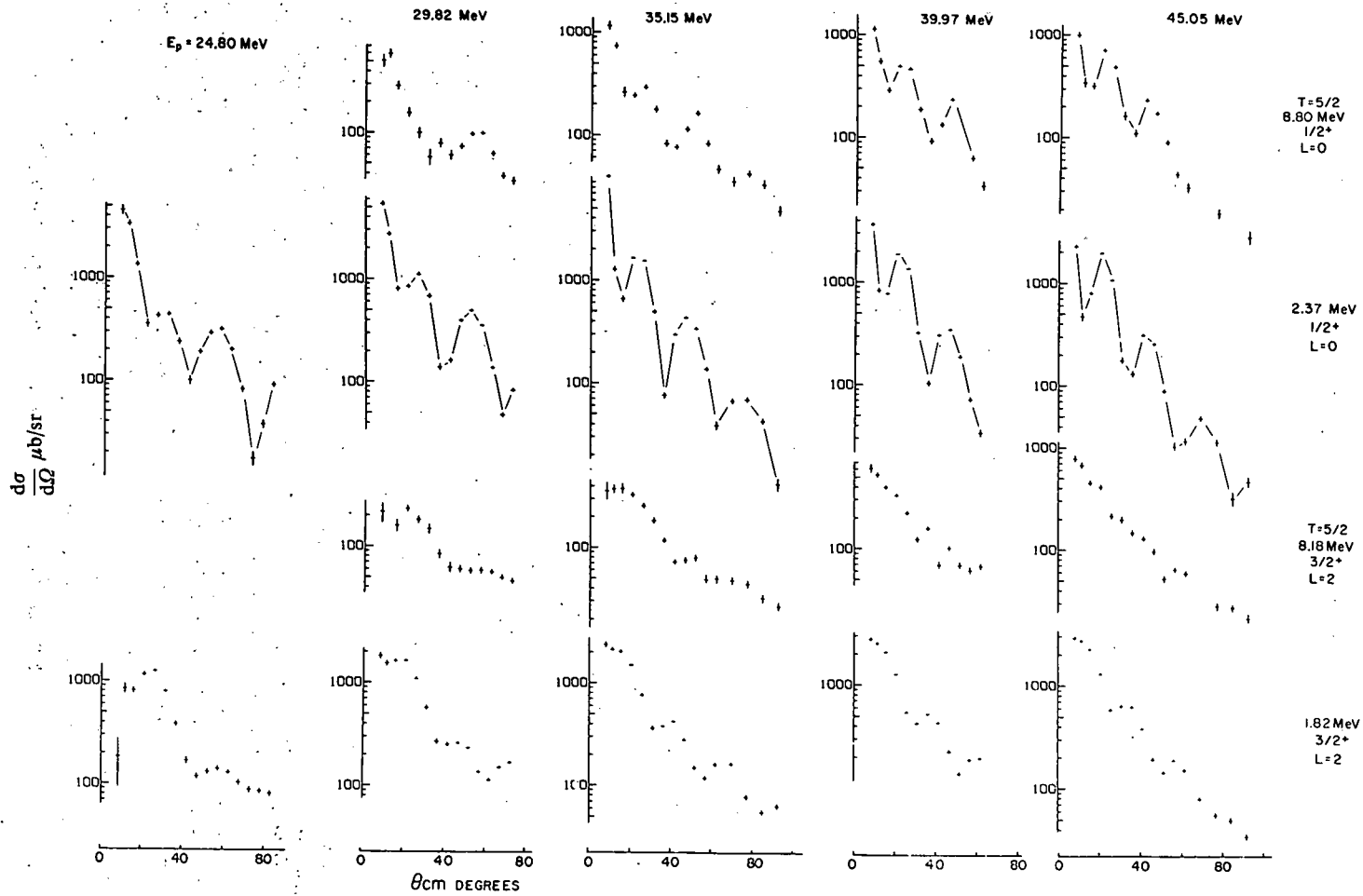


Fig. 3. Energy dependence of the cross sections of even-*l* transitions in  $^{48}\text{Ti}(p, d)^{47}\text{Ti}$ .



levels in  $^{47}\text{Ti}$ . The  $l$ -transfer,  $J$  and  $T$  assignments for the strong transitions are taken from earlier studies.

Note that the principal transition occurs to the 0.16 MeV first excited state and not to the ground state. The latter is known to have spin  $\frac{5}{2}^-$ , and is expected to consist mostly of three  $1f_{7/2}$  neutrons coupled to  $\frac{5}{2}^-$ . Since the direct pickup of a  $1f_{7/2}$  neutron from a  $0^+$  target cannot excite this state, the transition can only proceed in a one-step direct process via  $1f_{7/2}$  configuration admixtures in the target and final state wave functions. The  $1f$  spin-orbit splitting is known to be on the order of 5.5 MeV in this mass region<sup>17)</sup>, so the direct reaction cross section for this channel is expected to be small<sup>18)</sup>.

Thus the 0.16 MeV  $l = 3$  transition is of prime importance in the energy dependence investigation. Also included in the study are the strong  $l = 1$  transition at 1.55 MeV excitation and the  $l = 2$  transition at 1.82 MeV. The latter is known to be an unresolved doublet<sup>19)</sup>, which includes an  $l = 1$  transition. This component is relatively weak, as will be shown later, and does not strongly influence the shape of the cross section.

The three strong transitions between 7 and 9 MeV are to  $T = \frac{5}{2}$  analog states. One can locate such states by subtracting the n-p mass difference from the mass of the analogous state in  $^{47}\text{Sc}$ , then adding the Coulomb energy required to bring an additional unit of charge into the nucleus. Systematics of Coulomb energies in this region have been investigated<sup>20)</sup>, and usually agree with observed analog excitations to within 100 keV. Analog state transitions stand out as concentrated deuteron groups against a nearly continuous background of states of lower  $T$ .

Above these analog states, in fact up to 20 MeV excitation, no significant transitions are observed. Thus one can characterize  $^{48}\text{Ti}(p, d)^{47}\text{Ti}$  as leading principally to a few low-lying states in each isospin spectrum. Figs. 2 and 3 show the odd- $l$  and even- $l$  transitions described above at the 5 incident energies. In addition, the strong  $l = 0$  transfers measured at 2.37 and 8.80 MeV are displayed. Since these distributions are expected to have their principal maxima at  $0^\circ$ , they are not easily compared to calculated shapes and so play little role in the DWBA investigation.

All  $l = 3$  cross sections were found to increase linearly with energy up to about 35 MeV, then become fairly constant (see figs. 2 and 3). This is consistent with the data of Kashy and Conlon at 17.5 MeV and of Sherr *et al.*<sup>4)</sup>, at 28 MeV. The shape of these cross sections, however, undergoes a marked change, the shape apparently being a function of the energy of the outgoing deuteron (compare 7.38 and 0.16 MeV  $l = 3$  distributions of fig. 2). Other  $l$ -transfer cross sections also increase with energy, but more uniformly. Such differences in energy dependence must, of course, be reproduced by the DWBA calculations to produce consistent spectroscopic factors.

DWBA calculations were performed for the principal  $l$ -transfers described above at 25, 30, 35, 40 and 45 MeV. In the zero-range approximation, these included a series of lower radial cutoffs from 0 to 7 fm to bracket the nuclear surface, which is at about  $1.25A^{1/3}$  or 4.54 fm. For the case of no cutoff, measured spectroscopic factors for all

$l = 3$  transitions decreased by about 30 % from 35 to 45 MeV. Using cutoffs at the nuclear surface best reproduced the shapes of angular distributions for all  $l$ -transfers and, while this procedure did not eliminate the observed energy dependence, it gave consistent behavior for all transitions. This agrees with the findings of Snelgrove and Kashy <sup>6</sup>) in the oxygen-mass region:

Best results, however, were obtained by applying finite-range and non-locality corrections to the form factor. Energy dependence was not apparent, from 25 to 45 MeV, as table 5 shows for a variety of transitions. Moreover, the predicted shapes are best for no cutoff, and become much worse with increasing cutoff radius.

TABLE 5  
FRNL spectroscopic factors for some of the principal transitions to <sup>47</sup>Ti

$E_x$ (MeV)	$L$	$J$	25 MeV	30 MeV	35 MeV	40 MeV	45 MeV
0	3	$\frac{3}{2}$	0.13	0.14	0.13	0.14	0.13
0.16	3	$\frac{7}{2}$	3.5	3.5	3.7	3.4	3.4
1.56	1	$\frac{3}{2}$	0.19	0.18	0.18	0.19	0.17
1.82	2	$\frac{3}{2}$	2.1	2.2	1.9	1.8	1.9
7.38	3	$\frac{7}{2}$	0.46	0.54	0.52	0.47	0.45

The ability of the DWBA to reproduce the shapes of experimental angular distributions is displayed in fig. 4. The dashed curves are zero-range calculations with no integration cut-offs. In all cases, such calculations predict far too much scattering at larger angles. Even fits to the principal maximum become so poor at higher energies that meaningful comparison with the data is difficult. The solid lines represent zero-range calculations where the integration is cutoff near 4.5 fm. These curves track the data much more closely, particularly at back angles. While the agreement with data also deteriorates with increasing energy, it is better than for no cutoff. The finite-range non-local predictions (FRNL) with no cutoff are shown as dot-dash lines. At 25-30 MeV they are generally better than zero-range with cutoff, but tend to be not as good at back angles for the 40-45 MeV data.

Thus the predicted angular distributions, using FRNL corrections, deviate most from the data at back angles and at higher energies. Both are cases of large momentum transfer, or relatively deep penetration into the nucleus. From the study of integration cutoffs, it is evident that the deviations are caused by the nuclear interior contributing proportionately too much to the cross section. Finite-range and non-locality corrections damp this contribution, but apparently not enough.

Green <sup>21</sup>) has investigated yet another possible correction, the dependence of the  $p$ - $n$  interaction on the density of nuclear matter. As in the case of finite-range and non-locality, this correction tends to damp contributions from the nuclear interior. At present, calculations have been performed only for the oxygen mass region by Freedom *et al.* <sup>22</sup>). There the agreement of DWBA with ( $p$ ,  $d$ ) data is markedly im-

proved by using this correction<sup>22</sup>). The results of that study indicate that performing density-dependent corrections for titanium would result in similar improvement.

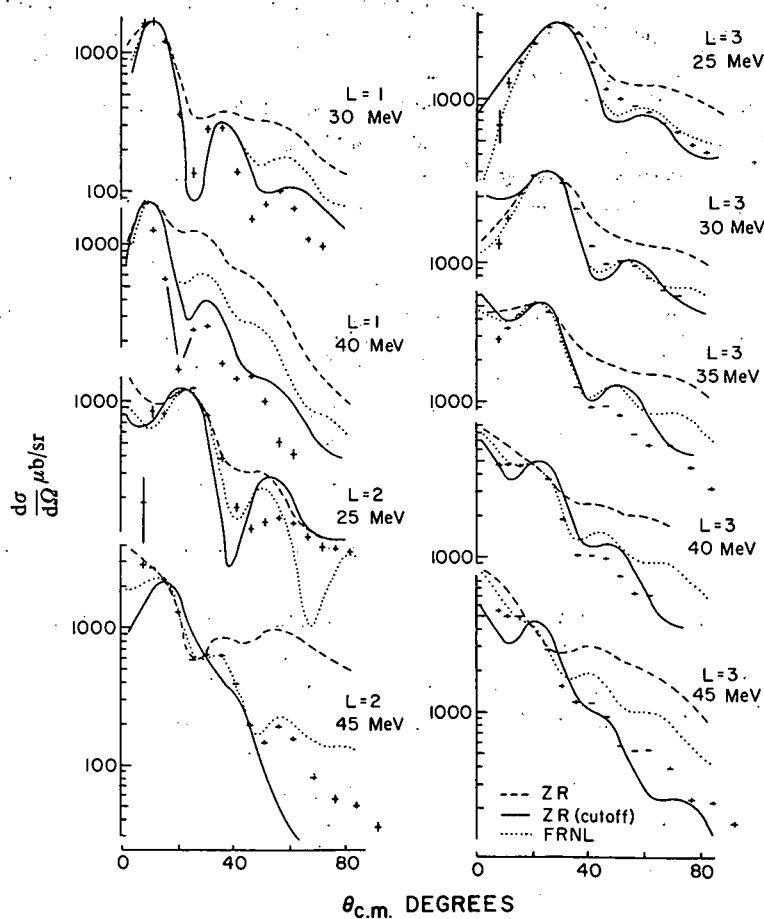


Fig. 4. DWBA calculations for  $l_n = 1$  (1.55 MeV),  $l_n = 2$  (1.82 MeV) and  $l_n = 3$  (0.16 MeV) in the  $^{48}\text{Ti}(p, d)^{47}\text{Ti}$  reaction for various bombarding energies.

#### 4. Spectroscopy of (p, d) reactions

The general features of  $^{48}\text{Ti}(p, d)^{47}\text{Ti}$  were discussed in the preceding section, and are displayed in fig. 1. Based on the conclusions of the energy dependence study, it was decided to study the spectroscopy of this reaction at 35.15 MeV, using FRNL corrections with no integration cutoffs in all DWBA calculations. Table 6 summarizes the observed data and spectroscopic analysis. The measured cross sections for all observed transitions are displayed in fig. 5.

Measured excitation energies are given in the first column of table 6. Low-lying

TABLE 6  
Summary of results for  $^{48}\text{Ti}(p, d)^{47}\text{Ti}$  at 35.15 MeV

$E_x$ (MeV)	Measured		$l$	Assigned				Previous	
	$\sigma_{\text{max}}$ (mb/sr)	$\theta_{\text{max}}$ (deg)		$J$	$S$	$T$	$E_x$ (MeV)	$J$	
0	0.14	22	3	$\frac{5}{2}^-$	0.12	$\frac{3}{2}$	0	$\frac{5}{2}^-$	
0.16	5.1	20	3	$\frac{7}{2}^-$	3.6		0.157	$\frac{7}{2}^-$	
1.25	0.02	flat					1.247		
1.44	0.05	30-60	(5)	$(\frac{3}{2}^-)$	0.01		1.442		
1.55	1.8	8	1	$\frac{3}{2}^-$	0.15		1.545	$\frac{3}{2}^-$	
1.82	0.48	8	1	$(\frac{3}{2}, \frac{1}{2})$	0.04		1.788	$\frac{1}{2}^-$	
	1.8	16	2	$\frac{3}{2}^+$	1.9		1.816	$\frac{3}{2}^+$	
2.16	0.40	10	1	$(\frac{3}{2}^-)$	0.03		2.157	$(\frac{1}{2}, \frac{3}{2})$	
2.26	0.16	@ 8					2.252		
							2.292		
2.37	1.6	22 <sup>a)</sup>	0	$\frac{1}{2}^+$	(0.59)		2.361	$\frac{1}{2}^+$	
2.60	0.22	22 <sup>a)</sup>	0	$\frac{1}{2}^+$	(0.08)			$\frac{1}{2}^+$	
	0.25	20	3	$\frac{7}{2}^-$	0.29				
2.82	0.22	22	3	$\frac{7}{2}^-$	0.25			$(\frac{5}{2}, \frac{7}{2})$	
3.22	0.48	22	3	$\frac{7}{2}^-$	0.46			$\frac{7}{2}^-$	
3.55	0.24	6	1	$(\frac{3}{2}^-)$	0.03		3.545	$\frac{3}{2}^-$	
4.15	0.14	8	(1)		0.02				
	0.14	16	(2)		0.37				
7.38	0.26	28	3	$\frac{7}{2}^-$	0.46	$\frac{5}{2}$	7.38	$\frac{7}{2}^-$	
8.18	0.37	14	2	$\frac{3}{2}^+$	1.4	$\frac{5}{2}$	8.18	$\frac{3}{2}^+$	
8.80	0.29	22 <sup>a)</sup>	0	$\frac{1}{2}^+$	(0.80)	$\frac{5}{2}$	8.80	$\frac{1}{2}^+$	

<sup>a)</sup> Second maximum.

states are compared with the precision  $^{46}\text{Ti}(d, p)^{47}\text{Ti}$  study by Rapaport, Sperduto and Buechner<sup>19)</sup> and the (d, p)  $J$ -dependence study by Lee and Schiffer<sup>23)</sup>. Earlier (p, d) investigations of  $^{47}\text{Ti}$  levels have been made by Kashy and Conlon<sup>3)</sup> and by Sherr *et al.*<sup>4)</sup>. Finally, there are the more recent ( $^3\text{He}$ ,  $^4\text{He}$ ) studies by L'Ecuyer and St-Pierre<sup>24)</sup> and by Lutz and Bohn<sup>25)</sup>. All previously established levels are included in the table down to the dashed line. Below this line the level density is too high for meaningful comparisons.

Since DWBA predictions are usually compared to data at the principal maximum, the cross section in mb/sr and the c.m. angle in degrees is listed at this point. If the distribution has no definite peak, the largest value measured is given, followed by the angle at which it was measured flagged with an @ sign. An exception is any state assigned  $l = 0$ , for which the data on the second maximum is recorded.

Several angular distributions were known or suspected to arise from unresolved doublets of different  $l$ -values. In such a case, least-squares fits were performed for the six possible linear combinations of two pure  $l = 0-3$  distributions, using angular distributions of isolated levels as a basis. From the variances of the fits, the most likely combination was determined. The computed variances of the coefficients, obtained

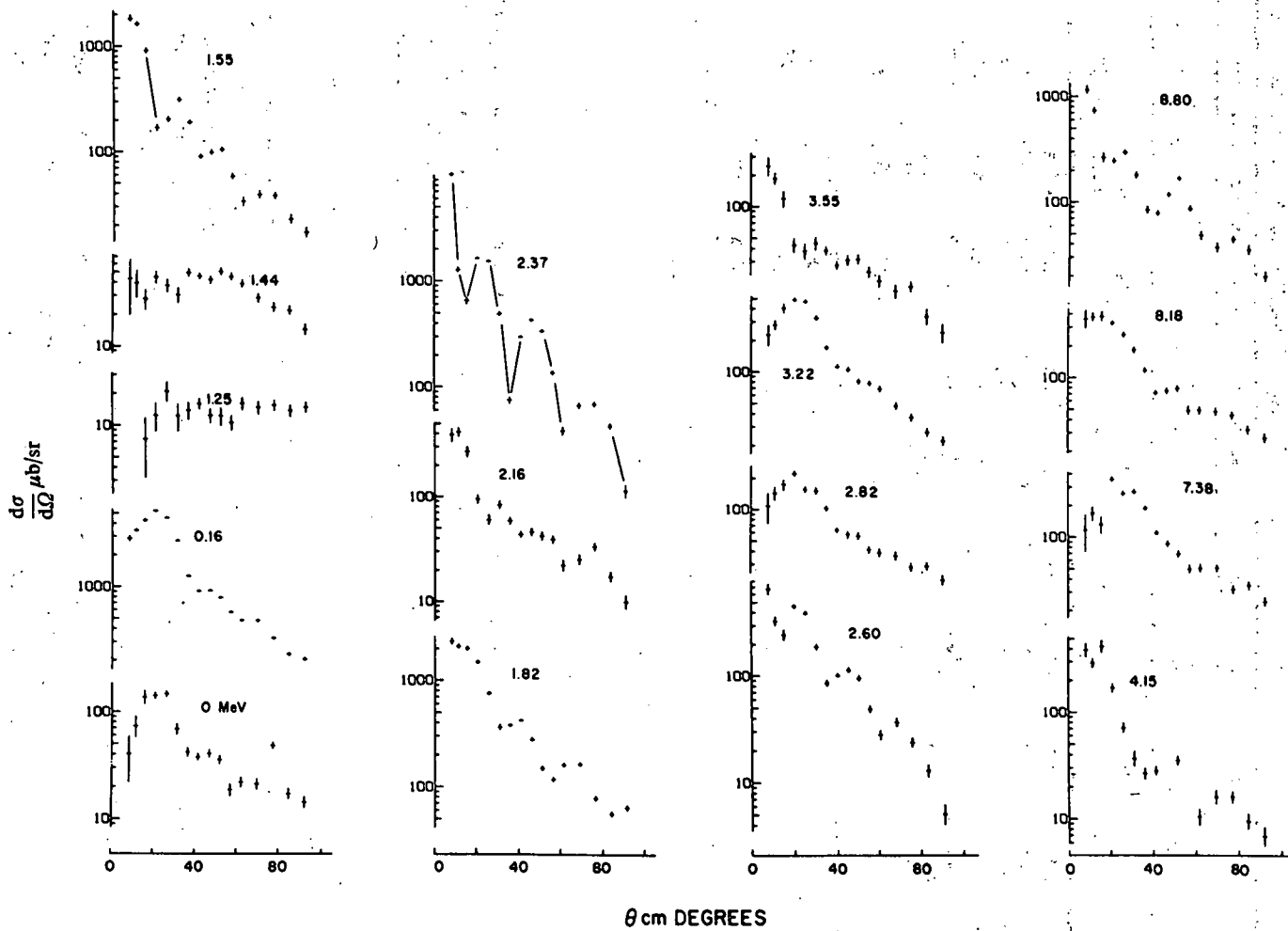


Fig. 5. Experimental angular distributions of  $^{48}\text{Ti}(p, d)^{47}\text{Ti}$  transitions at  $E_p = 35.15$  MeV.

from the inverted least-squares matrix<sup>26</sup>), indicated the validity of the fit and the sensitivity to individual contributions. Where such a fit has been made to the data, two lines of cross section are given, indicating the maximum for each contribution.

The *l*-transfers are generally determined by comparison with known transitions, aided in some cases by DWBA predictions. Strong non-zero *l*-transfers are almost

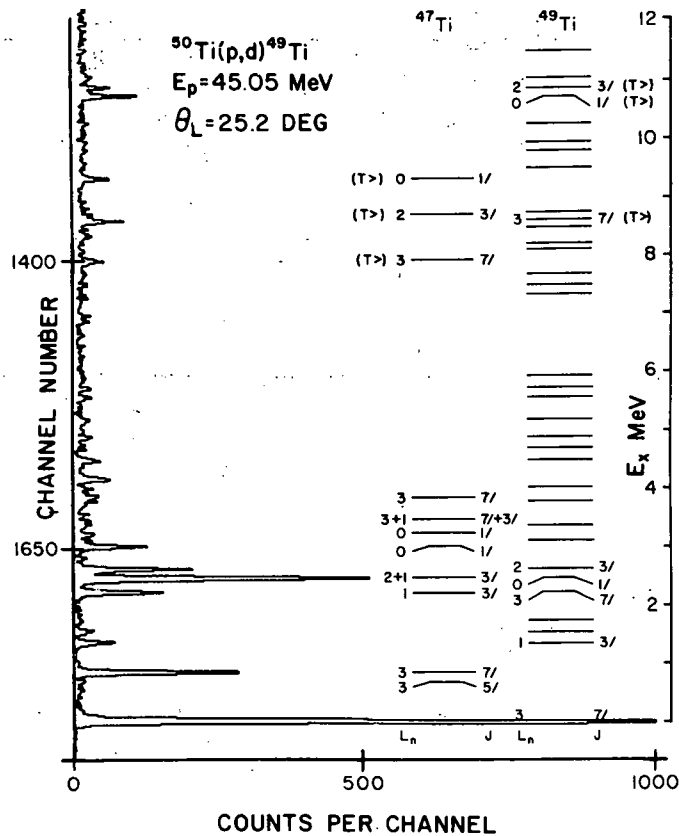


Fig. 6. Deuteron spectrum from the <sup>50</sup>Ti(p, d)<sup>49</sup>Ti reaction, aligned with the energy level diagram. The total spin *J* is in units of  $\frac{1}{2}\hbar$ . Transitions from <sup>48</sup>Ti contaminant present in the <sup>50</sup>Ti target are also indicated.

always assigned to the  $1d_{3/2}$ ,  $1f_{7/2}$  or  $2p_{3/2}$  shells because these lie nearest the Fermi surface. Following the usual convention, parentheses indicate tentative assignments. Thus, all  $l = 0$  assignments are given only tentative spectroscopic factors, due to the difficulty of comparing data to DWBA calculations. Isospin assignments are always to the lower allowed *T* unless specified otherwise.

As table 6 reveals, the qualitative description of this reaction given in the preceding section is quite precise – there are two isospin spectra, each with only a few strong

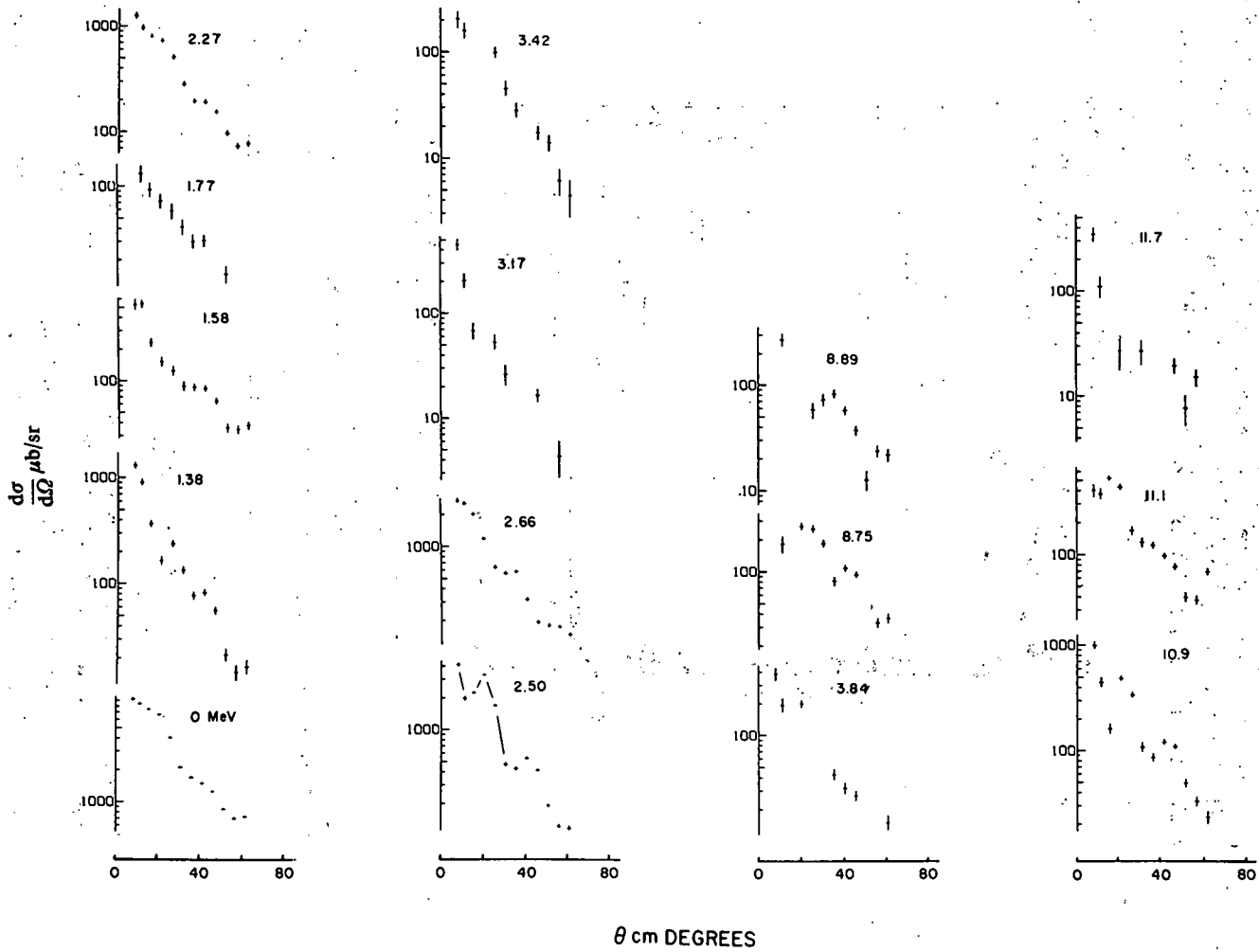


Fig. 7. Experimental angular distributions of  $^{50}\text{Ti}(p,d)^{49}\text{Ti}$  transitions at  $E_p = 45.05$  MeV.

transitions. A comparison with the predicted  $l = 3$  transfers of McCullen, Bayman and Zamick<sup>2,27</sup>) shows qualitative similarities between the data and the MBZ spectrum. The two unusual assignments at 1.44 and 1.82 MeV are of some interest. The former is a very weak transition having a definite direct reaction character, but peaking far back in angle. DWBA calculations for  $l = 5$  reproduce the wide change in peak angle observed from 25 to 45 MeV. If the  $l$  assignment is correct,  $1h_{\frac{3}{2}}$  is the lowest-lying candidate, closely corresponding to a  $\frac{3}{2}^-$  state predicted by MBZ. The  $l = 1$  component of the doublet at 1.82 MeV has been assigned spin  $\frac{1}{2}^-$  on the basis of  $J$ -dependence in back angle (d, p) scattering<sup>23</sup>). If this much  $2p_{\frac{1}{2}}$  admixture is known to occur, then weak  $l = 1$  assignments cannot be given a definite  $J$  in this study.

The large body of states between 4 and 7 MeV are too weakly populated to permit reliable assignment of  $l$ -values. Many show a direct reaction distribution having a strong dependence on scattering angle. Of these, it can only be concluded that they represent fairly complex configurations in terms of single-particle states. The excitation energies and distributions reported for this region are not necessarily for discrete states; rather they represent peaks in the (p, d) cross section.

TABLE 7  
Summary of results for  $^{50}\text{Ti}(p, d)^{49}\text{Ti}$  at 45.05 MeV

$E_x$ (MeV)	Measured		Assigned				Previous	
	$\sigma_{\max}$ (mb/sr)	$\theta_{\max}$ (deg)	$l$	$J$	$S$	$T$	$E_x$ (MeV)	$J$
0	9.0	8	3	$\frac{7}{2}^-$	3.6	$\frac{1}{2}$	0	$\frac{7}{2}^-$
1.38	1.3	8	1	$\frac{3}{2}^-$	0.19		1.382	$\frac{3}{2}^-$
1.58	0.48	8	1	$\frac{3}{2}^-$	0.07		1.542	
	0.04						1.586	$(\frac{3}{2}^-)$
							1.622	
							1.724	$\frac{1}{2}^-$
1.77	0.12	8	(3)		(0.05)		1.762	
2.27	1.2	8	3	$\frac{7}{2}^-$	0.58		2.261	$(\frac{7}{2}^-)$
							2.472	
2.50	2.5	20 <sup>a</sup> )	0	$\frac{1}{2}^+$	(1.5)		2.503	$\frac{1}{2}^+$
							2.505	
	1.3	8	(3, 2)		(0.6, 1.2)		2.516	$\frac{7}{2}, \frac{5}{2}$
							2.557	
2.66	2.6	10	2	$\frac{3}{2}^+$	2.4		2.665	$\frac{3}{2}^+$
3.17	0.44	8	1	$(\frac{1}{2}, \frac{3}{2})$	0.08		3.176	$\frac{1}{2}^-$
3.42	0.20	8	1	$(\frac{1}{2}, \frac{3}{2})$	0.04		3.430	$(\frac{1}{2}, \frac{3}{2})$
3.84	0.17	8	(3)	$(\frac{7}{2}^-)$	0.10		3.847	$(\frac{7}{2}, \frac{5}{2})$
	0.05	20 <sup>a</sup> )	(0)	$(\frac{1}{2}^+)$	(0.03)			
8.75	0.26	22	3	$\frac{7}{2}^-$	0.23	$\frac{7}{2}$	8.75	$\frac{7}{2}^-$
8.89	0.26	12	2	$(\frac{3}{2}^+)$	0.48			
10.9	0.47	22 <sup>a</sup> )	0	$\frac{1}{2}^+$	(0.77)	$\frac{7}{2}$	10.99	$\frac{3}{2}^+$
11.1	0.51	16	2	$\frac{3}{2}^+$	1.7	$\frac{7}{2}$	11.12	$\frac{1}{2}^+$
11.7	0.34	@ 8	(1)		1.0	$(\frac{3}{2})$		

<sup>a</sup>) Second maximum.



The  $^{50}\text{Ti}(p, d)^{49}\text{Ti}$  reaction was measured at 45.05 MeV over an angular range of 8 to 60° in the lab. Fig. 6 shows a typical deuteron spectrum obtained from the  $^{50}\text{Ti}$  foil, along with the levels observed. Since the target was 23%  $^{48}\text{Ti}$  (see table 1), its strong transitions are also indicated.  $l, J$  and  $T$  assignments for the principal transitions are taken from earlier work<sup>3,4,28,29</sup>.

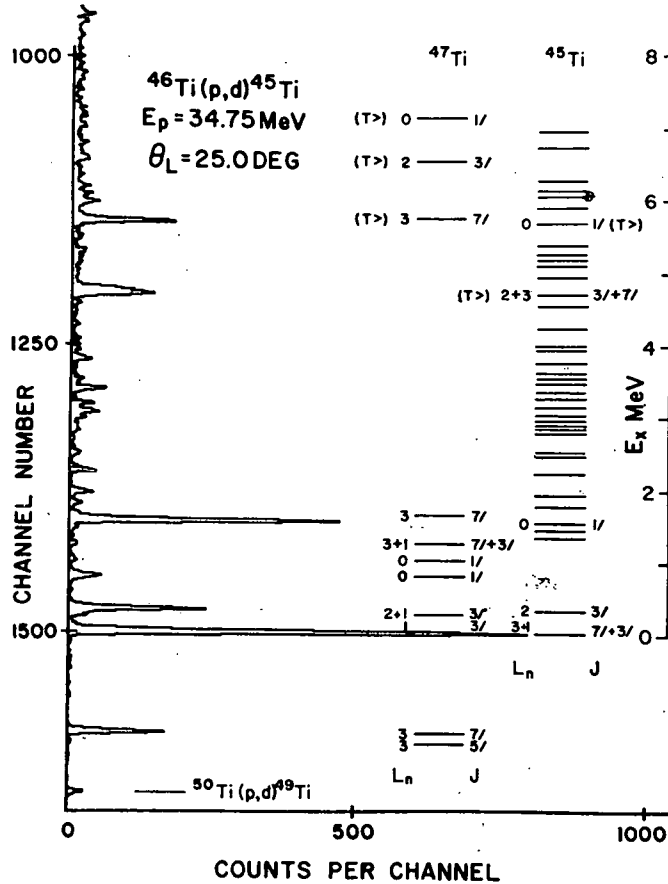


Fig. 8. Deuteron spectrum from the  $^{46}\text{Ti}(p, d)^{45}\text{Ti}$  reaction. The total spin is in units of  $\frac{1}{2}\hbar$ . Transitions from the  $^{50}\text{Ti}$  and  $^{48}\text{Ti}$  contaminants present in the  $^{46}\text{Ti}$  target are also indicated.

Besides the titanium studies mentioned in the previous section<sup>3,4,10,24,25</sup>) other investigations of the levels of  $^{49}\text{Ti}$  include the precision (d, p) work of Barnes *et al.*<sup>28</sup>) at 6.2 MeV and the consistent level scheme developed by Anderson *et al.*<sup>29</sup>). The measured angular distributions are presented in fig. 7, and results of the spectroscopic study are summarized in table 7. The same general remarks apply to this table as were made concerning table 6. All known levels<sup>29</sup>) are presented, down to

the dashed line, below which only states corresponding to relatively strong (p, d) transitions are reported.

Comparing this data to  $^{48}\text{Ti}(p, d)^{47}\text{Ti}$ , one is again struck by the selectivity of the

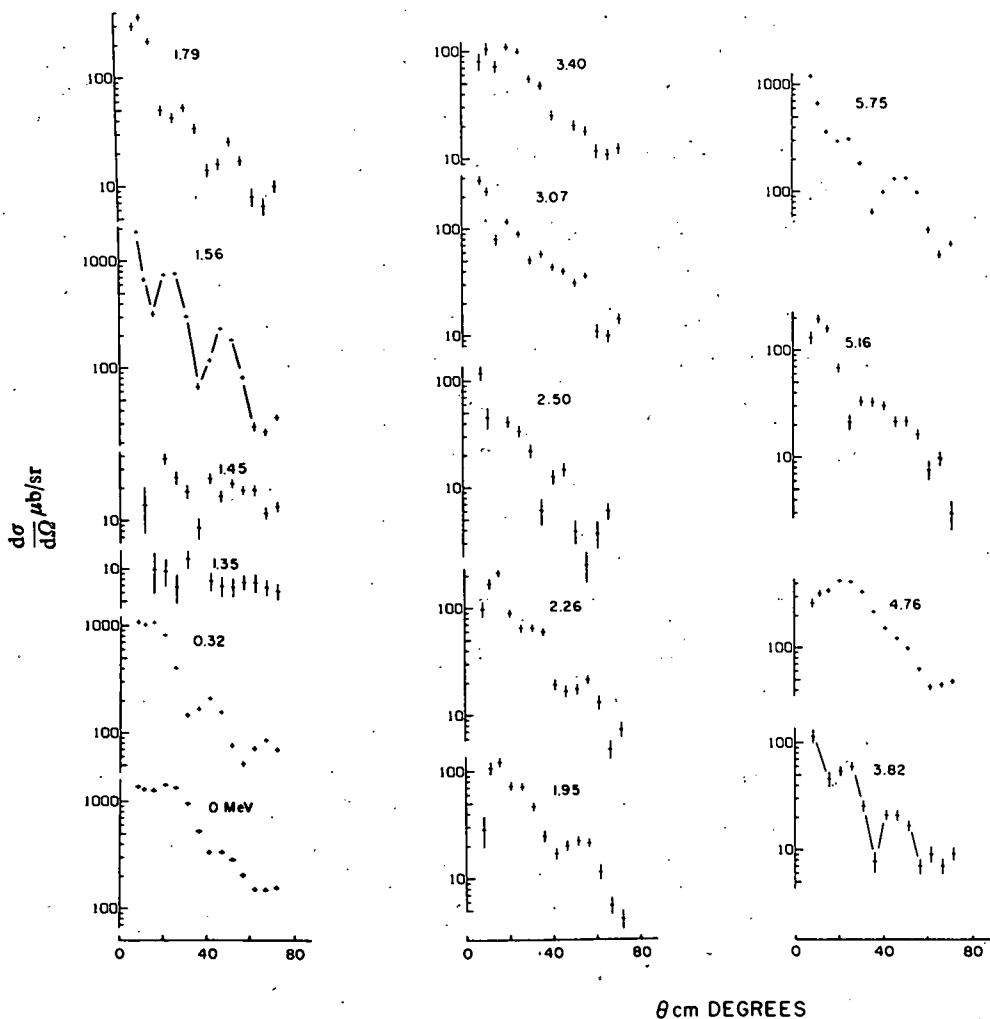


Fig. 9. Experimental angular distributions of  $^{46}\text{Ti}(p, d)^{45}\text{Ti}$  transitions at  $E_p = 34.78$  MeV.

(p, d) reaction. There is the strong  $l = 3$  transitions, this time to the ground state, a few strong low-lying transitions, a wide gap and then the analog states. Again the similarity to the MBZ predictions is only qualitative.

Of the states previously assigned spin  $\frac{1}{2}^-$ , the one at 1.724 MeV is not seen and that at 3.176 MeV apparently only weakly. For the doublet at 2.46 MeV measured excitation,

it was not possible to distinguish between an  $l = 0+2$  and an  $l = 0+3$  assignment. Due to the similarity of  $l = 2$  and  $l = 3$  angular distributions at this energy, several assignments are uncertain.

A strong  $l = 2$  transition was observed at 8.89 MeV in  $^{49}\text{Ti}$  which is not a candidate for being an analog state. It is possible that it is a  $1d_{3/2}$  hole state, since it lies at about the excitation predicted by the simple shell model. The single-particle strength of such a state would be much less likely to be distributed over other states in this nucleus, since in a simple model the configuration is  $d_{3/2}^{-1} f_{7/2}^8$  and the  $f_{7/2}^8$  term can only couple to  $0^+$ . Finally, a fairly strong transition was measured at 11.7 MeV which has been tentatively assigned  $l = 1$  and may be an analog state.

The  $^{46}\text{Ti}(p, d)^{45}\text{Ti}$  reaction was measured over an angular range of  $8$  to  $70^\circ$  in the lab at an incident energy of 34.75 MeV. Fig. 8 shows a typical spectrum, with the observed levels and principal contaminants. The quantities  $l$ ,  $J$  and  $T$  are given for the strongest transitions.

Since  $^{44}\text{Ti}$  is not stable, (d, p) stripping information is not available. The principal transitions have been reported<sup>3,24</sup>) and the excitation energies established for the isobaric analog states<sup>10</sup>). A low-lying triplet ( $0(\frac{7}{2}^-)$ ,  $37(\frac{3}{2}^-)$ ,  $40$  keV) has been reported by Jett, Jones and Ristinen<sup>30</sup>) for which some evidence has been found in this study, but other levels reported at 0.744 and 1.227 MeV are not observed. A level scheme based on 26 MeV (p, d) data has also been reported by Jones, Johnson and

TABLE 8  
Summary of results for  $^{46}\text{Ti}(p, d)^{45}\text{Ti}$  at 34.78 MeV

$E_x$ (MeV)	Measured		Assigned				Previous	
	$\sigma_{\max}$ (mb/sr)	$\theta_{\max}$ (deg)	$l$	$J$	$S$	$T$	$E_x$ (MeV)	$J$
0	1.4	22	3	$\frac{7}{2}^-$	1.2	$\frac{1}{2}$	0	$\frac{7}{2}^-$
	0.30	12	1	$\frac{3}{2}^-$	0.03		0.037	$(\frac{3}{2}^-)$
0.32	1.0	14	2	$\frac{3}{2}^+$	1.0			$\frac{3}{2}^+$
1.35	0.01	flat						
1.56	0.74	25 <sup>a)</sup>	0	$\frac{1}{2}^+$	(0.33)			$\frac{1}{2}^+$
1.79	0.35	12	1	$(\frac{3}{2}^-)$	0.04			$\frac{3}{2}^-$
1.95	0.07	22	3	$(\frac{7}{2}^-)$	0.07			$\frac{7}{2}^-$
2.26	0.07	22	(3)					$\frac{3}{2}^+$
	0.15	12	(1)					
2.50	0.04	22 <sup>a)</sup>	(0)	$(\frac{1}{2}^+)$	(0.02)			
3.07	0.08	22 <sup>a)</sup>	(0)	$(\frac{1}{2}^+)$	(0.05)			
	0.09	14	(2)	$(\frac{3}{2}^+)$	0.15			
3.40	0.11	20	3	$(\frac{7}{2}^-)$	0.14			
3.82	0.06	22 <sup>a)</sup>	0	$\frac{1}{2}^+$	(0.04)			
4.76	0.42	22	3	$\frac{7}{2}^-$	0.62	$\frac{3}{2}$	4.74	$\frac{7}{2}^-$
	0.18	14	2	$\frac{3}{2}^+$	0.50	$\frac{3}{2}$	4.81	$\frac{3}{2}^+$
5.16	0.19	12	1	$\frac{3}{2}^-$	0.04	$(\frac{3}{2})$		
5.75	0.30	22 <sup>a)</sup>	0	$\frac{1}{2}^+$	(0.40)	$\frac{1}{2}$	5.75	$\frac{1}{2}^+$

<sup>a)</sup> Second maximum.

Jett <sup>31</sup>) which gives excitation energies as much as 7 % different than those reported here. The assigned  $l$ -transfers for the first few states agree, however.

Measured angular distributions are presented in fig. 9, and the findings are summarized in table 8. The reaction strength is more uniformly distributed than for the other isotopes studied, but bears the same qualitative features. Only 10 states have cross sections greater than 0.15 mb/sr, 4 of which are assigned  $T = \frac{3}{2}$ . Thus the (p, d) reaction is highly selective for all three targets.

The lowest-lying transition has been fit with  $l = 3 + 1$  distributions, which is consistent with a low-lying  $\frac{7}{2}^-, \frac{3}{2}^-, \frac{5}{2}^-$  triplet <sup>30</sup>). Likewise the lowest analog transition, clearly a doublet in fig. 8, is best fit with  $l = 3 + 2$ , as expected <sup>10</sup>). An  $l = 1$  transition observed at 5.16 MeV is a good candidate for a  $\frac{3}{2}^-$  analog state. No single transition of significant strength was observed above 6 MeV.

### 5. Sum rules and $Q$ -dependence

Having made a spectroscopic analysis of the (p, d) data one is now in a position to compare the summed spectroscopic factors for pickup from each orbital with the predictions of French and Macfarlane <sup>5</sup>). For pickup from a given shell, the expected sum for all transitions to upper- $T$  states is

$$\sum = p/(2T+1), \quad (9)$$

where  $p$  is the number of protons in the same orbital and  $T$  is the isospin of the target. Table 9 lists the summed spectroscopic factors for the  $2s_{\frac{1}{2}}$ ,  $1d_{\frac{3}{2}}$ ,  $1f_{\frac{7}{2}}$  and outer shells for each of the three reactions studied. The sums are further divided into lower- and

TABLE 9  
Comparison of summed spectroscopic factors to predictions <sup>a)</sup>

Target	Shell	Total		Lower- $T$			Upper- $T$		
		exp	th	exp	th	exp/th	exp	th	exp/th
<sup>46</sup> Ti	$2s_{\frac{1}{2}}$	0.84	2	0.44	1.33	0.33	0.40	0.67	0.60
	$1d_{\frac{3}{2}}$	1.7	4	1.2	2.67	0.43	0.50	1.33	0.38
	$1f_{\frac{7}{2}}$	2.0	4	1.41	3.33	0.42	0.62	0.67	0.93
	outer	0.11	0	0.07			0.04		
<sup>48</sup> Ti	$2s_{\frac{1}{2}}$	1.5	2	0.67	1.60	0.42	0.80	0.40	2.0
	$1d_{\frac{3}{2}}$	3.7	4	2.3	3.20	0.72	1.4	0.80	1.8
	$1f_{\frac{7}{2}}$	5.1	6	4.6	5.60	0.82	0.46	0.40	1.2
	outer	0.4	0	0.40			0		
<sup>50</sup> Ti	$2s_{\frac{1}{2}}$	2.2	2	1.5	1.71	0.88	0.77	0.29	2.7
	$1d_{\frac{3}{2}}$	4.1	4	2.4	3.43	0.70	1.7	0.57	3.0
	$1f_{\frac{7}{2}}$	5.2	8	5.0	7.71	0.65	0.23	0.29	0.79
	outer	1.4	0	0.38			1.0		

<sup>a)</sup> As discussed in text, the spectroscopic factors are of limited reliability.

upper- $T$  transitions, and ratios of experimental results to the sum-rule predictions are obtained. Although it is of questionable validity, the analysis is carried through for  $l = 0$ .

Even allowing for the systematic uncertainty due to the optical parameters and for the unknown amount of transition strength lost to the weaker states, many of the results given in table 9 are improbable. If the sums are to be believed, fully half the expected number of particles are missing from the  $2s-1d$  shell in  $^{46}\text{Ti}$ , while essentially all are accounted for in the heavier two nuclei. A possible explanation here is that much more of the  $(p, d)$  strength is unaccounted for, proportionately, since the cross sections are observed to be more uniform and since no  $(d, p)$  spectroscopy is available to help identify weaker transitions. Doubling all sums for  $^{46}\text{Ti}$  would also bring the  $1\ f_{7/2}$  sum more into line.

One can argue that the  $0.9\ f_{7/2}$  neutrons missing from  $^{48}\text{Ti}$  is within reason, but it is difficult to explain away nearly 3 from  $^{50}\text{Ti}$ . It also appears that  $\approx 1.4$  of the missing  $f_{7/2}$  neutrons from  $^{50}\text{Ti}$  are in the  $2p$  shell. Yet the lighter nuclei promote at most 0.4 neutrons to this shell. Clearly something is wrong.

The sums of transitions to upper- $T$  states are uniformly larger than expected. An extreme case is the high-lying  $l = 1$  transfer to  $^{49}\text{Ti}$  which has  $S = 1$  even though the lower- $T$  sum is only 0.38. The common feature of these analog states that could lead to such a discrepancy is their large excitation energies, i.e. they have  $Q$ -values significantly more negative than the lower  $T$ -states. Evidently the calculations do not predict the proper dependence of cross section on  $Q$ , even with the first order correction of adjusting the real well depth in the deuteron channel.

This is not too surprising. The prescription for obtaining the single-particle bound state wave function, or form factor, is to pick the well depth that binds the proper orbital, with the right separation energy. But the data shows that pickup from the same orbital can lead to levels 7 or 8 MeV apart. To bind the particle with 7 MeV greater separation energy requires a well 10 MeV deeper. The particle is bound tighter, there is consequently less overlap in the transition amplitude integral, the predicted cross section is too small and so the resulting spectroscopic factor is too large. While the simple shell-model levels are known to be widely split by Coulomb or other residual interactions, each level is treated as a pure unperturbed single-particle level at the proper energy for the sake of the calculation.

One approach to this problem is to just ignore the change in binding energy. Sherr *et al.* in their study<sup>4)</sup> of isobaric analog states in the titanium-nickel mass region were able to improve agreement with predictions by using an effective binding procedure. In this scheme, the same bound state wave function is used for all  $Q$ -values, effectively ignoring the energy shifts caused by residual interactions. Unfortunately, this produces an incorrect exponential falloff outside the nucleus for the form factor, which the separation energy prescription is designed to produce correctly.

The use of a neutron bound state wave function to represent the nuclear overlap is strictly correct only for pickup of a single particle outside a closed core<sup>32)</sup>. Thus,

while the form of the overlap in the nuclear interior is open to question, the exponential falloff outside is rather closely defined by the separation energy. Pinkston and Satchler, in an investigation<sup>33)</sup> of the  $Q$ -dependence problem, conclude that other features of the bound state well must be changed, besides the depth, as a function of  $Q$  and that the effective binding procedure is essentially wrong.

Another manifestation of the  $Q$ -dependence problem is the  $^{48}\text{Ti}(p, d)^{47}\text{Ti}(\text{g.s.})$  transition, which proceeds by a small  $1f_{7/2}$  admixture. A well nearly 10 MeV deeper than for the 0.16 MeV state is required to give the proper separation energy. The predicted spectroscopic factor is almost certainly too high. Prakash<sup>32)</sup> has ameliorated this problem in  $(d, p)$  stripping by introducing pseudopotentials, due to the presence of interacting extra-core nucleons, into the bound state wave equation. Prakash and Austern have proposed a procedure which attaches the proper exponential tail to the correct inside nucleus function<sup>34)</sup>. Likewise Rost has developed a coupled-channels method<sup>34)</sup> for computing more realistic bound state wave functions, for use in  $l = 3$  transitions to analog states. The general problem, however, of properly reproducing  $Q$ -dependence in DWBA calculations is still a topic for discussion.

Thus, the spectroscopic factors presented in table 9 are of only limited reliability. One can conclude, however, from the systematics of the  $(p, d)$  reaction over the titanium isotopes presented here, that large discrepancies between DWBA spectroscopic strengths and sum rules can be attributed to incorrect  $Q$ -dependence in the calculations, giving spectroscopic factors which are relatively too large for the high-lying excited states.

We wish to thank L. Learn and G. F. Trentelman for help in acquiring some of this data, and B. Horning for his assistance in the data reduction. We are especially indebted to Prof. B. M. Freedom for his aid in the DWBA calculation and his helpful comments concerning the experiment, and to Prof. R. Sherr for many stimulating discussions of the spectroscopy of analog states in the Ti isotopes. We also wish to thank Mrs. Jean McIntyre who prepared this manuscript.

### References

- 1) G. R. Satchler, Nucl. Phys. **55** (1964) 1;  
R. H. Bassel, R. M. Drisko and G. R. Satchler, Oak Ridge National Laboratory Technical Report ORNL-3240 (1962) unpublished;  
Oak Ridge National Laboratory Memorandum to the users of the code JULIE (1966) unpublished
- 2) J. D. McCullen, B. F. Bayman and L. Zamick, Phys. Rev. **134** (1964) B515
- 3) E. Kashy and T. W. Conlon, Phys. Rev. **135** (1964) B389
- 4) R. Sherr, B. F. Bayman, E. Rost, M. E. Rickey and C. G. Hoot, Phys. Rev. **139** (1965) B1272
- 5) J. B. French and M. H. Macfarlane, Nucl. Phys. **26** (1961) 168
- 6) J. L. Snelgrove and E. Kashy, Nucl. Instr. **52** (1967) 153
- 7) H. G. Blosser and A. I. Galonsky, IEEE Trans. on Nucl. Sci., NS-B **4** (1966) 466
- 8) G. L. Miller and V. Radeka, Proc. NAS Conf. on instrument techniques in nuclear pulse analysis (Monterey, 1968)

- 9) D. L. Bayer, Michigan State University Cyclotron Laboratory Sigma 7 Program Description 0013 (1969) unpublished
- 10) B. Rosner and D. J. Pullen, *Phys. Lett.* **24B** (1967) 454
- 11) M. P. Fricke, E. E. Gross, B. J. Marton and A. Zucker, *Phys. Rev.* **156** (1967) 1207
- 12) P. Wilhelm, O. Hansen, J. R. Comfort, C. K. Bockelman, P. D. Barnes and A. Sperduto, *Phys. Rev.* **166** (1968) 1121
- 13) C. M. Perey and F. G. Perey, *Phys. Rev.* **152** (1966) 923
- 14) E. Newman, L. C. Becker, B. M. Freedom and J. C. Hiebert, *Nucl. Phys.* **A100** (1967) 225
- 15) G. R. Satchler, *Nucl. Phys.* **55** (1964) 1
- 16) G. R. Satchler, description of Oak Ridge National Laboratory FORTRAN-IV computer code WAVDAM (1969) private communication
- 17) T. A. Belote, E. Kashy, A. Sperduto, H. A. Enge and W. W. Buechner, Argonne National Laboratory Report ANL-6878 (1964) 109, unpublished
- 18) T. A. Belote, W. E. Dorenbusch, O. Hansen and J. Rapaport, *Nucl. Phys.* **73** (1965) 321
- 19) J. Rapaport, A. Sperduto and W. W. Buechner, *Phys. Rev.* **143** (1966) 808
- 20) R. Sherr, *Phys. Lett.* **24B** (1967) 321
- 21) A. M. Green, *Phys. Lett.* **24B** (1967) 384
- 22) B. M. Freedom, J. L. Snelgrove and E. Kashy, *Phys. Rev.* **C1** (1970) 1132
- 23) L. L. Lee, and J. P. Schiffer, *Phys. Rev.* **154** (1967) 1097
- 24) J. L'Ecuyer and C. St.-Pierre, *Nucl. Phys.* **A100** (1967) 401
- 25) H. F. Lutz and T. S. Bohn, *Nucl. Phys.* **A116** (1968) 112
- 26) R. H. Moore and R. K. Zeigler, Los Alamos Scientific Laboratory Report LA-2367 (1960) unpublished
- 27) J. D. McCullen, B. F. Bayman and L. Zamick, Princeton University Technical Report NYO-9891 (1964) unpublished
- 28) P. D. Barnes, J. R. Comfort, C. K. Bockelman, O. Hansen and A. Sperduto, *Phys. Rev.* **159** (1967) 920
- 29) S. A. Anderson, O. Hansen and L. Vistisen, *Nucl. Phys.* **A125** (1969) 65
- 30) J. H. Jett, G. D. Jones and R. A. Ristinen, *Phys. Lett.* **28B** (1968) 111
- 31) G. D. Jones, R. R. Johnson and J. H. Jett, *Nucl. Phys.* **A111** (1968) 449
- 32) A. Prakash, *Phys. Rev. Lett.* **20** (1968) 864
- 33) W. T. Pinkston and G. R. Satchler, *Nucl. Phys.* **72** (1965) 641
- 34) A. Prakash and N. Austern, *Ann. of Phys.* **51** (1969) 418
- 35) E. Rost, *Phys. Rev.* **154** (1967) 994

## Experimental Studies of the Neutron-Deficient Gadolinium Isotopes. II. $Gd^{145m}$

R. E. Eppley and Wm. C. McHarris

*Department of Chemistry\* and Cyclotron Laboratory,† Department of Physics,  
Michigan State University, East Lansing, Michigan 48823*

and

W. H. Kelly

*Cyclotron Laboratory,† Department of Physics, Michigan State University, East Lansing, Michigan 48823*

(Received 13 July 1970)

The  $N=81$  isomer  $Gd^{145m}$  is characterized as having a half-life of  $85 \pm 3$  sec and an  $M4$  isomeric transition of  $721.4 \pm 0.4$  keV. It also has a direct  $\beta^+/\epsilon$  branch to the  $h_{11/2}$  state at 716.1 keV in  $Eu^{145}$ . The intensity of this branch is 4.7% of the decay, implying a  $\log ft$  of 6.2. The  $M4$  transition probability is calculated and compared with the trends among other isomeric transitions in this region.

### I. INTRODUCTION

Gadolinium isotopes cover a wide range of nuclear types, extending from permanently deformed nuclei to spherical single closed-shell nuclei at  $N=82$ . As a result, systematic studies of their decay properties and structures should prove quite rewarding, for here is one of the few regions in the nuclidic chart where one can follow trends in

nuclear states when moving from one extreme nuclear type to another. We have embarked recently on such a systematic study. The first paper in this series described the electron-capture decay of  $Gd^{149}$ , a nucleus that lies midway between the spherical and spheroidal regions.<sup>1</sup> On the neutron-deficient side of  $N=82$  the Gd isotopes have not been very well characterized until quite recently, although their decays present some interesting



anomalies, such as the peculiar ground-state decay of  $Gd^{145}$  into what appear to be three-quasiparticle states in its  $Eu^{145}$  daughter, the subject of which will form the third paper in this series.<sup>2</sup> On the neutron-deficient side of  $N = 82$  a systematic study of the odd-mass isotones also appears well worthwhile because of the appearance of long series of nuclear isomers having quite different and distinct decay properties. The longest series of these isomers, in the  $N = 81$  nuclei, extended from  $Te^{133}$  to  $Sm^{143}$ , and it seemed reasonable that  $Gd^{145}$ , as the next nucleus in line, should also exhibit isomeric states.

We subsequently observed the metastable state in  $Gd^{145}$  and its isomeric transition. The energy of the transition was found to be  $721.4 \pm 0.4$  keV and the half-life of the state,  $85 \pm 3$  sec. These values were consistent with our predictions based on the systematics of the other  $N = 81$  isotones, and they were first reported in November 1968.<sup>3</sup> Since that time, Jansen, Morinaga, and Signorini<sup>4</sup> have published results in very good agreement with our  $\gamma$ -ray energy and half-life values. Since our first preliminary report we have also observed the conversion electrons from the isomeric transition, clearly identifying it to be of  $M4$  multipolarity, and we have observed a  $\beta^+/\epsilon$  branch from  $Gd^{145m}$  directly to states in  $Eu^{145}$ .

Even by 1951, some 77 nuclear isomers had

been classified by Goldhaber and Sunyar.<sup>5</sup> Since then, of course, isomers have been one of the prominent nuclear properties used to test the validity of nuclear models. In particular,  $M4$  transitions are of interest for testing the extreme single-particle model. If such a thing as a "pure" single-particle transition exists, these transitions are good candidates for that distinction. The  $M4$  transitions observed in the  $N = 81$  nuclei are thought to proceed from  $h_{11/2}$  to  $d_{3/2}$  states, and the  $h_{11/2}$  state should be particularly pure owing to its being the only odd-parity high-spin state at low excitations. We discuss the properties of these  $M4$  transitions in Sec. III.

## II. EXPERIMENTAL

We produced  $Gd^{145m}$  in this laboratory by both the  $Sm^{144}(\tau, 2n)Gd^{145m}$  and the  $Sm^{144}(\alpha, 3n)Gd^{145m}$  reactions. The calculated  $Q$  values for these reactions were  $-10.4$  and  $-30.9$  MeV, respectively.<sup>6</sup> For all of these experiments, separated isotope  $Sm^{144}$  (95.10%, obtained from Oak Ridge National Laboratory) in the form of  $Sm_2O_3$  was used as the target material. The  $\tau$  and  $\alpha$  beams, typically 20 and 40 MeV, respectively, were furnished by the Michigan State University (MSU) sector-focused cyclotron. Excitation functions were run to determine the energy for maximum  $Gd^{145m}$  yield in each

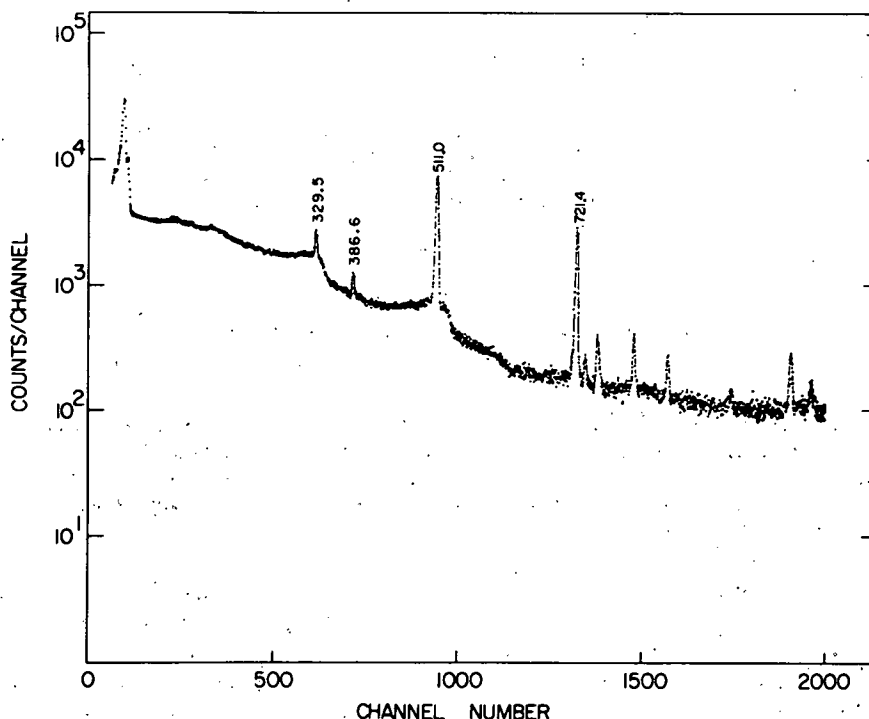


FIG. 1. Singles  $\gamma$ -ray spectrum from 85-sec  $Gd^{145m}$ . The 721.4-keV peak is the  $M4$  isomeric transition, while the 386.6- and 329.5-keV peaks come after a direct  $\beta^+/\epsilon$  branch from  $Gd^{145m}$  to the  $h_{11/2}$  state in  $Eu^{145}$ . The unlabeled peaks result from the decay of 21.8-min  $Gd^{145}$ .

case. Most of our experiments were performed with the  $\tau$  beam, and typically a 10-mg or smaller target would be bombarded with a 0.5- $\mu$ A beam for 1 min. Because of the short half-life of  $Gd^{145m}$ , no chemical separations could be carried out. Fortunately, they proved to be unnecessary, owing to the cleanness of the reactions. After most bombardments it took less than 2 min to retrieve the target and transport it to the counting area.

We also produced  $Gd^{145m}$  in a set of confirming experiments performed at the Yale University heavy-ion accelerator.  $C^{12}$  beams ranging between 70 and 120 MeV were used, and the reactions of interest were  $Nd^{142}(C^{12}, \alpha 5n)Gd^{145m}$  and  $Sm^{144}(C^{12}, 2\alpha 3n)Gd^{145m}$ . The latter was discovered quite by accident and has an unexpectedly large cross section. It must proceed by a combination of cluster stripping and compound-nucleus formation.

The  $\gamma$ -ray energies were determined by simultaneous counting with the standards listed in Table I. A  $\gamma$ -ray singles spectrum is shown in Fig. 1. The peaks appearing in this spectrum without energy assignments listed come from the decay of the ground state of  $Gd^{145}$ .<sup>2</sup> The detector used was a five-sided trapezoidal Ge(Li) detector fabricated in this laboratory. It has an active volume of  $\approx 7$  cm<sup>3</sup> and a resolution of 2.9 keV full width at half maximum (FWHM) for the  $Co^{60}$  1.333-MeV  $\gamma$  ray. The  $\gamma$  rays associated with the decay of  $Gd^{145m}$  had energies of  $721.4 \pm 0.4$ ,  $386.6 \pm 0.3$ , and  $329.5 \pm 0.3$  keV, as determined from the averages of a number of experiments.

The  $Gd^{145m}$  half-life was determined with the help of a computer code called GEORGE.<sup>7</sup> This code allows us to accumulate data through an 8192-channel analog-to-digital converter interfaced to the MSU Cyclotron Laboratory Sigma-7 computer. We can dump segments of the spectrum in successive time intervals: Counting can be stopped, the spectrum segment dumped onto a rapid access disk

TABLE I.  $\gamma$ -ray energy standards.

Nuclide	$\gamma$ -ray energies (keV)	Reference
$Ce^{141}$	$145.43 \pm 0.02$	a
$Cm^{243}$	$209.85 \pm 0.06$	b
	$228.28 \pm 0.08$	b
	$277.64 \pm 0.02$	b
$Co^{56}$	$846.4 \pm 0.5$	c
	$1038.9 \pm 1.0$	c
	$1238.2 \pm 0.5$	c

<sup>a</sup>J. S. Geiger, R. L. Graham, I. Bergström, and F. Brown, Nucl. Phys. 68, 352 (1965).

<sup>b</sup>R. E. Eppley, unpublished results (1969).

<sup>c</sup>R. L. Auble, Wm. C. McHarris, and W. H. Kelly, Nucl. Phys. A91, 225 (1967).

TABLE II. Transition data summary for  $Gd^{145m}$ .

	This work	Jansen, Morinaga, and Signorini (Ref. 4)
$E_{\gamma}(M4)$	$721.4 \pm 0.4$ keV	$721.3 \pm 0.7$ keV
$E_{\gamma}(M2)^a$	$386.6 \pm 0.3$ keV	...
$E_{\gamma}(M1)^a$	$329.5 \pm 0.3$ keV	...
$t_{1/2}$	$85 \pm 3$ sec	$85 \pm 7$ sec

<sup>a</sup>These transitions occur in  $Eu^{145}$  and result from the direct feeding of the  $h_{1/2}$  state in that nucleus by  $Gd^{145m}$ . The multiplicities are assumed from the properties of the states as determined from  $Gd^{145g}$  decay and scattering. Cf. Refs. 2 and 12.

(for punching on cards at a later time), the memory erased, and the counting resumed, all in considerably less than one second of elapsed time. In the present case the spectra were dumped at 15-sec intervals. A pulser peak was included in each spectrum for later determination of the proper dead-time corrections. The net peak areas, corrected for dead time, then yielded the half-life information in the usual manner. (A set of these spectra, together with the half-life curves can be found in Eppley.<sup>8</sup>) A listing of our  $E_{\gamma}$  and half-life values is given in Table II, where they are compared with those of Jansen, Morinaga, and Signorini.

The electron spectra were obtained by use of a 1000- $\mu$ -thick Si(Li) surface-barrier detector, cooled to methanol-dry-ice temperature and operating with a bias of +200 V. The resolution of this detector was typically 5 keV FWHM in the 600-keV region, the electrons having passed through a 0.25-mil Havar window. A resulting electron spectrum is shown in Fig. 2.

In order to arrive at a value for the conversion coefficient of the isomeric transition, the  $\gamma$ -ray and electron spectra were measured simultaneous-

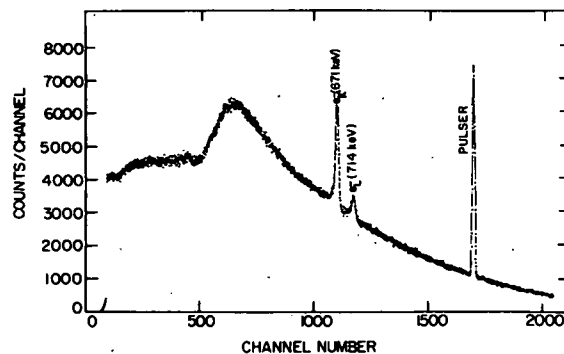


FIG. 2. Electron spectrum showing conversion lines from the 721.4-keV  $M4$  isomeric transition in  $Gd^{145}$ . This spectrum was taken with a 1000- $\mu$  Si(Li) detector mounted in a dipstick cryostat with a 0.1-mil Havar window.

ly from the same source, which was placed in a fixed, reproducible geometry. Again, owing to the short half-life, "mass-free" sources could not be made. However, as can be seen from the electron spectrum, our "thick" sources led to a minimum of straggling. For calibrating the detector efficiencies and the geometry corrections, a  $\text{Cs}^{137}$  source was used as a standard. A value of 0.094 was used for the  $\alpha_K$  of its 661.6-keV transition; this is an average of published values.<sup>9, 10</sup>

Two separate experiments made at widely differing times were performed to determine the  $\text{Gd}^{145m}$   $K$ - and  $L$ -internal-conversion coefficients. The results, compared with theoretical values for various multiplicities, are shown in Table III. The logarithms of the theoretical values were interpolated from a quadratic least-squares fit to the tabulated values of Hager and Seltzer.<sup>11</sup> The experimental  $\alpha_K$  value definitely shows the isomeric transition to be  $M4$  in character. The measured  $K/L$  ratio places it as being either  $M3$  or  $M4$ . The former is a more sensitive test, however, and an  $M4$  assignment fits in quite well with the systematics of transition probabilities in the  $N = 81$  isotones, as we shall see in the next section.

We shall see later that the 386.6- and 329.5-keV  $\gamma$  peaks fit between known<sup>2, 12</sup> states and imply that 4.7% of the decay of  $\text{Gd}^{145m}$  goes via a direct  $\beta^+/\epsilon$  branch to an  $h_{11/2}$  state in  $\text{Eu}^{145}$ , the other 95.3% going via the isomeric transition. The 4.7% branch was determined by correcting the 386.6-keV/721.4-keV photon ratio (found to be 0.048) for conversion, again using the conversion coefficients of Hager and Seltzer and assuming the 386.6-keV transition to be a pure  $M2$  transition. The 329.5-keV  $\gamma$  rays result also from the decay of the ground state of  $\text{Gd}^{145}$ , so no quantitative information about their intensity could be obtained from these experiments.

### III. $\text{Gd}^{145m}$ AND $N = 81$ $M4$ ISOMERS

Figure 3 shows our decay scheme for  $\text{Gd}^{145m}$ . While the other known  $N = 81$  odd-mass isotones have been assigned  $d_{3/2}$  ground-state configurations, there is some evidence<sup>2</sup> that in  $\text{Gd}^{145}$  the  $s_{1/2}$  state has replaced the  $d_{3/2}$  state as the ground state, which may account partly for the peculiar

TABLE III. Conversion coefficients for the isomeric transition in  $\text{Gd}^{145}$ .

	Experimental	Theoretical (Ref. 11)			
		$E3$	$E4$	$M3$	$M4$
$\alpha_K$	$0.12 \pm 0.2$	0.011	0.024	0.054	0.118
$\alpha_K/\alpha_L$	$5.4 \pm 0.7$	3.50	3.53	5.77	4.88

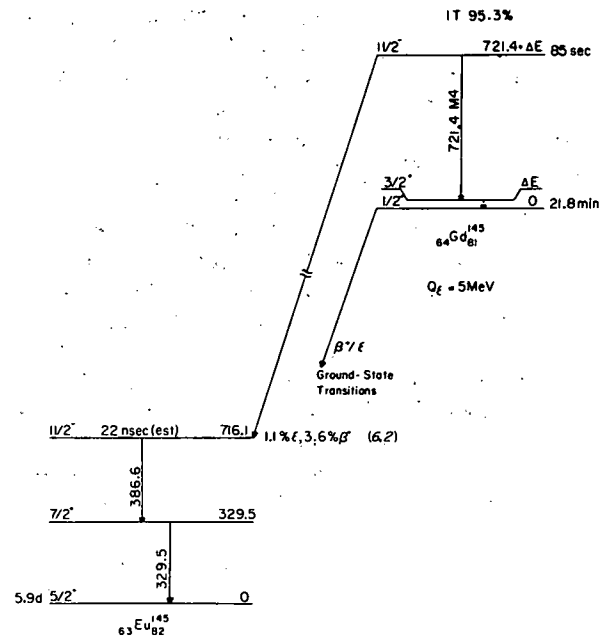


FIG. 3. Decay scheme of  $\text{Gd}^{145m}$ .

ground-state decay of  $\text{Gd}^{145}$ . Newman *et al.*,<sup>12</sup> also came to this conclusion when interpreting their scattering data from the  $\text{Sm}^{144}(\tau, d)\text{Eu}^{145}$  reaction in conjunction with their  $\text{Gd}^{145g}$  decay data. If the  $s_{1/2}$  assignment is correct, the  $M4$  isomeric transition in  $\text{Gd}^{145}$  does not proceed directly to the ground state but to a state  $\Delta E$  in energy above the ground state. This excited  $d_{3/2}$  state would then decay to the ground state via a predominantly  $M1$  transition.

In a search for a low-energy  $M1$  transition, we have utilized a  $\text{Si}(\text{Li})$  x-ray detector, which is useful in the 5–100-keV energy region for  $\gamma$  rays and is also sensitive to charged particles. No peaks that are in evidence in any of our spectra in the 10–100-keV range can be attributed to the decay of  $\text{Gd}^{145m}$ . The high positron flux, primarily from  $\text{Gd}^{145g}$  decay, contributed to a high background problem below 10 keV and ruled out observing a transition in that region. Assuming such a low-energy transition to be present, most likely  $M1$  in character, it would be converted primarily in the  $L_I$  shell, with  $\alpha_{L_I}$  having a value of 4.5 at 46 keV and increasing to 246 at 9.38 keV.<sup>11</sup> Consequently, assuming the transition to be low in energy, say, 20 keV or less, would preclude observing the photons. However, we should have been able to see the  $L_I$  conversion line if the energy were above 10 keV.

The radial matrix elements for the  $M4$  transitions in the  $N = 81$  odd-mass isotones were calculated using Moszkowski's<sup>13</sup> approximations for a single neutron hole,

$$T_{(\mu L)}^{SP} = \frac{2(L+1)}{L[(2L+1)!!]^2} \omega \frac{e^2}{\hbar c} \left(\frac{R_0}{c}\right)^{2L} \left(\frac{\hbar}{mcR_0}\right)^2 (\mu_N L)^2 \times |M|^2 S(j_i, L, j_f),$$

where  $L$  is the multipolarity of the transition,  $R_0$  is the effective nuclear radius,  $S(j_i, L, j_f)$  is a statistical factor (i.e., angular momentum portion of the matrix element), which for  $\frac{1}{2} - \frac{3}{2}$  transitions has the value  $\frac{1}{2}$ , and  $\mu_N$  is the dipole moment of the neutron. Symbolically,  $|M|^2$  has the form,

$$|M|^2 = \left[ \int_0^\infty R_f \left(\frac{r}{R_0}\right)^{L-1} R_i r^2 dr \right]^2.$$

Our results are plotted in Fig. 4, where we also show the differences in energy between the  $h_{11/2}$  and  $d_{3/2}$  states.

The resulting transition probabilities are consistently smaller than the approximation of a constant wave function,

$$|M|^2 = \left(\frac{3}{L+2}\right)^2 (\mu_N L)^2 = 14.6,$$

but this fact should not concern us particularly, for  $M4$  transitions are customarily retarded over such estimates and one needs much more detailed information about the nuclear wave functions in order to make detailed comparisons meaningful. What is of more importance is the fact that the values of  $|M|^2$  are not constant but show a definite trend in this series of isotones. [It is unusual for  $|M|^2$  not to be constant over such a series. For example, in the odd-mass neutron-deficient lead isotopes,  $|M|^2$  was constant to the point that an apparent 15% discrepancy at  $\text{Pb}^{203}$  suggested that an unobserved transition was competing with the  $M4$  isomeric transition, and this competing transition was subsequently discovered.<sup>14</sup> Examinations of more of these series of isomers can be found in Ref. 8.]

The complete answer as to why the discrepancy in magnitude and in trend exists between the experimental and theoretical values is still not forthcoming. Kotajima<sup>15</sup> summarizes several effects that could contribute to these deviations: (1) cancellation of the magnetic moments because of the mesonic effect, (2) configuration mixing or spin polarization, or (3) the use of too crude an approximation for the radial wave functions. In the same paper he explores the usefulness of applying a more realistic function for these radial wave functions, but the matrix elements were remarkably insensitive to changes in these wave functions. This effect, then, by itself could not explain even the deviations in magnitude, much less the "bowing" of the curve as seen in Fig. 4.

More recently, Jansen, Morinaga, and Signorini<sup>4</sup>

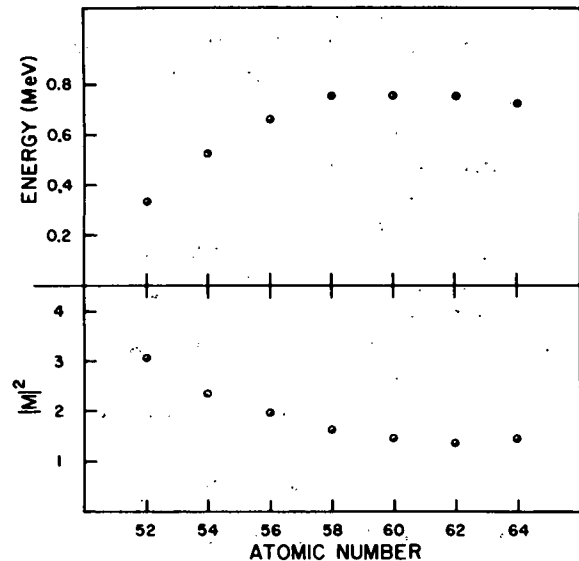


FIG. 4. Plots of the  $h_{11/2}$ - $d_{3/2}$  energy differences and of the squares of the radial matrix elements for the  $M4$  isomeric transitions that connect these states in the  $N=81$  odd-mass isotones.

have also sought to better the experimental-theoretical agreement. In a calculation similar to that used by Kotajima, they recalculated the radial matrix elements using a potential function consisting of a Woods-Saxon part and a spin-orbit part. In this manner they recalculated the radial part of the Schrödinger equation for these nuclei. In addition to this refinement, they took account of configuration mixing by utilizing the results of Horie and Oda.<sup>16</sup> In this manner, much of the  $Z$  dependence was removed. However, the experimental values are still lower than the theoretical ones for all reasonable values of  $R_0$ . For an  $R_0$  of 1.22 F, the experimental-to-theoretical ratio hovers around 0.5.

An alternate attack on this problem might prove to be useful. Recasting the problem in a quasiparticle framework would allow a simplified picture, with the transition probabilities depending only on the particle-hole character of the states involved. Stripping and pickup reactions are just now beginning to be carried out on nuclei in this region, so occupation numbers may very well become available from these before long. As soon as such information is available, this type of formulation can be explored more fully.

Finally, it should be noted that as  $Z$  increases there is an increase in the direct  $\beta^+/\epsilon$  decay to the  $h_{11/2}$  states in the daughter nuclei. On the neutron-deficient side of the  $N=81$  odd-mass isotones,  $\text{Ce}^{138m}$  does not have sufficient decay energy to populate such a state in  $\text{La}^{139}$ , but the decay is energetically possible for  $\text{Nd}^{141m}$ ,  $\text{Sm}^{143m}$ , and  $\text{Gd}^{145m}$ . We have made a careful search for direct

population of the  $h_{11/2}$  state in  $\text{Pr}^{141}$  by  $\text{Nd}^{141m}$  decay<sup>8,17</sup> and have been able to set an upper limit of 0.01% on any such population. This results in a  $\log ft$  greater than 7. From  $\text{Sm}^{143m}$  decay, however, Feldsteiner and Rosner<sup>18</sup> were able to detect a direct branch of 0.2% to the state in  $\text{Pm}^{143}$ , implying a  $\log ft$  of 6.7. And we find a direct branch of 4.7% from  $\text{Gd}^{145m}$  decay, resulting in a  $\log ft$  of only 6.2. We consider this to be an indication of the increased occupation of the  $h_{11/2}$  orbit by proton pairs as one moves up the series. A more detailed consideration of this phenomenon,

however, is beyond the scope of this paper and will be the subject of another paper to be forthcoming shortly.<sup>19</sup>

#### ACKNOWLEDGMENTS

We wish to thank Dr. H. Blosser and Mr. H. Hilbert for their help in the operation of the MSU cyclotron. We also wish to thank Dr. D. Beery for his assistance with the acquisition of some of the data and Mr. N. Mercer for his great help in the fabrication of the electron-detector mount.

\*Work supported in part by the U. S. Atomic Energy Commission.

†Work supported in part by the U. S. National Science Foundation.

<sup>1</sup>R. E. Eppley, Wm. C. McHarris, and W. H. Kelly, *Phys. Rev. C* **2**, 1077 (1970).

<sup>2</sup>R. E. Eppley, Wm. C. McHarris, and W. H. Kelly, to be published.

<sup>3</sup>R. E. Eppley, Wm. C. McHarris, and W. H. Kelly, *Bull. Am. Phys. Soc.* **13**, 1467 (1968).

<sup>4</sup>G. Jansen, H. Morinaga, and C. Signorini, *Nucl. Phys. A* **128**, 247 (1969).

<sup>5</sup>M. Goldhaber and A. W. Sunyar, *Phys. Rev.* **83**, 906 (1951).

<sup>6</sup>W. D. Myers and W. J. Swiatecki, University of California Radiation Laboratory Report No. UCRL-11980, 1965 (unpublished).

<sup>7</sup>GEORGE, a data-taking code with live oscilloscope display developed by P. Plauser for use on the MSU Cyclotron Laboratory Sigma-7 computer.

<sup>8</sup>R. E. Eppley, Ph. D. thesis, Michigan State University, 1970 (unpublished).

<sup>9</sup>H. Daniel and H. Schmidt, *Z. Physik* **168**, 292 (1962).

<sup>10</sup>S. Hultberg, D. J. Horen, and J. M. Hollander, *Nucl. Phys.* **28**, 471 (1961).

<sup>11</sup>R. S. Hager and E. C. Seltzer, *Nucl. Data A* **4**, 1 (1968).

<sup>12</sup>E. Newman, K. S. Toth, R. L. Auble, R. M. Gaedke, M. F. Roche, and B. H. Wildenthal, *Phys. Rev. C* **1**, 1118 (1970).

<sup>13</sup>S. A. Moszkowski, in *Alpha-, Beta-, and Gamma-Ray Spectroscopy*, edited by K. Siegbahn (North-Holland Publishing Company, Amsterdam, The Netherlands, 1965); *Phys. Rev.* **89**, 474 (1953).

<sup>14</sup>R. E. Doebler, Wm. C. McHarris, and C. R. Gruhn, *Nucl. Phys. A* **120**, 489 (1968).

<sup>15</sup>K. Kotajima, *Nucl. Phys.* **46**, 284 (1963).

<sup>16</sup>H. Horie and T. Oda, *Progr. Theoret. Phys. (Kyoto)* **32**, 65 (1964).

<sup>17</sup>D. B. Beery, W. H. Kelly, and Wm. C. McHarris, *Phys. Rev.* **171**, 1283 (1968).

<sup>18</sup>J. Felsteiner and B. Rosner, *Phys. Letters* **31B**, 12 (1970).

<sup>19</sup>Wm. C. McHarris, R. E. Eppley, and W. H. Kelly, to be published.

## ULTRA-HIGH RESOLUTION SPECTROMETER SYSTEM FOR CHARGED PARTICLE STUDIES OF NUCLEI\*

H. G. BLOSSER, G. M. CRAWLEY, R. DEFOREST, E. KASHY and B. H. WILDENTHAL

*Cyclotron Laboratory, Michigan State University, East Lansing, Michigan 48823, U.S.A.*

Received 14 August 1970

This paper describes an arrangement for introducing feedback into a charged particle magnetic analysis system for nuclear reaction studies. In initial tests of the system, a resolution of 5 keV has been obtained in  $(p,p')$  studies at 30 MeV with 70% of the cyclotron internal beam on target. This corresponds to a

resolving power  $p/\Delta p$  of 12000. Essential features of the system, in addition to the feedback, are a careful definition of the cyclotron source by means of internal slits and the use of dispersion matching to cancel the effect of coherent on-target energy spread.

### 1. Introduction

The crucial role of an intense source in determining the ultimate resolution of charged particle magnetic analysis systems has been discussed by Cohen<sup>1)</sup>, who concludes that the resolution in an optimized system is predominantly controlled by source luminosity. Generally, the effective source for such an analysis system consists of an object slit at the beginning of a beam preparation system. The accelerator is tuned to maximize the transmission through this slit and thus maximize the luminosity of this effective source. In such an arrangement the dispersive properties of the accelerator are normally ignored, which, for the case of a cyclotron, is a major error (as we explain in section 2). In the system described here this difficulty is avoided

by using the actual cyclotron ion source as the effective object for the system which, if all magnets are stable, is equivalent to an external slit with exactly correct "dispersion matching"<sup>2)</sup> (also see sec. 2). For the system we describe the stable magnet requirement is effectively provided by a feedback circuit which acts to maintain the position of the optic axis at a fixed point on the focal plane of the magnetic spectrograph.

A second important feature of our system is a "resolution meter" based on fractional transmission through a small slit in the spectrograph focal plane. Such a meter, in conjunction with "separated function" magnets<sup>3)</sup>, allows a quick empirical adjustment of quadrupoles and sextupoles to give the best linear focus, dispersion matching, cancellation of aberrations, etc.

\* Supported by the National Science Foundation.

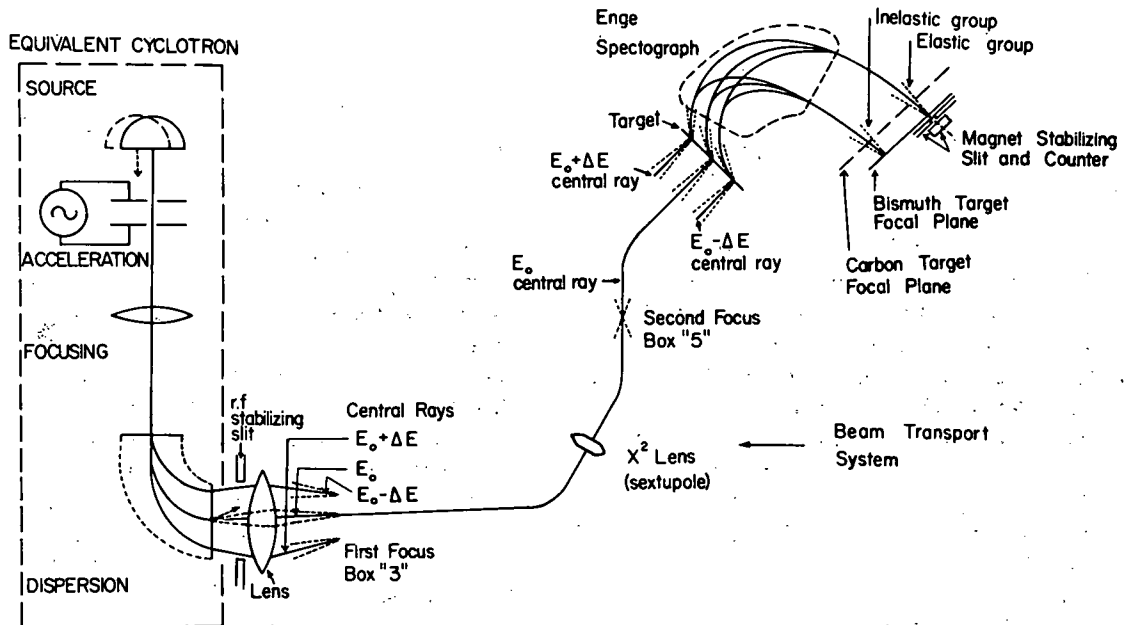


Fig. 1. "Equivalent circuit" of cyclotron and high resolution beam line.

Using this system, a number of exploratory nuclear reaction studies have been made – some initial results are presented in section 3.

## 2. Description of the system

Fig. 1 is an “equivalent circuit” drawing of the high-resolution beam line showing the essential features of the system. At the left of the figure is the “equivalent cyclotron” consisting of ion source, acceleration system and focusing and dispersing elements. For a cyclotron operating with single turn extraction (assumed as a condition in the following discussion), the simple equivalent circuit shown is in fact quite realistic. The sinusoidal acceleration produces a particle beam with a coherent spread in energy in direct proportion to the time variation of the voltage. The cyclotron magnet acts as a combined focusing and dispersing system and even though these actions are spread over hundreds of turns the net result is a transfer matrix identical to that of a simple bending magnet and quadrupole system. (Higher order multipoles may also be implied if non-linearities in the cyclotron are appreciable.) With such a configuration the size of the external beam is clearly determined by the combined action of dispersion and source size rather than source size alone. For example, fig. 2 shows the measured radial emittance of the external beam of our cyclotron. If we neglect dispersion and assume the observed area to be entirely due to the effective source an emittance of 5 mm-mrad results. If, however, the dispersion and spot size are separately determined [using techniques described elsewhere<sup>4</sup>] one obtains the detailed picture on the right of the figure, namely a beam whose instantaneous radial emittance is 0.7 mm-mrad and moving in time along a dispersion curve in accord with the coherent energy variation of the beam. Obviously a beam with properties as at the right of fig. 2 could equally well have been produced by the equivalent cyclotron of fig. 1.

(If the single turn extraction restriction is lifted the equivalent cyclotron is similar to the one shown except that particles from different turns appear to leave the cyclotron in a slightly different direction as if they had come from a displaced source. In fig. 1 this effect is indicated schematically by the dashed source and the heavy dashed arrow at the exit port. Such an enlarged source would have catastrophic consequences on the high resolution system described here – single turn extraction is therefore an essential requirement for this system.)

From the equivalent cyclotron the beam is directed to the target by the transport system, an array of fo-

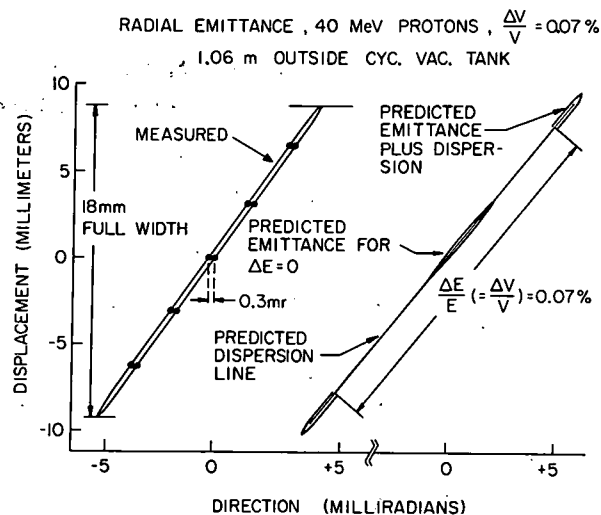


Fig. 2. Right: computer calculation of expected beam distribution due to combined emittance and dispersion. Left: measured radial distribution of the cyclotron external beam (100% of beam).

cusing and dispersive magnet elements, and finally brought to a dispersed focus on the target. The fact that the beam has in the process passed thru intermediate focii at locations called “box 3” and “box 5” is irrelevant since no slits are employed at either of these locations. The properties of the final dispersed focus on the target are qualitatively the same as would result from a single simple bending magnet, i.e., a rather large spot whose size is determined mainly by the total energy spread of the beam but with a coherence such that particles of energy  $E + \Delta E$  go to a small region on one side of the target, particles of energy  $E - \Delta E$  pass to a similar region on the other side of the target, and other energies correspondingly in between. Assuming no time variations in magnets, the size of the region in which particles of given energy focus is determined by the size of the cyclotron source and the total system magnification.

Beyond the target, scattered particles enter the Enge spectrograph<sup>5</sup> (another dispersive and focusing system) and come to a focus at the detector. At this stage the very important concept of “dispersion matching” as proposed by Cohen<sup>2</sup>) is used. This condition is achieved if rays of energy  $E$  and  $E \pm \Delta E$ , etc., when directed back from some assumed detector thru the spectrograph to the target, go to just the same points on the target as the corresponding energies coming from the cyclotron. Given this condition *all elastically scattered* particles will clearly come to a focus at the same position regardless of whether their original energy was  $E + \Delta E$ ,  $E - \Delta E$  or something be-

DETECTOR SETUP — ELASTIC PEAK

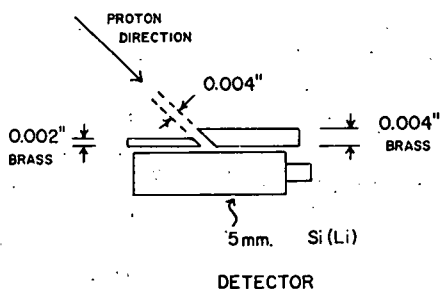


Fig. 3. Schematic drawing of the slit and counter arrangement used to detect the elastic peak. The width of the slit was measured accurately using a laser beam.

tween. In this condition the width of the observed elastic line at the focal plane of the spectrograph is then independent of the beam energy spread to first order and is in fact determined by the width of the cyclotron source and system aberrations. Such an arrangement is achieved in practice by appropriate

shifting of the strengths of quadrupole singlets in the transport system to give the desired dispersion.

In a similar fashion to the elastic scattering, inelastic lines will have all lost a fixed amount of energy corresponding to the excitation energy of the nuclear state and will also be focused to a narrow group at the appropriate focal plane position, and will also have line widths independent of the beam-energy spread. Since the ability to resolve particle groups corresponding to different nuclear states is determined by the ratio of line width to separation at the spectrometer focal plane, the narrowing of the lines from various nuclear levels leads directly to higher resolution.

An important detail is to provide a rapid means for adjusting parameters controlling the line width in order to optimize resolution. This function we accomplish with the "resolution meter" diagrammed in fig. 3. It consists of a 5 mm Si(Li) solid state detector with a brass entrance slit which has one jaw 0.1 mm thick, and the other 0.05 mm thick. With an aperture of

TYPICAL SPECTRA:

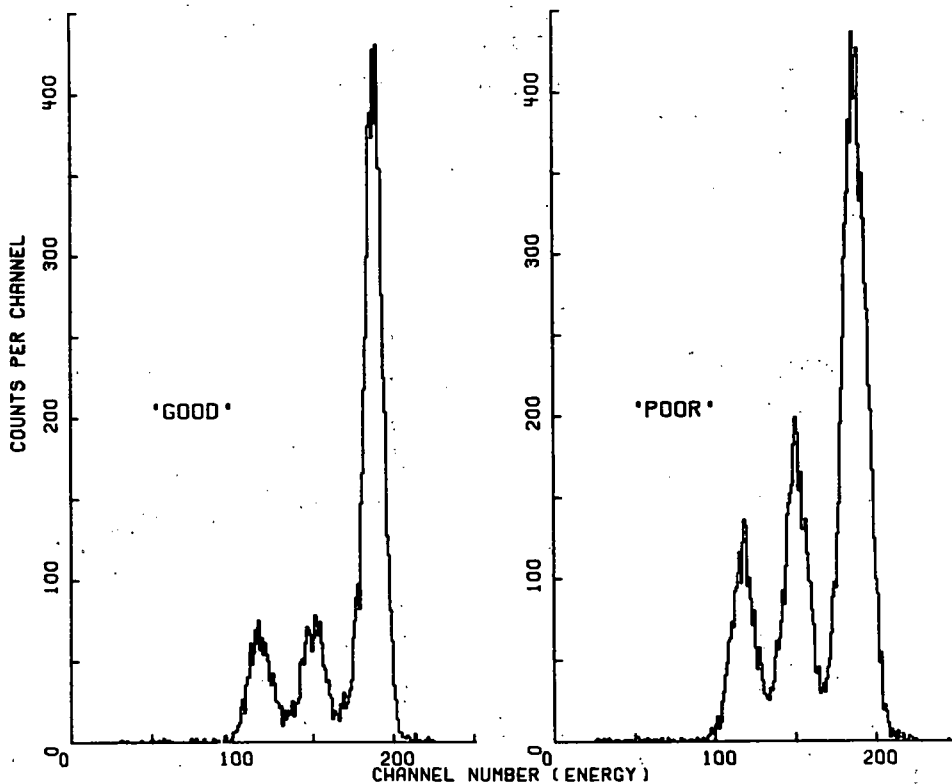


Fig. 4. Typical spectra obtained from the slit and counter arrangement shown in fig. 3. One spectrum shows good transmission through the central slit and the other spectrum a lower transmission and therefore poorer resolution.



typically 0.05 or 0.1 mm this slit and counter then serve as an ultra-sensitive position sensing system. Beam penetrating either jaw of the slit is degraded in energy and appears as a distinct energy group to the counter, giving typical spectra as shown in fig. 4. With appropriate circuitry and count rate meters the ratio of the high energy transmission peak to the total of the three peaks is presented on a console meter. Since the fractional transmission through this slit is approximately inversely proportional to line width, this ratio is the desired "resolution meter". Watching this meter, focusing elements, aberration corrections, dispersion controls, plate position, etc. can all be adjusted to optimize system resolution. The resulting changes from calculated control settings are generally small but nevertheless of great importance. Improvements in resolution by factors of 2 are typical.

Two special feedback stabilization circuits are employed in the system, one for compensating bending magnet drifts, the other to keep the cyclotron rf amplitude in its proper range. From fig. 1 it is obvious that a shift in the strength of any bending magnet will move the position of the central ray relative to the resolution meter slit. Given such a shift, a compensating change can be effected by any other magnet (at least in so far as the position error is concerned) i.e. one servo system on one magnet is adequate to

correct a small bending change in any element of the system. The slit counter gives a ready reference standard for this circuit. One desires to have a servo adjustment of some magnet so as to have equal counts in the two lower energy peaks of fig. 4, i.e. equal beam on the right and left jaws of the slit. Rather arbitrarily we have elected to control the spectrometer magnet with this servo system – the action of the circuit is then to keep the elastic line locked at a fixed position in the spectrograph focal plane. We note in passing that for small shifts, the action of this circuit leaves the position of the linear focus undisturbed; and even for large shifts a given fractional change in a dipole element has a vastly more catastrophic effect on resolution than a similar change in quadrupoles or sextupoles and so position is properly the primary reference for such a stabilization circuit.

The second special feedback circuit, on the cyclotron rf, is in principle unnecessary in a dispersion matched system since a small change in the rf (within the range allowed for single turn extraction) induces no effect other than a simple one-to-one change in the beam energy and such a change is of course compensated by the dispersion matching in a fully matched system. Nevertheless transmission considerations and non-linear phenomena make it convenient and valuable to stabilize the rf. This is accomplished by sensing the

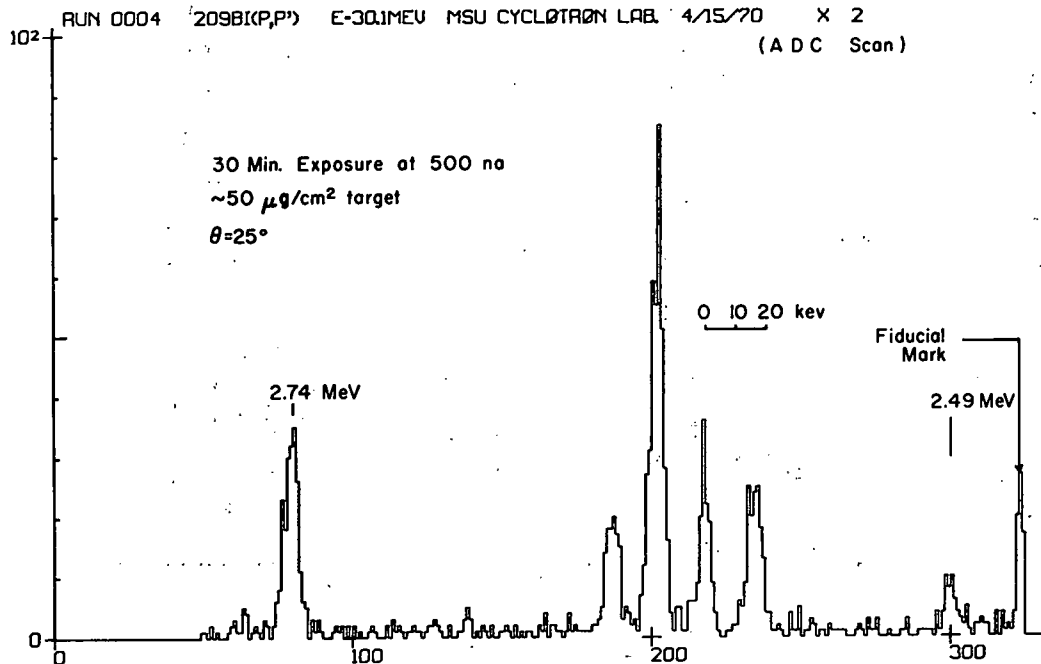


Fig. 5. Spectrum of inelastically scattered protons from  $^{209}\text{Bi}$  at a bombarding energy of 30 MeV, showing the states which arise from the coupling of the  $h_{3/2}$  proton to the octupole vibration.

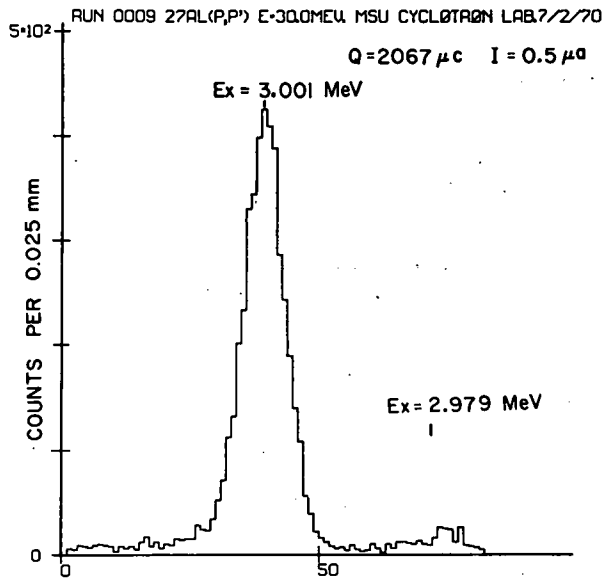


Fig. 6. Spectrum of inelastically scattered protons from  $^{27}\text{Al}$  at a bombarding energy of 30 MeV, showing the states near 3 MeV excitation energy.

beam on a feedback slit located just at the cyclotron exit port and sending an amplitude feedback correction to the rf to keep the beam balanced on this slit (an arrangement very similar to the standard feedback system on Van de Graaff accelerators). With this circuit in use the cyclotron beam remains very steady for periods of hours or longer without any control adjustment. (Interestingly, if the circuit is turned on in a multi-turn extraction situation it promptly acts to drive the external beam to nearly zero, apparently adjusting the rf to line up the bulk of the beam exactly on the deflector septum with fringes from the before and after turns reaching the slit.)

### 3. Results

Figs. 5 and 6 show spectra from (p,p') runs on typical heavy and light elements (bismuth and aluminum). The bismuth data shows the region from 2.5 to 2.7 MeV excitation and displays the well-known multiplet which arises from the weak coupling of an  $h_{3/2}$

proton to the collective  $3^-$  excitation. The aluminum data shows states in the region of excitation near 3 MeV. Both runs are at 30 MeV with a lab scattering angle of  $25^\circ$  and an acceptance angle of  $\pm 0.5^\circ$  in  $\Delta\theta$  and  $\pm 1^\circ$  in  $\Delta\phi$  (solid angle of 0.6 msterad) with the data recorded by exposing photographic plates.

The resolution for the bismuth is more than two times better than previously published charged particle data for this nucleus<sup>6</sup>) (13 keV resolution at 21 MeV bombarding energy) and is equivalent to (or slightly better than) recent gamma ray data<sup>7</sup>). The run on aluminum of course involves the well-known technique of shifting the position of the spectrometer focal plane to compensate for kinematic effects<sup>5</sup>).

### 4. Conclusions

With the experimental configuration which we have described, a well tailored isochronous cyclotron can be a powerful high resolution tool for nuclear reaction studies. Total system resolution hinges primarily on the quality of the accelerator source. With such a system (and assuming presently existing sources) cyclotrons with their high-luminosity positive ion sources should regularly achieve significantly higher resolution than accelerators depending on negative ion sources.

### References

- 1) B. L. Cohen, Rev. Sci. Instr. **33** (1962) 85.
- 2) B. L. Cohen, Rev. Sci. Instr. **30** (1959) 415.
- 3) National Accelerator Laboratory Design Report (Jan. 1968) sect. 5, and Beam Transport System of the Michigan State University Cyclotron; G. Mackenzie, E. Kashy, M. M. Gordon and H. G. Blosser; IEEE Trans. Nucl. Sci. NS-14, no. 3 (June 1967) 450.
- 4) H. G. Blosser, Proc. 1969 Intern. Cyclotron Conf. (Oxford, U. K., 1969) in press.
- 5) J. E. Spencer and H. A. Enge, Nucl. Instr. and Meth. **49** (1967) 181.
- 6) J. C. Hafele and R. Woods, Phys. Letters **23** (1966) 579.
- 7) J. W. Hertel, D. G. Fleming, J. P. Schiffer and H. E. Gove, Phys. Rev. Letters **23** (1969) 488; R. A. Broglia, J. S. Willey, R. Perazzo and W. R. Phillips, Phys. Rev. C **1** (1970) 1508.

## Precision Mass Measurement of ${}^9\text{C}$ , ${}^{13}\text{O}$ , and ${}^{21}\text{Mg}$ and the Isobaric-Multiplet Mass Equation\*

G. F. Trentelman, B. M. Freedom,† and E. Kashy

Cyclotron Laboratory and Physics Department, Michigan State University, East Lansing, Michigan 48823

(Received 23 February 1971)

The ground-state masses of  ${}^9\text{C}$ ,  ${}^{13}\text{O}$ , and  ${}^{21}\text{Mg}$  have been determined through measurement of the  $Q$  values of the  ${}^{12}\text{C}({}^3\text{He}, {}^6\text{He}){}^9\text{C}$ ,  ${}^{16}\text{O}({}^3\text{He}, {}^6\text{He}){}^{13}\text{O}$ , and  ${}^{24}\text{Mg}({}^3\text{He}, {}^6\text{He}){}^{21}\text{Mg}$  reactions. The measurements were made with 68–70-MeV  ${}^3\text{He}$  beams using a split-pole magnetic spectrograph. A new method for obtaining a precise calibration for the beam analyzer and magnetic spectrograph at these high bombarding energies is presented.

The mass excess of  ${}^9\text{C}$  has been measured as  $28.911 \pm 0.009$  MeV, that of  ${}^{13}\text{O}$  as  $23.103 \pm 0.014$  MeV, and that of  ${}^{21}\text{Mg}$  as  $10.912 \pm 0.018$  MeV. These nuclei represent the  $T_z = -\frac{3}{2}$  members of the  $T = \frac{3}{2}$  quartets for  $A = 9, 13,$  and  $21$ , respectively.

The present results show excellent agreement with a quadratic isobaric-multiplet mass equation for  $A = 13$  and  $A = 21$ , but there is some indication that a small cubic term is required for the  $A = 9$  multiplet.

### I. INTRODUCTION

The isobaric-multiplet concept has been successful in explaining the similar level structure of mirror nuclei and the existence of analog states. Using isospin formalism, it is possible to obtain from first-order perturbation theory an equation quadratic in  $T_z$  that relates the masses of members of an isobaric multiplet.<sup>1,2</sup> This isobaric-multiplet mass equation (IMME) can be written as

$$M(\alpha, T, T_z) = a(\alpha, T) + b(\alpha, T)T_z + c(\alpha, T)T_z^2,$$

where  $M$  is the mass of a multiplet member,  $T$  is the isospin,  $T_z$  is the specific isospin projection for the multiplet member, and  $\alpha$  represents all of the charge-independent quantities. These charge-independent quantities are assumed to be identical for all members of the multiplet.

Since this equation is quadratic in  $T_z$ , one must know the masses of at least an isobaric quartet ( $T = \frac{3}{2}$ ) to test its validity. Such quartets exist but the uncertainties in the mass of the most proton-rich member ( $T_z = -\frac{3}{2}$ ) have made most such tests inconclusive. The most accurately measured  $T = \frac{3}{2}$  multiplet ( $A = 9$ ) has shown indications that a term proportional to  $T_z^3$  should be included in the IMME, at least for this quartet.<sup>3-5</sup> The purpose of the work presented here was to accurately measure the masses of other  $T_z = -\frac{3}{2}$  nuclei in order to further test the IMME and to see if the need for a  $T_z^3$  term persists. Some of the results of this work have been reported previously.<sup>6</sup>

The experiments described here determined the ground-state masses of the nuclei  ${}^9\text{C}$ ,  ${}^{13}\text{O}$ , and  ${}^{21}\text{Mg}$  by measuring the  $Q$  values of the reactions  ${}^3\text{He}, {}^6\text{He}){}^9\text{C}$ ,  ${}^{16}\text{O}({}^3\text{He}, {}^6\text{He}){}^{13}\text{O}$ , and  ${}^{24}\text{Mg}({}^3\text{He}, {}^6\text{He}){}^{21}\text{Mg}$ . The measurements were made us-

ing an Enge-type split-pole magnetic spectrograph.<sup>7</sup> Since the spectrograph can compensate for the kinematic spread of the reaction products, it was possible to use a large detection solid angle. Magnetic analysis of the charged particles also removed the overwhelming background that would be caused by the elastically scattered  ${}^3\text{He}$  particles.

### II. BEAM SYSTEM AND PARTICLE DETECTION

This experiment used  ${}^3\text{He}$  beams from the Michigan State University sector-focused cyclotron. The analysis and transport system<sup>8</sup> was typically set to deliver a beam of maximum energy spread of  $\pm 20$  keV at 70 MeV and maximum radial divergence of  $\pm 2$  mrad. The direction of the beam on the target was defined by two sets of current sensitive slits. Continuous monitoring of these slits and the switching magnetic field assured constancy of incident beam direction. Slits defining detection solid angles of 1.2, 0.30, and 0.05 msr were used at the entrance to the spectrograph. For spectrograph calibration runs, the 0.30-msr slit was used, and for the ( ${}^3\text{He}, {}^6\text{He}$ ) reactions the 1.2-msr slit was used. Occasionally a reaction was observed through each of the three slits while the spectrograph field was kept constant. No centroid shift was produced that was significantly greater than the statistical error in the centroid itself.

Particle detection at the spectrograph focal plane was accomplished with a 300- $\mu$ -thick position-sensitive silicon surface-barrier detector which subtended 3.0 cm along the focal plane.<sup>9</sup> The energy-loss signals ( $E$ ) and the position signals ( $XE$ ) were digitized and used as input to an on-line XDS Sigma-7 computer. The position and identi-

fication of the particles were obtained using the code TOOTSIE<sup>10</sup> which plots the ratio  $XE/E$  vs  $E$ . This highly flexible code also calculated and displayed the centroids of various particle groups, thus allowing rapid access to the information necessary for the tuning of the various magnets during the calibration procedure. The  $E$  and  $XE$  signal amplifiers were used in an ac-coupled, doubly differentiated mode. The analog-to-digital-converter zero levels were set to obtain a true zero so that no error in the position signal ( $XE/E$ ) would arise due to any dc levels. Such dc biases would have given a different  $XE/E$  ratio for particles at the same position on the detector if their total energy losses ( $E$ ) were significantly different, as is the case in the present work for  $p$ ,  $d$ ,  $^3\text{He}$ , and  $^6\text{He}$  particles. Two different detector geometries were used; the first with particles incident at  $45^\circ$  in which the detector operated in the  $dE/dx$  mode, and the second with particles incident at  $53^\circ$  and the detector operating in a stopping mode for the  $^{12}\text{C}(^3\text{He}, ^6\text{He})^9\text{C}$  and  $^{16}\text{O}(^3\text{He}, ^6\text{He})^{13}\text{O}$  reactions. Rotating the detector  $8^\circ$  relative to the incident particles also increased the effective energy dispersion by about 20%.

It has been observed that the spectrograph magnetic field shape is sensitive to the field-recycling procedure used<sup>11</sup> and to the rate at which the central field is changed. Using a cycling time of 40 min for a field change of 0.0 to 15.3 to 0.0 kG, and taking all data on the cycle with the field always rising to the desired value considerably reduced this effect. Peak locations on separate cycles were repeatable to within the statistical uncertainty of their centroids.

Energy-dispersion matching between the transport system and spectrograph reduced the effects of small beam-energy shifts within the limits set by the beam transport-analysis system. The dispersion-matched condition was created by choosing quadrupole lens settings that gave the dispersed beams a width on target commensurate with that required by the dispersion characteristics of the spectrograph. The degree of dispersion match actually used in these experiments ranged from 50–75% of total match.

To guard against spurious effects on incident beam direction due to stray fields of the cyclotron, bending magnets, the earth's magnetic field, and particularly the spectrograph whose field was often changed, all exposed areas of the beam-transport system were wrapped with soft iron for magnetic shielding.

### III. SPECTROGRAPH CALIBRATION AND PARTICLE ORBITS

The spectrograph-field behavior was carefully

calibrated between 8.7–13.3 kG with proton beams, and extended to 14.7 kG using  $^3\text{He}$  beams. The calibration was made for particles in orbits corresponding to an effective radius of curvature ( $\rho$ ) of about 32.3 in., and all data were taken at a focal-plane position corresponding to this radius. The calibration was accomplished with a momentum-matching procedure developed at this laboratory.<sup>12</sup> The procedure involved the use of proton beams whose energies were determined by simultaneously detecting at the same focal-plane position (corresponding to  $\rho \approx 32.3$  in.) the elastically scattered protons and ground-state deuterons from reactions on  $^{12}\text{C}$ . Since the protons and deuterons have different charge-to-mass ratios, their magnetic rigidities were equal for a unique beam energy determined by the  $^{12}\text{C}(p, d)^{11}\text{C}$   $Q$  value, and the detection scattering angle. For this particular pair of reactions with a  $^{12}\text{C}(p, d)^{11}\text{C}$   $Q$  value of  $-16.4953$  MeV,<sup>13</sup> a beam energy of 33.691 MeV is required to give the deuterons and elastically scattered protons equal magnetic rigidities when they are detected at  $15.0^\circ$  in the laboratory.

The uncertainties associated with this beam energy came from the uncertainties in the  $Q$  value, the scattering angle, and in peak centroid positions. The scattering angle was determined by detecting protons from the  $^1\text{H}(p, p)^1\text{H}$  reaction on a very thin Formvar target. Since outgoing proton energies in this reaction are very sensitive to the detection angle, these angles could be measured to a precision of  $\pm 0.05^\circ$  using the beam-energy value given by the transport-analysis system. An uncertainty of  $\pm 0.05^\circ$  in the scattering angle yields an uncertainty of  $\pm 1.5$  keV in the momentum-matched beam energy.

The difference between proton and deuteron peak centroid positions could be determined to better than 0.1 mm. A 0.1 mm uncertainty in the relative centroid positions would give a beam energy uncertainty of  $\pm 1.5$  keV. Particle-energy losses in the targets were taken into account and are estimated to have contributed an uncertainty of less than 0.2 keV to the determination of the momentum-matched beam energy. The total uncertainty of the momentum-matched beam energy is therefore estimated to be no more than  $1 \times 10^{-4}$  of the beam energy.

This procedure for determining the beam energy and scattering angle also determined the magnetic rigidity of the scattered protons and deuterons and provided a normalization point for the remainder of the calibration. The value of the radius of curvature corresponding to the focal-plane position, where these and all following reaction products were detected, was defined as the ratio of the proton or deuteron rigidity (they are equal

ie momentum-matched condition) to the spectrograph-field strength measured by the nuclear-magnetic-resonance fluxmeter (NMR). The NMR was located in the flat field region of the spectrograph, between the large pole tips. A collimated  $^{241}\text{Am}$   $\alpha$  source was permanently mounted to the focal-plane apparatus below the normal detector position and provided a fiducial mark for the focal-plane position corresponding to this radius. The position on the detector corresponding to the centroid of the  $\alpha$  peak marked the required focal-plane position. When amplifier gains were changed to accommodate various particle-energy losses, the detector was lowered to the  $\alpha$  source for recalibration.

The remainder of the calibration was accomplished by taking advantage of the precise knowledge of the incident beam energy as determined by the momentum match, and observing reactions whose  $Q$  values are well established. The reaction products were detected at the standard focal-plane position. The magnetic rigidities of the resulting reaction products were calculated using the measured beam energy, scattering angle, and kinematic considerations. These calculated rigidities were compared with the empirical rigidities determined using the spectrograph field measured by the NMR and the radius of curvature associated with the standard focal-plane position. Since all reaction products were detected at this position, this comparison of calculated and empirical rigidities provided the required information about the spectrograph-field behavior.

TABLE I. Spectrograph calibrating reactions.

Reactions	Excitation of residual nucleus (MeV $\pm$ keV)	$Q$ value $Q_0 + E_{ex}$ (MeV $\pm$ keV)
$^{12}\text{C}(p, p')^{12}\text{C}^*$	$4.4398 \pm 0.3^a$	$-4.4398 \pm 0.3$
$^{16}\text{O}(p, p')^{16}\text{O}^*$	$6.1305 \pm 0.4^b$	$-6.1305 \pm 0.4$
$^{16}\text{O}(p, d)^{15}\text{O}$	0.0	$-13.4434 \pm 1.2^c$
$^{27}\text{Al}(p, d)^{26}\text{Al}$	0.0	$-10.8322 \pm 2.9^c$
$^7\text{Li}(p, d)^6\text{Li}$	0.0	$-5.0280 \pm 1.6^c$
$^7\text{Li}(p, d)^6\text{Li}^*$	$2.184 \pm 2.0$	$-7.212 \pm 3.0^d$
$^{12}\text{C}(^3\text{He}, ^3\text{He})^{12}\text{C}^*$	$4.4398 \pm 0.3$	$-4.4398 \pm 0.3$
$^{16}\text{O}(^3\text{He}, ^3\text{He})^{16}\text{O}^*$	$6.1305 \pm 0.4$	$-6.1305 \pm 0.4$
$^{12}\text{C}(^3\text{He}, ^4\text{He})^{11}\text{C}$	0.0	$1.8582 \pm 1.2^c$
$^{16}\text{O}(^3\text{He}, ^4\text{He})^{15}\text{O}$	0.0	$4.9101 \pm 1.3^c$

<sup>a</sup>C. Chasman, K. W. Jones, R. A. Ristinen, and D. E. Alburger, Phys. Rev. **159**, 830 (1967).

<sup>b</sup>J. B. Marion, University of Maryland Technical Report No. ORO-2098-58, 1967 (unpublished).

<sup>c</sup>See Ref. 13.

<sup>d</sup>T. Lauritsen and F. Ajzenberg-Selove, Nucl. Phys. **78**, 24 (1966).

The energies of the  $^3\text{He}$  beams were determined by measuring the rigidities of elastically scattered  $^3\text{He}$  from  $^{12}\text{C}$  and  $^{16}\text{O}$  using the calibrated spectrograph. The scattering angle was determined to  $\pm 0.03^\circ$  by measuring the rigidities of  $^3\text{He}$  from  $^1\text{H}(^3\text{He}, ^3\text{He})^1\text{H}$  scattering from a Formvar target.

Once the  $^3\text{He}$  beam energy and scattering angle were determined, more calibration data were taken in the same manner as indicated above. This supplemented the proton calibration data and al-

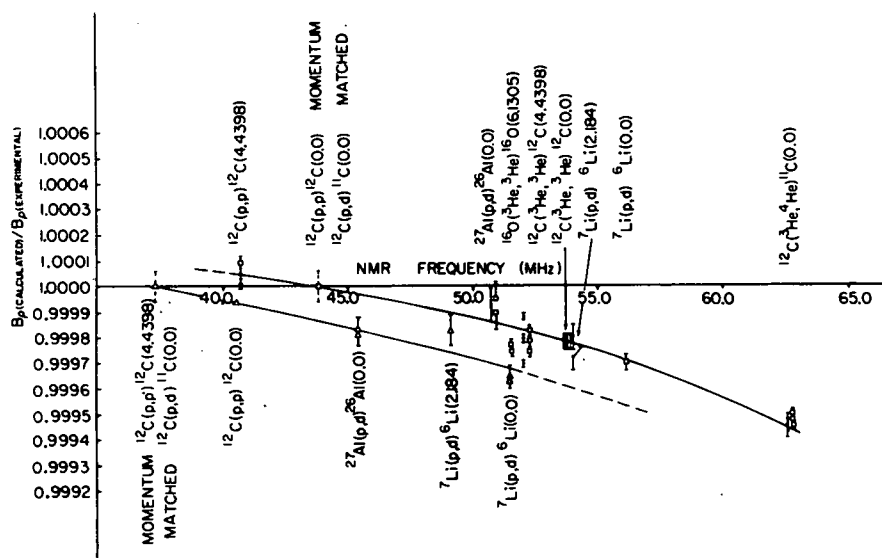


FIG. 1. Calibration of the effective spectrograph field. The calibration is for particles traveling in orbits corresponding to an effective radius of curvature of  $\sim 32.3$  in. The NMR frequency on the abscissa measures the spectrograph field in a flat field region and the ordinate gives the correction factor for obtaining the correct field.

lowed the calibration to be extended to spectrograph-field strengths of 14.7 kG. Table I lists all the calibration reactions used.

Figure 1 shows the calibration curve obtained from these data. The ordinate is the ratio of the calculated magnetic rigidities [ $B\rho$  (calculated)] to the rigidities determined from the product of the NMR field value and the standard radius of curvature [ $B\rho$  (experimental)]. This ratio is then plotted against the NMR frequency. The lower curve represents the same sort of calibration using a momentum match of different reactions and normalized at a different field value. As expected, the two curves are approximately parallel.

Since the detector holding apparatus must be moved to compensate for the kinematic energy spread of the various reaction products, this motion was controlled in such a way that the standard position on the focal plane moved along the defined particle orbits.

To preserve the independence of data from one run to another, each  $^3\text{He}$  run was preceded by its own proton calibration run. Three such runs were made. In addition, within each run, calibration data (including elastic  $^3\text{He}$  scattering) and  $^6\text{He}$  data were taken on each of several cycles of the spectrograph magnetic field. The elastic  $^3\text{He}$  data monitored any changes in beam energy between cycles. Several different carbon and SiO targets were used for the  $^{12}\text{C}$  and  $^{13}\text{O}$  measurements.

TABLE II. Targets used for ( $^3\text{He}$ ,  $^6\text{He}$ ) reactions for  $E(\text{beam}) = 68.0$  MeV.

Targets	Thickness (mg/cm <sup>2</sup> )	$\Delta E(^6\text{He})$ , average loss (keV)
$^{12}\text{C}$ No. 1	0.153	25 ± 3
SiO, F-80	0.227	34 ± 4
"Glass" SiO <sub>2</sub>	0.491	71 ± 8
$^{24}\text{Mg}$ foil	0.656	83 ± 13
SiO+C	0.432	66 ± 7
$^{12}\text{C}$ "F"	0.117	19 ± 3

#### IV. CALIBRATION UNCERTAINTIES

Uncertainty in the spectrograph calibration curve (Fig. 1) is the consequence of two separate phenomena; the uncertainty in the  $Q$  values of reactions used for momentum match, as discussed previously, and the uncertainty in the fit of the calibration curve to the calibrating reactions.

An error in a momentum-match  $Q$  value would translate the curve, with only a small change in its shape or tilt. Such a translation of the calibration curve would introduce an error in the calculation of the  $^3\text{He}$  beam and  $^6\text{He}$  energies. An error of +1.1 keV in the  $^{12}\text{C}(p, d)^{11}\text{C}$   $Q$  value would yield an error of +4.7 keV in the beam energy and +2.5 keV in the  $^6\text{He}$  energies for a  $^3\text{He}$  beam energy of 68.5 MeV. Since the ( $^3\text{He}$ ,  $^6\text{He}$ )  $Q$  value is essentially the difference between the  $^3\text{He}$  and  $^6\text{He}$  energies, the error in the  $Q$  value is the difference

TABLE III. Experimentally determined ( $^3\text{He}$ ,  $^6\text{He}$ )  $Q$  values.

Run number	Reaction	$Q$ value (MeV)	Total error (MeV)	Partial error (MeV)	$^3\text{He}$ beam energy (MeV)	$\theta_L$ (deg)	Target
1-121	$^{12}\text{C}(^3\text{He}, ^6\text{He})^9\text{C}$	-31.566	±0.020	±0.018	68.574 ± 0.010	14.82	$^{12}\text{C}$ No. 1
1-123	$^{16}\text{O}(^3\text{He}, ^6\text{He})^{13}\text{O}$	-30.510	±0.020	±0.018	68.577 ± 0.010	14.82	"Glass"
2-89	$^{12}\text{C}(^3\text{He}, ^6\text{He})^9\text{C}$	-31.574	±0.011	±0.010	68.476 ± 0.008	10.96	$^{12}\text{C}$ No. 1
2-89	$^{12}\text{C}(^3\text{He}, ^6\text{He})^9\text{C}$	-31.581	±0.011	±0.010	68.470 ± 0.008	10.96	$^{12}\text{C}$ No. 1
2-106	$^{12}\text{C}(^3\text{He}, ^6\text{He})^9\text{C}$	-31.597	±0.011	±0.010	68.470 ± 0.008	10.96	$^{12}\text{C}$ No. 1
2-93	$^{16}\text{O}(^3\text{He}, ^6\text{He})^{13}\text{O}$	-30.506	±0.012	±0.011	68.476 ± 0.008	10.96	SiO, F-80
2-101	$^{16}\text{O}(^3\text{He}, ^6\text{He})^{13}\text{O}$	-30.524	±0.012	±0.010	68.470 ± 0.008	10.96	SiO, F-80
2-107	$^{16}\text{O}(^3\text{He}, ^6\text{He})^{13}\text{O}$	-30.504	±0.011	±0.010	68.470 ± 0.008	10.96	SiO, F-80
2-103	$^{24}\text{Mg}(^3\text{He}, ^6\text{He})^{21}\text{Mg}$	-27.523	±0.018	±0.013	68.470 ± 0.008	10.96	$^{24}\text{Mg}$ foil
2-108	$^{24}\text{Mg}(^3\text{He}, ^6\text{He})^{21}\text{Mg}$	-27.519	±0.017	±0.010	68.470 ± 0.008	10.96	$^{24}\text{Mg}$ foil
3-15	$^{12}\text{C}(^3\text{He}, ^6\text{He})^9\text{C}$	-31.574	±0.011	±0.010	68.512 ± 0.008	11.01	$^{12}\text{C}$ No. 1
3-27	$^{12}\text{C}(^3\text{He}, ^6\text{He})^9\text{C}$	-31.577	±0.011	±0.009	68.512 ± 0.008	11.01	$^{12}\text{C}$ No. 1
3-17	$^{16}\text{O}(^3\text{He}, ^6\text{He})^{13}\text{O}$	-30.500	±0.011	±0.010	68.512 ± 0.008	11.01	SiO, F-80
3-28	$^{16}\text{O}(^3\text{He}, ^6\text{He})^{13}\text{O}$	-30.514	±0.022	±0.012	68.512 ± 0.008	11.01	"Glass"
3-21	$^{24}\text{Mg}(^3\text{He}, ^6\text{He})^{21}\text{Mg}$	-27.499	±0.016	±0.009	68.512 ± 0.008	11.01	$^{24}\text{Mg}$ foil
3-29	$^{24}\text{Mg}(^3\text{He}, ^6\text{He})^{21}\text{Mg}$	-27.505	±0.017	±0.011	68.210 ± 0.010	11.01	$^{24}\text{Mg}$ foil
3-88	$^{12}\text{C}(^3\text{He}, ^6\text{He})^9\text{C}$	-31.572	±0.012	±0.011	68.210 ± 0.010	10.68	$^{12}\text{C}$ "F"
3-77	$^{12}\text{C}(^3\text{He}, ^6\text{He})^9\text{C}$	-31.572	±0.013	±0.012	68.199 ± 0.010	10.68	$^{12}\text{C}$ "F"
3-78	$^{16}\text{O}(^3\text{He}, ^6\text{He})^{13}\text{O}$	-30.478	±0.014	±0.011	68.199 ± 0.010	10.68	SiO+C
3-89	$^{16}\text{O}(^3\text{He}, ^6\text{He})^{13}\text{O}$	-30.510	±0.014	±0.011	68.210 ± 0.010	10.68	SiO+C
3-90	$^{16}\text{O}(^3\text{He}, ^6\text{He})^{13}\text{O}$	-30.510	±0.014	±0.011	68.230 ± 0.010	10.67	SiO+C

their errors, i.e., +2.2 keV. Similarly, if the error in the  $(p, d)$   $Q$  value were  $-1.1$  keV, then the error in the  $(^3\text{He}, ^6\text{He})$   $Q$  value would be  $-2.2$  keV.

Using the quoted uncertainties of the calibration reaction  $Q$  values, and considering the consistency of the curve shape over several sets of experimental measurements, it is estimated that the uncertainty associated with the fit of the calibration curve, particularly over the region where  $^3\text{He}$  elastic scattering and  $^6\text{He}$  were detected, is not greater than  $\pm 0.5 \times 10^{-4}$  of the outgoing particle energy. This uncertainty was applied directly to the outgoing  $^6\text{He}$  energies and hence to the calculated  $Q$  value. Quantitatively it amounted to about  $\pm 2$  keV for  $^6\text{He}$  energies of approximately 36 MeV.

The systematic uncertainties associated with the absolute measurement of the  $^3\text{He}$  beam energies are so much a function of the calibration procedure and scattering-angle determination, that the values used for  $^3\text{He}$  beams are effectively defined by these procedures. Systematic errors in its value have therefore been absorbed into these other uncertainties.

Estimates of the beam-energy fluctuations during a run were obtained from the scatter of the  $^3\text{He}$  calibration reaction points over the course of the run. For example, nine individual measurements of the  $^{12}\text{C}(^3\text{He}, ^3\text{He})^{12}\text{C}$  elastic peak over the course of a 2-day run varied by a maximum of only 9 keV, with the other calibration reactions showing similar scatter commensurate with their sensitivity to beam energy. This remarkable stability of beam energy was of prime importance to the experiment. The largest such fluctuation for any of the runs was  $\Delta E(\text{beam}) = 10$  keV.

Fluctuations in the scattering angle caused by possible fluctuation in beam direction during a run was estimated to be no greater than  $\pm 0.03^\circ$ . Since this is reflected in the outgoing  $^6\text{He}$  energy through the kinematics for each reaction, this effect caused uncertainties in the  $Q$  values of  $\pm 4.5$ ,  $\pm 3.3$ , and  $\pm 2.1$  keV in the  $^9\text{C}$ ,  $^{13}\text{O}$ , and  $^{21}\text{Mg}$  measurements, respectively.

#### V. TARGETS

The  $^3\text{He}$  and  $^6\text{He}$  energy loss in the targets used in this experiment represent a significant correc-

tion to the measured  $^6\text{He}$  energies, and therefore careful measurement of all targets were made. The air-equivalent thicknesses of the targets were measured with an  $\alpha$ -source gauge, and the energy losses for various particles were calculated using published tables.<sup>14</sup> The specific ionization of the  $^6\text{He}$  was taken to be that of a  $^3\text{He}$  particle at half the  $^6\text{He}$  energy. Several measurements were made over the surface of each target foil. Since target thickness is measured relative to an equivalent amount of air, precise knowledge of the  $\alpha$  energy used is not critical if the stopping power of the target elements are commensurate with that of air. The average energy loss for the outgoing particles in the target was then introduced as an effective excitation energy in the corresponding reaction-kinematics calculations.

The uncertainty in the energy losses was estimated by making several separate measurements of each target and checking their consistency. Table II lists all targets used for this experiment, their air-equivalent thickness, the average energy loss of the  $^6\text{He}$  particle, and the estimated uncertainty in the energy loss.

For the  $^{24}\text{Mg}(^3\text{He}, ^6\text{He})^{21}\text{Mg}$  reaction one target was used for all measurements, and energy-loss uncertainty is treated as systematic and applied to the average of the  $Q$ -value measurements. For the  $^9\text{C}$  and  $^{13}\text{O}$  measurements several targets were used, and the uncertainties were applied to the  $Q$ -value measurements for the corresponding targets.

#### VI. DATA ANALYSIS

Each  $Q$ -value determination was assigned an uncertainty consisting of all relevant parameter fluctuations summed in quadrature. For a particular measurement this included beam-energy fluctuation, scattering-angle fluctuations, statistical error of the peak centroid, uncertainties due to detector nonlinearities for peak centroids not falling exactly at the standard focal-plane position, and any observed magnetic field fluctuations. A weighted average of the measurements for a reaction was then taken using these uncertainties. The systematic uncertainties such as those assigned to the calibration procedure and added to the uncertainty of the average  $Q$  value.

The standard deviation of the distribution of in-

TABLE IV. Average  $Q$  values and mass excesses for the  $T_z = -\frac{3}{2}$  nuclei.

Element	Reaction	$Q$ value (MeV)	Mass excess (MeV)
$^9\text{C}$	$^{12}\text{C}(^3\text{He}, ^6\text{He})^9\text{C}$	$-31.578 \pm 0.008$	$28.911 \pm 0.009$
$^{13}\text{O}$	$^{16}\text{O}(^3\text{He}, ^6\text{He})^{13}\text{O}$	$-30.506 \pm 0.013$	$23.103 \pm 0.014$
$^{21}\text{Mg}$	$^{24}\text{Mg}(^3\text{He}, ^6\text{He})^{21}\text{Mg}$	$-27.512 \pm 0.018$	$10.912 \pm 0.018$

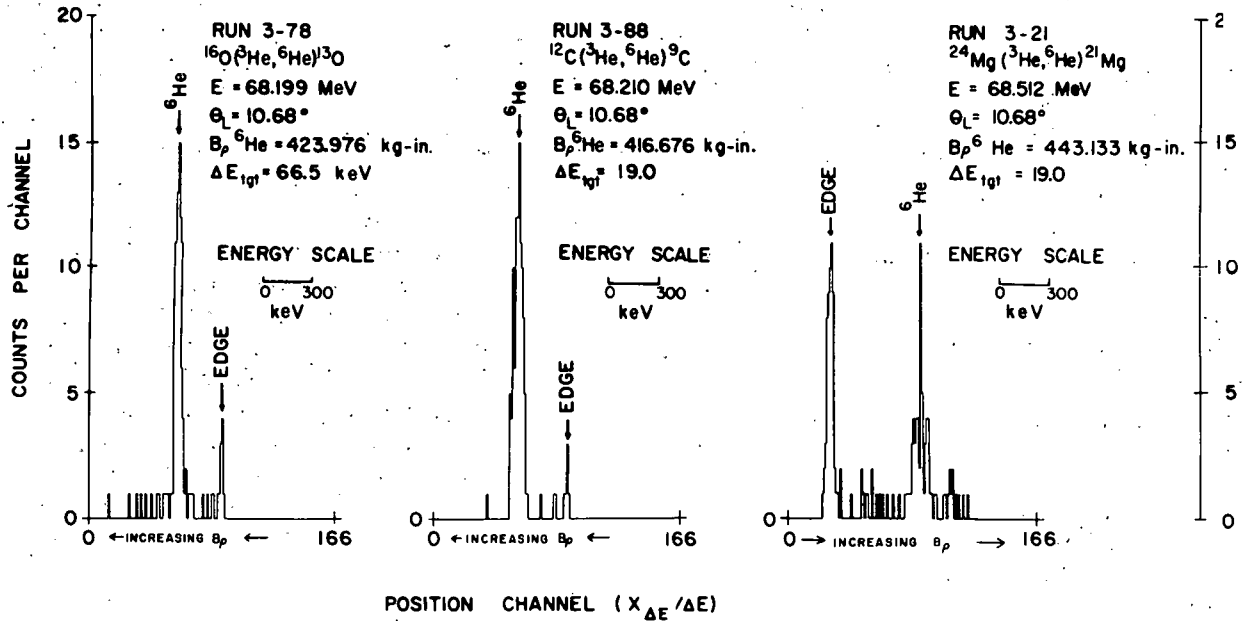


FIG. 2.  ${}^6\text{He}$  spectra from position-sensitive detector on spectrograph focal plane.

dividual measurements was also computed for each reaction. In each case the standard deviation of the distribution and the total experimental uncertainty described previously were nearly equal.

In computing the mass excesses of  ${}^9\text{C}$ ,  ${}^{13}\text{O}$ , and  ${}^{21}\text{Mg}$ , the uncertainties of the other masses involved,  ${}^3\text{He}$ ,  ${}^6\text{He}$ ,  ${}^{12}\text{C}$ ,  ${}^{16}\text{O}$ , and  ${}^{24}\text{Mg}$ , were also summed with the  $Q$ -value uncertainty in quadrature. The uncertainty of  $\pm 4.0$  keV associated with the  ${}^6\text{He}$  mass excess was not negligible in computing the total error of  ${}^9\text{C}$  and  ${}^{13}\text{O}$ . The masses of  ${}^3\text{He}$ ,  ${}^6\text{He}$ ,  ${}^{12}\text{C}$ ,  ${}^{16}\text{O}$ , and  ${}^{24}\text{Mg}$  were taken from Ref. 13.

### VII. EXPERIMENTAL RESULTS

Table III lists all individual measurements of the  $Q$  values obtained along with the experimental parameters pertinent to each. The column labeled "total error" represents all known experimental uncertainties for that run summed in quadrature as though that were the only measurement made. The column labeled "partial error" represents random errors associated with that particular run, excluding systematic errors that are applied later to the average of the  $Q$  values. In Table IV, the resulting average  $Q$  values, their uncertainties, and the resulting values for the mass excesses of  ${}^9\text{C}$ ,  ${}^{13}\text{O}$ , and  ${}^{21}\text{Mg}$  are given.

Figure 2 displays typical position spectra for the the  $({}^3\text{He}, {}^6\text{He})$  reactions where the abscissa is the position signal ( $X/E$ ). Figure 3 shows the angu-

lar distribution for the  ${}^{12}\text{C}({}^3\text{He}, {}^6\text{He}){}^9\text{C}$  reaction.

### VIII. DISCUSSION

Table V gives the coefficients of the IMME for the  $A=9$ , 13, and 21 isobaric quartets. The coefficients  $a(\alpha, T)$ ,  $b(\alpha, T)$ , and  $c(\alpha, T)$  were obtained from a least-squares fit of the form

$$M = a(\alpha, T) + b(\alpha, T)T_z + c(\alpha, T)T_z^2$$

to the mass excesses of the quartet members. The  $d(\alpha, T)$  coefficient is the coefficient of a  $T_z^3$

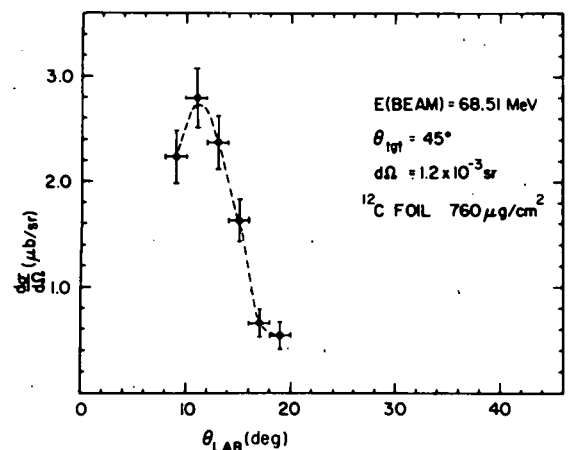


FIG. 3. Angular distribution of  ${}^6\text{He}$  for the reaction  ${}^{12}\text{C}({}^3\text{He}, {}^6\text{He}){}^9\text{C}$ . The curve is to guide the eye.



TABLE V. Empirically determined coefficients for the mass equation of the form  $M = a(\alpha, T) + b(\alpha, T)T_z + c(\alpha, T)T_z^2$  and  $M = a(\alpha, T) + b(\alpha, T)T_z + c(\alpha, T)T_z^2 + d(\alpha, T)T_z^3$  using the  $T_z = -\frac{3}{2}$  mass excess values of the present work. (For mass excesses of  $T_z = \frac{3}{2}, \pm\frac{1}{2}$ ; for  $T = \frac{3}{2}$  multiplet members see Table I in Ref. 2) The coefficients were determined from a weighted least-squares fit, and the  $\chi^2$  of the quadratic fit is indicated.

Mass	$a(\alpha, T)$	$b(\alpha, T)$	$c(\alpha, T)$	$d(\alpha, T)$	$\chi^2$
9	$26.343 \pm 0.004$	$-1.319 \pm 0.003$	$0.266 \pm 0.003$	...	4.0
13	$19.257 \pm 0.003$	$-2.180 \pm 0.004$	$0.256 \pm 0.003$	...	0.002
21	$4.899 \pm 0.005$	$-3.657 \pm 0.005$	$0.240 \pm 0.005$	...	1.28
9	$26.343 \pm 0.004$	$-1.334 \pm 0.008$	$0.265 \pm 0.003$	$0.008 \pm 0.004$	...
13	$19.257 \pm 0.003$	$-2.180 \pm 0.005$	$0.256 \pm 0.004$	$0.0002 \pm 0.0035$	...
21	$4.899 \pm 0.005$	$-3.665 \pm 0.009$	$0.238 \pm 0.005$	$0.0057 \pm 0.0051$	...

term when the same data are fit to the expression

$$M = a(\alpha, T) + b(\alpha, T)T_z + c(\alpha, T)T_z^2 + d(\alpha, T)T_z^3.$$

For both cases the mass-excess values for the  $T = \pm\frac{1}{2}, +\frac{3}{2}$  members are taken from Table 1 of Ref. 2. The term  $\chi^2$  represents the quality of the fit where

$$\chi^2 = \sum \left[ \frac{m(\text{calc}) - m(\text{exp})}{m(\text{exp})} \right]^2.$$

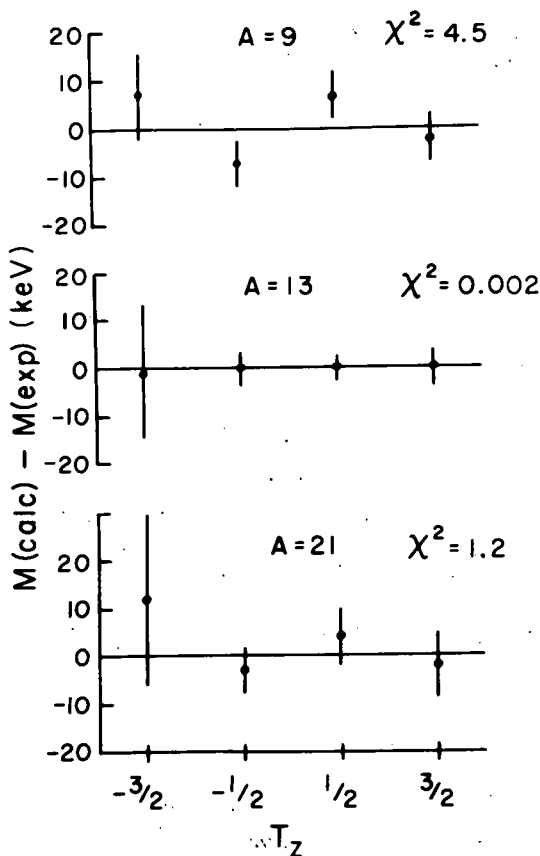


FIG. 4. Deviation of experimental  $T = \frac{3}{2}$  multiplet members from the quadratic mass equation using the coefficients of Table V. The  $T_z = -\frac{3}{2}$  members are from the present work, the  $T_z = +\frac{3}{2}, \pm\frac{1}{2}$  members from Ref. 2.

Deviations of the experimentally determined masses and predictions of the IMME with the  $a$ ,  $b$ , and  $c$  coefficients of Table V are displayed graphically in Fig. 4. Only the  $A = 9$  quartet shows deviations greater than the experimental uncertainty of the points.

The addition of higher-order terms such as  $T_z^3$  and  $T_z^4$  to the IMME are predicted if the nuclear forces are charge dependent or when the Coulomb potential is expanded as a second-order perturbation. Such a second-order perturbation can be treated in various ways. In Table VI,<sup>15-17</sup> various calculated values of the  $d$  coefficient are shown in comparison with the empirical values determined here.

Janecke<sup>15</sup> has used a second-order treatment that involves mixing of the  $T_z = \pm\frac{1}{2}$  members of the quartet with nearby states of the lower  $T$ . In this case the IMME is expanded to the fourth power of  $T_z$  and predicts that terms in  $T_z^3$  and  $T_z^4$  will be small, not so much because the perturbation is small, but because the major effects of such perturbations are absorbed mostly in the  $T_z$  and  $T_z^2$  terms. The calculated  $d$  coefficients are shown in the third column in Table VI.

Another attempt to make some estimate of the size of the cubic term is presented by Henley and Lacy,<sup>16</sup> where the Schrödinger equation is solved directly for a nuclear model. The model consists of three nucleons outside an inert core, with each of these extra nucleons in a Woods-Saxon nuclear potential, a Lane symmetry potential, and the Coulomb potential of a uniformly charged sphere with radius equal to that of the Woods-Saxon well. The coefficients for the  $T_z$  and  $T_z^2$  terms agree with experimental values, generally to within 10-20%. The predicted  $d$  coefficient is shown in the fourth column in Table VI.

Bertsch and Kahana<sup>17</sup> have calculated the coefficient of the cubic terms by considering just the specific second-order perturbation in the Coulomb interaction between protons. They also treated the  $T = \frac{3}{2}$  multiplet as three valence nucleons outside of an inert core, and used Woods-Saxon wave

TABLE VI. Comparison of experimental and theoretical values of the coefficient of a cubic term in the IMME.

Mass	Exp. value (keV)	Janecke <sup>a</sup> (keV)	Henley and Lacy <sup>b</sup> (keV)	Bertsch and Kahana <sup>c</sup> (keV)	$Z\alpha c$ <sup>b</sup> (keV)
9	8.3 ± 3.9	5.8 ± 4.2	0.064 65	1.6	9.0
13	-0.2 ± 3.5	...	-0.439 90	0.9	12.0
21	5.7 ± 5.1	...	-0.181 68	0.3	19.0

<sup>a</sup>See Ref. 15.<sup>b</sup>See Ref. 16.<sup>c</sup>See Ref. 17.

functions and a purely Coulomb force. Their values are shown in the fifth column in Table VI.

Also it has been estimated<sup>2,5,18</sup> that the size of the  $d$  coefficient may be  $\approx Z\alpha c$  where  $Z$  is the average charge of the multiplet,  $\alpha$  is the fine-structure constant, and  $c$  the coefficient of  $T_x^2$ . For the  $A=9$  quartet this would be  $\approx 9$  keV, and the data indicate a  $d$  term of this magnitude.

If we consider the Coulomb energy of a uniformly charged spherical nucleus, i.e.,  $3Z(Z-1)e^2/5R_0A^{1/3}$ , the term  $Z(Z-1)$  may be expanded in terms of  $T_x$  and  $T_x^2$  with resulting IMME coefficients<sup>2</sup>:

$$b = -0.6(A-1)e^2/R_0A^{1/3} + (M_n - M_p),$$

$$c = 0.6e^2/R_0A^{1/3},$$

where  $M_n - M_p$  is the neutron-proton mass difference. The radius parameter  $T_0$  can then be calculated from the empirically determined  $b$  and  $c$ , and the results are shown in Fig. 5, where  $R_0(b)$

and  $R_0(c)$  are extracted for the  $b$  and  $c$  coefficients, respectively. They should have the same value for a given  $A$  if the mass difference other than the proton-neutron mass difference between the members of the multiplet is attributable to the difference in the electrostatic energy of a uniform charge distribution. As can be seen in Fig. 5,<sup>19</sup> the  $b$  and  $c$  coefficients yield quite different results for some of the nuclei. This may reflect the effect of the contribution of individual protons to the total Coulomb energy as determined by the detail of their nuclear wave function.<sup>20</sup>

The IMME appears to be a rather insensitive probe of particular charge-dependent phenomena. As discussed in detail by Janecke,<sup>15</sup> Garvey,<sup>2</sup> and by Wilkinson,<sup>18</sup> the fact that very good IMME fits to the data of isobaric quartets may be obtained does not necessarily mean that the assumptions from which it may be derived are necessarily true. The reason for this lies in the fact that the quadratic nature of the equation enables it to ab-

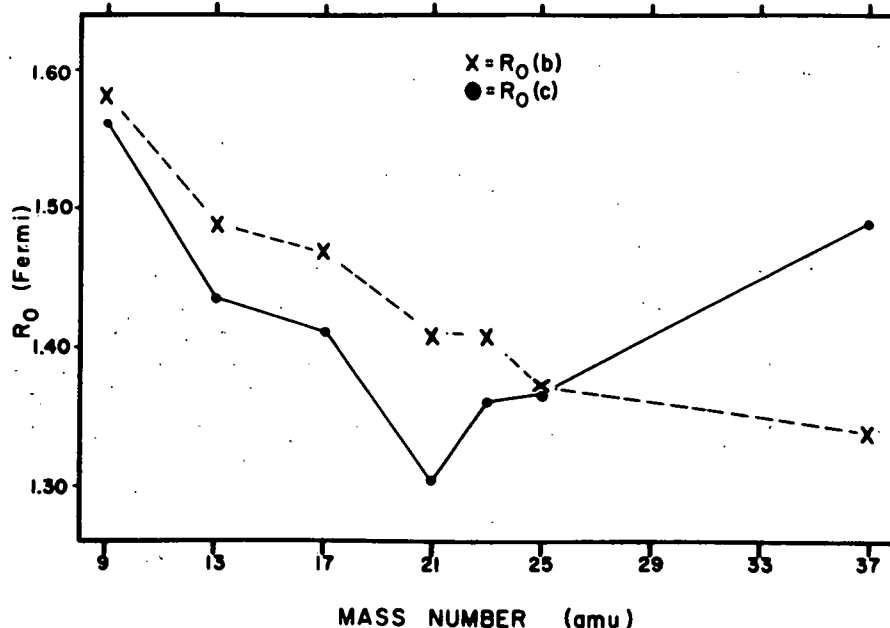


FIG. 5. Radius parameters as derived from the most recent determination of the  $b$  and  $c$  coefficients in the IMME. The Coulomb contribution to the mass difference between multiplet members is assumed to arise from a uniform spherical charge distribution of radius  $R_0A^{1/3}$ . Mass-equation coefficients  $b$  and  $c$  for  $A=9, 13, 21$  are from the present work; for  $A=17, 25, 37$  from Table I of Ref. 19; and for  $A=23$  from Table II, Ref. 2.

by many other phenomena as perturbations with accuracy sufficient to fit existing data well.

Even more accurate determination of the masses remains a worthwhile goal. The experimental procedures developed in this work allow one to make high-precision absolute  $Q$ -value measurements even at high bombarding energies and thus

makes possible the study of proton-rich nuclei that have been inaccessible by other techniques.

#### ACKNOWLEDGMENTS

We would like to thank the Michigan State University cyclotron laboratory staff for their continued support throughout this experiment.

\*Work supported by the National Science Foundation.

†Present address: Physics Department, University of South Carolina, Columbia, South Carolina.

<sup>1</sup>E. P. Wigner, in *Proceedings of the Robert A. Welch Foundation Conference on Chemical Research*, edited by W. O. Milligan (Robert A. Welch Foundation, Houston, Texas, 1957), p. 67.

<sup>2</sup>G. T. Garvey, in *Proceedings of the Second Conference on Nuclear Isospin, Asilomar-Pacific Grove, California, 13-15 March 1969*, edited by J. D. Anderson, S. D. Bloom, J. Cerny, and W. W. True (Academic Press Inc., New York, 1969), p. 703.

<sup>3</sup>C. A. Barnes, E. G. Adelberger, D. C. Hensley, and A. B. McDonald, in *Nuclear Physics: An International Conference*, edited by R. L. Becker, C. D. Goodman, P. H. Stelson, and A. Zucker (Academic Press Inc., New York, 1967), p. 261.

<sup>4</sup>J. M. Mosher, R. W. Kavanagh, and T. A. Tombrello, *Bull. Am. Phys. Soc.* **14**, 1167 (1969).

<sup>5</sup>J. Cerny, *Ann. Rev. Nucl. Sci.* **18**, 27 (1968).

<sup>6</sup>G. F. Trentelman, B. M. Freedom, and E. Kashy, *Phys. Rev. Letters* **25**, 530 (1970).

<sup>7</sup>J. E. Spencer and H. A. Enge, *Nucl. Instr. Methods* **49**, 181 (1967).

<sup>8</sup>G. H. Mackenzie, E. Kashy, M. M. Gordon, and H. G. Blosser, *IEEE Trans. Nucl. Sci.* **14**, 450 (1967).

<sup>9</sup>R. K. Jolly, G. F. Trentelman, and E. Kashy, *Nucl.*

*Instr. Methods* **87**, 325 (1970).

<sup>10</sup>D. Bayer, TOOTSIE XDS Sigma-7 Computer Assembly Language Code for On-Line Data Acquisition, Michigan State University Cyclotron Laboratory Internal Report, 1970 (unpublished).

<sup>11</sup>J. L. Snelgrove and E. Kashy, *Nucl. Instr. Methods* **52**, 153 (1967).

<sup>12</sup>G. F. Trentelman and E. Kashy, *Nucl. Instr. Methods* **82**, 304 (1970).

<sup>13</sup>C. Maples, G. W. Goth, and J. Cerny, University of California Radiation Laboratory Report No. UCRL-16964, 1966 (unpublished).

<sup>14</sup>C. F. Williamson, J. P. Bouyot, and J. Picard, Centre d'Etudes Nucléaires de Saclay, France Report No. CEA-R3042, 1966 (unpublished).

<sup>15</sup>J. Janecke, *Nucl. Phys.* **A128**, 632 (1969).

<sup>16</sup>E. M. Henley and C. E. Lacy, *Phys. Rev.* **184**, 1228 (1969).

<sup>17</sup>G. Bertsch and S. Kahana, *Phys. Letters* **33B**, 193 (1970).

<sup>18</sup>D. H. Wilkinson, *Phys. Rev. Letters* **13**, 571 (1964); *Phys. Letters* **12**, 348 (1964).

<sup>19</sup>R. Mendelson, G. J. Wozniak, A. D. Bacher, J. M. Losieaux, and J. Cerny, *Phys. Rev. Letters* **25**, 533 (1970).

<sup>20</sup>J. A. Nolen, Jr., and J. P. Schiffer, *Ann. Rev. Nucl. Sci.* **19**, 471 (1969).

**Ge(Li)-Ge(Li) SUM COINCIDENCE:  
A BONUS FROM Ge(Li)-Ge(Li) MEGACHANNEL COINCIDENCE EXPERIMENTS**

G. C. GIESLER, K. L. KOSANKE, R. A. WARNER and Wm. C. McHARRIS

*Department of Chemistry\* and Cyclotron Laboratory†, Department of Physics*

and

W. H. KELLY

*Cyclotron Laboratory†, Department of Physics, Michigan State University, East Lansing, Michigan, U.S.A.*

Received 17 November 1970

The sum-coincidence technique in Ge(Li)-Ge(Li)  $\gamma$ -ray spectroscopy is shown to be a viable and useful method for reducing Compton backgrounds and the resulting confusion they can cause. When used in conjunction with the digital readout from a two-dimensional "megachannel" coincidence experiment, many of the disadvantages and much of the tedium associated

with the technique can be eliminated. It thus becomes a valuable, complementary technique to be used as needed in processing the data from a  $\gamma$ - $\gamma$  coincidence experiment, requiring little or no additional experimental preparation. We present examples of its use in a relatively simple ( $^{63}\text{Zn}$ ) and a very complex ( $^{209}\text{Bi}$ ) spectrum.

**1. Introduction**

During the 1950's when  $\gamma$ -ray coincidence spectroscopy came into its own with NaI(Tl) detectors and the newly developed fast electronics, a number of modifications and improvements on the straightforward  $\gamma$ - $\gamma$  coincidence experiments were made. Most of these were designed to improve the poor peak-to-Compton ratios and the poor resolution of NaI(Tl) detectors. Among these improvements was the "sum-coincidence" method introduced by Hoogenboom<sup>1</sup>) in 1958. In this method the coincident pulses from two NaI(Tl) detectors were passed through a summing network, producing a "sum-coincidence" spectrum. A single-channel analyzer was used to set a window on a sum peak in this spectrum, and this window was then used to gate the output of one of the NaI(Tl) detectors.

Some major advantages of the sum-coincidence technique were readily apparent:

a. Attention was focused on the cascade de-excitation of nuclear states themselves rather than on individual  $\gamma$ -rays. Thus, in principle one could work his way up a level scheme, setting the sum-window gate on the energies corresponding to each state in turn and observing the various (two-component) cascades that de-excite this state.

b. The method does improve the peak-to-Compton ratio in the gate, thereby helping to eliminate some of the ambiguities caused by the underlying Compton backgrounds from stray, unwanted peaks.

c. The resolution of the NaI(Tl) detectors was effectively improved, especially at higher energies, for it was shown<sup>1</sup>) that

$$\Gamma_{S1} = \Gamma_1(\Gamma_2^2 + \Gamma_S^2)^{1/2} / (\Gamma_1^2 + \Gamma_2^2 + \Gamma_S^2)^{1/2},$$

where the  $\Gamma$ 's are the energy widths of the various  $\gamma$ -ray peaks in a cascade ( $\Gamma_1$  and  $\Gamma_2$ ), of the sum-coincidence peak ( $\Gamma_S$ ), and of the  $\gamma$ -ray peak appearing in the sum-gated spectrum ( $\Gamma_{S1}$ ). For  $\gamma$ -rays of equal energy this improvement in resolution approached a factor of  $\sqrt{2}$ , which could make a considerable difference in NaI(Tl) spectra.

Despite these advantages, the sum-coincidence technique never really became popular. Probable reasons for this can be seen fairly easily by considering its major disadvantages:

a. The method was cumbersome. One had to have some insight into the nature of a decay scheme before he could set the sum-window gates intelligently. As a result, one could often spend as much or more time in running sum-coincidence experiments as he would in running standard  $\gamma$ - $\gamma$  coincidence experiments.

b. In order to achieve the improvement in resolution - indeed, in order to prevent the actual broadening of the sum peaks or their becoming split into several components - the gains and energy zeros of the two detectors had to be matched as closely as possible. This, of course, could be a very tedious procedure.

c. The gates on the sum-coincidence peaks had to be set very carefully in order to avoid distortions in the peaks appearing in the final spectra. This introduced an added degree of uncertainty in determining  $\gamma$ -ray intensities and energies and made any stripping of peaks in complex spectra very difficult.

d. False peaks could be generated from the underlying Compton background. Because of the poor detector resolution involved, these peaks were difficult to

\* Supported in part by the U. S. Atomic Energy Commission.

† Supported in part by the U. S. National Science Foundation.

5

distinguish from those originating from bona fide  $\gamma$ -rays.

The necessity of having prior knowledge concerning a decay scheme before being able to set gates intelligently was emphasized in an adaptation of the sum-coincidence method called the "integral-bias" summing spectrometer<sup>2</sup>). Here one set lower-level discriminators (the "integral bias") or windows on the outputs of the individual detectors and used these to gate the sum spectrum itself. The appearance of a particular sum peak in a sum spectrum gated by, say, windows  $m$  and  $n$  thus indicated that its components lay in energy regions  $m$  and  $n$  in the respective singles spectra. In principle, with this method a clever setting of three or four gates could furnish all the coincidence information needed to unravel a reasonably complex decay scheme. In practice, however, one almost never succeeded in setting the windows "cleverly" before he already knew the specific locations of states in a major portion of the decay scheme.

The main application, then, of the sum-coincidence methods was for neutron-capture  $\gamma$ -rays<sup>3</sup>), where any technique that might simplify the spectra was welcomed. They have also found occasional uses in total absorption spectroscopy<sup>4</sup>), directional correlation experiments<sup>5</sup>), and some  $g$ -factor measurements<sup>6</sup>). And with the advent of Ge(Li) detectors one might reasonably expect the sum-coincidence methods to become quite obsolescent, for their operational difficulties appear to outweigh their advantages rather quickly. The problem of matching the gains of the detectors, for example, becomes all the more difficult and critical. A recent paper by Kantele and Suominen<sup>7</sup>) does extend the "integral-bias" sum-coincidence method to Ge(Li)-Ge(Li) systems, but in all fairness it must be concluded that their results show it to be more of a curiosity than a viable laboratory technique.

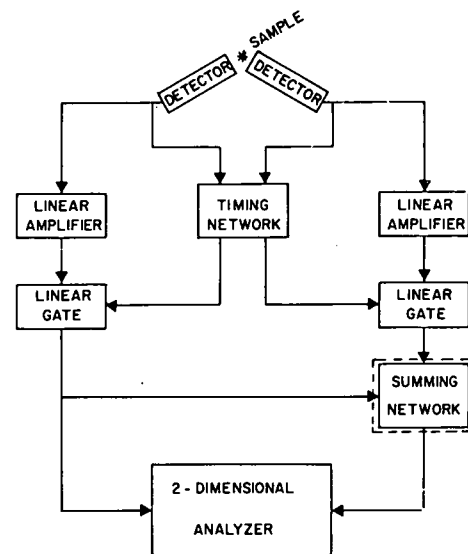
Recently, however, we have been making use of a variant of the sum-coincidence method in our laboratory, using Ge(Li)-Ge(Li) detector systems, and we have found it to be quite useful in helping to clarify complex spectra and decay schemes. Its usefulness depends critically on the fact that we use the sum-coincidence method only for off-line after-the-fact analysis of the recorded data from two-dimensional "megachannel"  $\gamma$ - $\gamma$  coincidence experiments. These are experiments in which two Ge(Li) detectors are operated in full (not gated) coincidence and the addresses of each coincident event are listed in a computer buffer and then written on magnetic tape. Spectra are obtained later by sorting the two-dimensional array in slices. During the sorting process one can easily per-

form sums, so little or no additional experimental effort is required to add the sum-coincidence method to the other methods of analysis. Also, since the data are available in *digital* rather than analog form, the computer can be made to perform some of the routine tasks that made the older sum-coincidence techniques so unwieldy. For example, it can correct for the energy calibration of the detectors after the experiment has been completed, making it no longer necessary to match the detector gains exactly. Or, since a record is available of which events originated from which detectors, one can immediately obtain meaningful sum spectra even without bothering to convert from channel number to energy, providing that the gains were only moderately mismatched (cf. below).

In other words, having a complete digital record of the data from a Ge(Li)-Ge(Li)  $\gamma$ - $\gamma$  coincidence experiment on hand and then performing sum-coincidence analysis on these data makes the sum-coincidence method a worthy supplement and complement to the standard  $\gamma$ - $\gamma$  coincidence analyses, especially for very complex spectra. In this paper we discuss its various advantages and disadvantages and present some results from its use on a moderately complex spectrum (<sup>63</sup>Zn) and a very complex spectrum (<sup>205</sup>Bi).

## 2. Experimental methods

Our sum-coincidence experimental set-up differs



$\gamma$ -SUM COINCIDENCE

Fig. 1. Block diagram of the sum-coincidence experiment. The addition of the "summing network" is the only way in which this differs from a standard two-dimensional  $\gamma$ - $\gamma$  "megachannel" coincidence experiment, and the "summing network" is merely an addition to the off-line computer recovery program.

very little in concept from a standard two-dimensional  $\gamma$ - $\gamma$  "megachannel" coincidence experiment. This is shown dramatically in fig. 1, where the only difference is the addition of a summing network to a  $\gamma$ - $\gamma$  coincidence block diagram in order to obtain the sum-coincidence block diagram – and this summing network is simply a modification of the off-line recovery program. It should be pointed out that all of the data presented in this paper had been taken prior to our decision to try a sum-coincidence analysis. The experimental methods used to record these data were developed strictly to optimize the  $\gamma$ - $\gamma$  coincidence results; yet the data could be analyzed quite successfully by sum-coincidence methods.

A description of our two-dimensional megachannel coincidence system, using ADC's interfaced to the MSU Cyclotron Laboratory Sigma-7 computer, has been given previously<sup>8</sup>), the only difference here being the specific detectors we used. For the  $^{63}\text{Zn}$  spectra the detectors were two five-sided coaxial Ge(Li) detectors obtained from Nuclear Diodes. One had a resolution of 2.2 keV fwhm for the 1333-keV  $\gamma$  from  $^{60}\text{Co}$  and an efficiency of 2.5% for the same  $\gamma$ -ray relative to a  $7.6 \times 7.6$ -cm NaI(Tl) detector (source distance 25 cm), the other a resolution of 3.4 keV and an efficiency of 2.0%. The 2.5% detector was also used for the  $^{205}\text{Bi}$  spectra, along with a 3.6% efficient, 2.1 keV resolution true coaxial detector obtained from ORTEC. The 2.5% detector used a cooled FET preamplifier, the others room-temperature FET preamplifiers.

The off-line recovery program<sup>9</sup>) was modified to perform sum-coincidence gating as well as the normal  $\gamma$ - $\gamma$  coincidence gating. Fig. 2 shows a simplified flow diagram of this modified program. The main modifications made involved summing the  $X$  and  $Y$  addresses of the event. From there on this sum was used as the second parameter of a two-parameter analysis, with either the  $X$  or the  $Y$  address as the other parameter, so the gating was done the same as would be done on  $\gamma$ - $\gamma$  coincidence data. Routines such as background analysis and subtraction were performed exactly as previously, again using the sum address as one side of the system. The additional limitation on the sum of  $X > Y$  or  $X < Y$  was performed because the gains of the detectors were not perfectly matched. In this way we prevent two peaks from appearing for the same sum without having to go through the procedure of converting the addresses to  $\gamma$ -ray energies.

### 3. Analysis of a moderately simple spectrum: $^{63}\text{Zn}$

As an example of the power of the sum-coincidence method to reduce a large background under weak

peaks, we present some results obtained on the decay of 38-min  $^{63}\text{Zn}$ . In fig. 3 we show portions of the spectra

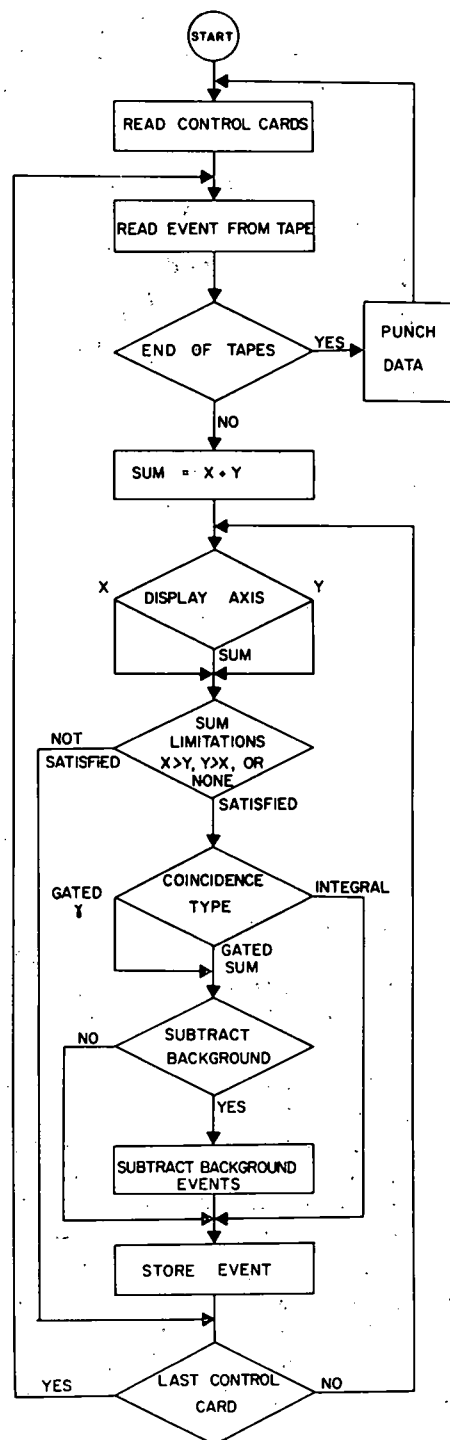


Fig. 2. Flow diagram of the program used to recover data from the magnetic tapes produced by the "megachannel" coincidence experiments at the MSU Cyclotron Laboratory.

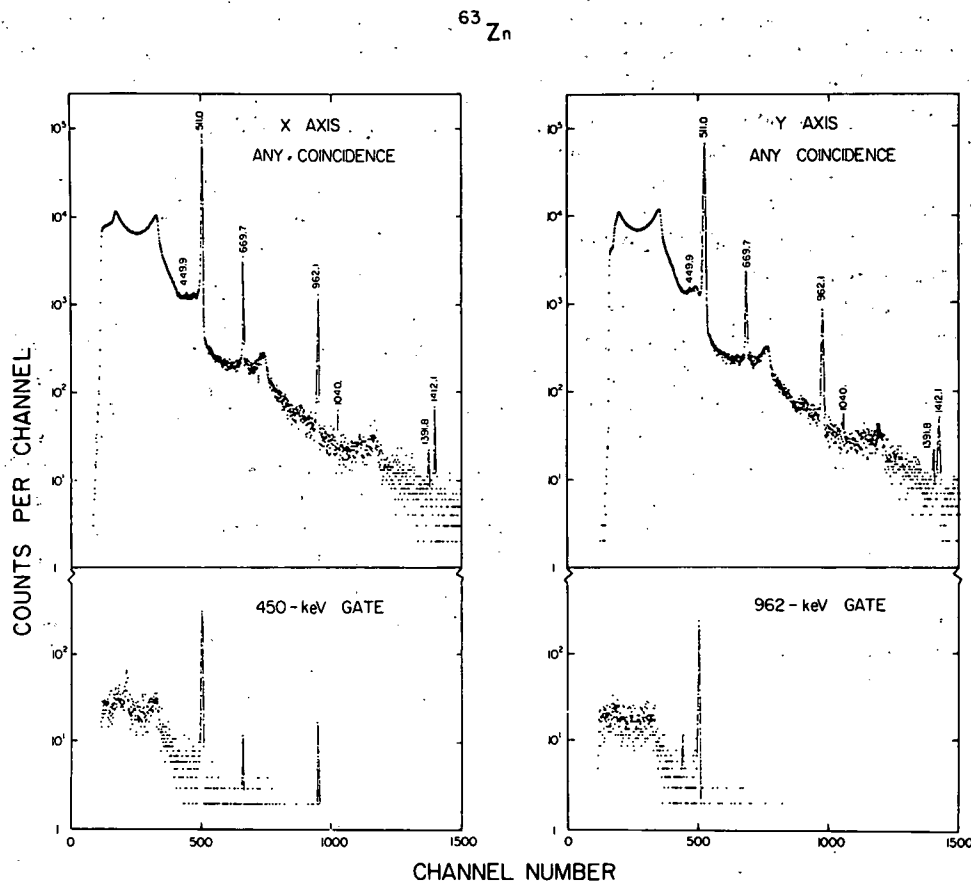
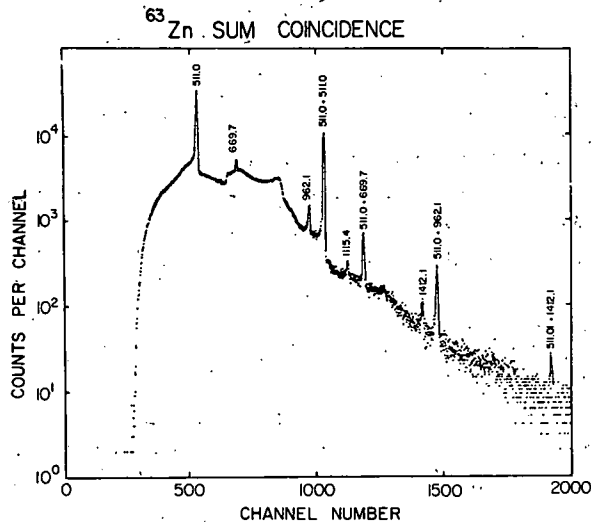


Fig. 3. Coincidence spectra for  $^{63}\text{Zn}$ . The integral or "any" coincidence spectra shown at the top were obtained by adding up all coincident events for each axis. The lower spectra are gated slices.

obtained from a two-dimensional  $\gamma$ - $\gamma$  coincidence experiment. The integral or "any" coincidence spectra, which were obtained by adding up all the listed events recorded by the 2.5% and the 2.0% detectors singly, are shown at the top as  $X$  and  $Y$ , respectively. All that need be said about the decay scheme itself<sup>10</sup>) is that the first and second excited states of  $^{63}\text{Cu}$  lie at 669.7 and 962.1 keV, both decay exclusively to the ground state, and the weak 449.9-keV  $\gamma$  feeds the 962.1-keV state from a state at 1412.1 keV. The 669.7-, 962.1-, and 1412.1-keV states are all strongly  $\beta^+$  fed. The cascade nature of the 449.9-keV  $\gamma$  is demonstrated by the gated spectra appearing in the lower half of fig. 3. Placing a gate on the 450-keV region causes an enhancement of the 962.1-keV  $\gamma$  over the 669.7-keV  $\gamma$ , although the latter is more intense in most of the other spectra. Also, placing a gate on the 962-keV region results in an enhancement of the 449.9-keV  $\gamma$ . It can be seen, however, that the background interference from the  $\gamma^\pm$  (in true coincidence with the 962.1-keV  $\gamma$ ) is quite severe in this last spectrum.

The spectrum resulting from summing each pair of  $X$  and  $Y$  addresses together is shown in fig. 4. Two types of peaks appear in this spectrum, sum peaks, as indicated, and Compton scattered peaks. The Compton scattered peaks are those that result from a Compton scattered photon from one detector being captured by the second detector. The peaks at 511.0, 669.7, 962.1, and 1115.4 keV are examples of this type. The peak at 1412.1 keV is mostly a sum peak but contains a Compton scattered component.

Fig. 5 shows examples of gating on each type of peak. At the top we see the  $X$  and  $Y$  components of all sums with  $Y > X$ . The result is that the  $Y$  axis shows a relatively normal integral coincidence spectrum, although skewed toward higher energies, while the  $X$  axis shows a spectrum whose intensity is greatly reduced at the higher energies. Gating on the 669.7-keV peak (a Compton scattered peak) as displayed in fig. 4, we see the following results: A sharp peak appears at 511 keV in the  $Y$ -axis spectrum, and it appears to be in coincidence with a peak at  $\approx 160$ .



keV in the X-axis spectrum. What we are seeing is a true coincidence between the 511-keV photopeak from one detector with that portion of the  $\gamma^\pm$  Compton distribution from the other detector that is required to add up to the 670-keV gate. The peak at  $\approx 160$  keV is narrow only because the gate on the 670-keV region was also quite narrow. (This whole business of generating peaks that can masquerade as photopeaks is discussed at length in ref. 8.)

In the 670-keV gated spectra three broader peaks also appear. The Compton edge from the 669.7-keV  $\gamma$  in the Y spectrum is in coincidence with the back-

Fig. 4. Total sum-coincidence spectrum for  $^{63}\text{Zn}$ . This spectrum was obtained by summing the addresses of each coincident event in the integral coincidence spectra of fig. 3.

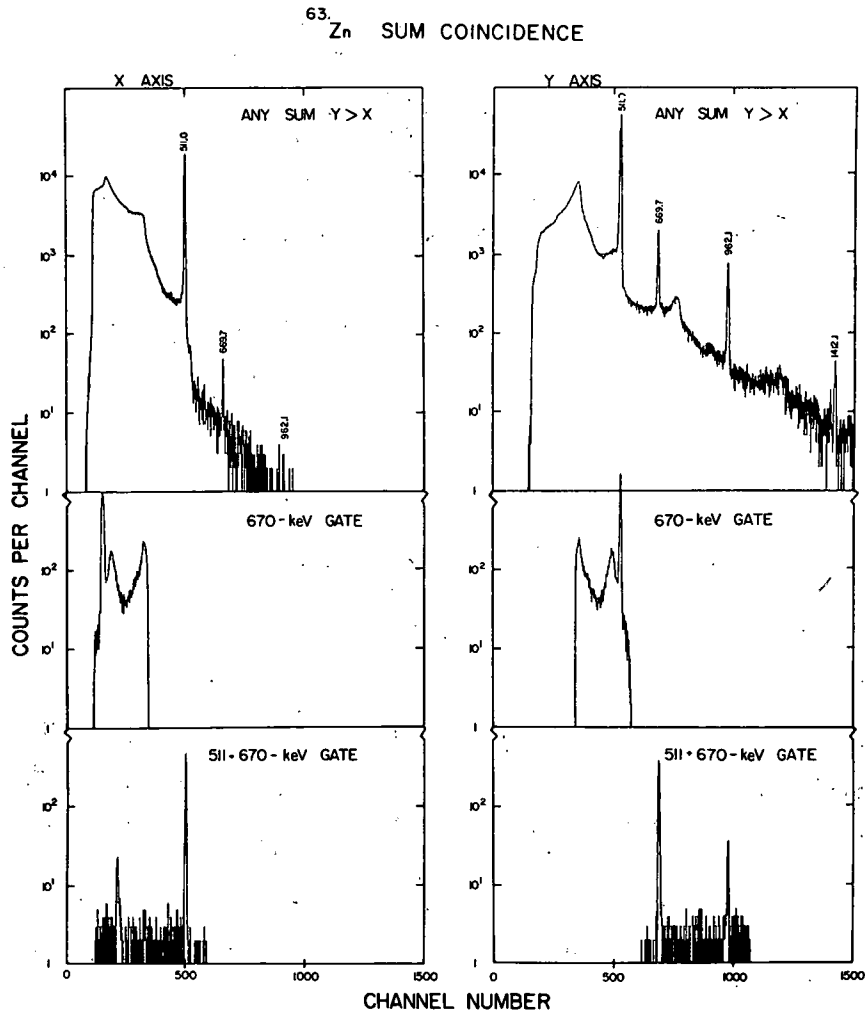


Fig. 5. Sum-coincidence spectra for  $^{63}\text{Zn}$ . All of the spectra shown were taken with the limitation  $Y > X$ , and the X-axis spectra are displayed on the left opposite their corresponding Y-axis spectra.



scatter peak from the same  $\gamma$ -ray in the  $X$  spectrum. And the broad Gaussian-looking peak that is split between the  $X$  and  $Y$  spectra represents those portions of the Compton continuum from the  $\gamma^\pm$  in each detector that, in true coincidence, add up to  $\approx 670$  keV.

The spectra gated on the 511+670-keV sum start to show the advantages of the sum-coincidence method. First, notice the welcome reduction in the Compton background in these spectra. Then notice the clean appearance of the 669.7-keV photopeak in the  $Y$  spectrum and the 511.0-keV photopeak in the  $X$  spectrum. The 962.1-keV peak (weak) in the  $Y$  spectrum arises from chance coincidences, as does the backscatter peak from the 669.7-keV  $\gamma$  in the  $X$  spectrum.

In fig. 6 we show the results of gating on the 1412-keV sum peak. The 449.8- and 962.1-keV peaks are very strongly enhanced, demonstrating conclusively that they are a cascade adding up to 1412 keV. The 511.0- and 669.7-keV peaks are present because of being in coincidence with the underlying Compton background. The fact that there is a 1412.1-keV ground-state transition is evidenced by the Compton edge of this transition appearing in coincidence with its backscatter peak. Subtracting a weighted background from each side of the sum peak improves the peak-to-Compton ratios further and removes some of the 511.0- and 669.7-keV peaks. Perhaps the strongest statement we can make in favor of the sum-coincidence technique is "compare the 449.8-keV peak in the lower

part of fig. 6 with the same peak in the 962-keV gated spectrum in fig. 3". We remind the reader that both spectra were extracted from the same set of magnetic tapes.

#### 4. Analysis of a complex spectrum: $^{205}\text{Bi}$

As our second example, we show how the sum-coincidence method can aid in resolving a weak, closely spaced triplet peak in the complex spectrum that results from the decay of 14.6-d  $^{205}\text{Bi}$ . The  $^{205}\text{Bi}$  singles spectrum presented in fig. 7, with its myriad of weak peaks, illustrates the complexity of the decay – a total of 99  $\gamma$ -rays have been identified as belonging to this decay. The peak of interest to us here is the weak peak near 1002 keV. Fig. 8, which shows only that small portion of the decay scheme<sup>11)</sup> necessary for the present discussion, indicates the reason for selecting this peak. All of the previous studies of this decay<sup>12)</sup> concluded that the 1002-keV peak represents a single  $\gamma$ -ray that feeds the 262.9-keV state. And although we noted a slight broadening of the 1002-keV peak, even the best Ge(Li) detectors did not have the ability to resolve the peak even partially. In our studies, however, considerable Ge(Li)–Ge(Li)  $\gamma$ - $\gamma$  coincidence data suggested a triplet with the placements indicated in fig. 8.

To substantiate the tentative placements of the transitions in the  $\approx 1002$ -keV triplet, we set sum-coincidence gate on the regions corresponding to the 1264.5-, 1705.0-, and 1764.5-keV states. The integral or "any"

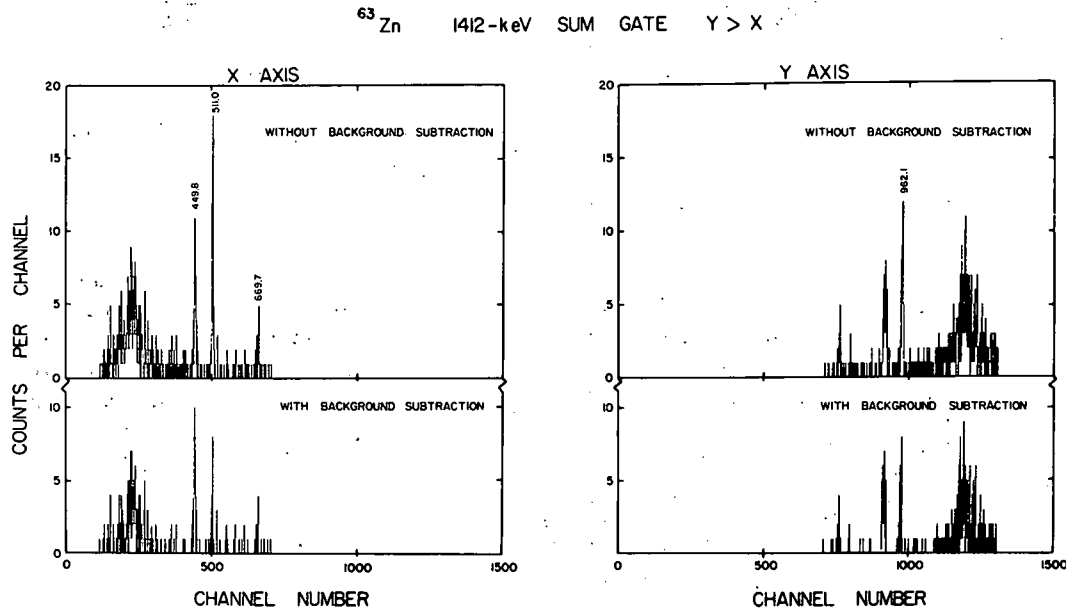


Fig. 6. Sum-coincidence spectra for  $^{63}\text{Zn}$  with the sum-gate set on the 1412.1-keV sum peak.

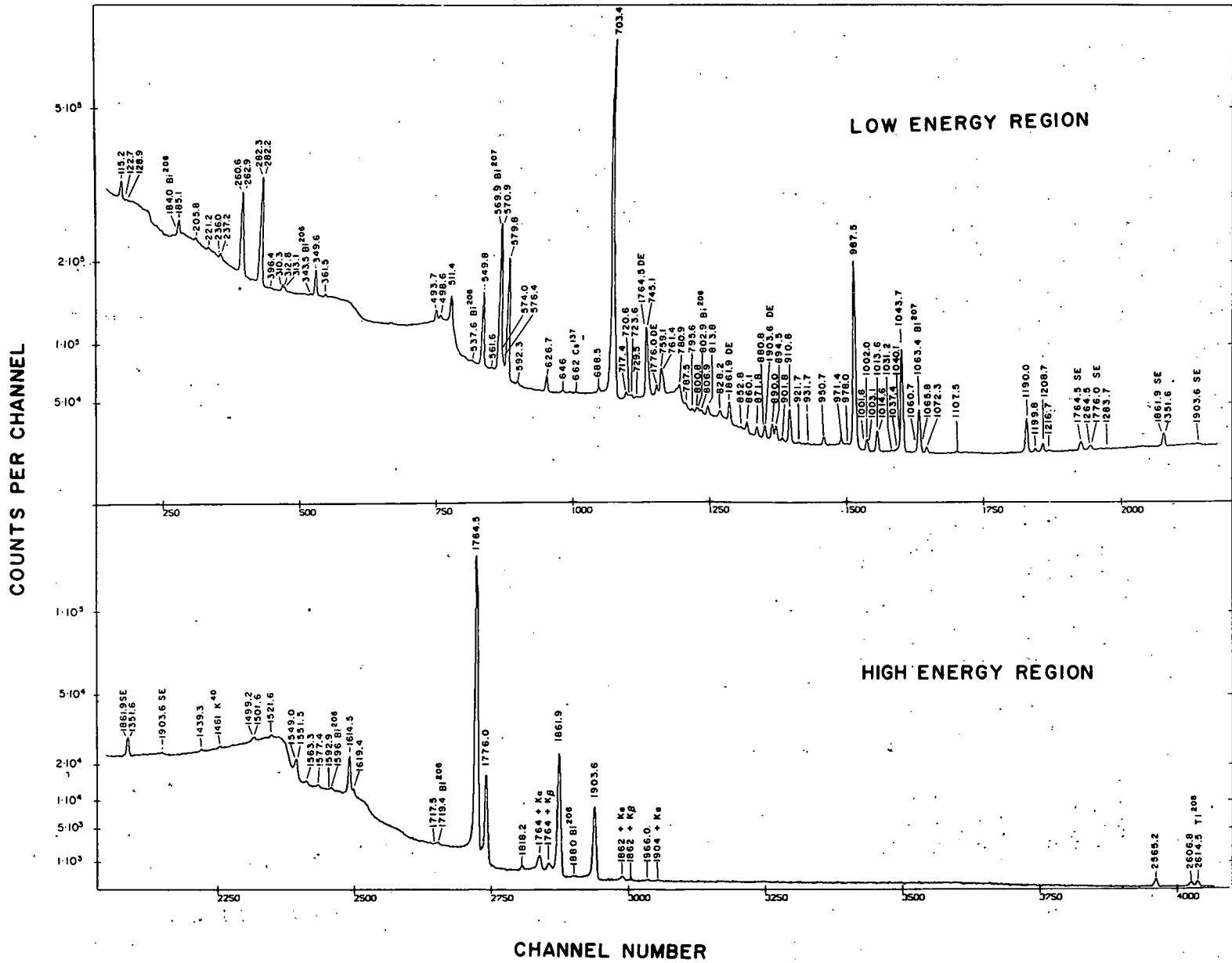


Fig. 7. <sup>205</sup>Bi singles  $\gamma$ -ray spectrum taken with a 7 cm<sup>3</sup> Ge(Li) detector.

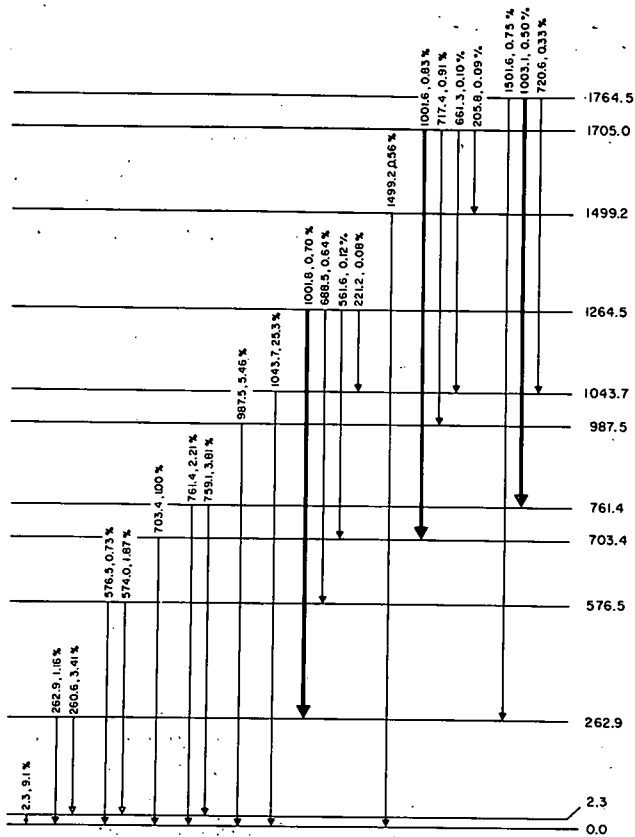


Fig. 8. A small portion of the  $^{205}\text{Bi}$  decay scheme showing those states and transitions of interest to the present discussion (from ref. 11). The three components of the  $\approx 1002$ -keV triplet are drawn as larger arrows to aid the eye in locating them.

sum spectrum is shown in fig. 9. There are relatively few clearcut sum peaks in this spectrum, considering the wealth of cascade  $\gamma$ -rays resulting from  $^{205}\text{Bi}$  decay. In fact, examining the positions of our three sum-coincidence gates does not lead to much initial optimism. The position of the 1264.5-keV gate shows no sign of an obvious sum peak – all that is present is a Compton-type background. At the location of the 1705.0-keV gate there is only a weak peak. Only at the location of the 1764.5-keV gate is the sum peak obviously present.

We show the spectra resulting from these three sum-coincidence gates in fig. 10. We display only composite spectra from the Y axis (the 3.6% detector), with the small arrows indicating where  $X > Y$  ends and  $Y > X$  begins. Even though the sum peaks were small in fig. 9, the gated spectra in fig. 10 show many well-defined peaks. A closer examination of each of these indicates that only a few are in coincidence with other  $\gamma$ -rays, while most of them result from Compton scattering.

In the top spectrum, resulting from a gate on the 1264-keV region, the 1001.8-keV  $\gamma$  is shown definitely to be in coincidence with the 260.6–262.9-keV doublet. Also present is the 576.5-keV and 688.5-keV coincidence pair. Both the 561.6- and the 221.2-keV  $\gamma$ 's are too weak to stand out from the background in this spectrum. Also present in the spectrum are strong  $\gamma$ -rays such as those at 549.8, 570.9, 703.4, and 1043.7 keV, which are present because of chance coincidences and because of Compton scattering, as discussed in the previous

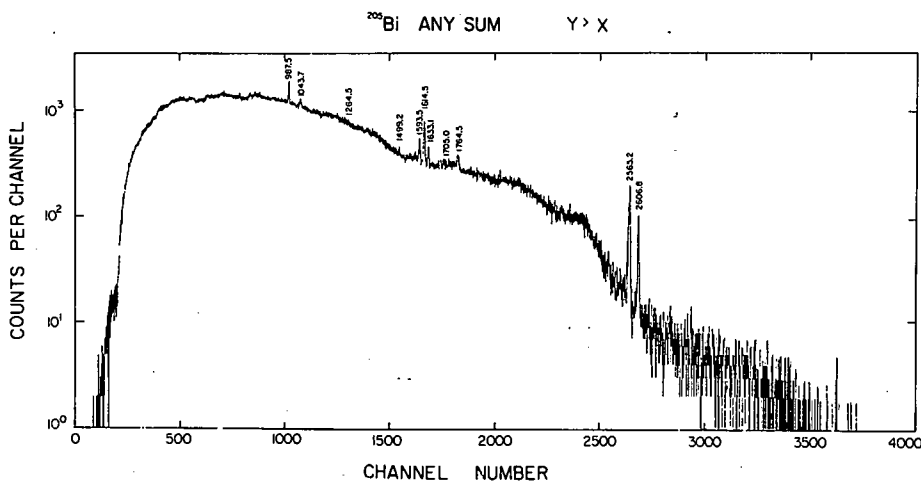


Fig. 9. Total or "any" sum-coincidence spectrum for  $^{205}\text{Bi}$ .

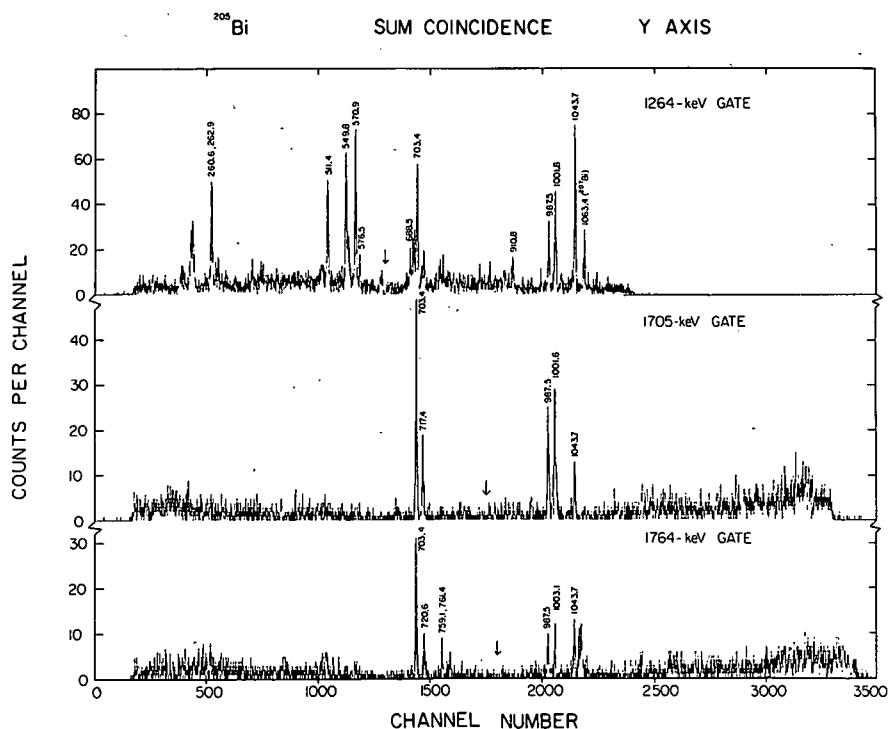


Fig. 10. Sum-coincidence spectra for  $^{205}\text{Bi}$  showing the results of gating on the 1264-, 1705-, and 1764-keV sum peaks. These are all Y-axis spectra. The small arrows show where the condition  $Y < X$  stops and  $Y > X$  begins.

section. The other peaks in the spectrum are caused almost solely by Compton scattering, as was verified by increasing the gate widths and observing the resulting changes in the intensities and shapes of these peaks.

The middle spectrum, resulting from a gate on the 1705-keV region, is considerably simpler. The 1001.6-keV and 703.4-keV coincident pair is definitely established, and so is the 717.4-keV and 987.5-keV pair. Both the 661.3- and 205.8-keV  $\gamma$ 's are too weak to stand out in this spectrum.

A few more peaks are present in the bottom spectrum, gated on the 1764-keV region. The 1003.1-keV and 759.1-761.4-keV and the 720.6-keV and 1043.7-keV coincident pairs are readily observed. Also present are the 703.4- and 987.5-keV  $\gamma$ 's, here only in coincidence with the Compton background in the gate, for their intensities are much lower than in the 1705-keV gated spectrum. In the spectrum drawn at the bottom of fig. 10 the 1501.6-keV and 262.9-keV coincident pair is not seen even though it is moderately intense. However, when using a wider gate width ( $\approx 20$  keV), this pair was easily seen. This result points out one of the problems that has not been completely solved here — that of unmatched gains for the two detectors. These peaks were far enough away in energy from the other

two coincident pairs that their sum peak produced simply by adding channel numbers was excluded from the narrow sum gate based on the other two pairs. In this instance the apparent difference in sum energy was almost 10 keV. Thus, although one can and does use detectors without perfectly matched gains, he must be on the lookout for this sort of sum-peak "jitter". That is, unless he is willing to convert the spectra from channel numbers to  $\gamma$ -ray energies before setting the sum-coincidence gates, a somewhat tedious procedure but one that can be performed readily by the computer.

Accordingly, the presence of the 260.6-262.9- & 1001.8-keV, the 703.4- & 1001.6-keV, and the 759.1-761.4- & 1003.1-keV pairs in the sum gates set both confirm the existence of the  $\approx 1002$ -keV peak as a triplet and also the placements of its components. Perhaps it is worth noting that the sum-coincidence method also added a confirmation of the new state at 1705.0 keV and by removing ambiguities in the  $\gamma$ - $\gamma$  coincidence results has allowed the definite placement of the 720.6-keV transition, the center member of a quite weak 717.4-720.6-723.6-keV triplet.

## 5. Conclusion

We have shown that the sum-coincidence technique

as applied to the digitally-stored data from a two-dimensional Ge(Li)-Ge(Li)  $\gamma$ - $\gamma$  "megachannel" coincidence experiments is a viable and useful tool for the nuclear spectroscopy laboratory. When thus applied using sum-coincidence gates to complement the standard  $\gamma$ - $\gamma$  coincidence gates in the off-line sorting of the spectra, the sum-coincidence method is quite useful for pulling weak peaks out of a strong Compton background. The analysis of spectra must be made carefully and cautiously, however, for the spectra resulting from sum-coincidence gates are not quite so easily interpreted as those resulting from standard  $\gamma$ - $\gamma$  coincidence gates. This is particularly true when there is significant Compton scattering between the detectors. Nevertheless, when used to supplement and complement these  $\gamma$ - $\gamma$  coincidence experiments and *not as a stand-alone technique*, the sum-coincidence method should find considerable use in high-resolution  $\gamma$ -ray spectroscopy.

We are indebted to Mr. R. Au, Dr. D. Bayer, Mr. R. DeForest, and the MSU Cyclotron Laboratory computer staff for their assistance in the writing of programs and in the operation of the Sigma-7 computer. We also thank Mr. H. Hilbert and Dr. H. Blosser for their aid in operating the MSU Cyclotron when we prepared the sources used in this work.

## References

- 1) A. M. Hoogenboom, Nucl. Instr. and Meth. **3** (1958) 57.
- 2) J. Kantéle and R. W. Fink, Nucl. Instr. and Meth. **15** (1962) 69.
- 3) J. E. Draper and A. A. Fleischer, Nucl. Instr. and Meth. **9** (1960) 67.
- 4) J. Kantele, Nucl. Instr. and Meth. **17** (1962) 33.
- 5) J. Hattula, J. Kantele and A. Sarmanto, Nucl. Instr. and Meth. **65** (1968) 77.
- 6) E. Bozek, A. Z. Hryniewicz, G. Zapalski, R. Kulesa and W. Waluś, Nucl. Instr. and Meth. **58** (1968) 325.
- 7) J. Kantele and P. Suominen, Nucl. Instr. and Meth. **86** (1970) 65.
- 8) G. C. Giesler, Wm. C. McHarris, R. A. Warner and W. H. Kelly, Nucl. Instr. and Meth. **91** (1971) 313.
- 9) EVENT RECOVERY, a mixed FORTRAN-machine language program written for the MSU Cyclotron Laboratory Sigma-7 computer by D. Bayer, D. B. Beery and G. C. Giesler.
- 10) G. C. Giesler, Wm. C. McHarris and W. H. Kelly, to be published; cf. also A. Kiuru and P. Holmberg, Z. Physik **233** (1970) 146.
- 11) K. L. Kosanke, Wm. C. McHarris and W. H. Kelly; to be published.
- 12) T. D. Rupp and S. H. Vegors, Jr., Preprint (1970) submitted to Nucl. Phys., and references cited therein.

## *N*-Shell Conversion Electrons from the 2.33-keV Transition in $^{205}\text{Pb}$

W. C. Johnston, W. H. Kelly, and S. K. Haynes

*Cyclotron Laboratory,\* Department of Physics, Michigan State University, East Lansing, Michigan 48823*

and

K. L. Kosanke and Wm. C. McHarris

*Department of Chemistry† and Cyclotron Laboratory,\* Department of Physics,  
Michigan State University, East Lansing, Michigan 48823*

(Received 18 March 1971)

We have measured the  $N_{II}$  and  $N_{III}$  conversion electrons from the  $\approx 2.33$ -keV transition in  $^{205}\text{Pb}$  with a  $\pi\sqrt{2}$ , iron-free, double-focusing  $\beta$ -ray spectrometer and have determined the energy of this transition to be  $2.328 \pm 0.007$  keV. We obtain an  $N_{II}/N_{III}$  ratio of  $0.70 \pm 0.25$  for this transition and a ratio  $(N_{II} + N_{III})/L_I$ , where the  $L_I$  is from the 26.22-keV  $M2$  isomeric transition in  $^{205}\text{Pb}$ , of  $0.48^{+0.15}_{-0.05}$ . These are in very good agreement with predicted conversion ratios and represent the first test of theoretical calculations for the  $N$  shell at such low energies.

The Michigan State University (MSU)  $\pi\sqrt{2}$ , iron-free, double-focusing  $\beta$ -ray spectrometer has been used to make measurements on the very low-energy portions of the electron spectra resulting from the EC decay of  $^{205}\text{Bi}$  and  $^{206}\text{Bi}$ . These were used to obtain the  $N$ -conversion spectrum for the 2.33-keV transition in  $^{205}\text{Pb}$ . At  $^{205}\text{Pb}$  the  $p_{1/2}$  and  $f_{5/2}$  neutron orbits have crossed and lie very close together, and indirect evidence<sup>1-3</sup> has established the 2.33-keV transition as being an  $E2$  from the (predominantly  $\nu p_{1/2}$ )  $\frac{1}{2}^-$  first excited state to the (predominantly  $\nu f_{5/2}$ )  $\frac{5}{2}^-$  ground state. Measurements on conversion electrons in this energy range are extremely rare, and the present experiments represent the first direct observation of this transition. In fact, we believe that this is only the second time that an  $\approx 2$ -keV transition has been measured,<sup>4</sup> and it is the first time such measurements have been made on an element with a high enough  $Z$  that the  $N$  subshell ratios could be used to test theoretical conversion coefficients directly.

The sources used for this study were prepared by bombarding mass-separated Pb isotopes (obtained from Oak Ridge National Laboratory) with protons from the MSU sector-focused cyclotron. The reactions  $^{206}\text{Pb}(p, 2n)^{205}\text{Bi}$  ( $t_{1/2} = 15.3$  day) and  $^{208}\text{Pb}(p, 3n)^{206}\text{Bi}$  ( $t_{1/2} = 6.24$  day), using 19- and 25-MeV protons, respectively, produced clean sources of the desired activities.

Standard precipitation and anion-exchange techniques were used to retrieve the active material from the targets. However, we found it necessary to take extreme precautions in order to minimize even trace amounts of impurities that would cause poor quality sources.<sup>5</sup> All glassware was replaced with quartz that had been specially washed and leached for several days in low-conductivity water (deionized, distilled, doubly deionized, distilled) whose purity was checked by measuring its conductivity. The acids used (HCl and  $\text{HNO}_3$ ) were either "Ultrex" commercial grade<sup>6</sup> or were prepared by bubbling HCl and  $\text{NO}_2$  gases through low-conductivity wa-

They were finally purified by passing them through ion-exchange columns. The ion-exchange resin used for the separations (Dowex 1×8) was also washed repeatedly with all of the acids and concentrations to be used in the separations.

Spectrometer sources,  $1 \times 12 \text{ mm}^2$  on 0.5-mil Al foil, were prepared by vacuum evaporation. Liquid source material (in 0.5N  $\text{HNO}_3$ ) was dried on a W boat that had just previously been flashed for several seconds in vacuum. Only after bringing the boat up to a temperature slightly lower than that needed for Bi evaporation were the backings put into place and a series of sources made. As many as five sources were prepared from one loading of the boat by collecting at successively slightly higher temperatures for longer times. Typically the second or third source gave the most favorable combination of activity and resolution.

The MSU  $\pi\sqrt{2}$ , iron-free, double-focusing spectrometer used to obtain the spectra includes a post-focusing acceleration technique<sup>7</sup> that extends its useful range down to less than 1 keV.

The energy resolution, which was limited by the source size and quality, was determined to be  $<0.3\%$  for the  $L_I$  line from the 26.22-keV transition in  $^{205}\text{Pb}$  (an  $M2$  transition that is primarily responsible for the de-excitation of the  $^{13/2}^+$  isomeric state at 1013.7 keV<sup>8,1-3</sup>). As source thickness became more critical at the lower energies, the linewidth increased to as much as 0.6% at 1 keV with a substantial tail as well. The energy calibration and instrumental transmission were monitored throughout the experiments by periodically running over the  $L_{III}$ - $M_{IV}M_V$ ,  $L_{III}$ - $M_V M_V$  Auger doublet in addition to the  $L_I$  conversion line from the 26.22-keV transition.

During the counting periods of three or more half-lives, a number of passes were made over the low-energy region of interest and these were compared for consistency. In the end, all of the data for each source were corrected for half-life and a point-by-point weighted average and three-point smoothing were carried out. In Fig. 1 we show a comparison of the  $^{205}\text{Bi}$  and  $^{208}\text{Bi}$  spectra.

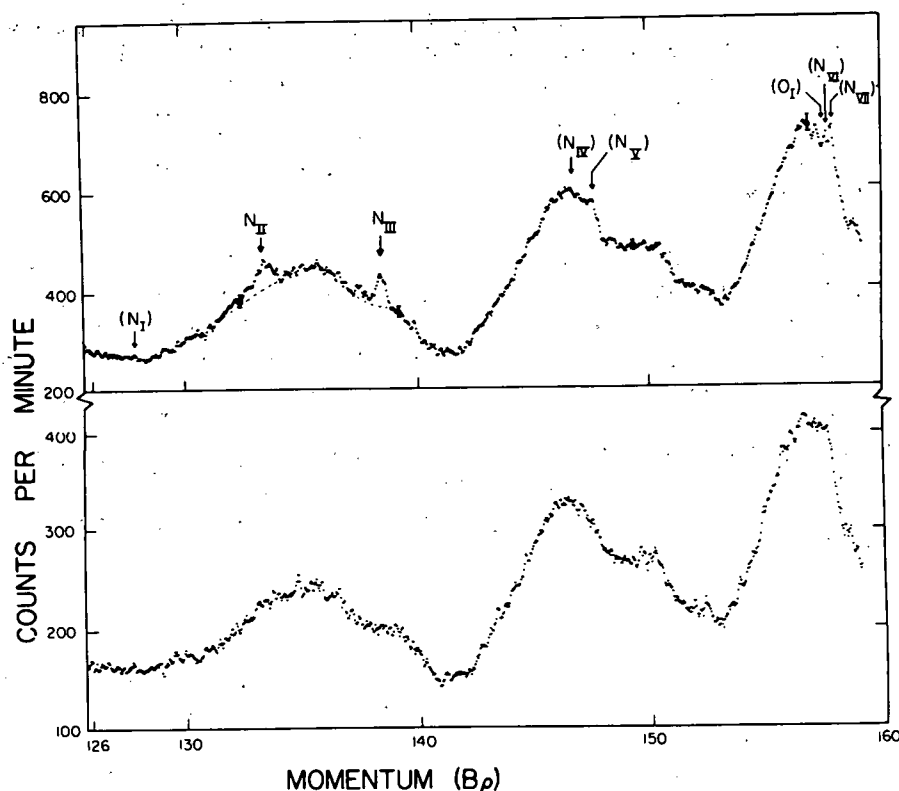


FIG. 1. (Top) The  $N$ -conversion spectrum of the 2.328-keV transition in  $^{205}\text{Pb}$  resulting from the EC decay of  $^{205}\text{Bi}$ . The  $N_{II}$  and  $N_{III}$  lines are clearly visible above the  $M$ -Auger background and have energies of  $1.564 \pm 0.007$  and  $1.683 \pm 0.007$  keV, respectively. The positions where other conversion lines would fall are indicated in parentheses. The dashed line represents the experimental Auger background under the  $N_{II}$  and  $N_{III}$  peaks. (Bottom) The  $^{208}\text{Bi}$  spectrum, which contains no low-energy conversion electrons, is shown for comparison. This spectrum was used to remove the Auger background from the  $^{205}\text{Bi}$  spectrum.

The gross features of these spectra are much what we expected—a rather intense Auger background with very broad peaks corresponding to many predicted unresolved *M* Auger lines. Since <sup>206</sup>Bi has no low-energy transitions, its spectrum appears to consist solely of Auger lines; however, in the <sup>205</sup>Bi spectrum the *N*<sub>II</sub> and *N*<sub>III</sub> (but not the *N*<sub>I</sub>) conversion lines from the 2.33-keV transition are present and quite discernable.

The higher energy conversion lines fall on top strong Auger lines and are not unambiguously solved from them.

To subtract out the Auger background we normalized the <sup>206</sup>Bi spectrum to the <sup>205</sup>Bi spectrum and did a point-by-point subtraction. It should be pointed out that this tacitly assumes that the Auger components are the same for the two spectra. This should be a fair approximation, al-

Table I. Conversion intensity data for the 2.328-keV transition in <sup>205</sup>Pb.

	This work	Other experiments	Theoretical <sup>a</sup>
$\alpha_{N_{III}}$	fiducial line ( $\approx 2.03 \times 10^7$ )	---	$2.03 \times 10^{7b}$
$N_I/N_{III}$	$< 5 \times 10^{-2}$	---	$5.8 \times 10^{-3b}$
$N_{II}/N_{III}$	$0.70 \pm 0.25$	---	$0.74^b$
$N_{IV}/N_{III}$	$< 5 \times 10^{-2}$	---	$1.7 \times 10^{-2b}$
$N_V/N_{III}$	$< 5 \times 10^{-2}$	---	$1.5 \times 10^{-2b}$
$O_{II}/N_{III}$	<i>O</i> <sub>II</sub> present	---	$1.4 \pm 0.3 \times 10^{-1c}$
$O_{III}/N_{III}$	<i>O</i> <sub>III</sub> present	---	$2.1 \pm 0.4 \times 10^{-1c}$
$P_{II}/N_{III}$	$< 5 \times 10^{-2}$	---	$1.0 \times 10^{-2c}$
$P_{III}/N_{III}$	$< 5 \times 10^{-2}$	---	$1.5 \times 10^{-2c}$
$\frac{N_{II} + N_{III}}{L_{I26.22}}$	$0.48^{+0.15}_{-0.05}$	---	---
$\frac{\Sigma 2.328^d}{L_{I26.22}}$	$0.59^{+0.21}_{-0.07}$	---	---
$\frac{\Sigma 2.328^e}{\Sigma 703.3}$	$0.10^{+0.04}_{-0.02}$	$\left\{ \begin{array}{l} 0.106 \pm 0.008^f \\ 0.112 \pm 0.008^g \end{array} \right.$	---

<sup>a</sup>All other conversion coefficients are at least a factor of 3 smaller than those listed.

<sup>b</sup>Graphical and numerical interpolation of Ref. 10.

<sup>c</sup>Linear extrapolation, on log-log paper, of Ref. 11 from 10 keV.

Errors represent extrapolation uncertainties.

<sup>d</sup> $(N_{II} + N_{III})/L_I$  multiplied by (total conversion/ $(N_{II} + N_{III})$ ) from the last column.

<sup>e</sup>I.e., the ratio of the total transition intensities; see text for method of calculation.

<sup>f</sup>Reference 2 with 26.22-keV conversion data from Ref. 8 and 703.4-keV conversion data from Ref. 9.

<sup>g</sup>Reference 3 with 26.22-keV conversion data from Ref. 8 and 703.4-keV conversion data from Ref. 9.



though  $M_I$  and  $M_{III}$  conversion of the 26.22-keV transition in  $^{205}\text{Pb}$  does cause some different  $M$  primary vacancy distributions, which in turn cause slight variations in the Auger spectra. Despite this and the statistical fluctuations, the  $N_{II}$  and  $N_{III}$  still stood out clearly. The line shapes and areas, including low-energy tails, were determined by demanding that the two lines have identical shapes and that the background ( $^{205}\text{Bi} - \text{const} \times ^{206}\text{Bi}$ ) have no maxima or minima under the lines.

Basing the energy calibration on the  $L_I$  line of the  $(26.22 \pm 0.01)$ -keV transition,<sup>8</sup> we measured the transition energy to be  $2.328 \pm 0.007$  keV. This compares with  $2.33 \pm 0.03$  keV, which was deduced in this laboratory from  $\gamma$ -ray studies.<sup>3</sup> A summary of the electron intensity data is given in Table I. The fact that the assumed baseline, affecting especially the low-energy tails, is more likely to be high than low accounts for the asymmetrical errors on the intensity ratios. The measured  $N_{II}/N_{III}$  ratio of  $0.70 \pm 0.25$  is in excellent agreement with the prediction of Dragoun, Pauli, and Schmutzler.<sup>10</sup> These are the first experimental data that have been available to test these predictions.

The total intensity of the 2.328-keV transition relative to the very prominent 703.4-keV transition from  $^{205}\text{Bi}$  decay (the second most intense transition, which de-excites a state of the same energy in  $^{205}\text{Pb}$ —cf. Refs. 1-3) can be obtained from the  $(N_{II} + N_{III})/L_{I,26.22}$  ratio by the following relation:

$$\frac{I_{2.328}}{I_{703.4}} = \left( \frac{N_{II} + N_{III}}{L_{I,26.22}} \right) \left( \frac{\alpha_{2.328}}{\alpha_{N_{II}} + \alpha_{N_{III}}} \right) \times \left( \frac{L_{I,26.22}}{K_{703.4}} \right) \left( \frac{\alpha_{K_{703.4}}}{1 + \alpha_{703.4}} \right),$$

where the second, third, and fourth terms on the right have respective values of  $1.24 \pm 0.05$  (from the last column of Table I), 14.9 (Ref. 8), and  $0.011 \pm 0.001$  (Ref. 9). As shown in Table I, this ratio has a value of  $0.10_{-0.02}^{+0.04}$ , which agrees well with the sum of the intensities of the  $\gamma$  rays<sup>2,3</sup> plus conversion electrons of the transitions feeding the 2.328-keV state. Assuming that the decay scheme is correct, this result then suggests that the predicted<sup>10</sup> ratio,  $\alpha_{2.328}/(\alpha_{N_{II}} + \alpha_{N_{III}})$ , also

agrees with experiment.

Only the  $N_{II}$  and  $N_{III}$  conversion lines were measured quantitatively in this work. There appears to be appreciable intensity at the momenta corresponding to the  $P_{II}$  and  $P_{III}$  lines, however, but the fluctuations in the difference curves mask the much weaker transitions. Further measurements on these lines are being made to accumulate better statistics and will be reported on elsewhere.

We are deeply grateful to Steve Park and Larry Tummel who helped operate the spectrometer and prepared many of the data for computer analysis. We also thank Harold Hilbert and Dr. Henry Blosser for their aid in operating the MSU cyclotron. Finally, we thank Mrs. Helen Michel, Lawrence Radiation Laboratory, Berkeley, for her valuable aid in the techniques of source vaporization.

\*Work supported in part by the U. S. National Science Foundation.

†Work supported in part by the U. S. Atomic Energy Commission.

<sup>1</sup>S. H. Vegors, Jr., R. L. Heath, and D. G. Proctor, Nucl. Phys. **48**, 230 (1963); also references to earlier work contained therein.

<sup>2</sup>T. D. Rupp and S. H. Vegors, Jr., to be published.

<sup>3</sup>K. L. Kosanke, W. C. McHarris, and W. H. Kelly, to be published; summarized by K. L. Kosanke in Michigan State University Nuclear Chemistry Annual Report No. COO-1779-49, 1970 (unpublished), p. 23.

<sup>4</sup>W. M. LaCasse and J. H. Hamilton, Bull. Amer. Phys. Soc. **15**, 1358 (1970), report their observation of  $M_{II}$ ,  $M_{III}$ ,  $M_{IV+v}$ , and  $\sum N$  electrons from the 2.17-keV  $E3$  transition in  $^{99}\text{Tc}$ :

<sup>5</sup>Details are given by K. L. Kosanke, *op. cit.*, p. 283.

<sup>6</sup>J. T. Baker Chemical Co., Phillipsburg, N. J.

<sup>7</sup>R. J. Kriescioaitis and S. K. Haynes, Nucl. Instrum. Methods **58**, 309 (1968).

<sup>8</sup>R. Stockendal, Ark. Fys. **17**, 553 (1960).

<sup>9</sup>R. Stockendal and S. Hultberg, Ark. Fys. **15**, 33 (1959).

<sup>10</sup>O. Dragoun, H. C. Pauli, and F. Schmutzler, Nucl. Data, Sect. A **6**, 235 (1969).

<sup>11</sup>O. Dragoun, Z. Plajner, and F. Schmutzler, "Tables of Approximate Conversion Coefficients for the  $N_6-N_7$ ,  $O_1-O_7$ ,  $P_1-P_5$ , and  $Q_1$  Atomic Subshells" (to be published).

INELASTIC DEUTERON SCATTERING FROM  $^{56}\text{Fe}$  AND  $^{58}\text{Fe}$ R. K. JOLLY<sup>†</sup>, B. H. ARMITAGE and A. K. SENGUPTA<sup>††</sup>

Atomic Energy Research Establishment, Harwell, Berks., England

Received 15 December 1969

**Abstract:** Angular distributions of inelastically scattered deuterons from  $^{56}\text{Fe}$  and  $^{58}\text{Fe}$  have been measured at incident deuteron energies of 11.5 and 11.8 MeV respectively using a broad-range spectrograph. The experimental angular distributions have been compared with the results of DWBA calculations using complex coupling and including the contribution from Coulomb excitation. Values of  $\beta_1$  have been extracted and in general the spin and parity assignments agree well with previous work.

E NUCLEAR REACTIONS  $^{56,58}\text{Fe}(d, d')$ ,  $E = 11.5$  MeV, 11.8 MeV; measured  $\sigma(E_d, \theta)$ .  $^{56,58}\text{Fe}$  deduced levels,  $J, \pi$ ; deformation parameters  $\beta_1$ . Enriched targets.

## 1. Introduction

A systematic study of the octupole and quadrupole states of even isotopes of Zn and Ni by inelastic deuteron scattering has already been reported<sup>1</sup>). In the present work the measurements have been extended to  $^{56}\text{Fe}$  and  $^{58}\text{Fe}$  and include angular distributions for all excited states up to an excitation energy of about 4.5 MeV in  $^{56}\text{Fe}$  and for the more intensely excited groups in  $^{58}\text{Fe}$ . Although  $^{56}\text{Fe}$  and  $^{58}\text{Fe}$  are well-studied nuclei<sup>2-21</sup>), the only detailed work on deuteron inelastic scattering which has as yet been reported is that of Majumder and Sengupta<sup>5</sup>) on  $^{56}\text{Fe}$ .

## 2. Experimental procedure

Deuterons of energy 11.5 MeV and 11.8 MeV from the Harwell Tandem Accelerator have been used to bombard targets of  $^{56}\text{Fe}$  and  $^{58}\text{Fe}$  enriched to 99.9 % and 61 % respectively. The inelastically scattered deuterons were detected with a broad-range magnetic spectrograph using nuclear emulsion plates, a brief description of which has already been given<sup>3,4</sup>). Some additional measurements on the first  $2^+$  states and the  $3^-$  states have been made with the broad-range spectrograph using position sensitive detectors. Here again a description of the arrangement has been given elsewhere<sup>1</sup>).

The precision elastic scattering data of Igo *et al.*<sup>2,5</sup>) was used to establish the cross-section scale of the inelastically scattered particle groups. This was achieved by comparing the elastic yield with the relevant inelastic yield in the present measurements.

<sup>†</sup> Now at Michigan State University, East Lansing, Michigan, USA.

<sup>††</sup> Now at Saha Institute for Nuclear Physics, Calcutta, India.

### 3. DWBA calculations

The calculation of differential inelastic scattering cross sections has been fully discussed in the literature<sup>35</sup>). Suffice it to say that the present calculations were made in the framework of the surface-coupling collective model using complex coupling and including the Coulomb excitation contributions for  $l = 2$  and  $l = 3$ . The validity of the surface-coupling model has been demonstrated in numerous analyses<sup>1, 31, 32</sup>). Furthermore it has been shown that a correct prediction of deuteron inelastic scattering cross sections<sup>31, 32</sup>) can be obtained using complex-coupling and including the contribution from Coulomb excitation. The DWBA calculations which were performed with the code JULIE<sup>26</sup>), enabled the angular momentum transfer ( $l$ ) to be assigned to one-phonon vibrational states. In addition the mean square deformation ( $\beta_l^2$ ) of the vibrational states was obtained from normalization of the calculated and observed differential cross sections. More specifically, the ratio of the experimental differential cross section to the calculated differential cross section was taken to be  $\beta_1^2/5014$ .

TABLE 1  
Optical-model parameters used in DWBA calculations

$V$ (MeV)	$r_0$ (fm)	$a$ (fm)	$W$ (MeV)	$r'_0$ (fm)	$a'$ (fm)	$r_c$ (fm)
89.1	1.15	0.81	20.9	1.34	0.68	1.15

A set of optical-model parameters was obtained by Perey and Perey<sup>36</sup>) from an analysis of elastic scattering data on  $^{56}\text{Fe}$  obtained by Igo *et al.*<sup>25</sup>) with 11.8 MeV deuterons. The optical-model parameters used in the present DWBA calculations, which are listed in table 1, are "set B" of those obtained by Perey and Perey<sup>36</sup>). The DWBA calculations were made using the same optical potentials in the entrance and exit channels. The effect of taking into account the energy dependence of the optical parameters in the exit channels for the  $3^-$  states of the Zn and Ni isotopes has already been described in an earlier work<sup>1</sup>). The result was that  $\beta_3$  was increased by about 4% on average while the shape of the calculated angular distribution hardly changed at all. No account has been taken of these effects in the present work.

### 4. $^{56}\text{Fe}$ results

The spectrum of inelastically scattered deuterons obtained at a laboratory observation angle of  $90^\circ$  is shown in fig. 1. This spectrum reveals that the strongest groups are associated with the first  $2^+$  and  $3^-$  states. This result is in accord with that observed in inelastic proton and inelastic  $\alpha$ -particle experiments<sup>8, 13-18</sup>). Angular distributions for a number of groups in  $^{56}\text{Fe}$  are compared with the results of DWBA calculations in fig. 2.

The agreement of the DWBA  $l = 2$  calculations with the experimental data is moderate for the 0.85 MeV ( $2^+$ ) state. As can be seen in table 3 the  $\beta_1$  for the 0.85 MeV  $^{56}\text{Fe}$  state agrees well with Coulomb excitation measurements<sup>27)</sup>.

The  $4^+$  nature of the 2.09 MeV state has already been established<sup>4)</sup> but the angular distribution is rather featureless and shows little agreement with the calculated  $l = 4$  angular distribution. This result lends some support to the view that this state has a

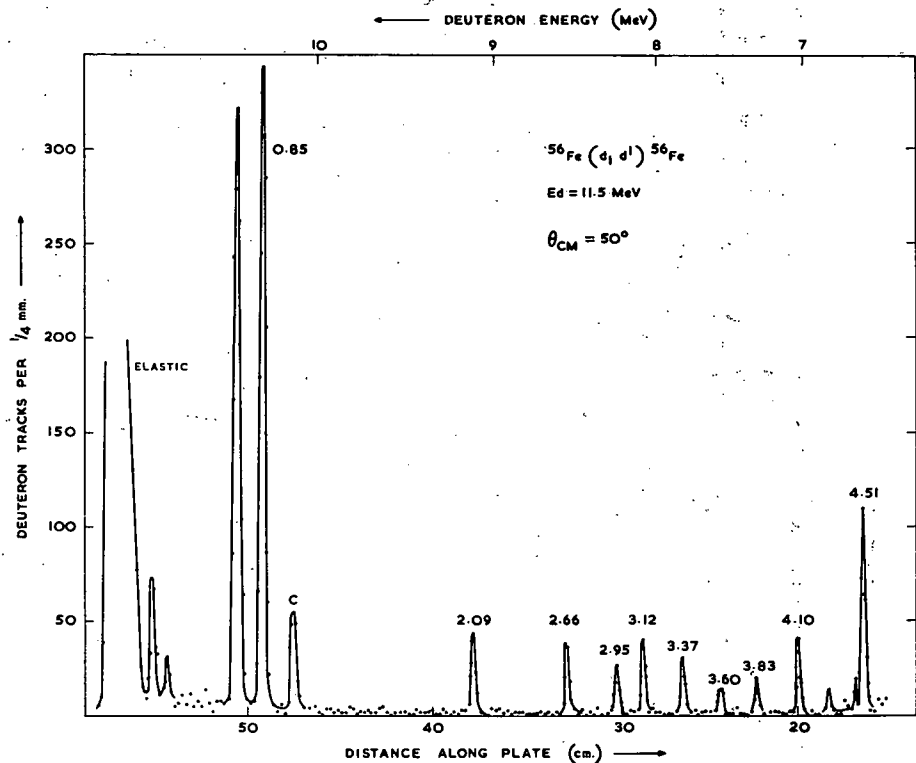


Fig. 1. Spectrum of deuterons obtained by bombarding an  $^{56}\text{Fe}$  target with 11.5 MeV deuterons. The energies in MeV of the excited states corresponding to the outgoing deuteron groups are shown.

strong two-phonon component since two-phonon angular distributions are predicted to be out of phase with one-phonon angular distributions<sup>30)</sup>. A combination of one-phonon and two-phonon cross sections might therefore lead to a featureless angular distribution.

The 2.66 MeV state is established<sup>4)</sup> as  $2^+$  and the angular distribution is in moderate agreement with the DWBA calculation for  $l = 2$ . In contrast, however, calculations made with other  $l$ -values are in definite disagreement with the experimental angular distributions.

The 2.95 MeV group is established as a ( $0^+$ ,  $2^+$ ) doublet<sup>4)</sup> with a spacing of about 18 keV. A combination of  $l = 0$  and  $l = 2$  DWBA angular distributions gives poor

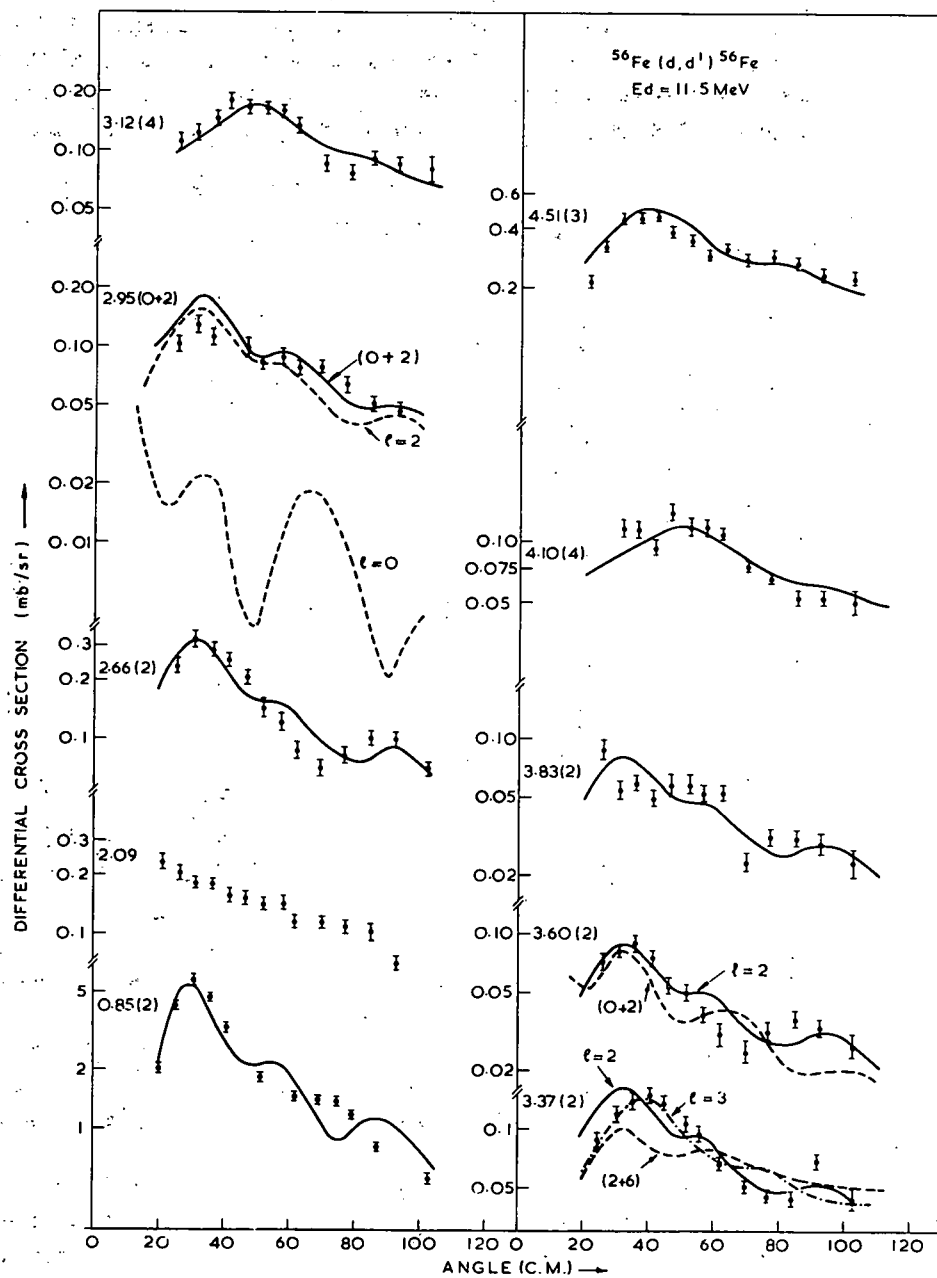


Fig. 2. Angular distributions of deuteron groups from  $^{56}\text{Fe}(d, d')^{56}\text{Fe}$  are compared with the results of DWBA calculations. The optical parameters are listed in table 1. The errors shown on the experimental points are both systematic and statistical.

agreement with experiment at forward angles up to  $40^\circ$ . A possible explanation is provided by the inclusion of two-phonon contributions in the combined angular distribution.

There is fairly good evidence that the 3.12 MeV group corresponds to a closely spaced ( $1^+$ ,  $4^+$ ) doublet<sup>4)</sup> or possibly a triplet<sup>23)</sup>. Good agreement between calculation and experiment is obtained with a single  $l = 4$  angular distribution. This result is consistent with a one-phonon  $l = 4$  excitation since the  $1^+$  level is of unnatural parity and would not be expected to be excited with an appreciable cross section in the present experiment. Cohen *et al.*<sup>2)</sup> obtained an assignment of  $5^-$  for this state; an assignment of  $4^+$  has, however, been obtained in a re-analysis of the data<sup>29)</sup>. Some support for the  $5^-$  alternative is provided by an  $l = 5$  assignment from the  $^{56}\text{Fe}(d, d')^{56}\text{Fe}$  data of Majumder *et al.*<sup>5)</sup>. In the present work, however, much better agreement is obtained with the experimental data with  $l = 4$  rather than  $l = 5$ .

The 3.37 MeV angular distribution agrees with the  $l = 2$  calculation at angles greater than  $50^\circ$  while at forward angles the  $l = 3$  calculation gives better agreement. The available evidence is that this group is composed of a ( $2^+$ ,  $6^+$ ) doublet<sup>4)</sup>, although the  $6^+$  assignment is obtained solely from the  $^{59}\text{Co}(p, \alpha)^{56}\text{Fe}$  reaction<sup>28)</sup>. The absence of the high-spin state in  $^{56}\text{Co}$  and  $^{56}\text{Mn}$  decay is consistent with this assignment. However, in the present work the agreement with experiment is worsened if any  $l = 6$  component (broken curve in fig. 2) is added to the  $l = 2$  cross section.

The 3.60 MeV group is probably a ( $0^+$ ,  $2^+$ ) doublet<sup>4)</sup>. The  $^{56}\text{Fe}(d, d')^{56}\text{Fe}$  angular distribution agrees reasonably well with the  $l = 2$  calculation. Again, any appreciable admixture of  $l = 0$  will worsen the agreement between calculation and experiment (broken curve in fig. 2). This result agrees with the general observation that  $0^+$  states are usually weakly excited in the (d, d') reaction.

A  $2^+$  assignment<sup>4)</sup> has been given for the 3.83 MeV level, which, in the present work has a poorly defined angular distribution. The situation here is unsatisfactory since the observed angular distribution is almost equally consistent with  $l = 1$ ,  $l = 2$  and  $l = 3$  calculations. As expected the nearby unnatural parity  $3^+$  state<sup>4)</sup> at 3.86 MeV is not observed in the present measurements.

The angular distribution of the 4.10 MeV group is in reasonable agreement with the  $l = 4$  DWBA calculation. Support is therefore given to the  $4^+$  assignment obtained from (t, p) measurements<sup>2)</sup>. It would appear, therefore, that the angular distribution does not contain an appreciable contribution from a three-phonon excitation.

The 4.51 MeV group corresponds to the well established  $3^-$  state and good agreement is obtained with the  $l = 3$  DWBA calculation.

There is some indication in the present work that the 2.09 MeV ( $4^+$ ) state can be equated with a two-phonon  $4^+$  state insofar as the angular distribution is in disagreement with the DWBA calculation for a one-phonon state. No light can be cast on the location of possible  $0^+$  and  $2^+$  two-phonon states in the present work since two  $0^+$  and three  $2^+$  states are contained in the 2.95 MeV, 3.37 MeV and 3.60 MeV groups which are all unresolved doublets. It should be pointed out, however, that theoretical

work has shown that the phonon model is not very useful in describing two-phonon states in the even mass Ni isotopes<sup>33</sup>).

The values of the deformation parameter ( $\beta_l$ ) for  $^{56}\text{Fe}$  obtained in the present work are listed in table 2. The quoted errors take into account experimental uncertainties only. The existing data on  $\beta_l$  for  $^{65}\text{Fe}$  is associated entirely with the first quadrupole and octupole states. The deformation parameters for the first  $2^+$  state agrees reasonably well with that obtained from Coulomb excitation. Fairly good agreement also exists with data obtained from (p, p') and ( $^3\text{He}$ ,  $^3\text{He}'$ ) experiments. The value of the deformation parameter obtained for the octupole state agrees well with that obtained from proton inelastic scattering.

TABLE 2  
Deformation parameters for  $^{56}\text{Fe}$  and  $^{58}\text{Fe}$

$^{56}\text{Fe}$			$^{58}\text{Fe}$		
Excitation energy (MeV)	<i>l</i> -value	$\beta_l$	Excitation energy (MeV)	<i>l</i> -value	$\beta_l$
0.85	2	$0.27 \pm 0.01$	0.81	2	$0.30 \pm 0.02$
2.66	2	$0.086 \pm 0.005$	1.67	2	$0.105 \pm 0.005$
2.95	2	$0.063 \pm 0.006$	2.61	4	$0.125 \pm 0.012$
3.12	4	$0.106 \pm 0.004$	3.63	2	$0.067 \pm 0.005$
3.37	2	$0.071 \pm 0.006$	3.88	3	$0.20 \pm 0.01$
3.60	2	$0.055 \pm 0.003$			
3.83	2	$0.056 \pm 0.003$			
4.10	4	$0.096 \pm 0.006$			
4.51	3	$0.20 \pm 0.01$			

### 5. The $^{58}\text{Fe}$ results

In comparison with the data obtained from  $^{56}\text{Fe}$ , that from  $^{58}\text{Fe}$  is of lower quality with poorer energy resolution and inferior counting statistics. The difference can be partly accounted for by the lower enrichment (sect. 2) of the  $^{58}\text{Fe}$  target in comparison with the  $^{56}\text{Fe}$  target. In addition the angular distribution data is limited to six angles for  $^{58}\text{Fe}$  in contrast with the thirteen angles for  $^{56}\text{Fe}$ .

The angular distribution of the more strongly excited  $^{58}\text{Fe}$  groups are compared with the results of DWBA calculations in fig. 3. Angular distributions from several weakly excited  $^{58}\text{Fe}$  groups are not included in fig. 3 as meaningful comparisons with DWBA calculations cannot be made.

The agreement of the DWBA  $l = 2$  calculations for the 0.81 MeV ( $2^+$ ) level is good, but the restriction of the data to six angles limits the value of the comparison.

The spin of the 1.67 MeV level is established as  $3^-$   $2^+$  and the angular distribution is consistent with the  $l = 2$  calculation.

The 2.61 MeV group has some features in common with the high-spin member of the 3.12 MeV doublet in  $^{56}\text{Fe}$ . The 2.61 MeV  $^{58}\text{Fe}$  level has been assigned as  $5^-$  or

$6^+$  by Cohen *et al.*<sup>3)</sup> from the  $^{56}\text{Fe}(t, p)^{58}\text{Fe}$  reaction, but the best agreement with the present (d, d') angular distribution is obtained once again for  $l = 4$  indicating a spin and parity of  $4^+$ .

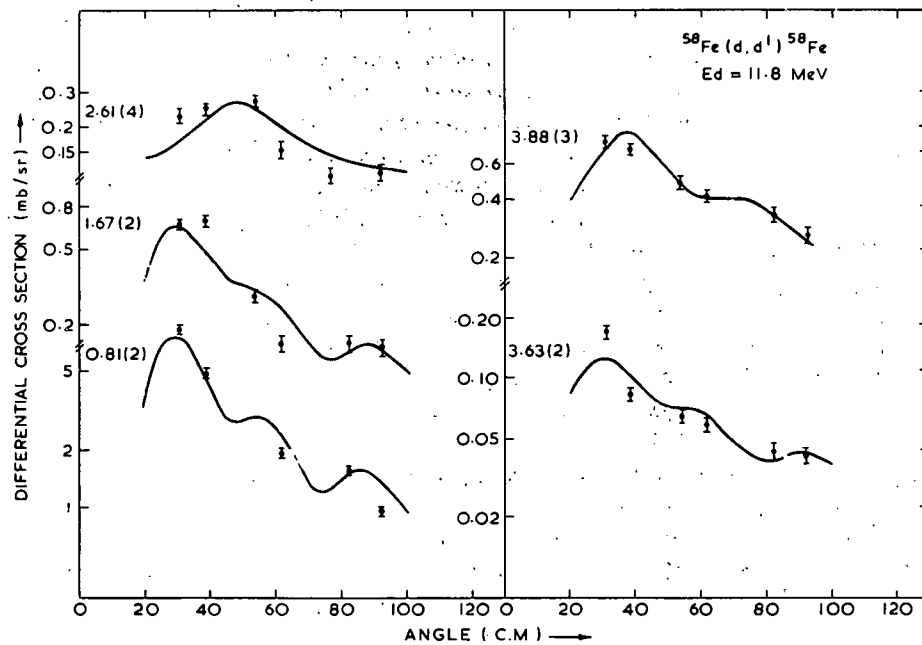


Fig. 3. Angular distributions of deuteron groups from  $^{58}\text{Fe}(d, d')^{58}\text{Fe}$  are compared with the results of DWBA calculations. The optical parameters are listed in table 1. The errors shown on the experimental points are both systematic and statistical.

TABLE 3  
Deformation parameters for  $^{56}\text{Fe}$  and  $^{58}\text{Fe}$

	This work	Mean (p, p') a)	( $^3\text{He}, ^3\text{He}'$ ) b)	( $\alpha, \alpha'$ ) c)	(d, d') d)	(e, e') e)	Adopted value f)
$^{56}\text{Fe}(2^+)$	0.27	0.24	0.22		0.38	0.18	0.23
$^{56}\text{Fe}(3^-)$	0.20	0.20	0.11		0.25	0.10	
$^{58}\text{Fe}(2^+)$	0.30	0.24	0.22	0.17			0.27
$^{58}\text{Fe}(3^-)$	0.20		0.082				

a) Refs. 13-18). b) Ref. 12). c) Ref. 8). d) Ref. 5). e) Ref. 20). f) Ref. 27).

Adopted value for  $^{56}\text{Fe}$  obtained from 5 Coulomb excitation and 3 resonance fluorescence measurements. Adopted value for  $^{58}\text{Fe}$  obtained from 2 Coulomb excitation measurements.

The angular distribution of the 3.63 MeV level is consistent with a  $l = 2$  calculation. This is in agreement with the assignment of  $2^+$  obtained from the  $^{56}\text{Fe}(t, p)^{58}\text{Fe}$  reaction<sup>3)</sup>.



The 3.88 MeV level which is known to be the collective  $3^-$  state <sup>3)</sup> agrees reasonably well with the DWBA  $l = 3$  calculation.

The values of the deformation parameters for  $^{58}\text{Fe}$  obtained in the present work are listed in table 2. As in the case of  $^{56}\text{Fe}$ , comparisons with existing data can only be made for the first  $2^+$  and  $3^-$  states. Here again the deformation parameter for the first  $2^+$  state agrees well with that obtained from Coulomb excitation: the agreement with the  $(p, p')$  and the  $(^3\text{He}, ^3\text{He}')$  data is moderate, and that with the  $(e, e')$  data is rather poor. The deformation parameter for the octupole state can only be compared with that obtained from inelastic  $^3\text{He}$  scattering with which the agreement is poor.

## 6. Conclusions

In general reasonably good agreement has been obtained between the DWBA calculations and the experimental angular distribution in the present work. This result is in accord with earlier measurements, at the same bombarding energy, on the Ni and Zn isotopes <sup>1)</sup>, but other work at lower incident energies has shown rather poor agreement between experiment and calculation <sup>37, 38)</sup>. The extent of the agreement for  $^{56}\text{Fe}$  and  $^{58}\text{Fe}$  has, however, been partly obscured by the considerable number of unresolved doublets in  $^{56}\text{Fe}$  and also by the lack of a sharp distinction between the shapes of the angular distributions for different  $l$ -values. Where comparisons can be made, the deformation parameters agree well with those obtained from Coulomb excitation and inelastic proton scattering. The fact that the deformation parameter obtained for the first  $2^+$  state of  $^{56}\text{Fe}$  agrees reasonably well with that obtained from a rather different technique i.e. Coulomb excitation, seems to indicate that the lack of really precise agreement between the shapes of the experimental and calculated angular distributions is not very important.

The authors wish to thank Dr. M. D. Goldberg for many very helpful suggestions. Thanks are also due to Professor R. M. Drisko for the loan of a copy of the DWBA code JULIE.

## References

- 1) R. K. Jolly, M. D. Goldberg and A. K. Sengupta, Nucl. Phys. A123 (1969) 54
- 2) B. L. Cohen and R. Middleton, Phys. Rev. 146 (1966) 748
- 3) B. L. Cohen, C. L. Flink, J. B. Moorhead and R. A. Moyer, Phys. Rev. 157 (1967) 1033
- 4) P. F. Hinrichsen, M. H. Shapiro and D. M. Van Patter, Nucl. Phys. A101 (1967) 81 and references cited therein
- 5) A. R. Majumder and H. M. Sengupta, Nucl. Phys. A118 (1968) 151
- 6) J. H. Bjerregaard, P. F. Dahl, O. Hansen and G. Sidenius, Nucl. Phys. 51 (1964) 641
- 7) B. H. Armitage, A. T. G. Ferguson, G. C. Neilson and W. D. N. Pritchard, Nucl. Phys. A133 (1969) 241
- 8) P. Darriulat, G. Igo, H. G. Pugh, J. M. Meriwether and S. Yamabe, Phys. Rev. 134 (1964) B42
- 9) A. Sperduto and W. W. Buechner, Phys. Rev. 134 (1964) B142
- 10) D. K. McDaniels, J. S. Blair, S. W. Chen and G. W. Farwell, Nucl. Phys. 17 (1960) 614
- 11) C. B. Fulmer, J. Benveniste and A. C. Mitchell, Phys. Rev. 165 (1968) 1218

- 12) E. R. Flynn and R. H. Bassel, *Phys. Rev. Lett.* **15** (1965) 168
- 13) S. F. Eccles, H. F. Lutz, V. A. Madsen, *Phys. Rev.* **141** (1966) 1067.
- 14) S. A. Fulling and G. R. Satchler, *Nucl. Phys.* **A111** (1968) 81
- 15) J. Benveniste, A. C. Mitchell, B. Buck and C. B. Fulmer, *Phys. Rev.* **133** (1964) B323
- 16) B. Buck, *Phys. Rev.* **127** (1962) 940
- 17) M. P. Fricke and G. R. Satchler, *Phys. Rev.* **139** (1965) B567
- 18) G. R. Satchler, R. H. Bassel and R. M. Drisko, *Phys. Lett.* **5** (1963) 256
- 19) G. Brown, S. E. Warren and R. Middleton, *Nucl. Phys.* **77** (1966) 365
- 20) J. Bellicard and P. Barreau, *Nucl. Phys.* **36** (1962) 476
- 21) K. Matsuda, *Nucl. Phys.* **33** (1962) 536
- 22) U. Fanger, W. Michaelis, H. Schmidt and H. Ottmar, *Nucl. Phys.* **A128** (1969) 641
- 23) K. Vaughan and B. D. Pate, *Nucl. Phys.* **A130** (1969) 62
- 24) W. W. Daechnick, *Phys. Rev.* **177** (1969) 1763
- 25) G. Igo, W. Lorenz and U. Schmidt-Rohr, *Phys. Rev.* **124** (1961) 832
- 26) R. H. Bassel, R. M. Drisko and G. R. Satchler, ORNL Report 3240 and supplement
- 27) P. H. Stelson and L. Grodzins, *Nucl. Data* **1** (1965) 1
- 28) R. Sherr, private communication to P. F. Hinrichsen *et al.*
- 29) R. Drisko, private communication
- 30) N. Austern, R. M. Drisko, E. Rost and G. R. Satchler, *Phys. Rev.* **128** (1962) 733
- 31) J. K. Dickens, F. G. Perey and G. R. Satchler, *Nucl. Phys.* **73** (1965) 529
- 32) R. K. Jolly, *Phys. Rev.* **139** (1965) B318
- 33) S. Cohen *et al.*, *Phys. Rev.* **160** (1967) 903;  
L. S. Hsu and J. B. French, *Phys. Lett.* **19** (1965) 135;  
N. Auerbach, *Phys. Rev.* **163** (1967) 1203
- 34) B. H. Armitage and R. E. Meads, *Nucl. Phys.* **33** (1962) 494
- 35) E. Rost, *Phys. Rev.* **128** (1962) 2708;  
T. Stovall and N. M. Hintz, *Phys. Rev.* **135** (1964) B330;  
M. M. Strautberg and J. J. Kraushaar, *Phys. Rev.* **151** (1966) 969
- 36) C. M. Perey and F. G. Perey, *Phys. Rev.* **132** (1963) 755
- 37) P. Wilhelm, Ole Hansen, J. R. Comfort, C. K. Bockelman, P. D. Barnes and A. Sperduto,  
*Phys. Rev.* **166** (1968) 1121
- 38) O. Hansen, T. A. Belote and W. E. Dorenbusch, *Nucl. Phys.* **A118** (1968) 41

A TRUNCATED SHELL MODEL CALCULATION OF  $^{23}\text{Na}$ ,  $^{24}\text{Mg}$  AND  $^{28}\text{Si}$ 

J. B. McGRORY

Oak Ridge National Laboratory\*, Oak Ridge, Tennessee, USA

and

B. H. WILDENTHAL

Michigan State University\*\*, East Lansing, Michigan, USA

Received 28 December 1970

Results of an s-d-shell model calculation of  $^{23}\text{Na}$ ,  $^{24}\text{Mg}$  and  $^{28}\text{Si}$  are discussed. An inert  $^{16}\text{O}$  core is assumed and states with up to four  $d_{5/2}$  holes and at most two  $d_{3/2}$  particles are included. The calculated level energies of  $^{23}\text{Na}$  and  $^{24}\text{Mg}$  are in excellent agreement with the observed spectra. Fair agreement for  $^{28}\text{Si}$  is also obtained if the  $d_{5/2}$ - $s_{1/2}$  interaction is strengthened by 400 keV over that used for  $A = 23$  and  $24$ .

Calculations of the structure of low lying states of  $^{24}\text{Mg}$  and  $^{28}\text{Si}$  have been relatively unsuccessful to date. Calculations in the complete s-d-shell model space are not presently feasible for these nuclei because the dimensions are too large. Deformed Hartree-Fock calculations of  $^{24}\text{Mg}$  are difficult because the lowest Hartree-Fock solution is ellipsoidal [1], which causes problems in the projection of states of good  $J$  and  $T$ . This same method has difficulties in  $^{28}\text{Si}$  because there are two nearly degenerate solutions for the ground state, each with a quite different shape.  $\text{SU}_3$  calculations [2, 3] have likewise met with only modest success for these nuclei. In this note, we present the results of an attempt to calculate the spectra of  $^{24}\text{Mg}$  and  $^{28}\text{Si}$  in terms of a truncated  $j$ - $j$  coupling shell model calculation. In addition we present the results of the energy level calculations for  $^{23}\text{Na}$ . We obtain excellent agreement with the model we describe below for  $^{23}\text{Na}$  and  $^{24}\text{Mg}$ , and fair agreement for  $^{28}\text{Si}$ .

We describe first the model we use. An inert  $^{16}\text{O}$  core is assumed, and the  $d_{5/2}$ ,  $s_{1/2}$  and  $d_{3/2}$  orbits are included in the active model space. The dimensions of the complete space of  $J=2$ ,  $T=0$  states for eight particles in the s-d shell is 1206. For  $^{28}\text{Si}$ , with twelve particles, the dimension of the complete  $J=2$ ,  $T=0$  space is

3276. To reduce these dimensions to manageable sizes, we have truncated the full s-d shell space. In the calculations we present here, we include only configurations of the form

$$(d_{5/2})^{n_1} (s_{1/2})^{n_2} (d_{3/2})^{n_3},$$

where  $A-20 \leq n_1 \leq A-16$ ,  $n_2 \leq 4$ ,  $n_3 \leq 2$ , and  $A$  is the mass of the nucleus involved. In other words, we allow no more than four particles outside the  $d_{5/2}$  shell, and we allow no more than two particles in the  $d_{3/2}$  shell. In this space there are 456 states in  $^{24}\text{Mg}$  with  $J=2$ ,  $T=0$ , and 249 states in  $^{28}\text{Si}$  with  $J=2$ ,  $T=0$ . The effective interaction is specified by three single-particle energies, and 63 two-body matrix elements. We use the single-particle energies inferred by the observed energy spectrum of  $^{17}\text{O}$ ; i.e.,

$$\epsilon_{5/2} = -4.25 \text{ MeV}; \quad \epsilon_{1/2} = -3.28 \text{ MeV}; \quad \epsilon_{3/2} = 0.93 \text{ MeV}.$$

The 63 two-body matrix elements were determined in the following way. The "realistic" matrix elements developed by Kuo [4] for this mass region were empirically modified to improve the quantitative agreement between calculated and observed spectra for nuclei with  $A = 18-22$  in the following manner. The 16 matrix elements which involve only  $d_{5/2}$  or  $s_{1/2}$  orbits were treated as free and independent parameters. All the other matrix elements were altered with the prescription

$$\langle j_1 j_2 JT | H | j_3 j_4 JT \rangle = A_1 \langle j_1 j_2 JT | H | j_3 j_4 JT \rangle_{\text{Kuo}} + A_2 \delta_{j_1 j_3} \delta_{j_2 j_4}$$

\* Research sponsored by the US Atomic Energy Commission under contract with Union Carbide Corporation.

\*\* Research supported in part by the National Science Foundation.

Thus, all the Kuo matrix elements involving at least one  $d_{3/2}$  orbit were multiplied by one constant  $A_1$ , and a constant  $A_2$  was added to all diagonal matrix elements which involve one or more  $d_{3/2}$  particles. The 16 independent matrix elements, and the constant  $A$  and  $B$  were then varied to optimize the fit between theory and experiment for a selected set of ground-state and excitation energies with  $A = 18 - 22$ . The resulting interaction is used in the calculations reported here. No properties of nuclei with  $A \geq 23$  were used to determine this interaction. In the final interaction  $A_1$  was essentially 1, and  $A_2$  was +600 keV, so that all diagonal matrix elements involving any  $d_{3/2}$  particles were weakened by 600 keV.

We have repeated the calculations of nuclei with  $A = 20 - 22$  in a model space truncated in the same way that we truncate the space for  $^{23}\text{Na}$ ,  $^{24}\text{Mg}$  and  $^{28}\text{Si}$ . We found no significant differences between the spectra of low lying states of these nuclei calculated in the truncated space and in the full space. This is a necessary, but hardly sufficient, test, since the percentage of states truncated is much larger for the heavier nuclei.

The calculated and observed [5, 6] spectra of  $^{23}\text{Na}$  and  $^{24}\text{Mg}$  are shown in fig. 1. In the experimental spectrum of  $^{23}\text{Na}$  shown in this figure, three states with probable negative parity below 4 MeV are omitted. The model space we use contains no negative parity states, so we cannot account for these levels. The positive parity spectrum can possibly be characterized as a  $K = 3/2^+$  ground state rotational band. Six members of the band, from  $J = 3/2$  to  $J = 13/2$  have been tentatively identified. For the lowest five members of this band, the agreement of theory with experiment is excellent. The observed and calculated positions of the 13/2 member of the band are not shown in fig. 1, but they are in fair agreement (5.27<sub>th.</sub> MeV versus 6.24<sub>exp.</sub> MeV). Above this ground state band there are several states in the observed spectrum with uncertain spin assignments, so that it is difficult to make any firm theory-experiment correlations. If the tentative assignments shown are correct, the only possible discrepancy is for the second  $3/2^+$  and  $5/2^+$  states. On the whole, the theory-experiment agreement is quite good for  $^{23}\text{Na}$ . To an only slightly less extent the same can be said for  $^{24}\text{Mg}$ . One of the interesting features of the experimental spectrum of  $^{24}\text{Mg}$  is the appearance of a  $K = 2^+$  band, of which the first state,  $2^+$ , is essentially degenerate with the  $4^+$  member of ground state  $K = 0^+$  band. In the  $\text{SU}_3$  calcula-

tions [2] of  $^{24}\text{Mg}$  reported so far, the  $K = 2$  band is always too low, by 1 MeV or more. We see here that the known members of both the  $K = 0$  and  $K = 2$  bands are well accounted for by the shell model calculation. The agreement is less satisfactory for states outside the two rotational bands. There are several possible sources of difficulty for these higher states. Configurations which are significant for states at this excitation may be omitted in our truncation scheme. Because of the way we have adjusted the effective interaction, we feel the interactions involving  $d_{3/2}$  and  $s_{1/2}$  particles are more accurate than those involving  $d_{3/2}$  particles. The discrepancies at higher excitations may reflect this. It is also possible that the entire effective Hamiltonian should be renormalized for the higher states.

We have made a partial check of truncation effects for the  $0^+$  states in  $^{24}\text{Mg}$ . It is possible to calculate these states in the complete s-d shell space. The first excited  $0^+$  state is at 8.0 MeV in the truncated space calculation, and at 8.16 MeV in the complete-space calculation. Thus, the 1.5 MeV discrepancy between theory and experiment for this excited  $0^+$  state is not due to omitted s-d shell configuration. A possible explanation for the  $0^+$  state at 6.44 MeV is that it is analogous to the deformed  $0^+$  state in  $^{16}\text{O}$  at 6.06 MeV. Such a state exists between 6 and 8 MeV in  $^{20}\text{Ne}$ .

The spectra of  $^{26}\text{Al}$  and  $^{28}\text{Si}$  have been calculated in this same model with less success. For both nuclei, the calculated spectrum of excited states is too high with respect to the ground state. We have found that this situation is significantly improved if we effectively lower the centroid of the  $s_{1/2}$  single-particle strength. This can be accomplished in one of two ways. One is to lower the  $s_{1/2}$  single-particle energy. The other is to lower the center-of-gravity of the  $d_{5/2} - s_{1/2}$  interaction. We have chosen to calculate the spectra of  $^{26}\text{Al}$  and  $^{28}\text{Si}$  in the same model space as is used above, but with the center-of-gravity of the  $d_{5/2} - s_{1/2}$  interaction lowered to obtain reasonable fits to these nuclei. This is accomplished by subtracting 150 keV from the four diagonal  $|d_{5/2}, s_{1/2}JT\rangle$  matrix elements for the  $^{26}\text{Al}$  calculation, and by subtracting 400 keV for the  $^{28}\text{Si}$  calculation. Thus, these calculations are identical to the calculations for  $^{23}\text{Na}$  and  $^{24}\text{Mg}$  with the addition of one parameter. The results for  $^{28}\text{Si}$ , with the interaction modified in this fashion, are shown in fig. 2. For the first five experimental states [6], there is reasonable agreement between theory and experiment. Above these levels, the agree-

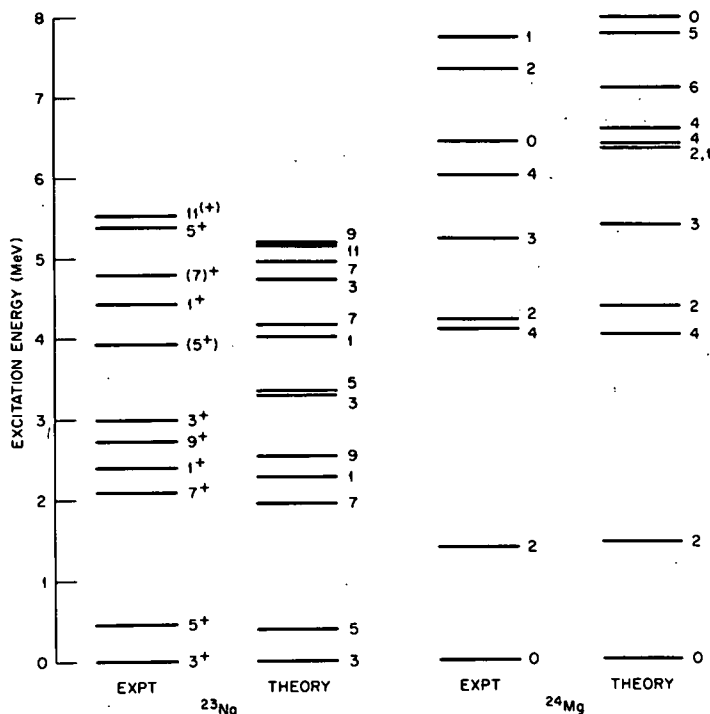


Fig. 1. Calculated and observed spectra of  $^{23}\text{Na}$  [5] and  $^{24}\text{Mg}$  [6]. All possible positive parity states below highest level shown are included in the calculated and observed spectra. For  $^{23}\text{Na}$ , we indicate  $2J$ .

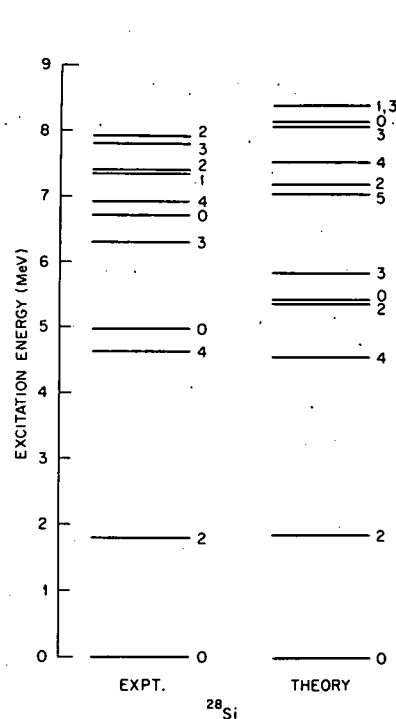


Fig. 2. Calculated and observed [6] spectra of  $^{28}\text{Si}$ . All possible positive parity levels below highest level shown are included in both calculated and observed spectra are shown.

ment is not so good. The possible reasons for this breakdown are the same as those for  $^{24}\text{Mg}$ .

We have calculated the  $B(E2)$ -values for transitions in  $^{24}\text{Mg}$  and  $^{28}\text{Si}$ . We use harmonic oscillator wavefunctions to evaluate the one-body matrix elements, and we determine the oscillator parameter from the relationship  $\hbar\omega = 41 A^{-1/3}$ . In these calculations we assume an added effective charge of  $0.5e$  for both the proton and neutron. This effective charge gives reasonable agreement for E2 observables in the complete s-d shell calculations of the  $A=18-22$  nuclei [7]. Since the transitions in  $^{24}\text{Mg}$  and  $^{28}\text{Si}$  are  $\Delta T=0$  transitions, the effective charge,  $\epsilon$ , enters only as a multiplication factor  $(1+2\epsilon)$  for the quadrupole moment operator and a factor  $(1+2\epsilon)^2$  for the E2-transition operator. The calculated  $B(E2)$ -value for the first  $2^+$  to ground state transition in  $^{24}\text{Mg}$  is  $63 e^2\text{fm}^4$ . Five different kinds of experiments have been used in the recent past to obtain values for this transition strength. Four of these, Coulomb excitation [8], resonance fluorescence scattering [9], inelastic electron scattering [10] and Doppler-shift attenuation [11], yield values falling within  $89 \pm 10 e^2\text{fm}^4$ . The fifth experiment, resonance

fluorescence self-absorption [12], yields a much larger value,  $152 \pm 18 e^2\text{fm}^4$ . Our calculated value is in reasonable agreement with the consensus result of the first four types of experiments. The average of recent measurements [8] of the quadrupole moments of the first  $2^+$  in  $^{24}\text{Mg}$  is  $-26 e\text{fm}^2$ . The calculated value is  $-16$ , so that the calculated shape is correct, but the magnitude is too small. In  $^{28}\text{Si}$ , the measured [13]  $B(E2)$  for the first  $2^+$  to ground state transition is about  $65 e^2\text{fm}^4$ . The calculated value is  $59 e^2\text{fm}^4$ , in good agreement. The calculated quadrupole moment is  $+16 e\text{fm}^2$ . Two recent measurements [13] of this moment give values of  $+11 \pm 5 e\text{fm}^2$  and  $+17 \pm 5 e\text{fm}^2$ .

In summary, we have extended a truncated shell model calculation which is successful in light s-d shell nuclei to the nuclei  $^{23}\text{Na}$ ,  $^{24}\text{Mg}$  and  $^{28}\text{Si}$ . The results for  $^{23}\text{Na}$  and  $^{24}\text{Mg}$  are excellent. For  $^{28}\text{Si}$ , it is necessary to modify the center-of-gravity of the  $d_{5/2}$ - $s_{1/2}$  interaction in order to obtain reasonable agreement with experiment. Since the space is fairly severely truncated, and any inaccuracies in the effective interaction are greatly magnified in a calculation

of a twelve-particle system such as  $^{28}\text{Si}$ , we think that overall the results of all these calculations are satisfactory. The results strongly suggest that the energy levels of most of the low lying states in these nuclei can be accounted for in terms of s-d shell configurations only.

We are grateful to R. A. Lindgren for making his experimental information on  $^{23}\text{Na}$  available to us prior to publication.

#### References

- [1] G. Ripka, *Advances in nuclear physics*, Vol. 1, eds. M. Baranger and E. Vogt (Plenum Press, New York, 1968); S. Das Gupta and M. Harvey, *Nucl. Phys.* A94 (1967) 602.
- [2] Y. Akiyama, A. Arima and T. Sebe, *Nucl. Phys.* A138 (1969) 273; K. Wathne and T. Engeland, *Nucl. Phys.* A94 (1967) 129.
- [3] J. P. Bernier and M. Harvey, *Nucl. Phys.* A94 (1967) 593.
- [4] T. T. S. Kuo, *Nucl. Phys.* A103 (1967) 71.
- [5] R. A. Lindgren, to be published.
- [6] P. M. Endt and C. van der Leun, *Nucl. Phys.* A105 (1967) 1.
- [7] E. C. Halbert, J. B. McGrory, B. H. Wildenthal and S. P. Pandya, *Advances in nuclear physics*, Vol. 4, edited by M. Baranger and E. Vogt (Plenum Press, New York, 1971) to be published.
- [8] A. Bamberger, P. G. Bizzeti and B. Povh, *Phys. Rev. Letters* 21 (1968) 1599; O. Hausser, B. W. Hooten, D. Pelte, T. K. Alexander and H. C. Evans, *Can. J. of Physics* 48 (1970) 35.
- [9] S. J. Skorka, D. Evers, J. Hertel, J. Morgenstern, T. W. Retz-Schmidt and H. Schmidt, *Nucl. Phys.* 81 (1966) 370.
- [10] O. Titze, quoted as private communication in Hausser et al. [8].
- [11] D. Pelte, O. Hausser, T. K. Alexander and H. C. Evans, *Can. J. of Phys.* 47 (1969) 1929.
- [12] D. Herrmann and J. Kalus, *Nucl. Phys.* A140 (1970) 257.
- [13] K. Nakai, J. L. Quebert, F. S. Stephens and R. M. Diamond, *Phys. Rev. Letters* 24 (1970) 903; O. Hausser, T. K. Alexander, D. Pelte, B. W. Hooten and H. C. Evans, *Phys. Rev. Letters* 23 (1969) 320.

\* \* \* \* \*

# States in Odd-Odd $Tl^{200}$ Populated by the Electron-Capture Decay of $Pb^{200}$

R. E. Doebler and Wm. C. McHarris

*Department of Chemistry,\* and Cyclotron Laboratory,† Department of Physics  
Michigan State University, East-Lansing, Michigan 48823*

and

W. H. Kelly

*Cyclotron Laboratory,† Department of Physics, Michigan State University, East Lansing, Michigan 48823*

(Received 11 June 1970)

Low-spin states in  $Tl^{200}$  have been studied via the decay of 21.5-h  $Pb^{200}$ , which was prepared by the reactions,  $Tl^{203}(p,4n)Pb^{200}$ ,  $Hg^{202}(\tau,5n)Pb^{200}$ , and  $Tl^{203}(\tau,6n)Bi^{200} \rightarrow Pb^{200}$ . Its  $\gamma$  rays were studied in singles, coincidence, anticoincidence, and Ge(Li)-Ge(Li) two-dimensional ( $2048 \times 2048$  channel) coincidence experiments. Nineteen  $\gamma$  transitions have been assigned to the decay of  $Pb^{200}$ , and all have been placed in a consistent level scheme. States in  $Tl^{200}$  populated by  $Pb^{200}$  decay lie at 0 ( $I\pi=2-$ ), 147.63 ( $0-$ ), 257.19 ( $1-$ ), 289.24 ( $2-,1-$ ), 289.92 ( $1-$ ), 450.56 ( $1-$ ), 525.54 ( $1-$ ), and 605.44 keV ( $1-$ ). Our spin and parity assignments are based on measured conversion coefficients, relative photon intensities, and  $\log ft$  values. The structures of the states are discussed in terms of the coupling of the possible single-particle states in adjacent odd- $A$  nuclei. We also place an upper limit of 1 sec on the half-life of any possible isomeric state in  $Pb^{200}$  itself.

## I. INTRODUCTION

As part of a continuing study of neutron-deficient nuclei in the Pb region, we present results on the states in the odd-odd nucleus,  $_{81}Tl^{200}_{119}$ , as populated by the electron capture ( $\epsilon$ ) of 21.5-h  $_{82}Pb^{200}_{118}$ . This is one of the more favorable regions for explaining properties of nondeformed odd-odd systems, for the single-particle states in many of the neighboring odd-mass nuclei are reasonably well characterized. We discuss our results and the properties of the  $Tl^{200}$  states in terms of the simple shell model, showing both the advantages and disadvantages of this approach.

The first published study of the decay of  $Pb^{200}$  was by Bergkvist and his coworkers<sup>1</sup> in 1955. They bombarded natural Tl with protons and investigated the conversion electrons in the energy region 10–1600 keV with a double-focusing  $\beta$  spectrometer. They measured the half-life of  $Pb^{200}$  to be  $21.5 \pm 0.4$  h and assigned 10 transitions to its decay. In 1956, Gerholm<sup>2</sup> proposed a decay scheme consisting of four excited levels at 148.0, 257.3, 289.5, and 525 keV; these were placed on the basis of electron-electron coincidence experiments. Åström, Johansson, and Berström<sup>3</sup> next measured the relative conversion-electron intensities more precisely and also measured the half-life of the 148-keV state to be 8 nsec. (The half-life of this state was later determined to be  $7.1 \pm 0.15$  nsec by Johansson, Alvåger, and Zuk.<sup>4</sup>) They characterized the 148.0-keV transition to the ground state as a “pure”  $E2$  transition, which allowed them to make an assignment of  $I\pi=0-$  for the 148-keV

state. (The  $Tl^{200}$  ground state had been assigned  $2-$  on the basis of its decay properties<sup>5</sup> to  $Hg^{200}$ , where the spin of 2 had been established previously by atomic spectra and atomic-beam methods.<sup>6</sup>)

The latest work on the decay of  $Pb^{200}$  was carried out by Wirhed and Herrlander<sup>7</sup> in 1962, who studied the conversion lines with flat-field permanent magnet  $\beta$  spectrometers having energy resolutions as good as 0.1%. They also performed some electron-electron coincidence experiments. Conversion lines corresponding to 15 transitions in  $Tl^{200}$  were found, and multipolarities were assigned for 10 of these on the basis of conversion-coefficient ratios. These workers devised a decay scheme including excited levels at 147.61, 257.15, 289.11, 289.92, 450.4, 525.6, and 605.3 keV. They also made several tentative spin and parity assignments for these levels.

Thus, although a reasonable amount of information on the decay of  $Pb^{200}$  had been obtained and assembled, many uncertainties remained. Especially since no  $\gamma$ -ray studies had been published, we felt that  $\gamma$ -ray spectroscopy using Ge(Li) detectors should allow us to clear up many of these. During the course of our studies we also searched for a possible high-spin isomeric state in  $Pb^{200}$ , but as of yet we have been unsuccessful and can place an upper limit of 1 sec on its half-life.

## II. SOURCE PREPARATION

Our  $Pb^{200}$  sources were prepared by three separate methods, the most frequently used one consisting of bombarding natural Tl foils (29.50%  $Tl^{203}$ , 70.50%  $Tl^{205}$ ) with 37-MeV protons from the Mich-

igan State University (MSU) sector-focused cyclotron to induce the  $Tl^{203}(p, 4n)Pb^{200}$  reaction. These targets were aged from 2 to 4 days before counting in order to minimize the 9.4-h  $Pb^{201}$  and 3.6-h  $Pb^{202m}$  activities. However, after 5 or 6 days, 52-h  $Pb^{203}$  from the  $Tl^{205}(p, 3n)Pb^{203}$  reaction became the dominant activity.

The second method made use of the  $Hg^{202}(\tau, 5n)Pb^{200}$  reaction, using a 50-MeV  $\tau$  ( $He^3$ ) beam from the MSU cyclotron on natural HgO targets. This method of preparation reduced the  $Pb^{203}$  contamination significantly. Again the sources were aged for 2 or 3 days to minimize contamination by the shorter-lived isotopes.

For both of the above methods the same chemical separations were performed to obtain Pb sources relatively free from Tl and Hg activities. The targets were dissolved in dilute  $HNO_3$ ;  $Pb^{++}$ ,  $Tl^{++}$ , and  $Hg^{++}$  carriers were added; and the Pb was precipitated as a sulfate.

The third method of preparation was more involved and was used only to a limited extent, primarily in our search for  $Pb^{200m}$ . It consisted of bombarding enriched  $Tl^{203}$  (70%  $Tl^{203}$ , obtained from Oak Ridge National Laboratory) with a 58-MeV  $\tau$  beam from the MSU cyclotron to induce the reaction,  $Tl^{203}(\tau, 6n)Bi^{200} \pm Pb^{200}$ . The Tl target was dissolved in concentrated HCl solution, the Tl was extracted with diethyl ether which had been saturated with HCl, and the remaining solution, containing Pb and Bi, was placed on an anion-exchange column consisting of Dowex 1 $\times$ 8 (200-mesh) resin. The  $Pb^{200}$  was then eluted from the column with 0.3M HCl as it grew in from the decay of 35-min  $Bi^{200}$ . This method produced  $Pb^{200}$  sources with less contamination than either of the two previous methods.

The principal contaminants in our sources were  $Pb^{201}$ ,  $Pb^{203}$ , and  $Tl^{200}$ , of which the last was difficult to avoid, although in most runs successive Tl-Pb chemical separations were made to minimize it. We did, however, observe some contaminant peaks that we could not identify. They were shown not to originate from  $Pb^{200}$  decay, because they had differing relative intensities throughout the many singles spectra taken at different times and with different sources.

### III. EXPERIMENTAL RESULTS

#### A. $\gamma$ -Ray Singles Spectra

Energies and intensities of the  $Pb^{200}$   $\gamma$  rays were determined using two five-sided trapezoidal Ge(Li) detectors having photopeak efficiencies at 1.332 keV of 0.42 and 2.5%. Typical resolutions were 3.0 and 2.3 keV full width at half maximum (FWHM) at the same energy. Both detector systems used

room-temperature field-effect-transistor preamplifiers, low-noise RC linear amplifiers with pole-zero compensation and near-Gaussian shaping, and 1024- to 4096-channel analyzers or analog-to-digital converters (ADC's) coupled to a PDP-9 or Sigma-7 computer.

The energies of the prominent  $\gamma$  rays were measured by counting the  $Pb^{200}$  sources simultaneously with the energy standards listed in Table I. The centroids of the photopeaks were determined with a live-display computer program<sup>8</sup> which used the upper two thirds of the photopeak after subtracting out the background. The background was determined for each peak by making a least-squares fit of selected points on both sides of the photopeak to a  $n$ th-degree (up to  $n=7$ ) polynomial. The centroids of the calibration peaks were used to define a quadratic calibration curve from which the energies of the  $Pb^{200}$  peaks were calculated. The energies of most of the weaker  $Pb^{200}$   $\gamma$  rays were then determined in a similar fashion by using the now well-determined energies of the prominent  $\gamma$  rays as secondary standards.

TABLE I.  $\gamma$  rays used as energy standards.

Nuclide	$\gamma$ -ray energy (keV)	Reference
Am <sup>241</sup>	59.543 $\pm$ 0.015	a
Co <sup>57</sup>	121.97 $\pm$ 0.05	b
	136.33 $\pm$ 0.04	b
Ce <sup>139</sup>	165.84 $\pm$ 0.03	c
Pb <sup>203</sup>	279.17 $\pm$ 0.02	b
Ta <sup>182</sup>	100.104 $\pm$ 0.002	d
	152.435 $\pm$ 0.003	d
	156.387 $\pm$ 0.003	d
	179.393 $\pm$ 0.004	d
	222.109 $\pm$ 0.005	d
	229.322 $\pm$ 0.008	d
	264.072 $\pm$ 0.009	d
Au <sup>198</sup>	411.795 $\pm$ 0.009	e
Bi <sup>207</sup>	569.63 $\pm$ 0.08	b
Cs <sup>137</sup>	661.595 $\pm$ 0.076	f

<sup>a</sup>T. Yamazaki and J. M. Hollander, Nucl. Phys. **84**, 505 (1966).

<sup>b</sup>J. B. Marion,  $\gamma$ -Ray Calibration Standards, University of Maryland Technical Report No. 653, 1957 (unpublished).

<sup>c</sup>J. S. Geiger, R. T. Graham, I. Bergström, and F. Brown, Nucl. Phys. **68**, 352 (1965).

<sup>d</sup>Average of: U. Gruber, R. Koch, B. P. Maier, and O. W. B. Schult, Z. Naturforsch. **20a**, 929 (1965); and E. J. Seppi, H. Henrikson, F. Boehm, and J. W. M. Dumond, Nucl. Instr. Methods **16**, 17 (1962).

<sup>e</sup>G. Murray, R. T. Graham, and J. S. Geiger, Nucl. Phys. **45**, 177 (1963).

<sup>f</sup>J. S. Geiger, R. T. Graham, and F. Brown, Can. J. Phys. **40**, 1258 (1962).



Figure 1 shows a  $\gamma$ -ray spectrum obtained in 7 h with the 2.5% detector. In this figure only those  $\gamma$  rays assigned to the decay of  $\text{Pb}^{200}$  are labeled. Nineteen  $\gamma$  transitions were so assigned, having the energies and intensities listed in Table II. Of these, the 155.29-, 139.39-, 348.23-, 377.92-, and 525.54-keV transitions had not been reported in the earlier studies.

The energies of the 142.28-, 147.63-, and 348.23-keV  $\gamma$  rays were determined by stripping these peaks by hand and then calculating the centroids. The 348.23-keV  $\gamma$  ray had to be stripped from an unresolved triplet that contained two contaminant peaks. Because even our best detector could not resolve the doublet consisting of the 289.24- and 289.92-keV  $\gamma$  rays well enough to allow us to strip these peaks, the energies for these transitions given in Table II were obtained from sum and difference relationships among the other transitions. The intensities were determined on the basis of the relative contributions necessary to reproduce the energy of the doublet, "289.66 keV." Evidence for the doublet nature of the 289.7-keV peak will be given in Sec. IIIB.

The uncertainties in the energies listed in Table II are based on the uncertainties in the energy standards, the heights of the peaks above backgrounds, and the reproducibilities of the calculated energies from many different spectra. The relative intensities listed are averaged from spectra obtained with both detectors. Their uncertainties are based on the reproducibilities of the intensities and the

uncertainties in our experimentally determined efficiency curves for the detectors. The photopeak efficiency curves for both detectors were determined by using sources that emit several  $\gamma$  rays whose relative intensities have been well established. The points so obtained were then fitted to an equation of the form,  $\log(\text{efficiency}) = A + B \log E + C(\log E)^2 + D(\log E)^3$ , where  $A$ ,  $B$ ,  $C$ , and  $D$  are empirical constants and  $E$  is the energy in keV.

The  $K$  x-ray intensity for  $\text{Pb}^{200}$  listed in Table II was obtained in the following manner. A  $\text{Pb}^{200}$  source was aged until the 9.4-h  $\text{Pb}^{201}$  was only a minor contaminant, thereby avoiding a correction for its x rays. This left  $\text{Pb}^{209}$  and  $\text{Tl}^{200}$  as the only major contributors to the total x-ray intensity. Since spectra of  $\text{Pb}^{209}$  and  $\text{Tl}^{200}$  could be obtained relatively free from contaminants, it was an easy matter to determine how much each of these contributed to the total x-ray intensity in the  $\text{Pb}^{200}$  spectrum. After subtracting out their contributions, the remaining  $K$  x-ray intensity belonged essentially to  $\text{Pb}^{200}$ .

#### B. Coincidence Spectra

In order to determine which  $\gamma$  rays appear in cascades and which are primarily  $\epsilon$ -fed ground-state transitions, we used the 0.42%-efficient  $\text{Ge}(\text{Li})$  detector in an anticoincidence experiment with an  $8 \times 8$ -in.  $\text{NaI}(\text{Tl})$  split annulus and a  $3 \times 3$ -in.  $\text{NaI}(\text{Tl})$  detector.<sup>9</sup> The  $\text{Pb}^{200}$  source was placed on top of the  $\text{Ge}(\text{Li})$  detector and this inserted into the other end. The single-channel analyzers associated with

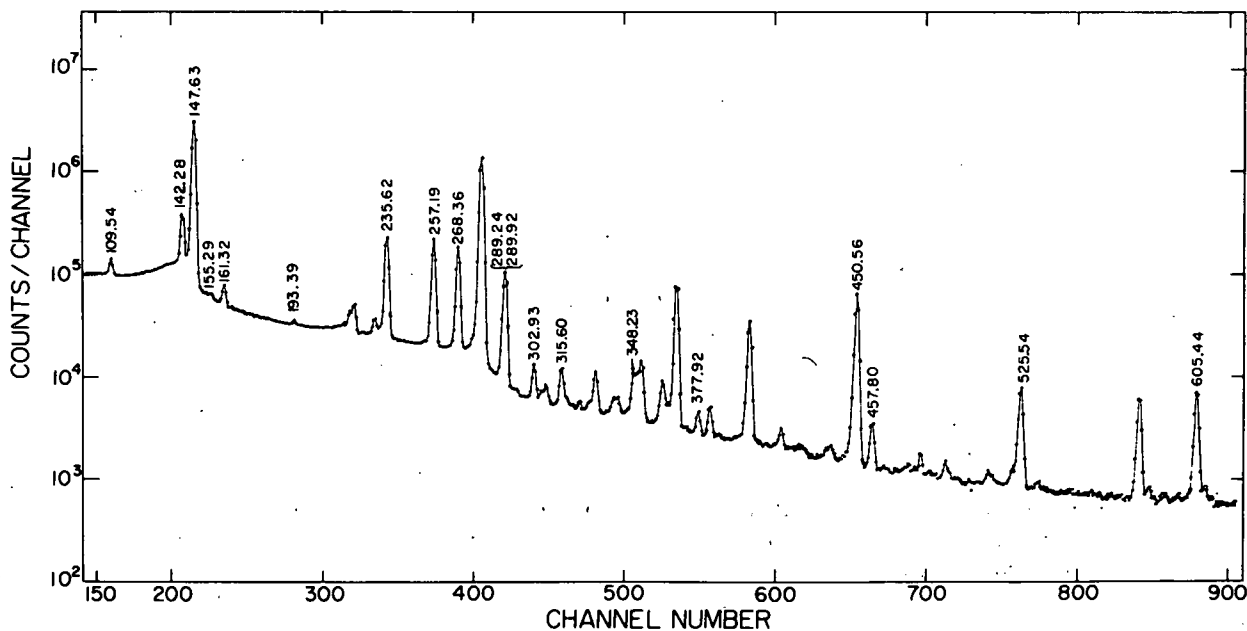


FIG. 1.  $\gamma$ -ray singles spectrum of  $\text{Pb}^{200}$  obtained in 7 h with a 2.5%-efficient  $\text{Ge}(\text{Li})$  detector. A chemical separation was performed each hour to remove  $\text{Tl}^{200}$ . Only those peaks belonging to the decay of  $\text{Pb}^{200}$  are labeled.

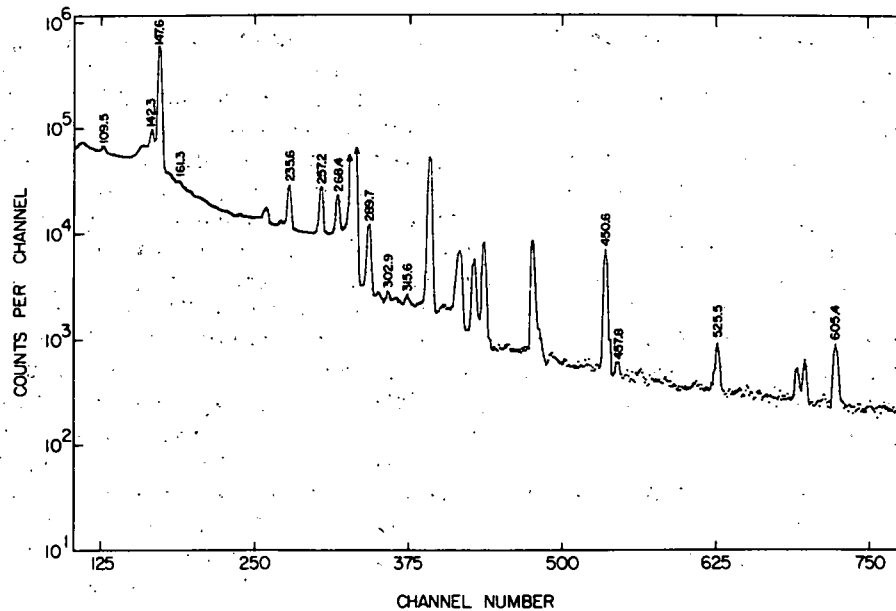


FIG. 2. Anticoincidence spectrum of  $Pb^{200}$   $\gamma$  rays. This spectrum was obtained with a 7-cm<sup>3</sup> Ge(Li) detector placed inside an 8×8-in. NaI(Tl) split annulus, with a 3×3-in. NaI(Tl) detector blocking the other end of the annulus tunnel. A chemical separation was performed every 2 h to remove  $Tl^{200}$ . Only peaks belonging to  $Pb^{200}$  decay are labeled.

each of the NaI(Tl) detectors were set to accept all  $\gamma$  rays above 90 keV to eliminate the Tl K x rays. A resolving time ( $2\tau$ ) of  $\approx 100$  nsec was used to obtain the spectrum shown in Fig. 2. The relative in-

tensities from the anticoincidence experiment are listed in Table II. The 147.63-, 450.56-, 525.54-, and 605.44-keV peaks are obviously greatly enhanced in the anticoincidence spectrum relative to

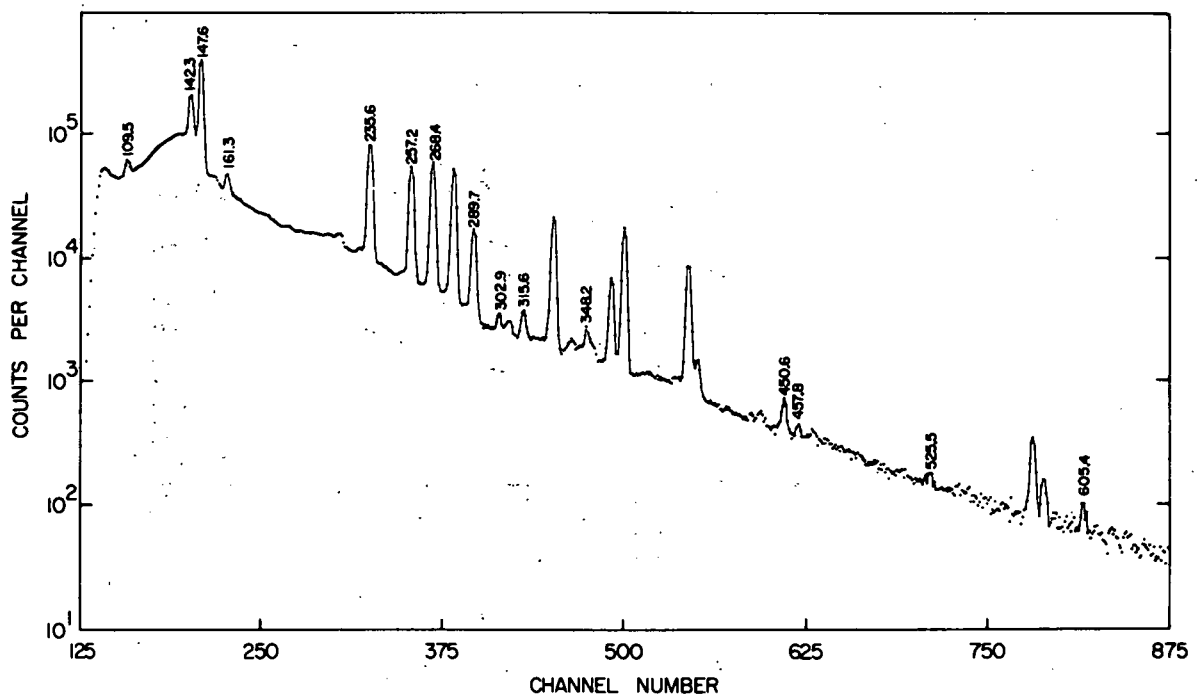


FIG. 3. Integral coincidence spectrum of  $Pb^{200}$   $\gamma$  rays. This spectrum was obtained by using the 7-cm<sup>3</sup> Ge(Li) detector in coincidence with the 8×8-in. NaI(Tl) split annulus. All  $\gamma$  rays above the K x rays were included in the gate.

air singles intensities. The 257.19- and 289.7-keV (289.24- and 289.92-keV doublet) peaks are also enhanced with respect to some peaks, such as the one at 235.62 keV.

To complement the anticoincidence experiment and determine which  $\gamma$  rays are involved in strong coincidences, we performed an integral coincidence experiment, using essentially the same set-up as for the anticoincidence experiment except the  $3 \times 3$ -in. NaI(Tl) detector was removed. The resulting spectrum is shown in Fig. 3 and the relative intensities are included in Table II. From the integral coincidence and anticoincidence experiments alone it is quite apparent that all of the  $\text{Pb}^{200}$   $\gamma$  rays are in relatively strong coincidences except for the 450.56-, 525.54-, and 605.44-keV  $\gamma$  rays, which we can safely assume are primarily  $\epsilon$ -fed ground-state transitions. We can also deduce that the 147.63-, 257.19-, and 289.24- and/or 289.92-keV  $\gamma$  rays are partially  $\epsilon$ -fed ground-state transitions that are also fed by  $\gamma$  rays from higher levels. These results are consistent with those of Wirhed and Herrlander.<sup>7</sup>

To aid in the placement of the remaining  $\gamma$  rays in a consistent decay scheme, we employed a two-dimensional "megachannel" Ge(Li)-Ge(Li) spectrometer system using the 2.5% detector and another of 2.0% efficiency. The two detectors were placed  $90^\circ$  to each other with a graded Pb absorber bisecting the  $90^\circ$  angle to prevent Compton scattering between the detectors. The  $\text{Pb}^{200}$  source was

placed equidistant from the centers of the detectors and was replaced with a freshly separated source every 3 h, as in most of the singles experiments. Figure 4 shows in flowsheet form the apparatus used in our two-dimensional experiment; it allows us to record two-dimensional spectra up to  $8192 \times 8192$  channels. The two 8192-channel ADC's are interfaced to a Sigma-7 computer, and the  $x$  and  $y$  addresses of each coincident event are stored in the two halves of a single word in a dedicated buffer in the computer. As the buffer fills, another buffer starts to receive events and the contents of the first are written on magnetic tape. The data on tape are recovered in gated "slices" later via an off-line program. This recovery program has provision for linearly interpolated background subtraction from each side of a gated region.<sup>10</sup> During a 24-h period we collected a total of about 500 000 events. The two integral coincidence spectra obtained with the 2.5 and 2.5% detectors are shown in Figs. 5(a) and 5(b), respectively. Some examples of other gated coincidence spectra having background subtraction are shown in Figs. 5(c)-5(k). Table III contains a summary of the coincidence data obtained from the two-dimensional experiments.

From these data we could confidently place all the observed transitions in a decay scheme, with the exception of the 155.29- and 193.39-keV  $\gamma$  rays, for which we had only weak-coincidence data. And even these two transitions could easily be placed in the decay scheme between well-defined existing

TABLE II. Energies and relative intensities of  $\gamma$  rays from the decay of  $\text{Pb}^{200}$ .

Measured energies (keV)	Relative intensities		
	Singles	Integral $\gamma$ - $\gamma$ coincidence	Anticoincidence
K x rays	3156 $\pm$ 350	...	...
109.54 $\pm$ 0.04	14.5 $\pm$ 2.0	370	12
142.28 $\pm$ 0.03 <sup>a</sup>	95.1 $\pm$ 5.0 <sup>a</sup>	4900	55
147.63 $\pm$ 0.03 <sup>a</sup>	1133 $\pm$ 30 <sup>a</sup>	21 500	1020
155.29 $\pm$ 0.10	1.4 $\pm$ 0.5	...	...
161.32 $\pm$ 0.04	9.1 $\pm$ 1.0	650	6.6
193.39 $\pm$ 0.10	1.0 $\pm$ 0.4	...	...
235.62 $\pm$ 0.04	129 $\pm$ 4.0	7000	81
257.19 $\pm$ 0.03	134 $\pm$ 4.0	5100	100
268.36 $\pm$ 0.03	119 $\pm$ 5.0	6000	80
289.24 $\pm$ 0.15 <sup>a</sup>	32 $\pm$ 10 <sup>a</sup>	...	...
289.92 $\pm$ 0.10 <sup>a</sup>	51.6 $\pm$ 10 <sup>a</sup>	1950	70
302.93 $\pm$ 0.05	5.0 $\pm$ 1.0	125	3.5
315.60 $\pm$ 0.08	6.7 $\pm$ 1.0	260	4.5
348.23 $\pm$ 0.08 <sup>a</sup>	4.8 $\pm$ 1.5 <sup>a</sup>	130	...
377.92 $\pm$ 0.05	0.8 $\pm$ 0.3	9.7	...
450.56 $\pm$ 0.05	$\approx$ 100	$\approx$ 100	$\approx$ 100
457.80 $\pm$ 0.07	3.5 $\pm$ 0.6	24	2.3
525.54 $\pm$ 0.06	12.6 $\pm$ 1.0	...	12
605.44 $\pm$ 0.06	16.9 $\pm$ 1.2	23	19

<sup>a</sup>Be sure to read the text for comments on how these energies and intensities were obtained.

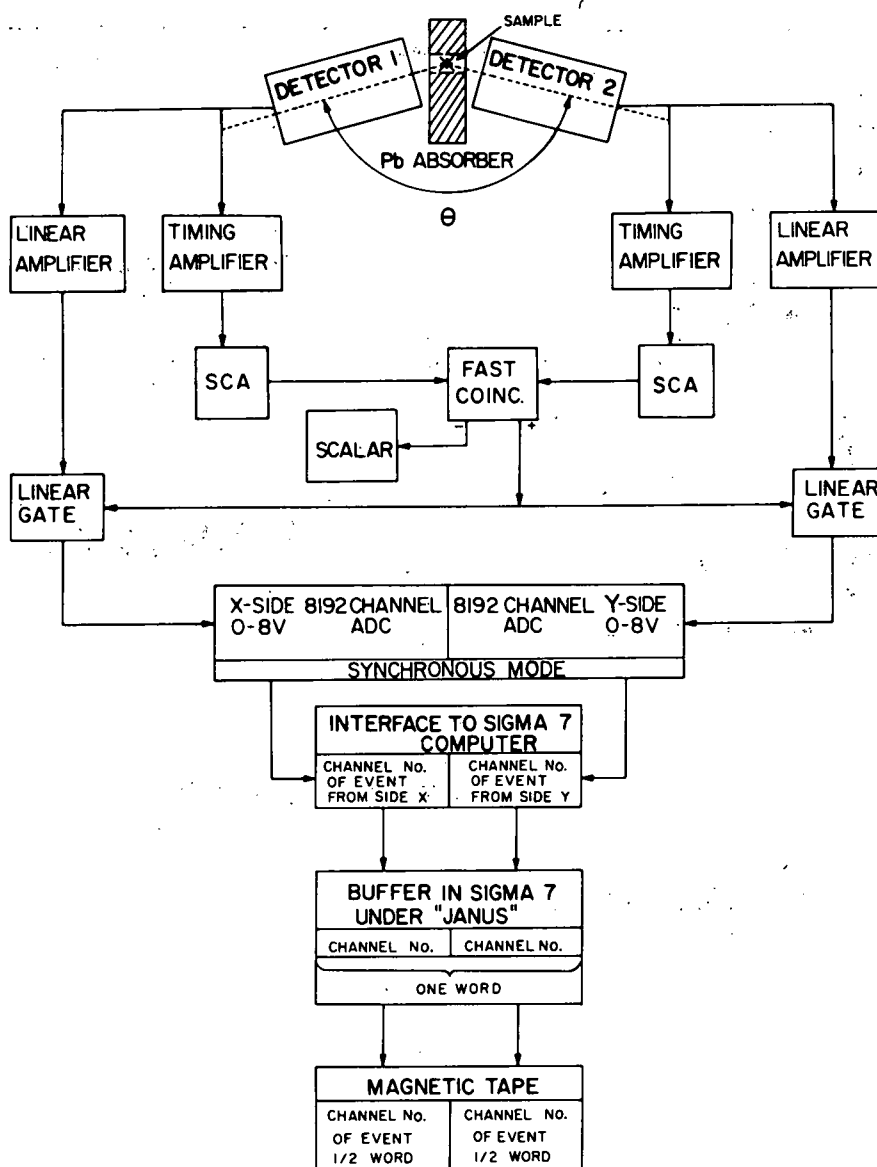


FIG. 4. Block diagram of the electronics used to collect two-dimensional "megachannel"  $\gamma\text{-}\gamma$  coincidence spectra, using the Sigma-7 computer.

levels by using sum and difference techniques. In addition to helping us place the transitions, the two-dimensional experiments aided in identifying peaks that were part of the unresolved multiplets. As mentioned before, the 348.23-keV  $\gamma$  ray is part of a triplet containing two long-lived contaminant peaks at 350.11 and 352.02 keV, as can be seen in Fig. 1. We had failed to identify this peak as belonging to  $Pb^{200}$  decay until we looked at the results of the two-dimensional experiments and observed a single peak at 348 keV that appeared to be in strong coincidence with the 257.19-keV transition [Fig. 5(f)] and fit nicely into the decay scheme.

The doublet nature of the 289.6-keV peak was confirmed by gating first on the 235.62- and 315.60-keV  $\gamma$  rays and then on the 161.32-keV  $\gamma$  ray. From energy sums we had determined that the first two appeared to populate a state at 289.92 keV, while the last one appeared to populate a state at 289.24 keV. We then carefully analyzed the resulting spectra, looking for a difference in the centroid of the 289.6-keV peak. This shift in centroid can be observed in Fig. 6. The energies obtained from this experiment were 289.22 and 289.79 keV, as compared with our adopted values of 289.24 and 289.92 keV obtained by sums and differences.

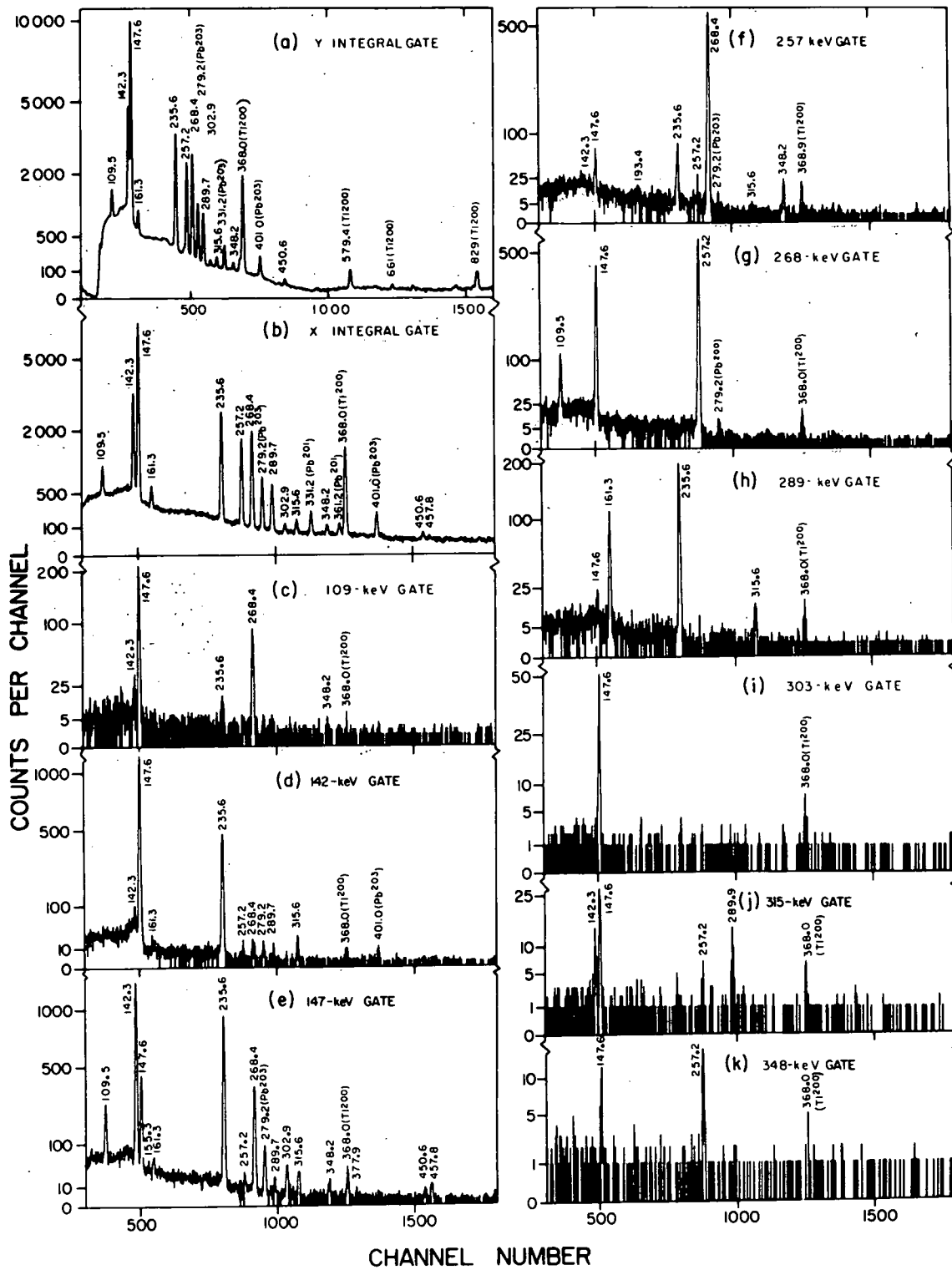


FIG. 5. Some results of a two-dimensional "megachannel"  $\gamma$ - $\gamma$  coincidence experiment using 2.5%- and 2.0%-efficient Ge(Li) detectors. During the 24-h counting period, a chemical separation was performed every 3 h to remove the Tl<sup>200</sup>. (a) and (b) show the two integral coincidence spectra as obtained with the 2.0 and 2.5% detectors, respectively. (c)-(k) show examples of gated coincidence spectra with background subtraction -gates from 2.0% spectrum, display from 2.5% spectrum.

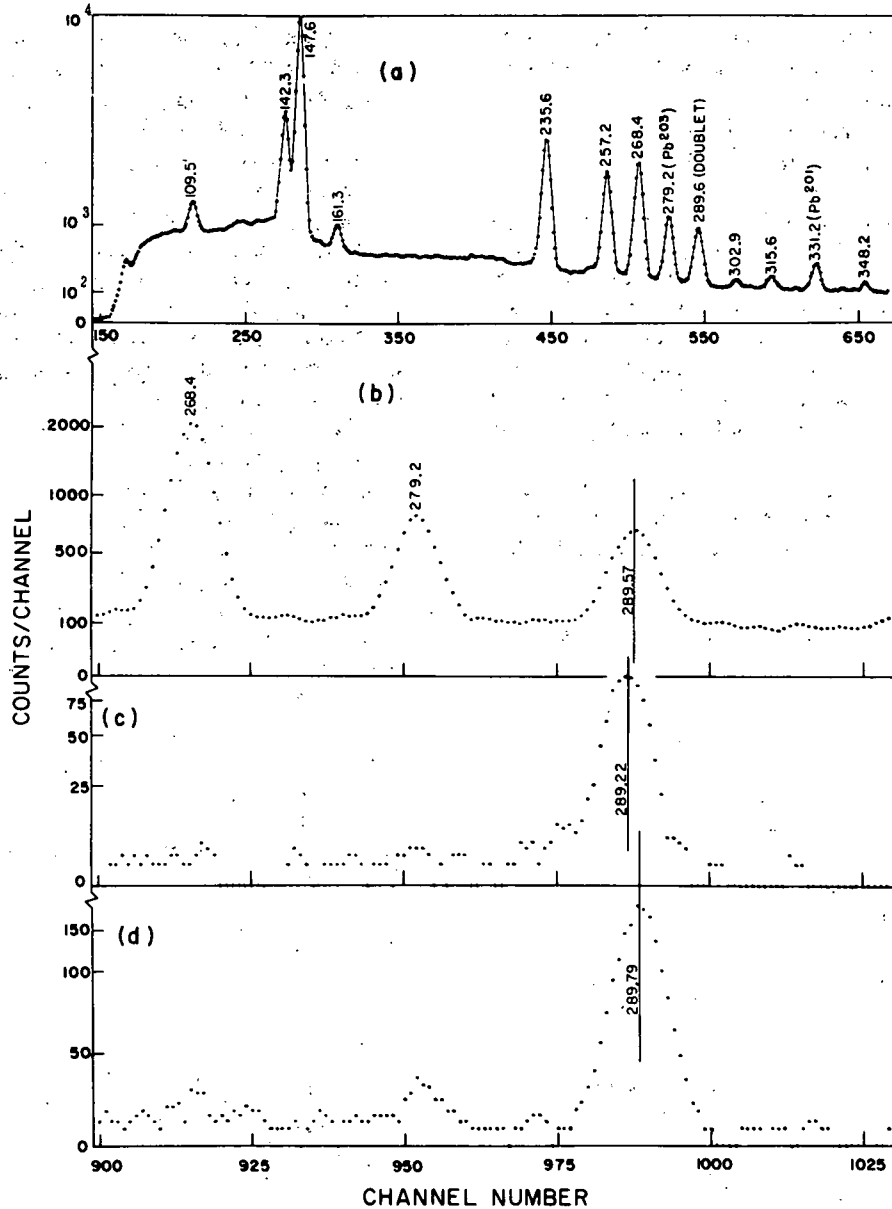


FIG. 6. Results of the two-dimensional coincidence experiment used to confirm the doublet nature of the 289.6-keV peak. (a) Y-side integral coincidence spectrum used for the gates. (b) X-side integral coincidence spectrum showing the region near the 289.6-keV peak on an expanded scale. (c) X-side spectrum in coincidence with the 161.3-keV peak (background subtracted). (d) X-side spectrum in coincidence with the 235.6-keV peak (background subtracted).

### C. Conversion Coefficients

Conversion coefficients for most of the transitions were determined using our photon intensities and the conversion-electron intensities of Wirhed and Herrlander.<sup>7</sup> In order to normalize the two sets of data, we assumed that the 147.63-keV transition was a pure  $E2$  transition<sup>8</sup> and used the theoretical conversion coefficients of Hager and Seltzer<sup>11</sup> for this transition. Table IV contains the

transition data for  $Pb^{200}$  along with the multipolarity assignments we propose for those transitions where both photon and electron intensities were available. Figure 7 shows the theoretical  $K$ -conversion coefficients of Hager and Seltzer together with the experimental points.  $K$ -shell conversion coefficients were determined for all but the 155.29-, 193.39-, 348.23-, 377.92-, and 525.54-keV transitions, and  $L$ - and  $M$ -shell conversion coefficients were determined for many of the transitions. The

multipolarity predictions all basically agree with those from the  $K/L$  and  $L$ -subshell ratios of Wirhed and Herrlander.

As can be seen from Fig. 7 and Table IV, all of the transitions are  $M1$  with the exception of the 147.63-keV  $E2$  and the 257.19-keV transition, which is  $\approx 40\%$   $M1$  and  $\approx 60\%$   $E2$ . These  $M1$  transitions all appear to have very little  $E2$  admixing, which is somewhat surprising, considering the  $E2$  enhancements that show up in some of the Pb isotopes much closer to the doubly closed shell. It would be helpful to have careful angular-correlation experiments performed on this nucleus in order to improve the limits on  $E2$  admixtures in the  $M1$  transitions.

On the basis of the experimental  $\alpha_K$ , the 457.80-keV transition would seem to be  $M2$ ; however, for reasons mentioned later we have assigned it also as  $M1$ .

#### IV. SEARCH FOR AN ISOMERIC STATE IN $Pb^{200}$

All of the odd-mass Pb isotopes known below  $N = 126$  have long-lived isomeric states based on the  $i_{13/2}$  neutron state. The three even-even isotopes,  $Pb^{206}$ ,  $Pb^{204}$ , and  $Pb^{202}$ , also have isomeric states, here 7- or 9- states resulting from coupling the  $i_{13/2}$  neutron hole to other holes. Since the  $i_{13/2}$  neutron hole decreases in energy with decreasing mass number, we hoped to be able to find a similar isomer in  $Pb^{200}$ .

TABLE III. Results of  $\gamma$ - $\gamma$  coincidence study using two-dimensional analysis.

Gated energy	Energies of $\gamma$ rays in coincidence with gate <sup>a</sup>		
	Strong	Weak	Very weak
109.5	147, 268	235	...
142.3	147, 235, 315	161	...
147.6	109, 142, 235, 268, 303, 315, 457	161, 348, 378	155
161.3	289.24	147	...
235.6	289.92, 142, 147, 257	109	...
257.2	268, 348, 235	193, 315	155
268.4	109, 147, 257	...	...
289.2	161, 235, 315	...	...
289.9	147	...	...
302.9	142, 147, 289	257	...
315.6	147, 257	...	...
348.2	...	147	...
377.9	...	...	155
450.5	147	...	...
457	...	...	...

<sup>a</sup>The actual numerical intensities and complete spectra can be found in R. E. Doebler, Ph.D. thesis, Michigan State University, 1970 (unpublished).

Figure 8 shows the basic aspects of the even-even Pb isomers. From the apparent systematic occurrence of these isomers, we expected to find the isomeric state in  $Pb^{200}$  at about 2150 keV. Bergkvist and his coworkers<sup>1</sup> made a search for this isomeric state with no positive results and set an upper limit of 1 h on the half-life of  $Pb^{200m}$ .

Our first attempts to produce  $Pb^{200m}$  involved bombarding Tl with protons to induce the reaction,  $Tl^{203}(p, 4n)Pb^{200m}$ . This type of reaction has been used to produce the other even-even isomers in good yield. Bombardments were made at proton energies of 31, 36, and 40 MeV. Four 1024-channel Ge(Li)  $\gamma$ -ray spectra containing the results of numerous bombardments were obtained at each energy, each source being counted consecutively for periods ranging from 5 sec to 15 min. For the very short counting periods we made use of a fast pneumatic target system (rabbit) to bring the target from the beam to the counting system in less than 3 sec.<sup>12</sup> These experiments failed to produce any evidence of a new isomer, and we set an upper limit of about 1 sec on the half-life of any new activity.

We next attempted to populate an isomeric state in  $Pb^{200}$  from the decay of  $Bi^{200}$ . This procedure was similar to that used successfully in our study<sup>13</sup> of 6.1-sec  $Pb^{203m}$ . 35-min  $Bi^{200}$  has an estimated  $Q_\alpha$  of 6.5 MeV and a ground-state spin of 7, so it

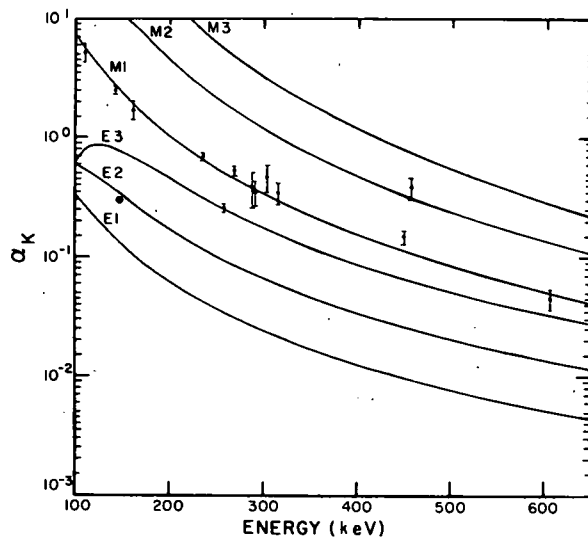


FIG. 7. Experimental and theoretical  $K$ -shell conversion coefficients for transitions following the decay of  $Pb^{200}$ . The smooth curves were drawn to fit the theoretical values of Hager and Seltzer (Ref. 12). The error bars on the experimental points represent the uncertainties in both the photon and electron intensities and also the uncertainty in the normalization factor. The normalization factor was based on the average of the  $K$ ,  $L_I(L_{II})$ , and  $L_{III}$  conversion factors for the 147.63-keV transition, assuming it to be a pure  $E2$ .

TABLE IV. Transition data for  $Pb^{200}$ .

Energy (KeV)	Photon intensity	Conversion-electron intensity (Ref. 7)	Experimental conversion coefficient	Theoretical conversion coefficient (Ref. 12)	Multipole order	
109.54	14.5	K	22	5.2±0.9	5.7	M1
		$L_I$	4.02			
		$L_{II}$	0.42	1.1±0.2	0.93	M1
142.28	95.1	K	69	2.5±0.2	2.7	M1
		$L_I(L_{II})$	14.2	0.51±0.06	0.48	M1
		$M_I$	3.4	0.12±0.02	0.095	M1
147.63	1133	K	100	0.30±0.03	0.34	E2
		$L_I(L_{II})$	137	0.41±0.04	0.43	E2
		$L_{III}$	90	0.27±0.04	0.27	E2
		$M_{II}M_{III}$	63	0.19±0.04	0.19	E2
161.32	9.06	K	4.5	1.7±0.3	1.9	M1
235.62	129	K	26.7	0.70±0.05	0.65	M1
		$L_I(L_{II})$	4.6	0.12±0.01	0.11	M1
		$M_I$	1.35	0.036±0.004	0.023	M1
257.19	134	K	10.1	0.26±0.02	0.51	M1
					0.091	E2
		$L_I(L_{II})$	2.8	0.071±0.009	0.092	M1
					0.048	E2
		$L_{III}$	0.5	0.013±0.005	0.00063	M1
			0.019	E2		
268.36	119	K	18.4	0.53±0.05	0.46	M1
		$L_I(L_{II})$	3.1	0.089±0.013	0.077	M1
		$M_I$	0.65	0.018±0.006	0.016	M1
289.24	32	K	3.7	0.39±0.13	0.37	M1
289.92	51.6	K	5.4	0.35±0.08	0.37	M1
302.93	5.03	K	0.70	0.47±0.12	0.32	M1
		$L_I(L_{II})$	0.12	0.081±0.026	0.057	M1
315.60	6.69	K	0.68	0.35±0.07	0.29	M1
		$L_I(L_{II})$	0.20	0.10±0.03	0.049	M1
450.56	100	K	4.4	0.15±0.02	0.11	M1
		$L_I(L_{II})$	0.76	0.026±0.003	0.019	M1
		M	0.16	0.0054±0.0008	0.0044	M1
457.80	3.49	K	0.40	0.39±0.08	0.11	M1
605.44	16.9	K	0.24	0.046±0.009	0.051	M1
		L	0.04	0.008±0.001	0.009	M1

should populate high-spin states in  $Pb^{200}$ . We produced  $Bi^{200}$  by bombarding separated isotope  $Tl^{203}$  with 50-MeV  $\tau$ 's to induce the reaction,  $Tl^{203}(\tau, 6n)-Bi^{200}$ . The  $Bi^{200}$  was chemically separated from the target and loaded onto an anion-exchange column similar to that described in Sec. II. The  $Pb^{200}$  activity was eluted with 0.3M HCl periodically and counted with Ge(Li) detectors. The rate of elution was varied for different experiments, the fastest being several drops every 5 sec. However, we failed to detect any evidence for an isomeric state in  $Pb^{200}$  longer than  $\approx 1$  sec in these experiments.

We are now in the process of performing delayed coincidence experiments on  $Bi^{200}$  decay in order to try to find isomeric states in the subsecond range.

#### V. DECAY SCHEME

Figure 9 shows the decay scheme we deduced

from our experiments. Transition and excited-state energies are given in keV, with the adopted energies for the levels being a weighted average based on our confidence in the respective cascade and crossover transitions. As mentioned in Sec. III A, the energies of the 289.24- and 289.92-keV levels are based on sum and difference relations. The  $Q_\alpha$  of  $\approx 939$  keV was calculated from the "experimental" masses listed in the table of Myers and Swiatecki.<sup>14</sup> We have included for the sake of completeness the levels in  $Tl^{200}$  populated by the decay<sup>15</sup> of 37-msec  $Tl^{200m}$ . It can be seen that there is little overlap in the two decay schemes, so we forego further discussion of the high-spin levels.

From the conversion coefficients in Table IV and from the theoretical conversion coefficients of Iser and Seltzer where experimental values were available, the total transition intensities, including



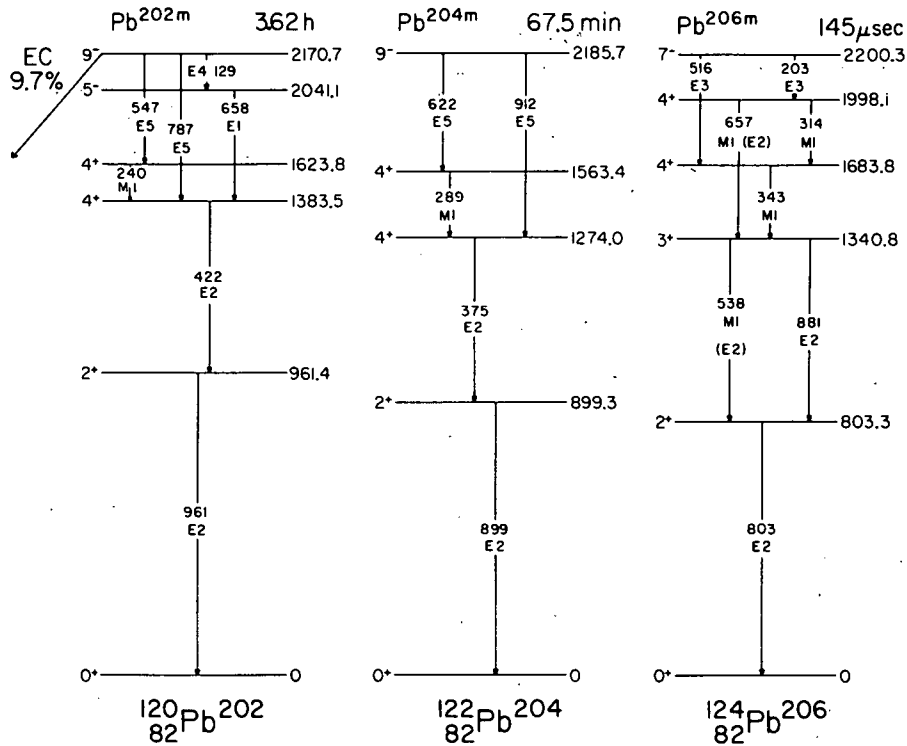


FIG. 8. Systematics and decay schemes of the known even-even Pb isomeric states.

conversion in higher shells, were calculated. These total transition intensities, in percent of the total  $Pb^{200}$  disintegrations, are given in the decay scheme. The total intensity for the 32.7-keV transition was obtained from the conversion intensity

measured by Wirhed and Herrlander.<sup>7</sup> This was corrected for the  $\gamma$ -ray intensity by using the  $L$ -shell conversion coefficients for an  $M1$  transition, which they assigned on the basis of its  $L$ -subshell ratios. From the measured  $K$  x-ray intensity,  $K$ -

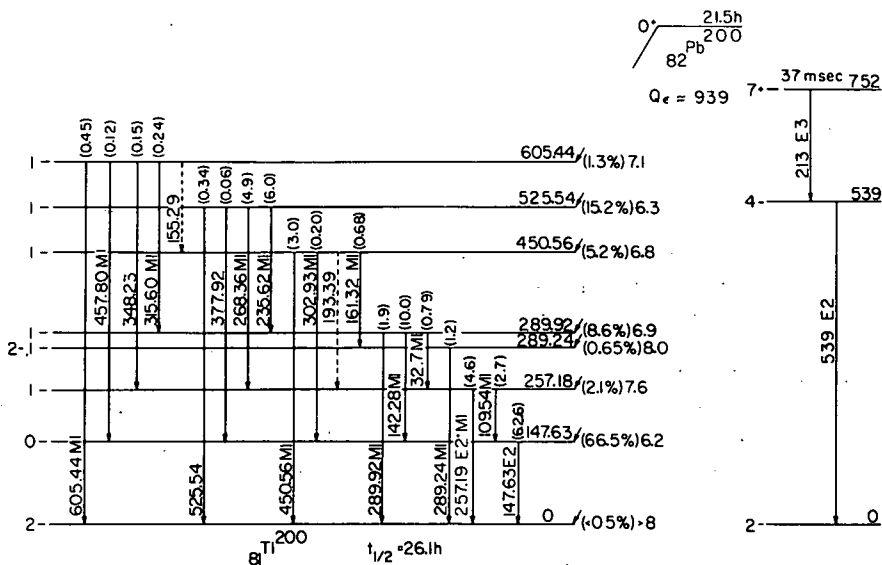


FIG. 9. Decay scheme of  $Pb^{200}$ . The intensities of all (total) transition are given in percent of the  $Pb^{200}$  disintegrations. The percent  $\epsilon$  decay to each state and the  $\log ft$  value for that state are listed to the right of the state. At the extreme right we show the states populated by the decay of  $Tl^{200m}$ ; these higher-spin states were not populated by the decay of  $Pb^{200}$ .

conversion intensities, and  $K$  fluorescent yield,<sup>16</sup> the total  $\epsilon$ -feeding intensity to the ground state was determined to be less than 0.5%. This corresponds to a  $\log ft > 8$ . The total  $\epsilon$ -feeding intensities for decays to each state were then calculated assuming that there was no ground-state feeding. These intensities are given in the decay scheme to the right of the energy levels.  $\log ft$  values based on them appear in italics at the extreme right of the levels.

## VI. SPIN AND PARITY ASSIGNMENTS

*Ground state.* Herrlander and Gerholm<sup>5</sup> assigned  $I\pi = 2-$  to the ground state of  $Tl^{200}$  on the basis of a Kurie analysis of the positron spectrum resulting from the decay of this state to the  $0+$  ground state of  $Hg^{200}$ . (The  $Tl^{200}$  ground state had a measured spin of 2 from atomic spectra and atomic-beam experiments.<sup>6</sup>) Our upper limit of 0.5% on direct  $\epsilon$  population to this state corresponds to a  $\log ft > 8$ . This is in agreement with a predicted first-forbidden unique  $\log ft \approx 9$  for such a  $0+ \rightarrow 2-$  transition.

*147.63-keV state.* The first excited state at 147.63 keV was previously assigned  $I\pi = 0-$  by Åström, Johansson, and Bergström<sup>3</sup> on the basis of the seemingly pure  $E2$  nature of the 147.63-keV  $\gamma$  transition and the strong  $\epsilon$  population of the state. Our work supports this  $0-$  assignment, as the  $\log ft$  of 6.2 lies in the range expected for a fairly rapid first-forbidden transition.

*257.18-keV state.* The  $\log ft$  for  $\epsilon$  decay to this state was found to be 7.6. This could indicate either an allowed or a first-forbidden transition, which would populate  $1+$  and  $0+$  or  $1-$  and  $0-$  states, respectively. From the definite  $M1$  assignment for the 109.5-keV  $\gamma$  ray to the 147.63-keV  $0-$  state, we can eliminate the  $1+$  and  $0+$  possibilities on the basis of parity and the  $0-$  state on the basis of observing the photons. The 257.2-keV  $\gamma$  ray to the  $2-$  ground state is a mixture of  $M1$  and  $E2$  multiplicities and also rules against the  $1+$ ,  $0+$ , and  $0-$  assignments. We can thus quite confidently assign  $I\pi = 1-$  to the 257.18-keV state.

*The four highest-lying states.* The  $\log ft$  values for these states range from 6.3 to 7.1, thus falling into the range of both allowed and first-forbidden (nonunique) transitions. This implies choices of  $1+$ ,  $0+$ ,  $1-$ , and  $0-$  for these states.

Based on the  $M1$  nature of the 289.92-keV  $\gamma$  ray, we can narrow the choice to  $1-$  for the 289.92-keV state. This is also supported by the  $M1$  nature of the 142.28- and 32.7-keV transitions. By analogous arguments the 450.56-keV state can also be assigned  $1-$ .

The  $M1$  nature of the 268.36- and 235.62-keV transitions allows the assignment for the 525.54-keV state to be narrowed to  $1-$  or  $0-$ . As we were

unable to determine the multipolarity of the 525.54 keV  $\gamma$  ray to the  $2-$  ground state, we could not distinguish between the  $1-$  and  $0-$  choices from this; however, the fact that we observed photons at all in the 377.92-keV transition from the 525.54-keV state to the 147.63-keV  $0-$  state strictly rules out the  $0-$  possibility. Again we are left with a  $1-$  assignment.

The 605.44-keV state can also be assigned  $1-$  from the  $M1$  nature of its ground-state  $\gamma$  transition, and this is consistent with the  $M1$  nature of the 315.60-keV transition. The only inconsistency in this assignment arises from the 457.80-keV  $\gamma$  ray, which goes to the  $0-$  state and has a measured  $\alpha_K$  in the range expected for an  $M2$  transition. If this  $\gamma$  ray were indeed an  $M2$ , the 605.44-keV state would be  $2+$  and the  $\epsilon$  decay would be second forbidden, obviously inconsistent with the  $\log ft$  of 7.1 as well as with the multiplicities of the other  $\gamma$  rays. Therefore, it appears that the measured  $\alpha_K$  is in error, and the multipolarity of the 457.80-keV  $\gamma$  ray is undoubtedly  $M1$  not  $M2$ .

*289.24-keV state.* The determined  $\log ft$  of 8.0 for  $\epsilon$  decay to this state is close enough to the range for a first-forbidden unique transition that we must include the possibility of a  $2-$  assignment to those of  $1+$ ,  $0+$ ,  $1-$ , and  $0-$ . From the  $M1$  multiplicity of the 289.24-keV  $\gamma$  ray to the ground state and also that of the 161.32-keV  $\gamma$  ray from the 450.56-keV  $1-$  state, we can exclude the positive parity and  $0-$  possibilities, leaving us with  $1-$  or  $2-$ . We prefer the  $1-$  assignment slightly because of the  $\log ft$  value but do not exclude the  $2-$  possibility. We shall discuss the assignment for this state further in the next section.

## VII. SHELL-MODEL ASSIGNMENTS AND DISCUSSION

$^{200}_{81}Tl_{119}$  is an odd-odd nucleus one proton removed from the closed shell at  $Z = 82$  and seven neutrons removed from the closed shell at  $N = 126$ . The simplest approach to such nuclei is to extend the odd-group model, as normally applied to odd-even and even-odd nuclei. In this model the properties of the nuclear states are assumed to be determined primarily by the odd group of particles. In extending it to odd-odd nuclei we assume that the wave functions for the states in the odd-odd nuclei are simple vector-coupled products of the wave functions of the two odd groups. If we assume that the residual  $p$ - $n$  interactions are weak compared with spin-orbit forces,<sup>17</sup> we can use  $jj$  coupling, with its resulting simplifications. With the assumption of  $jj$  coupling, a given proton and neutron configuration  $|l_p j_p l_n j_n\rangle$  can take on all integral spins,  $|j_p - j_n| \leq I \leq j_p + j_n$ , where the nature of the residual  $p$ - $n$

interaction will determine the ordering of these spins. The modified Nordheim coupling rules proposed by Brennan and Bernstein<sup>18</sup> can be useful in predicting the ordering of the spins resulting from a given configuration. Here  $j_p$  and  $j_n$  are the single-particle total angular momenta obtained from the adjacent odd-mass nuclei, while  $l_p$  and  $l_n$  (assumed to be pure) are the orbital angular momenta obtained from standard single-particle shell-model assignments. In order to keep our analysis as simple as possible, we have assumed that both odd groups are of the lowest possible seniority. Explicit calculations show that in many cases the admixtures of higher seniorities in the wave function of a given low-lying nuclear state are quite small,<sup>19</sup> so we are probably not going too far wrong here.

The question also arises concerning collective states and their effects on the odd-odd states, perhaps even core-coupled states. The positions of the first 2+ quadrupole vibrational state is known in three of the four nearest even-even nuclei: Pb<sup>202</sup>, at 961.4 keV<sup>20</sup>; Hg<sup>200</sup>, at 368.0 keV<sup>21</sup>; and Hg<sup>198</sup>, at 411.80 keV.<sup>22</sup> The energy range of states we are considering in Tl<sup>200</sup> starts to overlap with these, but the effects of blocking in this odd-odd system should make the nucleus a little more rigid, if anything, with respect to vibrations. This appears to be borne out by the lack of significant E2 admixtures in most of the M1 transitions, so in our discussion we do not consider collective effects ex-

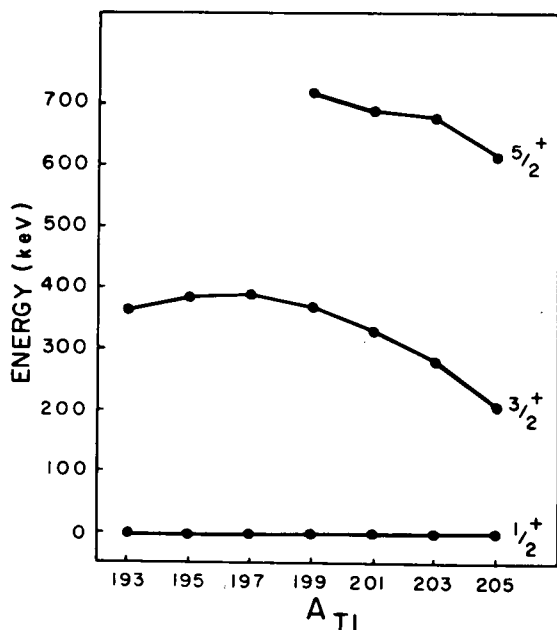


FIG. 10. Systematics of the low-lying  $\frac{1}{2}^+$ ,  $\frac{3}{2}^+$ , and  $\frac{5}{2}^+$  states in odd-mass Tl isotopes. These should be relatively pure  $s_{1/2}$ ,  $d_{3/2}$ , and  $d_{5/2}$  shell-model states.

licitly. It must be remembered, however, that we are discussing only a few low-spin states in a nucleus that must have a high level density even at low energies, so to obtain a more complete picture the effects of collective modes and configuration interactions will have to be included. As mentioned in Sec. III C, a more sensitive measurement of E2 admixtures, such as angular correlations, would be most welcome here.

In attempting to assign the shell-model configurations in this odd-odd nucleus, we assume that the low-lying states should result from combinations of the lowest configurations in the adjacent odd-proton and odd-neutron nuclei. The proton configurations contributing to the low-lying states were assumed to be the ground and first two excited states in the adjacent odd-mass Tl isotopes. The resulting spins of  $\frac{1}{2}^+$ ,  $\frac{3}{2}^+$ , and  $\frac{5}{2}^+$  are consistent with the shell-model assignments,  $s_{1/2}$ ,  $d_{3/2}$ , and  $d_{5/2}$ . The spacing of these states in the odd-mass Tl isotopes is shown in Fig. 10. The last two protons of the  $Z=82$  closed shell should fill the  $s_{1/2}$  orbit, so it is not surprising that the ground state for the odd-mass Tl isotopes is consistently  $\frac{1}{2}^+$ . The first two excited states in these isotopes then consist of the promotion of a proton from the filled  $d_{3/2}$  or  $d_{5/2}$  orbits to the  $s_{1/2}$  hole.

For neutron numbers just below the  $N=126$  closed shell, the odd neutron can populate the  $p_{1/2}$ ,  $i_{13/2}$ ,  $p_{3/2}$ , or  $f_{5/2}$  orbits in the ground or lowest excited states. Because of the large pairing energy of the  $i_{13/2}$  orbit, it should be filled in preferential-ly by pairs and not by odd particles, which may ac-

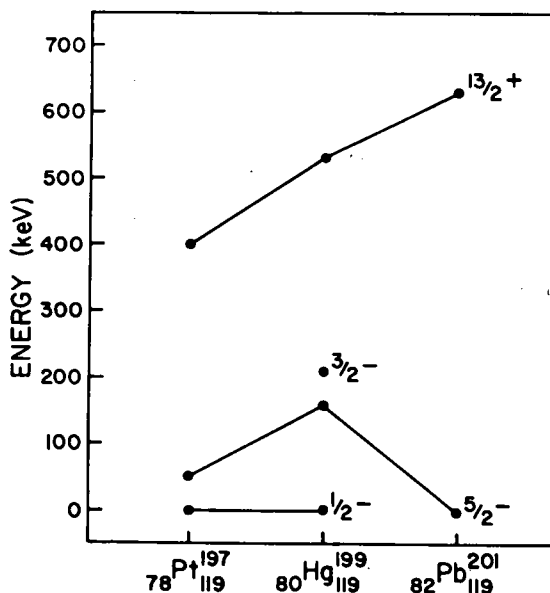


FIG. 11. Systematics of low-lying states in odd-mass isotones having 119 neutrons. These correspond to relatively pure  $p_{1/2}$ ,  $p_{3/2}$ ,  $f_{5/2}$ , and  $i_{13/2}$  shell-model states.

count for the fact that no  $i_{13/2}$  ground states have been observed. In order to obtain an idea of the ordering of the low-lying neutron configurations contributing to the states in Tl<sup>200</sup>, we would like to examine the ground and lowest excited states in the odd-mass isotones with 119 neutrons. Of particular interest are the states in Pb<sup>201</sup> and Hg<sup>199</sup>. As can be seen from Fig. 11, only the ground state is known in Pb<sup>201</sup> (excluding the  $i_{13/2}$  excited isomeric state). The  $I\pi = \frac{5}{2}^-$  suggests an  $f_{5/2}$  assignment as its primary component. We should be able to get some idea of the ordering of the excited states in Pb<sup>201</sup>, however, by looking at some of the systematics of the better-known odd-mass Pb isotopes, as shown in Fig. 12. From these systematics, it would appear that the neutron states (holes) of interest in order of increasing energy are  $f_{5/2}$ ,  $p_{3/2}$ , and  $p_{1/2}$ . The quasiparticle calculations of Kisslinger and Sorenson<sup>23</sup> for Pb<sup>201</sup> agree with this ordering. However, as is apparent from Fig. 12, the spacing between the  $f_{5/2}$  and  $p_{3/2}$  state is probably small in Pb<sup>201</sup>, as the two states have crossed between here and Pb<sup>197</sup>, where the ground state is  $p_{3/2}$ . It is not altogether certain whether the ground state of Pb<sup>199</sup> is  $f_{5/2}$  or  $p_{3/2}$ . Again referring to Fig. 11, we see that for Hg<sup>199</sup> and Pt<sup>197</sup> the ground state and first excited states are in the order  $\frac{1}{2}^-$  ( $p_{1/2}$ ) and  $\frac{5}{2}^-$  ( $f_{5/2}$ ), with the second excited state in Hg<sup>199</sup>

being  $\frac{3}{2}^-$  ( $p_{3/2}$ ). These isotones therefore suggest an ordering of  $p_{1/2}$ ,  $f_{5/2}$ , and  $p_{3/2}$ . It is obvious from this analysis that we cannot unambiguously assign an order to the single-neutron configurations contributing to the states in Tl<sup>200</sup>. This will make the assignment of configurations more difficult.

Based on the proton states and the neutron states available, we can immediately make the prediction that all the low-lying, low-spin states in Tl<sup>200</sup> should have negative parity. This is borne out without exception in the experimental states determined in our studies. (We do not include the  $i_{13/2}$  state in the list of available states for the additional reason that it would lead only to higher-spin states, which are not populated in Pb<sup>200</sup>  $\epsilon$  decay.)

Table V contains a summary of all the possible spins resulting from  $p$ - $n$  configurations using the  $s_{1/2}$ ,  $d_{3/2}$ , and  $d_{5/2}$  proton states and the  $p_{5/2}$ ,  $p_{3/2}$ , and  $f_{5/2}$  neutron states. We shall concern ourselves principally with the configurations giving rise to 0-, 1-, and 2- states, as these were the only states we observed populated in the  $\epsilon$  decay of Pb<sup>200</sup>.

It has been suggested by Bergström and Anderson<sup>24</sup> that the 2- ground state of Tl<sup>200</sup> has the configuration,  $[(\pi s_{1/2})(\nu f_{5/2})]_{2-}$ . This could be consistent with our analysis above. The "strong" coupling rule of Nordheim<sup>25</sup> predicts that the 2- state will lie lower than the 3- state for this configuration. However, de-Shalit and Walecka<sup>17</sup> have suggested a configuration of  $[(\pi s_{1/2})(\nu p_{3/2})]_{2-}$  for this ground state. Because of the uncertainty in ordering of the neutron states in this region, this also could be consistent with our above analysis. The 2- state is also predicted to lie lower than a 1- state from this configuration, according to Nordheim's "weak" rule and the modified rules of Brennan and Bernstein.<sup>18</sup> de-Shalit and Walecka proposed their assignment on the basis of the systematics of the states populated by the decays of the isomeric states in the odd-odd Tl isotopes. As

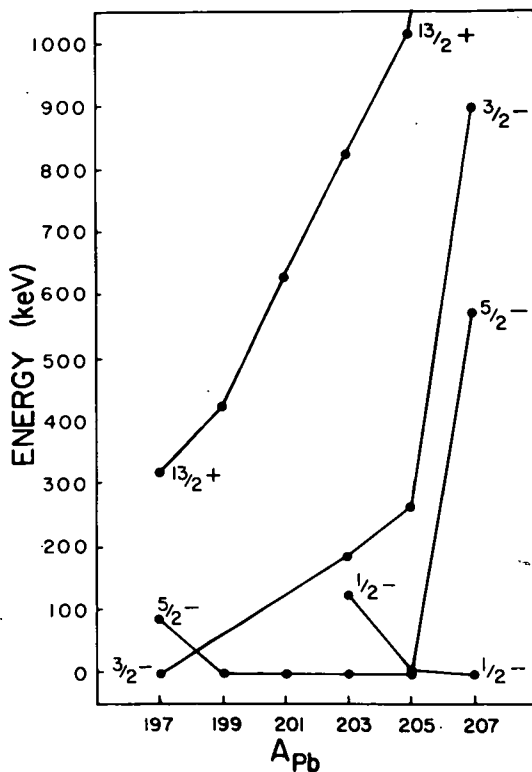


FIG. 12. Systematics of the  $f_{5/2}$ ,  $p_{1/2}$ ,  $p_{3/2}$ , and  $i_{13/2}$  states in the odd-mass neutron-deficient Pb isotopes.

TABLE V. Possible configurations for producing some low-lying odd-odd states in Tl<sup>200</sup>.

$I\pi$	$(\pi, \nu)$ configurations
0-	$(s_{1/2}p_{1/2}) (d_{3/2}p_{3/2}) (d_{5/2}f_{5/2})$
1-	$(s_{1/2}p_{1/2}) (s_{1/2}p_{3/2}) (d_{3/2}f_{5/2}) (d_{3/2}p_{1/2}) (d_{3/2}p_{3/2})$ $(d_{5/2}p_{3/2}) (d_{5/2}f_{5/2})$
2-	$(s_{1/2}f_{5/2}) (s_{1/2}p_{3/2}) (d_{3/2}p_{1/2}) (d_{3/2}f_{5/2}) (d_{3/2}p_{3/2})$ $(d_{5/2}p_{1/2}) (d_{5/2}p_{3/2}) (d_{5/2}f_{5/2})$
3-	$(s_{1/2}f_{5/2}) (d_{3/2}f_{5/2}) (d_{3/2}p_{3/2}) (d_{3/2}f_{5/2}) (d_{5/2}p_{3/2})$ $(d_{5/2}p_{1/2})$
4-	$(d_{3/2}f_{5/2}) (d_{5/2}p_{3/2})$
5-	$(d_{5/2}f_{5/2})$

shown in Fig. 13, the neutron-deficient odd-odd Tl nuclei have 2- ground and 0- first excited states. However, in  $Tl^{198}$  and  $Tl^{196}$  we see two closely spaced excited states with  $I\pi=2-$  and  $3-$  separated by 23 and 34 keV, respectively. The  $M1$  transitions between these states compete very favorably with the much more energetic  $M1$  transition to the ground state, which prompted de-Shalit and Walecka to assume that these states have the configurations,  $[(\pi s_{1/2})(\nu f_{5/2})]_{2-}$  and  $[(\pi s_{1/2})(\nu f_{5/2})]_{3-}$ . The 2- ground state of  $Tl^{200}$  must then be primarily one of the other possibilities listed in Table V, of which  $[(\pi s_{1/2})(\nu p_{3/2})]_{2-}$  seems to be the best choice. Since the  $M1$  transition  $[(\pi s_{1/2})(\nu f_{5/2})]_{3-} \rightarrow [(\pi s_{1/2})(\nu p_{3/2})]_{2-}$  is  $l$  forbidden, whereas the  $M1$  transition  $[(\pi s_{1/2})(\nu f_{5/2})]_{3-} \rightarrow [(\pi s_{1/2})(\nu f_{5/2})]_{2-}$  is not, this could explain the  $\gamma$  branching ratio for the cases in  $Tl^{198}$  and  $Tl^{196}$ . Also, the small splitting between the two states of the latter configuration is consistent with theoretical predictions, and many other examples of such doublets are presented in Ref. 17. However, the arguments are not conclusive for  $Tl^{200}$ , and, based on our present knowledge, we have to accept either possibility for the ground state.

Another potential source of information that might allow one to choose between the two above

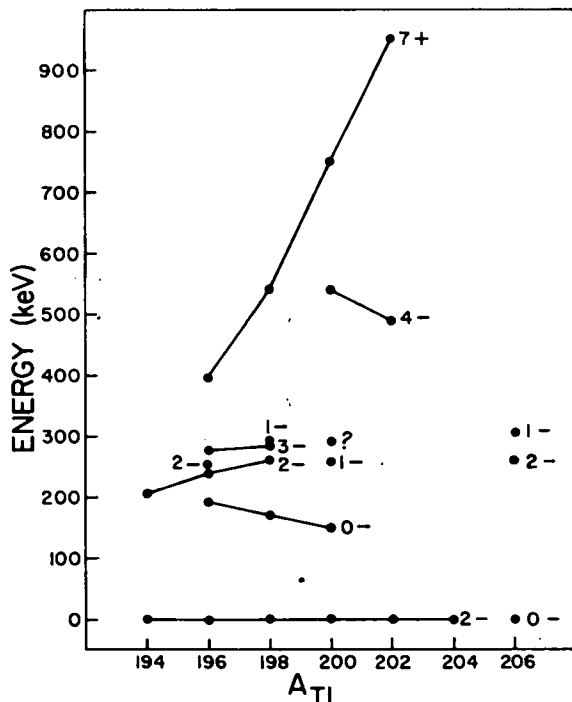


FIG. 13. Systematics of some selected states in odd-odd Tl isotopes. The states connected by lines are assumed to be primarily the same configurations. The 289.24-keV state in  $Tl^{200}$  is marked by a ?, for we have been unable to decide between 1- and 2- for its assignment.

configurations for the primary component of the  $Tl^{200}$  ground state is the magnetic moment of this state. This has been deduced from atomic spectral studies, where it was found that  $|\mu| < 0.15\mu_N$ . Now, relatively little has been done with respect to characterizing the magnetic moments of odd-odd states in terms of simple shell-model states, e.g., determining the damping effects of the odd proton and odd neutron on each other, so one can use such predictions only very qualitatively. Nevertheless, according to our somewhat simplistic estimates, one might expect the effective magnetic moment for each of the two above configurations to be almost the same, lying somewhere in the vicinity of  $+0.8\mu_N$ , an odd-odd "Schmidt limit." One cannot use this as a basis for choosing between the configurations either.

From Table V we find that there are three possibilities for the 0- first excited state. Because the  $s_{1/2}$  proton state lies much lower than the  $d_{3/2}$  and  $d_{5/2}$  states in this region, and the  $f_{5/2}$ ,  $p_{3/2}$ , and  $p_{3/2}$  neutron states are much closer together, we expect the lowest configurations to include the  $s_{1/2}$  proton state. We therefore conclude that the  $[(\pi s_{1/2})(\nu p_{1/2})]_{0-}$  configuration is the best choice for the first excited state. This follows the "strong" Nordheim rule, which suggests that the 1- state from this configuration will lie higher in energy than the 0- state. Since all the states above the first excited state that are populated by  $Pb^{200}$  decay have 1- assignments, with the possible exception of the 289.24-keV state, we cannot unambiguously assign the  $[(\pi s_{1/2})(\nu p_{1/2})]_{1-}$  configuration to any specific one of them. However, one would expect to observe a strong  $M1$  transition between the  $[(\pi s_{1/2})(\nu p_{1/2})]_{1-}$  and  $[(\pi s_{1/2})(\nu p_{1/2})]_{0-}$  states, which eliminates the 289.24-, 450.56-, 525.55-, and 605.44-keV states as contenders. This leaves the 257.18- and 289.92-keV states as possibilities for the major portion of the  $[(\pi s_{1/2})(\nu p_{1/2})]_{1-}$  strength. This is consistent with the prediction of a small splitting between the states of this configuration.<sup>18,26</sup> Based on the fact that the 142.28-keV  $M1$  transition between the 289.92- and 147.63-keV states competes very favorably with the more energetic ground-state transition, we tend to favor the  $[(\pi s_{1/2})(\nu p_{1/2})]_{1-}$  configuration for the 289.92-keV state. However, if the ground-state configuration were  $[(\pi s_{1/2})(\nu p_{3/2})]_{2-}$  and the 289.92-keV-state configuration were  $[(\pi s_{1/2})(\nu p_{3/2})]_{1-}$ , one could easily explain the weakness of the ground-state transition by its being  $l$  forbidden.

From Table V we see that there are seven possible configurations that can result in low-lying 1- states populated by the decay of  $Pb^{200}$ . Experimentally we have found six, possibly seven, such states. Considering the small energy differences

between these states, one would expect configuration mixing to play a very important role in this nucleus. Thus, one should take the foregoing arguments as an outline of the procedures to be followed in such assignments. And, of course, further attempts here to assign specific configurations to specific states could well be even more foolhardy, for the mixing could easily obviate simple selection rules for, say, the  $\gamma$  transitions.

As mentioned in Sec. VI, we have not been able to assign an unambiguous spin to the 289.24-keV state on the basis of the experimental data. There is some support for the  $2^-$  assignment in the systematics of the states in the other odd-odd Tl isotopes. In the  $\epsilon$  decays of  $Pb^{198}$  and  $Pb^{196}$ ,  $2^-$  states are reported to be populated at 259.5 and 240.3 keV, respectively.<sup>27,28</sup> A  $2^-$  state has also been tentatively observed at 205 keV in  $Tl^{194}$ .<sup>29</sup> Thus, we might expect to find a  $2^-$  state at about 280 keV in  $Tl^{200}$ . One possible configuration for this state could be  $[(\pi s_{1/2})(\nu f_{5/2})]_{2^-}$ , as suggested by de-Shalit and Walecka for the  $2^-$  states in  $Tl^{198}$  and  $Tl^{196}$ . On the other hand, if the ground state were  $[(\pi s_{1/2})(\nu f_{5/2})]_{2^-}$  and not  $[(\pi s_{1/2})(\nu p_{3/2})]_{2^-}$ , the 289.24-keV state might contain an appreciable fraction of the latter configuration. All other things being equal, one might expect the ground state of  $Pb^{200}$  to populate the latter configuration more strongly than the former, as the  $s_{1/2}$  protons are expected to lie closest to the Fermi surface in Pb. However, this is a very weak argument, and, in

fact, if one reasons in terms of the  $\epsilon$ -decay probabilities, then a  $1^-$  assignment is slightly favored for the 289.24-keV state, as was discussed in Sec. VI.

Although we have included the states populated by  $(7+?) Tl^{200m}$  decay<sup>15</sup> in Fig. 9 for the sake of completeness, we have purposely refrained from including them in our discussion. We expect very little overlap of these states with the ones we have just discussed, and to include them would have resulted in undue complexity. However, we would like to emphasize that odd-odd nuclei do provide one of the most convenient natural probes for studying the  $p$ - $n$  residual interaction, so a complete study of states in odd-odd  $Tl^{200}$  and the other odd-odd Tl isotopes would be most welcome. Now that high-resolution reaction-product spectrometers are coupled with moderate-energy, highest-resolution sector-focused cyclotrons, reactions such as  $(p, d)$  on  $Tl^{203}$  and  $Tl^{205}$  and  $(\tau, t)$  on the even-even Hg isotopes could well be a very profitable study.

#### ACKNOWLEDGMENTS

We are indebted to H. Hilbert for his help in the operation of the Michigan State University cyclotron. We also wish to thank Dr. D. B. Beery for help in setting up some of the initial coincidence experiments and Mrs. Carolee Merritt for aid in using the Sigma-7 computer.

\*Work supported in part by the U. S. Atomic Energy Commission.

†Work supported in part by the U. S. National Science Foundation.

<sup>1</sup>K. E. Bergkvist, I. Bergström, C. J. Herrlander, S. Hultberg, H. Slätis, E. Sokolowski, A. H. Wapstra, and T. Wiedling, *Phil. Mag.* **46**, 65 (1955).

<sup>2</sup>T. R. Gerholm, *Arkiv Fysik* **11**, 55 (1956).

<sup>3</sup>B. Åström, B. Johansson, and I. Bergström, *Arkiv Fysik* **12**, 205 (1957).

<sup>4</sup>B. Johansson, T. Alväger, and W. Zuk, *Arkiv Fysik* **14**, 439 (1959).

<sup>5</sup>C. J. Herrlander and T. R. Gerholm, *Nucl. Phys.* **3**, 161 (1957).

<sup>6</sup>R. J. Hull and H. H. Stroke, *Phys. Rev.* **122**, 1574 (1961).

<sup>7</sup>B. Wirhed and C. J. Herrlander, *Arkiv Fysik* **23**, 355 (1962).

<sup>8</sup>MOIRAE, a program developed for the Michigan State University Cyclotron Laboratory Sigma-7 computer by R. Au and G. Berzins.

<sup>9</sup>R. L. Auble, D. B. Beery, G. Berzins, L. M. Beyer, R. C. Etherton, W. H. Kelly, and Wm. C. McHarris, *Nucl. Instr. Methods* **51**, 61 (1967).

<sup>10</sup>EVENT RECOVERY, a FORTRAN program written

by D. Bayer and D. B. Beery, described in D. B. Beery, Ph. D. thesis, Michigan State University, 1970 (unpublished).

<sup>11</sup>R. S. Hager and E. C. Seltzer, *Nucl. Data A4*, 1 (1968).

<sup>12</sup>K. Kosanke, in Michigan State University Nuclear Chemistry Annual Report for 1969, No. COO-1779-13 (unpublished).

<sup>13</sup>R. E. Doebler, Wm. C. McHarris, and C. R. Gruhn, *Nucl. Phys.* **A120**, 489 (1968).

<sup>14</sup>W. D. Myers and W. J. Swiatecki, University of California Lawrence Radiation Laboratory Report No. UCRL-11980, 1965 (unpublished).

<sup>15</sup>R. M. Diamond and F. S. Stephens, *Nucl. Phys.* **45**, 632 (1963).

<sup>16</sup>R. W. Fink, R. C. Jopson, H. Mark, and C. D. Swift, *Rev. Mod. Phys.* **38**, 513 (1966).

<sup>17</sup>A. de-Shalit and J. D. Walecka, *Nucl. Phys.* **22**, 184 (1961).

<sup>18</sup>M. H. Brennan and A. M. Bernstein, *Phys. Rev.* **120**, 927 (1960).

<sup>19</sup>B. Oquidam and B. Jancovici, *Nuovo Cimento* **11**, 579 (1959).

<sup>20</sup>A. McDonnell, R. Stockendal, C. J. Herrlander, and I. Bergström, *Nucl. Phys.* **3**, 513 (1957).

<sup>21</sup>M. Sakai, H. Ikegami, T. Yamazaki, and H. Saito,

Nucl. Phys. 65, 177 (1965).

<sup>22</sup>G. Murray, R. L. Graham, and J. S. Geiger, Nucl. Phys. 45, 177 (1963).

<sup>23</sup>L. S. Kisslinger and R. A. Sorensen, Kgl. Danske Videnskab. Selskab, Mat.-Fys. Medd. 32, No. 9 (1960).

<sup>24</sup>I. Bergström and G. Andersson, Arkiv Fysik 12, 415 (1957).

<sup>25</sup>L. W. Nordheim, Phys. Rev. 78, 294 (1950); Rev. Mod. Phys. 23, 322 (1951).

<sup>26</sup>N. Zeldes, Nucl. Phys. 7, 27 (1958).

<sup>27</sup>B. Jung and G. Andersson, Nucl. Phys. 15, 108 (1960).

<sup>28</sup>J. Svedberg and B. Jung, Arkiv Fysik 19, 441 (1961).

<sup>29</sup>B. Jung, Nucl. Phys. 10, 440 (1959).

V. Ph.D. Thesis Titles (July 1970-June 1971)

- (1) Raymond Doebler      Gamma-ray Spectroscopic Studies of States in Neutron-Deficient Pb and Tl Isotopes
- (2) Thomas Kuo            Energy Dependence of Proton Inelastic Scattering from  $^{40}\text{Ca}$
- (3) G.F. Trentelman      An Experimental Test of the Isobaric Multiplet Mass Equation
- (4) William Pickles      Elastic Scattering and Reactions in the Bombardment of  $^{14}\text{N}$  by 20 MeV Deuterons